



ScuDo
Scuola di Dottorato ~ Doctoral School
WHAT YOU ARE, TAKES YOU FAR



Doctoral Dissertation
Doctoral Program in Energetics (31st Cycle)

Reduction of fuel consumption and pollutant emissions from vehicles

Implementation of low-temperature diesel combustion
and development of an advanced central tire inflation
system

Roberto Vitolo

* * * * *

Supervisor

Prof. S. d'Ambrosio

Doctoral Examination Committee:

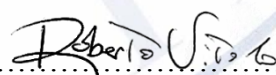
Dr. Z. Gao , Referee, Oak Ridge National Laboratory
Prof. Z. Samaras, Referee, Aristotle University of Thessaloniki
Dr. C. Beatrice, Istituto Motori - Consiglio Nazionale delle Ricerche
Prof. A. Ferrari, Politecnico di Torino
Dr. G. Fontaras, European Commission - Joint Research Centre
Dr. A. Vassallo, General Motors Global Propulsion Systems

Politecnico di Torino
September 23rd, 2019



This thesis is licensed under a Creative Commons License, Attribution - Noncommercial - NoDerivative Works 4.0 International: see www.creativecommons.org. The text may be reproduced for non-commercial purposes, provided that credit is given to the original author.

I hereby declare that, the contents and organisation of this dissertation constitute my own original work and does not compromise in any way the rights of third parties, including those relating to the security of personal data.



.....
Roberto Vitolo
Turin, August 19th, 2019

Summary

The high level of greenhouse gases as well as the presence of anthropogenic toxic gases in the atmosphere are responsible for climate change and diseases, and the transportation sector is recognized as one of the root causes of these issues. For this reason, the need for reduction of pollutant emissions and fuel consumption from vehicles has led to technological innovation in the automotive field, at least in the last sixty years. These topics can be addressed both through engine (or power unit) technologies and vehicle technologies, the first related to the process that leads to the production of mechanical power on-board, the latter referring to the vehicle power demand, i.e. how the mechanical power available from the engine is managed to overcome resistances. This dissertation presents a research work developed to address both these topics, and to assess the combined effect of two technologies, one related to combustion engines and the other related to the reduction of vehicle power demand. Specifically, the PhD activity here presented has developed two main projects in parallel: on the engine side, the aim of the research activity was the implementation of a non-conventional diesel combustion strategy, namely a premixed-charge compression ignition (PCCI) combustion mode, as a way to abate the production of soot and nitrogen oxides in the cylinder; on the vehicle side, the project work has been devoted to the development of an automatic system for smart management of tire pressure on board and to assess the effects of tire pressure on vehicle energy demand and fuel consumption. Finally, the combined effect of the two technologies has been assessed through simulations on a light-duty commercial vehicle.

More in detail, the potentialities of the abovementioned PCCI combustion has been experimentally assessed first on a production diesel engine for light-duty commercial vehicles, and later applied to a prototype version of the same engine, developed on-purpose to extend the range of application of the PCCI combustion mode. By means of a single early injection strategy and a high EGR rate, and keeping the overall air-fuel mixture in a narrow lean range close to the stoichiometric condition (i.e., $\lambda = 1.1-1.35$), it was possible to implement on the prototype engine the PCCI combustion mode up to 8.5 bar bmep and 3000 rpm. In this area, that is almost half of the speed-load map of the engine, it was possible to reduce by more than 85% the engine-out emissions of nitrogen oxides (NO_x) and by more than 90% the soot engine-out emissions. Nevertheless, this also produced an increase of fuel consumption by 3-11% and a high increase in the emissions of unburned hydrocarbons (HC) and carbon monoxide (CO), which have been

partially treated through a diesel oxidation catalyst. Major issues are highlighted at low engine load, where the catalyst does not reach the light off temperature due to the low temperature of the exhaust gases.

In order to improve the control over the combustion process, aiming at the enhancement of the application of PCCI combustion mode, combustion phasing controls have also been tested and models for the accurate control of EGR flow rate have been developed. These topics have been implemented and tested on the original production engine only, both under conventional diesel combustion and under PCCI combustion. The results of these activities, and their potential benefits on PCCI combustion, will also be discussed in this thesis.

For what concerns the reduction of vehicle power demand through the automatic management of tire pressure, the project was first developed on a passenger car, which included the design and test of a dedicated system to be installed on board, and the assessment of the potential effects of tire pressure management on driving cycles and on an annual mission. For passenger cars, the potentiality of this technology has been assessed as a reduction of 1-1.4% in fuel consumption on an annual basis, and up to 2.8% if the reference case is a common misuse condition. Then, the study has been extended and replicated on a light-duty and a heavy-duty commercial vehicle. For this purpose, a software tool was specifically developed to assess the effect of tire pressure on vehicle energy demand and fuel consumption, being this software designed to include the tire pressure as a variable parameter to be set for each simulation, and possibly also variable along a simulation. The fuel economy improvement obtainable on an annual basis through this kind of technology was estimated in 1.7-1.9% on a heavy-duty truck and of 1.7-2.1% on a light-duty commercial vehicle, if the reference case for comparison is a common misuse condition. Also for commercial vehicles, a dedicated system layout and its integration on board have been discussed and a preliminary design is reported in this dissertation.

Finally, the combined effect of the two technologies on a light-duty commercial vehicle has been simulated on some reference driving cycles and on annual missions. PCCI combustion has proved to reduce NO_x emissions by up to 20-73%, and soot by 32-78%, in highway and urban driving respectively. A significant increase in engine-out HC and CO emissions is remarked, although the tailpipe emissions with warm engine are estimated below Euro VI limits. The increase in fuel consumption due to PCCI combustion is estimated as 1.6-2.4% on an annual basis, and can be largely mitigated by the introduction of an automatic tire pressure management system. Considering also side benefits, i.e. the reduction of tire wear and urea consumption, the combined effect of the two technologies would lead to a reduction of the total cost of ownership of the vehicle, which would make these technologies of interest for the market of commercial vehicles.

Acknowledgments

First of all, I would like to express my gratitude to my tutor, Prof. Stefano d'Ambrosio, who I also have the privilege to call my friend. Stefano has been my mentor since 2011, when I moved my first steps in the engine test-bed at the Politecnico for my bachelor thesis. Thanks to him, I developed my passion in Automotive Research. Through him, I've learned the methodological approach in technical research, the need for accuracy and data quality, as well as the ability in presenting results. He has supported me in projects, and he gave strength and structure to my ideas and proposals. Definitely, I owe him all my professional growth from my bachelor thesis to now. Thank you, Stefano.

I also would like to thank the Reviewers, Prof. Samaras and Dr. Gao, for all their suggestions, which helped improving the quality of this dissertation, and the other members of the examination Committee, Dr. Beatrice, Prof. Ferrari, Dr. Fontaras, and Dr. Vassallo for taking time to go through my work.

Furthermore, I would acknowledge the co-authors of works that I have published and co-inventors of the patents that I have filed in these years, and especially all the colleagues at the Politecnico that in various ways have contributed to this work, and more generally to my professional growth: Nicolò Salamone, Elia Mameli, Edoardo De Mattei, Enrico Oliva, Alessandro Mancarella, Daniele Iemmolo. Working in team, having common goals, contributing together to each other's achievements, has been probably the best part of my PhD experience.

Moreover, thanks are due to the partner Companies, which funded and supported the projects that are the subject of this thesis. In particular, I would like to thank FPT Industrial, in the person of Gilles Hardy, and Iveco, in the persons of Alessio Sarcoli, Ivan Calaon, Vladi Nosenzo and Enrica Campitelli. I would also like to thank Centro Ricerche Fiat for the support on the Active Tire Pressure Control project, and Paolo Albano and Dario Messa from Michelin for sharing their knowledge and supporting the projects with data on tires.

Last, but not least, I would like to express my sincere gratitude to my family, and to my girlfriend Angelica, who have supported me on a daily basis along the path. They had the hard task of supporting me personally and morally, among ups and downs, being on my side to listen about my enthusiasm as well as about my doubts and outbursts, to celebrate my successes and to support the moments of daily stress, sharing my passions and my objectives. With unconditioned love. Thank you.

Contents

Introduction	1
---------------------------	----------

Chapter 1	20
------------------------	-----------

*Implementation of a non-conventional diesel combustion mode on a
3.0 liters engine for a light-duty commercial vehicle*

1.1	Experimental setup	25
1.2	Preliminary optimization of PCCI on the standard engine through a design of experiments and model-based calibration.....	30
1.3	Performance and emission comparison between the standard Euro VI diesel engine and an optimized PCCI version.....	46
1.4	Steady-state and transient operations of the standard engine with model- based and pressure-based combustion control techniques.....	58
1.5	Zero dimensional models for EGR and its unbalance estimation on the standard engine operated in conventional diesel combustion and in PCCI combustion modes	77

Chapter 2	108
------------------------	------------

*Development of an automatic system for on-board management of
tire inflation pressure*

2.1	Effects of tire pressure on rolling resistance	113
2.2	Generalities about CTIS.....	114
2.3	Potential effect of tire pressure management on fuel economy of passenger cars: simulations	116

2.4	Potential effect of tire pressure management on fuel economy of passenger cars: impact assessment of the technology on an annual mission	141
2.5	Potential effect of tire pressure management on fuel economy of commercial vehicles: simulations	153
2.6	Layout and design of the Active Tire Pressure Control (ATPC) system for Passenger Cars	183
2.7	Layout and on-board integration of the Advanced Central Tire Inflation System for commercial vehicles	215
2.8	Effect of the dynamics of the actuation system on fuel consumption ...	231
Chapter 3		241
<i>Assessment of the potential combination of PCCI combustion and ACTIS technology on a light-duty commercial vehicle</i>		
3.1	Performance comparison between the PCCI engine and the standard diesel engine on single mission profiles	247
3.2	Combining the PCCI engine with ACTIS: simulations on single mission profiles	269
3.3	Combining the PCCI engine with ACTIS: effect on the total cost of ownership on annual missions	279
Conclusions		2824
References		289
Abbreviations and Acronyms		309

List of Figures

- Figure 1** Regulated limits of NO_x and PM emissions in Europe and US: evolution of the emission regulations.
- Figure 2** Time evolution of the fuel economy regulated limits in Europe and US, expressed in CO₂ emissions per km (NEDC-equivalent).
- Figure 3** Objectives of the dissertation and fields of the current work.
- Figure 1.1** Simplified schematic of the engine installations at the test bench.
- Figure 1.2** Section view of the piston bowl and injector spray edge of the F1C Euro VI and the F1C PCCI engines.
- Figure 1.3** Schematic representation of the model based calibration methodology
- Figure 1.4** Results of preliminary tests on engine point 1800 rpm x 1 bar bmep. Brake specific soot vs. NO_x (a); CO (b) and CO₂ brake specific emissions (c), bsfc (d) as a function of the EGR rate, for different SOI angles.
- Figure 1.5** Barycenter of the combustion (a), angular duration of the combustion (b), angular duration of the ignition delay (c), angular duration of the first phase (d) and of the last phase of the combustion (e), peak firing pressure (f) and related angle (g), combustion noise (h), exhaust manifold temperature (i), intake manifold temperature (j) and pressure (k) as a function of EGR rate for different SOI.
- Figure 1.6** Tests performed at 1400 rpm and 3bar bmep attempting to get a proper PCCI combustion: SOI sweep at constant EGR rate (a,b) and EGR sweep at constant SOI (c,d).
- Figure 1.7** Test points of the V-Optimal DoE: values of the three control variables.
- Figure 1.8** bsfc: predicted vs. experimental values

Figure 1.9 NO_x (a), soot (b), HC (c) and CO (d) brake specific emissions, brake specific fuel consumption (e), MFB50 (f), combustion noise (g) and EGR rate (h): comparison between the base EU VI calibration and the optimized PCCI points.

Figure 1.10 (a) Percentage variations in COV_{imep} of cylinder #1 for the F1C PCCI and F1C Euro VI engines. (b) Percentage variations in COV_{PPF} of cylinder #1 for the F1C PCCI and for the F1C Euro VI engines.

Figure 1.11 Mass fraction burned x_b (a – left axis), apparent HRR (a - right axis), in-cylinder pressure of cylinder #1 (b – left axis), and its derivative (b - right axis) versus crank angle position at the 2000×2.3 point (rpm x bmep) for both the F1C Euro VI and the F1C PCCI engines.

Figure 1.12 Mass fraction burned x_b (a - left axis), apparent HRR (a - right axis), in-cylinder pressure of cylinder #1 (b - left axis), and its derivative (b - right axis) versus crank angle position at the 2000×7.5 point (rpm x bmep) for both the F1C Euro VI and the F1C PCCI engines.

Figure 1.13 Maximum in-cylinder pressure derivative of cylinder #1 for both the F1C Euro VI and the F1C PCCI engines (a) and λ values for the F1C PCCI engine (b).

Figure 1.14 NO_x, soot and bsfc as a function of λ at 2000×5 (speed x bmep) for different values of the input variables.

Figure 1.15 Percentage variations in engine-out NO_x (a), soot (b), CO (c), and HC (e) emissions between the F1C PCCI and the F1C Euro VI engine; percentage variations in CO (d) and HC (f) emissions after DOC between the F1C PCCI engine and the WHSC limit; percentage variations in bsfc (g) and CN (h) between the F1C PCCI and the F1C Euro VI engine.

Figure 1.16 Scheme of the RP setup for the pressure-based (a) and model-based (b) MFB50 control techniques.

Figure 1.17 EGR unbalance in the first cylinder with the map-based ECU strategy, evaluated as the difference between the cylinder-by-cylinder EGR rate and the average one, basing on the temperature of the intake air for each cylinder. Similar figures are obtained on the other cylinders.

Figure 1.18 Coefficient of variation of the peak firing pressure evaluated for the whole engine at various engine loads for three different engine speeds: 850 rpm (a); 2000 rpm (b); 3000 rpm (c): comparison among the map-based, the pressure-based and the model based controls.

Figure 1.19 Amplitude of the dispersion range of the MFB50 (a) and of the combustion noise (b) vs. engine load at 2000 rpm: comparison among the map-based, the pressure-based and the model based control strategy.

Figure 1.20 Brake specific soot and NO_x emissions at 2000 rpm: comparison among the map-based, the pressure-based and the model-based control strategy. The values are reported in adimensional units, referring all the values to the ones measured at $\text{bmep} = 1$ bar for the map-based control.

Figure 1.21 Brake specific engine-out soot and NO_x emissions at 1400 rpm \times 104 Nm (a) and 3000 rpm \times full load (b): comparison between the map-based and the pressure-based control strategy.

Figure 1.22 Coefficient of variation of the peak firing pressure evaluated for the whole engine on SOI sweep tests for two engine points: comparison among the map-based strategy and the pressure-based control strategy.

Figure 1.23 Example of mass fraction burned x_b (a) and pressure trace (b) for cylinder #1 in the case of clean signal (black solid line) and disturbed one (red solid line). Engine working point 1400 \times 104 (rpm \times Nm). Sinusoidal disturbance with amplitude = 2 bar and frequency = 7 kHz.

Figure 1.24 Coefficient of variation of the peak firing pressure (a) and of the indicated mean effective pressure (b) evaluated for the whole engine, and amplitude of the dispersion range of the combustion noise (c) on EGR sweep tests in PCCI combustion mode: comparison among the map-based strategy and the pressure-based control strategy.

Figure 1.25 WHTC points (blue markers), load ramps (red markers) and full load curve (black solid line).

Figure 1.26 Average MFB50 among cylinders as a function of engine speed and bmep on CDC engine mapping tests.

- Figure 1.27** Transient analysis in CDC: part of the reference load variation profile at 1400 rpm (a) and related MFB50 and SOI_{main} values: comparison among the map-based (b, without SOI correction), the pressure-based (c) and the model-based (d) controls. In all the graphs in this Figure the upper curves refers to MFB50 and the lower ones depict the SOI.
- Figure 1.28** Amplitude of the variation range of the MFB50 and related mean MFB50 variations during transient operations in CDC: comparison between the map-based (a, without SOI correction) and the pressure-based (b) controls.
- Figure 1.29** Geometric profile of the EGR poppet valve.
- Figure 1.30** Section of the minimum flow geometrical area at different poppet valve lift l_v : 2 mm (a), 5 mm (b) and 8 mm (c).
- Figure 1.31** EGR poppet valve geometric area (a) and electric duty cycle (b) as function of the lift.
- Figure 1.32** (a) Effective EGR flow area and geometrical flow area in function of the valve lift. (b) Flow coefficient in function of the valve lift.
- Figure 1.33** Comparison between EGR effective flow areas calculated with the hypothesis of compressible or incompressible flow (a). Mach number vs. pressure ratio across the valve (b).
- Figure 1.34** CFD simulations of the flow regime through the EGR poppet valve at three different valve lifts: 2 mm, 5 mm and 8 mm.
- Figure 1.35** Semi-physical approach for the estimation of the EGR flow rate: correlation between the experimental exhaust temperature (a) and pressure (b) and those estimated from ECU variables.
- Figure 1.36** Fluid-dynamic model vs. semi-physical approach: flow coefficients (a) and correlation between reference and estimated flow rate values (b).
- Figure 1.37** Assessment of the models for the prediction of EGR mass flow rate: engine map, trade-offs and PCCI tests.
- Figure 1.38** Correlation between the oxygen concentration in the intake manifold and the ratio between EGR rate and air-fuel ratio.
- Figure 1.39** First-attempt input/output model.

- Figure 1.40** Prediction of MFB10 (a) and MFB50 (b) based on a linear model with only air mass flow rate as input.
- Figure 1.41** Prediction of MFB90 based on linear model which consider as input: only the air mass flow rate (a), the air mass flow rate and the EGR rate (b), the air mass flow rate and the oxygen concentration in the intake manifold (c), the air mass flow rate and the air-fuel ratio (d).
- Figure 1.42** Predicted vs. reference EGR rate, where the prediction is obtained applying Equation 1.27.
- Figure 1.43** Modeling of combustion metrics and EGR rate in PCCI combustion: Prediction of MFB10 (a) MFB50 (b) and MFB90 (c) according to Eqs. 1.28-1.30, and correlation between oxygen concentration at the intake manifold and the ratio between the EGR rate and lambda, according to Eq. 1.23.
- Figure 1.44** Predicted vs. reference EGR rate, where the prediction is obtained applying Equation 1.33 (a) and Equation 1.34 (b).
- Figure 1.45** Schematic of the air and EGR path in the FIC engine.
- Figure 1.46** Picture of the intake manifold that shows the installation of the thermocouples.
- Figure 1.47** EGR rate spatial distribution in the intake manifold at IVC of cylinder 1 (right side) from CFD simulations.
- Figure 1.48** (a) Comparison of EGR unbalance in CDC estimated from mixing temperature technique and from in-cylinder pressure measurement on the reference engine map. (b) Maps of EGR rate and EGR mass flow rate as a function of engine speed and load.
- Figure 1.49** EGR unbalance in CDC estimated from mixing temperature technique and from in-cylinder pressure measurement vs. EGR rate (a) and vs. EGR mass flow rate (b).
- Figure 1.50** Average EGR rate estimated with mixing temperature technique compared with the average EGR rate obtained from in-cylinder pressure measurement.
- Figure 1.51** EGR unbalance in PCCI combustion estimated with mixing temperature technique and from in-cylinder pressure measurement vs. EGR rate (a) and vs. EGR mass flow rate (b).

- Figure 2.1** (a) Percentage rolling resistance variation as a function of tire pressure for a passenger tire according to LaClair [81]. The reference pressure for the cold tire is 2.1 bar according to ISO 18164:2005 [227]. (b) Percentage rolling resistance variation with tire pressure variation: comparison of LaClaire's relation provided for passenger cars and heavy trucks.
- Figure 2.2** Normalized rolling resistance coefficient of the reference passenger tire as a function of speed for different tire inflation pressure values.
- Figure 2.3** Test track (FCA Balocco Proving Ground), with highlighted the two straight sectors where the coast-down tests have been performed.
- Figure 2.4** Average coast-down characteristics of the tested passenger car for each test case.
- Figure 2.5** Variation of the F_0 coast-down parameter with tire inflation pressure for the tested passenger car: comparison of the test results with the calculated values.
- Figure 2.6** Vehicle velocity profiles of the driving cycles used as references for the study-case on passenger car.
- Figure 2.7** Percentage fuel consumption caused by variations in the inflation pressure of tires on the reference passenger car for different driving cycles. (a) Results normalized to the total fuel consumption on the NEDC cycle at the reference pressure of 2.1 bar. (b) Results of each cycle normalized to the total fuel consumption at the reference pressure of 2.1 bar.
- Figure 2.8** Absolute (left part of each graph) and relative (right part of each graph) contributions of the different terms to the energy demand for US06 (a) and HWFET (b): comparison between $p_{infl} = 2.1$ and 1.1 bar.
- Figure 2.9** Percentage variation in the energy demand due to rolling resistance at $p_{infl} = 1.1$ bar compared to $p_{infl} = 2.1$ bar for US06 and HWFET.
- Figure 2.10** Percentage fuel consumption variation with respect to the vehicle mass on the reference passenger car: comparison of the baseline case and the case in which the pressure is varied in order to maintain the same road contact patch area. The results are shown for an NEDC cycle (a) and for an HWFET cycle (b).

- Figure 2.11** Tire warm-up on a passenger car for three tire pressure levels: vehicle speed profile (a) and temperature of the rear right tire (b). The other tires show a similar behavior.
- Figure 2.12** (a) Percentage of rolling resistance versus time during tire warm-up on passenger cars: Michelin's data and parametrized curves. (b) Percentage of rolling resistance versus time during tire warm-up for the "baseline" and for the "variable pressure" cases (top) and corresponding inflation pressure (bottom).
- Figure 2.13** Fuel consumption benefits on the NEDC obtained through tire pressure management during tire warm-up on a passenger car: relative fuel consumption reduction (upper diagram) and cumulated saved fuel on a percentage basis (bottom graph).
- Figure 2.14** Fuel consumption variations on the reference passenger car: sensitivity to rolling resistance variations (a), sensitivity to mass variations (b) and instantaneous variation in fuel consumption during a warm-up and average worsening along the trip (c).
- Figure 2.15** Distributions of the percentage of trips per year for passenger cars as a function of the travelled distance per trip (a) and of the duration of each trip (b); percentage of trips (c) and number of trips (d) for each class of trip duration and travelled distance.
- Figure 2.16** CO₂ emissions and percentage variation of fuel consumption on the reference passenger car comparing the *reference* cases of the various considered *scenarios* (a); percentage variation of fuel consumption on misuse cases and pressure management strategies with respect to the *reference* case on each of the considered *scenarios* (b).
- Figure 2.17** Percentage of the rolling resistance variation with the tire pressure and vertical load.
- Figure 2.18** Coast-down curves of the reference heavy-duty vehicle, calculated for various vehicle loading conditions and tire inflation pressures.
- Figure 2.19** Percentage of the variation of the reference tire mileage with pressure.
- Figure 2.20** Percentage of the variation of rolling resistance during the warm-up period.

Figure 2.21 TyPE graphic user interface: main page of the software (a) and page for providing to the software the vehicle specifications.

Figure 2.22 TyPE graphic user interface: selection of embedded pressure management strategies.

Figure 2.23 Vehicle speed and gear profile in PerFECTS on a section of the *Custom HDV highway 1* cycle for different pressure combinations and loading conditions. *S*, *D* and *T* refer to the steer, drive and trailer axles and indicate the pressure set on the tires on each axle.

Figure 2.24 Comparison between TyPE and PerFECTS, when TyPE is run with a reference mission profile for all the pressure/load cases (a), and when the mission in TyPE is the same as that obtained from the PerFECTS simulations for each pressure/load case (b).

Figure 2.25 Percentage of the variation of HDV fuel consumption with tire inflation pressure on *long-haul* (a, b), *regional* (c, d) and *urban* (e, f) ACEA driving cycles, at truck curb weight (a, c, e) and maximum payload (b, d, f).

Figure 2.26 Percentage of the variation of LDV fuel consumption with tire inflation pressure on *highway*, *extra-urban* and *urban* driving cycles, at curb weight (a) and maximum payload (b).

Figure 2.27 Effects of tire cold-start and warm-up strategies on HDV on *long-haul* (a), *regional* (b) and *urban* (c) ACEA missions.

Figure 2.28 Effects of tire cold-start and warm-up strategies on LDV on *highway* (a), *extra-urban* (b) and *urban* (c) missions.

Figure 2.29 Effect of vehicle loading condition variations on fuel consumption on HDV on long-haul, regional and urban ACEA missions: effects of the application of the iso-deflection pressure management strategy.

Figure 2.30 Effect of vehicle loading condition variations on fuel consumption on LDV on the Custom LDV highway, Custom LDV extra-urban and Custom LDV urban missions: effects of the application of the iso-deflection pressure management strategy.

Figure 2.31 Schematic of the ATPC system layout.

Figure 2.32 Test-bench layouts for testing pneumatic components according to ISO 6358 [273].

- Figure 2.33** Test-bench layouts compliant with ISO 6358 [273] built to test several pneumatic components of the system (a), the toroidal pneumatic rotating joint under operating conditions (b), and additional layouts set-up to test an on-wheel deflation valve and a check valve (c) and the compressor/vacuum pump unit (d).
- Figure 2.34** Test-bench built to test several pneumatic components of the system. The pictures show the configuration setup to test the toroidal pneumatic rotating joint under operating conditions: (a) main view (b) top view.
- Figure 2.35** ATPC system: characteristics of the vacuum pump flow rate for several effective sections of the outlet port (a) and of the compressor for several sections of the intake port (b).
- Figure 2.36** Characteristics of the designed on-wheel deflation valve.
- Figure 2.37** Toroidal pneumatic rotating joint of the ATPC system: (a) statoric part (6), rotoric part (5), bearings (1), seals (2), spacers (3) and seeger rings (4); (b) photograph of the prototype.
- Figure 2.38** Volumetric flow rate characteristic of the pneumatic rotating joint of the ATPC system in non-rotating conditions: without any additional component upstream and downstream (a) and with the additional piping etc. that are needed to install it for measurements under rotating conditions (b).
- Figure 2.39** Time evolution of external surface temperature (a) and resistant torque (b) measured on the pneumatic rotating joint of the ATPC system, without putting the inner sealed chamber under pressure; steady state torque plotted as a function of the steady state temperature (c).
- Figure 2.40** Pressure-flow characteristic of the pneumatic rotating joint of the ATPC system at various rotating speeds (a-d) and choked flow-rate as a function of rotating speed (e).
- Figure 2.41** Resisting torque measured on the pneumatic rotating joint of the ATPC system as a function of the pressure ratio through the joint, for various inlet pressure levels, at 500 rpm (a) and 1000 rpm (b).
- Figure 2.42** Integration of the ATPC system in the wheel-end of a driving wheel: assembly of the parts from the toroidal pneumatic joint to the cv-joint (a) and the wheel-end components (b).

- Figure 2.43** Integration of the ATPC system in the wheel-end components of a non-driving wheel.
- Figure 2.44** Integration of the ATPC system in the wheel-end components of a driving wheel: photo of the prototype showing the solution with wheel-end valves and the final duct integrated into an aluminum alloy wheel.
- Figure 2.45** Integration of the ATPC system in the wheel-end components of a non-driving wheel: photo of the prototype showing the solution with wheel-end valves and the final duct fitted on the external surface of a steel rim.
- Figure 2.46** System prototype and test-bench used to test the performance of the complete ATPC system (a) and CAD of the final version of the system with the overall dimensions (b). Dimensions are reported in mm.
- Figure 2.47** Test-bench configuration used to test the performance of the complete ATPC system.
- Figure 2.48** Inflation operations for the tested configuration of the ATPC system: tire pressure variation in time during the tested operations (a), tire pressure variations as a function of the actuation times (b) and actual compressor working characteristic in the considered operating conditions (c).
- Figure 2.49** Deflation operations for the tested configuration of the ATPC system: tire pressure variation in time during the tested operations (a), tire pressure variations as a function of the actuation times (b) and actual vacuum pump working characterizing in the considered operating conditions (c).
- Figure 2.50** Linear correlation between tire pressure and pressure measured at the compressor outlet port on the ATPC system (a), estimated and measured tire pressure (b) and accuracy of the tire pressure estimation (c).
- Figure 2.51** Schematic of the ACTIS system layout for the tractor of HDV and for LDV with rear dual tires: version with an independent source of compressed air source (a) and version integrated with the pre-existing on-board compressed air distribution line (b).

- Figure 2.52** Preliminary design of the on-wheel valve group for single tires of LDV and HDV.
- Figure 2.53** Working principle of the wheel-end group for dual tires of LDV and HDV: example of the system response in case of a tire blowout (a) and Amesim model used to simulate it (b).
- Figure 2.54** Preliminary design of the on-wheel valve group for dual tires of LDV and HDV.
- Figure 2.55** Integration of the ACTIS system on HDV: solution for front steering (non-driving) wheels: global view of the wheel-end assembly.
- Figure 2.56** Integration of the ACTIS system on HDV: solution for front steering (non-driving) wheels: section (a) and exploded view (b) of the on-wheel valve block and its connection with the upstream parts of the circuit.
- Figure 2.57** Integration of the ACTIS system on HDV: solution for rear driving wheels: global view of the wheel-end assembly (a) and section of the on-wheel valve block and its connection with the upstream parts of the circuit (b).
- Figure 2.58** Integration of the ACTIS system on LDV: solution for front steering non-driving wheels: global view of the wheel-end assembly (a) and section of the on-wheel valve block and its connection with the upstream parts of the circuit (b).
- Figure 2.59** Integration of the ACTIS system on LDV: solution for rear driving wheels: global view of the wheel-end assembly (a) and section of the on-wheel valve block and its connection with the upstream parts of the circuit (b).
- Figure 2.60** Effects of the ATPC system, accounting for the tested dynamics of the system, when tire pressure is adjusted during the tire warm-up period (a and b) and during a pressure adaption to a vertical load (c and d): tire pressure variation in time (a and c) and effect on fuel economy (b and d).
- Figure 2.61** Inflation (a) and deflation (b) actuations as retrieved from Amesim 1D simulation model of the system for HDV.

- Figure 2.62** Effects of the ACTIS for HDV, accounting for the simulated dynamics of the system, when tire pressure is adjusted during the tire warm-up period (a and b) and during a pressure adaption to a vertical load (c and d) on a long-haul ACEA cycle: tire pressure variation in time (a and c) and effect on fuel economy (b and d).
- Figure 2.63** Benchmarking the designed ACTIS system for HDV against a commercial CTIS.
- Figure 3.1** Combination of the CDC and PCCI engine performance maps for the simulations of the PCCI/CDC hybrid combustion mode.
- Figure 3.2** Engine cumulated fuel consumption, gaseous emissions and urea consumption on the LDV *highway* mission. Fuel consumption (a), soot engine-out emissions (d) and urea consumption (f) are reported in terms of percentage of the cumulated values at the end of the cycle with the reference CDC engine. CO (b), HC (c) and NO_x (e) emissions are reported as percentage of the Euro VI limits.
- Figure 3.3** LDV *highway* cycle with the CDC and PCCI engines: DOC conversion efficiency for CO and HC emissions (a,c) and cumulated relative CO and HC tailpipe emissions (b,d) as a function of engine load; soot instantaneous (e) and cumulated relative emissions (f) as a function of engine load.
- Figure 3.4** LDV *highway* cycle with the CDC and PCCI engines: NO_x instantaneous (a, b) and cumulated relative emissions (c) as a function of engine load; instantaneous and cumulated relative urea consumption as a function of engine load (d, e).
- Figure 3.5** LDV *highway* cycle with the CDC and PCCI engines: normalized performance maps of bsfc and tailpipe CO/HC emissions.
- Figure 3.6** LDV *highway* cycle with the CDC and PCCI engines: normalized performance maps of engine-out soot and NO_x emissions.
- Figure 3.7** Engine cumulated fuel consumption, gaseous emissions and urea consumption on the LDV *highway* mission as a function of the vehicle mass.

- Figure 3.8** Engine cumulated fuel consumption, gaseous emissions and urea consumption on the LDV *extra-urban* mission. Fuel consumption (a), soot engine-out emissions (d) and urea consumption (f) are reported in terms of percentage of the cumulated values at the end of the cycle with the reference CDC engine. CO (b), HC (c) and NO_x (e) emissions are reported as percentage of the Euro VI limits.
- Figure 3.9** LDV *extra-urban* cycle with the CDC and PCCI engines: DOC conversion efficiency for CO and HC emissions (a,c) and cumulated relative CO and HC tailpipe emissions (b,d) as a function of engine load; soot instantaneous (e) and cumulated relative emissions (f) as a function of engine load.
- Figure 3.10** LDV *extra-urban* cycle with the CDC and PCCI engines: NO_x instantaneous (a, b) and cumulated relative emissions (c) as a function of engine load; instantaneous and cumulated relative urea consumption as a function of engine load (d, e)
- Figure 3.11** LDV *extra-urban* cycle with the CDC and PCCI engines: normalized performance maps of bsfc and tailpipe CO/HC emissions.
- Figure 3.12** LDV *extra-urban* cycle with the CDC and PCCI engines: normalized performance maps of engine-out soot and NO_x emissions.
- Figure 3.13** Engine cumulated fuel consumption, gaseous emissions and urea consumption on the LDV *extra-urban* mission as a function of the vehicle mass.
- Figure 3.14** Engine cumulated fuel consumption, gaseous emissions and urea consumption on the LDV *urban* mission. Fuel consumption (a), soot engine-out emissions (d) and urea consumption (f) are reported in terms of percentage of the cumulated values at the end of the cycle with the reference CDC engine. CO (b), HC (c) and NO_x (e) emissions are reported as percentage of the Euro VI limits.
- Figure 3.15** LDV *urban* cycle with the CDC and PCCI engines: DOC conversion efficiency for CO and HC emissions (a,c) and cumulated relative CO and HC tailpipe emissions (b,d) as a function of engine load; soot instantaneous (e) and cumulated relative emissions (f) as a function of engine load.

Figure 3.16 LDV *urban* cycle with the CDC and PCCI engines: NO_x instantaneous (a, b) and cumulated relative emissions (c) as a function of engine load; instantaneous and cumulated relative urea consumption as a function of engine load (d, e).

Figure 3.17 LDV *urban* cycle with the CDC and PCCI engines: normalized performance maps of bsfc and tailpipe CO/HC emissions.

Figure 3.18 LDV *urban* cycle with the CDC and PCCI engines: normalized performance maps of engine-out soot and NO_x emissions.

Figure 3.19 Engine cumulated fuel consumption, gaseous emissions and urea consumption on the LDV *urban* mission as a function of the vehicle mass.

Figure 3.20 Tire inflation pressure (a) and the relative variation of tire rolling resistance (b) during a cold start, with (red dashed line) and without (black solid line) the warm-up tire pressure management strategy actuated through the ACTIS on the reference LDV.

Figure 3.21 Results on LDV simulated on highway cycle. Fuel consumption, soot and NO_x engine-out emissions and urea consumption variations between the CDC and PCCI engines, with different tire pressure management situations: in a typical misuse case, when tires are always inflated at the nominal pressure (baseline) and in case of implementation of the ACTIS.

Figure 3.22 Results on LDV simulated on *highway* cycle. CO and HC engine-out and tailpipe emissions variations between the CDC and PCCI engines, with different tire pressure management situations: in a typical misuse case, when tires are always inflated at the nominal pressure (baseline) and in case of implementation of the ACTIS.

Figure 3.23 Results on LDV simulated on *extra-urban* cycle. Fuel consumption, soot and NO_x engine-out emissions and urea consumption variations between the CDC and PCCI engines, with different tire pressure management situations: in a typical misuse case, when tires are always inflated at the nominal pressure (baseline) and in case of implementation of the ACTIS.

Figure 3.24 Results on LDV simulated on *extra-urban* cycle. CO and HC engine-out and tailpipe emissions variations between the CDC and PCCI engines, with different tire pressure management situations: in a typical misuse case, when tires are always inflated at the nominal pressure (baseline) and in case of implementation of the ACTIS.

Figure 3.25 Results on LDV simulated on *urban* cycle. Fuel consumption, soot and NO_x engine-out emissions and urea consumption variations between the CDC and PCCI engines, with different tire pressure management situations: in a typical misuse case, when tires are always inflated at the nominal pressure (baseline) and in case of implementation of the ACTIS.

Figure 3.26 Results on LDV simulated on *urban* cycle. CO and HC engine-out and tailpipe emissions variations between the CDC and PCCI engines, with different tire pressure management situations: in a typical misuse case, when tires are always inflated at the nominal pressure (baseline) and in case of implementation of the ACTIS.

Figure 3.27 Annual missions of the reference light-duty vehicle: effect of the combination of PCCI engine and ACTIS technology on fuel consumption (a), cost of fuel (b), urea consumption (c) and tire life (d).

Figure 3.28 Annual missions of the reference light-duty vehicle: effect of the combination of PCCI engine and ACTIS technology on the Total Cost of Ownership.

List of Tables

- Table 1.1** Technical specifications of the conventional F1C Euro VI diesel engine and of the PCCI version of the engine.
- Table 1.2** DoE input boundary values.
- Table 1.3** Detail of the 32 test points of the V-Opt DoE at speed = 1500 rpm and bmep = 1 bar (i.e. torque = 27 Nm).
- Table 1.4** Statistical summary for each response model.
- Table 1.5** Parameters of the Euro VI point and of the optimization point parameters.
- Table 1.6** Optimum experimental points (boost pressure and exhaust pressure values expressed as relative pressures) of the PCCI engine.
- Table 1.7** Euro VI emission standards for heavy-duty diesel engines for the World Harmonized Stationary Cycle (WHSC).
- Table 1.8** Overview of the features concerning the three considered control methods.
- Table 1.9** Test conditions for EGR sweeps in PCCI combustion mode.
- Table 1.10** Effect of the tested control modes on fuel consumption and emissions: average percentage variation with respect to the map-based mode.
- Table 1.11** Best models tested to predict MFB10, MFB50 and MFB90 in PCCI combustion mode.
- Table 1.12** Comparison of EGR unbalance estimated with different methodologies in CDC.
- Table 2.1** Characteristics of the reference passenger car and of the related tire.

- Table 2.2** Test cases for the coast-down tests performed on track on a passenger vehicle.
- Table 2.3** Statistical accuracy and coast-down parameters of the tested passenger car for each test case.
- Table 2.4** Summary of the characteristics of the reference cycles for the study-case on passenger car.
- Table 2.5** Characteristics of the ATPC system.
- Table 2.6** Pressure variation with the loading conditions on the reference passenger car: test cases.
- Table 2.7** Test cases and results of tire pressure variations with the vehicle speed on the reference passenger car.
- Table 2.8** Characteristics of the reference light-duty vehicle.
- Table 2.9** Characteristics of the heavy-Duty vehicle.
- Table 2.10** Characteristics of the reference test cycles considered in the study for the reference heavy-duty vehicle (HDV) and light-duty vehicle (LDV).
- Table 2.11** Annual missions for the reference heavy-duty vehicle: effect of pressure management strategies on TCO.
- Table 2.12** Annual missions of the reference light-duty vehicle: effect of pressure management strategies on TCO.
- Table 3.1** Annual missions of the reference light-duty vehicle: effect of the combination of PCCI engine and ACTIS technology on the Total Cost of Ownership.

Introduction¹

The increasing technological capability in tracing and using energy resources has fostered the industrial revolution and the improvement in human wellbeing in the last two centuries. Quality of life, and related variables, have been found to be correlated to energy consumption per capita [1] as well as to indices related to energy availability, usage and distribution [2]. Transporting goods and people for medium and long distances is one of the factors that enabled the improvement of quality of life: historical evidence shows that aggregated distance travelled by vehicles has been increasing concurrently to the growth in the national GDP, although it is not possible to assess the causality between these two variables [3]. On the other hand, this development relied on the massive usage of fossil fuels [4], which caused a substantial increase in CO₂ emissions, therefore altering the Earth's radiative equilibrium [5]. Moreover, burning fossil fuels also contributes to the presence in the atmosphere of pollutants that affect the health of human beings and cause every year 3.3 million deaths all over the world, 5% of which (165'000 deaths/year) are due to transportation [6]. The foreseeable scenario about primary energy sources confirms the predominant role of fossil fuels, especially in the transportation sector, which accounts for 25% of the world's total energy consumption [4]. Road vehicles represent 81% of the transportation energy demand [7], and are responsible for nearly 60% of the global oil demand and 10% of global GHG emissions, 95% of which is CO₂ [8]. This scenario, which indicates transportation as one of the main responsible for energy consumption, GHG emissions and air pollution, has forced legislators and car makers to take countermeasures.

¹ Some parts of this chapter have been already published in:

d'Ambrosio, S., Mameli, E., Vitolo, R., "Impact assessment of an intelligent central tire inflation system for passenger cars", 7th Transport Research Arena TRA 2018, April 16-19, Vienna, Austria, 2018.
<https://doi.org/10.5281/zenodo.1486718>.

and

d'Ambrosio, S., Vitolo, R., "Potential impact of active tire pressure management on fuel consumption reduction in passenger vehicles", Proceedings of the IMechE, Part D: Journal of Automobile Engineering, 233(4):961-975, 2019, <https://doi.org/10.1177/0954407018756776>.

Vehicle Emissions Standards

The issue of pollution due to transportation was first recognized as a problem during the Sixties in California, where the visible smog and the increase of diseases due to low air quality brought the local public institutions to take some countermeasures. An investigation by the State Department of Public Health recognized internal combustion engines as one of the main contributors to anthropogenic air pollution, which led to the institution of an administrative organization devoted to face this issue, which was first named the Motor Vehicle Pollution Control Board [9]. The first regulation to limit the emissions of pollutants in the atmosphere was set by the Board in 1961, and it consisted in imposing the installation on new cars (and later also involved the retrofitting of existing models) of a device meant to recirculate blow-by gases from the crankcase to the engine intake system [9]. As a consequence, the concentration of pollutants – and especially of unburned hydrocarbons – in the Los Angeles area remained constant in the following years, despite the rapid increase of the circulating vehicles [9]. This result encouraged the extension of this regulation at the national level in the USA. Soon later, new regulations were adopted with the aim of pushing technological innovation to increase the combustion efficiency, to reduce the tailpipe pollutants through after-treatment systems (starting from 1966 in California) and to limit evaporative losses from the fuel tank and the carburetor [9, 10]. In 1970 the US Environmental Protection Agency (EPA) was founded, aiming to set legislations on air quality [11]. Since then, in the US two regulatory organizations exist: the EPA, which sets the federal emission standards and the related procedures, and the California Air Resources Board (CARB), which generally sets more stringent standards and procedures than EPA, which are valid for California and for other US states that agree on a voluntary basis to adopt CARB standards [12]. Thus, the State of California is still in charge for a leading role in the field. In 1970 also in Europe the first regulation was approved to set a limit to the emissions of unburned hydrocarbons and carbon monoxide emitted by vehicles endowed with spark ignition engine, which involved the definition of a test cycle to be operated at the vehicle dynamometer (roller test bench) [13].

Therefore, since the Sixties-Seventies, regulations on pollutant emissions have been one of the main factors to drive technological innovation, which had a strong impact on the evolution of vehicles, including their design. Furthermore, many technologies first developed to comply with pollutant emissions regulations, also had an impact on vehicle performance, fuel economy, drivability and safety [10]. As an example, the introduction of two-way catalysts first, and three-way catalysts later, raised the issue of combustion control, thus enabling the usage of electronic controls on the engine to properly adjust the amount of fuel injected by means of

electronically-controlled injectors through a closed-loop control of the current air-to-fuel ratio [10].

During the last twenty-five years the emission standards have been tightening the limits, till reaching, for passenger cars and light duty vehicles, the current Euro 6 limits in Europe and the EPA Tier 3 standards in USA [12]. Figure 1 shows the evolution of the emission regulation referring to the limits on NO_x and PM emissions. For gasoline vehicles the European regulations up to Euro 4 were not imposing any limitation on PM, (therefore, the NO_x limits corresponding to Euro 1 to Euro 4 regulations are represented through vertical lines). It is also worth to notice that Euro 2 regulation was setting two different limits on diesel vehicles, one for direct injection (DI) engines, and one for indirect injection (IDI) ones. It is also worth to mention that the plotted NO_x limits for Euro 1 and Euro 2 refer actually to limits on (NO_x+HC). Still referring to EU regulations reported in the graph, the limits plotted for light duty vehicles refer to the vehicles categorized as N1, Class II, i.e. with a mass between 1305 kg and 1760 kg. Concerning the US regulations, the EPA standards (Tier 1, Tier 2 and Tier 3) referred to the FTP-75 test cycle have been represented. As Tier 1 and Tier 2 set different limits for different mileage/life of the vehicle, while Tier 3 refer to the whole vehicle life, then for all the regulations the maximum considered mileage/life has been considered. For Tier 2 and Tier 3, the bins representative of the fleet average have been plotted. The graph clearly show the strong tightening of the emissions limits over time both in EU and in US.

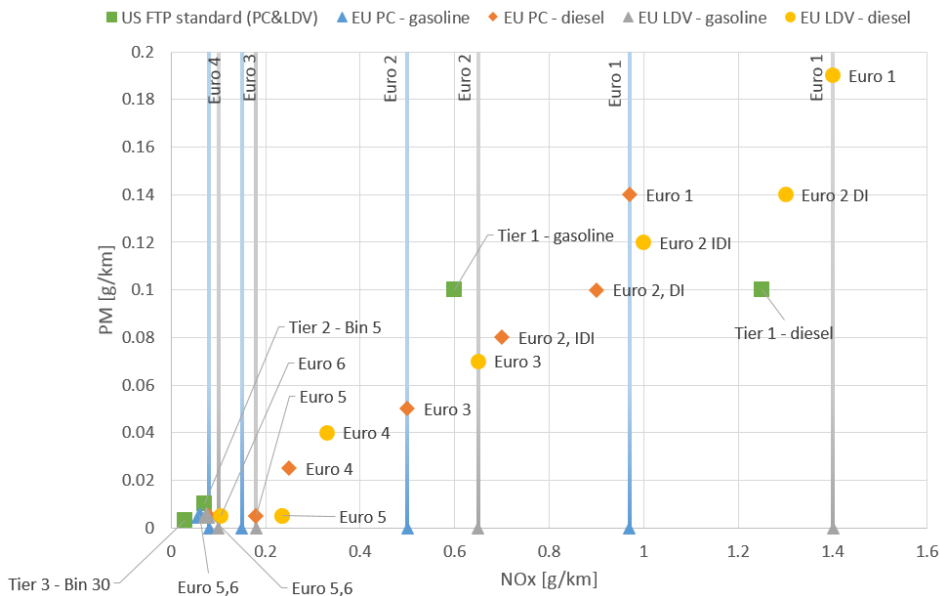


Figure 1: Regulated limits of NO_x and PM emissions in Europe and US: evolution of the emission regulations.

Anyway, in some cases these standards failed in catching realistic vehicles equipment and working conditions, especially for what concerns European Union regulations [14, 15]. As an example, some previous studies ([16-18] as reviewed in [15]) found that nitrogen oxides (NO_x) emissions from on-market Euro 6 diesel cars exceed the regulated limits by a factor equal to 5 when tested on dyno and 6-7 when tested on roads by means of Portable Emission Measurement Systems (PEMS). Some studies clearly showed that the main causes for this discrepancies lay both in the test cycle and in the testing procedure as a whole (e.g., [14]). In fact, on one side the NEDC test cycle represented an unrealistic driving behavior with light transients, low engine loads and some constant-speed driving periods, and on the other side the test procedure left to the OEMs wide shadow areas with a substantial freedom to choose the equipment of the vehicles tested for type approval. As a consequence, the OEMs used to type-approve vehicles with low weight and unrealistic road loads, which resulted in the increasing discrepancy between officially declared emissions and real-world ones. Due to these reasons, the European Union has recently introduced a new test procedure, in force since September 2017, whose aim is to constrain the OEMs to use realistic conditions for type-approval testing. The procedure is known as Worldwide Harmonized Light-Duty Test Procedure (WLTP), and includes the adoption of test masses, inertias and road loads that more properly represent the lower and upper boundaries of the on-market variants of the vehicle to be type-approved [14]. The procedure also includes a new test cycle, the Worldwide Light-Duty Test Cycle (WLTC), which has more transient conditions and covers a longer distance with respect to the NEDC. This cycle, anyway, does not result in any substantial increase of the average emissions per unit distance with respect to the NEDC, as most of the emissions are usually produced in the first period after the engine is switched on (cold-starts), and this period would have a lower relative weight on a longer trip distance [14]. The introduction of the WLTP/WLTC has been also accompanied with another initiative, aimed at introducing in the type-approval procedure the evaluation of on-road emissions by using the PEMS [10, 19]. This procedure, known as the Real Drive Emissions regulation, consists in a supplemental measurement of vehicle emissions during normal operation in on-road traffic conditions, in addition to dyno testing on WLTC [20]. The PEMS raw emission results are then post-processed to operate a normalization that accounts for the severity of the dynamic test conditions, and that provides for each specie a unique emission factor for comparison with the limits [15]. Currently, two normalization methods are allowed, and the OEM can choose which of the two would be used for the type-approval. Additionally, driving conditions that are considered too much severe are removed from the calculations, and some multiplicative factors are applied to the Euro 6 limits to evaluate the emissions conformity [15]. Especially, for NO_x an emissions factor of 2.1 is applied starting from September 2017, and it will be reduced to 1.5 from January 2020 [15,

20]. This means that, although Euro 6 limit for NO_x measured on dyno is 60 mg/km for gasoline passenger cars and light-duty commercial vehicles and 80 mg/km for diesel ones, the same limits raise to 126 mg/km and 168 mg/km from 2017 and to 90 mg/km and 120 mg/km from 2020, respectively, for RDE testing. Similarly, a conformity factor of 1.5 is defined for RDE particle number (PN) limit for diesel and gasoline direct injection (GDI) engines [20]. These factors should account for the higher severity of the test procedure with respect to dyno testing, as well as for the possibly higher inaccuracy of the PEMS devices compared to laboratory testing [15]. Finally, the limit thresholds for the acceptable emissions are further multiplied by an additional factor higher than one (namely, the *transfer function* coefficient) for those driving conditions that are not so severe to be excluded in the calculations, but still considered highly demanding [15]. Thus, although the positive intentions related to the introduction of real-world emissions measurements, a certain freedom and a number of facilitations are still provided to the OEMs. According to some authors [15] and to a large part of the public opinion [21-23], these facilitations, in the form of the various emissions factors, are to be considered a win for the automotive lobby, whose interest is to gain some time advantage to come on the market with suitable solutions for proper pollutant emissions reductions. If, on one side, it can be easily understood that Research needs suitable time to develop breakthrough technologies, on the other side it is obviously clear also the interest of the “automotive giants” (i.e., the larger OEMs) to maintain the “business-as-usual” condition as long as possible. Moreover, it is worth noticing that diesel vehicles represent 53% of the current European market share [14]. The abovementioned non-compliance with NO_x limits with respect to the Euro 6 limits on NEDC, and the discussed facilitations on NO_x and PM/PN in the introduction of the RDE regulation also are a consequence of such a diesel-oriented market [15], as diesel engines traditionally emit more NO_x and particulate with respect to gasoline ones. All these aspects result, in practice, in a substantial delay in the implementation of actions towards the improvement of air quality.

Nevertheless, the introduction of these new standards, together with the clear intention by the authorities to take countermeasures to limit air pollution, highlights the need for advanced technologies. The field of Research related to Automotive industry is working to provide solutions to the present and future markets. Recent improvements in diesel oxidation catalysts and three-way catalysts to lower the emissions of unburned hydrocarbons (HC) and carbon monoxide (CO) are mainly related to reducing the light-off time of the after treatment systems (ATS) [19], as catalyst warm-up is nowadays the vehicle utilization period in which most of the emissions are produced [10, 19]. This trend is further pushed by the application of engine technologies that tend to reduce the tailpipe temperatures, such as turbocharging or the implementation of low-temperature combustion processes

[19]. Engine-out nitrogen oxides (NO_x) and particulate matter (PM), typically associated to diesel engines, became also relevant on gasoline ones due to the introduction of gasoline direct injection (GDI). Therefore a number of solutions are being proposed, including improvements on selective catalytic reduction (SCR) systems, as well as the integration of SCR with diesel particulate filter (DPF), possibly including a lean NO_x storage catalyst (NSC) for the local production of ammonia [19]. Moreover, the recent introduction of limits on the particles number (PN), together with the stringent limits on PM, is pushing the study on the filtration-related phenomena, in order to propose advanced solutions for diesel and gasoline particulate filters [19]. If, on one side, the abatement of pollutants through improved after-treatment systems is still a relevant field for research, in-cylinder pollutant reduction techniques are also on the edge. These methods intervene on the development of the combustion process itself, in order to limit or avoid the activation of the chemical processes that lead to the formation of pollutants. This is the case, for instance, of: gasoline homogeneous charge compression ignition (HCCI) [24] and its “gasoline compression ignition” derivatives such as Mazda’s spark controlled compression ignition [25, 26]; diesel HCCI [27] and premixed charge compression ignition (PCCI) [28-30] concepts; and rate-controlled compression ignition (RCCI), where the combustion process is controlled by obtaining proper fuel reactivity, e.g. by combining different fuels (e.g., diesel and gasoline) and possibly using both direct injection and port fuel injection [31]. Also model-based combustion control techniques play a relevant role, especially to improve the engine response to transients, since traditional map-based controls produce high emissions during transients with respect to optimized steady-state calibration, mostly due to the different dynamic response of the fuel system and of the air-EGR (exhaust gas recirculation) path [32]. Additionally, combustion controls can compensate for engine drifts in time and correct cycle-to-cycle and cylinder-to-cylinder combustion variability, thus also becoming a key enabling technology for the implementation of some of the above-mentioned non-conventional combustion strategies [33-36]. Furthermore, not only engine-related technologies have the potential to reduce the vehicle pollutant emissions, but also vehicle-related ones: the reduction of vehicle inertia and road load through the introduction of lightweight materials and improvements in aerodynamics, rolling resistance, and passive resistances in general (e.g., mechanical frictions) not only have a direct effect on fuel consumption, but also allow the usage of smaller engines, as well as the better exploitation of areas of the engine map where the best performance can be possibly obtained in terms of pollutant emissions. Simulations based on steady-state engine performance map showed that reducing by 5% the weight of a Euro 4 small gasoline passenger car it is possible to reduce CO and NO_x tailpipe emissions by 14-15% and total HC by 11%, and an increase by 5% of the tire rolling radius reduced CO and HC emissions by 9-10% while increasing NO_x

by 9.5% [37]. Some experimental NEDC tests on roller test bench also showed a possible reduction by 30% in CO emissions from a Euro 4 gasoline passenger car and 8.5% reduction in NO_x emissions from a Euro 4 diesel passenger car reducing the rolling resistance of tires from 11.6 kg/ton to 9.7 kg/ton, and an additional 4.5% on CO emissions and 9.4% on NO_x from the gasoline and diesel cars, respectively, further reducing rolling resistance to 8 kg/ton [38]. The effect of reduced power requirement on NO_x emissions was also tested on a 12 liter truck in tests performed on track to simulate two highway driving conditions and one sub-urban driving case with starts-and-stops: the results showed that reducing rolling resistance and wheel inertia through the adoption of single wide tires and improving the trailer aerodynamics decreases fuel-consumption and NO_x emissions simultaneously, and that the NO_x emissions and fuel consumption are statistically correlated in the tested cases [39]. Last but not least, vehicle technologies can play a significant role in the further reduction of PM emissions from vehicles: as engine exhaust emissions have already been reduced by 99% since the introduction of Euro 5 regulation ([40, 41] as cited by [15]), further reductions of the particulates produced due to on-road transportation passes through the abatement of non-exhaust PM emissions, i.e. particulates coming primarily from tires, brakes and road [15]. These sources, although not mentioned yet by any regulation, are responsible for about 50% of the current vehicles-related PM10 and 25% of the PM2.5 emissions [15]. The interest in the field on non-exhaust emissions has been increasing in the last years, as demonstrated by a number of studies devoted to better explain the phenomena and quantify the impact of these sources [42-44], and by various projects aiming at finding technical solutions to the issue, e.g. the REBRAKE EU funded project and the companion LOWBRASYS project that aim at reducing by 50% the PM10 emissions from brakes with an expected overall reduction of PM10 by 4-14% in Europe [45]. This increasing interest is also motivated by the fact that non-exhaust PM emissions affect ICE-based vehicles as well as the recent and future generations of pure electric vehicles [46].

Fuel economy and greenhouse gases regulations

The usage of fossil fuels is also strictly linked – as widely known – to carbon dioxide emissions. Fuel consumption is often evaluated in terms of tailpipe carbon dioxide emissions to easily relate it to the effects on global GHG emissions. Therefore, in parallel to regulations on the reduction of pollutants, which are mainly addressing the emission of toxic gases such as the abovementioned HC, CO, NO_x and particulate matter, another priority raised, which strongly influenced the technological history of the automotive field. This is related to fuel economy and the corresponding emissions of CO₂. In the USA, the first need for regulations on fuel economy raised in 1975 in response to the oil crisis suffered during the

Seventies [10]. Therefore, this need was not originally derived by environmental purposes, but more by political-economical reasons. The so-called CAFE standard (Corporate Average Fuel Economy) resulted in a significant reduction (about 50%) of the fuel consumption of the vehicles in the period 1975-1985, thanks to the reduction of the displacement of engines, as well as the reduction of vehicle weight, improvement in aerodynamics and tires, and architectural choices such as front-drive wheels [10]. In Europe, although the first targets on the emissions of CO₂ were only applied in 1998, fuel consumption was also considered a priority since the Seventies, mostly due to the high taxation on gasoline fuel that was imposed in almost all the European Countries after the Second World War [15]. This attention of European market on fuel economy has been one of the main factors that have fostered the large adoption of diesel vehicles in the European market, as diesel engines are traditionally more efficient than gasoline ones [15], although this paradigm has been partly mitigated by the recent introduction of GDI engines and other gasoline technologies such as cooled EGR, high compression ratio, the adoption of the Miller cycle, etc... [15,19].

In the late Nineties, the increasing awareness in the scientific fields about the effect of greenhouse gases emissions [47-49] induced 180 Countries to set an agreement to reduce greenhouse gases emissions by at least 5% in the period 2008-2012 with respect to 1990 emissions [50]. This target could be obtained by the committing Parties jointly or individually [50]. This agreement, known as the *Kyoto Protocol* and developed within the United Nations Framework Convention on Climate Change (UNFCCC), was in force since 2005 in the State Parties that ratified it within that date, while other countries ratified it later. The Kyoto Protocol, therefore, substantially represents the first regulatory framework aimed specifically at reducing greenhouse gases emissions, including CO₂, due to their effect on the climate change. This posed a practical limitation to the emissions of greenhouse gases and in particular brought to the development of specific legislations to reduce CO₂ emissions from road fleets. In 1998 the European automotive OEMs signed an historical agreement (the so-called *ACEA agreement*) with the European Commission to reduce the CO₂ emitted by the vehicles to 140 g/km within 2008, i.e. 25% lower than 1995 [51]. Similar agreements were also signed by the associations of Japanese and Korean automotive manufactures with the European Commission [51], thus making Europe the world leader in the field of CO₂ emissions reduction on road transport. The adoption of these limits further increased the European diesel market thanks to the lower fuel consumption of diesel engines, together with the introduction of technologies that have further improved both the fuel efficiency and the pollutant emissions on diesel engines [15]. Anyway, as most of the OEMs were not able to reach the CO₂ target, the EU adopted in 2009 a regulation, based on the ACEA agreement, that was setting the limit of CO₂ emitted by vehicles to 130 gCO₂/km within 2015 [52,53]. A further reduction of 10 gCO₂/km had to be reached by means of improvements in other devices, whose benefits cannot be measured directly during the homologation cycle (e.g., air

conditioning systems, etc...). Moreover, a limit of 95 gCO₂/km has been set as a target that should be reached within 2020 [8, 54]. These reference limits are referred to a specific vehicle test mass, and they are adapted for different test masses, with an increase in in the maximum allowed CO₂ proportional to the increase of the vehicle mass [53].

In the US, after the abovementioned CAFE regulations in the 1975-1985 period, no additional standards were introduced until 2006-2010 (for light trucks and passenger cars, respectively), thus moving the attention of the vehicle OEMs to other fields, such as occupants safety, performance, etc... [10]. Then, in the first decade of the Twenty-First century, the raise of the oil price from about 24 US\$/barrel to about 110 US\$/barrel in the period 2002-2012 [55], as well as the mentioned growing concerns about the effects of anthropogenic CO₂ emissions on global warming, brought to a renewed interest in fuel economy of road vehicles. Therefore, in 2007 the US Congress recognized carbon dioxide as a pollutant to be regulated by EPA within the Clean Air Act. EPA, together with the National Highway Traffic and Security Agency (NHTSA, in charge for the CAFE standards), introduced some new regulations that were expected to result in an improvement in fuel economy of passenger cars to 33.3 mpg on model-year 2012 [8]. Data referred to 2012 reports the achievement of 35.4 mpg on model-year 2012, i.e., a fuel economy performance even better than expected [56]. An additional fuel economy improvement by 13% was expected within 2016 with respect to 2012 and by 48% in 2025 with respect to 2016, with the goal of 48.4-49.6 miles/gallon to be reached within 2025 [10, 57]. Type-approval tests in the US involve the Federal Test Procedure, i.e. and urban-extraurban driving cycle (FTP 75), a highway cycle (Highway Fuel Economy Test, HWFET) and, since 2008, includes a number of supplemental test procedure to represent also high-speed highly transient driving conditions (US06), the usage of air conditioning (SC03) and a cold-start FTP 75 [15, 57]. This procedure definitely results to be representative of realistic driving conditions [15]. The US 2025 fuel economy target roughly corresponds to 97 gCO₂/km when reported to NEDC-equivalent CO₂ emissions for comparison with EU standards ([15] based on [58,59]). Figure 2 shows the time evolution of the fuel economy regulations in Europe and US. All the data are expressed in terms of NEDC-equivalent CO₂ emissions in g/km. The ACEA agreement is highlighted in the graph, as it was not an actual limit set by regulation. For the US regulations, data are retrieved from [15, 57, 58] and converted to NEDC-equivalent according to [58]. Similar regulations have been set in other countries, such as South Korea, China and Japan with NEDC-equivalent targets of 97 g/km, 117 g/km and 122 g/km, respectively, to be reached in 2020 ([15] based on [58]).

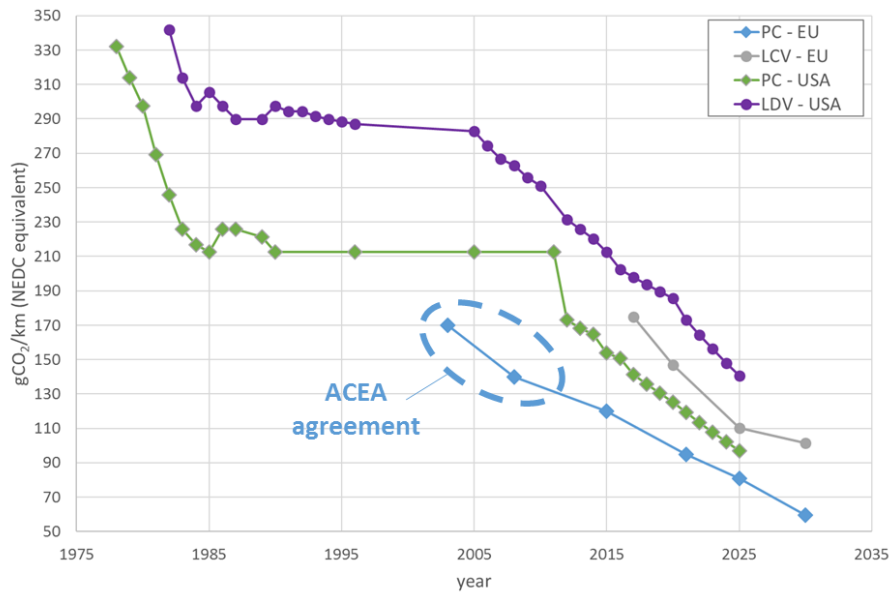


Figure 2: Time evolution of the fuel economy regulated limits in Europe and US, expressed in CO₂ emissions per km (NEDC-equivalent).

Although Europe has applied in time tighter fuel consumption and CO₂ emission limits, the regulatory effort has not been followed – in practice – by significant improvements in the real-world emissions of the circulating fleet. The nominal vehicle fuel consumption, derived from type-approval procedures, can be significantly different from what is actually experienced by drivers: the average difference was found to be about 11% for gasoline and 16% for diesel passenger cars for the European circulating fleet, when the NEDC is considered as the reference cycle [60]. Another recent study by the European Joint Research Center (JRC) reported that independent dyno testing on NEDC shows CO₂ emissions 8% ± 7% (average ± standard deviation) higher than the type-approved values for the tested vehicles [14]. Similar figures are also highlighted in other countries that have been using the NEDC and the related procedure: results related to the Chinese circulating fleet on real-life cycles have shown a 10-15% difference with respect to the NEDC [61,62]. The observed discrepancies are due to a lower average speed in real working conditions [61,62], to the differences between on-cycle and real load transients and to additional loads (i.e., air conditioning), especially on small vehicles [60]. Furthermore, there is an evident tendency for recent vehicles to increase this gap [60]: as the legislation becomes more demanding, OEMs tend to refine the vehicle set-up to pass type-approval tests, with the result that the loads reproduced on the roller test bench underestimate the behavior of real vehicles. The above-cited study by the JRC showed that the percentage exceedance of the limits has been increasing as the regulations became tighter, from a small discrepancy on Euro 4 cars with respect to declared type-approved fuel economy, to an average 8%

and 11% on Euro 5 and Euro 6, respectively [14]. Another study based on a wide database of European cars circulating on the roads, has shown a difference of about 8-9% between type-approved fuel consumption and real-world one in 2001, and up to 40-42% in 2014 ([63] as cited by [19, 15]). This means that, although the reduction of 28% in declared fuel consumption from 2001 to 2014, the real-world fuel economy only improved by 7% in the same period [19]. Notice that the huge difference between the JRC data and the last cited work stems from the different testing conditions: the latter study is referred to data acquired on roads on normal usage of the vehicles, while the JRC data refer to tests performed on NEDC cycle on roller test benches. Therefore, JRC tests have been nominally performed in the same testing conditions as type-approval procedure at the time of writing, and the difference between JRC figures and type-approved values stems only from the different equipment of the on-market vehicles with respect to type-approved ones.

The above-mentioned WLTP/WLTC have been studied and implemented also for the evaluation of vehicles fuel economy [14, 15, 19]. Although some previous studies on the WLTC showed almost no change in total CO₂ emissions by moving from NEDC to WLTC ([64-66] as cited by [14]), i.e. by applying the new driving cycle with same test conditions as for the NEDC, the abovementioned JRC study has demonstrated as a large difference between the old and the new test procedure exists if not only the cycle, but the whole procedure, is applied [14]. The JRC tested thirty-one vehicles, and for each of them chose a “best case” and a “worst case” in terms of test masses and road load, thus representing the lower and upper boundaries for testing the vehicle. In average the WLTP increased fuel consumption by $11\% \pm 6\%$ with respect to the NEDC in the “worst case” testing condition, and $1\% \pm 5\%$ in the “best case” one [14]. Diesel-based vehicles showed a larger worsening than gasoline ones, the former having generally an higher vehicle mass and being therefore more sensitive to the tightening of the test conditions in terms of test mass, rolling resistance and inertia [14]. Overall, testing the vehicles on WLTP increases the fuel consumption values about 15% with respect to current CO₂ emissions limits, and is expected to close the gap between declared values and in-use fuel economy [14]. Anyway, in order to maintain the limits set for CO₂ emissions with the current regulations, for the first period after the introduction of WLTP in 2017, the values measured on WLTP will be translated into NEDC-equivalent CO₂ emissions by means of a dedicated software tool developed by the JRC [15, 53]. RDE testing will not be applied, at the moment, for type-approval procedure on CO₂ emission testing, but PEMS CO₂ measurements on RDE will be used for monitoring purposes [15].

In December 2015 the Conference of Parties, still within the UNFCCC, signed a new agreement to define the maximum limit to the increase in the average global temperature to 2°C with respect to pre-industrial levels, in order to avoid

catastrophic consequences on the climate [67]. This agreement needs to be translated in effective solutions that can allow the fulfillment of this target without negative (and possibly with positive) effects on the quality-of-life de facto standards, including the field of transportation.

Impact of engine and vehicle technologies on fuel economy

The abovementioned desired reduction in fuel consumption passes through improvements in various fields: from the usage of lightweight materials to engine downsizing and improvement to the combustion efficiency, as well as improvements in aerodynamics, tires-to-road rolling resistance, reduction of powertrain frictions and parasitic losses in general, including those due to accessories [8, 10].

If the required fuel consumption reduction for 2025 targets would be addressed only by means of improvements in the engine, transmission and driveline, the overall efficiency of the propulsion system should be about 35%, which means 30% and 11% reduction on fuel consumption on the best on-market gasoline and diesel engines, respectively ([68] as cited by [19]). For what concerns engine technologies, direct injection high-speed diesel engines have been the reference for fuel economy thanks to the high thermal efficiency [69]. The introduction of new technologies such as variable valve timing and variable valve actuation was estimated to produce a 3-5% fuel economy improvement, while cylinder deactivation and start-and-stop strategies are expected to improve fuel economy by 7.5% and 8%, respectively [8]. Managing efficiently the engine operating conditions thanks to the increase of the number of gear ratios allowed a reduction in fuel consumption by 6-10% [68], while infinite gear ratios through continuously variable transmissions is expected to increase the fuel efficiency by about 10% [69]. Another relevant trend is relative to engine downsizing, coupled to power boosting through turbochargers and superchargers [8]. Comparing data from production gasoline vehicles in the period 1992-2003, it was shown that turbocharging allows to reduce engine displacement by 30-50%, with a consequent benefit by 10.5-12.5% on fuel consumption for a 150 kW gasoline turbocharged engine with respect to a naturally aspirated one with the same power [70]. A possible improvement of 18% in fuel economy was also shown with high pressure boosting and with 40% engine downsizing, with a possible additional improvement by 9% that could be obtained by means of a variable compression ratio (VCR) mechanism, which allows high boosting at high loads with a low compression ratio to avoid the risk of knock, while improving the low-end torque characteristic by increasing the compression ratio at low loads [70, 71]. A further fuel reduction by 15% can be obtained by means of regenerative braking [69]. Also, technologies for heat recovery from exhaust gases are widely studied as a mean to improve the vehicle energy balance, e.g. through

the application of a Rankine cycle using an organic oil with high molecular mass in order to improve the efficiency of the cycle (namely, organic Rankine cycle, ORC): according to the working condition, 5-13% of the thermal energy in the exhaust flow can be converted in electric energy to be stored on board [72-74] and used in a mild-hybrid layout.

Gasoline engines are getting closer to the fuel efficiency of diesel ones [19]. Brake thermal efficiency figures up to 40-45% have been experimentally reached on gasoline engines thanks to turbocharged downsized GDI engines, possibly implementing high compression ratios and lean-burn strategies to achieve a fast and efficient combustion, and with the usage of cooled EGR to allow the combustion to occur closer to TDC due to larger knock tolerance ([75, 76] as cited by [19]). Also diesel engines show a potential reduction of fuel consumption up to 15% with improvements in combustion efficiency, combustion chamber, frictions, etc [19]. More recently, the diversification of energy sources, with the introduction on the market of hybrid and electric vehicles, also represents a strong driver through the reduction of CO₂ emissions [8, 10]. Anyway, especially in the field of light and heavy commercial vehicles, diesel engines nowadays represent almost the entire market and are expected to be the leading on-market technology also for the next years. In the near future, CO₂ emissions target in the EU and the US are expected to be mostly met through some extent of hybridization and through diesel engines, also considering that the expected improvements required on diesel engines are still the most cost-effective ones for mass-production, both compared to hybridization and to improvements required in gasoline engines [19]. Nevertheless, future markets will also be strongly influenced by recent limitations set by the Governments of various States to specifically limit the circulation of diesel vehicles in urban areas, which would potentially mainly affect the market of diesel passenger cars in Europe.

Concerning vehicle technologies, a number of studies have shown the sensitivity of fuel consumption to various vehicle parameters. It was shown that about 5% of the fuel energy is spent to overcome air drag, and 33% is dissipated into frictions, including tire-road contact (11% of the total fuel energy), frictions in engine and transmission (17%) and frictions in brakes (5%) [77]. New technologies, including coatings and texturing of mechanical components, advanced lubricants and additives, and tires with lower width and higher inflation pressure, could reduce the friction losses by 18% in the short term and by 61% in the long term [77]. A parametric study conducted on 5 gasoline and 5 diesel vehicles has shown how fuel consumption varies with a variation in vehicle gross weight, aerodynamic resistance, rolling resistance and engine full-load characteristic [78]. The selected vehicle characteristics were parametrically varied, one factor at a time, by $\pm 10\%$

with respect to the reference value for each of the selected vehicles, and the analysis involved computer simulations on a number of different driving cycles characterized by different average speeds. The study shows that a 10% reduction in vehicle mass brings a reduction between 3% and 6% on fuel consumption, with a larger effect on those driving situations that show a highly transient behavior with respect to high-speed cycles with less transients. A reduction by 10% in the aerodynamic or rolling resistance was shown to reduce fuel consumption up to 5% and 3%, respectively, in high-speed driving cycles, while in low-speed driving modes the said reduction in rolling resistance reduces fuel consumption by about 1% and changes in aerodynamics are negligible. Changes in the full-load characteristic was shown to be significant on fuel consumption only for the smallest tested gasoline engine, and especially in highly transient conditions, while revealed to be uninfluential for bigger engines for which full-load conditions were not frequent with the selected test cycles [78]. Similarly, a 10% combined reduction of rolling resistance, vehicle mass and aerodynamic drag was estimated to improve by 4% the fuel efficiency of a naturally aspirated gasoline vehicle and by 8% that of a DI diesel one [69]. Optimizing the combined effect of wheel mass and wheel aerodynamic was shown to reduce fuel consumption by 1.8-2.1% [79].

An important role in the field of fuel economy improvements is played by tires. In road transportation, pneumatic tires represent the connection between the vehicle and the ground. Tire-road contact and tire deformation are therefore responsible for grip (related to power traction) as well as for rolling resistance (related to power dissipation), both of which are related to energy utilization. In general, an increase in the propensity of a tire to dissipate energy is considered to be beneficial from the grip point of view and detrimental for rolling resistance. Nevertheless, the two phenomena are decoupled, since they are related to different excitation frequency ranges [77, 80]. In fact, the frequency of the tire rubber deformation during rolling (which affects the tire rolling resistance) is much lower than during sliding (i.e., when braking), as the first is in the order of magnitude of the ratio between the vehicle speed and the length of the contact patch, and the latter is almost equal to ratio between the slip velocity and the diameter of a contact point between an asperity of the soil and the tire rubber [77]. Therefore, it is possible to obtain a tire that performs properly in the two frequency domains by properly defining the viscoelastic modulus of the rubber, i.e., by optimizing the ratio between the imaginary and the real parts of the viscoelastic modulus so that the ratio is as small as possible in the rolling frequency domain and as high as possible in the sliding frequency domain.

This complex role played by the tire makes it central for automotive safety and fuel economy. Given the geometry, structure and composition of a tire, the tendency

to dissipate energy depends on many different factors, including the tire temperature and inflation pressure, the vehicle speed and loading conditions and the characteristics of the road surface [80-84]. “Green tires” [85] represent an example of the efforts that have been made by manufacturers: the average reduction in rolling resistance obtained by replacing carbon black with silica in the rubber composition of the tire is about 3.5 kg/ton (expressed as kg of resistance force per 1 ton of vertical load acting on the tire), which corresponds to a reduction of 3.2-5.1% in fuel consumption, depending on the driving conditions [83]. Also tire inflation pressure has been proven to have an important effect on real-world fuel economy and, as a consequence, on the actual CO₂ emitted by the circulating fleet: a survey conducted in the US in 2007 [86] revealed an average loss of between 0.162 and 0.216 mpg in urban driving, and of between 0.216 and 0.288 mpg in highway driving, due to a general under-inflation of the tires. The data can be considered even more dramatic if it is taken into account that 78% of European drivers run vehicles with underinflated tires [87], and only 30% of the drivers in the US check their tire pressure regularly [88]. The compulsory labeling of tires related to fuel economy [89] and the prescribed installation of tire pressure monitoring systems (TPMSs) on new vehicles of the M1 category (passenger cars) [90] are examples of European legislation interventions, while analogous regulations have been set up in other countries, including the US [91] and South Korea. This generates a direct effect on real-world driving, in terms of improved both in-use vehicle economy and safety, and is aimed to correct inappropriate drivers’ behavior. Anyway, as TPMS only provides an indication about current tire pressure and alerts the driver when pressure is too low and the driver is still in charge for manually adjusting tire pressure, it does not ensure that all the vehicles equipped with TPMS have tires inflated at the proper pressure. Additionally, TPMS do not adjust tire pressure to the vehicle working conditions and their accuracy (for both direct and indirect models) is generally low.

Proposed work and aim of the dissertation

This general scenario clearly shows that the reduction of pollution and the increase in fuel economy have been two leading factors in the development of the automotive technologies at least in the last sixty years, and – also due to the regulatory framework – have strongly influenced the market and shaped the needs and the preferences of the customers. Drivers are conscious that mobility is growing over the years due to the growth of world population and due to the globalization of commerce and of human mobility, but are also aware about the need for the reduction of greenhouse gas emissions [92,93]. The perception of the importance of fuel economy is increasing and is becoming important also during vehicle purchase decisions. Technologies are assumed to penetrate the market based upon

a cost-effectiveness algorithm that compares the technology cost to the discounted stream of fuel savings and the value of performance to the consumer [94]. Therefore, the lower is the cost for the realization and the installation of an innovative technology, the higher the market share will be: for instance, variable valve timing, and 6-speed transmissions have been introduced on the market with a low impact on the cost and nowadays cover respectively 96% and 64% of market share [94]. Annual driven distance and fuel price are the two most significant parameters influencing consumers' cost-benefit result. On the other side, consumers often undervalue the benefits related to fuel economy, as they do not have sufficient awareness and proper habits to conduct a correct economical analysis to quantify the cost of fuel consumption and the economic effects of improved fuel efficiency, while they generally recognize that the value of fuel economy improvements is not merely economic but concerns environmental sustainability, and therefore assume a positive meaning [93]. Therefore, sustainable mobility is becoming an important goal for the automotive industry, both due to the need to comply with the standards imposed by regulations and in terms of customers' value.

Therefore, the role of Automotive Research nowadays is to propose technologies that are able to comply with the requirements set by the described context. Pollutant emissions and fuel consumption cannot be treated as two separate issues, as solutions designed for one aim may be beneficial or adverse for the other. As an example, it was already mentioned that the reduction of tires rolling resistance is first meant to improve fuel economy but also has a positive impact on tailpipe emissions [38,39], while the application of particulate filters usually results in an increase in fuel consumption due to increased engine back-pressure and due to the need for filter re-generation [95]. Similarly, as already mentioned, the introduction of GDI engines allows to increase engine efficiency, but increases PM/PN emissions of gasoline engines [15], as well as NO_x emissions in case of lean engine operation [69]. Therefore, a comprehensive view is needed to evaluate each technology in terms of its effect on both the topics. As a positive impact on pollution and fuel consumption is possible both through interventions on the powertrain efficiency and on the vehicle power demand, engineers and researchers, who are typically focused on a single specific field of the vehicle development, should also get familiar with the view of the vehicle as a whole: a complex of sub-systems that interact and influence each other, and that further interact with the external environment, including the market, the infrastructure, the drivers and the passengers.

The need for a global view of the "vehicle as a whole", while keeping significant details on specific technologies, is the prime mover of this dissertation, whose aim is to present the development of two different technologies, one related to internal combustion engines and the other related to the reduction of the vehicle

power demand. The two technologies have been developed aiming at applying both of them on the same vehicle to demonstrate their combined effect on the reduction of fuel consumption and pollutant emissions. More in detail, this thesis will discuss about an experimental work related to the implementation of an advanced diesel combustion strategy aiming at a NO_x -less and soot-less combustion, and about the development of an automatic system for smart and autonomous management of tire inflation pressure of vehicle tires, whose target is to avoid tire misuse and adapt tire pressure to the vehicle working conditions in order to reduce fuel consumption and improve vehicle safety and drivability. The former experimental activity has shown the potentialities of premixed charge compression ignition (PCCI) combustion on the reduction of NO_x and particulate, but also highlighted the weakness of this kind of combustion in terms of engine-out emissions of HC and CO and in terms of increased fuel consumption. While the increase of HC and CO emissions could be effectively compensated by proper after-treatment devices, the increase of fuel consumption can be partially neutralized by the reduced need for regeneration of the DPF. Additional benefits can be achieved if the PCCI combustion is coupled to any reduction of the vehicle energy demand, such as the abovementioned device for tire pressure management. Furthermore, the latter can have additional benefits on the reduction of tire wear and, as a consequence, on non-exhaust particulate emissions. Also, a reduction of NO_x could be achieved thanks to the reduction of the rolling resistance.

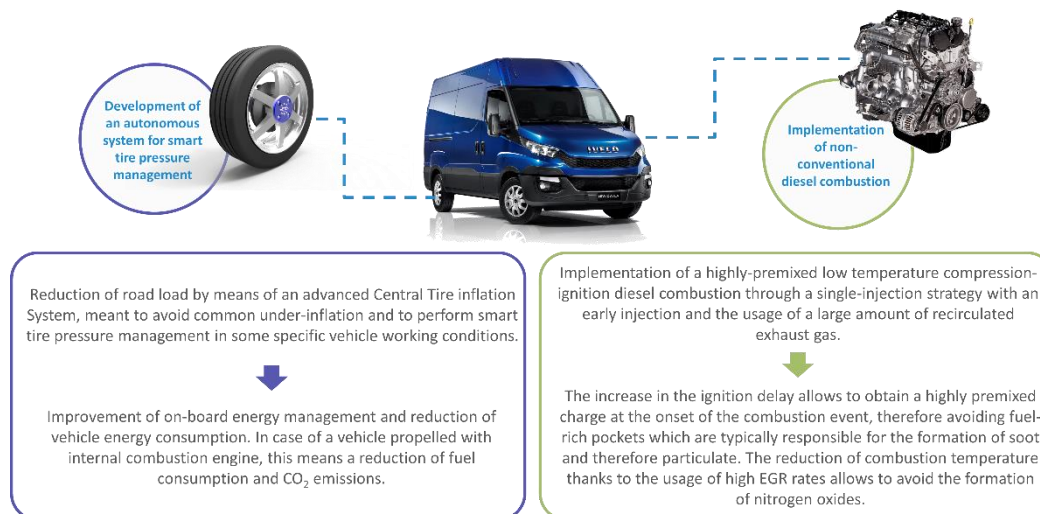


Figure 3: Objectives of the dissertation and fields of the current work.

The PCCI work has been developed in collaboration with FPT Industrial, targeting the implementation of such a type of combustion on a light-duty commercial vehicle (LDV). The tire pressure system was initially developed for the application on passenger cars and later also developed for commercial vehicles (both light-duty and heavy-duty) in a project in collaboration with Iveco. For the latter, the effect on fuel economy of passenger cars and commercial vehicles endowed with standard diesel engines has been assessed by means of a dedicated software tool for the estimation of fuel consumption, developed to account directly for the effect of tire pressure on road load. Finally, experimental data from the test-bench activity on the PCCI project have been used to simulate the combined effect of the two technologies on a light-duty commercial vehicle. The thesis has been therefore organized as follows:

- *Chapter 1* discusses about the experimental methodologies developed to implement the PCCI combustion and the related experimental results. The study has been first performed in a preliminary form by working on a standard on-market diesel engine, and later extended to a prototype version of the engine, specifically developed for the implementation of PCCI combustion. Experimental figures related to fuel consumption and gaseous emissions from steady-state tests are shown for both the engine configurations. Additionally, a model-based combustion control algorithm has been tested on the standard engine, both on steady-state and on transient tests, as a mean to improve combustion stability and therefore fostering the implementation of advanced combustion strategies. Moreover, as the control of EGR mass flow rate is a critical variable for implementing and controlling the PCCI combustion, control-oriented models for the estimation of EGR flow rate have been tested on the standard engine both in conventional diesel combustion mode and in PCCI combustion mode.
- *Chapter 2* shows the development of the tire pressure management system. Fuel consumption simulations were initially performed using an existing simulation tool that does not take directly into account tire pressure, therefore the effect of tire pressure variation was simulated by re-calculating the vehicle road load (i.e., the coast-down parameters) to account for the effect of tire pressure on rolling resistance. In order to apply the study to commercial vehicles, the same approach was then extended and implemented on a dedicated software tool. Such a tool is based on a kinematic vehicle model to define the engine working conditions starting from the vehicle mass and the road load in a specific condition, and then interpolates in experimental fuel consumption steady-state maps to obtain the instantaneous fuel consumption. Then, the design of the system for a passenger car (named Active Tire

Pressure Control, ATPC) and its impact on fuel consumption will be discussed. Finally, the preliminary design of the system for commercial vehicles (named Advanced Central Tire Inflation System, ACTIS) will be briefly presented.

- *Chapter 3* is devoted to the integration of the two technologies on a light commercial vehicle. Their combined effect is evaluated by means of computer simulations based on the said software tool, which has been further adapted to also simulate the effect on pollutant emissions, estimated by interpolating experimentally-derived maps. The overall effect is evaluated on some single driving cycles, and on an annual mission, the latter being intended as an assessment of the final effect on the total cost of ownership of the vehicle.

In order to perform estimations of on-cycle fuel consumption and pollutant emissions in *Chapter 2* and *Chapter 3*, a number of driving cycles have been simulated. Some of these cycles are those used in the abovementioned type-approval procedures, including the NEDC, FTP 75, HWFET and US06. Other used cycles are custom cycles defined with Iveco to be representative of real usage of the commercial vehicles in some reference missions. In any case, when the type-approval driving cycles are used, their application is purely intended as a way to have some reference speed-load profiles to compare the tests. Therefore, the cycles have been applied using various test masses that are representative of various loading cases of the vehicles and using a plurality of tire rolling coefficients both related to different tires, or to the same tire applied at different tire pressures, wear and loading conditions. Therefore, in none of the cases that will be reported, the application of a type-approval cycle can be intended as an application of the proper type-approval procedure. Moreover, as most of the cycle-based results that will be shown are obtained only by means of simulations, some effects which were not considered crucial for a preliminary analysis – such as the engine cold starts and the effect of ambient temperature – have been neglected. Therefore, the simulated results may differ from values measured during type-approval procedures or independent tests in similar conditions of those declared for simulations, also due to possible inaccuracies in the calculations. Nevertheless, although possible inaccuracies in the absolute values resulting from simulations, the relative difference between the compared cases are considered significant and relevant for the proposed analysis. For this reason, and for confidentiality of the data provided by Iveco and FPT, the results of the simulations in *Chapter 2* and *Chapter 3* will be only shown as percentage variations with respect to a baseline case.

Chapter 1²

Implementation of a non-conventional diesel combustion mode on a 3.0 liters engine for a light-duty commercial vehicle

The commercial sector involves about 335 million vehicles throughout the world [96] and includes heavy-duty vehicles and commercial vans. In Europe, 29 million vans and 6.5 million trucks deliver 14 billion tons of goods every year, i.e., 75% of all goods carried over land [97-99]. Despite the efforts that have been made to promote new powertrain technologies, possibly not based on fossil fuels, most of the commercial vehicles are powered by internal combustion engines fueled with diesel (98% of the trucks and 96% of the vans in Europe), while alternative powertrains only cover a very small market share [97, 98]. If compared to gasoline

² Most of the contents of this *Chapter* have been previously published in:

d'Ambrosio, S., Iemmolo, D., Mancarella, A., and Vitolo R., "Preliminary optimization of the PCCI combustion mode in a diesel engine through a design of experiments". Energy Procedia 101 (2016) 909 – 916, <https://doi.org/10.1016/j.egypro.2016.11.115>. In: 71st Conference of the Italian Thermal Machines Engineering Association, ATI2016, 14-16 September 2016, Turin, Italy

d'Ambrosio, S., Iemmolo, D., Mancarella, A., Salamone, N., Vitolo, R., Hardy, G., "Performance and Emissions Comparison between a Conventional Euro VI Diesel Engine and an optimized PCCI Version", SAE Technical Paper 2018-01-0221, 2018, <https://doi.org/10.4271/2018-01-0221>. In: SAE WCX 2018, April 10-12, 2018, Detroit, Michigan, USA

Spessa, E., d'Ambrosio, S., Iemmolo, D., Mancarella, A.; Vitolo, R., Hardy, G., "Steady-State and Transient Operations of a Euro VI 3.0L HD Diesel Engine with Innovative Model-Based and Pressure-Based Combustion Control Techniques", SAE Int. J. Engines 10(3):1080-1092, 2017, <https://doi.org/10.4271/2017-01-0695>.

d'Ambrosio, S., Iemmolo, D., Mancarella, A., Salamone, N., Vitolo, R., Hardy, G., "Zero Dimensional Models for EGR Mass-Rate and EGR Unbalance Estimation in Diesel Engines". SAE Technical Paper 2017-24-0070, 2017, <https://doi.org/10.4271/2017-24-0070>. In: SAE 13th International Conference on Engines and Vehicles, ICE 2017, Capri (Italy)

Some parts of the introduction to this *Chapter* is also retrieved from:

d'Ambrosio, S., Mameli, E., Vitolo, R., Calaon, I. et al., "Fuel Consumption Reduction on Heavy-Duty and Light-Duty Commercial Vehicles by Means of Advanced Central Tire Inflation Systems", SAE Int. J. Commer. Veh. 11(5):267-289, 2018, <https://doi.org/10.4271/2018-01-1334>.

engines, diesel ones show higher thermal efficiency, lower brake specific fuel consumption (bsfc) and CO₂ emissions, which makes them a preferential choice for both light-duty and heavy-duty commercial vehicles. Moreover, they ensure higher durability, higher reliability and lower pumping losses. Anyway, diesel engines suffer from high particulate matter (PM) and nitrogen oxide (NO_x) emissions: lowering these species in exhaust gases has long been a challenge, and still remains a major issue [100]. In Europe, the diesel transport sector is the largest contributor (about 40%) to the total ambient NO_x concentrations [17]. After-treatment technologies have proven to be effective for the abatement of NO_x and soot emissions. The currently available after-treatment technology is able to fulfil the Euro VI emission standards, but it leads to very high costs, in terms of research, development and maintenance, and to difficulties in engine packaging. These are important factors that have to be considered for future vehicles. Two main after-treatment technologies are currently available for NO_x abatement: lean-burn NO_x absorbers, which are also called lean NO_x traps or LNTs [101], and selective catalytic reduction, i.e. SCR [102]. In the former case, NO_x is absorbed by a catalyst during lean engine operations. When the catalyst is saturated, the system is regenerated over short fuel-rich condition periods, during which NO_x is catalytically reduced. In an SCR, a catalytic medium reduces NO_x to gaseous nitrogen and water in the presence of ammonia. However, in both cases, high costs, packaging and control issues still represent major drawbacks.

Although the vast majority of heavy-duty vehicles are able to fulfil Euro VI standards by means of the abovementioned after-treatment systems (ATS) [103], the current combustion engine technologies also make it possible to reduce engine-out emissions by adjusting the combustion process. Therefore, in-cylinder advanced combustion strategies have been widely investigated, with the aim of simultaneously reducing engine-out NO_x and soot emissions, thus minimizing, or even avoiding, the need for the employment of the above mentioned after-treatment technologies [28].

Low NO_x emissions can be accomplished through a combination of aggressive exhaust gas recirculation (EGR), compression ratio (CR) reduction [104] and variable valve lift and combustion chamber reshaping. Most of these in-cylinder techniques lead to penalties for the unburned hydrocarbon (HC) emissions, particulate matter emissions and fuel consumption. It is common practice, in diesel engines, to refer to the NO_x/PM trade-off [28] or the NO_x/bsfc trade-off: reducing NO_x emissions generally leads to an increase in PM emissions and in fuel consumption, and vice versa.

In direct-injection, conventional diesel combustion (CDC) fuel is injected during the last part of the compression stroke, just a few crank angle degrees before

the top dead center (TDC). The fuel spray atomizes, evaporates and mixes with the charge, which is made up of air, residual gases and, when is employed, recirculated exhaust gases (EGR). When the fuel auto-ignition temperature is reached, thanks to the compression caused by the piston, which moves toward the TDC, a portion of the mixture burns under premixed conditions and this portion is marked by a sharp cylinder pressure increase. The time interval between the start of the hydraulic injection and the start of combustion (SOC) is commonly referred to as ignition delay (ID). The term “premixed combustion” refers to the combustion of the portion of the fuel injected during the ID period. The fuel that does not participate to premixed combustion burns under diffusive combustion, i.e., a rate-controlled combustion, in which the consumption rate of this fuel is controlled by its rate of injection and its subsequent mixing with air.

In order to achieve a simultaneous reduction of both NO_x and PM emissions, new combustion concepts, which are generally defined as Low Temperature Combustions (LTC) [105], are emerging, with the aim of lowering the combustion peak temperatures. The potential advantages of LTC, with respect to conventional combustion, are related to the utilization of diluted mixtures, either with excess charge gas or with moderate to high EGR levels. This determines the absence of localized high temperature areas and high equivalence ratios, as a result of the homogeneity of the mixture, which allows the combustion process to prevent the formation of the NO_x and PM zones shown in the equivalence ratio vs. temperature (Φ -T) plot [106]. Different LTC strategies have been proposed in the literature. Homogeneous Charge Compression Ignition (HCCI) refers to a combustion mode in which the vaporized fuel is mixed with the charge gas prior to the end of the compression, thus obtaining an overall lean and homogeneous mixture. However, this is not a practical alternative to conventional diesel combustion, because the ignition event is decoupled from the start of injection (SOI) of the fuel [29], and this results in a more difficult control of combustion. The conditions necessary for low temperature combustion can also be reached by realizing a premixed combustion (even though not completely homogeneous), which is usually defined as Premixed Charge Compression Ignition (PCCI).

A premixed charge can be obtained by directly injecting the fuel into the cylinder and exploiting the effect of dilution by means of EGR [107]. Combustion is controlled by acting on the EGR rate and on the injection timing, according to the considered engine load and speed. PCCI strategies can generally be divided into two categories characterized by advanced or retarded fuel injection timing [27-30,108-110]. In the early injection method, the fuel is injected into the cylinder during the compression stroke, well before TDC, in order to enlarge the ID, and thus to ensure better air-fuel mixing. The latter consists in injecting the fuel after TDC (late injection), thus taking advantage of the expansion phase to increase the

ID, which results in a premixed charge. Under these working conditions, the combustion process and the mechanism of pollutant formation differ significantly from those of conventional diesel combustion. The combined effect of advancing or retarding fuel injections and using high EGR rates (which reduce the oxygen concentration of the intake charge) leads to a slower pre-ignition chemistry, and to a higher ignition delay. This in turn allows a better pre-combustion mixing than conventional diesel combustion [29], hence the formation of rich mixture pockets within the cylinder is avoided, which is the main cause of soot generation [111]. Moreover, high EGR rates diminish flame combustion temperatures, and thus lower NO_x emissions [28,111]. Also in cases where the mixture formation process is not significantly improved, the presence of very high EGR rate lowers in-cylinder temperatures so that the whole combustion process would occur in an area in which both soot and NO_x formation rates are very low [106], referring to an equivalence ratio vs. temperature diagram such as the one proposed by Kamimoto and Bae [112]. In detail, soot particles would not be formed due to the fact that the combustion temperatures are not high enough to allow the evolution of polycyclic aromatic hydrocarbons (PAH) to soot, while the presence of fuel rich pockets will produce a higher amount of unburned components which will result in higher presence of CO, HC (low boiling point fuel-derived particles) and the soluble organic fraction (SOF) which composes the particulate matter (PM) [106]. Late injection, compared to the early injection method, is characterized by a lower mixture homogeneity before SOC [113], while the relation between injection timing and SOC is stronger with respect to the case of early injection, thus making late injection more controllable. Therefore, the advantages of the PCCI combustion mode is the simultaneous abatement of NO_x and soot emissions [114,115]. On the other hand, due to heavily reduced oxygen content, low combustion temperatures and early injections, the formation of incomplete combustion products, such as carbon monoxide (CO) and unburned hydrocarbons (HC) deteriorate [116,117], which leads to the need for a higher conversion efficiency of the diesel oxidation catalyst (DOC) [118]. Penalties in fuel consumption have also been observed [111]. In addition, due to sharp rises in the in-cylinder pressure, high levels of combustion noise (CN) are generally related to PCCI combustion [116,117,119].

Exhaust gas sent back to the intake manifold is usually cooled to increase volumetric efficiency and to lower the charge temperature. Both EGR and the cooled charge air contribute to extending ID [120] and to reducing the peak temperatures responsible for the formation of high NO_x . However, high flow rates of cold EGR increase the SOF in the particle matter [121]. SOF can be treated through a diesel oxidation catalyst, but – on the other hand – it is the main agent, together with soot particles, that is responsible for EGR cooler fouling. The latter is defined as the accumulation of exhaust gas particles on the walls of the heat

exchanger, which forms an insulating layer [122]: this phenomenon is one of the predominant factors in the failure of EGR systems. Lowering the exhaust gas temperatures in an EGR cooler makes the PM deposit increase, especially when high concentrations of SOF are recirculated, as in the case of low temperature combustion [121]. The creation of a deposition layer on the walls of an EGR cooler degrades the heat transfer efficiency [121,123]. Moreover, it can cause an appreciable pressure drop, or even severe clogging [124], thus hindering the flow through the recirculating system. This could be a major problem when PCCI combustion is implemented, as the EGR quantity is one of the most important parameters that needs to be controlled.

One of the main issues of PCCI is the reduced load range over which it can operate. The maximum engine load is limited by intense combustion noise, significant in-cylinder pressure gradients and difficulties in managing very low oxygen concentrations, due to the high rate of EGR [34]. PCCI applications, such as PREDIC, which was developed by New Ace in Japan [125], UNIBUS, developed by Toyota [126] and NADI, developed by Institut Français Du Pétrole (IFP) [127], are not generally able to overcome the 5 bar load of brake mean effective pressure (bmep) [128,129]. This limit is much lower than the maximum load that can be achieved for conventional diesel combustion.

Many researches have been conducted in order to overcome the main limits of PCCI combustion. Some studies were conducted on the effects of CR [104, 130, 131], on increased fuel injection pressure [105], on variable valve timing [132] and on split injection [133], among others, in order to enhance this kind of combustion mode. The fuel properties can also have a profound impact on the performance and emissions of those engines that employ LTC [134-141]. It is necessary to consider that the suitability of a fuel blend depends on many factors, such as the engine features (nozzle characteristics, bowl shape, CR, etc.) and the operating conditions.

The work presented in this *Chapter* is devoted to the implementation of a PCCI combustion mode, featuring a single early injection strategy, to a four-cylinder, four-stroke 3.0-liter Euro VI engine for commercial vehicles, made by FPT Industrial. The engine has been tested in two different configurations: first, a production (or standard) version of the engine has been tested both under conventional diesel combustion and in PCCI. Testing the standard engine in PCCI mode was limited to low engine loads due to operational limits discussed above. Therefore, for the second phase of the project, FPT provided a modified version of the engine with hardware modifications that made it more suitable to PCCI combustion up to the medium load/speed range.

The first part (*Section 1.2*) of this *Chapter* will discuss the implementation of the PCCI combustion mode on the standard engine. Statistical design of

experiments (DoE) techniques have been used to find the optimal calibrations. For the sake of conciseness, only the results relative to one engine working point, namely the one at engine speed $n = 1800$ rpm and brake mean effective pressure $b_{mep} = 1$ bar, will be presented. Similar results were obtained in other working points in the low load/medium speed area. The second part (*Section 1.3*) of the *Chapter* will then show the results obtained by implementing the PCCI combustion mode in the modified engine, in comparison with the results obtained with CDC on the standard engine, in order to show the true potentialities of an optimized PCCI combustion mode. With the modified engine, PCCI working points covered an area of up to medium-high speed and a load of up to around 8.5 bar of b_{mep} . In *Section 1.4* the effects of a model-based and a pressure-based combustion controls are analyzed under steady-state and transient operations and compared to the standard map-based control. Both the models have been tested on the standard engine only, at the moment. As a preliminary assessment of the developed techniques, most of the tests here presented refer to the application of the abovementioned models to conventional diesel combustion, while a set of steady-state tests also involved PCCI combustion mode operations. The robustness of the controls has been assessed in order to evaluate the effectiveness in different working conditions, such as considering different EGR rates and SOI, and disturbing the in-cylinder pressure signal during steady-state tests. Finally, as properly controlling the EGR rate has a crucial role in obtaining the desired combustion mode while avoiding detrimental effects on combustion stability, in *Section 1.5* control-oriented models are proposed and assessed to estimate the real-time EGR rate, both intended as the average EGR in all the cylinders as well as the cylinder-by-cylinder distribution. The influence of EGR rate on combustion metrics is also analyzed. Also the models for EGR rate estimation have only been tested on the standard engine, both in conventional diesel combustion and in PCCI mode.

1.1 Experimental setup

As mentioned above, the activity concerned two different hardware configurations. The first engine, a conventional FPT F1C, homologated for Euro VI regulations and designed to run in conventional diesel combustion mode, is a four-stroke, four-cylinder 3.0L diesel engine manufactured by FPT Industrial, equipped with a single-stage variable geometry turbocharger (VGT), a high-pressure common-rail injection system and a short-route cooled EGR system. The main technical specifications are listed in Table 1.1, while a simplified engine schematic is depicted in Fig. 1.1. The EGR flow is driven by the pressure difference between the exhaust and the intake manifolds and is adjusted by the actuation of the EGR valve, which affects the cross-section flow area. Should the pressure

difference between the manifolds not be sufficient, an exhaust flap, placed downstream of the turbine, is activated to increase the pressure in the exhaust manifold. Moreover, the exhaust flap is also employed in the vehicle application to effectively shorten the warm-up time of the ATS by increasing the exhaust gas temperature during cold start operations. The ATS system installed on the vehicle is made up of a DOC, a diesel particulate filter (DPF) and an SCR system, while no ATS system was installed in the test bench applications, and the backpressure it causes in the vehicle was reproduced by a throttle valve placed at the cold-end of the exhaust line. As this engine has been designed to run under conventional diesel combustion mode, the desired PCCI combustion mode can only be implemented for quite low loads, and for low to medium rotational speeds.

A modified engine, here referred to as F1C PCCI, has been derived from the conventional F1C Euro VI engine, and it was specifically designed to run in PCCI combustion mode. Low temperature combustion is achieved by means of an early single-injection strategy and high levels of EGR. For this reason, some engine parts were redesigned accordingly. The combustion chamber (bowl shape, compression ratio, injector geometry) was optimized to reach a PCCI combustion mode of up to 9 bar of bmep. The design of the new combustion chamber was developed by FPT Industrial basing on 3D CFD combustion models developed in a parallel project by FPT Industrial in collaboration with the Politecnico di Milano [142-144]. The prototype of the F1C PCCI engine was fully produced and assembled by FPT Industrial, and provided to the Politecnico di Torino for research purposes. The details of the hardware modifications are summarized hereafter, and also reported in Table 1.1:

- the compression ratio was reduced from 17.5:1 to 14.6:1, with the aim of lowering the in-cylinder pressure and temperature conditions before the combustion event and the resulting flame peak temperature, which are the main parameters responsible for engine-out NO_x emissions;
- a modified piston bowl was designed to be more suitable for fuel spray-air mixing for advanced injection timings (Fig. 1.2);
- new injectors were installed, with reduced cone angles (cf. Fig. 1.2) and lower static flowrate (cf. Table 1.1), which was purposely considered to reduce the risk of cylinder wall impingement, as the reduced compression ratio and the generally advanced injection timings tend to increase the liquid penetration of the fuel spray inside the combustion chamber;
- the original EGR cooler was replaced by a larger one, from a production 11-liter displacement engine, to allow a greater cooling power for the high EGR mass flow rates that are usually involved in PCCI operations. Moreover, the

EGR cooling circuit in the F1C PCCI was separated completely from the engine cooling loop so as to provide a precise control of the exhaust gas temperature at the EGR cooler outlet (the tests on the F1C PCCI engine were carried out at a roughly constant gas temperature set at 85°C);

Engine type	FPT F1C Euro VI diesel	FTP F1C PCCI
Number of cylinders	4	
Displacement	2998 cm ³	
Bore / stroke	95.8 mm / 104 mm	
Rod length	160 mm	
Compression ratio	17.5 : 1	14.6 : 1
Valves per cylinder	4	
Turbocharger	Single-stage variable geometry turbine type	Single-stage variable geometry turbine type (smaller turbine with respect to the Euro VI diesel version)
Fuel injection system	Common rail injection system	
Injector static flowrate	990 cm ³ in 30 s at 100 bar	750 cm ³ in 30 s at 100 bar
Injector cone angle	139.8°	130°
EGR circuit type	Short-route, high pressure, cooled	
EGR valve type	poppet	throttle
EGR cooler	Max thermal power: 6kW Cooling water circuit integrated with block coolant circuit	Max thermal power: 32kW Dedicated external circuit for the cooling water

Table 1.1: Technical specifications of the conventional F1C Euro VI diesel engine and of the PCCI version of the engine.

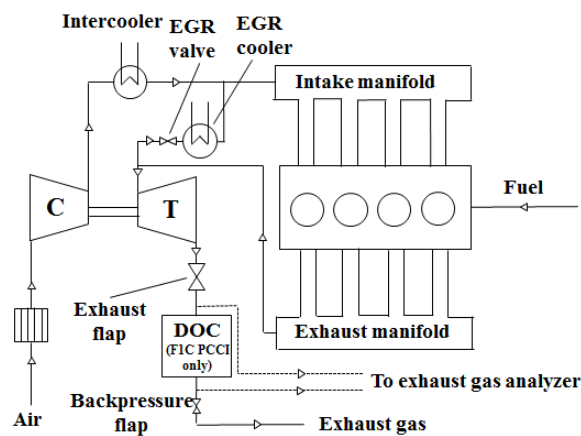


Figure 1.1: Simplified schematic of the engine installations at the test bench.

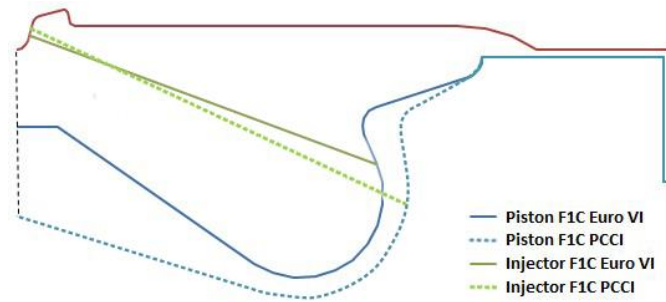


Figure 1.2: Section view of the piston bowl and injector spray edge of the F1C Euro VI and the F1C PCCI engines.

- the EGR poppet valve installed on the conventional hardware was replaced by a throttle valve, with the aim of increasing the maximum cross-section area and the resulting EGR mass flowrate toward the intake manifold;
- a smaller turbo-group was specifically designed and implemented for higher boost levels at lower engine loads;
- the ATS of the F1C PCCI engine was only endowed with a DOC.

On the software side, the standard engine is equipped with its reference software, where the original on-market calibration was originally present. This software and its calibration were used for testing in CDC, while some of the engine calibration maps and parameters were changed according to the need to obtain the desired PCCI combustion mode. In some specific activities aiming at testing some engine control functions, that will be discussed later in this *Chapter*, dedicated configurations were used to bypass some original functions of the conventional electronic control unit (ECU) by using dedicated electronic hardware and the related software: these specific configurations will be shown in a dedicated *Section* of this *Chapter* (cf. *Section 1.4.2*).

Referring to the software for the PCCI version of the engine, the same base software was used but the original air control implemented on the ECU of the F1C Euro VI was excluded and replaced by a dedicated rapid prototyping device, which was employed to control the position of the EGR valve and VGT actuators, independently of the conventional ECU.

The pressure and temperature were measured at different positions of the flow path (such as upstream and downstream of the turbocompressor, in the turbine and intercooler, as well as in the intake manifold and in the EGR circuit), by fully instrumenting both engines with several low-frequency piezo-resistive pressure transducers and thermocouples. Four Kistler 6058A high-frequency piezoelectric pressure transducers were placed in glow-plug adapters to acquire the combustion

chamber pressure traces of each cylinder on a crank angle basis. The latter piezoelectric sensors have a measuring range up to 250 bar, and a sensitivity of about -17 pC/bar, with a maximum sensitivity shift of $\pm 0.5\%$ with temperature up to $200 \pm 50^\circ\text{C}$ (at the sensor flameguard), which ensures a good thermal stability of the measurement with temperature. The piezoelectric signals are amplified through an AVL MicroIFEM indicating amplifier, with a hardware low-pass filter at 100 kHz and a linearity error lower than 0.01% of the full-scale output (14400 pC). The amplified signals are acquired at an angular frequency of 10 samples/ $^\circ\text{CA}$. In-cylinder pressure sensors are pegged on the signal of the intake manifold pressure measured by means of a high-frequency Kistler 4007C piezo-resistive transducer, with a measuring range of 0-5barA (absolute pressure), having an integrated amplifier and a digital compensation of the measurement with temperature in the range between 25°C and 180°C . The piezo-resistive sensor is located in front of cylinder #1, and its signal is also acquired every 0.1°CA . Similarly, also a water-cooled high-frequency Kistler 4049B piezo-resistive sensor is installed in the exhaust manifold, with a measuring range between 0 barA and 10 barA. All the high-frequency pressure sensors are acquired through the AVL indicating system Indicom, and phased on the crank angle basis by means of an AVL 350C encoder which provides a TTL signal with 720 pulses/round to an AVL 365Z01C pulse converter, thus acquiring angular position of the crankshaft with a resolution of 0.5°CA .

The test bench equipment consists, inter alia, of a cradle-mounted AC dynamometer and an AVL KMA 4000 fuel flowrate system, which is able to perform a continuous measurement of the engine fuel consumption with an accuracy of 0.1%. The raw gaseous emissions from the engine can be measured by means of two complete AVL AMAi60 measuring analyzers, both of which are endowed with devices that are able to simultaneously provide gaseous concentrations of NO_x/NO , HC, CH_4 , CO, CO_2 and O_2 . NO and NO_x concentration are measured by means of two heated chemiluminescence detector (CLD), with a measuring range up to 1000 ppm (low concentration range) and a response time lower than 2 seconds. On each of the two measurements streams, a flame ionization detectors (FID) with heated inlet lines and with a measuring range up to 10000 ppmC₃ are used to measure HC and CH_4 , with a response time below 1.2 s. Carbon monoxide and dioxide concentrations are measured through non dispersive infrared measuring instruments (NDIR): for the CO, two different analyzers are used, one for the low concentrations up to 5000 ppm, and the other for concentrations above 5000 ppm and up to 5%, while the CO_2 is calibrated in the measuring range between 0% and 20%. The NDIR devices have a response time within 1.5 s. Finally, the oxygen concentration is measured by means of a paramagnetic sensor, with a measuring range of 0-25% and a response time below 4.5 s. All the gas analyzers

have a reproducibility within $\pm 0.5\%$ of the full scale and a linearity error within $\pm 2\%$ of the measured value (or within $\pm 1\%$ of the full scale, whichever is smaller). A third analyzer is only endowed with a CO₂ measuring device, which is used to evaluate the EGR rate to the engine. As far as soot emissions are concerned, an AVL 415S smokemeter is used for steady-state tests, which has a reading range from 0.002 FSN to 10 FSN with a resolution of 0.001 FSN and a repeatability of $\pm(0.005 \text{ FSN} + 3\% \text{ of the measured value})$. When transient measurements are needed, an AVL 439 opacimeter is adopted. Smoke opacity is evaluated in percentage with a resolution of 0.1%, a rise time of 0.1 s, a linearity error lower than $\pm 0.5\%$ and a zero stability of 0.1% over 30 min of testing. In order to ensure a good accuracy, the zeroing procedure is performed every 30 min of testing. All of the abovementioned measurement devices are controlled by AVL PUMA Open 1.3.2 automation system. AVL CAMEO 3R8 software has been set for automatic tests related to design of experiments (DoE) analysis.

1.2 Preliminary optimization of PCCI on the standard engine through a design of experiments and model-based calibration

The increasing complexity of the phenomena involved in engine technology makes the task of optimal calibration complex and challenging. As a result, there is growing interest in model-based approaches, in which design of experiments, statistical modeling and optimization techniques are employed, as these can simplify and efficiently produce high quality engine calibrations [145].

Experiments at the engine test-bed are expensive and time consuming. Therefore, there is the need for properly designing and planning experiments. For this purpose, DoE is an efficient technique and can lead to significant reduction of the empirical data collection at the test bench. Experiments are expressed in terms of ‘factors’, which are the independent input variables varied at each test point in order to understand the effect on the dependent parameters, known as ‘responses’ [146]. After the selection of the factors of greatest influence based on the physical knowledge of the system under investigation, specific values, or ‘levels’, have to be determined, in order to specify a ‘level-combination’ for each test [146]. Different kinds of designs can be applied when DoE is adopted: classical (including full factorial, central composite designs, etc.), space-filling, and computer-generated optimal designs [147]. The tests obtained with DoE can be analyzed and can provide accurate data to create the statistical models that relate the experimental input factors to the measured response outcomes [148]. Many alternative models

and methods exist, but probably the most adopted is the “response surface methodology”, which generally uses second-order polynomial equations as response surface approximating functions, and least squares regression analysis as a fitting method [146].

If the resulting regression models show a good fit (a correlation coefficient close to one), they can be used to generate an optimal calibration, applying optimization techniques in order to find which input values should be set in order to obtain certain desired outputs. It is possible to set some constraints, and search for an optimum calibration point within the feasible area defined by these constraints [145, 147]. For example, once models for exhaust emissions are defined, it is possible to search the values of the inputs that minimizes NO_x with constraints in terms of CO, soot, etc.

In this work, aiming at implementing the PCCI combustion mode, the statistical techniques of the design of experiments were applied in order to efficiently plan tests, analyze acquired data and provide cause-and-effect relationships about the observed phenomena. First, based on experimental evidence, the variables that mostly influence the ignition delay were identified, which are: the SOI, the EGR rate and the fuel injection pressure. The activity was then performed according to the steps described hereinafter and graphically illustrated in Figure 1.3:

- i. preliminary tests are performed in order to identify which ECU variables are more relevant to reach the desired combustion mode and corresponding variation ranges;
- ii. based on preliminary test results, statistical design of experiments is applied: a variation list is obtained which combines various factors and their values according to a specific DoE technique;
- iii. designed experiments are tested on engine test-bench, and experimental readings are obtained from tests;
- iv. regression models are built on experimental readings, in order to predict desired outputs (emissions, fuel consumption, combustion noise) as a function of selected inputs;
- v. model-based optimization is performed to provide suitable input values to reach desired output targets, which basically consists in inverting the statistical models built on experimental values in order to get the input values (i.e., the calibration values) needed in order to obtain response variables at certain targets or within certain limits;
- vi. optimal calibrations are implemented in the engine ECU are experimentally validated by comparing the measured responses to the expected ones resulting from model-based optimization.

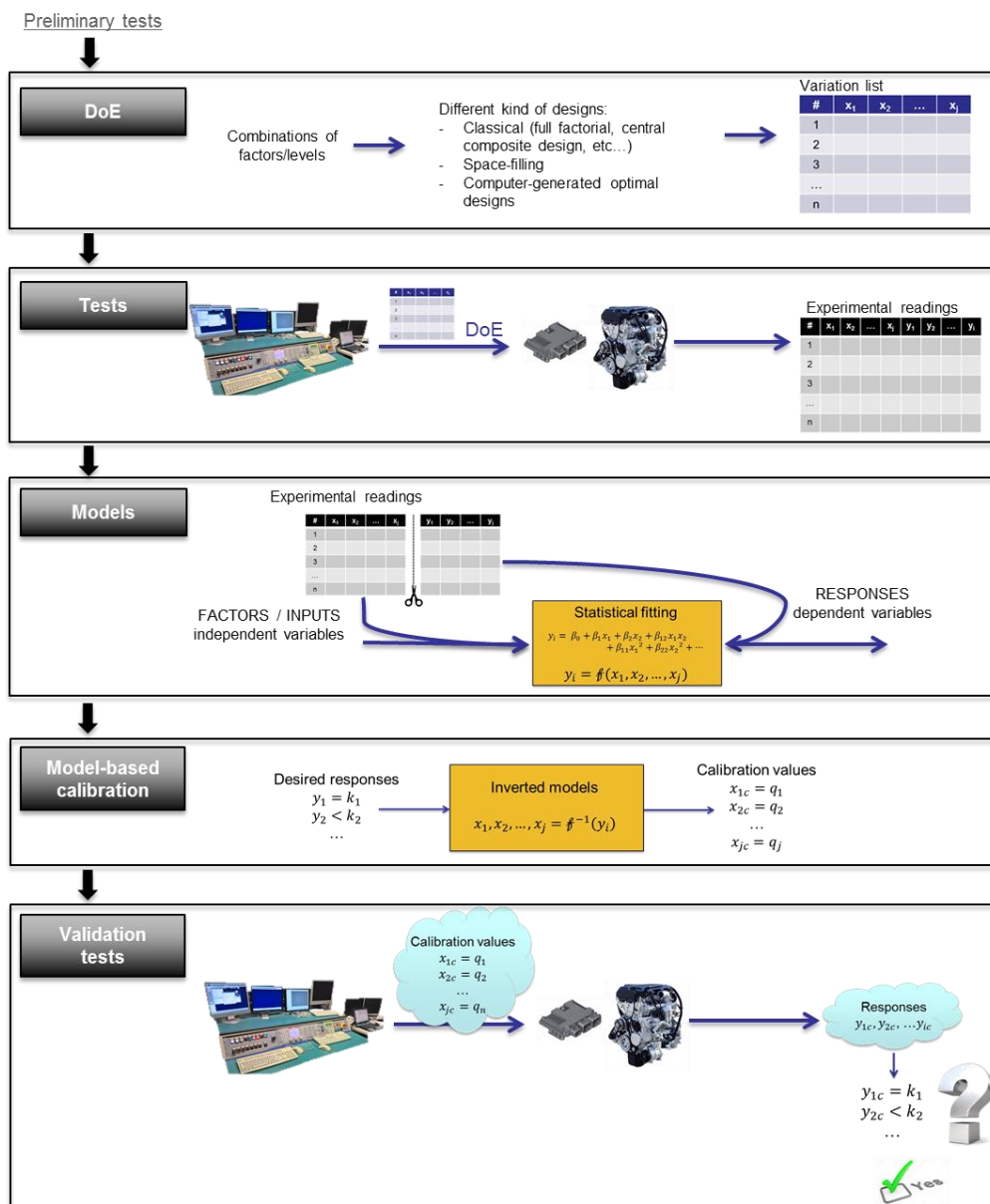


Figure 1.3: Schematic representation of the model based calibration methodology.

In this study, a “V-optimal” experimental design algorithm and optimization techniques [147] were applied at different steady-state speed and torque conditions, in order to define optimum calibrations of SOI, EGR rate and injection pressure to run the engine under PCCI combustion mode, meeting various constraint criteria. In particular, the focus has been to reduce the smoke and NO_x exhaust emissions from the engine accepting some penalties in terms of CO and HC exhaust emissions

and bsfc. For sake of conciseness, only the results relative to one engine working point, namely at engine speed $n = 1800$ rpm and brake mean effective pressure $b_{mep} = 1$ bar, will be presented in the following sections.

1.2.1 Preliminary experimental analysis on PCCI combustion

A preliminary test activity has been performed in order to identify the main engine control variables that can be managed in order to obtain a PCCI combustion strategy.

In conventional diesel combustion, the mixture ignites in the region where the local equivalent ratio is between 2 and 4 [149], i.e. in fuel-rich conditions. The targets of PCCI combustion strategies are, first, to ignite the charge at much lower local equivalent ratios in order to reduce the formation of soot, and, secondly, to slowdown the combustion development to lower peak temperatures, and consequently decrease the formation of NO_x [112]. The attainment of PCCI combustion conditions basically means increasing the ignition delay (ID) [29, 150, 151]. The duration of the ID depends on the charge density, fuel and oxygen concentrations and in-cylinder temperature [152]. The oxygen concentration and in-cylinder temperature for a certain engine working point are affected to a great extent by the EGR rate. This clearly points out that EGR is the most important engine working parameter to attain PCCI combustion.

SOI timing also plays an important role when direct injection engines are considered. As already mentioned, PCCI combustion strategies usually involve a very early [27, 30, 108, 109] or late [110] injection event. In the former case, the in-cylinder charge density and temperature at SOI are relatively low, with a consequent prolongation of the time available for the charge to mix, together with an increase in wall impingement phenomena. In the latter case (late injection), the fuel is injected just after TDC, when the high density of the charge requires additional EGR to increase the ignition delay. The potentialities of these two strategies, with respect to the reduction in the local equivalence ratio and in the combustion temperatures, have been clearly shown in [153]. The fuel injection pressure may also play a relevant role as it affects the fuel atomization process as well as the liquid penetration length, which is the cause of wall impingement phenomena, especially when very early injection strategies are employed.

Moreover, a reduction of temperature and pressure in the intake manifold would be beneficial to increase the ignition delay [154]. On the other hand, an increase in boost pressure reduces CO and HC emissions thanks to the overall leaner mixture and higher availability of oxygen in the combustion chamber, and extends the amount of EGR that the engine can tolerate [154]. Although the potential effect

of these variables on the implementation of PCCI combustion, the intake air temperature and pressure were not explicitly considered as control variables, nor for the preliminary tests neither for the following DoE, as they were not directly controllable in the tested system. In fact, due to high EGR rates and – consequently – low exhaust flow rate expanding in the turbine, the boost pressure was generally low (in the order of 10 mbar) although the turbine blades of the VGT were set at the closest position. Therefore, the boost pressure obtained was always lower than the target set in the ECU, and there was no chance to further increase the boost pressure with the current hardware. Also the temperature at the intake manifold was not directly controllable as it was a consequence of the EGR mass flow and temperature. The temperature of intake air after the compressor, before mixing with EGR, was controlled and set to 15°C. Nevertheless, the temperature of the EGR gases was conditioned by means of an EGR cooler integrated within the cooling circuit of the engine block, and therefore it was not possible to directly control the temperature or the flow of the coolant water in the EGR cooler. Therefore, as not directly controllable, intake air temperature and pressure were excluded from the set of possible engine control variables for the tests.

Further improvements may be obtained by increasing the mixing rate through a design which would enhance the swirl motion, and by on-purpose design of the combustion chamber geometry and the injectors [109].

In order to limit the variables to be included in the DoE and the degrees of freedom of the models, an early injection strategy, with a single injection event, has been chosen for this activity. Preliminary tests were performed on the reference engine working points by gradually changing the relevant variables (i.e. EGR rate, SOI and rail pressure) with a “one-factor-at-a-time” approach [147]. The limit values of the variables that allow the realization of a PCCI-like combustion event were then identified as a preliminary step for the DoE activity. Limits on the lower values of SOI and EGR were set, taking into account the trends in the engine-out concentrations of NO_x and soot: these two pollutants generally have opposite trends in conventional combustion, while a simultaneous reduction in both pollutants is obtained in PCCI combustion. Maximum values for SOI advance were dictated by the increase in HC and CO emissions above acceptable levels. Limits on the highest EGR rate value are imposed by two phenomena: first, an increase in the EGR rate above a certain value generates high combustion instability and high cylinder-to-cylinder variations (even though the relative EGR unbalance not always increases with EGR rate – cf. *Section 1.5* – an increase in the EGR mass flow can determine a larger cylinder-to-cylinder difference in the amount of EGR mass per cylinder); second, because large amounts of EGR are obtained by opening the EGR valve wide and, at the same time, increasing the engine backpressure by means of a dedicated flap valve. The increase in backpressure degrades fuel consumption and,

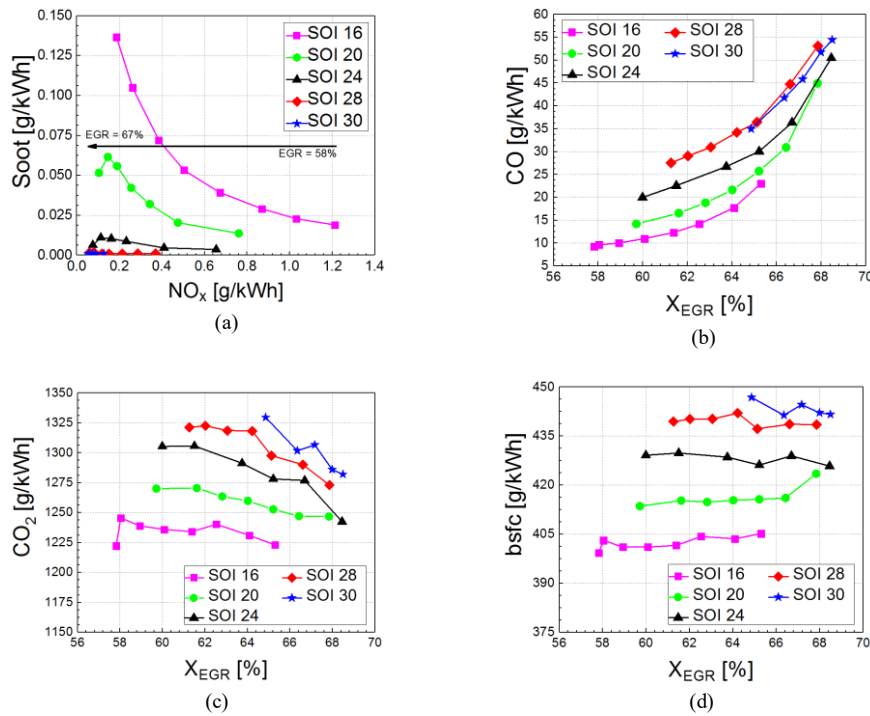


Figure 1.4: Results of preliminary tests on engine point 1800 rpm x 1 bar bmep. Brake specific soot vs. NO_x (a); CO (b) and CO_2 brake specific emissions (c), bsfc (d) as a function of the EGR rate, for different SOI angles.

after certain levels, increases combustion instability and the occurrence of misfiring, due to the difficulties involved in managing the inlet and outlet flows from the cylinders.

The results of the preliminary tests are shown Fig. 1.4 and Fig. 1.5. All the data refer to a single engine working point, namely 1800×1 (engine speed in rpm \times bmep in bar). The engine-out pollutants are considered in terms of brake specific emissions, evaluated as the ratio between the pollutant flow rate and the engine brake power. Soot emissions have been evaluated, starting from the measurement of the filter smoke number (FSN), according to [155]. The reference EGR rate in the Euro VI CDC calibration point was 38%.

Fig. 1.4a shows the soot vs. NO_x emissions and EGR rate for various values of SOI, where the SOI is expressed in terms of crank angle degrees before TDC ($^{\circ}CA$ bTDC). Soot is reduced, for constant NO_x emissions, by advancing the injection event due to the longer mixing time. Soot increases, for a certain SOI value, for decreasing NO_x , to a certain point where the soot starts to decrease simultaneously with NO_x . This is obtained at high EGR rates, and the specific EGR value at which the standard trend is inverted depends on the SOI. This inversion does not occur if the start of injection is set to 16 $^{\circ}CA$ bTDC, even at the maximum possible EGR

rate, and this condition cannot therefore be considered suitable for PCCI combustion. For earlier injection events, e.g. when SOI occurs at 20 or 24 °CA bTDC, the simultaneous decrease of the two pollutants is obtained for higher EGR rates than 66%. If SOI is advanced further, e.g. to 28 or 30 °CA bTDC, the soot emissions are almost null, and the corresponding variations are therefore not significant. On the other hand, Fig. 1.4d shows an increase in the brake specific fuel consumption with SOI, due to the advance in the barycenter of combustion, while – given an SOI value – the increase in the EGR rate does not significantly affects bsfc for the tested conditions. Moreover, advanced injection in a low density and low temperature environment leads to possible wall impingement and lean-charge pockets, which determine an increase in CO (Fig. 4b) and HC emissions, which partially contributes to a deterioration in combustion efficiency. The HC emissions have not been reported since they show a similar trend to that of CO, that is, HC is roughly one fourth of CO: the increase in unburned hydrocarbons that can be observed as the SOI is advanced may also be due to the increase in the oil dilution phenomena, and to a general deterioration of the fuel atomization process, due to a lower in-chamber density when the fuel is injected. Furthermore, the dilution effect of EGR contributes to the increase in HC and CO emissions. In these conditions, as the HC and CO emissions are extremely high, the CO₂ emissions (Fig. 1.4c) are not directly proportional to bsfc, and tend to decrease slightly as the EGR rate for a given SOI value increases, although increasing the EGR rate also produces an increase in the amount of CO₂ in the intake gases.

Figs. 1.5 shows the effect of EGR and SOI on the development of the combustion event. The dashed lines in the graphs refer to the Euro VI calibration point, where the EGR rate of the latter was not reported in order to maintain the graph compact on the x axis. In some of the graphs the value referred to the Euro VI calibration point was omitted for confidentiality reasons. The advanced injection event leads to a dramatic advance of the combustion barycenter (MFB50, Fig. 1.5a), which is one of the causes of the reduction of the combustion efficiency and the consequent increase in bsfc (Fig. 1.4d). Generally, the MFB50 is more advanced as the SOI is advanced, although the relation between the two quantities is not linear, as the effect of increasing the SOI is weakest for higher SOI values. Moreover, an increase in the EGR rate tends to retard the combustion event. Therefore, an appropriate combination of the two control parameters can provide acceptable values of MFB50, although still highly advanced with respect to CDC. Both SOI and EGR have an almost linear effect on the total duration of the combustion, evaluated as the angular difference between the crank angle at which 90% and 10% of the fuel has burnt (MFB10-90, Fig. 1.5b). The angular interval from the SOI and the MFB10 is reported in Figure 1.5d, as it is representative of the ignition delay, and the duration of the first phase of combustion (MFB10-50) and of the latest phase

of combustion are reported in Fig. 1.5e-f. Figure 1.5d shows that the ignition delay elongates from about 4°CA in CDC to values ranging from 13-15°CA with SOI = 16°CA bTDC to 25-29°CA with SOI = 30°CA bTDC (notice that in CDC a triple-injection strategy is applied, and the MFB0-10 is evaluated from the SOI of the main injection). As most of the fuel mass accumulates and mixes in the chamber during the ignition delay, the bulk of charge rapidly burns in the first phase of the combustion event, which therefore results extremely more rapid than in CDC Euro VI point (c.f. Figure 1.5 d). It is worth to notice that the EGR rate also affects the duration of the first phases of the combustion (MFB10-50), while, for a fixed EGR rate, variations of the SOI have a small effect on MFB10-50 (within 0.5°CA). As the combustion event is anticipated, also the peak firing pressure occurs earlier, i.e. closer to the TDC (c.f. Figure 1.5 g), leading to higher PFP (c.f. Figure 1.5 f): advancing the SOI anticipates both the combustion barycenter and the angle at which the PFP occurs, thus leading to higher PFP values, while an increase in EGR slows the development of combustion, and reduces the corresponding PFP. Having a fast combustion during the first combustion phase leads to a higher pressure derivative, thus impacting also the combustion noise (CN, Fig. 1.5 h), which in PCCI is 6-13 dB higher than in CDC, and reduces with the increase in EGR rate. The duration of the second phase of the combustion event (MFB50-90, Fig. 1.5 e) is almost linearly influenced both by the SOI and by the EGR rate: the combustion duration shortens when the SOI is advanced, and elongates with the increase in the EGR rate. Exhaust temperature (T_{exh} , Figure 1.5 i) increases as the combustion duration increases and combustion phase is retarded: the later the combustion event occur, the lower the peak pressure and the slower the pressure decrease during the expansion phase, which leads to higher exhaust temperature and pressure at the exhaust valves opening. It is also worth to notice that the exhaust temperature in the examined point are always higher than the same engine point calibrated in CDC, which shows exhaust temperature around 185°C, i.e. 30-50°C lower than the PCCI combustion. This is partially justified considering that the temperature at the intake manifold, i.e. the in-cylinder charge temperature at the beginning of the compression phase, is 15-30°C higher in PCCI than in CDC (Figure 1.5 j), due to the higher temperature and mass flow of EGR, which leads to a higher temperature of the intake mixture at the mixing point, although the fresh air temperature after the intercooler is lower in the PCCI case. Moreover, as mentioned above, since the engine is equipped with a short-route EGR system, the higher the EGR rate, the lower the flow rate through the turbine blades and – as a consequence – the lower the work available to compress the fresh air, and therefore the lower the boost pressure (Figure 1.8 k).

The discussed analysis of the PCCI combustion mode implemented on the conventional F1C Euro VI engine showed that it was not possible to exceed the

load of 2 bar of bmep. For higher engine loads, it was not possible to reach a premixed combustion due to: (1) the higher amount of fuel injected per cycle, (2) the richer composition of the EGR, (3) the low intake pressure. As the engine load is increased and the fuel injected per cycle increases accordingly, the ignition delay tends to shorten due to the higher amount of chemical energy in the combustion chamber. Therefore, the SOI should be further anticipated with respect to engine points at lower load in order to obtain a sufficient pre-mixing of the charge. Nevertheless, advancing further the SOI leads to higher fuel impingement, with higher unburned hydrocarbons and worsening in fuel consumption. One engine point was tested in these conditions, at 1400 rpm and 3 bar bmep (cf. Figure 1.6). Tests showed an increase in HC emissions from 2 g/kWh to 5 g/kWh and an increase in specific fuel consumption by 6.5% moving the SOI from 15°CA bTDC to 30°CA bTDC with an EGR rate of 60% (Figure 1.6a). The soot emissions were measured between 1g/kWh and 0.015 g/kWh, where the Euro VI emission limit is 0.01 g/kWh on PM (Figure 1.6b). Further increase in the EGR rate would provide a longer ignition delay, but it was not possible to increase the EGR rate as the EGR valve was always operated in the fully-open position, and the exhaust flap was operated in a very narrow range close to the fully-closed position. An additional increase in the backpressure through a further closure of the exhaust flap was found to be extremely detrimental on fuel consumption and in terms of combustion stability. In the mentioned test point at 1400 x 3 (rpm x bar bmep), with an SOI of 24°CA bTDC, an increase in EGR rate from 60% to 62% through the regulation of the exhaust flap (from 93.2% to 94% of the full stroke) led to a further increase of 4.8% in fuel consumption, caused by an increase in the engine backpressure of only 5 mbar (Figure 1.6c). In these extreme conditions, combustion stability worsened up to reach the misfire condition in several cycles. Therefore, in these conditions the worsening in bsfc, CO and HC were comparable to those measured for points at lower loads, but soot emissions were higher than the Euro VI limit and there was no chance to further decrease them. Moreover, due to the limitations in boost pressure caused by the high amount of EGR and due to the higher amount of fuel per cycle, the charge results relatively richer than for points at lower loads, thus affecting also the composition and the temperature of exhaust gases. As a consequence, given a certain EGR mass flow, the intake temperature increases and the oxygen concentration at the intake manifold decreases as the load is increased. The higher intake temperature leads to an increase of the combustion peak temperature, thus increasing the formation of NO_x. The lower concentration of oxygen limits the fuel-air mixing, thus leading to higher local fuel-to-air ratios, which increases the soot emissions. Furthermore, the lack of oxygen in the last phases of the combustion further increases CO and HC emissions due to missing late oxidation.

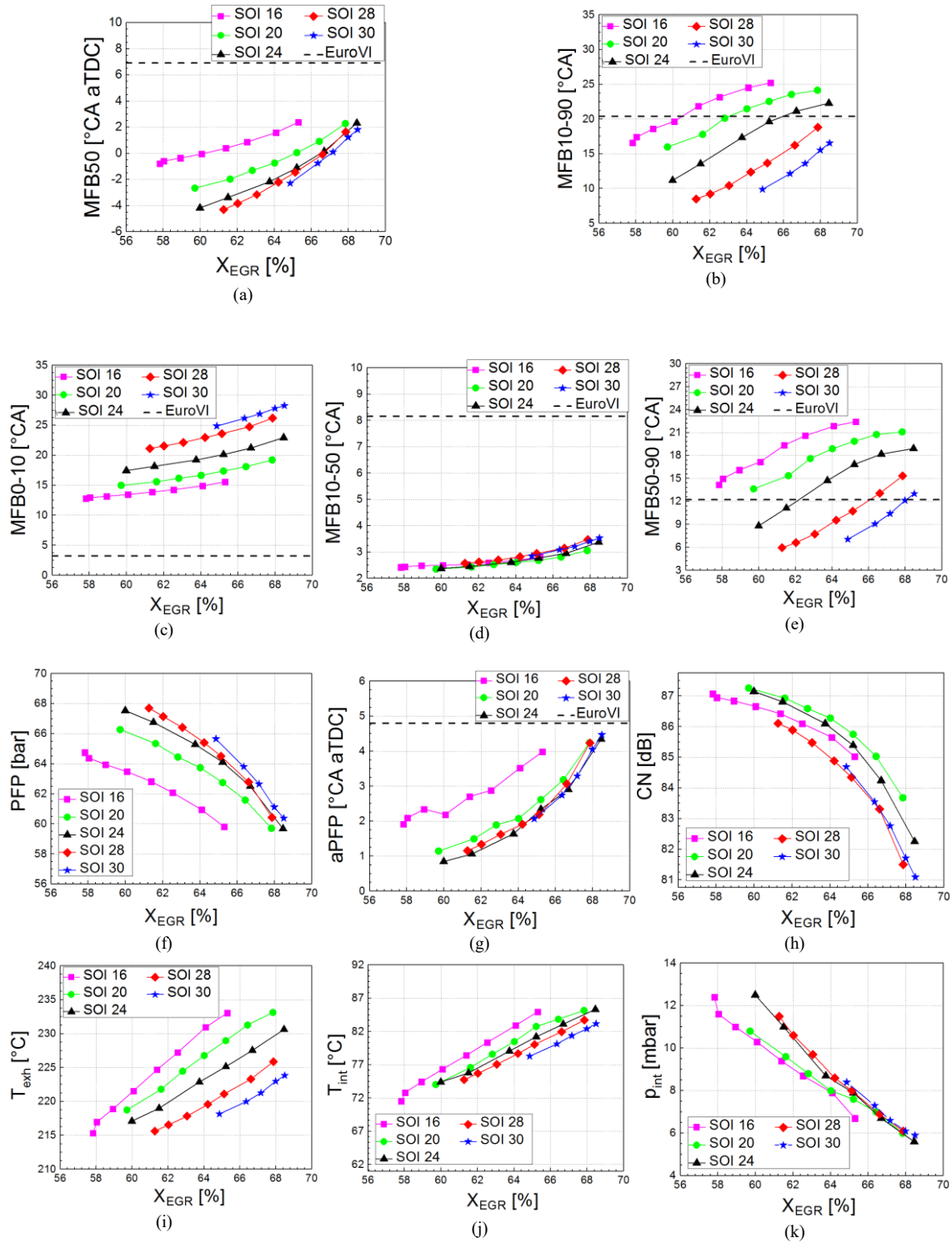


Figure 1.5: Barycenter of the combustion (a), angular duration of the combustion (b), angular duration of the ignition delay (c), angular duration of the first phase (d) and of the last phase of the combustion (e), peak firing pressure (f) and related angle (g), combustion noise (h), exhaust manifold temperature (i), intake manifold temperature (j) and pressure (k) as a function of EGR rate for different SOI.

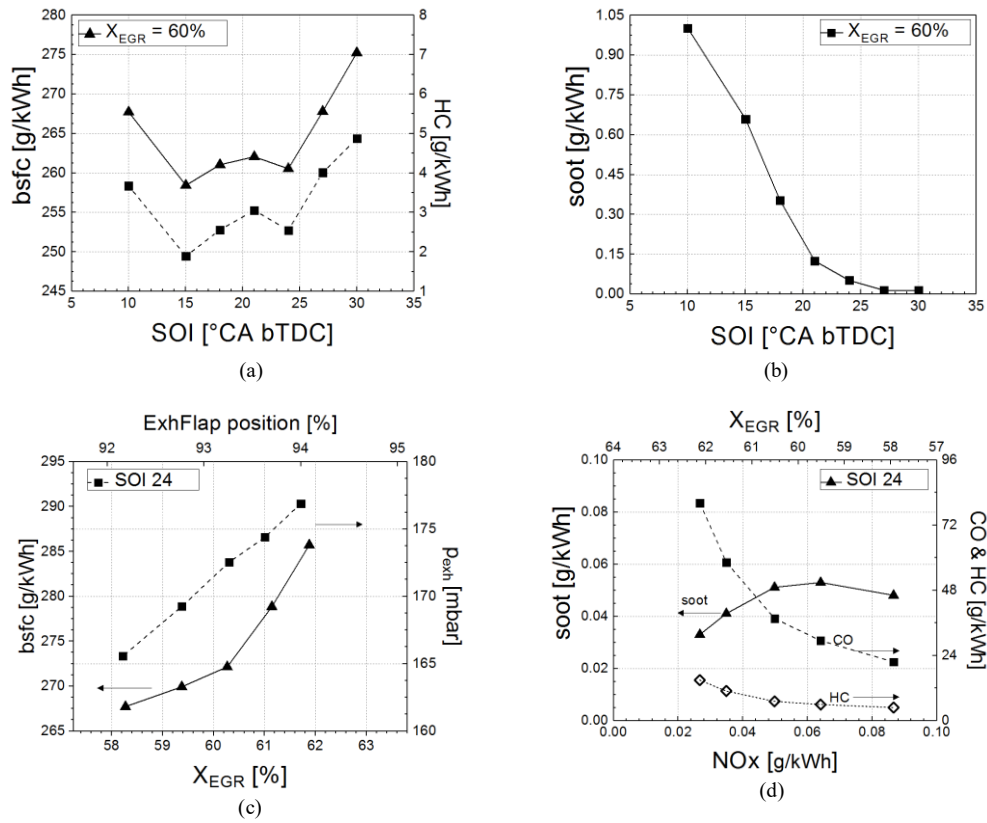


Figure 1.6: Tests performed at 1400 rpm and 3bar bmep attempting to get a proper PCCI combustion: SOI sweep at constant EGR rate (a,b) and EGR sweep at constant SOI (c,d).

1.2.2 Design of experiments and model-based optimization of PCCI combustion

The limit values of the input parameters to perform a DoE have been set according to the above presented preliminary analysis, and are reported in Table 1.2. The following input parameters have been identified as the ones that mainly affect PCCI combustion: the rail pressure, the start of injection and the position of the backpressure flap valve used to regulate the EGR rate, since the EGR poppet valve was fully open in all the PCCI working conditions. Considering the limit values for each of these variables, and provided there is an appropriate number of levels, a “V-optimal” design, which minimizes the values of the predicted error variance in the test plan, has been implemented by means of the “MBC model” Matlab software tool. The optimal design of experiments provided a number of 32 combinations of the control variables, whose values are shown in Figure 1.7. These combinations of EGR flap position, SOI and rail pressure have been tested on the reference engine point. A detailed list of the tested engine points is reported in Table

1.3. Moreover a number of repetitions of the central point of the DoE (reported as test #1 in the table) have been evenly run during the test plan in order to check possible drifts.

The experimental values of the main outputs, i.e. bsfc, brake specific emissions (NO_x , soot, HC and CO), CN and MFB50, were used to fit second order polynomial regression functions of the input control variables (rail pressure, SOI, EGR flap position). Moreover, the Box-Cox transformation [156] was applied, where necessary, in order to normalize the distribution of the residuals and the “stepwise regression” method [146] was used to eliminate any regressors that showed a negligible effect on the outputs. Summary statistics of the obtained models are reported in Table 1.4. According to the reported statistical indexes the models show a good correlation with the experimental values. As an example of the results obtained with the modeling, Fig. 1.8 depicts the predicted bsfc versus the experimental one. The validation root mean square error (RMSE), obtained by comparing the validation tests with the model outcomes, was generally very similar to the model RMSE.

Input	Lower Limit	Upper Limit
EGR flap position [%]	85	95
SOI [$^{\circ}\text{CA}$ bTDC]	18	30
Rail pressure [bar]	500	700

Table 1.2: DoE input boundary values.

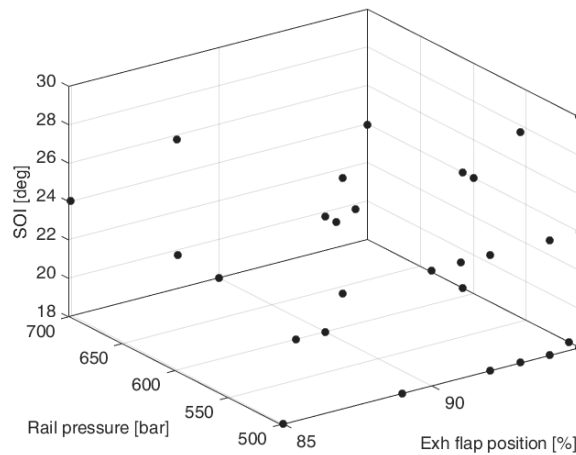


Figure 1.7: Test points of the V-Optimal DoE: values of the three control variables.

	EGR flap position [%]	SOI [°CA bTDC]	Rail pressure [bar]
1	90	24	600
2	90	18	600
3	87	30	500
4	92	24	500
5	87	24	500
6	95	18	500
7	93	18	500
8	91	24	500
9	90	24	590
10	95	24	600
11	95	24	500
12	85	24	600
13	92	18	500
14	95	30	590
15	94	18	500
16	85	18	500
17	85	30	600
18	85	24	700
19	88	30	700
20	95	18	510
21	91	24	600
22	95	18	610
23	95	30	500
24	89	18	500
25	95	24	700
26	90	18	700
27	93	30	500
28	94	24	500
29	93	30	700
30	90	24	500
31	95	24	610
32	89	18	600

Table 1.3: Detail of the 32 test points of the V-Opt DoE at speed = 1500 rpm and bmep = 1 bar (i.e. torque = 27 Nm).

Among the models, the lowest coefficient of determination was obtained for the soot specific emissions, due to the high dispersion in the low-end of the measurement range of the smokemeter: as mentioned in *Section 1.1*, the repeatability of the instrument is $\pm (0.005 \text{ FSN} + 3\% \text{ of the measured value})$, i.e. a repeatability error of between 53% and 11% when the measured value ranges from 0.01 FSN to 0.06 FSN, where 80% of the soot samples in the DoE lied. As a consequence, considering that the root cause of the dispersion of the model could not be improved and that the root mean square error is equal to the resolution of measuring instrument itself, the model was validated although the coefficient of determination was slightly lower than 0.9.

Once the response models had been validated, a model-based optimization of the PCCI combustion in the considered engine working point was set up. Different optimization strategies were tested and the results were compared. In particular, the focus was on the minimization of the NO_x emissions or of the bsfc, and some upper boundaries were sometimes set on other output parameters. A “conjugated gradient optimization” method was adopted for single-objective optimizations, while multi-objective optimizations were computed employing a Normal Boundaries Intersection algorithm. Details on the optimizations are reported in Table 1.5, which reports, for each of the optimizations, the values of the control variables obtained through the model-based optimization, as well as the optimization criteria (i.e., the variable to be minimized) and the applied constraints. The first and the second

Response model	Parameters	Box-Cox	R ²	R ²	PRESS	PRESS	RMSE	Validation
		λ		adjusted	R ²	RMSE		
bsHC [g/kWh]	8	1	0.960	0.951	0.933	0.161	0.140	0.184
bsNO _x [g/kWh]	8	0.5	0.994	0.992	0.989	0.346	0.268	0.282
bsCO [g/kWh]	8	-0.5	0.983	0.980	0.973	1.071	0.879	0.633
bsSoot [g/kWh]	10	1	0.880	0.837	0.749	0.002	0.001	0.001
bsfc [g/kWh]	8	1	0.938	0.925	0.913	2.537	2.392	3.616
CN [dB]	7	1	0.977	0.973	0.957	0.132	0.106	0.095
EGR rate [-]	6	1	0.996	0.995	0.994	0.411	0.369	0.494
MFB ₅₀ [°CA]	8	0.5	0.998	0.997	0.995	0.190	0.148	0.177

Table 1.4: Statistical summary for each response model.

Point	EGR valve	EGR flap	SOI	Rail pressure	Minimization	Constraints
	[%]	[%]	[°CA bTDC]	[bar]		[-]
Euro VI	100	71.4	6.9	583		
Opt 1	100	95.0	30	700	NO _x	
Opt 2	100	95.0	30	500	NO _x	CO/CO _{REF} < 8.5
Opt 3	100	91.5	18	500	bsfc	NO _x /NO _{x,REF} < 0.5 Soot/Soot _{REF} < 0.4
Opt 4	100	95.0	21	500	NO _x bsfc	HC/HC _{REF} < 2 Soot/Soot _{REF} < 0.2

Table 1.5: Parameters of the Euro VI point and of the optimization point parameters.

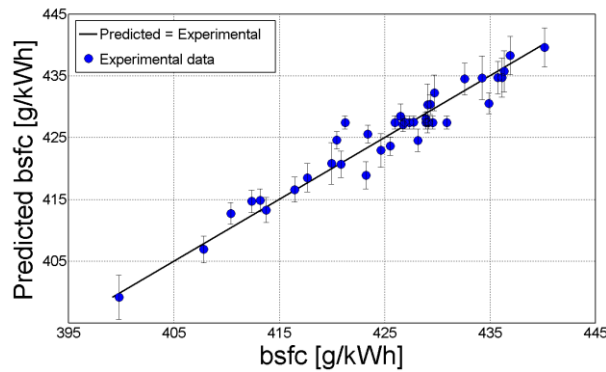


Figure 1.8: bsfc: predicted vs. experimental values

optimization points (Opt 1 and Opt 2) were obtained by minimizing the NO_x emissions, and the second differs from the first one for the application of a constraint on the maximum CO emissions. The third optimization (Opt 3) was computed minimizing the brake specific fuel consumption and applying constraints on both NO_x and soot emissions, and the fourth optimization point (Opt 4) is set to minimize NO_x emissions and bsfc at the same time, while limiting HC and soot emissions to constrained levels.

Fig. 1.9 shows a comparison of the experimental results pertaining to the optimized PCCI combustion modes and the standard engine calibration conducted in conventional diesel combustion mode. The first and second optimizations (Opt 1 and Opt 2) resulted in a reduction in the NO_x brake specific emissions of more than 90% (Fig. 1.9a), and smokeless combustion (Fig. 1.9b), thanks to an increase in the EGR rate to more than 60% (Fig. 1.9h). On the other hand, the CO and HC emissions increased by more than 2-fold and 8-fold, respectively (Figs. 1.9c-d), while the bsfc increased by 13% (Fig. 1.9e), due to an advance of the barycenter of the combustion of more than 11 °CA (Fig. 1.9f, Opt 1 and Opt 2 with respect to EUVI). The third optimization resulted to be the best trade-off for the tested conditions: in this case, it was possible to reduce the NO_x emissions by 60% and the soot by more than 80%, while the bsfc penalty was slightly lower than 10%, the increase in CO was contained to less than 3-fold and the HC emissions were almost the same as the reference condition.

Experimental tests performed with the Opt 4 calibration provided even lower NO_x levels than Opt 1 and Opt 2 (due to the model and experimental uncertainty for such low values), while bsfc was slightly higher than in Opt 3, and HC and CO were considerably lower with respect to Opt 1 and Opt 2, but much higher than Opt 3. Soot emissions were reduced by 46%, but were still far from the target of a PCCI-like combustion. In all the tested conditions, the combustion noise was considerably higher than in the reference condition, with an increase from 11.7 to 13.1 dB, which was in part due to the fact that the PCCI tests were performed with a single injection strategy, while the Euro VI calibration used a triple injection strategy for the considered engine point. Moreover, the advance in the combustion event and the longer ignition delay had to be accounted for as additional causes of the increase in combustion noise.

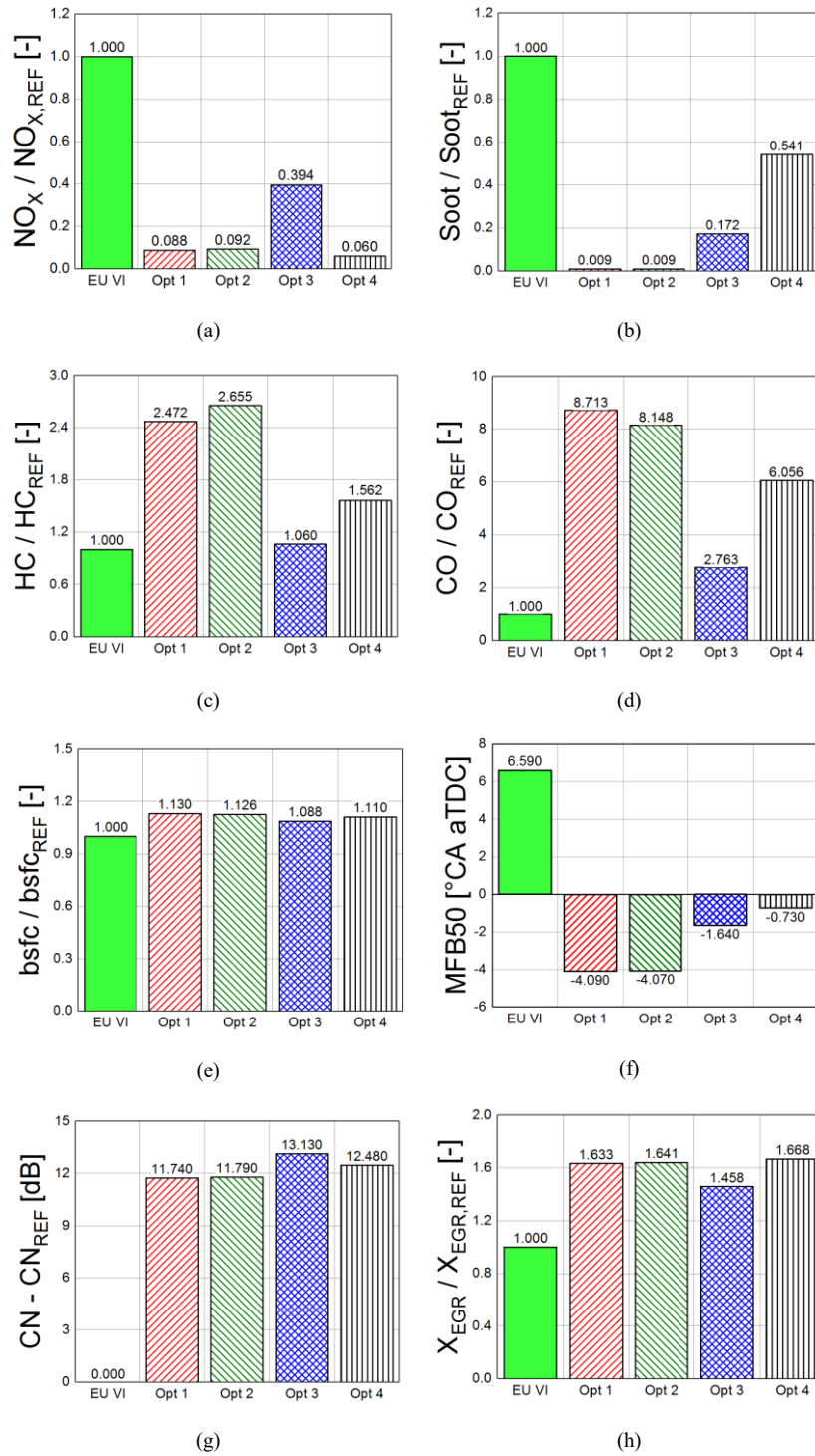


Figure 1.9: NO_x (a), soot (b), HC (c) and CO (d) brake specific emissions, brake specific fuel consumption (e), MFB50 (f), combustion noise (g) and EGR rate (h): comparison between the base EU VI calibration and the optimized PCCI points.

1.3 Performance and emission comparison between the standard Euro VI diesel engine and an optimized PCCI Version

Starting from the commercial Euro VI on-road engine, as mentioned in *Section 1.1*, the engine hardware has been modified to optimize PCCI operations. This has involved adopting a smaller turbo group, a new combustion chamber and injectors, and a dedicated high-pressure exhaust gas recirculation system. The results obtained on the modified version of the engine, in terms of engine performance and exhaust emissions, under steady-state operation conditions, are presented in this *Section*, where the original Euro VI calibration of the conventional engine has been compared with the PCCI calibration of the optimized hardware engine, in order to identify the potentialities of the PCCI combustion strategy on the optimized hardware engine.

As far as the F1C Euro VI engine is concerned, the experimental tests were run adopting the original OEM calibration on the ECU (which cannot be reported here for confidentiality reasons), featuring a conventional combustion mode with a triple injection strategy (two pilot injections and one main injection). In particular, a full engine map was experimentally obtained at the following angular speeds: 850, 1000, 1200, 1400, 1600, 2000, 2500, 3000 and 3500 rpm and for the following loads: 7%, 12.5%, 25%, 37.5%, 50%, 62.5%, 75%, 87.5% and 100% of the maximum bmep at each angular speed. Hereafter, the blue filled circles reported in Figs. 1.10, 1.13, 1.15 refer to this engine map.

As mentioned in the previous *Section*, the implementation of PCCI combustion on the Euro VI engine was limited to low loads. In order to overcome this limit, the new hardware was designed to explore the suitability of PCCI operations to up to medium loads and at medium-high speeds, as mentioned in *Section 1.1*. Also in this case, an early single injection strategy was chosen to provide the charge premixing during the last part of the compression phase. The following engine control variables were used to implement the PCCI combustion mode: electric start of injection (SOI) of the single injection pulse, exhaust flap position (flap), variable geometry turbine (VGT) position and rail pressure (p_{rail}). Therefore, most of the used control variables are the same as for the PCCI mode on the conventional diesel engine, with exception for the VGT position that was added in this cases since the smaller turbo was expected to provide a boost pressure higher than environment also at high EGR rates. It is worth pointing out that, also in this case, although a larger section of the EGR valve, the EGR valve was always kept in the completely open position in order to obtain high EGR rates, and it was therefore not considered

as an input in the following analysis. In this investigation, the PCCI combustion mode was mainly explored according to a “one-factor-at-a-time” (OFAT) approach [147]. The experimental optimum PCCI calibration for each engine operating point was chosen through the use of an objective function, in order to achieve the best compromise in terms of simultaneous reduction of soot, NO_x and bsfc. In the following figures, a smaller area of the full engine map was investigated, as it was not possible to acceptably extend the performance of PCCI operations any further. In particular, the engine operating points listed in Table 1.6 were tested on the F1C PCCI engine.

The maximum experimental load explored in PCCI combustion mode was about $\text{bmep} = 8.5$ bar, as it was limited by the increased injected fuel mass. As the load rises, a higher injected fuel quantity is required, so that the λ range in which the engine can be operated effectively becomes narrow and very close to the stoichiometric value. As a consequence, in order to re-establish the desired λ value (cf. Fig. 1.14), the exhaust flap has to be opened to reduce the EGR flow rate and increase the air flow rate. Combustion becomes unstable at low λ values and soot increases, whereas other quantities, such as bsfc, CN and NO_x , tend to become too high at high λ values, because MFB50 occurs appreciably before TDC. The SOI has to be advanced, with respect to CDC, so that the fuel has the necessary time to premix with the surrounding charge. Furthermore, the link between MFB50 and SOI is not straightforward in the PCCI combustion mode, as it is instead in the CDC mode. In fact, in the PCCI combustion mode, an appreciable difference in SOI has a minor influence on MFB50. Therefore, if a higher load is required, this cannot be obtained under PCCI combustion and it is necessary to switch to CDC. Further details about quantities that have not been graphically reported (such as SOI, rail pressure, EGR rate, exhaust pressure and temperature) are available in Table 1.6, where the values related to the conventional engine are not reported for confidentiality reasons. SOI and p_{rail} are calibration parameters, p_{exh} and T_{exh} refer to the values downstream of the engine and upstream of the flap (cf. Fig. 1.1), p_{boost} is evaluated in the intake manifold. The rail pressure was increased, with respect to the calibration of the CDC mode. In fact, in PCCI combustion mode, the fuel must be evaporated and at least partially mixed prior to the SOC reactions. Fuel droplets that survive the start of reactions will burn in diffusion flames, and this would lead to a dramatic increase in the production of soot and NO_x [105].

speed [rpm]	bmep [bar]	SOI [°bTDC]	p _{rail} [bar]	EGR rate [%]	p _{boost} [mbar]	p _{exh} [mbar]	T _{exh} [°C]	λ [-]
1000	4.0	22	1000	51.2	49	13	254	1.25
1400	3.0	28	650	55.5	45	29	236	1.44
1400	4.4	28	1000	49.7	89	18	282	1.25
2000	2.3	22	1000	54.6	171	41	219	1.81
2000	5.0	35	1100	52.4	279	68	310	1.18
2000	6.7	34	1400	49.5	522	69	323	1.13
2500	2.3	26	1000	53.2	220	74	238	1.82
2500	5.0	34	1400	51.6	505	98	294	1.36
2500	6.7	40	1600	54.1	808	113	308	1.15
3000	2.3	26	1400	53.8	384	124	242	1.76
3000	5.0	35	1800	48.7	379	139	351	1.21
3000	6.4	44	1800	52.5	838	157	327	1.16
2000	7.5	32	1600	46.3	589	60	336	1.13
2000	8.4	32	1600	43.6	698	59	347	1.13
2500	7.5	38	1600	48.1	811	84	331	1.18
2500	8.4	44	1600	46.4	865	96	354	1.09
3000	7.5	46	1800	47.4	862	108	358	1.10

Table 1.6: Optimum experimental points (boost pressure and exhaust pressure values expressed as relative pressures) of the PCCI engine.

In order to highlight the cycle-to-cycle variations in both the F1C Euro VI and the F1C PCCI engines, data relative to 100 consecutive combustion cycles were acquired for each of the four cylinders in all the experimental tests to calculate the coefficient of variation for the indicated mean effective pressure (CoV_{imep}) and for the peak firing pressure (CoV_{PFP}). The results, depicted in Fig. 1.10a and Fig. 1.10b, which are relative to cylinder #1 (but similar results were also found for the other cylinders) show that CoV_{imep} and CoV_{PFP} are rather small in both engines and for

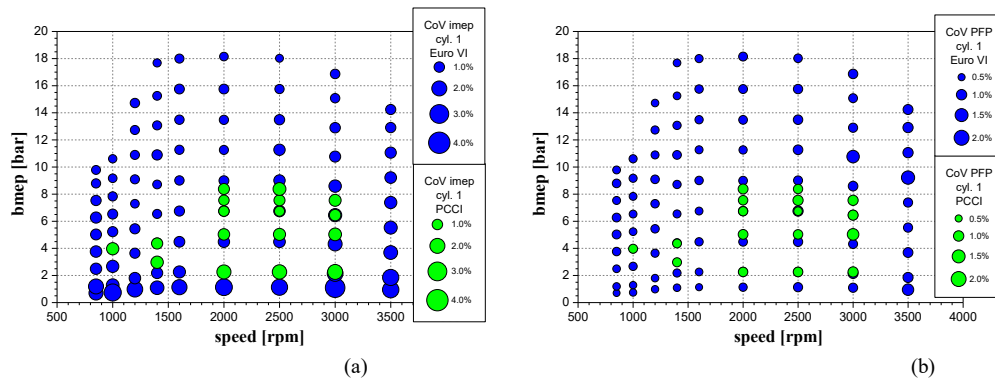


Figure 1.10: (a) Percentage variations in CoV_{imep} of cylinder #1 for the F1C PCCI and F1C Euro VI engines. (b) Percentage variations in CoV_{PFP} of cylinder #1 for the F1C PCCI and for the F1C Euro VI engines.

almost all the investigated points. This suggests that a very stable combustion can also be obtained for the high EGR rates and advanced injection timings of F1C PCCI, as a result of the hardware modifications highlighted in *Section 1.1*. Considering the four cylinders together, the COV_{imep} dispersion proved to be similar for both engines, whereas the COV_{PFPP} resulted to be slightly higher for F1C PCCI (but lower than 3%). The F1C Euro VI running in PCCI combustion mode had shown higher values of CoV_{imep} and CoV_{PFPP} , as it will be shown in one of the following *Sections* of this *Chapter* (cf. *Section 1.4*).

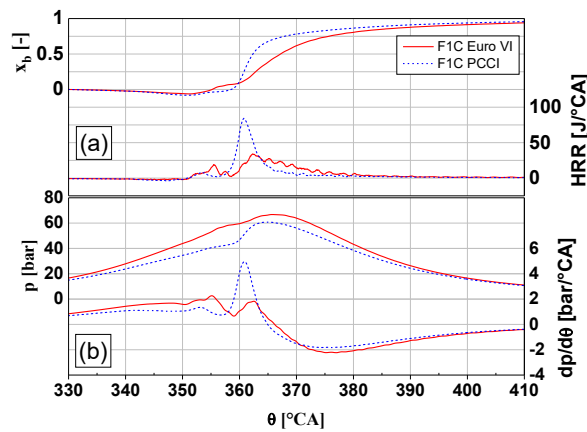


Figure 1.11: Mass fraction burned x_b (a – left axis), apparent HRR (a - right axis), in-cylinder pressure of cylinder #1 (b – left axis), and its derivative (b - right axis) versus crank angle position at the 2000×2.3 point (rpm x bmep) for both the F1C Euro VI and the F1C PCCI engines.

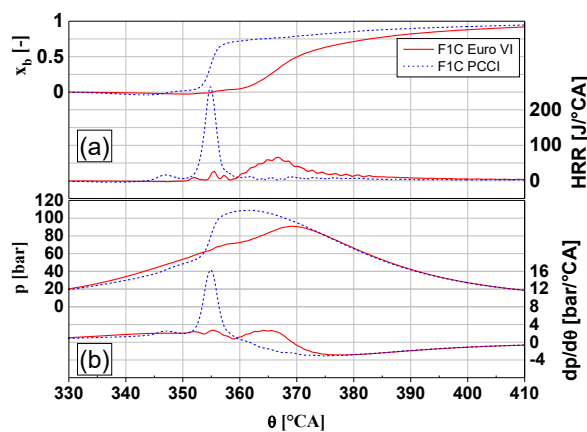


Figure 1.12: Mass fraction burned x_b (a - left axis), apparent HRR (a - right axis), in-cylinder pressure of cylinder #1 (b - left axis), and its derivative (b - right axis) versus crank angle position at the 2000×7.5 point (rpm x bmep) for both the F1C Euro VI and the F1C PCCI engines.

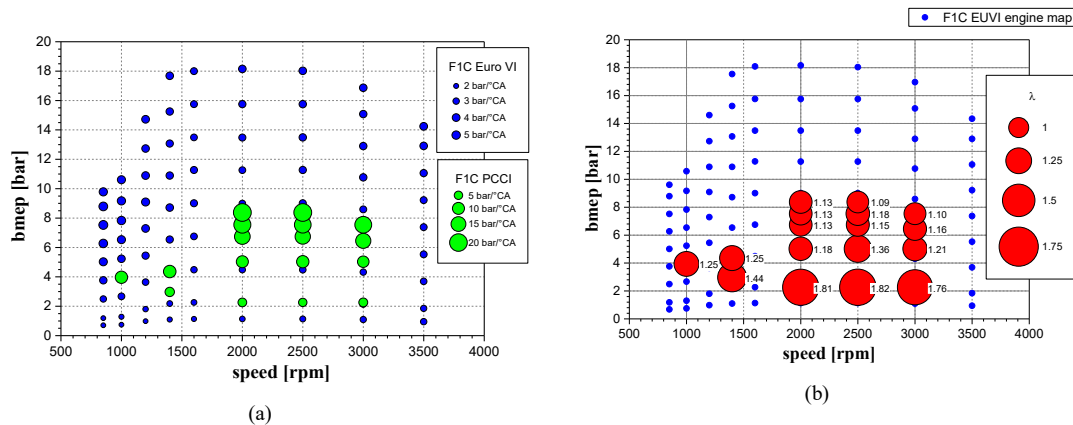


Figure 1.13: Maximum in-cylinder pressure derivative of cylinder #1 for both the F1C Euro VI and the F1C PCCI engines (a) and λ values for the F1C PCCI engine (b).

As expected, significant differences were found when the pressure traces of the optimum points of the F1C Euro VI and the F1C PCCI were compared. Figs. 1.11 and 1.12, which are related to 2000×2.3 and to 2000×7.5 , respectively, show, in the bottom part, the in-cylinder pressure and its derivative in cylinder #1 and, in the upper part, the corresponding apparent heat release rate (HRR) and mass fraction burned (x_b), as evaluated in a single zone analysis implemented in the AVL Concerto software for indicating analysis. The PCCI engine shows an advanced and faster combustion. The peak firing pressure (PFP) values for the F1C PCCI decrease for low loads and increase for higher loads, with respect to the F1C Euro VI. At low loads, e.g. at 2000×2.3 , the ID is extended, due to a higher dilution that the engine can tolerate, so that PFP is achieved during the expansion phase and, consequently, the maximum pressure derivative is attenuated. At higher loads, e.g. at 2000×7.5 , the combustion develops well before TDC, i.e. during the compression phase, with a large increase in PFP and in the maximum pressure derivative. The maximum values of the pressure derivative in the explored PCCI area ranged between 5-20 bar/°CA. These values are much higher than those observed for the F1C Euro VI, which ranged between 1.5-5 bar/°CA, as shown in Fig. 1.13a. This result could be used to set a limit to the maximum explored bmep in PCCI combustion mode. However, the PFPs of all the working points of F1C PCCI engine never exceeded the PFPs of the full-load curve of the F1C Euro VI engine.

In order to provide indications on how the optimum PCCI calibration should be chosen, Fig. 1.14 depicts NO_x , soot and bsfc as a function of the relative air-fuel ratio (λ), at the 2000×5 (speed x bmep) working point. The tests are related to the OFAT approach and therefore involve different values of the abovementioned inputs. It is worth to remark that the dyno was always operated in the speed/torque control mode, and therefore all the points in Fig. 1.14 are related to the same engine

brake torque. In general, the λ values are affected by all the input variables, and in particular by the flap and VGT positions. As soot was quite low at 2000×5 , due to the high premixing, the aim of the calibration was to reduce the engine-out NO_x while limiting the bsfc penalty. This was achieved over a narrow range of λ , that is, around 1.15, for this engine point. To this aim, a suitable objective function was defined in order to find the best combination of inputs that result in a simultaneous minimization of NO_x , soot and bsfc. The black dashed horizontal lines in Fig. 1.14 refer to the emission limits of the World Harmonized Stationary Cycle (WHSC) [157], which are reported in Table 1.7 and which were taken as a reference, whereas the dashed red line represents the 10% increase in the bsfc experimentally measured for the corresponding Euro VI point.

A similar methodology was adopted for the other PCCI tested points. It was generally found that the input variables had to be chosen so that an average λ , corresponding to a slightly lean mixture, in the 1.1-1.35 range, was obtained. The values of λ for each optimum working point of FIC PCCI are reported in Fig. 1.13b. The λ values increase when the engine load decreases, because it is not possible to further increase the EGR rate (and hence to reduce the λ values), due to the onset of combustion instabilities (higher cylinder-to-cylinder and cycle-to-cycle variations till misfiring events occur) and a dramatic increase in engine-out CO and HC emissions. This increase was ascribed to the air handling system, which was optimized for medium loads, since NO_x and soot emissions at low loads do not represent a major issue. Starting from the experimental tests, statistical models (featuring second-order polynomial functions with linear coefficients, which was proved in the previous *Section* of this *Chapter* to be quite accurate for this application) were built in order to understand the influence of the input parameters on λ and on the desired outputs. In general, the rail pressure does not have an important effect on λ , while the flap was the most important parameter on λ . A closer position of the flap determined a larger difference between the exhaust and intake manifold pressures, and this resulted in a higher EGR rate, and therefore a reduction in the air flowrate. The VGT position and SOI both affected the pressure and temperature in the intake and exhaust manifolds, so that the dependence of λ on the considered inputs was found to be quite complex and did not show monotonic behavior.

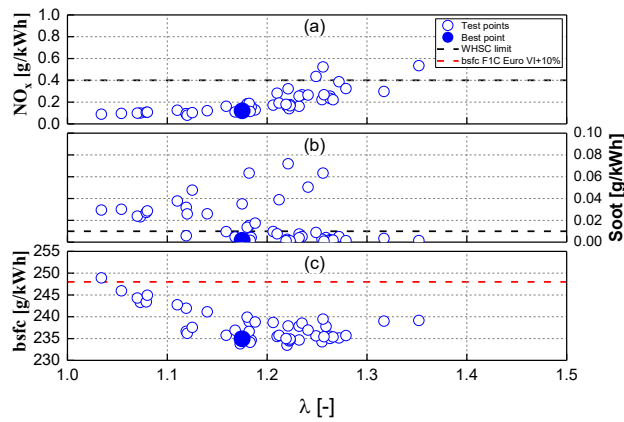


Figure 1.14: NO_x , soot and bsfc as a function of λ at 2000×5 (speed \times bmep) for different values of the input variables.

CO [g/kWh]	1.5
HC [g/kWh]	0.13
NO_x [g/kWh]	0.40
PM [g/kWh]	0.01

Table 1.7: Euro VI emission standards for heavy-duty diesel engines for the World Harmonized Stationary Cycle (WHSC).

The values of SOI in the considered calibrations ranged from 22 to 46 °CA bTDC and generally increased with engine speed and load. The advanced SOI values also determined advanced MFB50 values, which occurred before TDC at the highest PCCI loads. The considered p_{rail} for the F1C PCCI was about 150–450 bar higher than that of the F1C Euro VI and the greatest differences were generally measured at the lowest loads. The exhaust flap was observed to be closed more in the F1C PCCI, especially at higher loads, and this determined, together with the advanced MFB50, an expected increase in bsfc (cf. Fig. 1.15g).

The following graphs (Fig. 1.15) show the percentage variation of exhaust pollutant emissions, bsfc and combustion noise of the optimum points on the F1C PCCI engine, with respect to the corresponding points on the F1C Euro VI engine, for all the PCCI working points. In Fig. 1.15, the green or red filled circles, with their size being proportional to the percentage variation, highlight a reduction or an increase, respectively, in the F1C PCCI engine, compared to the F1C Euro VI one.

Fig. 1.15a depicts the percentage reduction in engine-out NO_x emissions. The tested PCCI points show a massive reduction in NO_x emissions for the explored

area, that is, ranging from 85% to 97%. This is due to the high dependence of the NO_x formation rate on the available oxygen concentration and on the maximum in-cylinder temperatures, which are significantly lower when very high EGR rates are implemented in the PCCI operation mode to dilute the charge [29,105]. The current SCR systems manufactured for heavy-duty applications guarantee a conversion efficiency that ranges from 90% to 92%, when a cooled EGR is employed [103], and which can thus reach comparable values, in terms of NO_x tailpipe emission reduction, compared with those of the F1C PCCI, which was not endowed with any NO_x after-treatment system, as already mentioned in *Section 1.1*.

Fig. 1.15b shows the percentage reduction of engine-out soot emissions for all the tested PCCI operating points, with respect to the corresponding Euro VI calibration. An average reduction of more than 90% is obtained, with peak values of nearly 100% (which means an ultra-low soot combustion), thanks to the advanced combustion phasing featured in the PCCI operation mode. Advanced SOI values provide enough time for the injected fuel to mix within the in-cylinder charge [29], and this leads to a more homogeneous mixture than in the conventional combustion mode, with a reduction of charge-fuel rich pockets, which are generally thought to be responsible for the formation of soot [158].

On the other hand, all the premixed combustion modes, including the SI engines (gasoline and natural gas), produce high levels of CO and HC. HC is mainly due to trapped fuel in the valve pockets and piston crevices, whereas CO occurs in regions where not enough O_2 is available. When a strongly diluted charge is employed, as in this case, the local maximum temperature in the cylinder at low loads can be so low that it causes wall-quenching phenomena, and this leads to high HC emissions. The percentage variations of brake specific CO emissions, measured before and after DOC, are shown in Fig. 1.15c and Fig. 1.15d, respectively. The comparison, in the case of CO exhaust emissions after DOC, was not evaluated with respect to the F1C Euro VI engine, but was instead evaluated with respect to the WHSC limit (cf. Table 1.7), because no ATS system was installed on the engine in the original Euro VI configuration at the test bench. The reduced flame temperatures of PCCI operations, in addition to the reduced oxygen contents, due to EGR, tend to prevent the final stage of oxidation from CO to CO_2 [118]. This problem occurs under nearly all PCCI operating conditions (with dramatic, up to 20 times higher penalties than those of the corresponding Euro VI engine), so that DOC plays a key role. Above a certain load (about $\text{bmep} = 4$ bar), the exhaust gas temperatures are hot enough to make the DOC reach its light-off temperature, with a CO conversion efficiency of nearly 100%. Light-off temperatures cannot be reached below this load, and the engine-out CO emissions are not mitigated (with a partial exclusion of high speed and low load points, for which the DOC conversion

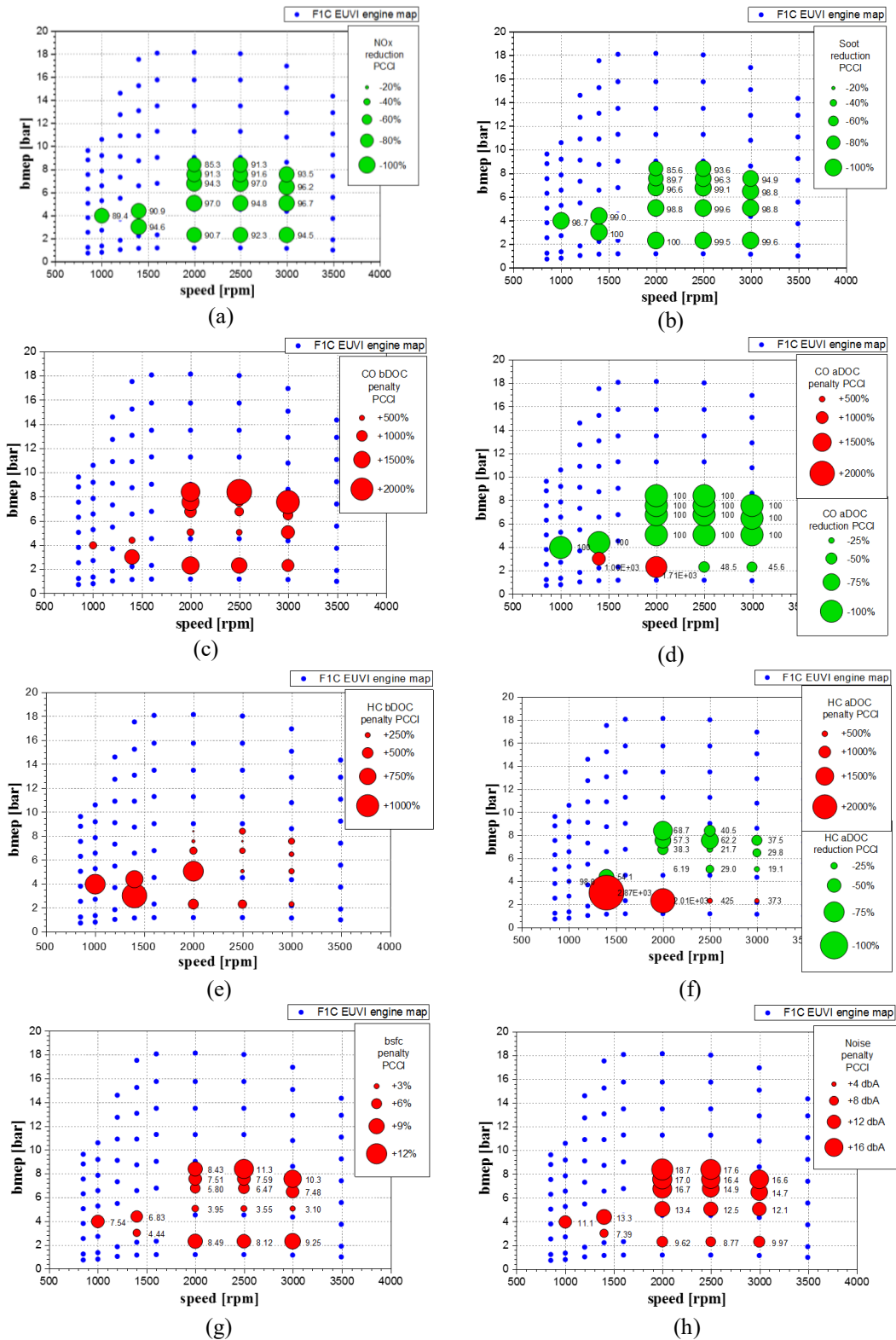


Figure 1.15: Percentage variations in engine-out NO_x (a), soot (b), CO (c), and HC (e) emissions between the F1C PCCI and the F1C Euro VI engine; percentage variations in CO (d) and HC (f) emissions after DOC between the F1C PCCI engine and the WHSC limit; percentage variations in bsfc (g) and CN (h) between the F1C PCCI and the F1C Euro VI engine.

efficiency, even though not high, is still able to reduce CO tailpipe emissions by about 45%, with respect to the WHSC limit).

Similarly to what was shown for CO emissions, the percentage variations of the brake specific HC emissions, measured before and after DOC, are shown in Fig. 1.15e and Fig. 1.15f, respectively. Again, no comparison of HC emissions after DOC, was performed for the F1C Euro VI, but was instead performed with reference to the WHSC limit (cf. Table 1.7). Apart from promoting high mixing of the injected fuel with the inlet charge, advanced injection timings in PCCI mode tend to increase the fuel penetration length, due to lower in-cylinder pressure conditions at the injection event [159], and this leads to wall impingement phenomena and a high number of unburned hydrocarbon emissions. As mentioned above, the cone angle [29,105] and the static flowrate were both reduced to decrease the drawback of wall wetting. However, wall wetting cannot always be avoided, but when it occurs, it is on the piston crown and not on the cylinder walls. As the temperature of the piston is higher, this impingement is less critical to avoid fuel evaporation [29]. As Fig. 1.15e shows, the increase in HC engine-out emissions is particularly high for low loads and speeds, with peaks of about 10 times the corresponding levels obtained with the F1C Euro VI. Fig. 1.15f highlights the benefits that DOC can have on reducing the tailpipe HC emissions: at bmep values above 4 bar, its conversion efficiency is high enough to keep these emissions lower than the WHSC limit. Major problems are encountered at low load and low speed points, where the exhaust gas temperatures are too low to allow the DOC to reach its light-off temperature. At low load and low speed, further reductions of λ were not considered due to poor combustion quality and unacceptable increase in fuel consumption. Comparing Fig. 1.15d and Fig. 1.15f, it is possible to see that the conversion efficiency is higher for CO than for HC, as was also found in [160]. Fig. 1.15g shows that PCCI operations leads to a fuel consumption penalty of up to 11%, but about 4% is obtained at intermediate loads. The detrimental effects, in terms of bsfc obtained for the F1C PCCI engine, are partly due to the decrease in efficiency of the standard ideal air cycle with a lower CR (about 2.5%), and to the decrease in combustion efficiency (over the 0.5-3% range). Furthermore, bsfc is also negatively affected by the implemented values of SOI (an early SOI advances MFB50, i.e. combustion occurs mainly during the last part of the compression stroke) and the considered exhaust flap positions (a closure of the flap determines an increase in engine backpressure), which affects the mechanical efficiency over the 0.5-5% range.

The F1C Euro VI engine equipped with an SCR system and tested by the OEM, featured a urea consumption that ranged from 0.5% to 4.5% of the fuel consumption, within the same portion of engine map tested for the F1C PCCI. In addition, according to literature [95], the fuel consumption penalty associated with

DPF backpressure and regeneration strategies ranges from 4.5% to 7.0%, depending on the frequency of the regeneration events. Typically, DPF regeneration occur with a soot loading in the order of 6 g/l, which leads to an increase in fuel consumption by 5.5-6% [95]. In the case of the implementation of PCCI combustion strategies, the low NO_x and low soot production would allow the injection of urea in the SCR system to be avoided when the engine is working within the area of the engine map that features the PCCI combustion mode. The frequency of DPF regeneration events would be also minimized. The reduction in urea and fuel used for regeneration makes it possible to tolerate some fuel penalties that are derived from the implementation of the PCCI strategy itself.

As already mentioned in *Section 1.2*, one of the major issues related to the PCCI concept, caused by the advanced injection timings and the highly premixed combustion, is CN. Fig. 1.15h shows its increment in relation to PCCI operation, with respect to the baseline Euro VI calibration. The increase in CN is due to the considerable increase in the maximum pressure derivative (cf. Fig. 1.11) [117, 135]. As the increment in CN is huge, appropriate countermeasures should be taken into account to limit the increase in acoustic noise and mechanical stress when a PCCI engine is installed on a vehicle.

Nevertheless, it is worth to remark that some examples exist in literature of premixed combustion modes where a substantial reduction of NO_x and soot emissions was obtained without penalties in CO and HC emissions, as well as in brake specific fuel consumption and noise. For example, Toyota observed the high potentiality of split injection strategies in PCCI combustion, if the injection timing and of the second injection and the fuel quantity ratio between the first and the second injections are properly optimized [161-163]. The optimal calibration was obtained injecting 70% of the fuel in an early-injection event, and starting the second injection (accounting for the remaining 30% of the total amount of fuel to be injected on the cycle) just before the start of the heat release associated with the first injection event [161]. With respect to a single-injection PCCI strategy, it is possible to lower the peak of the heat release rate of the first injection, thus reducing combustion temperature (lower NO_x, lower cooling losses) and the combustion noise [161]. Moreover, the second injection allows to obtain a fast combustion in the late phase of the combustion event, thus allowing the oxidation of the products of incomplete combustion (soot, HC, CO) and shortening the combustion duration [161]. Optimal timing and quantity of the second injection was demonstrated to affect the formation of intermediate chemical species and the flame propagation [162, 163]. Proper injection timing allows to propagate the flame towards the center of the combustion chamber after the second injection, thus allowing proper utilization of the lean charge in the center of the combustion chamber, where unburned species can oxidize due to the presence of oxygen, but extinguishing the

flame before it reaches the near-nozzle area where fuel-rich pockets are formed, thus avoiding the formation of soot [162]. The potentiality of controlling the ignition timing of the first injection through the management of the second injection event was also demonstrated through chemical kinetic simulations in combination with a multi-zone combustion model [163]. Finally, also the possibility to apply this strategy for reducing the combustion noise was discussed: as the combustion events related to the two injections excite the same frequencies in the combustion chamber, optimal timing of the second injection also leads to pressure waves in counter-phase with the pressure waves generated by the combustion of the first injection, thus leading to a “noise cancelling” effect [162, 163]. This combustion strategy, named “Diesel Staggered Premixed Ignition with Accelerated oxidation” (D-SPIA), was calibrated on a 2L research diesel engine, with compression ratio equal to 15, up to 8 bar bmep [161]. The engine was tested on dyno on the NEDC cycle and showed the potentiality of reducing NO_x emissions to a level 42% lower than Euro VI limit without SCR or DeNO_x, while CO₂ emissions were also reduced by 7% with respect to the base calibration of the engine in CDC (calibrated for Euro V emission limits) [161].

The literature study-case here described is meant to highlight that further potentialities exist to improve the performance of PCCI combustion, which encourages future researches on the topic. Recent advances of the PCCI project at the Politecnico di Torino also involved the investigation of two-injections, and three-injection strategies on PCCI combustion. Preliminary results showed the potentiality to decrease fuel consumption and CO/HC emissions, with small increases in NO_x and soot emissions with respect to single-injection PCCI. This was achieved with two-injection strategies where the quantity of the fuel injected per cycle is equally distributed between an early injection event (occurring at crank-angles close to the optimal SOIs obtained for the single-injection cases), and a later injection event occurring 15-20°CA later than the first. These results are still preliminary, and will be further investigated and presented in future works of the Research team of the Politecnico di Torino.

1.4 Steady-state and transient operations of the standard engine with model-based and pressure-based combustion control techniques

Real-time combustion control can highly improve diesel combustion, which is commonly affected by cycle-by-cycle and cylinder-by-cylinder variations both caused by internal and external factors (ambient conditions, coolant temperature, EGR unbalance, engine components aging, etc.). Besides, these combustion control techniques are of interest as they can dramatically reduce the time-consuming calibration of today's engine control systems [164]. The conventional control architecture for modern electronic control unit (ECU) is map-based, requiring great experimental activity to be carried out in order to consider all possible engine operating conditions (e.g. taking into account transient corrections, multiple maps in function of the number of injections, etc.). With the adoption of innovative combustion control methods, exploiting the computational capabilities of modern ECUs, the main parameters related to engine performance could be determined in real-time on the basis of inputs directly measured on the engine itself [34, 164, 165].

In this context, being combustion phasing recognized to be one of the most important features affecting combustion, MFB50 [33, 34] and start of combustion [35, 36] represent the most frequently used parameters for such types of real-time controls. In some applications, other quantities, such as indicated mean effective pressure (imep) and maximum of heat release rate [33] are considered, possibly in addition to the abovementioned quantities.

Two different ways of controlling the MFB50 and the SOC in real-time are possible: pressure-based and model-based approaches. The former [33, 34, 165] needs a pressure transducer for the instantaneous measurement of in-cylinder pressure, from which the corresponding mass fraction burned x_b and the actual value of MFB50 are calculated. The latter is generally based on semi-empirical modeling of in-cylinder phenomena: one possibility is proposed in [36] based on the identification of the SOC by modeling and estimating the ignition delay. Another possible methodology is based on an improved accumulated fuel mass (AFM) approach to estimate the heat release rate and the MFB50 by a low-throughput model which requires as inputs a set of engine quantities already measured or estimated by the standard ECU (such as engine speed, rail pressure, air mass, pressure and temperature in the intake manifold, fuel injected quantities and related injection timings) [166-168].

Another important benefit of combustion phasing control is related to the increased engine stability when new combustion concepts such as LTC and PCCI

are employed [34-36, 169]. As already discussed in the previous *Sections* of this *Chapter*, among the possible drawbacks for such a type of combustion mode, high combustion instability can occur (especially related to the very high EGR rate used and uneven distribution among cylinders), thus making almost mandatory the use of combustion control to implement PCCI concept in on-road vehicles [34, 36]. As a matter of fact, in these conditions the combustion is highly sensitive to variations of the intake conditions [36, 169] and this may easily cause instability, i.e. wide cylinder-by-cylinder variations in terms of imep and MFB50 up to the occurrence of misfiring events. For speed and load transient operations, the different delay of the airpath with respect to the fuelpath determines that actual intake conditions may substantially deviate from steady-state calibrated values. This becomes especially critical for PCCI/HCCI combustion, leading to high pressure and imep fluctuations. Due to the slow dynamic behavior of the airpath, closed-loop control on airpath controllers/actuators cannot provide fast enough adaptation to the transient conditions. Therefore, combustion control may be effectively provided only through an accurate control of injection parameters in order to cope with requirements in terms of combustion and torque distribution stability, acoustic comfort and pollutant emissions.

For this reason, the effects of both model-based and pressure-based combustion controls have been analyzed under steady-state and transient operations and compared to the standard map-based control. The analysis has been performed on the standard engine only, as this activity was held before the availability of the PCCI version of the engine. As a preliminary assessment of the developed techniques, most of the tests here presented refer to the application of the abovementioned models to the conventional diesel combustion mode, while a set of steady-state tests also involved PCCI combustion mode operations. The robustness of the controls has been assessed in order to evaluate the effectiveness in different working conditions, such as considering different EGR rates and SOI, and disturbing the in-cylinder pressure signal during steady-state tests.

1.4.1 Pressure-based and model-based techniques for MFB50 control

The standard ECU calibration relies on a map-based approach, i.e. quantities are interpolated from look-up tables that mainly depend on the estimated fuel injected quantity (which is related to the engine load), the engine speed and other measured quantities, such as the intake air mass and the boost pressure. In particular, SOI maps depend on the total injected quantities and on the engine speed as well as on the number of pilot injections. When transient operations are considered, the ECU applies several corrections to account for the delays in terms

of injection pressure, boost pressure, EGR, etc. Anyway, when SOI and ignition delay are no longer directly correlated, e.g in PCCI combustion mode, a new calibration of SOI would be necessary in order to achieve a correct MFB50 for all conditions, and transient operation corrections would become less effective. The calibration task would be much more time consuming and less robust compared to approaches that are able to control directly the MFB50, such as pressure-based and model-based controls.

The pressure-based control for the MFB50 stems from the measurement of the time-history of the in-cylinder pressure in the combustion chamber. The actual MFB50 value is obtained from the net energy release Q_{net} , which in turn is evaluated from the measured instantaneous in-cylinder pressure p and chamber volume V , on the basis of a single-zone approach [170], as follows:

$$dQ_{\text{net}} = \frac{\gamma}{\gamma-1} p dV + \frac{1}{\gamma-1} V dp \quad \text{Eq. 1.1}$$

where $\gamma = c_p/c_v = 1.37$. To have a short computational time a constant value of γ is chosen, even if, in a more refined calculation, γ would depend on the composition of the burned gas [166]. The integration of the dQ_{net} provides the net heat release profile Q_{net} , which is then normalized to its maximum value in order to get the mass fraction burned curve x_b and, in particular, to evaluate the MFB50, i.e. the crank angle at which the mass fraction burned is equal to 0.5. The evaluated cycle-by-cycle MFB50 is compared to the MFB50 target (i.e., $\text{MFB50}_{\text{tgt}}$) and the error between the target and the actual value is calculated. The SOI_{main} of the following cycle is then adjusted in order to minimize the MFB50 error. The method has been developed by researches affiliated to the same research group at the Politecnico di Torino, and is described into details in a previous work [171]. In order to avoid instability problems of the controller, the entity of the correction on SOI_{main} is generally lower than the MFB50 error. As all the cylinders are instrumented with piezoelectric transducers, the MFB50 error calculation and the SOI correction can be performed not only cycle-by-cycle but also cylinder-by-cylinder.

The model-based control implements a procedure that evaluates a low-throughput predictive heat release curve based on a refined version of the AFM

Control type	Features
Map-based	Standard ECU control based on SOI look-up tables.
Pressure-based	Closed-loop control on MFB50 evaluated cylinder-by-cylinder from the pressure signal.
Model-based	Open-loop control on MFB50 calculated from a predictive heat-release model.

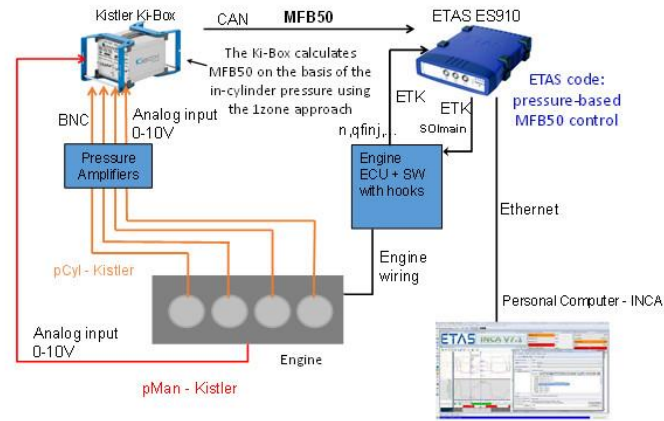
Table 1.8: Overview of the features concerning the three considered control methods.

approach [166]. As the MFB50 is not measured but estimated, the model is therefore of the open-loop type. The AFM approach considers, at any time instant, that the rate of chemical energy released by the fuel is proportional to the energy associated with the in-cylinder accumulated fuel mass, i.e. the difference between the chemical energy of the injected fuel mass and the fuel released chemical energy [166, 167, 171]. The model was assessed on steady-state tests evaluated on the considered engine. In particular, a complete engine map (made up of 126 tests at different speeds and loads) and 12 EGR sweeps were considered. Therefore, the model is capable of predicting the effects of variations in engine speed, load and intake oxygen concentration on MFB50. The root mean square error between the predicted and the experimental MFB50 was around 0.8 °CA. The control is performed by means of the model inversion. The combustion predictive model is in fact able to simulate the heat release and the consequent MFB50 for a considered set of injection parameters and working conditions. The inverted model receives as an input the desired MFB50 target, and provides as output the corresponding SOI_{main} value that allows to obtain the desired target, adopting an iterative procedure with a fixed number of three iterations [171], capable of providing the desired SOI_{main} with an uncertainty lower than 0.2 °CA [167]. An overview of the three models is reported in Table 1.8.

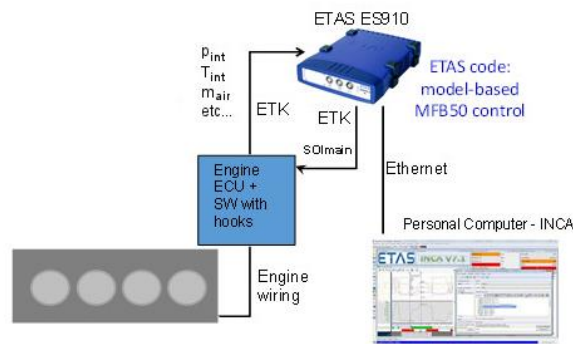
1.4.2 Rapid Prototyping setup

The rapid prototyping (RP) setup is aimed at running new control strategies bypassing only the corresponding original ones present in the ECU, thus avoiding the need of completely reprogramming the ECU. For this purpose, an ETAS ES910 RP device has been used to implement the MFB50 controls. The control algorithms were developed in Simulink and were deployed on the ETAS ES910 using the ETAS Intecrio software tool. The functionalities of the new developed controls were initially tested in a Hardware-in-the-Loop configuration in which the RP device was connected to a real-time engine emulator running on a National Instruments PXIe-8135 device [171]. In a following step, the RP device was directly connected to the engine ECU.

With reference to the setup for the pressure-based technique (Fig. 1.16a), a Kistler Kibox is used to calculate from the pressure signals acquired in all the cylinders the cycle-by-cycle real-time MFB50, using a single-zone model. The MFB50 values are sent in real-time to the RP device via CAN communication. The pressure-based control technique running on the RP device calculates the cycle-by-cycle SOI_{main} values needed to match the actual MFB50 for each cylinder to the target value. Then, it sends the updated SOI_{main} values to the engine ECU for each



(a)



(b)

Figure 1.16: Scheme of the RP setup for the pressure-based (a) and model-based (b) MFB50 control techniques.

injector via ETK communication, thus bypassing the SOI_{main} values evaluated by the map-based control.

As far as the model-based technique setup (Fig. 1.16b) is concerned, the RP device receives the input signals needed for the low-throughput heat release model from the ECU via ETK. Then, the control algorithm calculates the SOI_{main} value, equal for all the cylinders, that allows the target MFB50 value to be reached, and sends this value to the ECU via ETK, thus bypassing the standard values derived from the ECU look-up tables.

1.4.3 Steady-state tests in conventional diesel combustion mode

The experimental activity was performed with the map-based, the pressure-based and the model-based controls above described. The steady-state tests were relative to:

- Complete engine mapping with the three controls;
- SOI/MFB50 sweeps for three engine operating points with the map-based and the pressure-based control;
- Tests with a disturbed pressure signal to simulate a degradation of the pressure signal or a pressure transducer of a lower quality.

Engine mapping

The engine mapping tests here considered are the same already mentioned in *Section 1.3* as a baseline for comparing the CDC to PCCI. In detail, 85 engine points were considered and tests were performed for each of the three controls at the following speeds: 850, 1000, 1200, 1400, 1600, 2000, 2500, 3000, 3500 rpm and the following loads: 7%, 12,5%, 25%, 37,5%, 50%, 62,5%, 75%, 87,5% and 100% of the maximum torque at each speed (cf. Fig. 1.10, blue filled circles).

The considered tests practically showed the same values in terms of bsfc and specific emissions (CO, HC, NO_x and soot) measured upstream of the after-treatment device and calculated from the emission analyzers according to [172]. Therefore, pressure-based and model-based controls are able to provide results aligned to the ones of the map-based calibration, under conventional combustion mode. In order to highlight the influence of the three controls on engine combustion stability, results pertaining to the coefficient of variation (CoV) of imep and peak firing pressure (PFP) were analyzed. $CoV_{imep\ cyl}$ and $CoV_{PFP\ cyl}$ were evaluated cylinder-by-cylinder considering 100 consecutive cycles for each cylinder, while when referring to $CoV_{imep\ eng}$ and $CoV_{PFP\ eng}$, 400 pressure cycles, 100 cycles per each cylinder, were evaluated. Therefore, $CoV_{imep\ cyl}$ and $CoV_{PFP\ cyl}$ take into account the cyclic variability, whereas $CoV_{imep\ eng}$ and $CoV_{PFP\ eng}$ can be thought as parameters that encompass both cycle-by-cycle and cylinder-by-cylinder variability. The highest values of CoV_{imep} , both considering each cylinder and the whole engine, are around 4% at the lowest loads whereas at high loads they become even lower than 1% considering the map-based control, thus showing a really stable cycle-by-cycle and cylinder-by-cylinder behavior of the engine in all working conditions. As a reference, Heywood [170] indicates limit values between 2% and 5% on CoV_{imep} in order to avoid drivability issues. The high cylinder-by-cylinder engine stability with the map-based strategy can be partially justified considering a very low dispersion of the EGR rate among the cylinders in most of the map, thanks

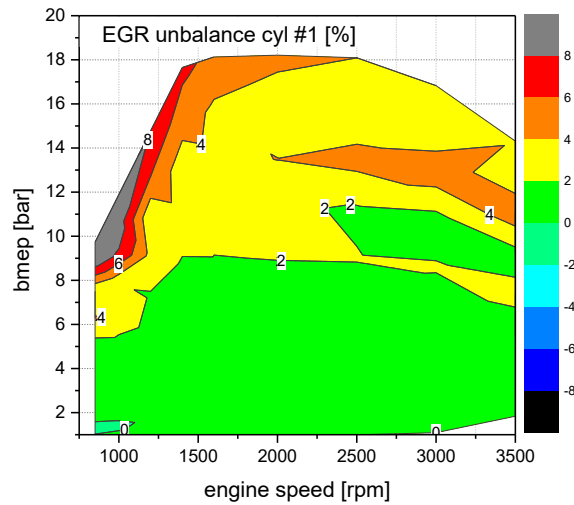


Figure 1.17: EGR unbalance in the first cylinder with the map-based ECU strategy, evaluated as the difference between the cylinder-by-cylinder EGR rate and the average one, basing on the temperature of the intake air for each cylinder. Similar figures are obtained on the other cylinders.

to a proper design of the intake system specifically intended to reduce the EGR unbalance. As an example, Fig. 1.17 shows the EGR unbalance relative to cylinder #1 (evaluated according to [172], cf. *Section 1.5*).

The $CoV_{imep\ cyl}$ and $CoV_{PFP\ cyl}$ showed similar values for the three controls. However, in the case of pressure-based control an appreciable decrease in the $CoV_{PFP\ eng}$ was generally found, especially at medium-high loads and speeds. More in detail, Figs. 1.18a-c show the $CoV_{PFP\ eng}$ as a function of the engine load, comparing the three controls at three different engine speeds. For medium to high load, it can be noted that the pressure-based control allows to achieve a reduction from 0.2 % to 0.7 % of the $CoV_{PFP\ eng}$. As the cycle-by-cycle variability was low and similar for all the controls, a reduction of $CoV_{PFP\ eng}$ can be mainly ascribed to a lower dispersion of PFP among the cylinders. Hence, the pressure-based model can provide the potentiality to reduce cylinder-by-cylinder variations related to PFP by keeping the same MFB50 target for each cylinder. The effect of the implemented strategies on the cylinder-by-cylinder combustion variations can be observed with reference to Fig. 1.19a, which reports the difference of the maximum and the minimum MFB50 (averaged on 100 cycles) among the cylinders as a function of the brake mean effective pressure, comparing the map-based strategy to the pressure-based and to the model-based methods. The graph reports the results obtained for various engine loads at 2000 rpm; similar trends are obtained for the other engine speeds. In particular, it can be noted a certain cylinder-by-cylinder dispersion of the MFB50 both in the map-based control and in the model-based one, where the difference is about 0.8 °CA between the cylinder which shows the most

advanced combustion event and the one in which the combustion tends to be more retarded. On the other hand, the pressure-based method shows practically no cylinder-by-cylinder fluctuations. As a consequence, this provided a slightly more uniform distribution of CN among the cylinders. As an example, Fig. 1.19b shows the results relative to a speed section at 2000 rpm and different loads. However, as previously mentioned, the difference in terms of emissions was practically negligible, as can also be seen considering for example engine-out soot and NO_x emissions for the speed section at 2000 rpm, reported in Fig. 1.20b. For confidentiality reasons emissions are reported in adimensional units, referring the values to the ones measured at $\text{bmep} = 1$ bar for the map-based control.

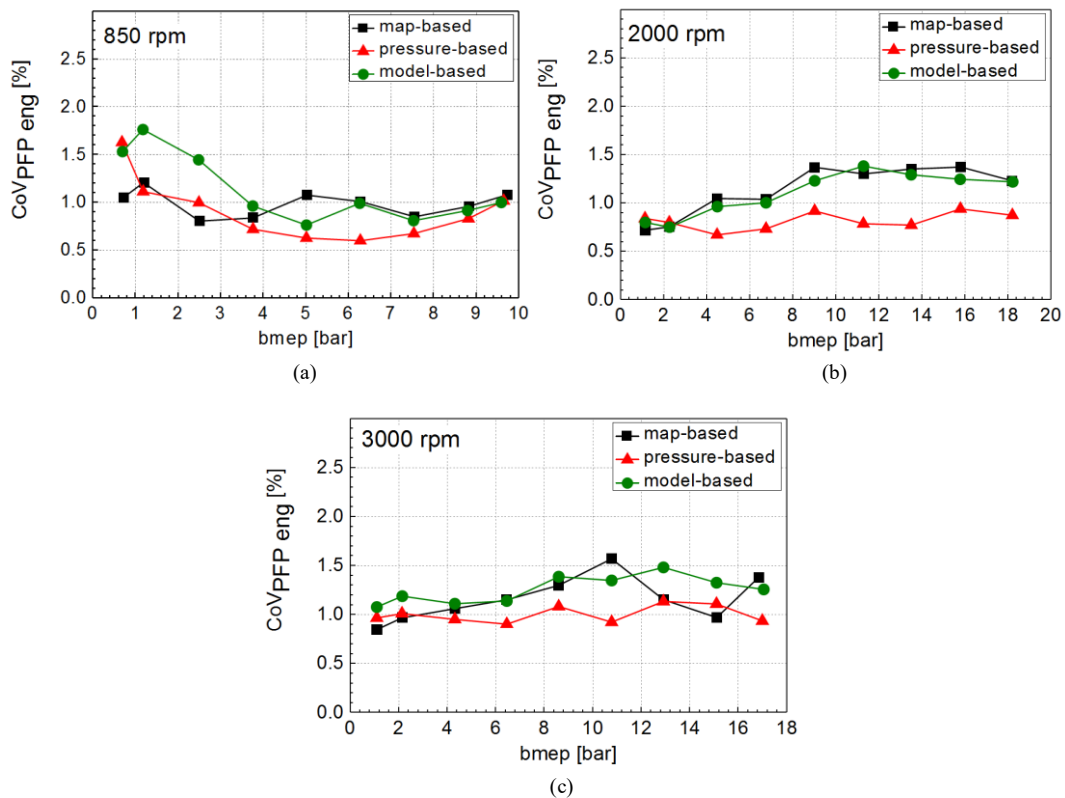


Figure 1.18: Coefficient of variation of the peak firing pressure evaluated for the whole engine at various engine loads for three different engine speeds: 850 rpm (a); 2000 rpm (b); 3000 rpm (c): comparison among the map-based, the pressure-based and the model based controls.

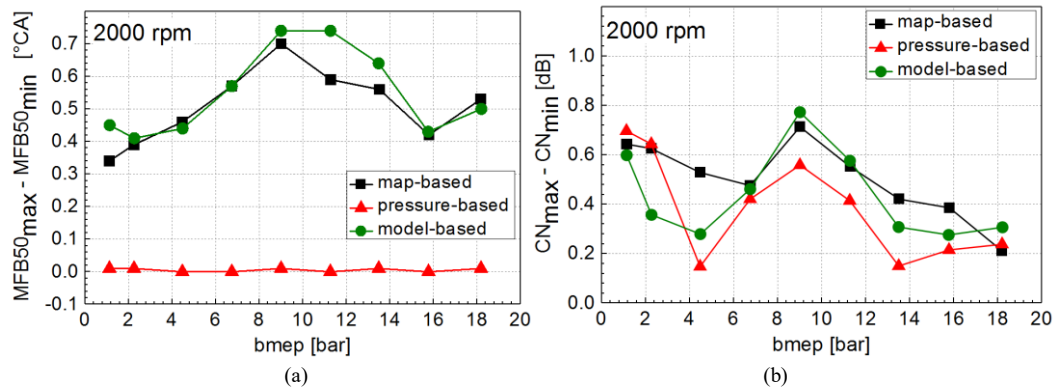


Figure 1.19: Amplitude of the dispersion range of the MFB50 (a) and of the combustion noise (b) vs. engine load at 2000 rpm: comparison among the map-based, the pressure-based and the model based control strategy.

Similar results were found at different speed sections and load sections. The improved cylinder-by-cylinder uniformity is obtained although the EGR unbalance does not vary between the two controls (map-based and pressure-based): this shows that the cylinder-by-cylinder SOI correction applied through the pressure-based strategy allows a more precise control of the in-cylinder conditions regardless from other parameters which would normally affect the development of the combustion.

SOI/MFB50 sweeps

In the SOI/MFB50 sweep tests the map-based control and the pressure-based one were compared. At two different working points, namely 1400×104 (the number before the × symbol represents the engine speed in rpm whereas the other number is the torque in Nm) and 3000 rpm at full load, a trade-off of SOI was considered for a single injection pattern (i.e. the pilot injections were disabled) for the map-based control and the corresponding values of MFB50, averaged on 100 cycles for each cylinder, were calculated. In the pressure-based control the average of the 4 values of MFB50 of the map-based control was set as a target for the pressure-based control. The model-based method was not considered because the model was calibrated considering the base engine mapping at standard SOI and multiple injection pattern. A model-based control could be applied only after having acquired all the tests necessary for the calibration of the model in these working conditions.

As for mapping, similar results were obtained in terms of bsfc and emissions, as can be noted in Fig. 1.21, which reports engine-out soot and NO_x emissions in adimensional units, in which all the values are normalized according to the values measured at the reference SOI (the lowest value) for the map-based control. Also in these tests, a reduction in the CoV_{PPF_{eng}} was obtained by the pressure-based with

respect to the map-based control, as shown in Fig. 1.22. On the other hand, similar dispersions in terms of CN were found applying the two controls, which cannot be compared to the results shown on the engine mapping since the former were performed with a triple-injection strategy while the latter presented a single injection.

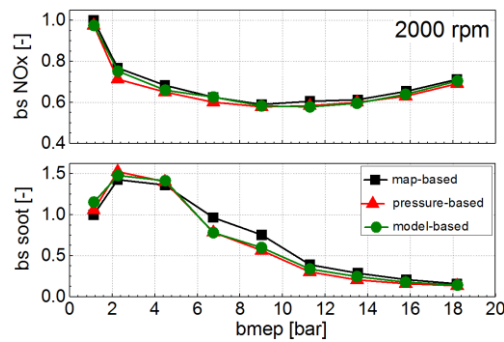


Figure 1.20: Brake specific soot and NO_x emissions at 2000 rpm: comparison among the map-based, the pressure-based and the model-based control strategy. The values are reported in adimensional units, referring all the values to the ones measured at $\text{bmep} = 1$ bar for the map-based control.

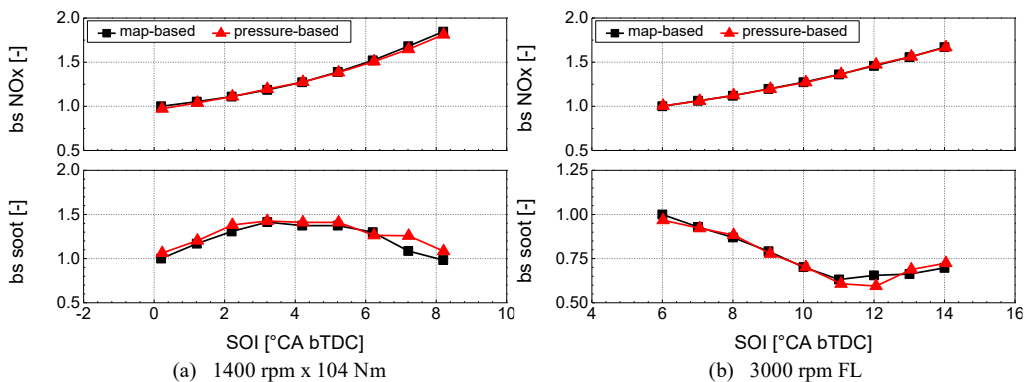


Figure 1.21: Brake specific engine-out soot and NO_x emissions at 1400 rpm \times 104 Nm (a) and 3000 rpm \times full load (b): comparison between the map-based and the pressure-based control strategy.

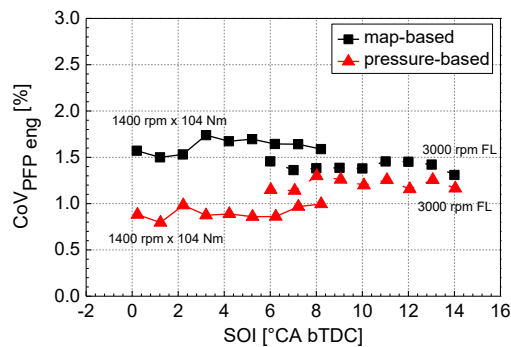


Figure 1.22: Coefficient of variation of the peak firing pressure evaluated for the whole engine on SOI sweep tests for two engine points: comparison among the map-based strategy and the pressure-based control strategy.

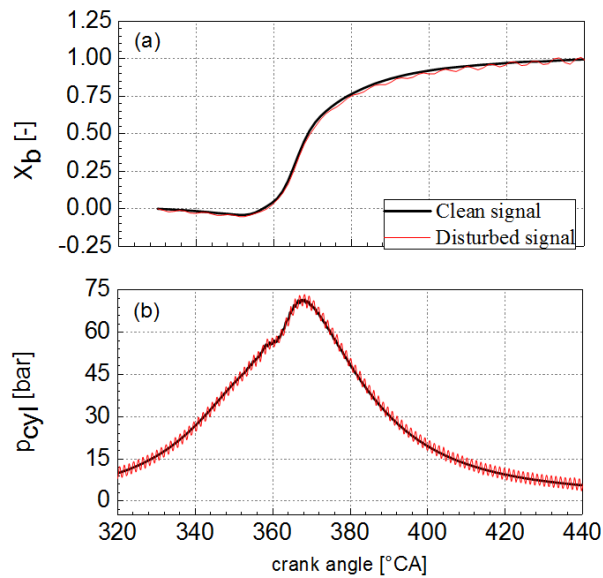


Figure 1.23: Example of mass fraction burned x_b (a) and pressure trace (b) for cylinder #1 in the case of clean signal (black solid line) and disturbed one (red solid line). Engine working point 1400×104 (rpm × Nm). Sinusoidal disturbance with amplitude = 2 bar and frequency = 7 kHz.

Disturbed pressure signal

A sinusoidal noise has been added to the pressure signals in order to replicate the behavior of a low-quality or aged in-cylinder pressure transducer and check whether the pressure-based model could still control properly the SOI_{main} . The resulting disturbed pressure signals were sent to the indicating device, i.e. the Kistler Kibox, which calculates the MFB50. To compute the MFB50, the pressure signal is filtered out by means of a moving average filter, and then the HRR curve

is calculated and integrated to get the crank angle corresponding to the 50% of burned mass.

In order to check the stability of the pressure-based control different sinusoidal disturbances, in particular 3 amplitudes – 0.7 bar, 1.4 bar, 2 bar – and 4 frequencies – 4 kHz, 5kHz, 6kHz, 7kHz, have been added to the pressure signal of every cylinder. Tests were performed for several working points setting the highest amplitude signal (i.e. 2 bar) within the selected range. Fig. 1.23 depicts the clean and disturbed signals for cylinder #1 and the corresponding fraction of burned mass. It was verified that the value of the resulting MFB50 is affected in a minor way by the disturbance, hence the pressure-based control preserves its stability even for this condition.

Further investigations could include the application of a delay to the signal, a low-frequency disturbance and a gradual attenuation of the measured pressure, the latter being a possible way to simulate a possible gradual drift in the sensor sensitivity. All these factors can occur in case of application of a pressure-based closed loop combustion control on a mass production engine, and therefore studying their effect on the combustion control stability would be of big interest for future investigations.

1.4.4 Steady-state tests in PCCI combustion mode

Some PCCI tests were carried out as a preliminary test campaign with the standard engine configuration. The comparison involved original map-based control and pressure-based model. The tests were performed at 1600×54 (rpm × Nm) with a high EGR ratio (>60%) and an advanced single injection pattern in order to obtain a PCCI combustion regime. As for the PCCI tests presented in the previous *Sections*, in order to achieve such high EGR rates, the EGR poppet valve was kept fully open and the flow rate of the recirculated exhaust gas was increased by raising the engine backpressure (i.e., the pressure difference across the EGR poppet valve) by means of the actuation of the already mentioned exhaust flap placed downstream of the turbine.

In the original map-based control strategy, the SOI was fixed at 23°CA bTDC, while in the pressure-based model MFB50 values were set to the average value from the different cylinders obtained during EGR sweep tests with map-based control. In both control strategies, the EGR sweep was performed by progressively closing the exhaust flap, until combustion instability was reached. Table 1.9 summarizes the conditions of the performed tests, where the SOI values in the case of the pressure-based method were obtained as a result of the strategy once set the target MFB50 (notice that a 100% exhaust flap position corresponds to a totally

closed flap). Due to the implemented combustion mode, soot and NO_x values were close to zero in every test condition, while similar values of bsfc, CO and HC were obtained for both controls, as it has been obtained in the previous tests.

The purpose of this part of the investigation was to check the influence of the three controls on engine combustion stability. $\text{CoV}_{\text{imep eng}}$ and $\text{CoV}_{\text{PFP eng}}$ were lower for pressure-based, with a lower CN dispersion among the cylinders. With reference to Figs. 1.24a-b, it can be observed that similar values are obtained with the two controls for the lower-end of the considered working range, while significant reductions are obtained for higher values of the flap position, i.e. in the conditions in which the combustion tends to be more unstable. As a consequence, pressure-based control also allowed to operate the engine with the flap in a more closed position, by maintaining the engine working point limit more stable. This allowed to obtain a stable combustion even with high EGR rates in PCCI operation, which increases the chances of application of this combustion mode as a mean to reduce in-cylinder formation of NO_x and PM. Moreover, a significant reduction on the dispersion in the combustion noise CN is observed, as depicted in Fig. 1.24c: for each point the difference among the cylinder which shows the maximum CN and the one with the minimum CN is reported.

As a consequence, the pressure-based combustion control is expected to be beneficial on the combustion stability of non-conventional diesel combustions, especially when PCCI is applied to a wide range of engine working conditions, as it happens on the PCCI engine configuration discussed in the previous *Sections* of this *Chapter*. Nevertheless, at the time of testing these control strategies, the PCCI engine configuration was not available yet, nor it was possible to plan this testing activity since the PCCI engine was set-up and until the time of writing. Therefore, testing these control strategies on the PCCI engine configuration is a future task of the research project.

Exhaust flap position	Map-based	Pressure-based				
	SOI ($^{\circ}\text{CA}$ bTDC)	target MFB50 ($^{\circ}\text{CA}$)	SOI ($^{\circ}\text{CA}$ bTDC)			
			Cyl #1	Cyl #2	Cyl #3	Cyl #4
94.5%	23	0.1	23.5	23.2	23.1	21.6
95.0%	23	1.8	23.7	23.2	23.1	21.2
95.2%	23	3.2	23.8	23.1	23.0	20.9
95.3%	23	4.3	23.6	22.8	22.7	20.5
95.4%	23	5.1	23.5	22.6	22.6	20.3
95.5%	23	6.6	23.9	22.7	22.6	20.3
95.5%	23	7.5	23.4	22.3	22.2	19.9
95.6%	unstable	7.5	27.4	25.1	25.1	22.3

Table 1.9: Test conditions for EGR sweeps in PCCI combustion mode.

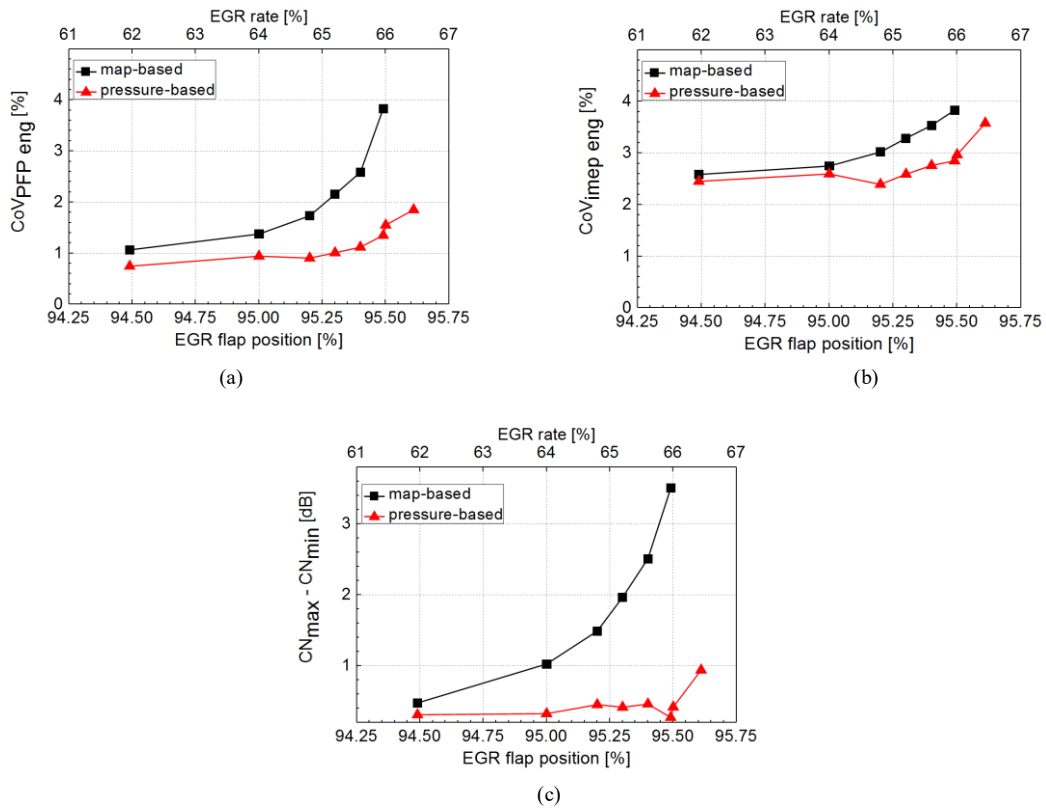


Figure 1.24: Coefficient of variation of the peak firing pressure (a) and of the indicated mean effective pressure (b) evaluated for the whole engine, and amplitude of the dispersion range of the combustion noise (c) on EGR sweep tests in PCCI combustion mode: comparison among the map-based strategy and the pressure-based control strategy.

1.4.5 Transient tests in conventional diesel combustion mode

The transient analysis hereby proposed is based on the results obtained on engine load ramps at two different engine speed levels, namely 1400 rpm and 2000 rpm, and on WHTC (Fig. 1.25).

A preliminary analysis was performed to check the influence of speed, load and a combination of them on SOI_{main} and MFB50 and therefore the engine behavior on ramps of a progressively reduced time, i.e. 10, 5, 3 s. Since the MFB50 does not vary significantly with the engine speed (Fig. 1.26), the influence of a speed variation was negligible on SOI_{main} variation. Therefore, in a successive step only fast load ramps were considered at two different fixed speeds. The slope of the ramps were chosen to be comparable with a fast transient cycle as in WHTC.

As previously stated, the map-based calibration implemented in the ECU sets SOI_{main} through look-up tables according to engine speed and load, expressed as injected fuel per cycle. Afterwards, if a load-increasing transient maneuver is detected, a correction on SOI_{main} is applied taking into account the actual p_{rail} and boost pressure in order to avoid huge increase of smoke and excessive in-cylinder pressure. Considering the performed transient tests, this correction also produces a significant reduction of NO_x . In order to perform a coherent comparison between map-based control and the new ones here proposed, based on MFB50, the transient correction of the original calibration was bypassed, because at the current development status the pressure-based and model-based controls do not perform a dynamic correction based on other engine variables (e.g. p_{rail} and boost pressure). Therefore, when talking about the map-based calibration in this *Section* it is meant

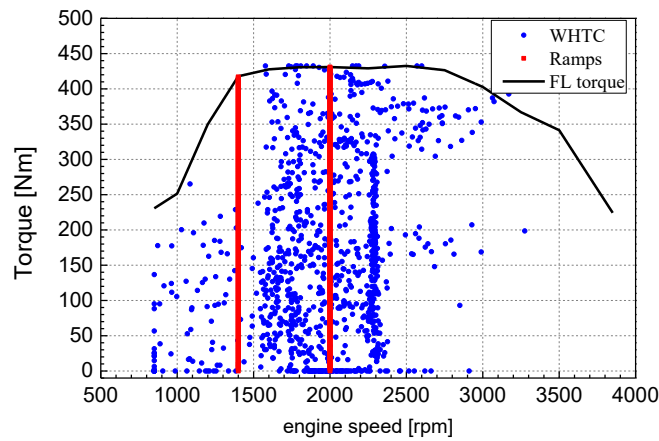


Figure 1.25: WHTC points (blue markers), load ramps (red markers) and full load curve (black solid line).

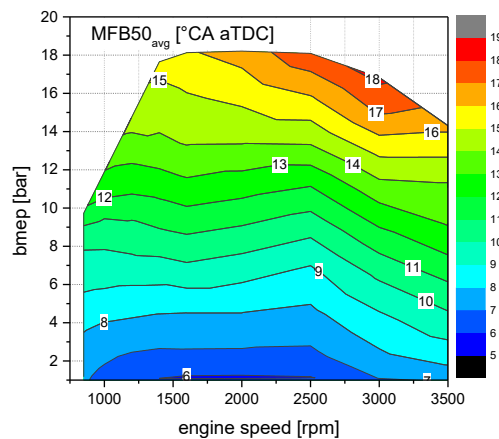


Figure 1.26: Average MFB50 among cylinders as a function of engine speed and bmep on CDC engine mapping tests.

the calibration without the transient correction, bypassed by setting the SOI_{main} referring to the steady-state map by means of the RP device.

A portion of the performed ramps is depicted in Fig. 1.27 in which the SOI_{main} and MFB50 are reported for the map-based control (Fig. 1.27b) the pressure-based control (Fig. 1.27c) and the model-based control (Fig. 1.27d). In all the graphs of Fig. 1.27, the orange thick line represents the MFB50 target relative to the pressure-based control, whereas the thin colored lines close to it represent the actual MFB50 values for the different cylinders. The SOI_{main} indicated with the thick red line in all the graphs represents the SOI of the main injection evaluated interpolating the steady-state map. For the map-based control (Fig. 1.27b), this corresponds to the SOI_{main} actuated in all the cylinders, while when the pressure-based control (Fig. 1.27c) is applied, the actual cylinder-by-cylinder SOI_{main} varies with respect to the map-based one (as indicated by the different colored lines close to the thick red one) in order to match the MFB50 target. In the model-based control (Fig. 1.27d) the SOI_{main} , reported with a green thin line, is calculated by means of the implemented strategy based on the estimated MFB50. It can be observed that the pressure-based model allows to limit the dispersion of the cylinder-by-cylinder MFB50 with respect to the target one, although – differently from what highlighted by steady-state tests – the target is not perfectly matched due to the highly dynamic nature of the transient operation. To further highlight this effect, Fig. 1.28 shows the amplitude of the cylinder-by-cylinder variation of the MFB50 in transient operation: with pressure-based control, the dispersion is less spread around a lower mean value compared to the map-based control. Still concerning the MFB50, the model-based control showed a similar cylinder-by-cylinder variation bandwidth as in the map-based control due to the absence of a cylinder-by-cylinder SOI_{main} control. Moreover, it shows an undershoot behavior of the set SOI_{main} at the beginning of the load ramp and an overshoot after it (Fig. 1.27d) possibly due to uncertainties in the real-time estimation of the intake O_2 necessary for the control [171] during high transient operation.

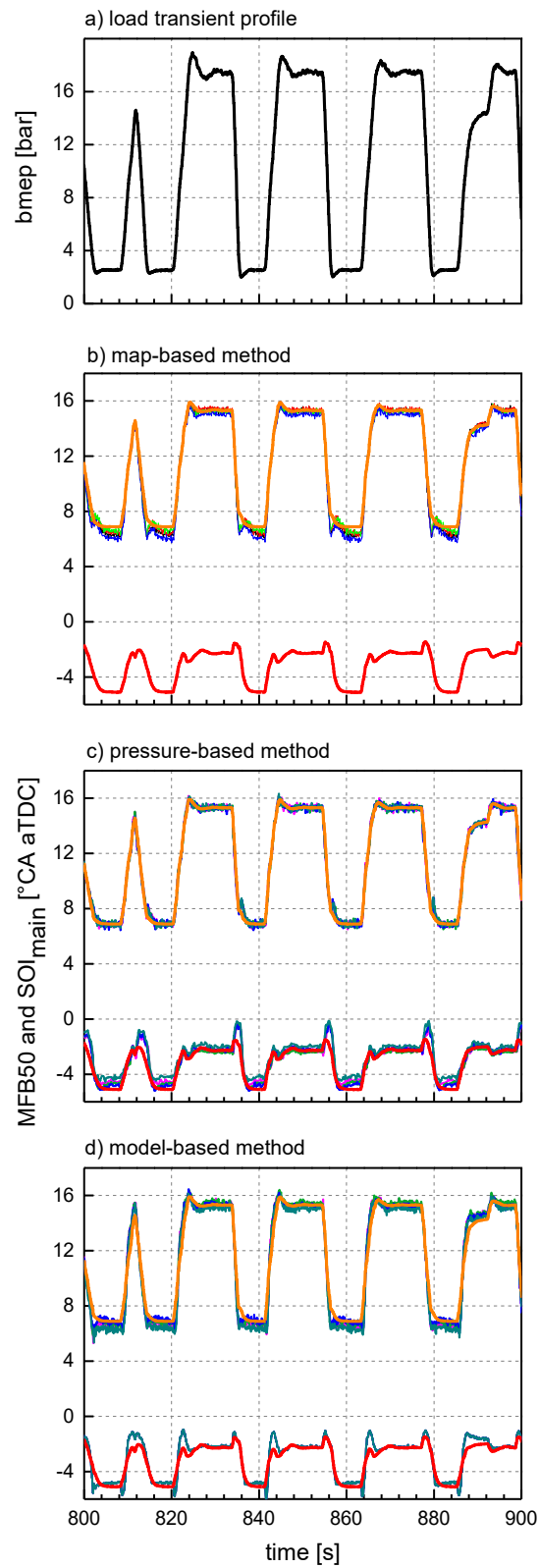


Figure 1.27: Transient analysis in CDC: part of the reference load variation profile at 1400 rpm (a) and related MFB50 and SOI_{main} values: comparison among the map-based (b, without SOI correction), the pressure-based (c) and the model-based (d) controls. In all the graphs in this Figure the upper curves refers to MFB50 and the lower ones depict the SOI.

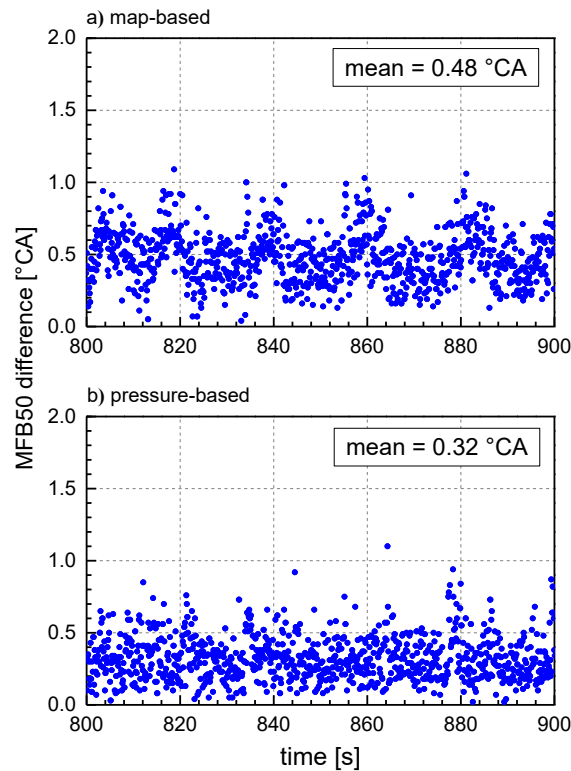


Figure 1.28: Amplitude of the variation range of the MFB50 and related mean MFB50 variations during transient operations in CDC: comparison between the map-based (a, without SOI correction) and the pressure-based (b) controls.

With reference to Table 1.10, the values of fuel consumption are virtually unaffected by the considered control. Possible variations in terms of cumulated HC emissions were difficult to be estimated as the integral value was quite low. Values of cumulated CO showed a certain dispersion among different repetitions, however pressure-based and model-based controls showed lower values up to 6% with respect to the map-based control on a single repetition of the cycle (and up to 4.8% on the average value of the various repetitions). As far as cumulated NO_x are concerned, the results were similar for the three controls (pressure-based control showed an improvement around 1.5% with respect to the map-based one, whereas a no definite trend was always found for the model-based control, considering about 10 repetitions of the considered cycles). The reasons for a decrease in NO_x can be ascribed to possible EGR delay difference between transient and steady-state conditions, especially when a decreasing load ramp is considered, and dispersion among the cylinder not accounted for by the map-based calibration.

In general, the results confirm that the proposed controls are always comparable to the standard map-based one in terms of fuel consumption and emissions, without any detrimental effect under conventional combustion. Moreover, in some cases some minor positive effects have been found. This encourages the research in the application of this methodology to transient operation under PCCI combustion mode, where larger benefits are expected due to significant improvements achievable on combustion stability. Furthermore, the pressure-based control technique allows to reduce time needed for engine calibration and improves the combustion stability with engine ageing thanks to its ability to automatically compensate for any time drift or for other random or systematic variations in the boundary conditions with respect to the reference ones. Therefore, pressure-based control is considered of interest also under conventional combustion modes.

	fc [%]	CO [%]	HC [%]	NOx [%]
Map-based	0.000	0.00	0.00	0.00
Pressure-based	0.021	-2.52	-0.49	-1.80
Model-based	-0.086	-4.76	-0.86	0.74

Table 1.10: Effect of the tested control modes on fuel consumption and emissions: average percentage variation with respect to the map-based mode.

1.5 Zero dimensional models for EGR and its unbalance estimation on the standard engine operated in conventional diesel combustion and in PCCI combustion modes

Exhaust gas recirculation (EGR), consisting in driving part of the exhaust gas flow-rate back to the intake manifold and mixing it with fresh air before the cylinder suction stroke, is a well-known and widely adopted technique to reduce NO_x emissions in modern diesel engines [168, 170, 173, 174]. The main advantage of its application is the reduction of the oxygen in-cylinder content and of the high temperature combustion flames, mostly responsible for nitrogen oxides (NO_x) formation [170]. The combination of three different basic effects induced by EGR, which are generally summarized as “dilution effect”, “thermal effect” and “chemical effect”, gives the opportunity to obtain this result [174]. When part of the oxygen content present in the inducted charge is replaced by exhaust gases, the injected fuel has to diffuse over a wider volume in order to find the necessary stoichiometric oxygen quantity to burn, thus increasing the quantity of inert gases absorbing the heat release (dilution effect). Moreover exhaust gases, containing a great amount of triatomic species (i.e. CO_2 and H_2O), are characterized by higher specific heat (thermal effect) if compared to fresh air, mainly containing diatomic molecules (i.e. N_2 and O_2). Finally, carbon dioxides and water contained in the EGR tend to undergo dissociating phenomena during combustion (chemical effect), thus contributing to the reduction of the peak combustion temperature and the consequent NO_x formation inhibition [111, 120]. In general, dilution and chemical effects are more important than the thermal effect for both conventional [173] and non-conventional combustion modes [111].

However, some drawbacks in terms of fuel consumption as well as increased particulate matter (PM), carbon monoxide (CO) and unburned hydrocarbons (HC) emissions should be taken into account when considering EGR utilization. A high EGR rate can also cause increased wear between cylinder liner and piston rings and adversely affect the quality of lubricating oil [175].

Hence, the recirculated exhaust gas flow-rate as well as the in-cylinder oxygen concentration (both parameters difficult to be measured on-board in a conventional production engine) should be known as precisely as possible to achieve the best compromise between advantages and drawbacks related to the EGR application. This is particularly true for non-conventional combustion modes, such as HCCI and PCCI, or more generally for LTC modes. In facts, as mentioned in the above *Sections*, these kinds of combustion exploit heavy amounts of recirculated gases to achieve the desired target of low engine-out NO_x and PM exhaust emissions, but

they must operate with a very precise control to limit the risk of combustion instability. A balanced cylinder-to-cylinder EGR distribution plays a fundamental role for ensuring equal combustion processes over all the cylinders [176, 177]. A higher or lower amount of EGR delivered to one cylinder with respect to the optimal target, can lead to higher average emissions formation and, in critical cases, to unstable combustion events (e.g. misfire events). For these reasons, addressing a proper methodology to estimate the EGR rate and the related unbalance is an important requirement when targeting the implementation of non-conventional diesel combustion modes.

Many possibilities exist to estimate the EGR flow-rate. This is generally estimated from the measurement of CO₂ concentration in the intake manifold, requiring a dedicated NDIR (Non Dispersive Infrared) sensor installation, and possibly one for each intake cylinder runner to have the chance of evaluating the unbalance distribution among them. Moreover, a thermal anemometer can be installed as an EGR flow-rate sensor [178]. Beyond these alternatives, many types of models have been proposed in the literature for the estimation of the EGR flow-rate, with different spatial and time resolutions [179-183]. In particular, great interest has been demonstrated towards the so-called “zero-dimensional models”, relatively simple models exploiting only lumped parameters variables with no spatial resolution [182]. The main advantage of these 0D models, also referred to as “mean value engine models”, is the low computational effort requested, characteristic that makes them particularly suitable for on-board ECU applications, especially if only input signals from conventional sensors connected to the ECU are needed for the calculations.

The aim of this *Section* is to propose and assess control-oriented models to estimate the real-time EGR rate, both intended as the average EGR in all the cylinders as well as the cylinder-by-cylinder distribution. The influence of EGR rate on combustion metrics is also analyzed.

At the time when this analysis was performed, the PCCI version of the engine was not available yet for experimental activities. Therefore, this activity has been performed on the standard diesel engine, i.e. the reference on-market engine designed for conventional diesel combustion and used for the first part of the activity also for implementing the PCCI operating mode in the low speed – low load range. The main features of the engine and of the testbed have been previously discussed in *Section 1.1* (c.f. Figure 1.1 and Table 1.1). Future activities will involve a similar analysis to be performed on the PCCI version on the engine for the development of proper control-oriented functions to be possibly implemented in the engine ECU.

1.5.1 Estimation of the mass flow through the EGR valve

In order to develop a model able to predict the flow rate recirculated in the intake manifold through the EGR system, four different approaches are developed and compared:

1. a physical-chemical method, which estimates the EGR mass flow rate starting from the chemical reaction of fuel with air and taking into account gaseous emissions and smoke level measurements in exhaust gases as well as the concentrations of various chemical species in the inlet flow rate [172];
2. a fluid-dynamic model, based on the description of the valve geometry (Figure 1.29) and on the application of the compressible-flow nozzle equation [170, 184], applied knowing the values of pressure and temperature measured upstream and downstream of the valve;
3. a semi-physical model, in which the nozzle equation is applied estimating exhaust pressure and temperature in the exhaust manifold upstream of the turbine (thermodynamic state of the fluid upstream of the control valve) as a function of relevant engine parameters by means of statistical modeling;
4. a pure statistical method, modeling the EGR flow rate as a polynomial function with linear coefficients, having as input a proper set of engine parameters.

The first approach is universally adopted for EGR rate estimation and is highly accurate if the measurements of the concentrations of the various chemical species is performed with a low uncertainty. Therefore, this method is taken as the reference for the assessment of the other models.

The fluid-dynamic model, as well as the physical-chemical approach, requires data that can be collected on a testbed but dedicated sensors are not generally available on-board engine. Therefore, the semi-physical and statistical model have been applied in order to obtain an estimation of the EGR flow rate using only variables that are already available in the engine ECU.

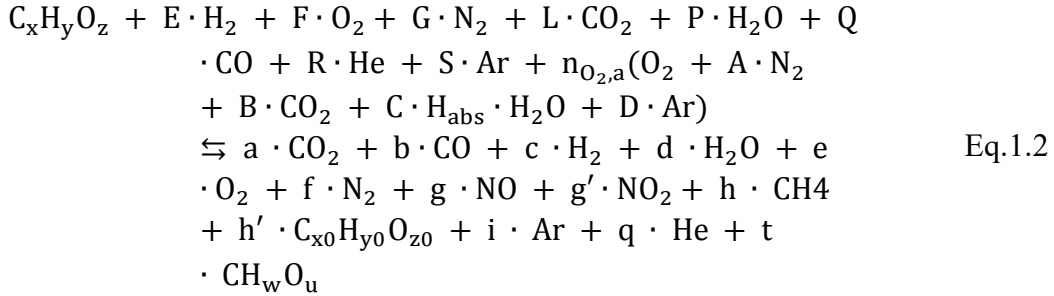
All the models were developed and tested on a set of 120 tests performed to describe a complete engine working map in the standard configuration and calibration of the engine, i.e. under conventional diesel combustion mode.

Physical-chemical method

The following description of the physical-chemical method for the estimation of EGR rate from the measurement of the concentrations of chemical species in the

exhaust gases and from the measurement of the concentration of CO₂ in the intake manifold is provided according to what reported in [172].

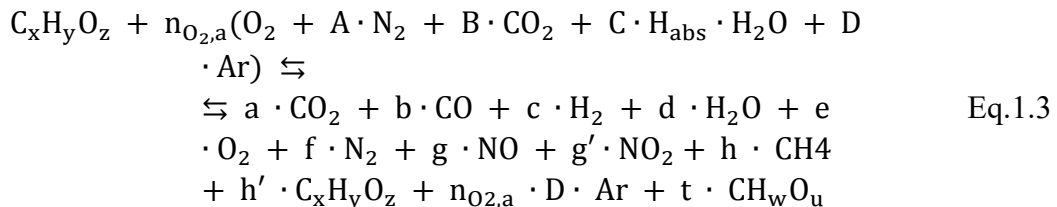
A real combustion reaction from a chemical point of view can be expressed as:



where:

- $C_xH_yO_z$ is the chemical composition of the fuel hydrocarbon molecule,
- coefficients E, F, G, L, P, Q, R and S account for the composition of gaseous fuel mixture that cannot be expressed by means of an average hydrocarbon formulation,
- $n_{O_2,a}$ is the number of moles of oxygen that react with fuel,
- A, B and D are the relative concentration of N₂, CO₂ and Ar in ambient air with respect to O₂,
- C accounts for the presence of water in the wet air,
- a, b, c, d, e, f, g, g', h, h', i and q are the number of moles of the various gaseous species at the engine exhaust, calculated from the dry measured concentrations of these species in the exhaust gas flow and corrected to account for the possible residues of water that have not condensed in the coolers inside the analyzers (whether some species are measured as “wet” concentrations, they need to be converted to dry concentrations),
- t accounts for the presence of soot (non-gaseous specie) in the exhaust.

Considering a liquid fuel, and taking into account that the concentrations of certain species (such as argon and helium) are not usually measured in the exhaust gas analyzers, the previous chemical reaction can be simplified as:



where helium has been neglected in the combustion products, and the amount of argon is considered unchanged in the two terms of the reaction.

According to the previous chemical reactions, the mass of combustion air can be written as:

$$m_a = n_{O_2,a}(M_{O_2} + A \cdot M_{N_2} + B \cdot M_{CO_2} + C \cdot H_{abs} \cdot M_{H_2O} + D \cdot M_{Ar}) = n_{O_2,a} \Omega_a \quad \text{Eq.1.4}$$

where the coefficients A, B, C and D are known for ambient air and M refers to the molar mass of the various chemical species, which are also known. Still referring to the general chemical reaction, under the hypothesis that the composition of EGR is the same as for the exhaust gases, the mass of EGR is known as:

$$M_{EGR} = n_{CO_2,EGR} \left(M_{CO_2} + \frac{b}{a} \cdot M_{CO} + \frac{c}{a} \cdot M_{H_2} + \frac{d}{a} \cdot M_{H_2O} + \frac{e}{a} \cdot M_{O_2} + \frac{f}{a} \cdot M_{N_2} + \frac{g}{a} \cdot M_{NO} + \frac{g'}{a} \cdot M_{NO_2} + \frac{h}{a} \cdot M_{CH_4} + \frac{h'}{a} \cdot M_{C_xH_yO_z} + \frac{i}{a} M_{Ar} + \frac{t}{a} \cdot M_{PM} \right) = n_{CO_2,EGR} \Omega_{EGR} \quad \text{Eq.1.5}$$

Therefore, the EGR rate can be evaluated as:

$$X_{EGR} = \frac{m_{EGR}}{m_{EGR} + m_a} = \frac{n_{CO_2,EGR} \Omega_{EGR}}{n_{CO_2,EGR} \Omega_{EGR} + n_{O_2,a} \Omega_a} = \frac{\Omega_{EGR}}{\Omega_{EGR} + \frac{n_{O_2,a}}{n_{CO_2,EGR}} \Omega_a} = \frac{\Omega_{EGR}}{\Omega_{EGR} + X \Omega_a} \quad \text{Eq.1.6}$$

The concentration of CO₂ in the inlet manifold, i.e. after fresh air is mixed to EGR, is given by the amount of CO₂ in the fresh air and the amount of CO₂ in the EGR flow, therefore it can be written as the number of moles of CO₂ in fresh air and EGR divided by the total number of moles in the intake mixture (air+EGR). In formula:

$$[CO_2]_{dry,intake} = \frac{n_{CO_2,EGR} + n_{CO_2,a}}{n_{tot,EGR} + n_{tot,air}} \quad \text{Eq.1.7}$$

where:

$$n_{CO_2,a} = B n_{O_2,a} \quad \text{Eq.1.8}$$

$$n_{tot,a} = n_{O_2,a} (1 + A + B + D) = n_{O_2,a} \Psi_a \quad \text{Eq.1.9}$$

$$n_{tot,EGR} = n_{CO_2,EGR} \left(1 + \frac{b}{a} + \frac{c}{a} + \frac{e}{a} + \frac{f}{a} + \frac{g}{a} + \frac{g'}{a} + \frac{h}{a} + \frac{h'}{a} + \frac{i}{a} + \frac{t}{a} \right) = n_{CO_2,EGR} \Psi_{EGR} \quad \text{Eq.1.10}$$

therefore:

$$[\text{CO}_2]_{\text{dry,intake}} = \frac{n_{\text{CO}_2,\text{EGR}} + B n_{\text{O}_2,\text{a}}}{n_{\text{CO}_2,\text{EGR}} \Psi_{\text{EGR}} + n_{\text{O}_2,\text{a}} \Psi_{\text{a}}} = \frac{1 + B \frac{n_{\text{O}_2,\text{a}}}{n_{\text{CO}_2,\text{EGR}}}}{\Psi_{\text{EGR}} + \frac{n_{\text{O}_2,\text{a}}}{n_{\text{CO}_2,\text{EGR}}} \Psi_{\text{a}}} = \frac{1 + B x}{\Psi_{\text{EGR}} + x \Psi_{\text{a}}} \quad \text{Eq.1.11}$$

$$x = \frac{1 - \Psi_{\text{EGR}} [\text{CO}_2]_{\text{dry,intake}}}{\Psi_{\text{a}} [\text{CO}_2]_{\text{dry,intake}} - B} \quad \text{Eq.1.12}$$

Therefore, as:

- B , Ω_{a} , Ψ_{a} are known from the composition of ambient air,
- x is known from the measured CO_2 concentration in the intake manifold,
- Ω_{EGR} and Ψ_{EGR} are calculated from the measured concentration of the chemical species in the exhaust gases,

the EGR flow rate can be estimated from Eq. 1.6.

Fluid-dynamic model

In order to determine the flow-rate, as a first step the restricted flow area through the poppet-type valve is calculated as a function of the valve lift and of the command duty-cycle. The geometric profile of the analyzed poppet valve and of its seat are reported in Figure 1.29. The two profiles and their relative position have been parametrically described on the section plane (x,y) represented in Figure 1.29. In Figure 1.29 the letters H_{v} and H_{s} indicate the point in which the conjugated profiles of the valve and of the seat are in contact when the valve is closed, and the distance between these two points along the axis y represents the valve lift l_{v} .

As long as the valve profile is curve, it was not possible to define a priori the smallest distance between the valve and the seat for each j-th value of the valve lift. Once defined the equations to describe parametrically the two profiles, an algorithm has been generated to calculate, for each considered j-th valve lift $l_{\text{v},j}$, the distance between the poppet and the seat (s_i in Figure 1.29) for each i-th segment s_i within a discrete set of segments that connect the two profiles. For each lift value $l_{\text{v},j}$, the minimum geometrical area between the poppet and seat profiles is calculated as the minimum of the areas of

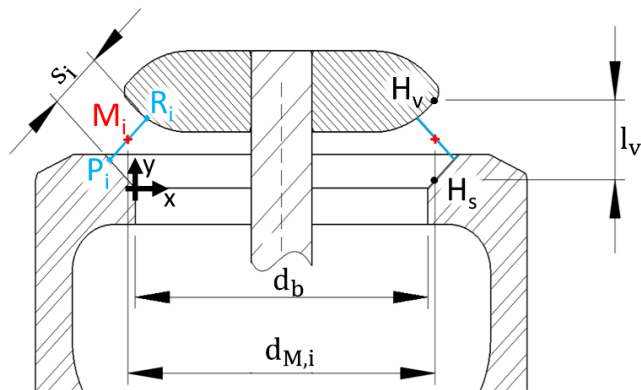


Figure 1.29: Geometric profile of the EGR poppet valve.

the surfaces of revolution generated by a 360° rotation of these segments [185]:

$$A_v(l_{v,j}) = [\min(\pi \cdot d_{M_i} \cdot s_i)]_j \quad \text{Eq.1.13}$$

$$d_{M,ij} = d_b - 2 \cdot x_{M,ij} \quad \text{Eq.1.14}$$

$$s_{ij} = \left[\sqrt{(x_{P,i} - x_{R,i})^2 + (y_{P,i} - y_{R,i})^2} \right]_j \quad \text{Eq.1.15}$$

being d_{Mij} the diameter corresponding to the barycenter of the segment s_{ij} and d_b the minimum seat diameter corresponding to the origin of the xy plane.

Figure 1.30 reports the section of the restricted area calculated for three valve lift values and Figure 1.31a shows the geometric restricted area as a function of the lift, according to the performed calculations. Moreover, the valve lift has been characterized as a function of the duty cycle of the electric signal provided to the valve (Figure 1.31b). Notice that the maximum lift which can be obtained through the electric actuation of the valve is much lower than the maximum one which can be obtained operating the valve manually.

The flow rate is then estimated assuming that the system could be described as a convergent nozzle in subsonic conditions, having measured on the testbed the pressure and temperature upstream and downstream of the valve:

$$\dot{m}_{EGR} = A_{EGR} \frac{p_{exh}}{\sqrt{RT_{exh}}} \sqrt{\frac{2k}{k-1} \left[\left(\frac{p_{co}}{p_{exh}} \right)^{\frac{2}{m}} - \left(\frac{p_{co}}{p_{exh}} \right)^{\frac{m+1}{m}} \right]} \quad \text{Eq.1.16}$$

where p_{exh} and T_{exh} are the pressure and temperature in the exhaust manifold, p_{co} is the pressure downstream of the EGR cooler (ref. Figure 1.1) and R is the elastic constant of the exhaust gas calculated from the concentration of chemical species in the raw exhaust gas flow. Although the polytropic coefficient for burned gases is generally assumed equal to 1.3 [170], in a previous case study (similar to the

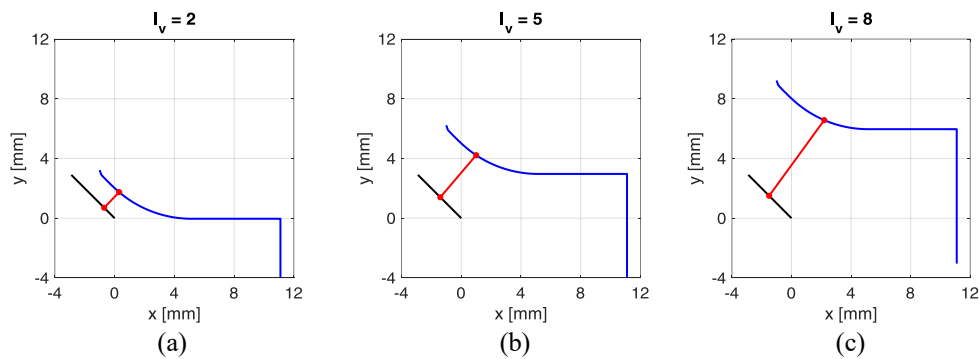


Figure 1.30: Section of the minimum flow geometrical area at different poppet valve lift l_v : 2 mm (a), 5 mm (b) and 8 mm (c).

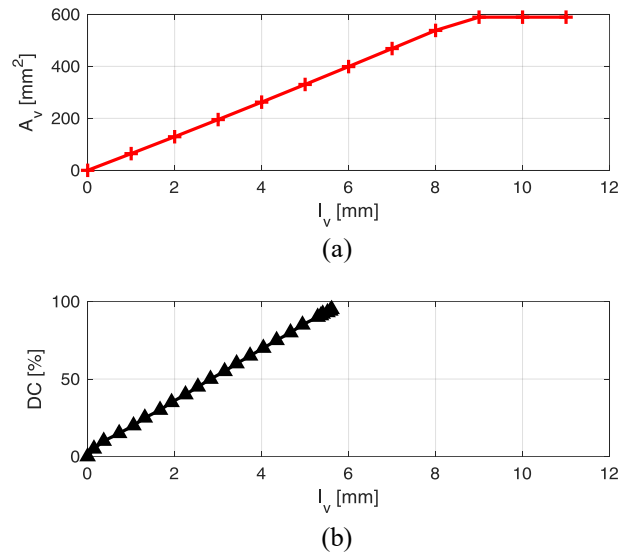


Figure 1.31: EGR poppet valve geometric area (a) and electric duty cycle (b) as function of the lift.

current application) related to evaluation of the mass flow through a cooled EGR valve the polytropic coefficient was calculated considering pressure and temperature measured upstream and downstream of the valve and it was found to be about 1.5 [184]. Therefore, in Eq. 1.16 m was assumed equal to 1.5. Due to the configuration of the EGR system it was not possible to install any sensor between the valve and the cooler, therefore the pressure downstream of the EGR cooler is the first possible measurement available downstream of the EGR valve. Consequently, the pressure losses along the cooler are neglected and the pressure p_{co} is assumed equal to the pressure on the restricted section of the valve.

Applying Equation 1.16 to working conditions in which the EGR flow rate is known by means of the physical-chemical method, an effective EGR flow area A_{EGR} can be evaluated and compared to the geometric restricted area A_v in Figure 1.32a. A discharge coefficient μ_v is estimated as the ratio between the effective flow area and the geometrical one:

$$\mu_v = \frac{A_{EGR}}{A_v} \quad \text{Eq.1.17}$$

Notice that the coefficient μ_v is calculated as the ratio between the fitting curves shown in Fig. 1.32a, where the geometric restricted area A_v is fitted through a linear function and the experimentally-derived flow area A_{EGR} has been fitted through a second-order polynomial function. This discharge coefficient is reported in Figure 1.32b as a function of the valve lift. It can be observed that it is constant for small lift values l_v and decreases for lift values higher than a critical lift $l_{v,e}$.

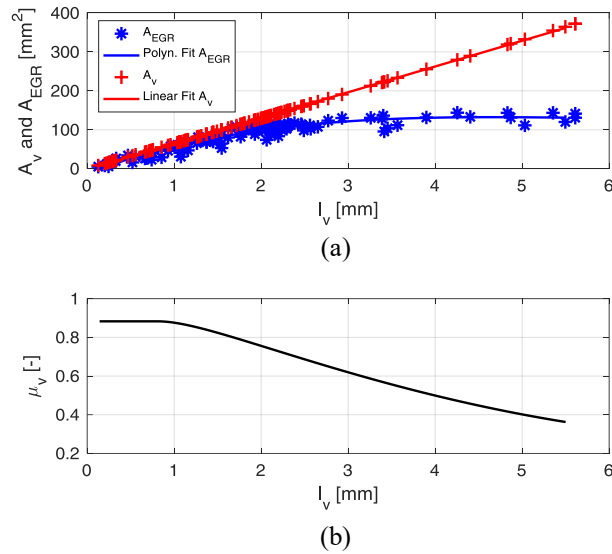


Figure 1.32: (a) Effective EGR flow area and geometrical flow area in function of the valve lift.
 (b) Flow coefficient in function of the valve lift.

Describing $\mu_v(l_v)$ through a proper regression function, i.e. a second-order polynomial function for $l_v > l_{v,e}$ and a constant value for $l_v \leq l_{v,e}$, or referring to a look-up table directly obtained as result of the calculation and interpolating linearly between the breakpoints, it is possible to correct the estimation provided in Equation 1.16 by replacing $A_{EGR}(l_v)$ with $\hat{A}_{EGR} = A_v(l_v) \mu_v(l_v)$. Similar calculations were repeated considering the hypothesis of incompressible flow, which produced a difference up to 10% with respect to the estimate obtained with Eq. 1.16. The results are shown in Figure 1.33. The hypothesis of incompressible flow provides a lower accuracy, as the Mach number reaches values up to 0.6, for the considered tests.

The discharge coefficient μ_v mostly accounts for flow detachment from the geometrical profile, which generates a vena contracta smaller than the geometrical area. In order to show this effect, some CFD simulations were performed using SolidWorks Flow simulations, setting the surrounding conditions according to data available on some experimental tests. The results are shown in Figure 1.34 in terms of fluid velocity for three values of the valve lift: 2 mm, 5 mm and 8 mm. The figure clearly shows the supposed effect of the flow detachment, which occurs more and more clearly as the lift increases, while the flow remains attached to the profiles for small values of the valve lift and of the fluid velocity.

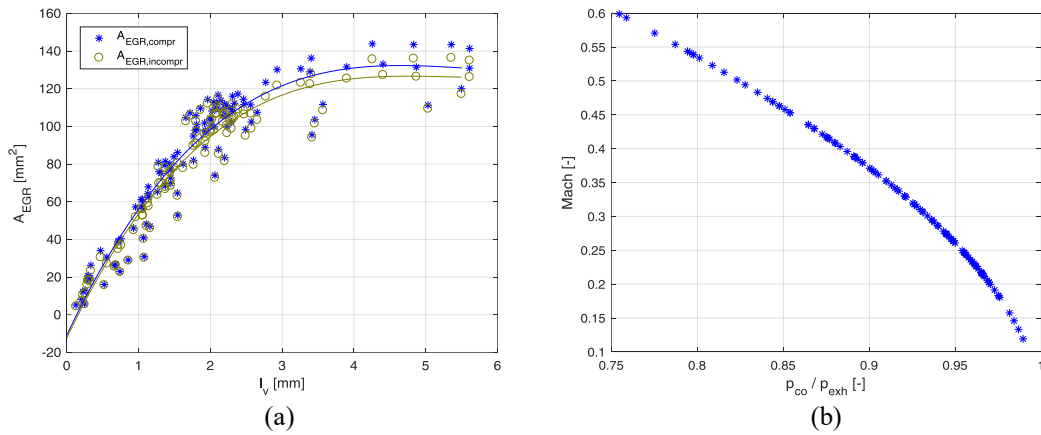


Figure 1.33: Comparison between EGR effective flow areas calculated with the hypothesis of compressible or incompressible flow (a). Mach number vs. pressure ratio across the valve (b).

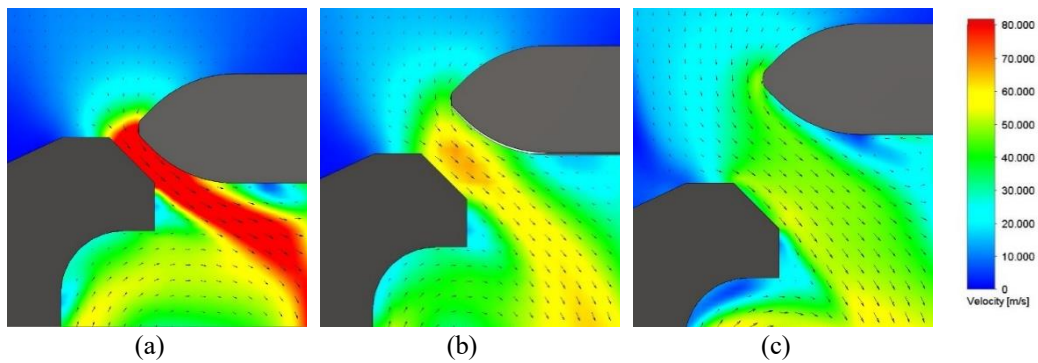


Figure 1.34: CFD simulations of the flow regime through the EGR poppet valve at three different valve lifts: 2 mm, 5 mm and 8 mm.

Semi-physical model

As long as the models are developed for control purposes, the described fluid-dynamic model would require the measurement of the exhaust pressure and temperature, which are not usually measured by the ECU. Therefore, in order to allow the implementation of this algorithm in the ECU, two sub-models have been developed through statistical techniques to estimate the exhaust temperature and pressure, i.e. the conditions upstream of the EGR valve, as a function of engine parameters. On the other hand, the pressure in the manifold p_{boost} , measured by the ECU, is considered as a good approximation of the pressure at the EGR cooler output.

For the exhaust temperature, T_{exh} a good estimation has been obtained modeling it as a linear function of the pressure and temperature in the intake manifold (p_{boost} and T_{IM}) and of the air-fuel ratio (λ):

$$\hat{T}_{\text{exh}} = \alpha_0 + \alpha_1 p_{\text{boost}} + \alpha_2 T_{\text{IM}} + \alpha_3 \lambda \quad \text{Eq.1.18}$$

which provides a coefficient of determination $R^2 = 0.977$ and a root mean square error $\text{RMSE} = 20.8^\circ\text{C}$, where the modeled variable ranges from 140°C to 640°C on the reference engine map.

Regarding the exhaust pressure p_{exh} , it was found that it is correlated with p_{boost} and λ , such as with the inlet air flow rate \dot{m}_{air} and with the engine speed n . Reducing the number of regressors up to a minimum significant set, a second order model with 6 terms is obtained, in the form:

$$\hat{p}_{\text{exh}} = \beta_0 + \beta_1 n + \beta_2 p_{\text{boost}} + \beta_3 p_{\text{boost}}^2 + \beta_4 \dot{m}_{\text{air}}^2 + \beta_5 \lambda^2 \quad \text{Eq.1.19}$$

with $R^2 = 0.999$ and $\text{RMSE} = 11.8$ mbar, where the modeled variables ranges from 1 bar to 3 bar over the complete engine map. Figure 1.35 shows the correlation between the measured and the modeled variables. Other variables, such as the amount of fuel injected and the start of injection, were also considered but were found to have a negligible effect on the estimation of the variables of interest.

The estimation of the EGR flow rate can be then obtained as:

$$\dot{m}_{\text{EGR,ss}}(l_v) = A_v(l_v) \mu_{v,ss}(l_v) \frac{\hat{p}_{\text{exh}}}{\sqrt{RT_{\text{exh}}}} \sqrt{\frac{2k}{k-1} \left[\left(\frac{p_{\text{boost}}}{\hat{p}_{\text{exh}}} \right)^{\frac{2}{m}} - \left(\frac{p_{\text{boost}}}{\hat{p}_{\text{exh}}} \right)^{\frac{m+1}{m}} \right]} \quad \text{Eq.1.20}$$

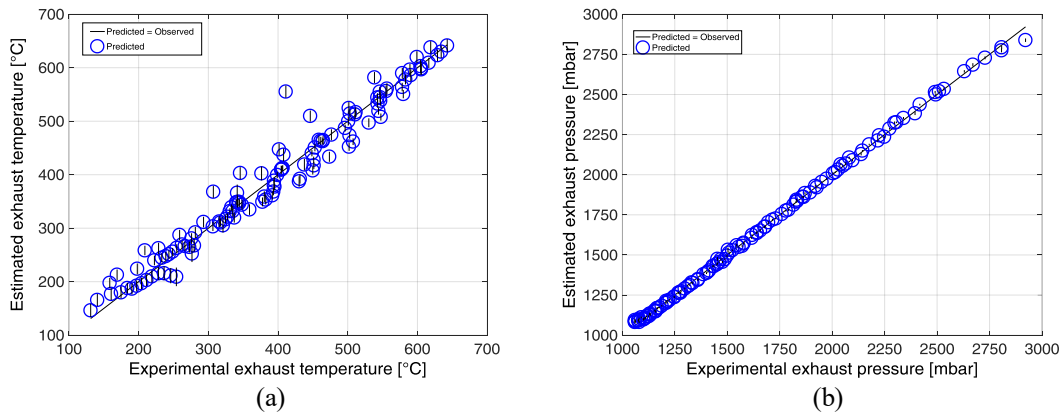


Figure 1.35: Semi-physical approach for the estimation of the EGR flow rate: correlation between the experimental exhaust temperature (a) and pressure (b) and those estimated from ECU variables.

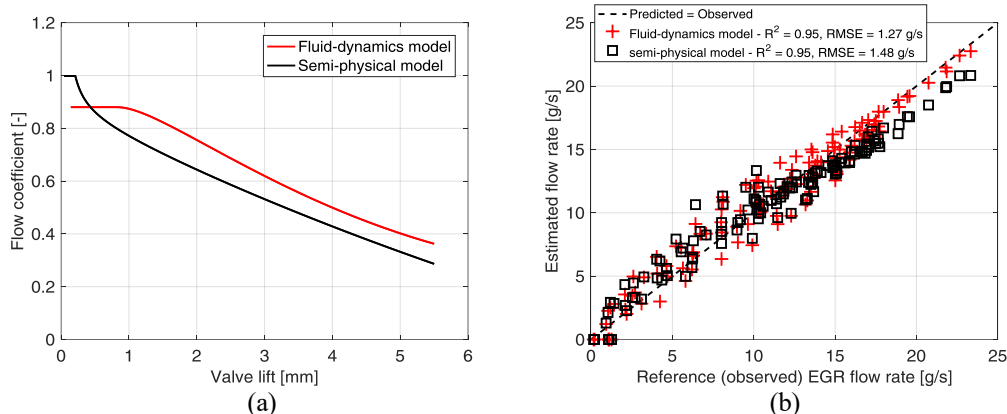


Figure 1.36: Fluid-dynamic model vs. semi-physical approach for the estimation of the EGR flow rate: flow coefficients (a) and correlation between reference and estimated flow rate values (b).

where the coefficient $\mu_{v,ss}$ is re-calculated comparing the result obtained by the model of Eq. 1.20 and the mass flow rate calculated by means of the analysis of the concentration of chemical species in the intake and exhaust manifolds. This is justified considering $\mu_{v,ss}$ as a fitting coefficient that accounts for the flow detachment as well as for other non-idealities, including modeling uncertainties.

Figure 1.36a shows the comparison between the flow coefficient μ_v of Eq. 1.17 and the coefficient $\mu_{v,ss}$ in Eq. 1.20. Figure 1.36b reports a graphical comparison between the fluid-dynamic and the semi-physical models for the estimation of EGR flow rate on the calibration dataset. The dispersion of the data around the bisector shows that both the models provide reliable results, with a slightly higher dispersion for the semi-physical model. Both the models show a higher dispersion for high flow rates, which is justified considering that the two flow coefficients have been obtained as the ratio between regression functions used to describe the geometric and effective areas.

Pure statistical approach

A further approach analyzed for modelling the EGR mass flow rate is a pure statistical one: without applying any constraint related to the valve geometry, the variable of interest is described through a polynomial model as a function of a set of input variables selected among those available in the ECU. The engine variables taken into account, which are supposed to have an effect on the EGR flow rate, are:

- engine speed, n ;
- mass of fuel injected in each cylinder per cycle, q_b ;
- pressure in the intake manifold, p_{boost} ;

- duty cycle of the EGR valve, DC_{EGR} ;
- duty cycle of the exhaust flap valve, DC_{flap} ;
- start of injection of the main injection, SOI_{main} ;
- position of the blades of the variable geometry turbine, VGT_{pos} .

This set of variables are chosen still with reference to Eq. 1.16, selecting those ECU variables which should affect the pressure at the intake and exhaust manifold, the temperature of the exhaust gases as well as the valve flow area.

The model is originally built as a second-order polynomial model, including also the regressors related to interactions of the inputs. Other models are then built choosing some subsets of the regressors of the initial model. The best performance on the dataset used to fit the model is obtained with a very simple linear model, in the form:

$$\hat{m}_{EGR,s1} = \gamma_{01} + \gamma_{11}n + \gamma_{21}Q_b + \gamma_{31} p_{boost} + \gamma_{41}VGT_{pos} \quad \text{Eq.1.21}$$

Other models were set and tested, all providing similar results on the original dataset, i.e. full engine maps realized with the standard calibration tuned for conventional combustion. As an example, another model is also considered for comparison:

$$\begin{aligned} \hat{m}_{EGR,s2} = & \gamma_{02} + \gamma_{12}n + \gamma_{22}Q_b + \gamma_{32} p_{boost} + \gamma_{42}VGT_{pos} + \\ & + \gamma_{52}DC_{EGR} + \gamma_{62}DC_{flap} + \gamma_{72}SOI_{main} + \gamma_{82} VGT_{pos}^2 \quad \text{Eq.1.22} \end{aligned}$$

The first model, i.e. Eq. 1.21, shows a determination coefficient $R^2 = 0.966$ and $RMSE = 1.11$ g/s. The latter (Eq. 1.22) has $R^2 = 0.91$ and $RMSE = 1.77$ g/s. The modeled variable ranges from 0 to 23 g/s. The maximum error is about 1.5% for the first model and 4% for the second one, being both models – and especially the second one – affected by a higher error in the estimation of small flow rates.

Assessment and validation of the models

All the models described have been developed and tuned taking as a reference a complete engine map tested with the standard Euro VI engine calibration in conventional diesel combustion. As a further step, the models have been validated through the assessment of their performance on other datasets, including other tests on the standard engine map, further tests in conventional combustion including trade-offs of air quantity and a sweep of the EGR valve or of the exhaust flap, and tests in PCCI combustion mode. The aim is to verify which models are able to provide a good estimation also in working conditions fairly different from those used for calibration. This would be an essential benefit for any model-based control.

Figure 1.37 shows the result of this analysis, where the models described, reported on y axis, have been compared with the reference one, i.e. the EGR flow rate estimated with the physical-chemical method, on x axis. Figure 1.37a shows the validation on a replicated test of the engine map. The graph shows that, on a dataset nominally equivalent to the calibration map, all the models are comparable in terms of determination coefficient R^2 and root mean square error RMSE: R^2 is always between 0.91 and 0.95 and RMSE is in the range 1.27-2.28 g/s, where the variable to be predicted ranges from 0 to 23 g/s. Figure 1.37b shows the models validation on trade-off tests realized on 10 engine working points from low to medium loads and on the whole engine speed range. The validation dataset includes air quantity sweeps on each of the considered engine working point, realized according to a one-factor-at-a-time approach. Therefore these tests include working conditions that are outside of the standard engine calibration. The graph shows a general worsening of the models performance. The fluid-dynamic model results to be the most accurate one, and its performance is comparable to what obtained on the engine maps. More in details, it can be observed that a worsening in the model performance is visible for flow rates higher than those reached on the engine map. The semi-physical model in Figure 1.37b provides a slightly lower determination coefficient with respect to the purely physical one, and higher RMSE up to 2.21 g/s (around 7% of the maximum flow rate). The pure statistical models, on the other hand, show a significant worsening of the performance: the first one (i.e., the simplest) has a higher dispersion on all the range with high errors for small flow rates, while the second has critical fitting errors also for medium flow rates, with a generally poor correlation between the phenomenon and its description. Similar results were also obtained on a set of EGR valve sweeps and exhaust flap sweeps realized on 9 engine working points.

Finally, the four models were validated on some tests in PCCI combustion mode, namely four engine points at low-medium engine speed and low engine loads: 1200 rpm \times 23 Nm, 1400 rpm \times 71 Nm, 1600 rpm \times 54 Nm, 1800 rpm \times 27 Nm. These tests were performed as part of the activity discussed in *Section 1.2* through the application of the statistical design of experiments in order to explore some engine working conditions, which allow to implement this non-conventional combustion mode. These datasets were then used to perform a model-based calibration of these engine points in PCCI, as discussed in *Section 1.2*. Figure 1.37c shows that the fluid-dynamic model provides a good estimation of the flow-rate also in these working conditions, with statistical indicators which are comparable to those obtained with the same model on other kind of validation tests. As already pointed out for all the PCCI tests, it can be highlighted that these tests have been performed keeping the EGR valve always in the fully-open condition and varying the flow-rate only managing the exhaust flow partialization through the flap exhaust

valve. Referring to the semi-physical model, although the determination coefficient is 0.93, the RMSE is higher than in the other tested cases: this highlights a systematic error which increases as the mass flow rate increases. On the other hand, both the statistical models show an extremely poor performance on these tests: the first model results to be completely uncorrelated with the phenomenon to be described, while the second model shows a clear worsening of the correlation for flow rate values close to or bigger than the maximum value in the calibration map.

The analysis shows that the fluid-dynamic model is able to properly describe the phenomenon in every working condition. Also the semi-physical model generally provides a good correlation, although a systematic error is highlighted in PCCI combustion mode, possibly due to the dependence of the estimated exhaust pressure and temperature on some engine variables that may have a negligible influence in the model calibration with the original dataset. On the other hand, purely statistical polynomial models built without a background knowledge of the

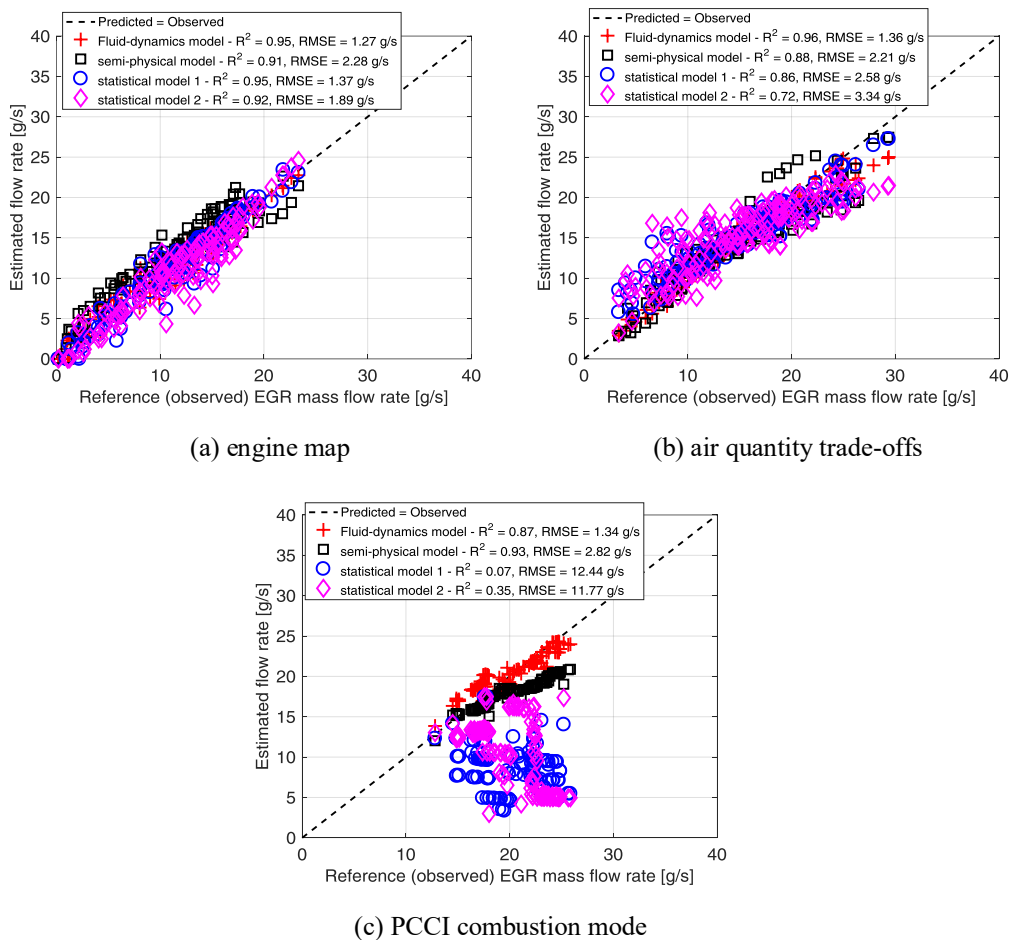


Figure 1.37: Assessment of the models for the prediction of EGR mass flow rate: engine map, trade-offs and PCCI tests.

physics of the system were not able to predict properly the EGR flow rate in working conditions different from the calibration tests. Apart from the two presented purely statistical models, a large number of other models, obtained with the same procedure, were analyzed and provided similar or lower performance.

1.5.2 Correlation of the EGR rate with combustion metrics

When high EGR rates are used to lower combustion temperature and NO_x emissions, especially in PCCI and low-temperature combustion modes, the combustion process and exhaust emissions tend to exhibit a marked sensitivity to small changes in the operating conditions because the engine is close to the limit of combustion stability, as also discussed in *Section 1.4*. As in PCCI engines the EGR influence on combustion development is high [150], the correlation of some combustion markers to the EGR rate has been investigated.

A single-zone net heat release rate approach (cf. Eq. 1.1) has been considered to evaluate the crank angle positions at which 10, 50 and 90% of the injected fuel has burnt, i.e. MFB10, MFB50 and MFB90. Each value is obtained for each cylinder as the average of 100 engine cycles. Moreover, in this *Section* these values are considered in terms of an average value of the 4 cylinders.

The correlation between the oxygen volume concentration [O₂] in the intake manifold and the ratio between the EGR rate (X_{EGR}) and the air-fuel ratio (λ) is known in the literature [186] and its validity has been verified also on the tested engine, on a complete engine map. The result is shown in Figure 1.38, where a linear correlation is verified in the form:

$$[O_2] = \delta_0 - \delta_1 \frac{X_{EGR}}{\lambda} \quad \text{Eq.1.23}$$

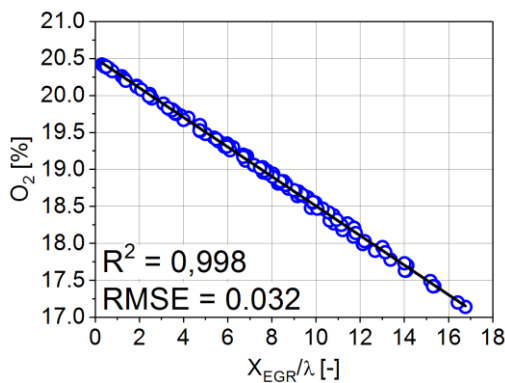


Figure 1.38: Correlation between the oxygen concentration in the intake manifold and the ratio between EGR rate and air-fuel ratio.

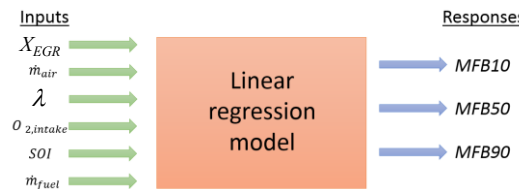


Figure 1.39: First-attempt input/output model.

where the EGR rate (X_{EGR}) is defined as the ratio between the EGR mass flow rate (\dot{m}_{EGR}) and the total intake mass flow-rate ($\dot{m}_{EGR} + \dot{m}_{air}$), and is evaluated according to the abovementioned physical-chemical method [172]. If a correlation among MFB10/50/90 and the EGR rate is sought, also $[O_2]$ and λ can be included among the inputs for the investigation. Moreover, other variables that are considered to have a strong influence on the phasing of the combustion process are air and fuel flow-rates and SOI_{main} . Therefore, the set of inputs and outputs is depicted in Figure 1.39. In order to analyze the factors that have a major influence on combustion phasing and its duration among those shown in Figure 1.39, a Matlab code has been developed which, given a set of variables and the associated values resulting from tests, builds all the polynomial linear models up to the second order that can be obtained combining all the input variables in order to fit the selected output variable. For each of the models the software provides the coefficient of determination and the root mean square error, together with the values of the constants associated to each of the regressors. By analyzing these results, considering only the models with independent regressors (i.e., excluding all the models where some regressors have a known cross-dependence), it is possible to individuate some minimum sets of regressors to provide a suitable description of the output variables. This approach was applied using the set of inputs and outputs shown in Figure 1.39. The best models were then further analyzed using the Model Based Calibration tool embedded in Matlab, in order to check the results, individuate and possibly eliminate outliers, etc...

On the reference analyzed condition, i.e. an engine map (120 engine points) in conventional diesel combustion, the SOI_{main} and the fuel flow rate have been found to have only a negligible effect on the studied responses, therefore they have been eliminated from the original set of inputs. The variable that was found to have the highest influence is the air flow rate. Figure 1.40 shows the results obtained by

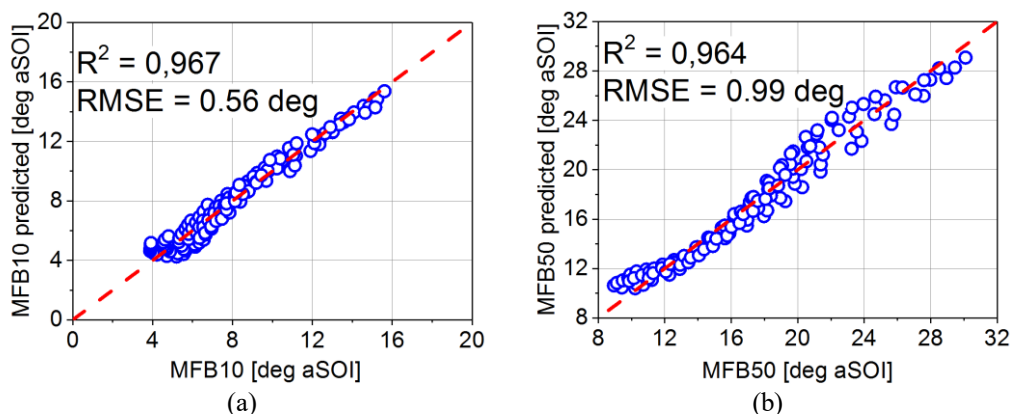


Figure 1.40: Prediction of MFB10 (a) and MFB50 (b) based on a linear model with only air mass flow rate as input.

predicting MFB10 and MFB50 using a linear model having as input only \dot{m}_{air} . In these cases a linear correlation between the combustion markers and the air mass flow rate is really strong, therefore the dependence on any other parameter cannot be assessed.

On the other hand, Figure 1.41a shows that the correlation between MFB90 and \dot{m}_{air} , although strong, is not sufficient to completely describe this combustion marker on all its variation range. Figure 1.41b and Figure 1.41c show also the results obtained through two estimation model obtained considering \dot{m}_{air} and X_{EGR} (Figure 1.41b) and \dot{m}_{air} and $[\text{O}_2]$, (Figure 1.41c) which also generate a poor correlation between the predicted and the measured MFB90. Finally, a model has been tested which describes the MFB90 as a linear function of \dot{m}_{air} and λ , whose result is shown in Figure 1.41d. The graph shows a very good correlation between the predicted and the measured MFB90, with a coefficient of determination of 0.93 and an RMSE of 1.46. The statistical model is in the form:

$$\text{MFB90} = \varepsilon_0 + \varepsilon_1 \dot{m}_{\text{air}} + \varepsilon_2 \lambda \quad \text{Eq.1.24}$$

Combining Eq. 1.23 and Eq. 1.24, it is possible to obtain a relationship among MFB90, X_{EGR} , $[\text{O}_2]$ and \dot{m}_{air} :

$$\text{MFB90} = \alpha_0 + \alpha_1 \dot{m}_{\text{air}} + \frac{\alpha_2 \delta_1 X_{\text{EGR}}}{[\text{O}_2] - \delta_0} \quad \text{Eq.1.25}$$

The same relation could be inverted to evaluate the EGR rate starting from the MFB90:

$$\begin{aligned} X_{\text{EGR}} = & \frac{\alpha_0 \delta_0}{\alpha_2 \delta_1} - \frac{\delta_0}{\alpha_2 \delta_1} \text{MFB90} + \frac{\alpha_1 \delta_0}{\alpha_2 \delta_1} \dot{m}_{\text{air}} - \frac{\alpha_0}{\alpha_2 \delta_1} [\text{O}_2] + \\ & + \frac{1}{\alpha_2 \delta_1} \text{MFB90} \cdot [\text{O}_2] - \frac{\alpha_1}{\alpha_2 \delta_1} \dot{m}_{\text{air}} \cdot [\text{O}_2] \quad \text{Eq.1.26} \end{aligned}$$

Introducing some new constants $\gamma_{0,1,2,3,4,5}$, given by the products and ratios of the constants in Eq. 1.26, the last relationship can be rewritten in the final form:

$$\begin{aligned} X_{\text{EGR}} = & \gamma_0 - \gamma_1 \text{MFB90} + \gamma_2 \dot{m}_{\text{air}} - \gamma_3 [\text{O}_2] + \\ & + \gamma_4 \text{MFB90} \cdot [\text{O}_2] - \gamma_5 \dot{m}_{\text{air}} \cdot [\text{O}_2] \quad \text{Eq.1.27} \end{aligned}$$

The result is shown in Figure 1.42, in which the EGR rate predicted by Eq. 1.27 is compared with the reference one, obtained through the physical-chemical method.

This analysis shows that the EGR rate (or other correlated quantities such as the oxygen concentration in the intake manifold or the air-fuel ratio) has a minor

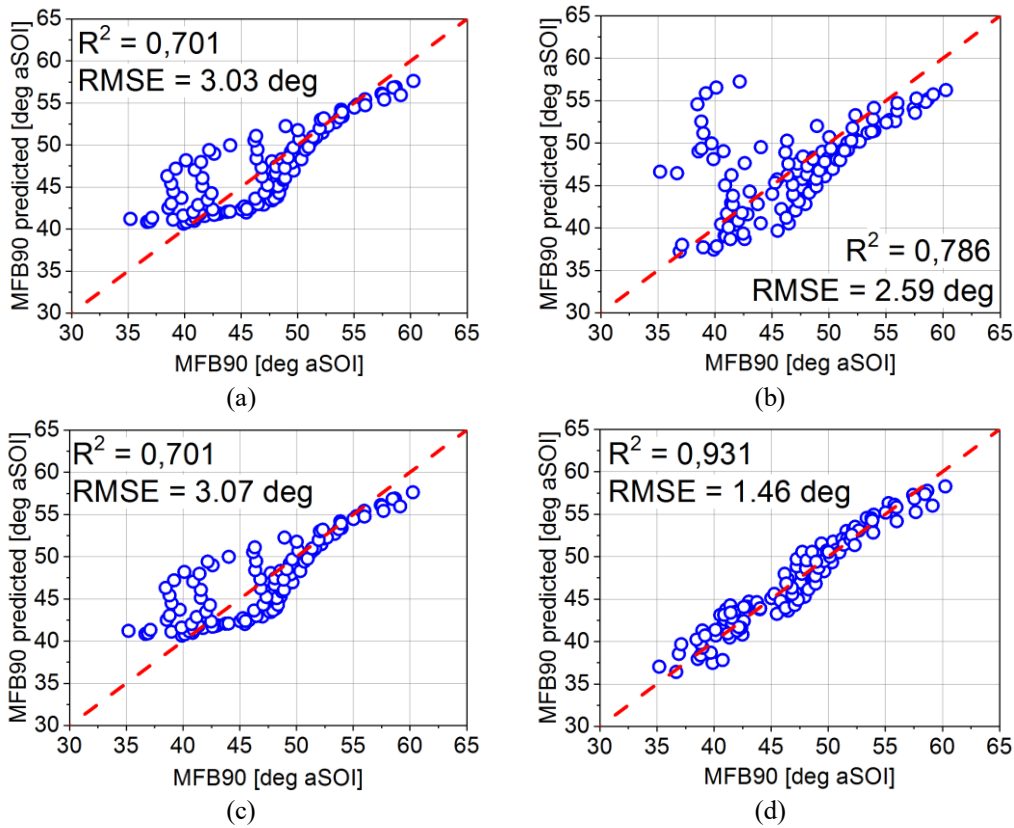


Figure 1.41: Prediction of MFB90 based on linear model which consider as input: only the air mass flow rate (a), the air mass flow rate and the EGR rate (b), the air mass flow rate and the oxygen concentration in the intake manifold (c), the air mass flow rate and the air-fuel ratio (d).

effect on the combustion rate during the first phases combustion, while it has an appreciable effect on the last part of the process. Given a certain oxygen concentration in the intake mixture, the last phase of the combustion is slowed down by an increase of EGR since it makes more difficult for the remaining unburned or partially burned fuel particles to find some fresh air to oxidize.

The same analysis was also extended to EGR sweeps in PCCI combustion mode at 1200×23 and

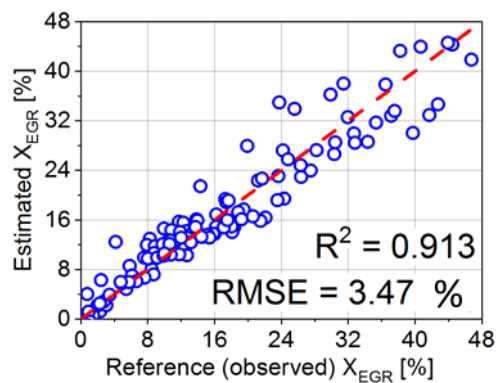


Figure 1.42: Predicted vs. reference EGR rate, where the prediction is obtained applying Equation 1.27.

1400 × 71 (rpm × Nm) performed on the standard F1C engine, where the EGR rate was changed in a range between 48% and 63.6%. In this case the results are significantly different. In particular, for MFB10 and MFB50, considering only air flow rate \dot{m}_{air} as a regressor, and using a first-order linear relation as for the results shown in Figure 1.40 for CDC, would result in prediction models with a lower coefficient of determination, i.e. R^2 equal to 0.85 and 0.83, respectively. This shows that, although the amount of inducted air is a main factor to determine these combustion metrics also in PCCI (as the air flow rate is related both to the engine speed and load, in a turbocharged engine with VGT), in this combustion mode some additional factors have to be considered to get a proper prediction of the combustion phasing. Both for MFB10 and MFB50, a coefficient of determination equal to 0.95 can be obtained by means of a first-order polynomial model that considers as regressors the air mass flow rate and the EGR rate, confirming that in this combustion mode the amount of EGR has a topic function in determining the development of the combustion process, especially for what concerns ignition delay. Anyway, a better fitting of the models can be obtained in the form:

$$\text{MFB10} = \kappa_{01} + \kappa_{11}\dot{m}_{\text{fuel}}^2 + \kappa_{21}[\text{O}_2] \quad \text{Eq.1.28}$$

$$\text{MFB50} = \kappa_{02} + \kappa_{12}\dot{m}_{\text{fuel}}^2 + \kappa_{22}[\text{O}_2] \quad \text{Eq.1.29}$$

where the mass flow rate of fuel accounts for the engine load, and the oxygen concentration accounts for both the amount of fresh air and for the amount of EGR. The result of this fitting is shown in Figs. 1.43a-b.

Concerning MFB90, considering only air mass flow rate as a regressor would provide a model with a coefficient of determination lower than 0.1. On the other hand, considering only lambda as a regressor would provide a coefficient of determination of 0.86, and a first-order linear model with air mass flow rate and lambda (as the one used for CDC and shown in Eq. 1.24) would provide a determination coefficient of 0.89. A more accurate model can be obtained considering a second-order model with air and oxygen as regressors, in the form:

$$\text{MFB90} = \kappa_{03} + \kappa_{13}\dot{m}_{\text{air}} + \kappa_{23}[\text{O}_2] + \kappa_{33}[\text{O}_2]^2 \quad \text{Eq.1.30}$$

The result of this last model is reported in Figure 1.43c. A summary of the main models of interest is also reported in Table 1.11, where for each of the most relevant models the constants of the considered regressors are reported, together with the related coefficient of determination and root mean square error. As the MFB90 shows a poorer correlation with respect to MFB10 and MFB50, with a slightly lower R^2 and a considerably higher RMSE, this parameter has not been considered for further evaluations concerning these models.

Furthermore, the relation between intake oxygen concentration and the ratio of EGR rate to lambda, i.e. Eq. 1.23, was also verified in PCCI combustion mode, and the result is shown in Figure 1.43d. therefore, this correlation has been proven to be robust in wide range of oxygen concentration/EGR rate.

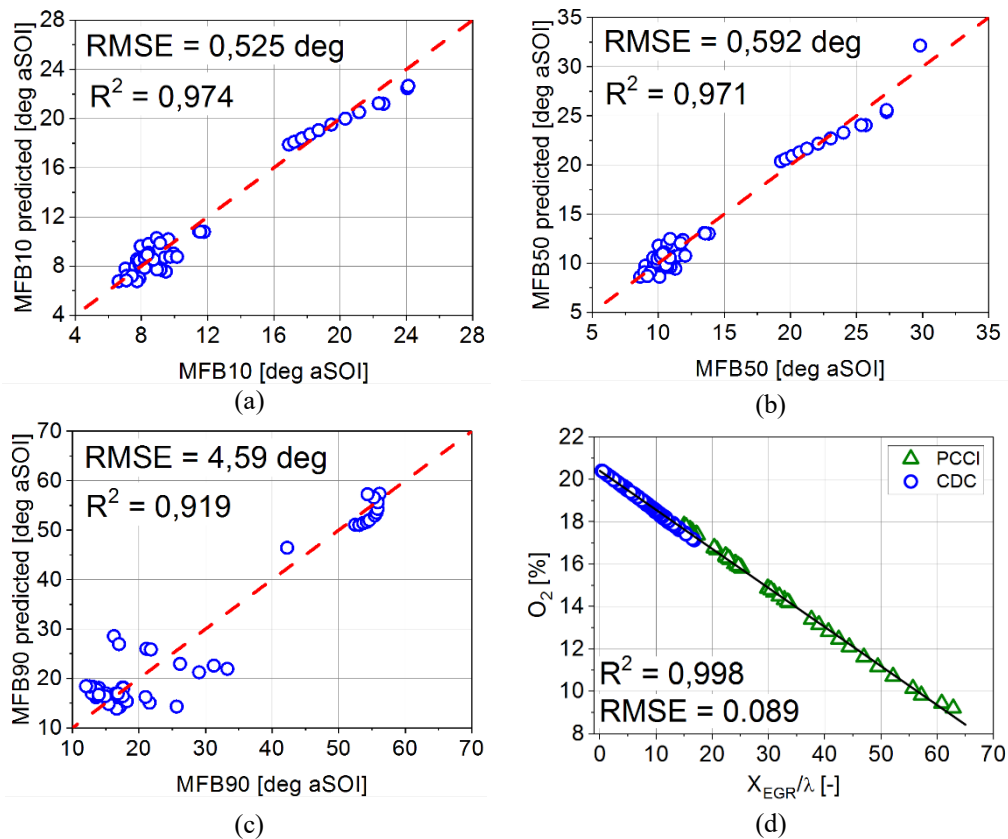


Figure 1.43: Modeling of combustion metrics and EGR rate in PCCI combustion: Prediction of MFB10 (a) MFB50 (b) and MFB90 (c) according to Eqs. 1.28-1.30, and correlation between oxygen concentration at the intake manifold and the ratio between the EGR rate and lambda, according to Eq. 1.23

Combining Eq. 1.23 with Eqs. 1.28 and 1.29, as for the CDC case, it is possible to get a relationship to express the EGR rate as a function of combustion phasing:

$$X_{EGR} = -\frac{\kappa_{01} + \kappa_{21}\delta_0}{\kappa_{21}\delta_1} \lambda + \frac{1}{\kappa_{21}\delta_1} \lambda \cdot \text{MFB10} - \frac{\kappa_{11}}{\kappa_{21}\delta_1} \lambda \cdot \dot{m}_{\text{fuel}}^2 \quad \text{Eq.1.31}$$

$$X_{EGR} = -\frac{\kappa_{02} + \kappa_{22}\delta_0}{\kappa_{22}\delta_1} \lambda + \frac{1}{\kappa_{22}\delta_1} \lambda \cdot \text{MFB50} - \frac{\kappa_{12}}{\kappa_{22}\delta_1} \lambda \cdot \dot{m}_{\text{fuel}}^2 \quad \text{Eq.1.32}$$

which can be rewritten as:

$$X_{EGR} = \zeta_{01} + \zeta_{11} \cdot \lambda + \zeta_{21} \cdot \lambda \cdot \text{MFB10} + \zeta_{31} \cdot \lambda \cdot \dot{m}_{\text{fuel}}^2 \quad \text{Eq.1.33}$$

$$X_{EGR} = \zeta_{02} + \zeta_{12} \cdot \lambda + \zeta_{22} \cdot \lambda \cdot \text{MFB50} + \zeta_{32} \cdot \lambda \cdot \dot{m}_{\text{fuel}}^2 \quad \text{Eq.1.34}$$

	Constant	\dot{m}_{fuel}	X_{EGR}	\dot{m}_{air}	$[\text{O}_2]$	λ	\dot{m}_{fuel}^2	$[\text{O}_2]^2$	R ²	RMSE	Number of regressors
MFB10	28.26	-	-	-0.32	-	-	-	-	0.850	1.26	1
	22.00	-	-	-	-0.98	-	0.03	-	0.974	0.525	2
	-412.52	-	4.00	3.86	-	-	-	-	0.950	0.726	2
	89.59	1.49	-0.78	-0.99	-	-	-	-	0.982	0.436	3
MFB50	31.85	-	-	-0.35	-	-	-	-	0.833	1.41	1
	25.70	-	-	-	-1.08	-	0.03	-	0.971	0.592	2
	-432.04	-	4.21	4.05	-	-	-	-	0.946	0.799	2
	100.95	1.58	-0.86	-1.10	-	-	-	-	0.978	0.514	3
MFB90	76.73	-	-	-	-	21.08	-	-	0.857	6.10	1
	59.74	-	-	-0.64	-	-	-	-	0.031	15.8	1
	8.80	-	-	1.52	-	-	-	-0.26	0.905	4.97	2
	45.60	-	-	0.68	-	22.66	-	-	0.888	5.40	2
	21.42	-3.65	-	3.15	-	-	-	-0.50	0.924	4.46	3
	-54.63	-	-	1.69	8.53	-	-	-0.58	0.919	4.59	3

Table 1.11: Best models tested to predict MFB10, MFB50 and MFB90 in PCCI combustion mode.

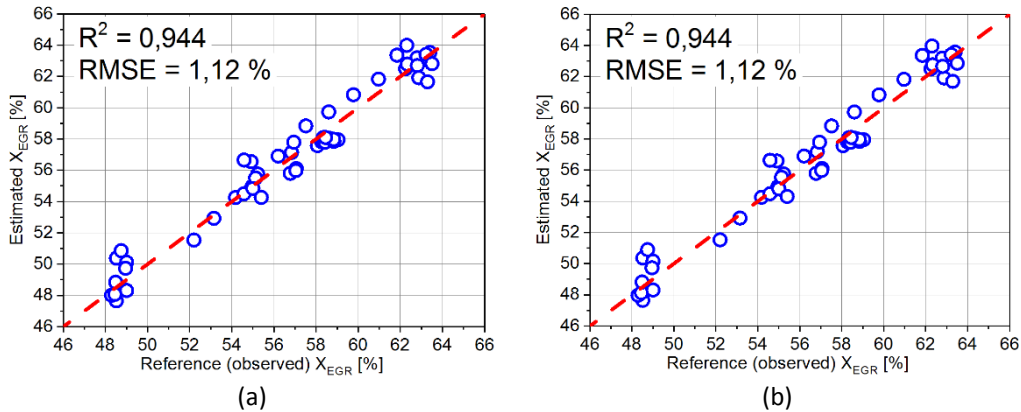


Figure 1.44: Predicted vs. reference EGR rate, where the prediction is obtained applying Equation 1.33 (a) and Equation 1.34 (b).

where in the last two equations a constant term ζ_0 has been included, which was not in Eqs. 1.31 and 1.32, in order to improve the quality of the fit. The results obtained estimating the EGR rate through Eqs. 1.33 and 1.34 are reported in Figure 1.44. The two graphs show that the result that is obtained is equivalent for Eqs. 1.33 and 1.34.

1.5.3 Evaluation of the EGR unbalance

In a multi-cylinder engine, the composition of the intake charge may be slightly different from one cylinder to the other. One of the reasons is the amount of EGR that is sent to each cylinder, which – especially in engines with separated intake runners for each cylinder – may be due to an improper mixing of the recirculated exhaust gas with the fresh air. This strongly depends on the geometry of the intake line and on its matching with the EGR system. Since a correlation exists between the EGR rate and the combustion rate, this unequal distribution of the EGR among the cylinders can be one of the causes of cylinder-to-cylinder variation in the

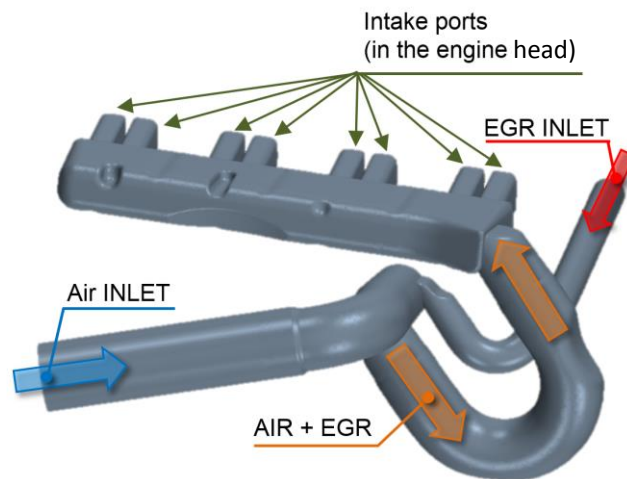


Figure 1.45: Schematic of the air and EGR path in the FIC engine.



Figure 1.46: Picture of the intake manifold that shows the installation of the thermocouples.

combustion cycle. Therefore, this can be used to provide a quantification of the EGR unbalance, i.e. the difference in the EGR rate between each cylinder and the average EGR rate. This may be especially important for PCCI combustion mode, due to its sensitivity to changes in boundary conditions: in the presence of high EGR rates, this uneven distribution may lead to combustion instability in some cylinders.

Usually, some evaluations are made by engine manufacturers about the EGR unbalance, which are meant as a proper way to validate the design of an intake/EGR system. Different methods could be exploited for this purpose:

- mixing concentration technique, based on the concentration of CO₂ at the inlet of each cylinder, which can be measured on each of the runners in an intake system that has one runner for each cylinder [176];
- CFD simulations, based on the exact geometry of the intake/EGR system and on the boundary conditions of the fluid at certain control surfaces that describe the control volume;
- mixing temperature technique [172, 187], based on the enthalpy balance between the fresh air outgoing from the intercooler (in a turbocharged engine), the EGR rate, and the total flow rate at the intake ($\dot{m}_{\text{EGR}} + \dot{m}_{\text{air}}$).

The engine on which this study is based has a manifold without runners, i.e. it has a unique manifold volume where air is mixed with EGR and that is directly connected to the engine head. Figure 1.45 shows the manifold of the F1C engine. The air and EGR inlets are highlighted together with the ducts where the two fluids are mixed before tangentially entering the manifold volume. The intake ports shown in the picture are not part of the manifold but of the engine head. As the runners are not present in this engine the mixing concentration technique cannot be applied to evaluate EGR unbalance since the CO₂ measurement can be only performed for the whole manifold and not for each cylinder. The intake charge used to evaluate the average EGR rate is taken in three different points of the manifolds and the samples are mixed in a Kempt chamber before being sent to the CO₂ analyzer in order to have an average measurement.

The mixing temperature technique requires the measurement of the temperature of the intake flow for each cylinder, i.e. in each runner. Since the present engine has a manifold without runners, four thermocouples have been installed in the manifold to have the measuring point as close as possible to the intake ports, in the central point between the two intake ports for each cylinder. Figure 1.46 shows the installation of the four thermocouples.

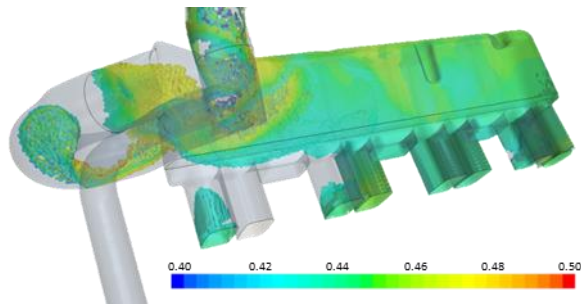


Figure 1.47: EGR rate spatial distribution in the intake manifold at IVC of cylinder 1 (right side) from CFD simulations.

In addition to the previous techniques, a further method is here proposed, based on the application of the correlation found between the EGR rate and the MFB90, i.e. Eq. 1.27 in CDC mode and Eqs. 1.33 and 1.34 in case of PCCI mode.

CFD simulations

CFD simulations are used as a reference to compare different methods. The study has been based on a complete detailed engine model running on GT-Power calibrated on experimental data, coupled with a CFD model (starccm+) representing the geometric model of the manifold and intake ducts shown in Figure 1.45. Four engine points (expressed as engine speed \times bmep) in CDC have been considered, nominally 1000 rpm \times 1.3 bar, 2000 rpm \times 6.7 bar, 2500 rpm \times 1.1 bar and 3250 \times 13.9 bar, corresponding to conditions of low, medium and high EGR rates (from 7% to 45%). It is worth to notice that in these conditions the EGR mass flow rate varies in a narrow range from 11.5 to 21.5 g/s, while the air mass flow rate ranges from 14 to 154 g/s. Moreover, not only the EGR rate varies but also its composition, having higher O₂ concentration at lower engine loads.

These simulations have been performed by FPT Industrial in order to support the current study, using a simulation model that was internally developed in the company. Therefore, the development and validation of the models are not discussed in detail here, as they were not directly performed as part of this study, and only the results that are relevant for this activity will be briefly presented hereinafter.

Figure 1.47 shows the result obtained at 1000 rpm \times 1.3 bar, i.e. the engine point with the highest EGR rate among those considered. The picture refers to EGR between 43% and 47% in the manifold. The frame refers to the intake valve closure of cylinder 1 (right side of the picture). Therefore, the flow is higher on the right side of the manifold.

CFD simulations demonstrated that EGR unbalance on the tested engine-manifold is extremely low, ranging from 0.01 to 0.25%, with the highest unbalance obtained on the fourth cylinder (i.e., the one closer to the air-EGR inlet in the manifold) at the highest EGR rate.

Mixing temperature technique

This technique applies an enthalpy balance to the air and EGR flows which are mixing in the manifold [172, 187]:

$$\dot{m}_{\text{EGR}}c_{p,\text{EGR}}(T_{\text{EGR}} - T_{\text{MAN}}) = \dot{m}_{\text{air}}c_{p,\text{air}}(T_{\text{MAN}} - T_{\text{air}}) \quad \text{Eq.1.35}$$

$$X_{\text{EGR}} = \frac{\dot{m}_{\text{EGR}}}{\dot{m}_{\text{EGR}} + \dot{m}_{\text{air}}} = \frac{(T_{\text{MAN}} - T_{\text{air}})}{(T_{\text{MAN}} - T_{\text{air}}) + \frac{(T_{\text{EGR}} - T_{\text{MAN}})}{c_{p,\text{air}}}} \quad \text{Eq.1.36}$$

where T_{air} is the temperature of the air flow before mixing with EGR, T_{EGR} is the temperature of EGR before mixing with air and T_{MAN} is the temperature of the air-EGR mixture in the manifold. Applying Eq. 1.36 to each single cylinder, i.e. considering the temperature in each runner or just upstream of the intake valves of each cylinder instead of the average manifold temperature, the EGR rate for each cylinder can be calculated.

Basically, this technique assumes that any temperature difference in the intake flow among the various cylinders is due to an uneven distribution of the hot EGR mixing with fresh air. This applies only to short-route EGR and results in an approximation which may lead to some significant bias of the EGR unbalance effect.

Evaluations on the reference engine map highlighted that the average EGR rate calculated as mean of the values for each cylinder through Eq. 1.36 is appreciably different from the overall EGR estimated through the application of the physical-chemical method for the estimation of the EGR mass flow rate. Therefore, the value calculated for each single cylinder has been re-scaled considering as average EGR the one from the physical-chemical method, which is considered to be a more reliable evaluation.

Moreover, it was found, by testing the whole engine map without EGR, that significant temperature variations in the manifold are present also in the case of absence of EGR: this is justified by heat exchanges between the manifold (in the test case, an aluminum-made component) and the surrounding engine parts: conductive heat transfer with engine block, convective heat transfer with surrounding air. Therefore, a not even cooling of the engine block or the presence of some hot parts which irradiates heat in the air close to one side of the manifold may result in some temperature gradients along the manifold itself. Finally, the

residence time of the gas should be considered, taking into account that the gas provided to the cylinder farthest from the air-EGR inlet in the manifold will remain in the manifold for a longer residence time with respect to the other cylinders, therefore having more time for heat exchanges with the manifold.

Some corrections may be applied to mitigate this bias, e.g. correcting the mix temperature of each runner considering the same temperature measured without EGR and the convective heat transfer with the manifold temperature [187]:

$$T_{MAN,i,corr.} = T_{MAN,i} + (T_{MAN,i,NO-EGR} - T_{MAN,avg,NO-EGR}) \frac{T_{MAN,avg} - T_{surface}}{T_{MAN,avg,NO-EGR} - T_{surface}} \quad \text{Eq.1.37}$$

Additionally, measurement uncertainties should be taken into account, especially considering the position of the temperature probes as well as the sensitivity of the measure to this position, also taking into account that thermocouple installations in the manifold may be difficult and that their position and orientation may change in time during a testing activity due to vibrations. Finally, it is worth to underline that additional uncertainty is added in the case of a unique-volume manifold with respect to runners.

EGR estimation from in-cylinder pressure measurement

Finally, a further method is proposed, which consists in applying to each single cylinder the correlation between combustion metrics and EGR discussed in the previous *Section* and represented by Eq. 1.27 for CDC mode and by Eqs. 1.33 and 1.34 for PCCI mode. When piezoelectric transducers are available on each cylinder, in case of CDC mode this method can be applied to obtain the EGR rate cylinder-by-cylinder as a function of MFB90 (evaluated for each cylinder), the air-fuel ratio measured at the exhaust through a lambda sensor and the oxygen concentration in the intake manifold. Similarly, for PCCI mode also an accurate measurement or estimation of the fuel mass flow rate is required.

As long as these measures are not available on ECUs (apart from λ), this method, such as the temperature-based one, is not suitable for engine control purpose. On the other hand, these measurements are often available on test engines during development, calibration and validation activities. Therefore, these methodologies may provide, without significant test or computational effort, an estimation of the EGR unbalance.

It is worth to underline that cylinder-to-cylinder variations in the combustion cycle, and therefore on the combustion metrics such as MFB10/50/90, may be due to different reasons: e.g. differences in the injected quantities due to imperfections

or uneven clogging of the injectors, variations in the volumetric efficiency among the cylinders, uneven cooling of the cylinder jackets, etc. The estimation of the EGR unbalance based on cylinder-to-cylinder combustion metrics lays on the assumption that all the cylinder-to-cylinder variations are due to differences in EGR unbalance.

Comparison of the methodologies: conventional diesel combustion

The methodologies based on intake temperature measurements and on combustion metrics evaluated from in-cylinder pressure measurement have been applied on a reference complete engine map acquired on the tested engine. Results obtained with the two methods have been compared among them and with the CFD simulations where available, in order to assess the validity of these methodologies as an alternative to CO₂ measurements in each runner and CFD simulations.

Table 1.12 shows this comparison among the three methods for the points in CDC where the CFD results are available: it can be easily noted that both the mixing temperature method and the one based on in-cylinder pressure significantly overestimate the EGR unbalance effect with respect to CFD simulations.

Figure 1.48 reports the comparison over the whole engine CDC map between the two tested methods, excluding CFD (as only few points are available from CFD simulations): the dimension of each circle is proportional to the difference between the maximum and minimum EGR rate evaluated on the 4 cylinders for each engine working point. It can be noticed that the two methods provide comparable results in most of the engine working map. Significant differences are highlighted in the low speed-high load range and in the medium/high speed-low load area. In the first case (low end of the full-load curve), the mixing temperature technique significantly overestimates EGR unbalance with respect to the method based on combustion metrics: this happens in an area with low air mass flow rates and EGR mass flow rate. In these conditions, the differences in temperature distribution of the mixture in the manifold increase due to the higher residence time of the gases

	speed	bmep	EGR rate (avg)	EGR unb. #1	EGR unb. #2	EGR unb. #3	EGR unb. #4
	rpm	bar	%	%	%	%	%
CFD	1000	1.3	45.3	0.10	0.10	0.04	-0.25
Mix. Temp				2.26	0.88	-1.89	-1.25
In-cyl pressure				13.90	-4.40	-6.35	-3.35
CFD	2000	6.7	18.7	0.06	-0.04	-0.09	0.07
Mix. Temp				1.42	0.88	-1.23	-1.07
In-cyl pressure				0.27	1.25	0.74	-2.26
CFD	2500	1.1	31.8	-0.02	0.02	0.00	-0.01
Mix. Temp				1.12	0.83	-1.23	-0.72
In-cyl pressure				3.38	7.16	1.63	-12.15
CFD	3250	13.9	7.02	0.04	-0.01	-0.05	0.01
Mix. Temp				0.33	0.38	-0.56	-0.14
In-cyl pressure				1.05	0.7	0.42	-2.17

Table 1.12: Comparison of EGR unbalance estimated with different methodologies in CDC.

in the manifold and due to the increase of heat drained by the engine. The considered method ascribes the reason of this temperature difference to EGR unbalance, although the EGR rate is almost null. As a reference, Figure 1.48b reports a map of EGR rate and EGR mass flow rate (estimated with the physical-chemical method) as a function of engine load and speed: the dimension of the circles is proportional to the value associated to the shown variable.

On the other hand, calculations based on combustion metrics generate an overestimation of the EGR unbalance in the low-load area for medium to high engine speeds. It has been verified that this area is the one with largest cylinder-to-cylinder variations in terms of in-cylinder pressure trace and mass fraction burned, which can be possibly due to causes not related to EGR unbalance, e.g. higher sensitivity of the combustion to differences in coolant temperature among cylinders.

Figure 1.49, shows the EGR unbalance as estimated with mixing temperature technique and from in-cylinder pressure measurement, plotted as a function of the EGR rate and of the EGR mass flow rate. It is clearly shown that the mixing temperature model tends to estimate an increasing EGR unbalance as the amount of EGR decreases, with an opposite trend with respect to reasonable expectations. The EGR unbalance evaluated with the mixing temperature method shows a lower dispersion when plotted as a function of the EGR mass flow rate, which confirms that the result is strongly influenced by fluid transportation time and residence time. On the other hand, when the EGR unbalance is estimated basing on in-cylinder pressure (and, more in detail, on the MFB90 angle, expressed as crank angles after the start-of-injection), the EGR unbalance – as expected – tends to increase with the amount of EGR. In this latter case the EGR unbalance shows a lower dispersion

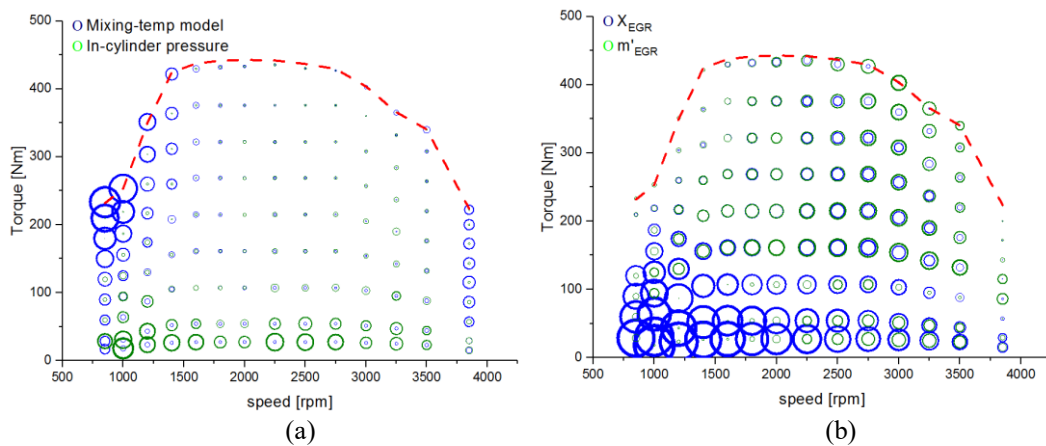


Figure 1.48: (a) Comparison of EGR unbalance in CDC estimated from mixing temperature technique and from in-cylinder pressure measurement on the reference engine map. (b) Maps of EGR rate and EGR mass flow rate as a function of engine speed and load.

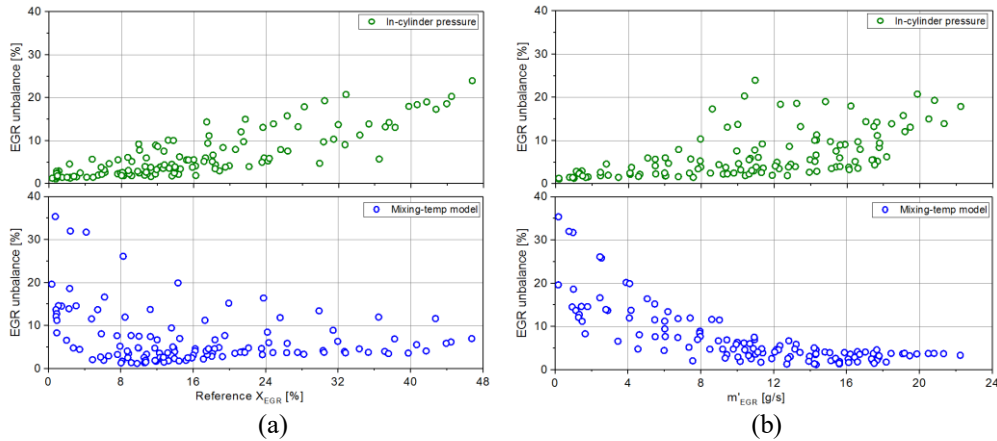


Figure 1.49: EGR unbalance in CDC estimated from mixing temperature technique and from in-cylinder pressure measurement vs. EGR rate (a) and vs. EGR mass flow rate (b).

when plotted as a function of EGR rate (Fig. 1.49a), which confirms that the result is more affected by the mixing of air and EGR than by transportation and residence time of the gases within the manifold.

Comparison of the methodologies: PCCI

Also for the case of PCCI combustion, the mixing temperature technique and the method based on combustion phasing have been both applied to estimate the EGR unbalance.

For the mixing temperature technique, the temperature correction of Eq. 1.37 is applied. As for the previous case, it was found that the average EGR rate calculated as mean of the values for each cylinder through Eq. 1.37 is appreciably different from the reference overall EGR (cf. Figure 1.50). Therefore, also in this case the value calculated for each single cylinder has been re-scaled considering as average EGR the one from the physical-chemical method.

Referring to the estimation of EGR unbalance based on combustion phasing, Eq. 1.33 and 1.34 are applied on each single cylinder and the EGR

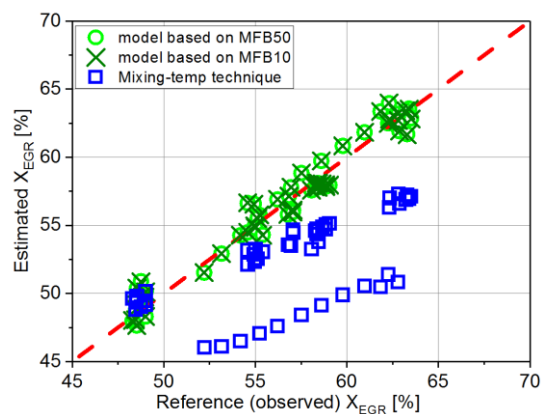


Figure 1.50: Average EGR rate estimated with mixing temperature technique compared with the average EGR rate obtained from in-cylinder pressure measurement.

unbalance is evaluated as a consequence as the maximum difference between two cylinders.

The tests used for this comparison are the EGR sweeps at 1200×23 and 1400×71 (rpm \times Nm) used to build the models of Eq. 1.33 and 1.34.

The comparison is shown in Figure 1.51. Differently from what seen in CDC, in this case the mixing temperature technique shows an increase in EGR unbalance as the amount of EGR increases. On the other hand, the estimations based on MFB10 and MFB50 show an extremely low EGR unbalance, always in the range 0.02-0.04%. This last result is well aligned with the results of CFD simulations, that showed generally an extremely low EGR unbalance, always below 1% (cf. Table 1.12).

This last sub-section of *Chapter 1* aimed at finding an alternative methodology to estimate EGR unbalance based on experimental data that are commonly available during testing activities. The two methodologies have been compared in some study cases both in CDC and PCCI combustions. Definitely, at the moment it is not possible to assess if one method is generally more accurate than the other. Further investigations are needed to better clarify the validity of the two methodologies. For this purpose, a detailed comparison of both the studied methodology with an accurate EGR unbalance estimation method would be required for a proper assessment. This would involve a massive amount of CFD simulations to reproduce all the tested conditions in simulation environment, or the measurement of CO₂ concentration at the intake of each single cylinder in an intake manifold with separated intake runners for each cylinder.

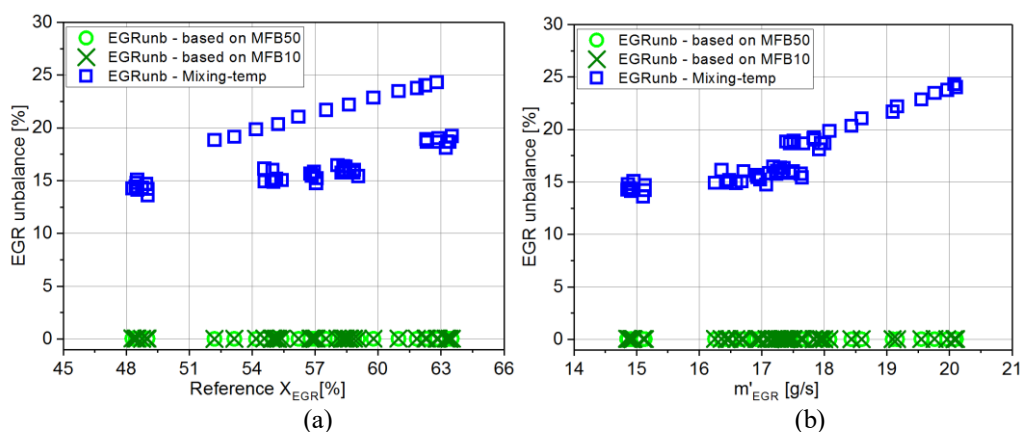


Figure 1.51: EGR unbalance in PCCI combustion estimated with mixing temperature technique and from in-cylinder pressure measurement vs. EGR rate (a) and vs. EGR mass flow rate (b).

Chapter 2³

Development of an automatic system for on-board management of tire inflation pressure

The energy consumption of a vehicle, given a certain powertrain and mission profile, is determined by the resistant forces which oppose its motion, i.e.: aerodynamic drag, rolling resistance and resisting torques due to friction along the driveline and (possibly) in the brakes. Among these, rolling resistance accounts for 30-40% of the vehicle resistances [38]. Therefore, reducing the rolling resistance decreases energy consumption, which in turn is translated into an improved battery energy management in an electric vehicle or into a reduced fuel consumption if the vehicle is propelled by a combustion engine.

As already mentioned in the *Introduction*, reducing the tire rolling resistance by 3.5 kg/ton is expected to produce a reduction by 3.2-5.1% in fuel consumption on passenger cars [83]. Similarly, a reduction in the rolling resistance coefficient of a heavy-duty truck of 1 kg/t has been shown to reduce fuel consumption by 3.3-5.4%, if the vehicle is half loaded, and by 3.4-6% if the vehicle is fully loaded, the lower percentage advantage being associated with a sub-urban driving condition

³ Part of the contents of this chapter has been previously published in:

d'Ambrosio, S., Vitolo, R., "Potential impact of active tire pressure management on fuel consumption reduction in passenger vehicles", Proceedings of the IMechE, Part D: Journal of Automobile Engineering, 233(4):961-975, 2019, <https://doi.org/10.1177/0954407018756776>.

d'Ambrosio, S., Oliva, E., Salamone, N., and Vitolo, R., "Active Tire Pressure Control (ATPC) for Passenger Cars: Design, Performance, and Analysis of the Potential Fuel Economy Improvement," SAE Int. J. Passeng. Cars – Mech. Syst. 11(4):321-339, 2018, <https://doi.org/10.4271/2018-01-1340>.

d'Ambrosio, S., Mameli, E., Vitolo, R., Calaon, I. et al., "Fuel Consumption Reduction on Heavy-Duty and Light-Duty Commercial Vehicles by Means of Advanced Central Tire Inflation Systems," SAE Int. J. Commer. Veh. 11(5):267-289, 2018, <https://doi.org/10.4271/2018-01-1334>.

d'Ambrosio, S., Mameli, E., Vitolo, R., "Impact assessment of an intelligent central tire inflation system for passenger cars", 7th Transport Research Arena TRA 2018, April 16-19, Vienna, Austria, 2018. <https://doi.org/10.5281/zenodo.1486718>.

and the larger with long-haul use [38] (it is worth noting that the average fuel consumption is lower in long-haul conditions due to the quasi-stationary working condition of the engine in a high-torque high-efficiency area of the engine map). According to ACEA, reducing tire rolling resistance through an improved tire design would produce an improvement of between 3% and 4% by 2020, in the regional and long-haul use of heavy commercial vehicles, respectively [188]. ICCT has reported a reduction of 2.5% and 2% in tractors and trailers during long-haul operations when the current tires have been replaced by low rolling resistance ones [189]. Additionally, a reduction of 4.9 kg/t to 3.85 kg/t on trailer tires has been shown to reduce fuel consumption by 3.9% and NO_x emissions by 4.7% on a EURO III heavy-duty truck [38].

An additional option to further reduce rolling resistance concerns the adoption of the so-called Central Tire Inflation Systems. A central tire inflation system (CTIS) is an on-board device that is able to check the tire inflation pressure, compare it to a target value and manage inflation and deflation actuations in order to realize and maintain the target inflation pressure [190-201]. It is generally composed of a number of valves and connections that allow fluid communication between the tire volume and a central part of the system. It includes a positive pressure source [194, 198] and sometimes also a negative one [195] in order to increase or reduce the tire pressure. A rotating pneumatic connection connects the wheel to the central parts of the circuit [199-202].

This kind of system was first developed during the Second World War for military applications [203] and was then extended to other vehicles. Primarily, the intended purpose of this kind of device is to adapt the vehicle traction ability to different kinds of soils for vehicles that may operate on compact soils as well as on soft ones [203, 204]. The utilization of CTISs on forestry logging trucks running on gravel soils and with heavy road grades has demonstrated significant improvements in the truck traction abilities, a reduction in the truck and soil maintenance operations and an improvement in ride comfort, thanks to the reduction in tire pressure in off-road conditions and the restauration of a suitable pressure for highway operation [204]. The reduction in the tire pressure of trucks through CTISs on asphalt roads and crushed aggregate roads cracked and weakened by thawing ice or snow has also been studied as a solution to highway load restrictions on trucks, and has proved to increase road life [205]. Modern CTISs on military vehicles, earth-moving machines, all-terrain vehicles, tractors, etc. usually implement semi-automatic solutions: an on-board panel, accessible to the driver inside the cabin, is used to select the target tire pressure from among a discrete number of choices according to the kind of soil and the loading conditions [206, 207].

Nowadays, due to the great attention to vehicle energy management, CTISs of the “automatic” type are also being extended to on-road trucks mainly in order to

avoid the risk of tire under-inflation, as a way of improving vehicle fuel economy and safety [88]. Tire pressure affects fuel consumption [81], as well as the dynamic behavior of a vehicle [208]. Under-inflated tires increase rolling resistance [81, 209], have a negative effect on the fuel consumption of vehicles propelled by internal combustion engines (or, in general, on the global vehicle energy balance) [81], and induce an improper deformation of the tire tread and sidewalls [210], thus reducing the useful life of the tires [211]. Moreover, low tire pressure produces a decrease in the forces that can be transmitted between the tire and the road through the contact patch [88], thus reducing the braking and handling performance of the vehicle.

Referring to passenger cars, a report by the Australian Government [211] has claimed that fuel savings, due to the use of tire inflation systems, can be between 1% and 4%, with an extension of the tire life of up to 10%. An improper inflation pressure is believed to generate an increase of 35 to 48 kg of CO₂ emissions per vehicle per year, which means that in the US alone about 12 billion kilograms of CO₂ and 4 billion dollars could be saved per year if the recommended tire pressure were to be maintained [86]. Tire maintenance is also critical for road safety: if the average tire under-inflation were to be limited to 25% (e.g., by means of the adoption of TPMSs), it would be possible to reduce crashes, and to annually avoid 124 fatalities and about 9000 injuries in the United States alone [88].

For which concerns the sector of commercial vehicles, the advantage that can be obtained by adopting this solution is quantified as being between 1% [189] and 1.4% [212] on fuel consumption on an annual basis, with additional benefits on tire life [212], both of these aspects being effective in reducing the Total Cost of Ownership (TCO). According to data presented by ICCT, the fuel economy improvement obtainable through the use of automatic tire inflation systems is comparable with that which can be obtained through improvements in transmission and axle efficiency, engine friction reduction and vehicle accessories improvements [189]. Moreover, an accurate inflation pressure would have a significant impact on road safety: properly inflated tires allow the best braking and steering performance to be obtained, thereby reducing the risk of crashes [213]. Additional benefits could be obtained by adapting the tire pressure to the load carried by the vehicle or to the road conditions [214, 215]. As an example, experimental tests conducted within the framework of the ADTYRE project on a light-duty commercial vehicle have shown a potential reduction of up to 16 m of the stopping distance on wet asphalt in a braking maneuver from 100 km/h, a reduction which could be obtained through a fast-dynamic tire pressure management system [215].

In order to reduce the drawbacks related to the presence of underinflated tires on the roads, all new passenger cars sold in the US since 2008, and in Europe since 2012, are required to be equipped with a Tire Pressure Monitoring System (TPMS) [52, 91]. These systems provide a measurement, or an estimation, of the tire pressure and alert the driver when the pressure is significantly low.

CTIS, intended as a means of maintaining the nominal pressure (indicated by the vehicle manufacturer) in normal driving conditions, offers some main advantages with respect to TPMS:

- the system does not require the intervention of the driver and can therefore always guarantee a suitable pressure over a narrow tolerance range;
- a direct pressure measurement provides a much more accurate result than indirect TPMS, and the usage of low-cost wired sensors provides a higher measurement accuracy and lower installation complexity than direct wireless TPMS. In fact, since the tire volume in a CTIS is connected to the central part of the system, pressure measurement may be obtained through the use of wired sensors – or even just one wired sensor – installed in the stationary part of the system [196, 198, 199].

Moreover, CTISs can be used not only to maintain one reference pressure level under all driving conditions, but also to adjust the tire pressure to the current vehicle state and surrounding conditions [216]. Therefore, further benefits can be obtained, with respect to TPMSs, in terms of handling and fuel consumption.

The impact of such a topic would surely be on a large scale, considering that about 78% of the passenger cars circulating in Europe and 70% of the US fleet have underinflated tires [87, 88]. Similarly, only 44% of the commercial vehicle tires tested in 2008 by the U.S. Federal Motor Carrier Safety Administration were properly inflated (over a range of ± 0.35 bar with respect to the target pressure) and 7% were underinflated by more than 1.3 bar [217]. As the benefits of CTISs are becoming more and more evident, in the sector of commercial vehicles the interest in this technology by truck owners and fleet managers has been increasing, as demonstrated by the increased popularity of this product on the market: 2.9 million CTIS units are expected to be on the roads by 2021, with a compound annual growth rate of 29.2%, driven by the high penetration of the product in the heavy-duty truck and trailer segments in the EMEA region [218].

Until recently, CTISs have not been considered as a suitable technology for light-duty commercial vehicles and passenger road vehicles. The reasons CTISs have not been proposed on the market for light-duty applications are mainly related

to safety issues, related to the fact that the tire air chamber is connected to an external circuit through pipes and connections that could be damaged, thus generating potential causes of risk. It is worth mentioning that many aftermarket products suggest the installation on the external side of the wheel (an unacceptable solution for cars for both safety and aesthetic reasons), while installation on some off-road vehicles is simplified due to the specific wheel-hub assembly architecture. Additional issues that have limited the diffusion of this kind of system on light duty vehicles and passenger cars are related to the wear of the rotating pneumatic joint and to the difficulties encountered in the integration of the system on board.

In order to address these issues, an active electro-pneumatic central tire inflation system, which is able to automatically manage tire pressure through inflation and deflation actuations, has been proposed for light-duty vehicles, including passenger cars and light-duty commercial vehicles, and for trucks. The aim of this *Chapter* is to present novel solutions specifically developed for the utilization of such a system on the target vehicle segments and to propose an analysis concerning the advantages that can be obtained from its installation on-board. The study concerns the design of the system layouts, and the evaluation of the potential benefits, through computer simulations, to estimate the effects of active pressure management on fuel consumption.

After an introduction on the effect of tire pressure on rolling resistance and some generalities on CTISs (*Section 2.1* and *Section 2.2*), the case study related to passenger cars will be first addressed in *Sections 2.3* and *2.4*. The effects on fuel economy were first assessed, for the case of passenger cars (*Section 2.3*), using an internal proprietary software used in FCA and Iveco. Moving from these results, also the effect of the system on an annual mission of a passenger vehicle are assessed in *Section 2.4*, and extended to the whole European fleet for a preliminary impact assessment of the technology on a large scale. As the FCA/Iveco software for fuel economy assessment does not directly and explicitly account for tire pressure, a dedicated software tool was then developed in a subsequent phase of the project (held in collaboration with Iveco), and this new tool is used for the assessment of the effects of tire pressure and potential tire pressure management strategies on commercial vehicles. Details on the development of this software tool, and on the results obtained through it, are discussed in *Section 2.5*. In *Section 2.6* the design of the system for passenger cars is presented. In this case study, a test-bench prototype has also been set-up, and details on sizing and on experimental results related to the single components of the system and to the overall system prototype are presented. In *Section 2.7*, the layout of the system designed for commercial vehicles and a preliminary solution for its integration on-board are also discussed. Finally, in *Section 2.8*, some final simulations are reported that show the

effect on the potential fuel economy benefit of the designed CTISs of the system dynamics (i.e. the actuation time required for a target pressure variation).

2.1 Effects of tire pressure on rolling resistance

Rolling resistance is the contribution, due to the tire, to the resistant forces which oppose vehicle motion [81], and it is, in general, defined as the energy dissipation per unit distance of a rolling tire. This force is mainly caused by the energy required for wheel and soil deformation [81, 84, 219]; soil deformation is negligible for typical on-road applications [220]. Rolling dissipation has been attributed to large-scale tire deformations, related to the structure and tread pattern of the tire, as well as to the small-scale deformation that is generated by the local tread deformations caused by the roughness of the road [221]. The rolling resistant coefficient (C_{rr}) is defined as the force due to rolling (F_{rr}) divided by the weight acting on the tire ($m \cdot g$):

$$C_{rr} = \frac{F_{rr}}{mg} \quad \text{Eq. 2.1}$$

Tire inflation pressure affects tire deformation to a great extent and, as a consequence, rolling resistance: the lower the tire stiffness, the higher its deformation and absorbed energy [84]. LaClair [81] described the phenomenon in terms of the percentage variation of the rolling resistance coefficient C_{rr} (at the reference speed of 80 km/h) with inflation pressure (p_{inf}). LaClair's graphical relation for passenger vehicle tires is fitted well by the following power equation reported in Fig. 2.1:

$$C_{rr}[\%] = 1.3447 \cdot p_{inf}^{-0.398} \quad \text{Eq. 2.2}$$

A similar graphical relation was also available for pressure ranges that are typical of truck applications [83]. These relations were then normalized in order to obtain the same relation as a function of the percentage variation of tire pressure (cf. Fig. 2.1b) and were found to be equivalent over the range of interest. Therefore, the same curve was also adopted for vans and light-duty commercial vehicles.

Similar results have been obtained, regardless of the tire and application [219, 220, 222]. Loading conditions have a significant effect on the slope of the curve, with a greater influence of inflation pressure on rolling resistance for higher loads [219]. However, appreciable differences are only evident for very large load variations, which are generally not experienced by light duty vehicles. The influence of tire pressure on fuel economy depends on the above relation, but is also

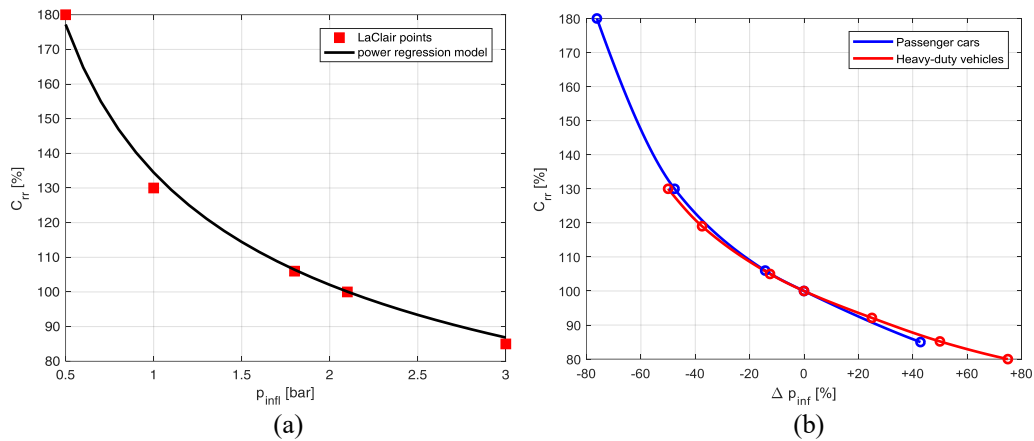


Figure 2.1: (a) Percentage rolling resistance variation as a function of tire pressure for a passenger tire according to LaClair [81]. The reference pressure for the cold tire is 2.1 bar according to ISO 18164:2005 [227]. (b) Percentage rolling resistance variation with tire pressure variation: comparison of LaClair's relation provided for passenger cars and heavy trucks.

affected to a great extent by the engine efficiency map, vehicle type, loading conditions, road-tire grip and driving conditions [83]. Different studies [83, 223, 224] have reported that a 10% variation in rolling resistance increases fuel consumption by about 1% for urban driving and almost 2% for highway driving.

The analysis of different vehicle models and driving cycles shows that rolling resistance has a larger relative effect in light vehicles [78]. Rolling resistance makes an even greater relative contribution to hybrid or electric vehicles, due to the higher efficiency of the propulsion system compared to ICE-based ones [221].

2.2 Generalities about CTIS

The importance of keeping tires inflated at the correct pressure level in order to reduce both the rolling resistance and the risk of damaging the rubber-made air chamber has been known almost since the pneumatic tire was invented by Robert William Thomson in the first half of the nineteenth century [225]. Furthermore, great importance has been given to the elastic properties of the air chamber under different inflation pressures. Many efforts were made in the late nineteenth century and at the beginning of the twentieth century – when the spread of motor vehicles and the general improvement of road transport conditions gave rise to an increase in the usage of pneumatic tires – to improve tires safety and performance. Some early precursors of modern TPMSs, such as on-rim graduated (proportional) pressure indicators [226] and pressure switches able to provide an electric signal to

the driver dashboard [228, 229], were already proposed in the first two decades of the twentieth century in order to warn the drivers when the tire pressure was lower than a desired threshold.

The advantages related to the chance of automatically varying the inflation pressure of a tire soon became known in the timeline of the pneumatic tire history: in the late 1940s, this kind of system was presented as a relevant innovation for military motor vehicles [203].

Several schematics have been proposed over the years for CTIS applications, and the general schematic, initially presented by Turek [191], has substantially been confirmed and improved with the introduction of electronic control devices and electro-valves [194-196]. Moreover, special designs have been introduced to solve some of the characteristic problems:

- isolation of the tire volume from the central part of the system when actuations are not ongoing, both to reduce the consequences of the possible failure of ducts, pipes, fittings, etc., and to reduce the frictions and the wearing of the pneumatic rotating joint [192-195]. This is attained by means of wheel valves that are opened for inflation and deflation: in the case of inflation actuations, the valves are always opened by generating a sufficient overpressure upstream of the tire, while they may be opened for deflating operations by generating a positive [194, 198] or negative [195] pressure upstream of the tire. In the latter case, a vacuum generator, which can be obtained through an ejector fed by the positive pressure source, as seen in [195], is needed;
- the type and placement of the components which allow the on-wheel rotating parts to be fluidly connected to the stationary part of the circuit [192, 195-201, 230];
- integration within the wheel-end components of the ducts that connect the pneumatic rotating junction to the wheel valve or valves [200, 202, 230-232];
- identification of measurement, control and actuation strategies that allow a good performance, robustness, reliability and flexibility to be obtained [196-199].

Modern CTIS controls may be of the “semi-automatic” type, where the target pressure is selected by the driver [195, 196] or may evaluate the target pressure autonomously, i.e. as a function of the slip rate and of the vehicle speed [197] or of such parameters as ambient conditions, vehicle speed, GPS-derived information, vehicle loading condition and data from other sub-systems such as dynamic controls, ABS, brake pedal and steering wheel inputs [216].

Many solutions have specifically been designed for, although not limited to, vehicles with pneumatic brake systems [193, 195], where a pressure source and an air circuit are already present on board. When they are not present, a dedicated pressure source is needed: some patents specify that this can be an electrically-driven [201] or an engine-driven compressor. In the latter case, it could be actuated by the engine crankshaft through a pulley-belt mechanism [195, 201], or by means of a turbocharger [193, 233].

Tire pressure can be measured in CTISs without the need to have sensors on the wheel. Owing to the presence of the wheel valves, measurement operations require on-purpose actuations to connect the tire to the central part of the system where the wired pressure sensor is placed. The in-wheel valve is opened to pressurize the central part of the circuit, and the measurement occurs in steady zero-flow conditions [199], or at the end of a pressure transient [198].

2.3 Potential effect of tire pressure management on fuel economy of passenger cars: simulations

In order to check the influence of tire pressure on fuel consumption, some computer simulations have been performed. Features of the vehicle and of the tire used for the simulations are reported in Table 2.1. The total driving resistance force and rolling resistance coefficient are described as a function of the vehicle speed [234]:

$$F_{\text{res}} = F_{\text{aer}} + mg C_{\text{rr}} + F_{\text{dvl+brk}} = F_0 + F_1 v + F_2 v^2 \quad \text{Eq. 2.3}$$

$$C_{\text{rr}} = B_0 + B_1 v + B_2 v^2 \quad \text{Eq. 2.4}$$

where F_{aer} is the aerodynamic resistance, $mg C_{\text{rr}}$ the rolling resistant force and $F_{\text{dvl+brk}}$ the term that takes into account power dissipations due to frictional losses in the driveline downstream of the gearbox (including also the differential), and any possible remaining torque between the pads and the disks in the braking system. Typical values for passenger cars range from 70 to 380 N for the coast-down coefficient F_0 , and from 0.017 to 0.09 N/(km/h)² for F_2 [235], while F_1 is often neglected in practical applications. The rolling resistant coefficient C_{rr} for passenger car tires ranges from values lower than 6.5 kg/ton (class A label according to EU tire labeling system) to 12.1 kg/ton (class G) [89]. The dependence

of the rolling resistance on vehicle speed is negligible for vehicle speed below 100 km/h and often neglected in practical applications.

Simulations have been performed using the proprietary software PerFECTS, developed and validated by Fiat Chrysler Automobiles (FCA) for fuel consumption calculations [236-238]. Providing the speed profile of the desired cycle, as well as the main vehicle and tire-related parameters, the software outputs results on the fuel and energy consumption, an estimation of the engine-out pollutant emissions and various parameters related to different vehicle sub-systems (e.g., the air conditioning system). The approach is similar to that presented in [78]. Given a mission profile in terms of vehicle speed and gear in time, the engine power and torque are calculated considering the resistant forces that oppose to vehicle motion and the power required to accelerate the vehicle:

$$\eta_{gbx}P_e - F_{res}v = m_{eq} \frac{dv}{dt}v \quad \text{Eq. 2.5}$$

being P_e the brake engine power, η_{gbx} the gearbox efficiency and m_{eq} the equivalent (apparent) mass, given by the current vehicle mass m increased by a

Reference Vehicle Data	
Vehicle segment	B – light passenger car diesel common-rail, 1.3 l
Version (engine)	75 metric HP @ 4000rpm FWD, synchronized MT 5 gears +
Transmission	reverse
Curb weight	1185 kg
Max load	500 kg
Full-load weight	1685 kg
Type-approval (NEDC) fuel consumption	Urban: 6.5 l/100km Extra-urban: 4.4 l/100km Combined: 5.2 l/100km Combined - CO ₂ emissions: 138 gCO ₂ /km
Reference Tire Data	
Tire	185/65 R15 88T (tubeless radial)
Manufacturer/Brand	Michelin / Energy Saver +
Max load capacity	560 kg @ 2.5 bar
Max permitted inflation pressure	3.2 bar
Rim	6.0 J 15

Table 2.1: Characteristics of the reference passenger car and of the related tire.

term due to the inertia ($J_i\omega_i^2$) of each i -th rotating part, including the engine, the primary and secondary shaft of the gearbox, the differential, the axles and the wheels:

$$\frac{1}{2}m_{eq}v^2 = \frac{1}{2}mv^2 + \frac{1}{2}\sum_i J_i\omega_i^2 \quad \text{Eq. 2.6}$$

Resistance forces are obtained through the coast-down coefficients, according to Eq. 2.3. Engine speed ω_e is calculated starting from the vehicle speed and gear ratio τ_{gear} imposed by the cycle:

$$\omega_e = \frac{v \tau_{final} \tau_{gear}}{R_w} \quad \text{Eq. 2.7}$$

where τ_{final} is the final drive ratio and R_w is the wheel loaded radius. The fuel consumption is then estimated by interpolating in a fuel consumption map, obtained through engine test-bed steady state tests and expressed as fuel consumption fc (g/h) as a function of engine speed and brake engine torque, evaluated as:

$$T_e = P_e/\omega_e \quad \text{Eq. 2.8}$$

or brake mean effective pressure, evaluated as:

$$bmep = \frac{2\pi T_e}{V_e} \iota \quad \text{Eq. 2.9}$$

being V_e the total engine displacement and ι the number of crankshaft rotations per engine cycle ($\iota=2$ for four-stroke engines). The instantaneous fuel consumption is then integrated over the mission to obtain the cumulated fuel consumption. The approach presented here above, in its simplest application, considers the instantaneous vehicle speed equal to the reference imposed speed profile, and the vehicle acceleration is derived from the theoretical speed profile. The engine speed and load are calculated as a consequence considering the kinematics of the transmission. This approach is therefore known as “kinematic approach” for fuel consumption estimations.

The software used for the simulations presented in this *Section* is the state-of-the-art software used in Iveco and FCA for fuel economy estimations, PerFECTS (Performance and Fuel Economy for Cars and Trucks Simulation) [236, 237]. It is based on the abovementioned procedure but it also includes a sophisticated closed-loop driver model, which operates on the pedals in such a way to minimize the difference between the actual speed and the imposed mission profile [237]. The

accelerator position is used as input for a refined engine ECU model, which determines an injected fuel quantity and a consequent torque. Dedicated models for the clutch and gearbox transfer the torque to the wheels, which determines the actual vehicle speed. The driver model, then, uses this information to act on the pedals in order to reproduce the mission profile. This software provides several features that can be used to test various vehicle configurations, including different gearboxes and powertrains, and various electric loads, as well as different driving conditions, from type-approval procedures to on-road acquisition profiles, including engine hot-start and cold-start conditions. Nevertheless, it does not directly take into account the tire inflation pressure, as vehicle tests, especially for homologation purposes, consider the reference tire pressure only [227]. The software allows a vehicle configuration to be set that considers a fixed set of coast-down parameters, which is only valid for a certain set of tires inflated at a reference pressure. Additionally, this tool allows a simulated coast-down curve to be calculated if a suitable set of data is provided in terms of aerodynamic coefficient C_xA and rolling resistance, whenever the rolling resistance is evaluated at a rated vertical load and tire pressure [227]. Therefore, the software users cannot evaluate the fuel economy for different tire pressures from the reference ones, nor can they analyze the effect of a variation in the rolling resistance over time during the execution of the test cycle.

All the vehicle specifications of the simulated car model, including detailed engine fuel consumption maps and full-load curve, coast-down coefficients, transmission ratios, efficiency maps and gearshift profiles, were provided by FCA. The tire specifications of the tested tire were provided by Michelin. The F_0 , F_1 , F_2 , B_0 , B_1 and B_2 coefficients were evaluated experimentally at the reference inflation pressure equal to 2.1 bar gauge for a cold tire, according to ISO 18164:2005 [227]. Coast-down coefficients F_0 , F_1 and F_2 can be set as input by the user of the software when configuring the dataset for the simulation model. On the other hand, the software does not allow to configure the tire coefficients B_0 , B_1 and B_2 , as they are already included in the coast-down coefficients. Indeed, the experimental coast-down coefficients F_0 , F_1 and F_2 are obtained with a specific tire inflated at a certain pressure. Therefore, the contribution of the rolling resistance of such a tire, which could be described through the coefficients B_0 , B_1 and B_2 in Eq. 2.4, is naturally included in the experimental coast-down coefficients F_0 , F_1 and F_2 (cf. Eq. 2.3 and Eq. 2.4).

All the tires were considered to be inflated at the same pressure. All the tests were performed with no road grade, according to standard specifications.

If the aerodynamic drag and the residual resistant force in the brakes are made explicit, Equation 2.3 can be rewritten as:

$$F_{\text{res}} = \frac{1}{2} \rho C_x A v^2 + mg C_{\text{rr}} + F_{\text{dvl}} + \sum_{i=1}^N \frac{T_{\text{brk},i}}{R} = F_0 + F_1 v + F_2 v^2 \quad \text{Eq. 2.10}$$

where ρ is the air density, C_x the longitudinal drag coefficient, A the frontal area of the vehicle, F_{dvl} the resistance in the driveline downstream of the gearbox (usually described, with a semi-empirical relationship, as linearly dependent on the vehicle speed), T_{brk} the possible residual torque in the brakes of each wheel, N the number of wheels, v the vehicle speed, m its mass and R the loaded tire rolling radius. Considering also the dependence of C_{rr} on the vehicle velocity (Eq. 2.4), the coast-down coefficients F_0 , F_1 and F_2 can be defined as:

$$F_0 = mgB_0 + F_{\text{dvl}} + \sum_{i=1}^N \frac{T_{\text{brk},i}}{R} \quad \text{Eq. 2.11}$$

$$F_1 = mgB_1 \quad \text{Eq. 2.12}$$

$$F_2 = \frac{1}{2} \rho C_x A + mgB_2 \quad \text{Eq. 2.13}$$

As a standard, the coast-down coefficients and rolling resistance coefficients in Eqs. 2.10-2.13 are provided at the reference pressure [227]. If the coefficients B_0 , B_1 and B_2 are known as a function of pressure, neglecting other effects induced by tire pressure variation (e.g., changes in aerodynamic drag), the coast-down coefficients can be computed for different inflation pressures by replacing the values of B_0 , B_1 and B_2 at the reference pressure with the values known for any inflation pressure. As in the previous equations not all the terms were explicitly known, the new coast-down parameters as a function of pressure were computed by subtracting the rolling resistant terms at the standard pressure and adding the rolling resistant term recalculated for the current pressure. In formula:

$$F_{0,1,2}(p_{\text{inf}}) = (F_{0,1,2,\text{std}} - mgB_{0,1,2,\text{std}}) + mgB_{0,1,2}(p_{\text{inf}}) \quad \text{Eq. 2.14}$$

The subscript ‘‘std’’ stands for standard and is related to the known data at the reference pressure.

Assuming that $C_{\text{rr}}(p_{\text{inf}})$ [%] is independent of the vehicle speed, the $C_{\text{rr}}(v)$ curves for different inflation pressures were obtained by vertically shifting the

reference curve on the $C_{rr} - v$ diagram according to Eq. 2.2. As an example, Figure 2.2 shows an experimentally-derived baseline $C_{rr}(v)$ curve at the standard inflation pressure of 2.1 bar, and the $C_{rr}(v)$ curves recalculated for different inflation pressure values by applying to the baseline curve the percentage variations calculated from Eq. 2.2. In Fig. 2.2 all the values have been normalized according to the reference value of C_{rr} at 2.1 bar and 80 km/h. The coefficients $B_0(p_{inf})$, $B_1(p_{inf})$ and $B_2(p_{inf})$ were then computed by means of second-order regressions as a function of the vehicle velocity of the $C_{rr}(v, p_{inf})$ curves.

2.3.1 Experimental coast-down tests at various tire pressure levels

In order to validate the proposed approach, some coast-down tests have been performed on track thanks to the collaboration of the Vehicle Dynamics testing division of FCA. The tests have been performed at the Balocco Proving Ground (FCA track, cf. Fig. 2.3). The vehicle and tires used for the tests are the same used for the simulations and described in Table 2.1. Pressure and temperature during the tests were measured inside the tires through a Stack batteryless TPMS Lite: the sensors installed inside the tires communicate to the central module via dual-band antennas, and the acquired signals are then transmitted via CAN and acquired through a Dewesoft on-board acquisition system provided by FCA for these tests.

The coast-down test has been performed at 2 different test masses, nominally a “standard B” case, i.e. vehicle in standard running conditions including the driver, and a full-load case, where the vehicle has been loaded with mannequins on the rear seats and with ballast in the trunk up to reach its maximum payload. For each of the

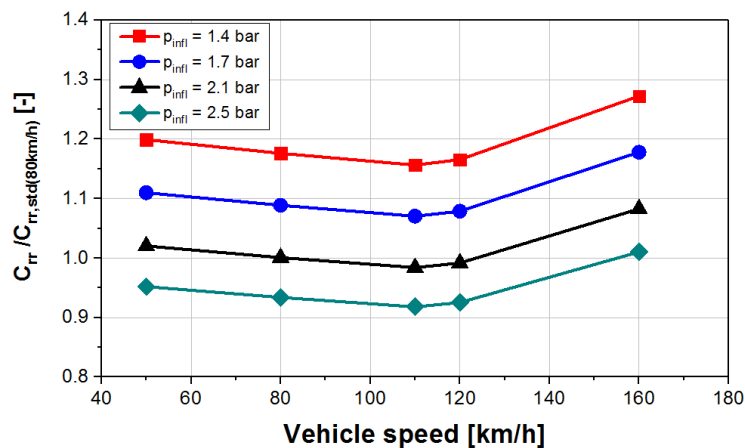


Figure 2.2: Normalized rolling resistance coefficient of the reference passenger tire as a function of speed for different tire inflation pressure values.

test masses, 3 levels of tire pressures were tested: a reference tire pressure value of 2.4 bar, and a case of overinflation as well as a case of underinflation with respect to the reference tire pressure. In order to reduce the statistical dispersion of the result, each test case has been repeated 10 times. Table 2.2 reports the list of the tested cases, including the mass distribution among the wheels, as the loaded vehicle was weighted on a balance before testing. It is worth highlighting that the tire pressure values reported in the table are obtained by averaging the pressure measured in the 4 tires along the 10 coast-down maneuvers, after normalizing instant-by-instant the measured pressure to a reference temperature of 25°C.

	Tire inflation pressure levels [bar]
Test set 1 – standard B weight <i>FL 31.9 % - FR 31.2 %</i> <i>RL 18.8 % - RR 18.1 %</i>	2.2
	2.4
	2.8
Test set 2 – Full-load weight <i>FL 24.6% - FR 23.9 %</i> <i>RL 25.9 % - RR 25.6 %</i>	2.0
	2.4
	2.7

Table 2.2: Test cases for the coast-down tests performed on track on a passenger vehicle.

The tests were performed by a professional test driver and following the internal FCA procedures for this kind of tests, in compliance to SAE J2263 regulation [234] and to the internal best common practices. The testing procedure includes: setting the tires at the desired pressure in cold conditions, then warming up the tires by high-speed driving on the track, and then performing 10 test repetitions. Each test consists in accelerating the vehicle up to about 140 km/h and then letting it decelerate to 35 km/h, without acting on the brakes, on a planar and straight road, with the clutch engaged and with neutral gear. Figure 2.3 shows the test track: the two straight sectors where the coast-down tests were performed are highlighted in blue and in red. The track is driven in the anti-clockwise direction, and – as the two straight sectors are almost parallel, the effect of the wind is averaged by performing half of the tests on one sector and half of the tests on the other sector. As one of the two straight sectors was shorter than the other, in some cases the vehicle could not reach the target final speed to complete the test in a single run: in these cases the test was split in two runs, i.e. a first acquisition included the vehicle starting at 140 km/h down to a final speed (e.g., 60 km/h), and the following acquisition was starting at a speed lower than 140 km/h (e.g., 70 km/h) down to the final speed of 35 km/h. In these cases, the tests have been then unified in post-processing.

Accurate vehicle speed measurement is obtained through a Corrsys-Datron Correvit S-350 2-axis optical sensor at 500 Hz. The longitudinal speed signal is



Figure 2.3: Test track (FCA Balocco Proving Ground), with highlighted the two straight sectors where the coast-down tests have been performed.

then re-sampled at 25 Hz and filtered through a moving average on a 50-sample window width (2 seconds) in post processing. Data analysis is performed according to the procedure described by SAE J2263 [234]. The vehicle resistant force is calculated in the interval between 120 km/h and 40 km/h. This speed interval is discretized into sub-intervals of width $2x$ and centered on the values v . For each speed value v , the resistant force is obtained as:

$$F_{res}(v) = m_{eq} \frac{\Delta v}{\Delta t} = m_{eq} \frac{(v+x)-(v-x)}{t(v+x)-t(v-x)} = 1.03 \cdot m \cdot \frac{2x}{t(v+x)-t(v-x)} \quad \text{Eq. 2.15}$$

being m_{eq} the equivalent (apparent) translating mass of the vehicle, assumed equal to the vehicle test mass increased by 3%, and being the width interval $2x$ chosen equal to 2 km/h. This equation is applied to each single coast-down maneuver. The European Directive 70/220/EEC [13] defines the following parameter in order to evaluate the dispersion of the results of coast-down tests:

$$p = \frac{K_N \cdot \text{std}(F_{R100}) \cdot 100}{\text{mean}(F_{R100})} \quad \text{Eq. 2.16}$$

where

- K_N is a parameter dependent on the number of repetitions of each test ($K_N = 0.73$ for 10 repetitions)
- F_{R100} is the resistant force at 100 km/h and converted in kg/ton according to the equation:

$$F_{R100} = \frac{F_{res}\left(v=100\frac{\text{km}}{\text{h}}\right)[\text{N}]}{9.81 \left[\frac{\text{m}}{\text{s}^2}\right] \cdot m_{eq}[\text{ton}]} \quad \text{Eq. 2.17}$$

- “std” and “mean” indicate the standard deviation and the mean value of F_{R100} .

The European regulation defines as acceptable the coast-down tests where the statistical accuracy p calculated through Eq. 2.16 is lower than 3. Table 2.3 reports the results of the calculation of the statistical accuracy parameter, which resulted in any case lower than 3. Therefore, all the tests can be considered acceptable.

The coast-down parameters F_0 , and F_2 can be obtained for each repetition of each test case by means of a second-order interpolation of the resistant force as a function of speed, calculated according to Eq. 2.15. Table 2.3 reports for each test case the average coast-down parameters for the tests performed on each straight road sector of the track, and finally the overall average for each test case. It is possible to notice that the values F_0 are always higher on the road sector 2 with respect to the road sector 1, which may be due to the non-null road grade and/or due to the presence of wind during the test. For this purpose the SAE regulation prescribes to run the tests in both the travelling directions, in order to compensate

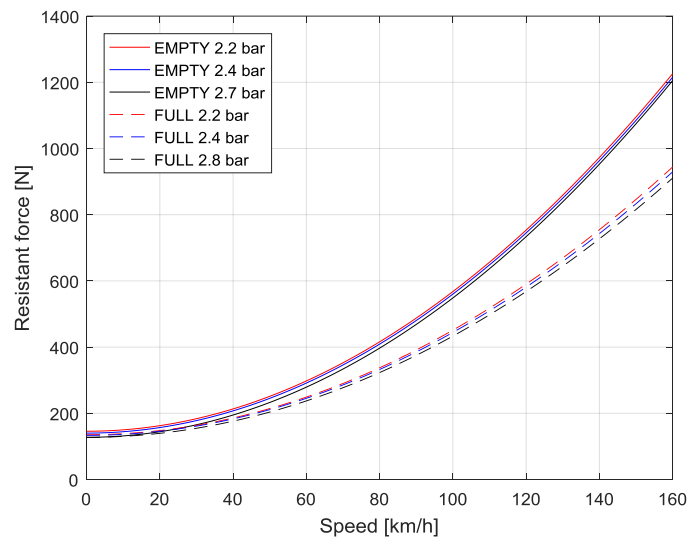


Figure 2.4: Average coast-down characteristics of the tested passenger car for each test case.

	Tire inflation pressure levels [bar]	Statistical accuracy p	Road sector 1		Road sector 2		Overall	
			F_0	F_2	F_0	F_2	F_0	F_2
Test set 1 Standard B weight <i>FL 31.9 % - FR 31.2 %</i> <i>RL 18.8 % - RR 18.1 %</i>	2.2	2.37	140.9	0.041	150.7	0.043	145.8	0.042
	2.4	0.58	132.2	0.042	148.2	0.042	140.2	0.042
	2.8	0.65	124.8	0.042	130.3	0.042	127.5	0.042
Test set 2 Full-load weight <i>FL 24.6% - FR 23.9 %</i> <i>RL 25.9 % - RR 25.6 %</i>	2.0	0.52	114.2	0.032	156.5	0.033	135.3	0.032
	2.4	0.59	117.0	0.029	149.9	0.033	133.4	0.031
	2.7	1.67	121.4	0.031	133.2	0.030	127.3	0.031

Table 2.3: Statistical accuracy and coast-down parameters of the tested passenger car for each test case.

for possible effects related to wind and road grade by averaging tests performed in two opposite travelling directions.

Figure 2.4 shows the coast-down characteristics deriving from the overall average coast-down parameters calculated for each test case and shown in the last columns of Table 2.3. The result shows an unexpected behavior, which can be further highlighted by looking at the numerical values in Figure 2.4: the full-load case shows lower resistant force than the standard B case, with both lower F_0 and F_2 parameters, while it would be reasonable to expect a higher resistance with an higher test mass. As the statistical accuracy of the test is good, and also the same result has been obtained for all the test cases with the higher test mass, this result cannot be considered as erroneous or affected by measurement issues nor by issues related to the repeatability of the maneuver. Therefore, the hypothesis that was formulated to justify this result is that loading the vehicle mainly on the rear with ballast has produced a higher pitch towards the rear axle, with a positive lift effect on the front that resulted in a reduction in F_0 , and in an unpredicted substantial change on the vehicle aerodynamics. Anyway, not enough data were available to perform a more detailed analysis on this topic.

Moreover, Figure 2.4 shows the effect of tire pressure on the vehicle coast-down characteristic. For both the test masses, the effect of changing tire pressure is evident, and results in a shift of the coast-down curve towards higher values of resistance when tire pressure is decreased, as expected. The effect on the aerodynamic coefficient F_2 is negligible. The percentage variation of the F_0 coefficient with tire pressure is plotted in Figure 2.5, where the results of the experimental tests are compared to the calculation performed according to Eq. 2.2 and Eq. 2.14. It can be noted that in all the cases the experimental result shows the expected trend, and in most of the case the calculation well fits the experimental

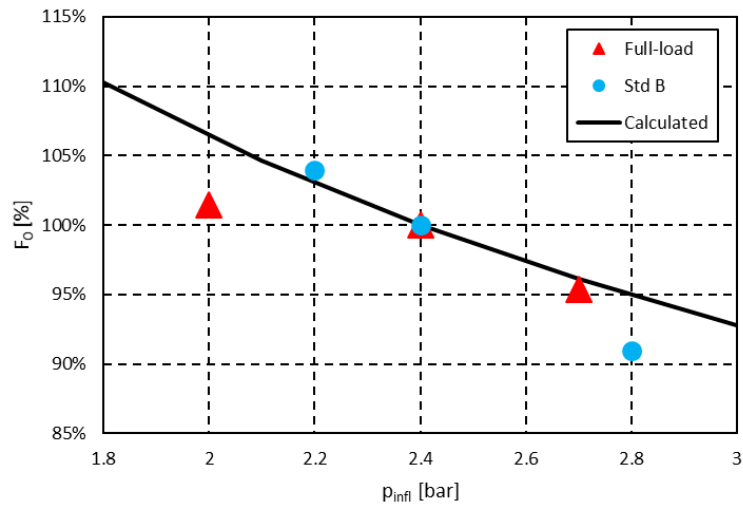


Figure 2.5: Variation of the F_0 coast-down parameter with tire inflation pressure for the tested passenger car: comparison of the test results with the calculated values.

results. Generally the experimental result show a slightly higher variability with tire pressure. Apart from the case at 2 bar and full-load weight, where the experimental result shows an increase by 1% on F_0 , while the calculation estimates an increase by 6%. Moreover, it can be noted that the trend in experimental data looks affected by the loading condition of the vehicle: the standard B case shows a steeper characteristic than the calculation, i.e. F_0 is more sensitive than predicted to a change in tire pressure, while the characteristic at full load looks less sensitive to tire pressure variations. Anyway, it is worth to underline that the calculated curve is based on Eq. 2.2, which is derived as a general rule valid for a wide population of vehicles and tires, while the experimental results here shown only refer to a single tire tested on a single vehicle.

2.3.2 Effects of tire pressure on fuel consumption

Simulations were performed on the different homologation driving cycles reported in Fig. 2.6, and a summary of their characteristics is reported in Table 2.4: the NEDC (New European Driving Cycle) has been the reference type-approval cycle in Europe until September 2017, and accounts for urban and extra-urban driving; the Federal Test Procedure (FTP75) is a US cycle representative of urban driving; the supplemental test procedure US06 was introduced in 2008 to integrate FTP75 with a more aggressive driving cycle; the Highway Fuel Economy Test cycle (HWFET) simulates highway driving and is used by US EPA, together with FTP75, to evaluate fuel economy of light-duty vehicles.

Fig. 2.7a shows the fuel consumption values as a function of the tire inflation pressure, normalized to the cumulated fuel consumption on the NEDC at the reference pressure (2.1 bar gauge): NEDC and FTP75 are quite similar, US06 has a similar trend to NEDC and FTP75 but the values are higher, and the difference between 1.1 and 2.1 bar is slightly higher with respect to NEDC. The HWFET trend is similar to the other cycles, but it has a much lower consumption. Fig. 2.7b reports a similar graph to Fig. 2.7a, but the fuel consumption of each curve refers to the value evaluated at the reference pressure (2.1 bar gauge) on the same cycle. Note that the tire pressure is always expressed as a gauge pressure, measured when the

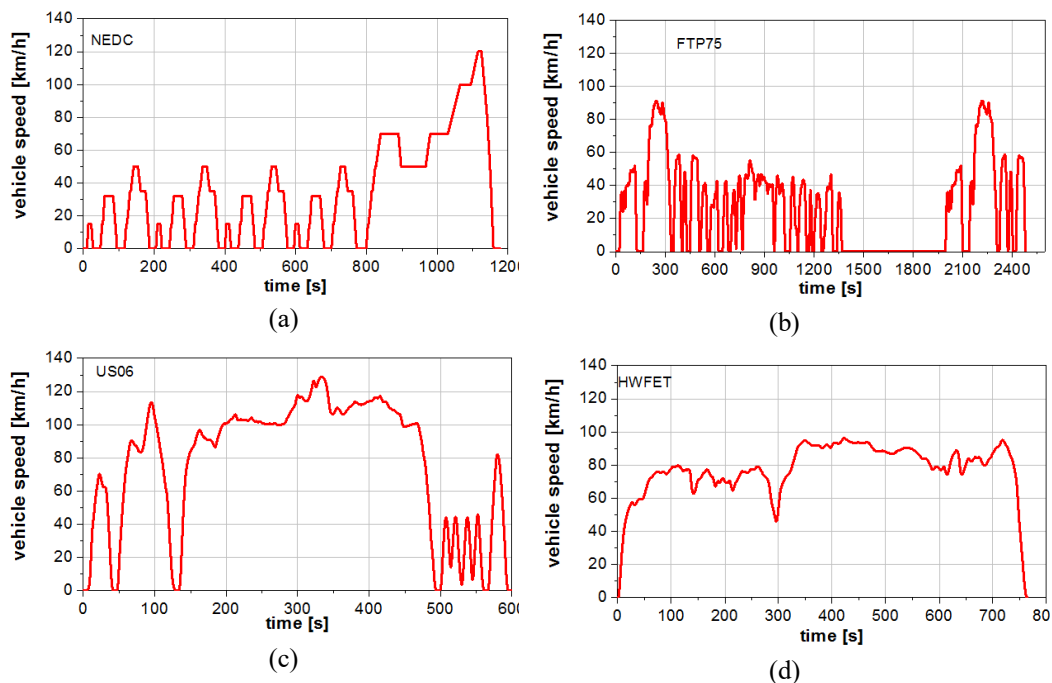


Figure 2.6: Vehicle velocity profiles of the driving cycles used as references for the study-case on passenger car.

Test cycle	Average speed - incl. idle [km/h]	Average speed - excl. idle [km/h]	Idle duration [%]	Driving time [s]	Driving distance [km]
NEDC	33.4	43.1	22.6	1180	10.9
FTP75	34.1	39.5	45.8	1877	17.8
US06	77.9	78.6	0.96	596	12.8
HWFET	77.7	77.7	0	765	16.5

Table 2.4: Summary of the characteristics of the reference cycles for the study-case on passenger car.

tire is cold. The values here obtained are coherent with those found in [223]: considering a decrease in the tire inflation pressure to 1.6 bar, which corresponds roughly to a 10% increase in rolling resistance, with respect to the reference pressure of 2.1 bar, fuel consumption increases by 1-2%, depending on the driving conditions, which corresponds to an increase in CO₂ emissions of 1.25-1.45 gCO₂/km. The differences among the cycles are negligible, apart from the HWFET. In fact, comparing various cycles for a given rolling resistance variation, the fuel consumption change rate generally increases with the mission average speed [78].

However, when two high-speed cycles are compared, the higher change rate on fuel consumption is not always obtained on the mission with higher average speed, which leads to the conclusion that accelerations also have an impact on rolling resistance [78]. Comparing US06 and HWFET, it can be noted that even though the average speed is almost identical (cf. Table 2.4), US06 presents a much higher top speed and a significant presence of heavy transients in the first and in the last parts of the cycle (cf. Fig 2.6). In order to provide an explanation of the obtained difference in fuel consumption between US06 and HWFET that can be observed in Fig. 2.7b, the energy demand for the two cycles was split in Fig. 2.8 into different contributions: rolling resistance (evaluated both at $p_{inf} = 1.1$ bar and $p_{inf} = 2.1$ bar), accelerations, and other resistances (aerodynamics, braking, driveline). As abovementioned, the variation in inflation pressure practically only affects the term related to rolling resistance. Moreover, according to the performed calculations, the percentage variation in energy demand due to rolling resistance between $p_{inf} = 1.1$ bar and $p_{inf} = 2.1$ bar is practically the same for the two cycles (cf. the difference between the black bar and red bar on US06 and HWFET of Fig. 2.9). However, the contribution of accelerations to the energy demand is much higher for US06 (Fig. 2.8a) with respect to HWFET (Fig. 2.8b). Therefore, the similar contribution of rolling resistance due to tire pressure variation (Fig. 2.9) provides a higher percentage contribution on HWFET (Fig. 2.8), because the total energy demand is lower. However, it is worth pointing out that Fig. 2.7b refers to fuel consumption, whereas Figs. 2.8 and 2.9 refer to energy demand, and that the two quantities are not simply correlated, since the same requested traction power can be provided at different engine working points, which correspond to different fuel consumptions.

According to [239], an increase in tire pressure could produce an increase in the power lost due to longitudinal slip, so that the slide loss contribution should be evaluated together with the rolling resistance in order to provide a complete analysis over the effects on fuel consumption. Furthermore, increasing the road load (i.e., grade) at a given pressure leads to an increase in the effect of pressure variations on

sliding losses. Although these losses have not been accounted for in the present study, it should be pointed out that the sliding power losses are much lower than the rolling resistance for a negative grade or for no grade. Finally, slide only occurs on traction wheels, and the desired combined effect can therefore be obtained through a selective adjustment of the rear and front wheels at different pressure levels [239]. The effective contribution of this loss depends on the specific characteristics of the tire.

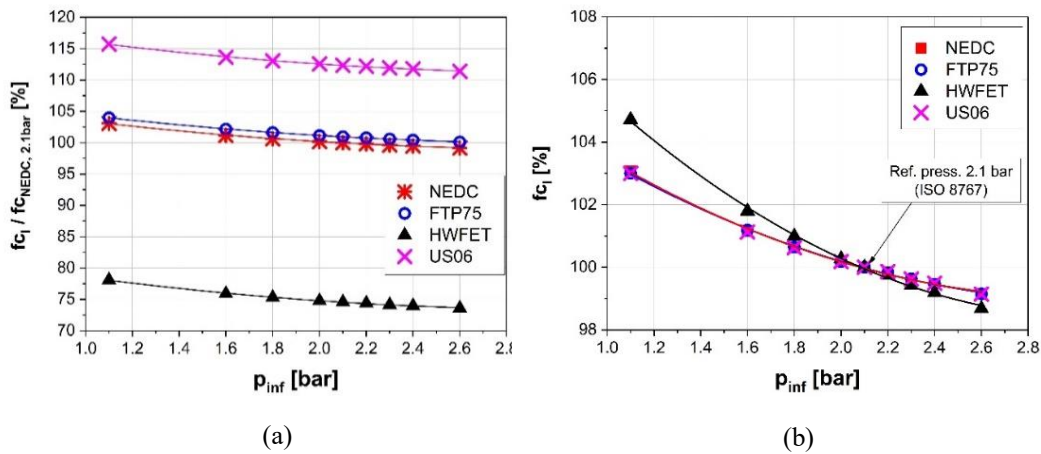


Figure 2.7: Percentage fuel consumption caused by variations in the inflation pressure of tires on the reference passenger car for different driving cycles. (a) Results normalized to the total fuel consumption on the NEDC cycle at the reference pressure of 2.1 bar. (b) Results of each cycle normalized to the total fuel consumption at the reference pressure of 2.1 bar.

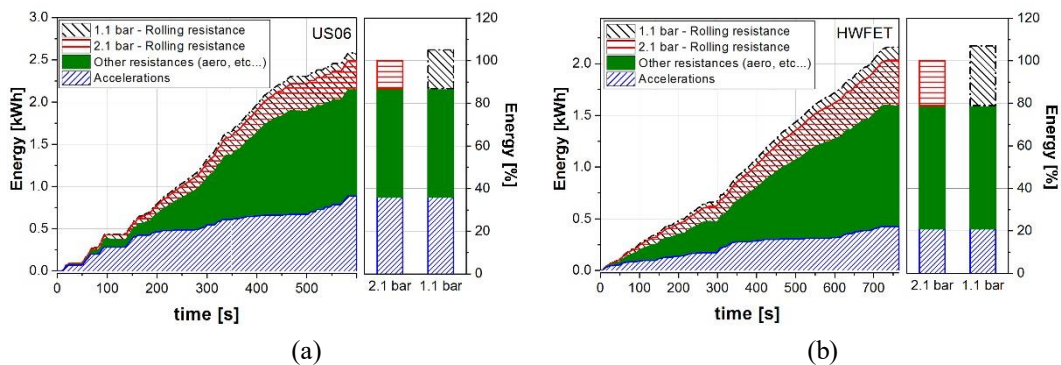


Figure 2.8: Absolute (left part of each graph) and relative (right part of each graph) contributions of the different terms to the energy demand for US06 (a) and HWFET (b): comparison between $p_{infl} = 2.1$ and 1.1 bar.

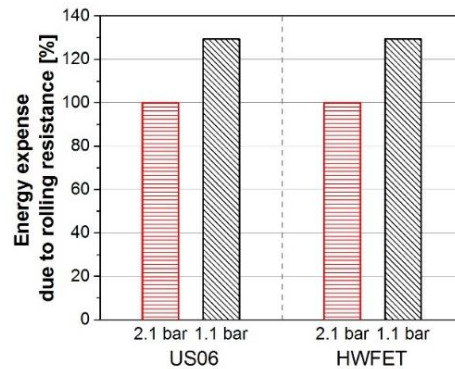


Figure 2.9: Percentage variation in the energy demand due to rolling resistance at $p_{infl} = 1.1$ bar compared to $p_{infl} = 2.1$ bar for US06 and HWFET.

2.3.3 Pressure management strategies and the related benefits

In order to quantify the possible benefits that can be achieved by means of a flexible pressure management through a CTIS, some strategies were chosen and the corresponding simulations were performed to evaluate the fuel consumption in the proposed cases. Three pressure management strategies were proposed and studied:

- 1 – inflation pressure adaptation to a vertical load;
- 2 – inflation pressure variation during tire warm-up;
- 3 – inflation pressure adjustment according to the average speed (urban/highway driving).

In order to obtain a result that does not depend on the specific design of the system, and can be therefore generalized, in the first two cases, the fuel economy advantages were evaluated neglecting the negative contributions on fuel consumption due to the vehicle curb mass increment. Anyway, for the considered system the mass increment is lower than 0.4% of the reference vehicle mass: therefore, the influence in terms of fuel consumption is minor (about 0.10% of the fuel consumption and about 0.18% of the energy available at the traction wheels along a NEDC under the reference inflation pressure of 2.1 bar). Additionally, the system is actuated as an electric load, which affects the total energetic balance, but the corresponding fuel consumption is not straightforward. Therefore, since the analysis of the first two cases is discussed with reference to fuel consumption, the negative contribution due to the activation of the system is not included. The evaluation concerned a comparison of the reference standard case, in which the standard tire pressure was set, and a case in which the proposed strategy was used.

ATPC system characteristics	
Weight of the system	4.4 kg
Nominal compressor/vacuum pump flow rate	35.4 l/min (in open air)
Maximum compressor flow rate in operating conditions (c.f. Fig 2.48)	14.5 l/min (p=2.8bar @ compressor outlet)
Maximum vacuum generator flow rate in operating conditions (c.f. Fig 2.49)	5 l/min (@ 67% vacuum level)
Minimum geometric flow section (diameter)	1.5 mm (M3 pipe fitting on the outlet port of the toroidal pneumatic rotating joint)
Reference actuation for each tire	inflation, from 2.2 bar to 2.3 bar
Duration	10 s (ca.)
energy absorption	0.61 Wh

Table 2.5: Characteristics of the ATPC system.

The third analysis concerned the global energy balance and it also took into account the negative contributions due to the installation and energization of the system, and involved the additional case of a vehicle with underinflated tires.

The simulations were performed over an NEDC and an HWFET cycle. In all the tested conditions, the four tires were considered to be inflated at the same pressure. The influence of the inflation pressure was evaluated in terms of the variations produced on the rolling resistance coefficient (c.f. Eq. 2.2) and as a consequence on the F_0 , F_1 , F_2 , B_0 , B_1 and B_2 coefficients (c.f. Eq. 2.14), according to the methodology illustrated above.

The study was carried out taking the vehicle and the tire already illustrated in Table 2.1 as references as well as the CTIS developed at the Politecnico di Torino for application on passenger cars, named Active Tire Pressure Control (ATPC), which will be discussed in detail in *Section 2.6*, whose weight and performance are reported in Table 2.5.

Inflation pressure adaptation to the vertical load

This control strategy concerns tire pressure adjustment with the vehicle loading conditions. A number of solutions exist for estimating on-board the vehicle loading conditions [240-245]. Some of these solutions require the installation of additional hardware, such as accelerometers to be installed inside the tire [240], while other solutions propose a software approach, as the estimation of the vehicle mass in the current working conditions can be based on some variables already available in

modern vehicle ECUs, such as the speed of each wheel and, possibly, tire inflation pressure [241-245]. One software solution for the estimation of the vehicle loading conditions, i.e. total vehicle mass and its distribution among the tires, was also proposed as a side project of the current study, and its details are discussed in [246]. The method is based on three main steps, briefly reported in the following:

- 1) evaluation of the total vehicle mass (m) from the apparent translating mass (m_{eq}) through Eq. 2.6, where the apparent vehicle mass is estimated through Eq. 2.5 from the engine torque and speed (available in the engine ECU) and from the total resistant force, evaluated at the current tire pressure (Eq. 2.10, 2.14);
- 2) evaluation of the static vertical force on each tire by means of tire structural data, including the correlation of tire effective rolling radius to inflation pressure and vertical load, where tire pressure is known as measured by a TPMS and tire rolling radius is evaluated from wheels rotational speeds and vehicle longitudinal speed;
- 3) iteration of the calculation of the vertical force per each tire, in order to improve the estimation by minimizing the error between the total vehicle mass estimated at point 1) and the sum of the tire-by-tire vertical load estimated at point 2).

The method has been developed and tested in real-time in a Hardware-in-the-Loop environment. The mass estimation algorithm was implemented in a real-time hardware, and it was tested by providing as input real-time data acquired on-board from the vehicle CAN during several tests on road and on track. The tests proved that the algorithm allows the estimation of the total vehicle mass within +2.5% error, while the maximum error on the percentage vehicle load distribution is 2% (the maximum error is obtained when the real load distribution is 63% front – 37% rear and the algorithm estimates 61% front – 39% rear). The convergence time depends on the availability of suitable data on the vehicle CAN: during the tests it was highlighted that the engine torque is often overestimated during transients, which led to the need for introducing plausibility logics in order to evaluate if a torque sample is acceptable for the calculation. The convergence of the algorithm was obtained in 390 valid torque samples in the best tested case.

Regardless of which method is used to provide real-time information about the vertical load acting on a tire, due to the vehicle loading condition, tire pressure can

be adapted to the vertical load in order to reduce fuel consumption, and to improve the tire dynamic response.

A number of simulations were performed, each at a specific load and for a specific tire inflation pressure. The vehicle load was varied between a base-load case and the full-load weight case; the vehicle mass distribution (percentage on front and rear axle) was considered to not vary with the vehicle mass. The simulations have been grouped together in order to represent two cases for comparison purposes:

- the “baseline” case: the vehicle mass was varied while the inflation pressure was kept constant (2.1 bar);
- the “variable pressure” case: the inflation pressure was varied with the vehicle mass according to a strategy which ensured that the tire-road contact patch area was maintained roughly constant for each loading condition and equal to the baseline case for the base loading condition.

The considered test conditions are summarized in Table 2.6.

The results of each of the computer simulations were evaluated, in terms of the average fuel consumption per cycle, normalized to the result obtained in the reference condition (base load and reference inflation pressure of 2.1 bar). The obtained results are reported in Fig. 2.10. In the “baseline” case, the fuel consumption increased by up to 9.3% for NEDC and by up to 8.0% for HWFET, when the vehicle was in the full load condition with respect to the reference loading condition. The advantage that can be obtained with the proposed strategy grows as the vehicle mass increases, and it reaches a maximum for the full load weight condition, where the saving in fuel consumption that can be obtained with a variable

#	0	1	2	3
Case	“baseline” (constant pressure)			
vehicle mass [kg]	1285	1416	1547	1678
vehicle mass [% #0]	100	110	120	130
inflation pressure [bar]	2.1	2.1	2.1	2.1
Case	“variable pressure”			
vehicle mass [kg]	1285	1416	1547	1678
vehicle mass [% #0]	100	110	120	130
inflation pressure [bar]	2.1	2.4	2.6	2.9

Table 2.6: Pressure variation with the loading conditions on the reference passenger car: test cases.

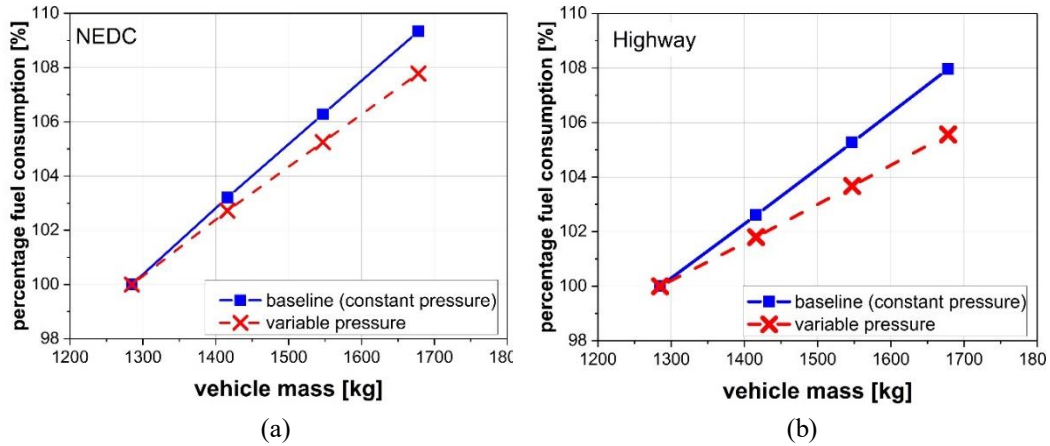


Figure 2.10: Percentage fuel consumption variation with respect to the vehicle mass on the reference passenger car: comparison of the baseline case and the case in which the pressure is varied in order to maintain the same road contact patch area. The results are shown for an NEDC cycle (a) and for an HWFET cycle (b).

pressure can be quantified as 1.6% for NEDC (Fig. 2.10a, vertical difference between solid and dashed curve) and 2.4% for HWFET (Fig. 2.10b), which, in terms of CO₂ tailpipe emissions, correspond to 2.2 and 2.5 gCO₂/km, respectively with a maximum rolling resistance variation of about 12%.

Inflation pressure variation during tire warm-up

The proposed strategy concerns the reduction in rolling resistance and fuel consumption for a cold tire: according to Michelin [83], the rolling resistance increases by up to 35%, with respect to the reference condition, when the tire temperature is low. The rolling resistance transient is generated by two effects: the dependence of the elasticity of the tread rubber on the tread temperature, i.e., the increase in energy that is needed to deform the rubber when its elasticity is low as a result of a low temperature [81, 83]; and tire pressure variation with temperature. As far as the latter is concerned, the tire pressure is usually set at cold-tire conditions in such a way that it is taken into account that this pressure will then increase until it reaches the correct working pressure as the tire is in a steady thermal state. In addition, the tire warm-up time is usually considered to be about 30 minutes, and the equilibrium temperature ranges from 20 to 60°C. The proposed strategy has been designed in order to compensate for this effect: having an advanced CTIS on board, it is possible to set, when the tire is still cold, the tire pressure that would be

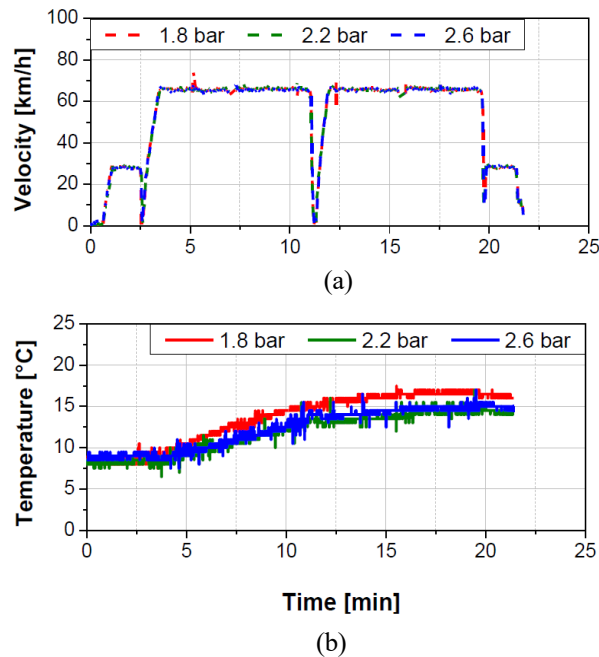


Figure 2.11: Tire warm-up on a passenger car for three tire pressure levels: vehicle speed profile (a) and temperature of the rear right tire (b). The other tires show a similar behavior.

reached at the end of the thermal transient and then keep this pressure by releasing air as the tire becomes warmer during the warm-up period.

Starting from the rolling resistance evolution during warm-up time t reported in [83], an evaluation of the fuel consumption over the heating time was performed for the “baseline” case (constant pressure), and applying the proposed strategy, which consists of an initial over-inflation to $p_{\text{std}} + 0.4$ bar and a gradual decrease in pressure until the p_{std} pressure (2.1 bar) is reached at the end of the thermal transient. The pressure was considered to decrease by a 0.1 bar step, with ideal instantaneous actuations every 5 minutes. The application of such a strategy was studied under the assumption that – as for warm tires – cold-tire pressure variations within the optimal working range of a tire do not have a significant effect on the vehicle dynamics.

Another hypothesis is implicit in the methodology reported above. It is assumed that the tire warm-up time does not vary with the tire inflation pressure and load, although the tire temperature is determined by the vertical deformation of the tire [81], which depends on the vertical load and inflation pressure. This would generate a different steady-state temperature of the tire and therefore a different

rolling resistance at the end of the thermal transient. Therefore, a tire with a higher vertical deflection is expected to reach a higher working temperature than a tire with a lower deflection, starting from the same ambient temperature. Nevertheless, the more deflected tire would also undergo a more rapid temperature variation in time. Therefore, it is reasonable to assume, at least as a first approximation, that the duration of the warm-up phase does not depend on the tire deflection. In order to support this assumption, Figure 2.11 reports the warm-up of a passenger car tire acquired on-board by means of a high-accuracy TPMS system during a test campaign realized at the Politecnico di Torino. The vehicle speed trace acquired via GPS is also reported as a reference. The driving cycle has been repeated for three different levels of tire pressure, that is, 1.8 bar, 2.2 bar and 2.6 bar, and for a single loading condition (driver only on board). The speed profile is reported for the three tests in order to point out the repeatability of the maneuver. The graph reports the temperature of the air inside the tire, which can be considered correlated to the tread temperature. The maneuver was realized during winter on a public asphalt road. The tested tire is a winter tire, which justifies the fast warm-up and the low steady-state temperature reached at the end of the transient. The graph shows no significant variation in the steady-state temperature at 2.2 bar or at 2.6 bar, while the tire underinflated at 1.8 bar reaches a slightly higher working temperature than in the other cases, due to its higher deflection. On the other hand, the warm-up time appears to be almost identical for the three pressures.

It is worth underlining that this result can be considered valid if the tire is working over a suitable range of pressure-load combinations, while excessive over-inflation or under-inflation, with respect to the reference iso-deflection, is expected to also generate differences in the duration of the warm-up period.

The “baseline” case was studied starting from the parametrization, through the following equation, of the graphical curve $C_{rr,std}(t)$ provided in [83], in which time t is expressed in minutes:

$$C_{rr,std}(t)[\%] = [1 - k(t)] \cdot C_{rr,std}(t - 1)[\%] + 100k(t) \quad \text{Eq. 2.18}$$

which is valid for $t \geq 1$ min, where $C_{rr,std}(t = 0) = 134.7\%$ and

$$k(t) = 0.0011t^2 - 0.028t + 0.2645 \quad \text{Eq. 2.19}$$

Fig. 2.12a shows a comparison between the data derived directly from the original graph (Michelin’s dotted curve) and the results obtained by means of the application of Eq. 2.18 and Eq. 2.19 (solid curve indicated as *diff_model*). A third curve (dashed curve), which represents the approximation of the original graph by

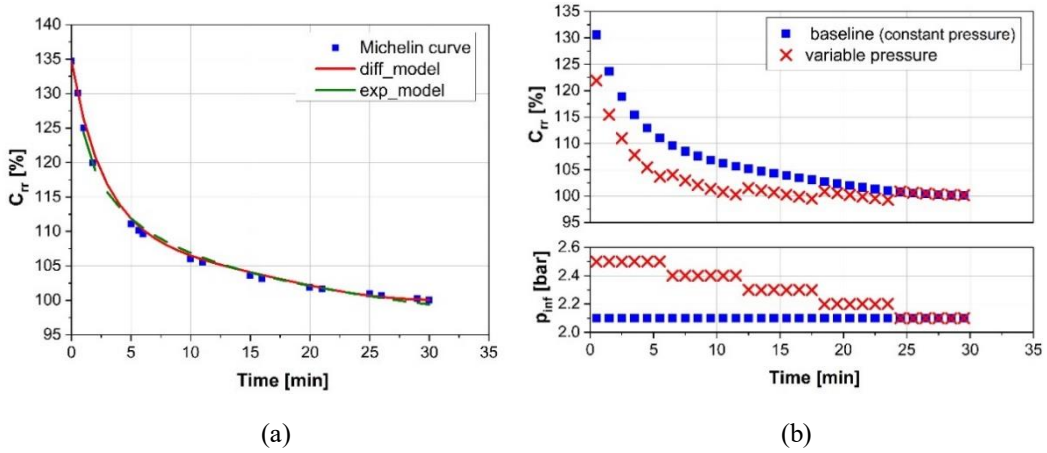


Figure 2.12: (a) Percentage of rolling resistance versus time during tire warm-up on passenger cars: Michelin's data and parametrized curves. (b) Percentage of rolling resistance versus time during tire warm-up for the "baseline" and for the "variable pressure" cases (top) and corresponding inflation pressure (bottom).

means of the following power equation (valid for $t \geq 1$ min) is shown in the same figure:

$$C_{rr,std_POWER}(t)[\%] = 124.42t^{-0.066} \quad \text{Eq. 2.20}$$

The points and the curves in Fig. 2.12a refer to the nominal tire inflation pressure of 2.1 bar.

The calculations for the "baseline" case were performed considering a discretization of the $C_{rr,std}(t)[\%]$ curve: the 30 minute time interval was divided into a number of sub-intervals, each of 1 min. The time-average value of the rolling resistance for each i -th interval was computed as follows:

$$C_{rr,std,i}[\%] = \frac{C_{rr,std}(t_{fin,i})[\%] + C_{rr,std}(t_{in,i})[\%]}{2} \quad \text{Eq. 2.21}$$

For the "variable pressure" case, the rolling resistance was evaluated for each i -th interval under the assumption that LaClair's $C_{rr}(p_{infl})[\%]$ curve (Fig. 2.1) is valid for both warm and cold tires:

$$C_{rr,i}(p_{infl})[\%] = (1.3447 \cdot p_{infl,i}^{-0.398}) \cdot C_{rr,std,i}[\%] \quad \text{Eq. 2.22}$$

The results, shown in Fig. 2.12b, were obtained considering the *diff_model* (Eq. 2.18 and Eq. 2.19). It is evident that similar results would be obtained, regardless of which parametrization is chosen for the $C_{rr,std}(t)[\%]$ curve in Fig 2.12a.

Two percentage values of rolling resistance were obtained for each sub-interval, one referring to the “baseline” case and the other representing the “variable pressure” case. A set of coast-down parameters (B_0, B_1, B_2, F_0, F_1 and $F_2,$) was computed for each calculated percentage value of the rolling resistance, according to Eq. 2.14.

The computer simulations were performed for each of the obtained parameter sets, in order to evaluate the fuel consumption of the reference vehicle over the NEDC under the given rolling resistance condition. All the simulations were performed for the reference loading case (1285 kg). The PerFACTS software used for the fuel consumption simulations does not allow variations in the coast-down parameters over time to be taken into account, and each simulation therefore refers to a single rolling resistance condition. The results of the various simulations were combined in order to evaluate a cumulated fuel consumption over the NEDC considering the temperature evolution of the tire after a cold start for both cases (“baseline” and “variable pressure”).

The NEDC was divided into 19 one-minute long sub-intervals and a 20-th sub-interval whose length covered the residual duration of the cycle (40 s). The fuel consumption for each j -th interval can be computed for each i -th simulation of the NEDC as:

$$fc_{i,j} = \int_{t_{j,in}}^{t_{j,f}} fc_i(t) dt \quad \text{Eq. 2.23}$$

where $fc_i(t)$ [g/s] is the instantaneous fuel consumption of the i -th simulated NEDC, j is the generic sub-interval of the i -th simulation, and $t_{j,in}$ and $t_{j,f}$ are the initial and final time instants of the j -th sub-interval, respectively. The cumulated fuel consumption for each of the two case studies (“baseline” and “variable pressure”) was obtained as the sum of the different one-minute fuel consumptions with variable rolling resistance (Eq. 2.23), according to the following equation:

$$fc_{tot} = \sum_{n=1}^{n=20} fc_{i,j} \quad i, j = n \quad \text{Eq. 2.24}$$

The percentage difference between the two case studies during warm-up (WU) was evaluated as

$$fc_{tot,WU,diff}[\%] = \frac{fc_{tot,WU,baseline} - fc_{tot,WU,VP}}{fc_{tot,WU,baseline}} \quad \text{Eq. 2.25}$$

where VP stands for “variable pressure” case. The proposed strategy could improve fuel economy by 0.48% over the NEDC, starting from a “cold tire” condition. Fig.

2.13 reports the results of the simulations: in the upper graph, the results of each j -th sub-interval for the “variable pressure” case are normalized with respect to the results of the baseline case for the same sub-interval, while the cumulative evaluation of the percentage fuel saving versus time, calculated according to Eq. 2.24, is reported in the bottom diagram.

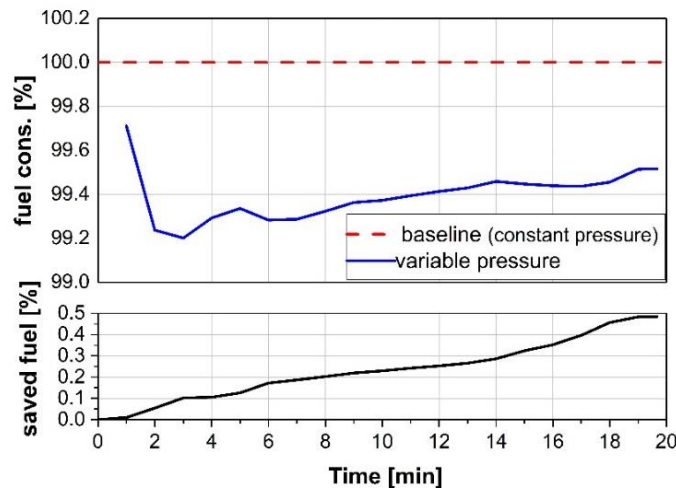


Figure 2.13: Fuel consumption benefits on the NEDC obtained through tire pressure management during tire warm-up on a passenger car: relative fuel consumption reduction (upper diagram) and cumulated saved fuel on a percentage basis (bottom graph).

Inflation pressure adjustment according to the average speed

The last of the proposed strategies regards the possibility of varying the tire inflation pressure according to the average cruising speed, as suggested in [216]. In fact, the fuel economy can be significantly improved, especially when driving at high speed, by increasing the tire pressure (Fig. 2.7b). A hypothetical mission system would recognize the driving condition, i.e., distinguish between urban and extra-urban/highway driving, on the basis of on-board information (average vehicle speed, radar-measured distances from other vehicles, etc...) as well as of information about the traffic and road conditions obtained from infrastructure-to-vehicle communication systems. Furthermore, it should be considered that high-speed driving (i.e., on a highway) usually determines larger vehicle-to-vehicle distances and smaller steering wheel angles than urban driving: the steady-state dynamic behavior of the car (e.g., the response to a ramp-steer maneuver) can be considered to be negligibly affected by tire pressure at small steering wheel angles.

On the other hand the effect of tire pressure on the understeering/oversteering characteristic in the high-speed range, as well as the response to a high-speed transient maneuver, such as a lane change or a step steer maneuver, has to be taken into account.

Regardless of which method is used to recognize the current working conditions of the vehicle, the tire pressure management system will increase the inflation pressure by 0.3 bar when a generic extra-urban mission is recognized.

The analysis of this case-study was performed comparing three different conditions:

- a “baseline” case: standard “cold” tire pressure 2.1 bar, reference loading case (1285 kg);
- an “underinflated” case: “cold” tire pressure 1.6 bar, reference loading case (1285 kg);
- an “ATPC” case: the active pressure management system is supposed to be installed on the vehicle. The curb vehicle mass is increased by the weight of the system (4.4 kg). The energy consumed to actuate the system is also taken into account and is considered equal to 0.61 Wh per tire for each 0.1 bar pressure variation. The system is actuated once for each test cycle to operate

	underinfl.	baseline	ATPC
Cycle	HWFET		
vehicle mass [kg]	1285	1285	1289
tire inflation pressure [bar]	1.6	2.1	2.4
Energetic expense - vehicle[kWh]	2.082	2.035	2.014
Energetic expense – ATPC system [Wh]	0	0	1.83
Energetic expense - total [kWh]	2.082	2.035	2.016
Energetic expense - total [%]	102.34	100	99.09
Cycle	NEDC		
vehicle mass [kg]	1285	1285	1289
tire inflation pressure UDC [bar]	1.6	2.1	2.1
tire inflation pressure EUDC [bar]	1.6	2.1	2.4
Energetic expense - vehicle UDC [kWh]	0.544	0.532	0.534
Energetic expense - vehicle EUDC [kWh]	0.979	0.960	0.953
Energetic expense – ATPC system [Wh]	0	0	1.83
Energetic expense - total [kWh]	1.523	1.493	1.489
Energetic expense - total [%]	102.01	100	99.73

Table 2.7: Test cases and results of tire pressure variations with the vehicle speed on the reference passenger car.

a pressure increase of 0.3 bar, starting from the reference “cold” pressure (2.1 bar gauge): the actuation occurs on the NEDC when passing from the urban to the extra-urban part of the cycle, while it occurs on the HWFET cycle at the beginning. The pressure variations are considered to be instantaneous for each case, i.e., the vehicle is run on tires inflated at the nominal pressure over the urban part of the NEDC, while the tires are inflated to 2.4 bar (gauge, equivalent pressure at ambient temperature) over the extra-urban part of the NEDC and over the HWFET cycle.

The results of the simulations are reported in Table 2.7, in terms of global energy balance. The net reduction in energy consumption obtained comparing the “ATPC” case with the “baseline” one is 0.9% of the total energetic expense on HWFET and 0.3% on combined urban/extra-urban driving. The advantage is much larger if the “ATPC” case is compared with the “underinflated” one, which is realistic for many circulating passenger cars: 3.3% of the global energy expense could be saved over the HWFET cycle and 2.3% over the NEDC.

2.4 Potential effect of tire pressure management on fuel economy of passenger cars: impact assessment of the technology on an annual mission

Stemming from the results of the simulations presented in the previous *Section*, the effect in terms of fuel consumption, fuel cost and CO₂ emissions has been assessed considering an annual mission of the reference vehicle. Then, the analysis is extended to show the potentialities of the technology if applied to the whole EU circulating fleet. An economic estimation is also provided taking into account the social cost of carbon emissions that could be saved through the application of this technology and the possible reduction of tire life in case of improper tire pressure management. Additionally, an active management of tire pressure could avoid a number of road crashes. These costs are quantified in order to provide a general prediction of the economic return which could be obtained by governments and by the European Commission by fostering the diffusion of an on-board technology for autonomous management of tire inflation pressure.

The vehicle considered for this study is the one already mentioned in the previous section, whose characteristics have been reported in Table 2.1. In order to perform the estimation of the effects of tire pressure management on an annual basis, the results of the previous simulations on single driving cycles have been

combined according to the methodology that is described hereinafter. Three main effects will be taken into account:

1. The variation of fuel economy performance due to a change in tire inflation pressure, through the relative variation of rolling resistance coefficient with pressure (Fig. 2.1a). For this purpose, the results of fuel consumption simulations presented in *Section 2.3.2*, performed at the reference vehicle mass M_{ref} and for a set of tire inflation pressures p_{inf} , have been exploited. A coefficient α_R , representative of the fuel consumption sensitivity to variations of the rolling resistance coefficient [38], has been estimated as the angular coefficient of the interpolating function shown in Fig. 2.14a. Two sensitivity coefficients, $\alpha_{R,U}$ and $\alpha_{R,EU}$ respectively, have been calculated on the urban and extra-urban parts of the NEDC. The values obtained for these coefficients are aligned with the reference one indicated by Michelin for diesel passenger cars, although these values have been found to be slightly underestimated with recent vehicle [247]. Once the reference pressure of 2.1 bar is defined as corresponding to the nominal rolling resistance coefficient $C_{rr,nom}$, a percentage variation of the rolling resistance coefficient can be evaluated through the LaClaire's function (Fig. 2.1a and Eq. 2.2) for any change in the tire pressure. Therefore, the corresponding variation in fuel consumption is evaluated as:

$$\Delta fc(p_{inf})_{(U,EU)} \left[\frac{l}{100 \text{ km}} \right] = \alpha_{R,(U,EU)} M_{ref} \Delta C_{rr}(p_{inf}) \quad \text{Eq. 2.26}$$

2. The variation of fuel economy performance due to a change in vehicle mass M at the reference tire inflation pressure, evaluated through the estimation of a sensitivity coefficient α_M obtained, as for the previous case, both for urban and extra-urban driving conditions, as a linear interpolation of the average fuel consumption as a function of the vehicle mass on the reference cycles (Fig. 2.14b):

$$\Delta fc(M)_{(U,EU)} \left[\frac{l}{100 \text{ km}} \right] = \alpha_{M,(U,EU)} (M - M_{ref}) C_{rr,nom} \quad \text{Eq. 2.27}$$

3. The variation of fuel economy performance as a function of rolling time during tire warm-up at the reference inflation and loading condition. A

warm-up time of 30 minutes is assumed and, as a first approximation, it is considered independent of the vehicle mission [83]. Therefore, referring to the graphic relation reproduced in Fig. 2.12a, it is possible to evaluate the variation of tire rolling resistance $\Delta C_{rr}(t_{roll})$ at a certain time instant t_{roll} after a cold start through Eqs. 2.18-2.19. Applying the sensitivity coefficients $\alpha_{R,U}$ and $\alpha_{R,EU}$ (cf. Fig. 2.14a) it is then possible to obtain the corresponding instantaneous worsening in fuel consumption with respect to the nominal one, during the rolling time (red dashed curve in Fig. 2.14c):

$$\Delta fc(t_{roll})_{(U,EU)} \left[\frac{l}{100 \text{ km}} \right] = \alpha_{R,(U,EU)} M_{ref} \Delta C_{rr}(t_{roll}) \quad \text{Eq. 2.28}$$

The worsening $\Delta fc_{trip,CS}$ due to cold-start of the tires along the trip duration is then calculated as the temporal average over the whole trip, between the initial instant t_0 and the instant t_{eot} corresponding to the end of the trip (blue solid curve in Fig. 2.14c):

$$\Delta fc_{trip,CS} \left[\frac{l}{100 \text{ km}} \right] = \frac{1}{t_{eot} - t_0} \int_{t_0}^{t_{eot}} \Delta fc(t_{roll}) dt \quad \text{Eq. 2.29}$$

As Δfc in Eqs. 2.26-2.28 is linearly dependent on ΔC_{rr} and ΔM and as the abovementioned effects, at least as a first approximation, are independent one of the other, the effects are combined by applying the superposition principle. In particular, the minor dependence of C_{rr} on the vertical load on the tire is neglected. Therefore, the final average fuel consumption along a trip in a generic loading condition M , with tires inflated at a certain pressure p_{inf} , where the vehicle is started with cold tires and whose time duration is $(t_{eot} - t_0)$, is calculated summing the worsening terms of Eq. 2.26, Eq. 2.27 and Eq. 2.29 to the average fuel consumption in reference conditions:

$$\begin{aligned} fc_{trip} \left[\frac{l}{100 \text{ km}} \right] = & fc_{ref} + \alpha_{R,(U,EU)} M_{ref} \Delta C_{rr}(p_{inf}) + \\ & + \alpha_{M,(U,EU)} (M - M_{ref}) C_{rr,nom} + \frac{1}{t_{eot} - t_0} \int_{t_0}^{t_{eot}} \Delta fc(t_{roll}) dt \end{aligned} \quad \text{Eq. 2.30}$$

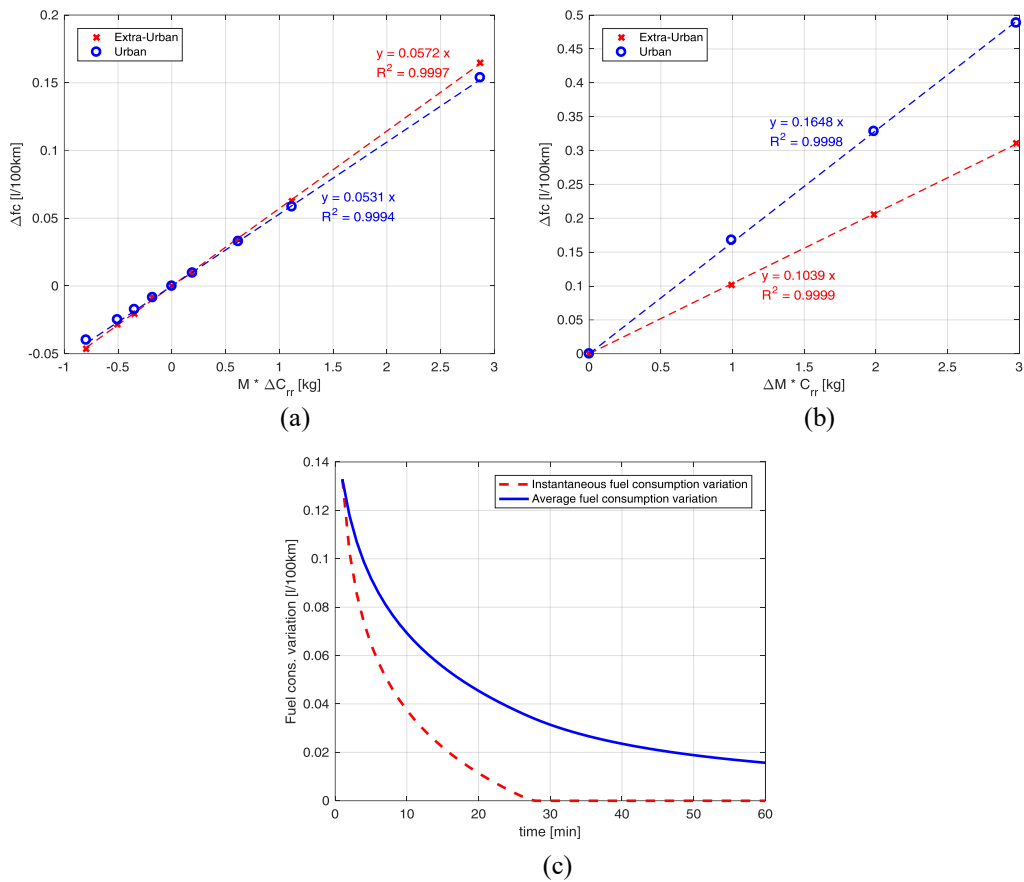


Figure 2.14: Fuel consumption variations on the reference passenger car: sensitivity to rolling resistance variations (a), sensitivity to mass variations (b) and instantaneous variation in fuel consumption during a warm-up and average worsening along the trip (c).

where the last term, related to tire cold-start cases, is not considered for trips that start with warm tires.

In order to refer the calculation to the annual mission of a mid-size vehicle, the following data are considered:

- 4.4 trips per day, i.e. the average daily trips in Florence, Italy [248, 249];
- distributions of the percentage of trips f_T as a function of the travelled distance x_d and of the trip duration x_t , being x_d and x_t divided into classes k_d and k_t (Fig. 2.15a-b), respectively, obtained from the elaboration of the cumulative number of trips acquired in Florence [248, 249].

The two distributions of the percentage of trips f_T as a function of the travelled distance x_d and of the trip duration x_t are multiplied between them in order to obtain a 3D distribution in which each element represents the percentage of trips per year

whose travelled distance is within the class k_d and whose duration is within the class k_t (cfr. Fig. 2.15c). In order to obtain the number of trips for each class combination (k_t, k_d) , the obtained matrix is then multiplied by the total number of trips per year, i.e. 4.4 trips per day for 365 days. The result is shown in Fig. 2.15d. By summing all the contributions of each time class k_t for a single distance class k_d , and multiplying the number of trips per each class of distance k_d by the corresponding trip distance $x_{k,d}$, a distribution of kilometers per distance class is obtained. Finally, the contribution of all the distance classes, can be summed to get the total number of travelled kilometers. According to the abovementioned input data and procedure, a yearly mileage of approximately 14'900 km/year is obtained, which is close to the average travelled distance per year per vehicle in Europe according to ACEA [250], i.e. 13'000 km/year.

In order to take into account the effects of urban and extra-urban driving conditions on total annual fuel consumption, 55% of the annual mileage obtained from above calculations is supposed to be travelled in urban mode, and the remaining part is considered as extra-urban mileage [86]. The trips distribution of Fig. 2.15b is therefore rescaled according to the abovementioned driving mode percentages.

Moreover, a distribution of loading conditions M_{kl} is supposed, which considers that a fraction $f_{T,kl} = 50\%$ of the trips are travelled in the reference loading condition (driver only), $f_{T,kl} = 25\%$ of the trips in full-load weight condition, and the remaining trips are travelled in an intermediate loading condition evaluated as the average between the full-load weight and the driver-only case. Such a distribution is applied to each of the classes defined in the previous distributions (cf. Fig. 2.15a and Fig. 2.15b).

In case of trips with tire hot-start, for each of the three considered classes M_{kl} of mass, Eq. 2.30 is applied (neglecting the warm-up term) to calculate average fuel consumption (in l/100km). Absolute fuel consumption (in liters) is then calculated, multiplying the corresponding average fuel consumption by the yearly travelled distance in urban and extra-urban modes and for each class M_{kl} . The contributions of the various masses and of the urban and extra-urban modes are then summed to provide the total annual fuel consumption. In formula:

$$fc_{year}[l] = \sum_{(U,EU)} \sum_{\forall k_l} \left\{ f_{T,kl} \cdot d_{(U,EU)} \cdot \frac{1}{100} [fc_{ref} + \Delta fc(p_{inf}) + \alpha_{M,(U,EU)} (M_{kl} - M_{ref}) C_{rr,nom}] \right\}$$

Eq. 2.31

being $d_{(U,EU)}$ the total yearly travelled distance in km in urban and extra-urban mode, respectively.

In case of tire cold-starts, Eq. 2.30 is applied, including the warm-up term, to each single class combination (k_t, k_d) of the distributions represented in Fig. 2.15a and Fig. 2.15b. The duration $(t_{eot} - t_0)$ of the trip in Eq. 2.30 corresponds to the value x_{kt} representative of the corresponding class k_t . The obtained result is then multiplied by the travelled distance per trip x_{kd} representative of the class k_d to obtain a fuel consumption value $fc_{(x_{kt}, x_{kd})}$ [l] representative of each trip referred to the combination (k_t, k_d) . The total yearly fuel consumption is then obtained multiplying these values times the number of trips related to the corresponding combination $n_{T,(x_{kt}, x_{kd})}$ and summing all these contributions. This calculation is repeated for each loading condition M_{kl} and the contributions are then summed:

$$fc_{trip,(x_{kt}, x_{kd}, M_{kl})} \left[\frac{1}{100km} \right] = fc_{ref} + \alpha_{R,(U,EU)} M_{ref} \Delta C_{rr}(p_{inf}) + \alpha_{M,(U,EU)} (M_{kl} - M_{ref}) C_{rr,nom} + \frac{1}{(t_{eot} - t_0)_{kt}} \int_{t_0}^{t_{eot,kt}} \Delta fc(t_{roll}) dt$$

Eq. 2.32

$$fc_{year} [l] = \sum_{\forall(k_t, k_d)} \sum_{\forall k_l} \left[f_{T,kl} \cdot n_{T,(x_{kt}, x_{kd})} \cdot \frac{1}{100} \cdot x_{kd} \cdot fc_{trip,(x_{kt}, x_{kd}, M_{kl})} \right]$$

Eq. 2.33

2.4.1 Scenarios and pressure management strategies

The methodology described above has been applied considering different combinations of the effect of tire cold-starts and trips with variable loading condition. The following scenarios, relative to the vehicle utilization, have therefore been analysed:

- *scenario 0*: the annual fuel consumption is evaluated considering the annual mileage in urban and extra-urban modes. All the trips start with warm tires and at the reference loading condition (driver only).
- *scenario 1*, stemming from *scenario 0*, considers the worsening in fuel consumption (Fig. 2.14c), assuming that all the trips in a year are started with cold-tires. This is meant to represent a realistic daily usage of the passenger car, where the car is mainly used for commuting (tires cool-down to ambient temperature between one trip and the following one).

- *scenario 2*, based on *scenario 0* and *1*, considers that 80% of the trips start with cold tires, while the remaining ones are started with tires already at the rated temperature to take into account short stops.
- *scenario 3*, stemming from *scenario 0*, considers half of the trips in the reference condition of mass (driver only) and the remaining trips equally distributed on loading conditions with intermediate vehicle mass and with the full-load weight.
- *scenario 4* considers the effect of variable loading conditions with 100% of the trips starting with cold tires. It is the superposition of the effects considered in *scenario 1* and *scenario 3*:

$$f_{c_{sc4}} \left[\frac{l}{100 \text{ km}} \right] = f_{c_{ref}} + \Delta f_{c_{sc1}} + \Delta f_{c_{sc3}} \quad \text{Eq. 2.34}$$

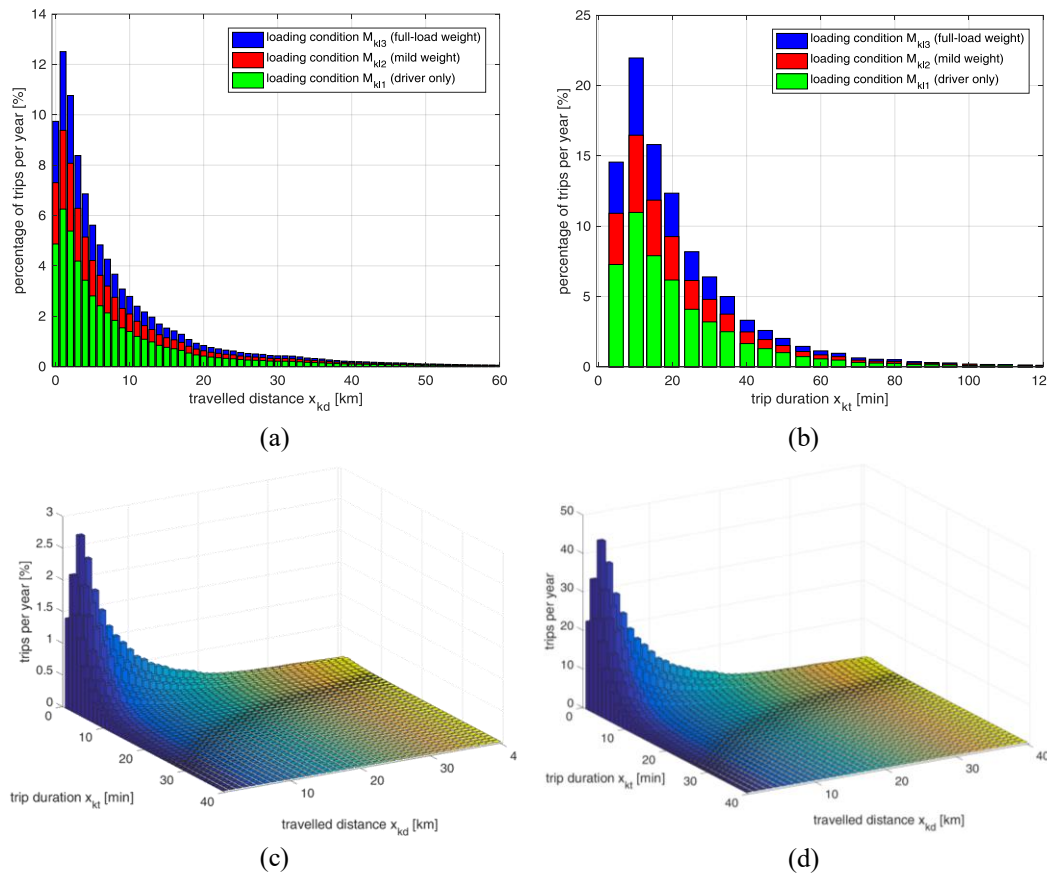


Figure 2.15: Distributions of the percentage of trips per year for passenger cars as a function of the travelled distance per trip (a) and of the duration of each trip (b); percentage of trips (c) and number of trips (d) for each class of trip duration and travelled distance.

- *scenario 5* considers the effect of variable loading conditions with a percentage of the trips starting with cold tires, indicated by the symbol %CS, being %CS equal to 80%. Therefore, %CS of fuel consumption calculated in *scenario 4* (variable mass, 100% cold start) is summed to (1-%CS) of the contribution of *scenario 3* (variable mass, 100% hot start):

$$fc_{sc5} \left[\frac{1}{100 \text{ km}} \right] = \%CS \cdot fc_{sc4} + (1 - \%CS) \cdot fc_{sc3} \quad \text{Eq. 2.35}$$

For each of these scenarios, different pressure management situations have been considered:

- *reference*: tires are always inflated at the nominal pressure indicated by the vehicle manufacturer for the driver-only case. Therefore, this case is representative of a driver which properly maintains the tires, or to the usage of an on-board system able to keep always a reference pressure (but not able to adapt the pressure to the vehicle working conditions). The reference tire pressure considered is 2.1 bar.
- *misuse 75%*: tires are always inflated at 75% of the reference pressure. This corresponds to improper tire maintenance where the tire pressure is, in average along the year, 25% lower than the nominal one. Considering a natural decrease of tire pressure of 0.1 bar per month, this misuse condition corresponds to checking tire pressure two times per year.
- *misuse 85%*: tires are always inflated at 85% of the reference pressure. This corresponds to a case of improper tire maintenance, but less critical than the one described above, e.g. with a lower natural deflation rate or checking the tires more often.
- *strategy 1*: it is considered that an automatic system is installed on-board [251]. Pressure is adapted to load variations in order to maintain always the same static tire radius. Moreover, an initial small over-inflation is realized for the trips which are started with cold tires, and then some air is gradually released as the tire temperature increases, according to an isobaric transformation.
- *strategy 2*: based on *strategy 1*, considers the additional pressure management strategy which slightly increases tire pressure in extra-urban conditions.

2.4.2 Single vehicle analysis: results and discussion

With reference to Fig. 2.16, the results of this analysis concerning a single vehicle are reported in terms of relative variations in fuel consumption and increase of annual CO₂ emissions. More in detail, Fig. 2.16a shows a comparison among the *reference* cases calculated for the various *scenarios*, i.e. highlights the effect of considering different loading conditions as well as of tire cold-starts keeping always the nominal tire inflation pressure. Loading conditions different from the reference one (curb weight + driver) contribute to increase real-world fuel consumption with respect to type-approval procedures. Additionally, Fig. 2.16b reports, for each *scenario*, the variations obtained due to improper or advanced tire pressure management with respect to the *reference* case.

As previously stated, *scenario 0* represents the condition with tires always at the rated temperature and vehicle at the reference loading condition. Since all the trips are at reference load and temperature, *strategy 1* has no effect and *strategy 2* has a minor improvement (-0.3%) due to the variation of pressure only on extra-urban driving conditions.

Comparing the *reference* case in *scenario 0* with those in *scenario 1* and 2, the consequence of introducing in the calculation the effect of tire cold-starts is highlighted (Fig. 2.16a). This corresponds to an increase of about 1% in fuel consumption, 8.4-6.7 litres of fuel and 22.3-17.8 kg of CO₂ per year per vehicle, considering 100% and 80% of the trips starting with cold-tires, respectively. Referring to *scenario 2* (80% cold-start), *misuse 75%* and *misuse 85%* increase fuel consumption by 1.43%-0.79% (up to 28.5 kg of CO₂), respectively, if compared to *reference* case of the same scenario (Fig. 2.16b). On the other hand, still referring to *scenario 2*, the proposed strategies reduce fuel consumption up to 0.8% with respect to *reference*, allowing to save up to 16.3 kg of CO₂ emissions.

The *reference* case of *scenario 3* shows that real-world operating loading conditions, not considered by current type-approval procedures, account for an increase of 3% of fuel consumption (59 kg of CO₂, cf. Fig. 2.16a). The *misuse 75%* case determines a worsening in fuel consumption of about 1.4%, as for the previous scenarios. On the other hand, pressure management strategies allow improving fuel economy up to 0.9% with respect to the *reference* case.

Scenario 4 and 5 show a linear combination of the cold-start and of the operating mass effects. Referring to *scenario 5*, the two considered effects account for an increase up to 3.9% of real-world fuel consumption (77 kg of CO₂, cf. Fig. 2.16a) – with respect to *scenario 0* – if the nominal pressure is maintained in all the trips (*reference* case). Misuse further increases fuel consumption by 1.4% and up to 28 kg of CO₂ per year (*misuse 75%* with respect to *reference* case of *scenario 5*,

cf. Fig. 2.16b). Proposed pressure management strategies can reduce fuel consumption of about 1-1.4% (*strategy 1* and *strategy 2*, respectively) if compared to the *reference* in *scenario 5*, with a reduction of 20-29 kg of CO₂ per year (Fig. 2.16b). Still with reference to *scenario 5*, considering *misuse 75%* as representative of the average current driving condition in Europe and *strategy 2* as the best case obtainable through an active tire management, the maximum potentiality of the studied technology on the reference car is about 2.8% on the reduction in fuel consumption and 58 kg of CO₂.

2.4.3 Impact assessment on European scale

Moving from the results obtained for a single vehicle, for each of the considered scenarios and strategies, the total effect on CO₂ emissions in Europe and the related Social Cost of Carbon (SCC) [252] have been calculated, considering 256 million vehicles that correspond to all the European fleet of passenger cars [250]. Results are based on the hypothesis that all the European circulating fleet has the same fuel economy figures as the reference vehicle, which is mid-size 2010 passenger car. Anyway, the circulating fleet is more heterogeneous and with an average vehicle age of 10 years [250], which determines an underestimation of the global effects.

The SCC metric is a valuable way to quantify, in current monetary value, the long-term effect of CO₂ emissions. Since SCC is strongly sensitive to the discount

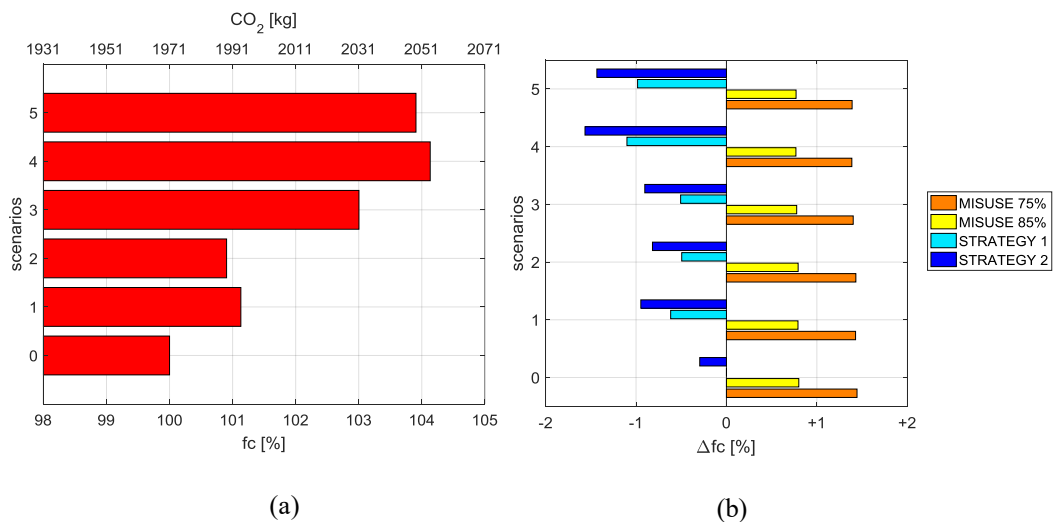


Figure 2.16: CO₂ emissions and percentage variation of fuel consumption on the reference passenger car comparing the *reference* cases of the various considered *scenarios* (a); percentage variation of fuel consumption on misuse cases and pressure management strategies with respect to the *reference* case on each of the considered *scenarios* (b).

rate, i.e. to the present value of future damages, and due to the uncertainties associated to this kind of estimation, instead of using a single figure, three different discount rates are used to provide a possible variation range of the costs/benefits value. Therefore three different integrated assessment models are applied (5%, 3% and 2.5% discount rates). For each of the models, the US EPA indicates as reference carbon price the average of the three frequency distributions, which corresponds to assume an average damage scenario. Moreover, considering that greenhouse gases emissions may produce negative effects higher than the potential damage that can be quantified nowadays, the 95th percentile of the distribution obtained at 3% discount rate is also considered. Although these models do not include all the damages produced by carbon emissions, they are effective in case of cost-benefits analysis or in case of a comparison among different technologies devoted to the reduction of greenhouse gases emissions. The SCC figures have been estimated in 2007 US dollars and reported in euros according to the current rate of change, equal to 1.1988 \$/€ (September 2017).

If *scenario 5* is taken into account, therefore considering the effect of tire pressure management under the hypothesis that 80% of the trips start with cold tires and in various loading conditions, common underinflation (*misuse 75%* and *misuse 85%* compared to *reference*) causes the waste of 10 to 17 million barrels of fuel (1'500'000 to 2'700'000 m³) and the emission of 4'040'000 to 7'290'000 metric tons of CO₂ every year in Europe. Considering that the transportation sector corresponds to 6.86 GtCO₂eq/year, i.e. 14% of the total anthropogenic greenhouse gases emissions [253], tire underinflation on passenger cars accounts, therefore, for 0.06% to 0.1% of the total. According to the estimations of the social cost of carbon provided by US EPA [252], the economic value of this yearly increase in CO₂ emissions will be 73 to 377 million € in 2020 (*misuse 75%*), depending on the average discount rate considered for the integrated assessment models used for the SCC analysis (5 to 2.5%), and up to 748 million € considering 95th percentile SCC estimate according to a 3% discount rate. Since the SCC increases over time to take into account of the increased incremental damage, if no action is taken to reduce tire underinflation – and supposing that the possible increase in the number of circulating vehicles in the coming decades will be compensated by fuel economy improvements – the same amount of emissions in 2050 would cost 158 to 578 million € (5 to 2.5% discount rate), up to 1'289 million € (3% discount rate, 95th percentile). On the other hand if the application of an active tire pressure control system is taken into account (*strategy 2* compared to *reference, scenario 5*), it would be possible to save 17.8 million barrels of fuel (2'836'000 m³) and 7'500'000 metric tons of CO₂ per year, that corresponds to a reduction of SCC up to 771 million € in 2020 and 1'329 million € in 2050 (3% discount rate, 95th percentile).

Moreover, referring to the in-use vehicle economy and considering an average cost of diesel on 1.154 €/l in Europe [254], the increase in fuel consumption due to underinflation costs in total up to 3.2 billion €/year (*misuse 75%* with respect to *reference, scenario 5*) to European drivers, while the reduction which could be obtained through advanced pressure management strategies would allow to save 3.3 billion €/year, with respect to *reference* case. Overall, advanced pressure management would allow to save 6.5 billion €/year with respect to a typical misuse case.

A further economic advantage could be obtained from the consequent increment in tire life. Tire durability reduction can be calculated by linearizing some figures provided by TUV [255], which show a reduction of 10%, 25% and 45% of tire life for a tire inflation pressure respectively 0.2, 0.4 and 0.6 bar lower than the reference. Therefore *misuse 75%* and *misuse 85%* correspond to 37.5% and 18.6% tire life reduction, respectively. Considering a nominal tire life of 50'000 km (warranted mileage on the North-American market by Michelin [256]), an annual mileage of 14'900 km and an average tire cost on the market of about 80 €, it is possible to estimate an increase of costs between 22 € and 57 € per year per vehicle, i.e. 5.6 to 14.7 billion €/year for the whole European fleet.

Additionally, 3.3% of all the crashes related to tire are due to improper inflation, which are responsible for 35 fatalities, 370 severe injuries and 3654 slight injuries per year in Europe [257]. Assuming that an active central tire inflation system may potentially avoid all the crashes due to improper tire inflation, this kind of system may generate a further economic benefit of 207.6 million €. For these quantification, the cost of personal damage, property damage and congestion caused by road crashes have been considered by updating the values reported in [257], referred to 2005, by taking into account the current value of money with respect to 2005.

2.5 Potential effect of tire pressure management on fuel economy of commercial vehicles: simulations

Commercial vehicles are responsible for about 6% of the total anthropogenic CO₂ emissions [258], i.e., about 2.3 GtCO₂eq/year, taking into account that the total CO₂ emissions were about 38 GtCO₂eq/year in 2010 [259].

Despite the fact that commercial vehicles have a significant impact on greenhouse gas emissions, no regulations have been adopted to limit the fuel consumption of heavy-duty vehicles. In fact, as these vehicles are used for business purposes, and since fuel represents almost 30% of the total operational costs of a commercial vehicle, fuel economy improvements in this field are mostly market-driven [258]. Nevertheless, although a reduction of two-thirds in fuel consumption has been obtained on heavy-duty trucks in the past 40-50 years, no significant variations have been registered over the last 13 years [189, 258]. This could partially be related to the introduction of regulations to limit pollutant emissions, such as NO_x and PM, and the subsequent adoption of technologies that generally worsen fuel economy [258]. This is the case, for example, of the installation of diesel particulate filters [260], of the usage of high exhaust gas recirculation rates to reduce the formation of NO_x [111], and of the adoption of non-conventional diesel combustion modes, such as premixed-charge compression ignition (c.f., *Chapter 1*). For these reasons, the US has recently adopted a fuel efficiency standard in two phases, with the first phase, which was introduced in 2014, aimed at reducing fuel consumption by 7-20% by 2017, with respect to 2010, and by 15-27% by 2027, with respect to 2017 [261]. Although some measures are being implemented in Europe, no regulation exists to limit carbon emissions from heavy trucks [262]. This surely does not foster innovative solutions on fuel economy reductions, especially when considering that the total CO₂ emissions due to heavy-duty vehicles have increased by more than 30% in the last 25 years, due to the increase in road freight traffic [262]. Nevertheless, the European Commission has been funding research projects with the aim of improving truck fuel economy by up to 30% by combining the already existing technologies under a smart on-board energy-management [263].

On the other hand, the fuel economy of light-duty commercial vehicles (i.e., vans) is regulated in both Europe and in the US together with passenger cars [53, 264].

Moving from this scenario and from the studies on passenger cars previously presented, the evaluation of the effects of tire inflation pressure management on vehicle energy demand and fuel economy has also been extended to commercial vehicles. This paragraph focuses on setting-up a methodology to evaluate the

effects of tire pressure management on the fuel economy of a heavy-duty truck and a light-duty truck. This section of the work is part of a joint research project, involving the Politecnico di Torino and Iveco, on the analysis of the potentialities of an advanced CTIS (ACTIS). The project work is devoted to the development of a completely autonomous tire pressure management system that would be able to recognize the current vehicle and road working conditions and to set an optimal tire inflation pressure as the result of a multi-objective optimization that would involve the truck performance on fuel consumption, braking distance and lateral vehicle dynamics response. Therefore, the device is intended as part of the on-board energy management strategies, as well as an active safety technology. Additionally, as for the case study on passenger cars, some pressure management strategies have been proposed in order to adapt the tire pressure to the vehicle loading conditions and during tire warm-up.

In the previous *Section*, the proprietary software used in FCA and Iveco for fuel economy simulations was applied. Nevertheless, the limits of this tool were highlighted in cases where it is needed to account for various tire inflation pressure conditions different from the reference one, and possibly tire pressure that vary along a mission profile. To overcome these issues, in a first stage of the project described in *Section 2.3*, coast-down parameters were manually calculated for different tire inflation pressures and then provided to the software as different datasets. In case of pressure variations along the cycle, as in the case of simulations that considered rolling resistance to vary along time because of tire warm-up at fixed tire pressure and with tire pressure varying in time, a complex pre-processing and post-processing procedure had to be adopted in order to obtain the desired result (c.f. *Section 2.3.3*).

In this section, aiming at extending the previous study to a larger set of vehicles, a dedicated software has been set up, which is able to perform fuel consumption simulations by directly taking into account the tire pressure, and pressure management strategies. Tire wear is also evaluated, in order to both account for the effect of pressure management on the tire life, and to consider variations in the rolling resistance with tire wear. The effects of tire pressure variations on the various axles and of the implementation of the specific strategies have been assessed on some reference driving cycles that are representative of urban, extra-urban and highway driving. Finally, these results have been combined in order to evaluate the impact of the advanced CTIS on an annual basis as a preliminary step for a cost-benefit analysis.

As in the previous sections (cf. *Section 2.1*), the LaClaire's relation [81, 83] was used to calculate the variation in the rolling resistant coefficient with tire pressure with respect to the reference value $C_{rr, std}$, provided by the tire

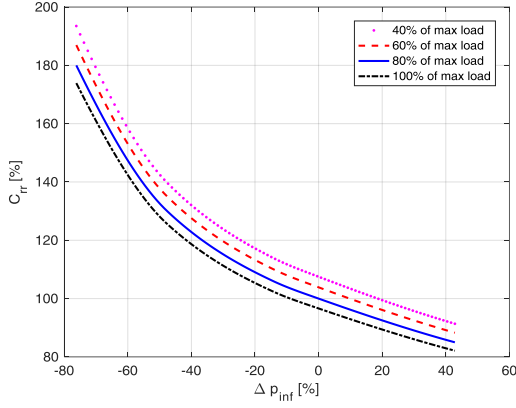


Figure 2.17: Percentage of the rolling resistance variation with the tire pressure and vertical load.

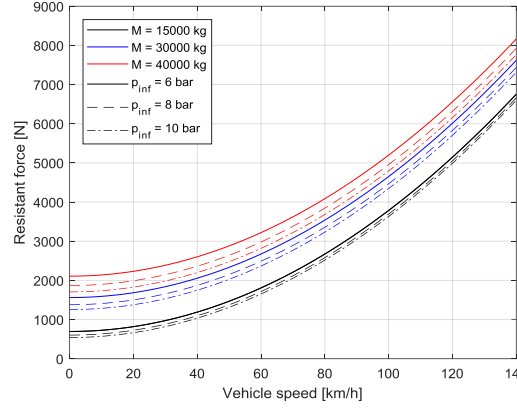


Figure 2.18: Coast-down curves of the reference heavy-duty vehicle, calculated for various vehicle loading conditions and tire inflation pressures.

manufacturers in compliance with [227]. Moreover, in the present *Section* of the work, the dependence of the rolling resistance coefficient on the vertical load F_z was also considered, according to what is reported in [83]. The contribution of each i -th tire was then calculated taking into account its inflation pressure and vertical force, the latter being evaluated according to the vehicle mass and its distribution over the axles:

$$C_{rr,i}(p_{inf}, F_z) = (\alpha \cdot \Delta p_{inf,i}^\beta) \cdot (a \Delta F_{z,i} + b) \cdot C_{rr,i,std} \quad \text{Eq. 2.36}$$

where the terms reported in parenthesis express a percentage variation of the standard $C_{rr,std}$, being the standard $C_{rr,std}$ related to the reference pressure and mass used for the experimental coast-down. Figure 2.17 reports the percentage variation of the rolling resistance as a function of the pressure and vertical load, according to Eq. 2.36. The B_0 , B_1 and B_2 coefficients were evaluated for each inflation pressure by means of a second-order regression of the curves obtained by translating the curve of $C_{rr}(v)$ vertically, according to Eq. 2.36. Finally, the F_0 , F_1 and F_2 coefficients can be evaluated for any tire inflation pressure and loading conditions as:

$$F_{0,1,2}(p_{inf}, F_z) = (F_{0,1,2,std} - m_{std}gB_{0,1,2,std}) + \sum_i F_{z,i}B_{0,1,2}(p_{inf,i}) \quad \text{Eq. 2.37}$$

With Respect to Eq. 2.14, where all the tires were considered to be inflated at the same pressure and loaded with the same vertical load, in Eq. 2.37 the total resistance force is computed taking into account possible different inflation pressures and vertical loads on each tire. Figure 2.18 reports the coast-down curves obtained for the tested cases on the reference heavy-duty truck used for this study.

2.5.1 TyPE: a new software tool

The described methodology has been used to develop a new software tool, specifically developed to take into account the effect of tire pressure and other causes that can determine a variation of the rolling resistance. The software, developed at the Politecnico di Torino and named TyPE (acronym for Tyre Pressure Effect), is based on the abovementioned kinematic approach for fuel consumption estimations (cf. *Section 2.3*). The fuel economy simulation procedure has been simplified with respect to PerFECTS, since the actual speed profile is considered equal to the reference one and is not recalculated through a dynamic driver model.

On the other hand, unlike all the known software programs used for fuel economy estimations, TyPE allows the following effects that influence tire rolling resistance to be taken into account:

- the effect of a tire pressure variation, with respect to the reference value used to identify the reference rolling resistant coefficient $C_{rr, std}$;
- the effect of the vertical load acting on each tire;
- the effect of tire wear on rolling resistance, according to [265];
- the effect of rolling time on rolling resistance, in the case of a tire cold-start, according to [83].

The software uses a 5-dimension matrix as a reference and interpolates, within this matrix, each time instant of the tested mission cycle, for each single i -th tire, to obtain a percentage variation of the rolling resistance with pressure, load, wear and time. This percentage is then multiplied by $C_{rr, std}(v)$ (cf. Eq. 2.4) in order to obtain the actual rolling resistance under the considered conditions:

$$C_{rr,i}(t) = \Delta C_{rr,i}(p_{inf,i}(t), F_{z,i}, w_i(t, F_{z,i}, p_{inf,i}), t) \cdot (B_{0, std} + B_{1, std}v(t) + B_{2, std}v(t)^2) \quad \text{Eq. 2.38}$$

where:

- the vehicle speed is a mission profile as a function of time t ;
- tire inflation pressure is considered to possibly vary along the cycle;

- tire wear starts from a reference value that is imposed by the software user (by default, $w = 0$ to consider new tires), increases in time due to usage and also depends on the tire inflation pressure and vertical load;
- rolling time t is taken into account in the case of a tire cold start.

The result of Eq. 2.38 is used to calculate the resistance force at each instant of the simulated cycle, and the abovementioned procedure is then applied to estimate fuel consumption through the evaluation of instantaneous engine speed and load (Eqs. 2.5-2.9) and the subsequent interpolation in fuel consumption maps.

Since the dependence of the rolling resistance on tire pressure is included in Eq. 2.38, tire pressure can be used as an “external” variable for the fuel economy estimation. In other words, knowing the coast-down coefficients $F_{0,std}$, $F_{1,std}$ and $F_{2,std}$ and the rolling resistant coefficients $B_{0,std}$, $B_{1,std}$ and $B_{2,std}$ in a reference condition, the tire pressure can be set as a variable parameter in the simulation. Furthermore, since the software executes the calculation in Eq. 2.38 at each instant of the cycle, the tire pressure can be considered variable in time. This allows strategies in which the tire pressure is changed in time to be tested. Moreover, it also makes it possible to test real-time variations of the tire pressure by taking into account the dynamics of the pneumatic system: since the pressure variations induced by a CTIS cannot be instantaneous, it is possible to consider how the pressure actually varies in time, for each tire, according to the sizing and working logic of the real system under test. In this way, it is possible to evaluate the effects of the system design choices on the fuel economy benefits provided by the system, in order to individuate an adequate compromise in the trade-off between system size (and weight) and its performance (cf. *Section 2.8*).

The vertical load F_z is intended as a static vertical force caused by the vehicle weight and is therefore not considered as a function of time, i.e., load transfers due to fast maneuvers are neglected.

In order to evaluate the tire wear in time, the total expected tire mileage, which corresponds to the tire life if the tire is always used at the rated vertical load and pressure, is given as input to the software. Under this hypothesis, it is considered that each travelled distance unit subtracts a percentage of the useful tire life. If the tire load and pressure are not at the rated levels, the current load and pressure conditions are compared with those in the reference pressure-load tables provided by the tire manufacturer: the cases reported in the table can be considered as iso-deflection curves, i.e. curves that report the variation in the tire pressure with the vertical load so that the vertical tire deflection is always the same (and the contact patch is also roughly the same). The reference iso-deflection condition is considered the one that provides the minimum tire wear for each loading condition. Therefore, if the current vertical force is different from the rated one, a corresponding reference tire pressure is evaluated from the pressure-load table. Whenever the current tire pressure is different from the reference pressure obtained from the iso-deflection curve, the tire wear per unit distance is increased according to the graphic relation provided by Michelin [266] in terms tire life variation with pressure, and reproduced as a reference in Figure 2.19.

In the case of a tire cold-start, as already mentioned in the previous *Sections*, the rolling resistance starts from a higher value than the reference one and decreases gradually over the warm-up period, T_{CS} , till reaching the reference (standard) value when $t \geq T_{CS}$ [83]. As no data were found in the technical literature on the variation of rolling resistance during the tire warm-up for vans and trucks, the same curve as that of passenger cars (Eq. 2.20 and Fig. 2.12a in *Section 2.3.3*) was parametrically adopted for commercial vehicles: the software user can select the total duration of the warm-up time, T_{CS} , which is set by default to 30 minutes for passenger cars [83,

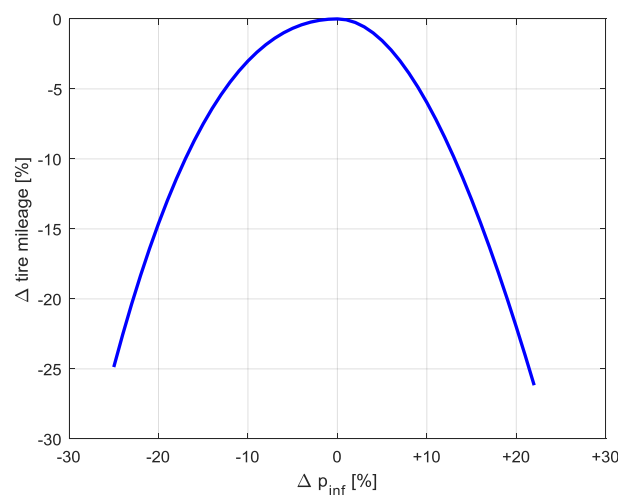


Figure 2.19: Percentage of the variation of the reference tire mileage with pressure.

267], 60 min for light-duty vans and 90 min for heavy-trucks [83]. Whatever the duration of the warm-up, the rolling resistance at the first instant of the cycle is set to an increment of about 35% of the nominal value under steady-state thermal conditions (cf. Fig. 2.20).

The effect of ambient temperature on rolling resistance [268] has not been taken into account in this study, and neither have some other ambient-related variables. In fact, the aim of the work has been to assess the variations in fuel economy due to tire pressure with respect to a reference case, i.e., the case in which the nominal pressure at rated load is selected and maintained. As a first approximation, although ambient temperature affects the steady-state rolling resistance, its effect can be considered as being independent from the others cited above. Therefore, if two conditions are compared, given a certain ambient and/or asphalt temperature, the relative variations between the two would not change as the external conditions change. A similar approach was also discussed in [267], where the effect of ambient and ground temperature on rolling resistance is considered negligible in the case of a relative comparison of two test vehicles running in parallel (i.e., in the same external temperature conditions).

TYPE: user options

The software realized at the Politecnico di Torino was thought up to work for passenger cars (PC), as well as light-duty vehicles (LDV) and heavy-duty ones (HDV).

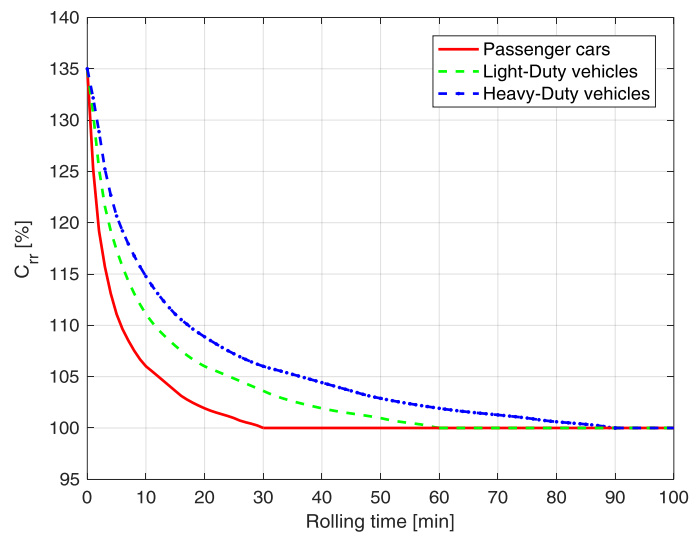


Figure 2.20: Percentage of the variation of rolling resistance during the warm-up period.

With reference to Figure 2.21a, the user is asked to insert vehicle data through the “Vehicle type and characteristics” section. Selecting the “Load vehicle” button, the user is provided with a form (cf. Figure 2.21b) that has to be filled out with all the required vehicle specifications. Among the more relevant data, are:

- the engine characteristics and its fuel consumption map as a function of engine speed and torque;
- the gearbox ratios and efficiencies (or efficiency maps as a function of inlet torque);
- the final drive ratio and efficiency (or efficiency map as a function of inlet torque);
- the number of axles and wheels per axle;
- the reference mass of the vehicle (for PC and LDV) or of the tractor (HDV), and the load distribution in the reference loading case;
- for HDV, the distance between the coupling and the steer axle and between the coupling and the trailer axle (note that in the case of multiple axles on the trailer, a single equivalent axle, placed in the middle of the real axles, is considered);
- for HDV, the reference mass of the trailer and its load distribution in the reference loading condition;
- the frontal area and the longitudinal drag coefficient;
- the experimental standard coast-down coefficients, including the loading case and the tire pressure combination at which they have been obtained;
- tire data: iso-deflection reference curve (i.e., pressure-load table), rolling resistance, rolling circumference, wheel inertia, maximum vertical force, expected total mileage, initial tread wear and cost of each axle type (steer, drive or trailer);
- fuel density and cost.

Additionally, it is possible to load a file in the vehicle configuration section that reports the characterization of the performance of the CTIS, in terms of actuation times, as a function of the initial and final (desired) tire pressure and of the temperature of the air inside the tire (“Actuation file” field in Figure 2.21b).

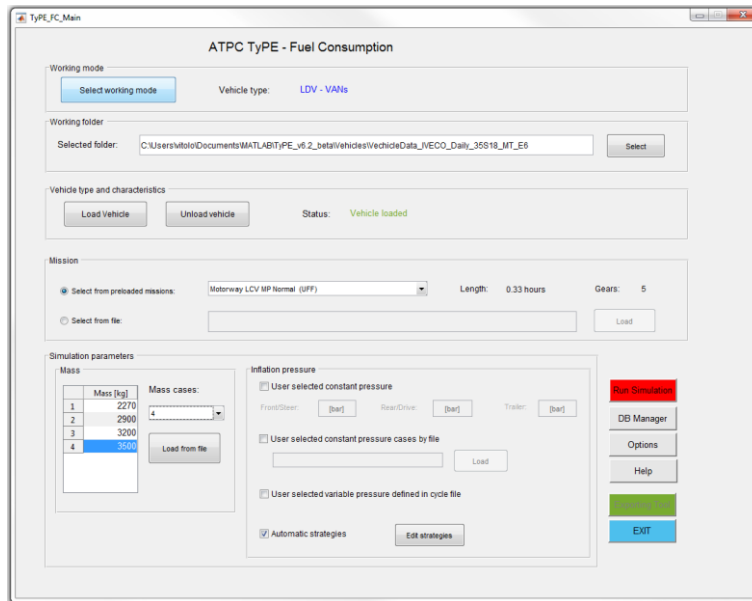
Again with reference to Figure 2.21a, the user can select a mission profile from among those that are already available in the software database, or load a new user-defined mission profile from an Excel file. Mission profiles are defined as vehicle speed, selected gear and road grade as a function of time.

In the “Simulation parameters” section (cf. Figure 2.21a), the user configures the cases that will be simulated by selecting the test mass cases and tire pressure levels. The user can select one or more simulation conditions with tire pressure constant along the driving cycle, or can define a variable pressure as a function of

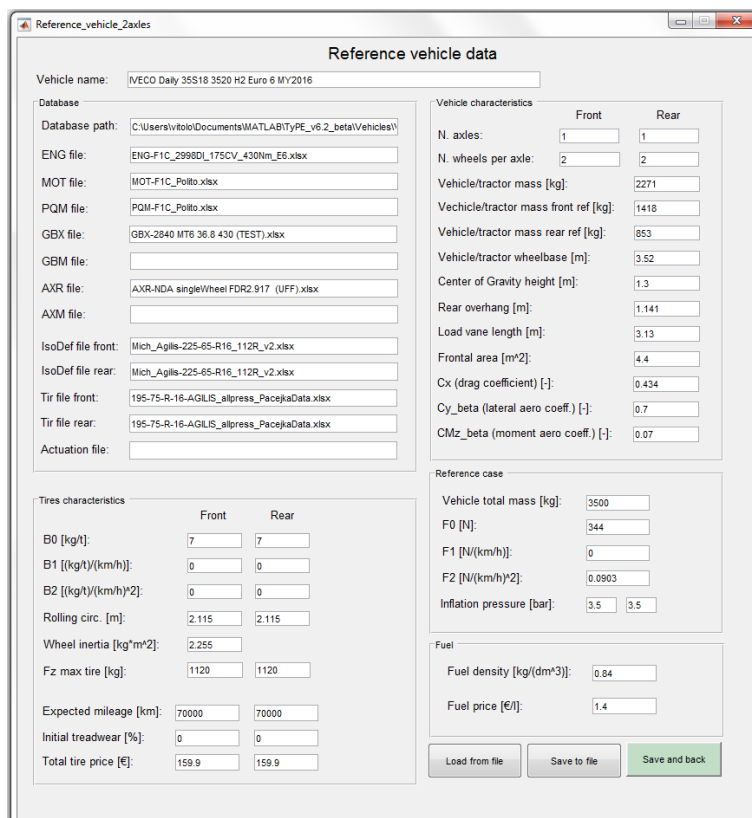
time through an Excel file. Moreover, the software has certain embedded strategies that can be applied (cf. Figure 2.22):

- pressure adaption to the vertical load, according to the pressure-load table (iso-deflection case, pressure constant over a simulated cycle);
- pressure variation during the warm up period: the user can select a number of possible warm-up strategies, specifying for each of them the duration of the warm-up transient, the initial over-inflation to be applied with cold tires (with respect to the reference pressure), and the axles where the strategy is intended to be applied. If this option is selected, two cases are simulated: a case in which a cold-start is applied with the pressure at the nominal level, and a case in which a cold-start is applied and the pressure is varied according to the strategy. If this option is not selected, all the simulations are considered to start with warm tires;
- misuse cases: as vehicles without any automatic pressure control may suffer from underinflated tires, this case is also considered by the software. The user can define one or several levels of under-inflation (pressure constant along a simulated cycle), expressed as a percentage value of the nominal pressure.

Once a number of loading cases and pressure cases have been defined, the software will produce a full-factorial test plan and will calculate – for the specified vehicle and mission profile – all the possible combinations from among the selected simulation parameters.



(a)



(b)

Figure 2.21: TyPE graphic user interface: main page of the software (a) and page for providing to the software the vehicle specifications (b).

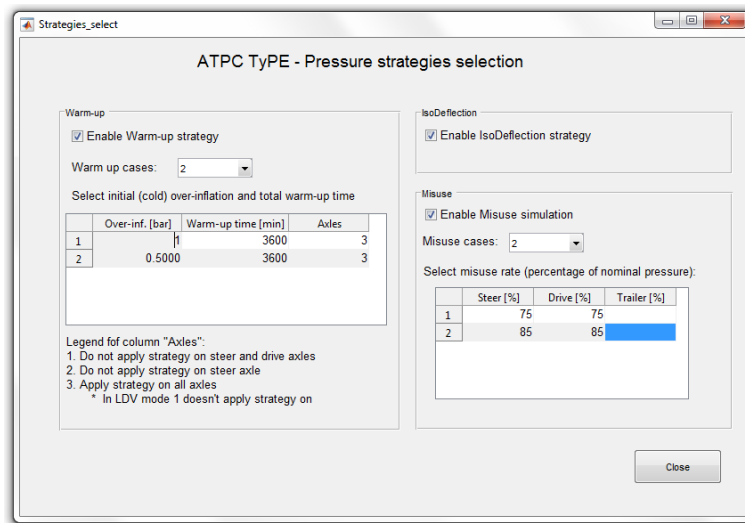


Figure 2.22: TyPE graphic user interface: selection of embedded pressure management strategies.

2.5.2 Results and discussion

Using the software tool described above, a number of computer simulations were performed to analyze the effect of a pressure variation on fuel consumption. An HDV and an LDV, whose main features are reported in Table 2.8 and Table 2.9, have been simulated. The analysis of the HDV was performed considering three ACEA cycles [269] that were defined to simulate urban, extra-urban (regional) and highway (long-haul) driving conditions. Moreover, in the validation tests, two cycles, which had been internally defined by Iveco as representative of two typical highway missions for Italian customers, were considered. The latter are referred to as *Custom HDV highway 1* and *Custom HDV highway 2* in the graphs. Three driving cycles were considered for LDV as being representative of urban, extra urban and highway driving conditions. These cycles were defined internally by Iveco and are referred to as *Custom LDV urban*, *Custom LDV extra-urban* and *Custom LDV highway*. Table 2.10 reports the main characteristics of the cycles: the average and maximum vehicle speed, the average and maximum acceleration, the average and maximum positive (adverse) grade, the percentage of time spent with the absolute acceleration of the vehicle higher than 0.1 m/s^2 (i.e., accounting for both accelerations and decelerations), and the percentage of time spent with the vehicle stopped and with the engine running at idle.

Validation of the simulation tool TyPE

In order to validate the fuel consumption results obtained from the developed TyPE software tool, a number of cases were simulated in parallel in the PerFACTS reference software. PerFACTS was taken as a reference for the comparison as it is the software currently used for fuel economy simulations in Iveco, and it was internally validated by the OEM on experimental data [236-238]. The results of this validation are presented with reference to the tested HDV, studied on two ACEA cycles and on the two *Custom* highway missions. The vehicle was simulated in three tire pressure configurations and in two loading conditions, corresponding to the vehicle curb weight (tractor + trailer) and to the maximum allowed vehicle load (40 t, including the curb weight and the maximum payload).

In order to evaluate the results, it should be taken into account that PerFACTS is based on a dynamic simulation model that considers the driver's action on the pedals, as well as the dynamic response of the engine and of other mechanical subsystems. Furthermore, in the case of a truck, the driver's action on the gearshift is also simulated, considering the typical strategies used by expert drivers.

Table 2.8: Characteristics of the reference light-duty vehicle.

Total vehicle curb weight	2271 kg	
Axles	1 steering, 2 wheels/axle 1 drive, 2 wheels/axle	
Gearbox	6 gears, manual transmission	
	ratio	efficiency
	I 5.38	0.965
	II 3.15	0.965
	III 2.04	0.965
	IV 1.37	0.965
	V 1	0.965
	VI 0.79	0.970
Final drive	ratio	efficiency
	2.92	0.98
$C_x \cdot A$	0.43 · 4.4 m ²	
Engine	3.0 l, diesel	
max power	132 kW @ 3500 rpm	
max torque	430 Nm @ 1500 rpm	
Tires	225/65 R16 112R	
reference $C_{rr, std}$	7.0 kg/ton	
maximum vertical load	1120 kg	
reference inflation pressure	3.5 bar	

Therefore, the actual speed and gear profiles were different for the same route or mission, according to the vehicle conditions. As a reference, Figure 2.23 reports a section of the *Custom HDV highway 1* cycle realized for two different pressure combinations at full-load vehicle weight (40 t), and for the reference pressure combination in the curb weight case (15 t). It can be observed that, although a change in inflation pressure generates a variation in the resistant forces, this effect is not large enough to determine a significant change in the gear selection or of the

Table 2.9: Characteristics of the heavy-Duty vehicle.

Total vehicle curb weight	7090 kg (tractor) + 6160 (semi-trailer)				
Axles	1 steering, 2 wheels/axle 1 drive, 4 wheels/axle 3 trailer, 2 wheels/axle				
Gearbox	12 gears, manual transmission				
	ratio	efficiency	ratio	efficiency	
	I 15.86	0.977	VII 3.57	0.985	
	II 12.33	0.977	VIII 2.7	0.987	
	III 9.57	0.977	IX 2.01	0.986	
	IV 7.44	0.978	X 1.63	0.987	
	V 5.87	0.977	XI 1.29	0.986	
	VI 4.57	0.989	XII 1	0.998	
Final drive	ratio	efficiency			
	2.64	0.973			
$C_x \cdot A$	0.6 · 10 m ²				
Engine	11.0 l, diesel				
max power	353 kW @ 1900 rpm				
max torque	2300 Nm @ 970 rpm				
Tires – steering axle	315/70 R22.5 (single)				
reference $C_{rr, std}$	5.0 kg/ton				
maximum vertical load	4000 kg				
reference inflation pressure	8.5 bar				
Tires – drive axle	315/70 R22.5 (twinned)				
reference $C_{rr, std}$	4.9 kg/ton				
maximum vertical load	3750 kg				
reference inflation pressure	8 bar				
Tires – trailer axles	385/65 R22.5 (single)				
reference $C_{rr, std}$	5.4 kg/ton				
maximum vertical load	4500 kg				
reference inflation pressure	9 bar				

		Time	Distance	Avg speed	Max speed	Avg positive accel.	Max positive accel.	Avg positive grade	Max positive grade	Accel. perc.	Stop perc.
		[s]	[km]	[km/h]	[km/h]	[m/s ²]	[m/s ²]	[%]	[%]	[%]	[%]
HDV	ACEA long-haul	4547	100.2	79.3	85	0.3	1.6	1.0	6.5	0.8%	0.0%
	ACEA regional	5980	100.0	60.2	85	0.2	1.3	1.0	6.1	4.4%	1.3%
	ACEA urban	3172	27.8	31.5	85	0.2	1.5	1.6	6.1	9.0%	68.9%
	ACEA municipality	4074	9.9	8.8	85	0.4	1.4	0.4	2.6	14.7%	12.0%
	Custom HDV highway 1	11414	247.2	78.0	80	0.1	1.2	1.2	5.1	3.5%	0.0%
	Custom HDV highway 2	8276	183.3	79.7	80	0.3	1.3	0.4	3.2	11.3%	18.6%
LDV	Custom LDV highway	1201	35.0	104.8	137	0.5	1.6	0.0	0.0	48.1%	0.4%
	Custom LDV extra-urban	1804	26.9	53.7	121	0.6	1.6	1.9	8.8	44.8%	7.0%
	Custom LDV urban	2584	13.5	18.8	74	0.6	1.9	0.0	0.0	62.9%	31.8%

Table 2.10: Characteristics of the reference test cycles considered in the study for the reference heavy-duty vehicle (HDV) and light-duty vehicle (LDV).

vehicle speed. On the other hand, having a light vehicle allows an adverse road grade or other additional resistances to be overcome more easily: therefore, the vehicle can face steeper speed gradients, and the driver would use higher gears more often to save fuel, which would also have an effect on the vehicle speed. It can be noted, again with reference to Figure 2.23, that, at a certain point, the strategy implemented in PerFECTS simulates a downshift to the 9th-10th gear when the vehicle is loaded by 40 t, while it continues to use the highest gear in the case where the vehicle is loaded by 15 t.

However, these effects are not considered in TyPE, which – as mentioned above – is based on a simpler kinematic approach, and it interprets the reference gear and speed profiles provided through the configuration panel as the actual ones.

The preferred approach in TyPE is to have a single reference mission profile, in which the speed and gear are not changed according to the other simulation parameters, such as the vehicle mass or tire pressure. This simplification was made deliberately, as more accurate dynamic models are beyond the scope of this work. However, this choice produces some changes in the selected engine working points with respect to PerFECTS, and also in the fuel consumption, and these changes contribute to the difference between the results obtained by the two software programs.

Therefore, a number of simulations were performed for validation purposes, in which exactly the same dynamic mission profile simulated by PerFECTS was provided to TyPE, for each single loading case and pressure combination. The developed simulation tool was validated by comparing the results with those

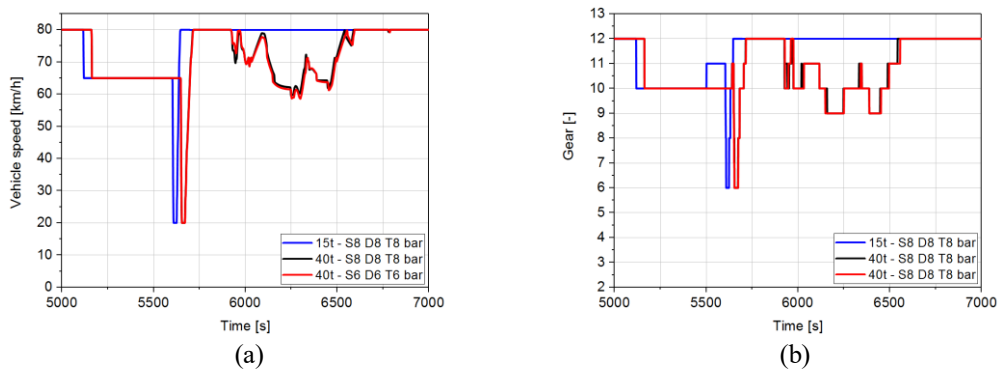


Figure 2.23: Vehicle speed and gear profile in PerFACTS on a section of the *Custom HDV highway 1* cycle for different pressure combinations and loading conditions. *S*, *D* and *T* refer to the steer, drive and trailer axles and indicate the pressure set on the tires on each axle.

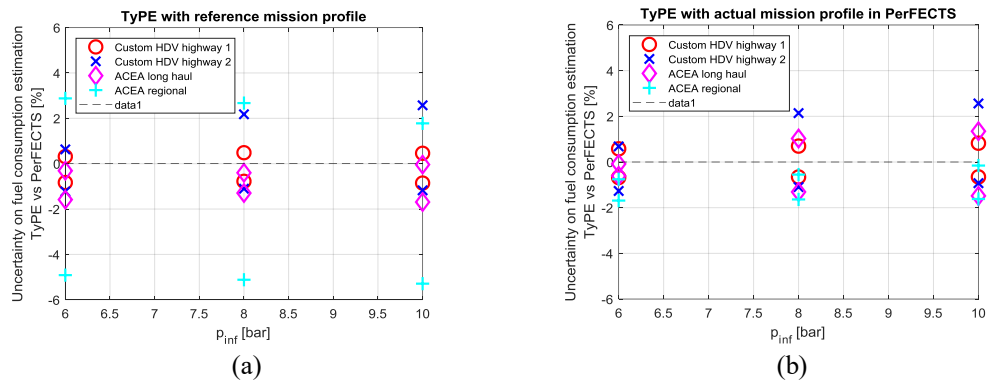


Figure 2.24: Comparison between TyPE and PerFACTS, when TyPE is run with a reference mission profile for all the pressure/load cases (a), and when the mission in TyPE is the same as that obtained from the PerFACTS simulations for each pressure/load case (b).

obtained from the PerFACTS reference software. This comparison was based on a full-factorial test plan of 9 tests obtained with 3 pressure levels and 3 vehicle loading conditions (vehicle mass and load distribution).

Figure 2.24 shows the uncertainty on the average fuel consumption obtained by TyPE with respect to the one obtained by PerFACTS. The comparison is shown for the case in which TyPE is always simulated with a reference mission profile, regardless of the current set mass and tire pressure combination (Figure 2.24a), as well as for the case in which the same mission is simulated by the two software tools for each single loading case and pressure combination (Figure 2.24b). A high relative error can be noted in the left-hand graph for the *regional ACEA* cycles when the vehicle is simulated at curb weight. Owing to the low load and highly transient

nature of the cycle, this is the case in which the maximum differences can be noted in the mission profiles and in the engine speed and torque. By eliminating these differences, (i.e., with reference to Figure 2.24b), the uncertainty range is much smaller, i.e. $\pm 2.5\%$. The case that presents the maximum difference is the *Custom HDV highway 2* mission in the full load condition, and it also shows a certain trend of the difference with pressure. Other missions also show this trend, although it is smaller: this can be justified considering that the rolling resistance variations considered in PerFACTS are calculated according to Eq. 2.36, while TyPE applies a more complete strategy concerning the evaluation of the rolling resistance, as shown in Eq. 2.38. All the TyPE simulations were performed considering that each cycle starts with a warm tire, since PerFACTS does not take into account tire warm-up.

The obtained results can be considered as a validation of the TyPE software.

Effect of the tire pressure on the fuel consumption of a single mission profile

Simulations were performed, for all the cycles reported in Table 2.10, with the aim of assessing the effect of a pressure variation on the fuel consumption of an HDV and an LDV. Studying different cycles provides the sensitivity of this analysis to the driving condition. A number of loading conditions between the two extreme cases (curb weight and maximum payload) were tested. The pressure combinations were set by incrementing or reducing the tire pressure on each axle by fixed amounts with respect to what is indicated in Table 2.8 and Table 2.9 as the reference pressure combinations. The pressures were changed in such a way to always keep the pressure-load combination within the safety limits provided by the tire manufacturers. The results obtained for the HDV are shown in Figure 2.25, where the x axis represents the pressure variation applied to the tires on each axle, with respect to the reference pressure on the same axle, and the y axis is the percentage variation of the average fuel consumption, with respect to the case in which all the tires are set according to the reference tire pressure combination.

The effect of changing the tire pressure on all the tires, on the drive and trailer axles only, and on the trailer only has been simulated for each loading case and pressure combination with reference to Figure 2.25. This simulation provided a wide scenario of cases of interest to analyze the effect of a CTIS if it were to be installed only on the trailer or on the whole vehicle. Considering that the companies that own the tractors are often not the owners of the semi-trailers they carry, the analysis of the effect of tire pressure variation on trailer axles can be of interest for two reasons: first, in the case in which a well-maintained truck (or a truck with a CTIS) is carrying a semi-trailer with underinflated tires; second, in the case the

trailers are only equipped with CTIS to reduce the cost and the complexity of the solution. Moreover, the case in which only the steering axle is excluded was analyzed to take into account the case in which a vehicle OEM decides not to adopt any pressure management strategy on the steer axle, which is the most important one for steering and braking maneuvers. Always maintaining a single reference tire pressure on this axle may be a good choice, and the CTIS may therefore be installed on that axle, possibly without applying any pressure management strategy to it, but only a “pressure-keeping” function. Another possibility is to avoid the installation of the CTIS on the steering axle in order to avoid complexities.

The results in Figure 2.25 show that, if the tire pressure is 2 bar (about 22-25%) lower than the reference one on all the tires (the *all axles* case in the graphs), fuel consumption increases by 1.5-3% if the vehicle is fully loaded (40 t) and by 1.2-2% if the vehicle is completely empty, depending on the driving conditions. The semi-trailer tires account for about half of the fuel penalty. As the vehicle mass increases, the steering axle is the one that is less sensitive to pressure variations: comparing the *all axles* case with the *drive and trailer axles* case, it is possible to notice that the difference between the two curves is smaller in the 40 t case than at 15 t. This is due to the fact that, as the vehicle is loaded, its barycenter moves backward, and the steer axle therefore bears a lower percentage of the total weight as the total weight increases (about 15% at full-load weight).

On the other hand, if the tire pressure in all the tires is increased by 1 bar, with respect to the reference tire pressure combination shown in Table 2.9, the fuel economy would improve by 0.5-1.1% in the 40 t case and 0.5-0.8% in the 15 t case. If the vehicle is loaded with its maximum payload, no significant difference is noted, if the steer axle is excluded. On the other hand, the relative advantage obtained by increasing tire pressure in the curb weight case is drastically reduced if the steering axle is excluded: in this case, the barycenter of the vehicle is positioned in such a way that the steering axle bears about 35% of the total load, that is, as much as the axles on the semi-trailer.

As expected, the lower the vehicle mass and the average speed are, the lower the sensitivity on fuel consumption to pressure variations. Although the urban ACEA cycle presents much more transient conditions than regional and long-haul ones, the effect of the average vehicle speed prevails due to the large difference in the average speed among the analyzed cycles.

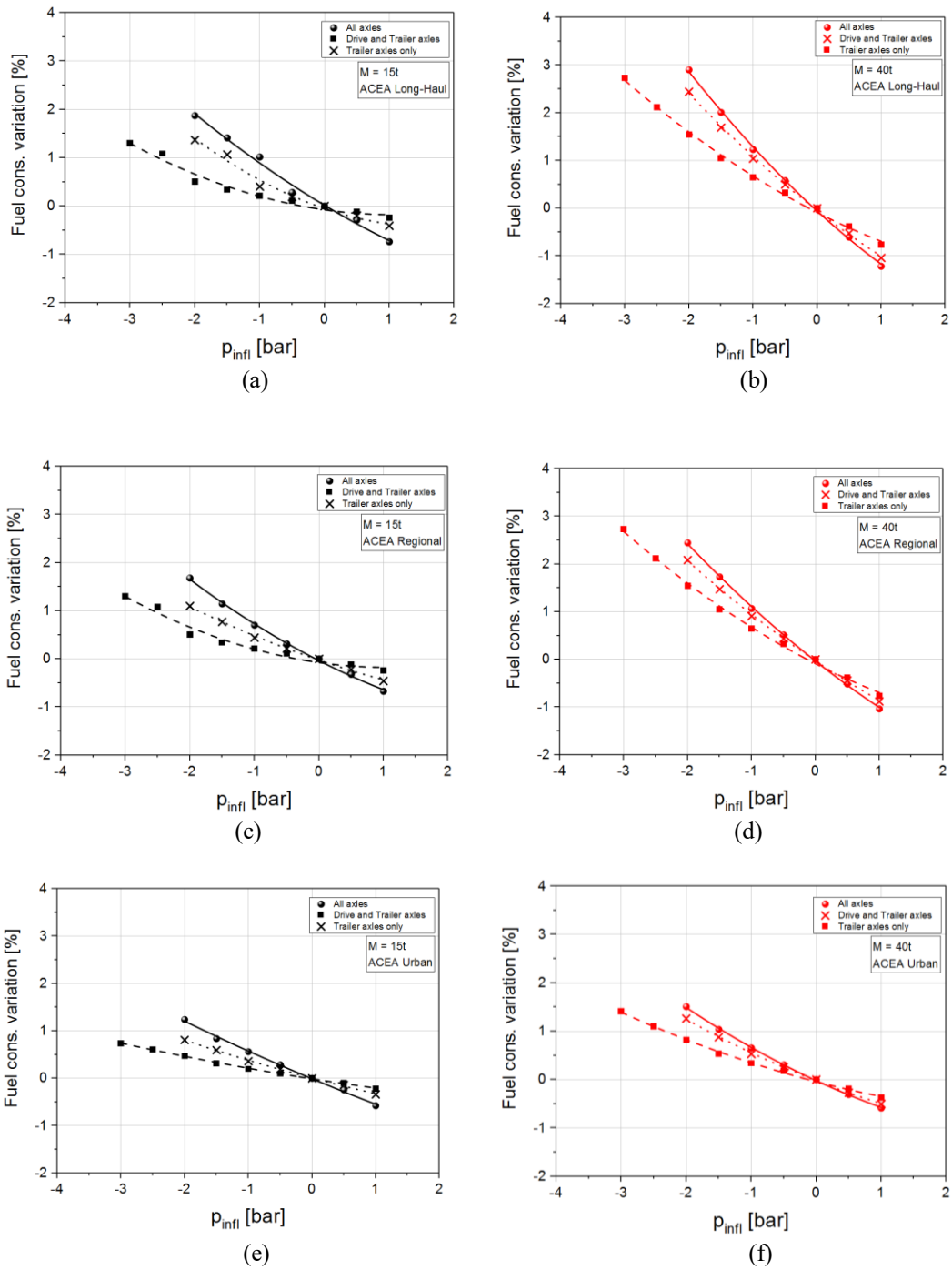


Figure 2.25: Percentage of the variation of HDV fuel consumption with tire inflation pressure on *long-haul* (a, b), *regional* (c, d) and *urban* (e, f) ACEA driving cycles, at truck curb weight (a, c, e) and maximum payload (b, d, f).

With reference to Fig. 2.26, the tire pressure variations of the LDV were applied to all the tires simultaneously. A 1 bar lower tire inflation pressure than the reference one (3.5 bar, according to what is reported in Table 2.8), i.e. a 25% under-inflation, increases fuel economy by 1.25-1.42% on the reference cycles for *urban*, *extra-urban* and *highway* driving, if the vehicle is only loaded with the driver, and by up to 1.30-1.87% if the vehicle is fully loaded. On the other hand, a 0.5 bar increase in tire pressure, with respect to the reference one, generates a reduction in fuel consumption of 0.47-0.57% in urban driving and of 0.49-0.69% in *highway* driving, the *urban* cycle being less sensitive and the *highway* cycle more sensitive to pressure variations.

Effect of the proposed pressure management strategies on the fuel consumption of a single mission profile

As mentioned above, some pressure management strategies have been proposed, and their effects have been analyzed and are discussed hereafter. The two here proposed strategies are: adaptation of the tire pressure to the vertical load acting on each tire under various loading conditions; tire pressure management during the tire warm-up period.

Each strategy is analyzed with reference to both its effect on fuel consumption and on tire wear. However, analyzing tire wear on a single mission profile does not provide useful information, and the results in this section are therefore only presented with reference to fuel economy.

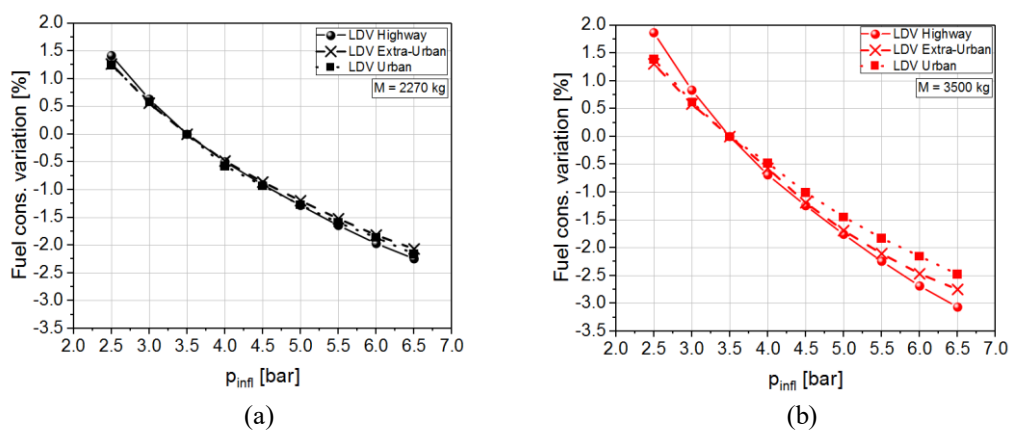


Figure 2.26: Percentage of the variation of LDV fuel consumption with tire inflation pressure on *highway*, *extra-urban* and *urban* driving cycles, at curb weight (a) and maximum payload (b).

The effect of a tire cold-start is generally not taken into account in fuel economy simulations, but it does in fact affect fuel consumption. The reference warm-up curves in Figure 2.20, which describe the percentage variation of tire rolling resistance as a function of the rolling time after a cold start, were taken into account. A warm-up time of 90 minutes has been considered for the HDV. The proposed strategies have been set in order to obtain the reference tire pressure on each axle at the end of the warm-up period, starting from a certain over-inflation. The initial increase in the pressure is the same for all the axles. The results obtained for the reference HDV are shown in Figure 2.27. Two options were tested, that is, increasing the tire pressure by 1 bar (referred to as *warm-up 1*, *warm-up 3* and *warm-up 5* in Figure 2.27) and by 2 bar (referred to as *warm-up 2*, *warm-up 4* and *warm-up 6* in Figure 2.27) with respect to the reference cold-tire pressure. The worsening in fuel consumption during a normal tire warm-up (*no strategy* cases in Figure 2.27), with respect to the case in which the tires are warm when the mission is started (*hot-start*), was taken as a reference to evaluate the potentiality of the proposed strategy. The strategies were applied considering the application of the pressure management logic to all the axles (*warm-up 1* and *warm-up 2*), to the drive and trailer axles only (*warm-up 3* and *warm-up 4*) and to the semi-trailer axles only (*warm-up 5* and *warm-up 6*).

The relative effect of the tire warm-up on fuel consumption is highly dependent on the mission characteristics. The tire warm-up period was considered the same, regardless of the driving condition, and as a result, the longer the cycle is, the lower the relative effect of tire warm-up on the cumulated fuel consumption over the whole mission. However, since the duration of the considered missions was similar for the three cycles, this effect was not the most relevant. On the other hand, the average fuel economy is better under highway driving conditions, due to the almost-steady working condition of the engine with respect to regional and urban modes, which are characterized by highly transient conditions. Therefore, a worsening of the rolling resistance produces a larger relative effect in the case where the average fuel consumption is lower, i.e. on the *long-haul ACEA* cycle. In other words, tire cold start generates a worsening of the fuel consumption, that is, from 1% for the *regional ACEA* and *urban ACEA* missions, to 1.9% for the *long-haul ACEA* mission, if the vehicle is loaded with its maximum payload, and from 0.7% for the *regional ACEA* missions to 1.2% for the *long-haul ACEA* missions, if the truck is travelling empty (15 t). The relative worsening due to the tire cold-start is less sensitive to vehicle loading conditions in a highly transient cycle, such as the *urban ACEA* mission.

The best performance of the proposed strategy can be obtained by implementing the strategy which starts from an initial over-inflation of 2 bar (*warm-up 2* in Figure 2.27) on all the axles. This would allow the fuel penalty due to the

warm-up to be reduced to 0.14-0.48% for the *regional ACEA* mission and for the *long-haul ACEA* mission, respectively, for the 40 t case, and to up to 0.09% for the *regional ACEA* cycle in the 15 t case. Therefore, depending on the considered cycle, in the best considered case, the advanced CTIS could drastically reduce the effect of tire cold-starts.

If the same initial over-inflation of 2 bar is only applied to the drive and trailer axles (*warm-up 4* in Figure 2.27), the obtained fuel consumption increase for the *regional ACEA* cycle is about 0.3%, compared to a hot-start case, where, if no strategy is applied, it would be 0.7-1%, thereby reducing the effect of a cold-start by 3/4. Similarly, a reduction of 2/3 of the effect of the tire cold start can be obtained for the *long-haul ACEA* cycle, and about 1/2 for the *urban ACEA* cycle. If the CTIS is only installed on the semi-trailer, the effect would be a reduction of 1/2 of the effect of the tire cold-start for the *regional ACEA* mission, and would be smaller for the other reference cycles.

If the initial over-inflation is limited to 1 bar (*warm-up 1* and *warm-up 3* in Figure 2.27), the benefits that can be obtained are significantly reduced. Again in this case, the *regional ACEA* cycle is the one that shows the best compensation of the cold-start effect, and the minimum increase in fuel consumption, with respect to the hot-start case, is about 0.4-0.55%.

The initial tire over-inflation can be chosen by taking into account the tire characteristics, i.e. considering the actual temperature and pressure transient that the tire would undergo in normal conditions. Moreover, the application of this strategy, as well as for the other options proposed here or in other works, should be the subject of further evaluations about the effect of these pressure changes on the longitudinal and lateral dynamics of a vehicle.

A similar analysis on the effect of a tire cold-start and of the proposed warm-up strategies was also conducted on the reference LDV (cf. Fig. 2.28). The tire cold-starts increased fuel consumption by 0.93-1.39% when the vehicle was loaded with only the driver (2270 kg), and by 1.02-1.85% when the vehicle was loaded with the maximum payload (3500 kg). In these ranges, the lower value refers to the *Custom LDV extra-urban* mission, and the higher value to the *Custom LDV highway* cycle. For this vehicle, it has always been considered that the advanced CTIS would be installed on all the wheels. By applying an initial over-inflation of 1 bar at the beginning of the mission (*warm-up 3* in Figure 2.28), and then deflating the tire until the target pressure at the end of the warm-up transient is reached (60 min), it is possible to reduce the effect of the warm-up on fuel consumption to 0.03-0.45%, where the lower value refers to the *Custom LDV extra-urban* mission at 2270 kg and the upper value is related to the *Custom LDV highway* cycle at 3500 kg. If the initial over-inflation is instead set to 0.5 bar (*warm-up 1* in Figure 2.28), the fuel penalty, with respect to the hot-start case, would be between 0.44% and 1.08%.

The adaptation of the tire pressure to the loading condition has been performed according to an iso-deflection strategy, and has been defined in each of the considered loading conditions, assuming the corresponding tire pressure obtained from the load-pressure tables provided by the tire manufacturer for each tire. This situation corresponds to the conditions that produce the same vertical deformation at rated speed for all the pressure-load combinations. According to what is mentioned above, this strategy would allow the tire mileage to be maximized, i.e. to keep the vehicle working condition on the vertex of the parabola shown in Figure 2.19.

The results of this strategy, applied to the reference HDV, are shown in Figure 2.29, where all the values obtained for the different tire pressure and loading conditions are considered as percentage variations with respect to the fuel consumption obtained at 15 t, with the reference tire pressure combination given in Table 2.9. The curves compare the performance of the described iso-deflection strategy and the case in which the reference pressure combination is maintained for all the loading conditions. In the analyzed case, the reference tire pressure combination has been set at the maximum allowed load. Therefore, the tire pressure combinations calculated through the load-pressure tables are always lower than the reference case, and are equal for the maximum-load case. This determines an obvious worsening of the truck fuel economy for the analyzed strategy. The fuel penalty induced by the iso-deflection strategy is 2.7% at 15 tons for the *long haul ACEA* cycle, 2.5% at 15 tons for the *regional ACEA* cycle, and 1.9% at 15 tons for the *urban ACEA* cycle. Moreover, it can be noted in the iso-deflection case (dashed lines in Fig. 2.29), that the rate of variation of fuel consumption with the total weight (expressed by the slope of the curves) is lower than in the “reference” case (solid lines). This means that if the reference tire pressure were lower, due to the selection of a different criteria or due to under-inflation caused by incorrect maintenance, the presented strategy would have a fuel saving potential.

Nevertheless, as mentioned above, the iso-deflection strategy allows the tire mileage to be maximized and could be beneficial considering vehicle dynamics. An analysis on the effect of the various strategies on the Total Cost of Ownership is provided in the next paragraph with reference to an annual mission profile, while additional evaluations on the effect on vehicle dynamics will be the topic of future work.

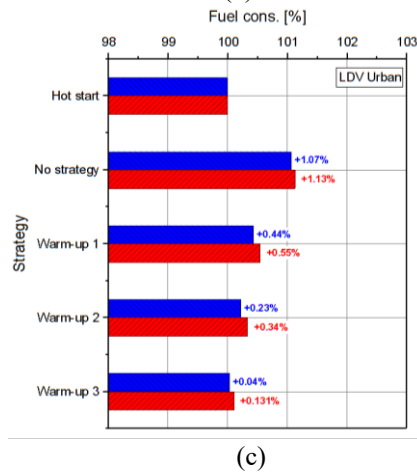
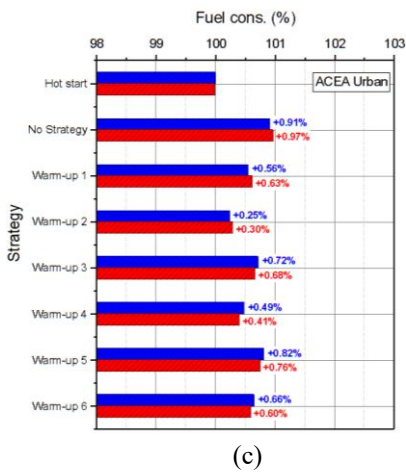
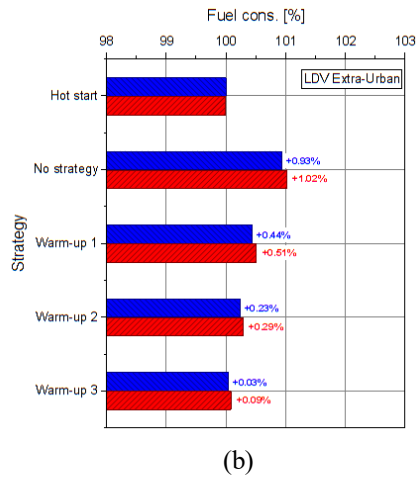
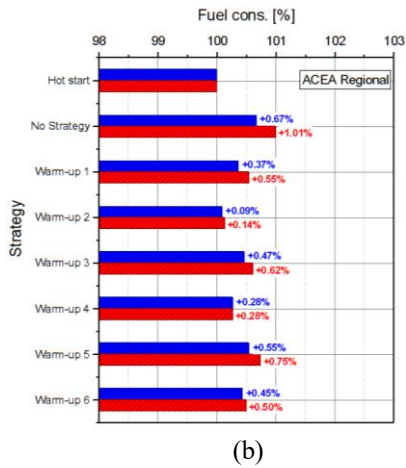
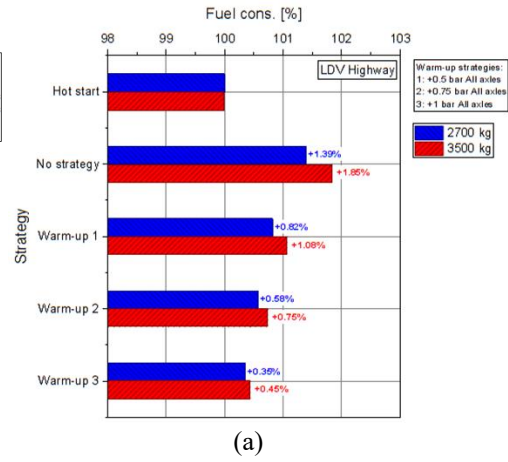
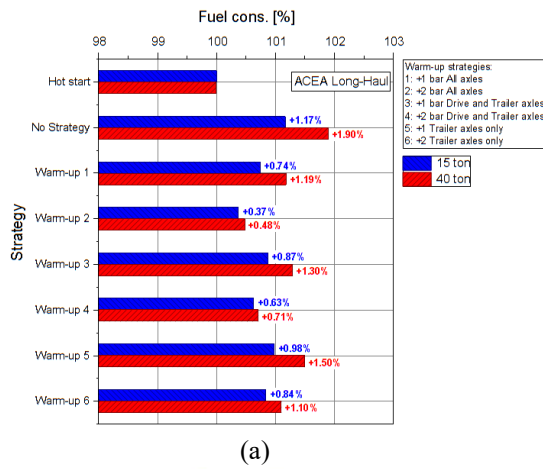


Figure 2.27: Effects of tire cold-start and warm-up strategies on HDV on *long-haul* (a), *regional* (b) and *urban* (c) ACEA missions.

Figure 2.28: Effects of tire cold-start and warm-up strategies on LDV on *highway* (a), *extra-urban* (b) and *urban* (c) missions.

A similar analysis, concerning the iso-deflection strategy, was also tested in the simulation of the considered LDV. Since a reference pressure-load table was not available for the studied tire, an iso-deflection curve was obtained considering the pressure-load combinations prescribed by ETRTO [270], and changing it to the load range of interest. The ETRTO manual in fact provides a reference pressure for the maximum load (4.75 bar at 2240 kg) and an equation to evaluate the maximum load allowed for different pressures. This provides the critical iso-deflection with the maximum allowed vertical deformation. Provided that the maximum load and maximum pressure are not exceeded, the reference iso-deflection can then be defined parallel to the ETRTO reference pressure-load combination, but moved to lower loads, i.e., in the range of interest for the studied application. Therefore, the following reference combinations were selected: 3.5 bar for the empty vehicle (1135 kg per axle), 5 bar for the full vehicle (1750 kg per axle). In this case, the reference tire pressure given in Table 2.8 (3.5 bar) was considered to refer to a loading condition with an empty vehicle and only the driver on-board. Considering the reference pressure-load combination, with reference to Figure 2.30, the iso-deflection strategy allows a reduction in fuel consumption of up to 1.84% to be reached for the *Custom LDV urban* cycle and 2.18% for the *Custom LDV extra-urban* mission.

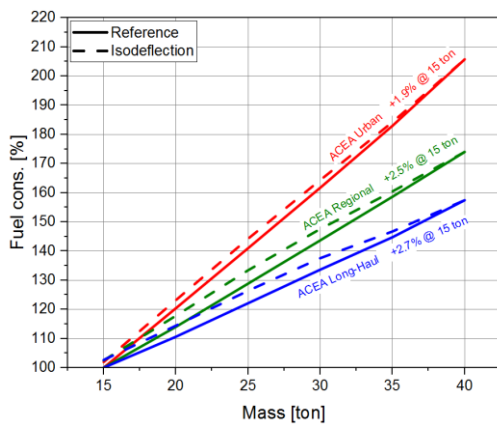


Figure 2.29: Effect of vehicle loading condition variations on fuel consumption on HDV on long-haul, regional and urban ACEA missions: effects of the application of the iso-deflection pressure management strategy.

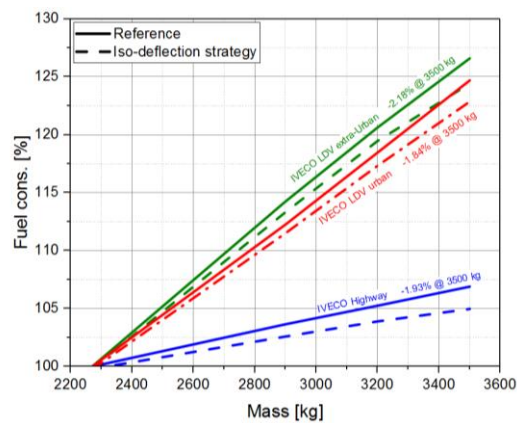


Figure 2.30: Effect of vehicle loading condition variations on fuel consumption on LDV on the Custom LDV highway, Custom LDV extra-urban and Custom LDV urban missions: effects of the application of the iso-deflection pressure management strategy.

Effect of the proposed strategy on the characteristic annual mission profiles

On the basis of the results obtained for the single cycles, the effects of an advanced pressure management system were analyzed on representative annual missions of the selected vehicles. After defining realistic annual missions, in terms of total mileage, fractions of this mileage in urban/extra-urban/highway and loading conditions, the results of the previously presented simulations were combined in order to simulate the following scenarios:

- case #1 – REFERENCE: all the trips were simulated for the reference tire inflation pressure combination (cf. Table 2.8 and Table 2.9), and all the trips were supposed to start with warm tires;
- case #2 - MISUSE (UNDERINFLATION): 50% of all the trips (in each mode: highway, extra-urban and urban) were simulated for the reference tire inflation pressure combination, the remaining 50% were simulated with a 25% lower tire inflation pressure than the reference one on all the axles, and all the trips were supposed to start with warm tires;
- case #3 – ISODEFLECTION: all the trips were simulated with the tire inflation pressure (on all the axles) set according to the load, with reference to the pressure-load table provided by the tire manufacturer of the selected tires, and all the trips were supposed to start with warm tires;
- case #4 - COLD-START / NO STRATEGY: a percentage of the trips were considered to start with cold tires. This percentage was changed according to the type of annual mission, in order to consider approximately 2 cold-starts per day. The fuel penalty, resulting from the additional resistance of the cold tire, was considered. No pressure management strategy was applied, i.e. the pressure was set to be the same as case #1;
- case #5 - COLD-START / WARM-UP STRATEGIES: a percentage of trips (the same percentage as case #4) were considered to start with cold tires. The fuel penalty, resulting from the additional resistance of the cold tire, was considered, taking into account the most suitable tire pressure management strategies that adapt the pressure during the tire warm-up transient.

A representative mission of intensive usage on long-distance trips was considered for the HDV. With reference to Table 2.11, the vehicle was supposed to travel 180'000 km/year. Of this distance, 85% was travelled on highways, 10% on extra-urban roads and 5% on urban roads. The average fuel consumption of the

corresponding ACEA cycle for each of these driving conditions was taken as a reference. A second annual mission was also considered, with a total yearly mileage of 90'000 km, 65% of which were travelled on highways, 30% on extra-urban roads and 5% under urban conditions. For both of the missions, the truck was supposed to be at full load (40 t) for 50% of its mileage, at part load (30 t) for 40% of its mileage and completely empty (15 t) for the rest of the trips.

For case #2, an under-inflation of 2 bar was considered on all the axles (22-25%) for 50% of the yearly mileage to account for any possible improper maintenance of the tire pressure. For case #4 and case #5, the warm-up duration was considered to be 90 min, and the best-case strategy of those presented in the previous section was applied for case #5, i.e. the case of an initial over-inflation of 2 bar on all the axles. The percentage of trips with a cold start was set to 35% for the 180000 km annual mission and 65% for the 90000 km annual mission (2 trips/day, with 5 and 1 daily repetitions of the highway cycle, respectively). The total tire life (if the tire was always used according to the pressure-load table provided by the tire manufacturer) was considered equal to 1'100'000 km [271], and included 2 regrooving and 1 retread operation, as well as a total cost of a single tire of about € 1'200 (including regrooving and retreading). The total tire mileage did not take into account the possible reduction due to utilization on different kinds of soil, or the kind of route or missions.

With reference to Table 2.11, for the 180'000 km/year mission, the analysis shows that the usual under-inflation due to misuse (case #2) produces an increase in the annual fuel consumption of 1.3%. Considering a cost of 0.911 €/l for diesel fuel for commercial trucks [272], this corresponds to an increase in the annual cost of fuel of about € 700 per truck. Misuse leads to more tire wear, and as a result the total tire mileage was considered to be reduced by 3%, with a cost impact of 83 €/year. Therefore, misuse produces an overall increase of € 783 in the Total Cost of Ownership of a truck. The application of an iso-deflection strategy leads to an increase in the total fuel consumption of 1.4%, with respect to the reference case. As mentioned above, this depends on how the reference pressure is set with reference to the reference loading condition: since the pressure in the reference case was set according to the maximum vehicle load and was considered the same for all the loading conditions with a lower vehicle mass, the iso-deflection strategy resulted in a worsening of the fuel economy. On the other hand, the tire mileage was increased by 12.5% in the iso-deflection case. Therefore, the adjustment of the tire pressure to a vertical load allows the tire life to be maximized, with an annual cost impact of about € 290. However, the increase in fuel consumption has a much greater effect on TCO than the decrease in the tire cost, and this strategy therefore negatively affects the TCO. Cold-starts increase the annual fuel consumption by 0.6% and the cost by about € 313 per year per truck. By applying the proposed

pressure management strategy to the warm-up, it would be possible to reduce the negative effect of cold-starts on fuel economy to 0.14%, and the related cost to about € 177 if the negative effect of the pressure increase on tire wear were also taken into account. Therefore this means a reduction of the TCO of about 136 €/year for the cold-starts (i.e., comparing case #5 with case #4). Similar percentage variations were found for the 90'000 km/year mission, with a greater effect for cold-starts, due to the higher percentage of trips considered to start with cold tires (2 trips/day, on 2 daily repetitions of the highway cycle). On the other hand, the effect on TCO was lower due to the lower annual mileage, i.e. due to the lower total cost of fuel.

Considering that a truck without an advanced CTIS is subject to usual under-inflation and does not compensate for the effects of a tire cold-start (i.e., combining the effect of case #2 and case #4), the increase in TCO, with respect to the reference case, was 660-1'094 €/year. On the other hand, if the system were installed, it would be possible to avoid usual under-inflation, and adapt the pressure during tire warm-up. Therefore, it would be possible to reduce the increase in TCO with respect to the reference case to 153-177 €/year.

The net reduction of TCO obtainable through the application of an advanced CTIS on a commercial truck can therefore be quantified as 507-917 €/year.

A similar analysis was also performed on the reference LDV. Three different annual missions were taken into account with reference to Table 2.12: a logistic mission, with 70'000 km travelled per year, with 80% of the trips in extra-urban mode and the remaining divided equally between urban and highway driving; a parcel delivery mission, with 40'000 km/year distributed almost equally over different driving modes (35% urban, 30% extra-urban, 35% highway); and an additional delivery mission with a total mileage of 56'000 km/year and most of the trips (70%) in highway mode (10% urban, 20% extra-urban). The duration of the warm-up phase for case #4 and case #5 was considered to be 60 min and the application of an initial over-inflation of 1 bar on all the tires was considered for case #5. Again considering 2 cold-starts per day, the percentage of trips with a cold start was calculated with respect to the total number of repetitions of highway and extra-urban trips per day. This provided a cold-start percentage of 24% for the logistic mission, 35% for the 56'000 km/year delivery mission and 46% for the 40'000 km/year mission. The total tire life (if the tire were always used according to the reference pressure-load calculated as mentioned above for the iso-deflection strategy) was considered equal to 50'000 km for the tire wear calculations, and the total cost of a single tire was about € 160. The cost of fuel was taken as 1.4 €/l.

With reference to Table 2.12, the considered misuse increases fuel consumption by 0.67-0.78%, and reduces tire life by about 3.5%. The final effect is an increase in the TCO of 57-93 €/year.

Adapting the tire pressure to the vertical load allows the fuel consumption to be reduced by 0.89-1.06% and increases tire life by about 25%, with a total reduction of TCO from 140 €/year to 230 €/year.

Moreover, the effect of tire cold-starts is an increase in fuel consumption of 0.14-0.32%, which can be reduced to 0.01-0.05% by applying the proposed warm-up strategy. Additionally, since it was supposed that the reference tire pressure was set in the driver-only loading case, and therefore that the vehicle was running on underinflated tires most of the time (with respect to iso-deflection), the over-inflation due to the warm-up strategy also produced a benefit on the reduction of tire wear, and a corresponding increase in tire life of 2.5-5.7%. Finally, the warm-up strategy allows TCO to be reduced by 18-25 €/year.

A van without an advanced CTIS is subject to under-inflation and is not able to compensate for the effects of a tire cold-start (i.e., combining the effect of case #2 and case #4), which leads to an increase in TCO, with respect to the reference case, of 75-111 €/year. On the other hand, if the system is installed, it would be possible to avoid under-inflation, and to adapt the pressure to the vertical load and during tire warm-up. As a first approximation, if these effects were considered as being independent of each other, i.e. summing the effects of case #3 and case #5, it would be possible to reduce TCO by 161-250 €/year.

The net reduction of TCO obtainable through the application of an advanced CTIS on a commercial van can therefore be quantified as 237-354 €/year.

HDV mission 1 - 180'000 km/year

	Urban	Extra-urban	Highway	% Load factor	Mission Load [t]
	5%	10%	85%	5%	15
	5%	10%	85%	45%	30
	5%	10%	85%	50%	40
	Total fuel cons. [% ref.]	Δ cost of fuel [€/year]	Tire life variation [% ref.]	Δ cost of tire wear [€/year]	Δ TCO [€/year]
<i>Case #1 - reference</i>	0.00%	0.0	0.0	0.0	0.0
<i>Case #2 - misuse (underinflation)</i>	1.28%	698.9	-3.05	82.6	781.5
<i>Case #3 - Load (isodeflexion)</i>	1.40%	768	12.5	-292.3	475.6
<i>Case #4 - Cold-start / NO STRATEGY (90 min)</i>	0.57%	312.8	0.00	0.00	312.8
<i>Case #5 - Cold-start / WARM-UP STRATEGY 2</i>	0.14%	75.1	-3.7	102	177.2

HDV mission 2 - 90'000 km/year

	Urban	Extra-urban	Highway	% Load factor	Mission Load [t]
	5%	30%	65%	5%	15
	5%	30%	65%	45%	30
	5%	30%	65%	50%	40
	Total fuel cons. [% ref.]	Δ cost of fuel [€/year]	Tire life variation [% ref.]	Δ cost of tire wear [€/year]	Δ TCO [€/year]
<i>Case #1 - reference</i>	0.00%	0.0	0.0	0.0	0.0
<i>Case #2 - misuse (underinflation)</i>	1.23%	349.2	-3.01	42.2	391.4
<i>Case #3 - Load (isodeflexion)</i>	1.36%	384.0	12.6	-149.4	234.7
<i>Case #4 - Cold-start / NO STRATEGY (90 min)</i>	0.95%	268.6	0.03	0.00	268.6
<i>Case #5 - Cold-start / WARM-UP STRATEGY 2</i>	0.22%	61.1	-6.4	91.7	152.8

Table 2.11: Annual missions for the reference heavy-duty vehicle: effect of pressure management strategies on TCO.

LDV parcel delivery mission - 40'000 km/year

	Urban	Extra-urban	Highway	% Load factor	Mission Load [kg]
	35%	30%	35%	10%	2270
	35%	30%	35%	35%	2900
	35%	30%	35%	40%	3200
	35%	30%	35%	15%	3500
	Total fuel cons. [% ref.]	Δ cost of fuel [€/year]	Tire life variation [% ref.]	Δ cost of tire wear [€/year]	Δ TCO [€/year]
<i>Case #1 - reference</i>	0.00%	0.0	0.0%	0.0	0.0
<i>Case #2 - misuse (underinflation)</i>	0.63%	35.5	-3.3%	15.6	51.1
<i>Case #7 - Isodeflexion</i>	-1.01%	-56.8	23.2%	-84.7	-141.5
<i>Case #3 - Cold-start / NO STRATEGY (60 min)</i>	0.60%	33.5	0.00%	0.00	33.5
<i>Case #6 - Cold-start / WARM-UP STRATEGY 1 (+1 bar)</i>	0.09%	5.1	8.0%	-33.4	-28.3

LDV logistic mission - 70'000 km/year

	Urban	Extra-urban	Highway	% Load factor	Mission Load [kg]
	10%	80%	10%	15%	2270
	10%	80%	10%	35%	2900
	10%	80%	10%	35%	3200
	10%	80%	10%	15%	3500
	Total fuel cons. [% ref.]	Δ cost of fuel [€/year]	Tire life variation [% ref.]	Δ cost of tire wear [€/year]	Δ TCO [€/year]
<i>Case #1 - reference</i>	0.00%	0.0	0.0%	0.0	0.0
<i>Case #2 - misuse (underinflation)</i>	0.59%	55.2	-3.3%	27.0	82.2
<i>Case #7 - Isodeflexion</i>	-0.95%	-87.9	22.6%	-144.0	-231.8
<i>Case #3 - Cold-start / NO STRATEGY (60 min)</i>	0.26%	24.3	0.00%	0.00	24.2
<i>Case #6 - Cold-start / WARM-UP STRATEGY 1 (+1 bar)</i>	0.02%	2.2	3.7%	-27.6	-25.5

LDV delivery mission - 56'000 km/year

	Urban	Extra-urban	Highway	% Load factor	Mission Load [kg]
	10%	20%	70%	10%	2270
	10%	20%	70%	35%	2900
	10%	20%	70%	40%	3200
	10%	20%	70%	15%	3500
	Total fuel cons. [% ref.]	Δ cost of fuel [€/year]	Tire life variation [% ref.]	Δ cost of tire wear [€/year]	Δ TCO [€/year]
<i>Case #1 - reference</i>	0.00%	0.00	0.00%	0.0	0.0
<i>Case #2 - misuse (underinflation)</i>	0.70%	55.9	-3.3%	21.8	77.7
<i>Case #7 - Isodeflexion</i>	-1.11%	-88.9	23.2%	-118.6	-207.4
<i>Case #3 - Cold-start / NO STRATEGY (60 min)</i>	0.54%	43.1	0.00%	0.00	43.1
<i>Case #6 - Cold-start / WARM-UP STRATEGY 1 (+1 bar)</i>	0.11%	9.0	6.0%	-35.6	-26.6

Table 2.12: Annual missions of the reference light-duty vehicle: effect of pressure management strategies on TCO.

2.6 Layout and design of the Active Tire Pressure Control (ATPC) system for Passenger Cars

When the target for the application of the system is a light-duty passenger vehicle with a conventional wheel-end architecture, the system layout needs to be fail-safe, robust, cost effective and easily installable at the same time. Therefore, the integration of the system with existing wheel-end designs needs to be studied carefully, in order to minimize the economic and installation complexity drawbacks of special designs. Therefore, some limits of the technical literature discussed in *Section 2.2* have been here highlighted. While some of the cited solutions for non-driving wheels may be appropriate for passenger vehicles [200, 230], most of the abovementioned patents were developed to fit the typical wheel-end designs of heavy-duty vehicles [198, 231]. As an example, the installation of the pneumatic rotating unit on a passenger vehicle cannot include an axle housing (as, e.g., in [192, 193]), since the hub-axle design is different. Finally, solutions that require the air conduit to pass through the bearing [198] or the hub-carrier, or involve a duct which reaches the rim in a non-coaxial position, with respect to the wheel rotation axis [194, 232], would also require high complexity in the design, production and installation of the system.

All these factors have limited in the past the opportunities for the application of this kind of system on passenger cars.

The main target of this *Section* is therefore the development of a specific solution that would allow the installation of a central tire inflation system on a light-duty passenger vehicle, in which the following points are addressed:

- the design of a pneumatic layout which would guarantee tire volume isolation when the system is not actuated in order to realize a highly fail-safe device, with no critical parts exposed;
- the design of a dedicated solution to allow the integration of parts of the system within the wheel-end mechanical parts of a driving and a non-driving wheel of a passenger vehicle, with a low impact on the wheel-end design and on the vehicle assembly procedure;
- the experimentally-driven design of a purposely sized solution that would allow a suitable combination of size/weight and performance;

- the study of pressure management strategies that exploit the system functionalities to improve safety and fuel economy.

Active Tire Pressure Control addresses all the above mentioned issues with the aim of producing a specifically developed CTIS for light-duty passenger applications in order to exploit the advantages of pressure management on fuel economy (c.f. *Sections 2.3, 2.4*), which required relevant innovations, with respect to the previous state of the art, due to the peculiarities of the application field. A small-size vehicle has been considered as a reference to study this application. A first version of the designed solution has been prototyped, installed on a test-bench that reproduces the wheel-end components of a standard passenger car and tested to analyze the performance discussed hereinafter in this *Section*.

The following qualitative requirements were considered as the starting points for the current study:

- the system weight and volume have to be as low as possible in order to limit the drawbacks related to the increase in vehicle weight and the reduction in usable volume due to the installation of the system on-board;
- the product cost should be as low as possible;
- the assembly process during vehicle manufacturing as well as the post-selling service operations should be as simple as possible and comparable with standard procedures;
- the system has to be highly fail-safe to satisfy high safety standards;
- the vehicle aesthetics should not be affected.

The constructive solutions have been designed in order to avoid modifications of the basic wheel-end architectures and so that the interventions required on the involved mechanical parts are as non-invasive as possible. The design was based on the study of mass-production components that have been modified to cope with the specific needs of the target application. The modifications of the standard parts were designed to be easily introduced during the conventional design and production process of the aforementioned components. Although the effect of the designed solution on production cost and vehicle assembly procedure have not been quantified yet, minimizing the modification of the standard parts and layouts in the design process was meant as a way to limit the impact of the new technology on cost and assembly.

The methods and the hardware used to fluidly connect the various components of the system have been defined and purposely designed in such a way that the mounting and dismounting operations of the wheel and of the system itself are easy and robust.

A brief description of the electro-pneumatic schematic of the Active Tire Pressure Control (ATPC) system is presented as a reference in Figure 2.31. The system is made up of a central part composed of a series of electro-valves (mounted on a central manifold), positive-pressure and negative-pressure air sources, and pneumatic lines which introduce air into the tires. The central (stationary) part and the wheel-end (rotating) part of the system are connected by means of pneumatic rotating joints. An on-wheel valve, or valve assembly, is opened by a pneumatic inflation and deflation command, while it remains closed when the system is not actuated, to both reduce the consequences of possible failure of the ducts, pipes, fittings, etc. and to reduce the friction and wear of the pneumatic rotating joint. One or several sensors are required to measure the current tire pressure.

Different solutions may be exploited to provide a suitable vacuum source. As an example, a vacuum source that is already present on board, such as the vacuum pump of the servo-brake system, can be used, if available. As an alternative, an on-purpose built vacuum pump, such as an electrically-driven pump, may be used, or a vacuum source can be introduced through a venturi ejector fed with the pressurized air flow provided by the compressor [195, 251]. A different solution, which allows a suitable performance to be obtained, in conjunction with a low

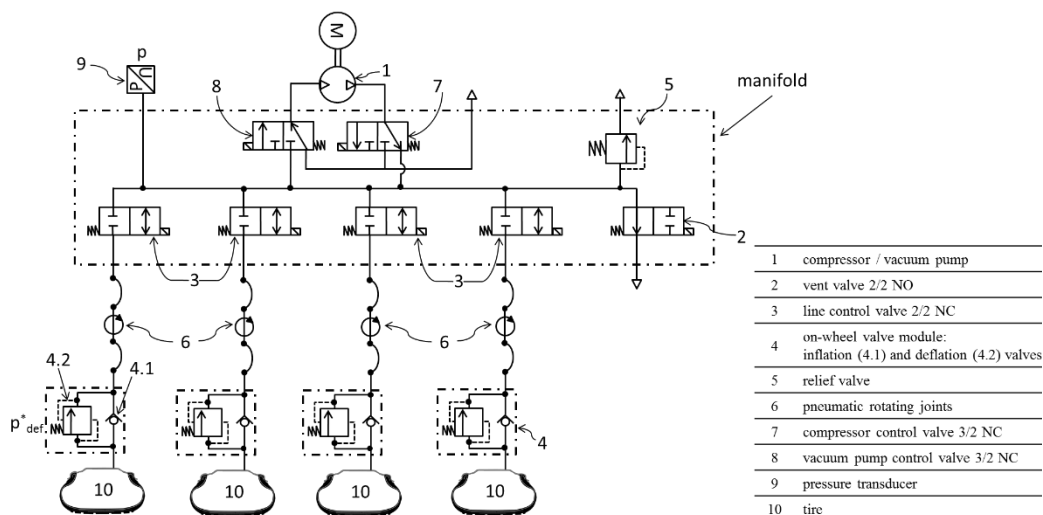


Figure 2.31: Schematic of the ATPC system layout.

complexity and high versatility of the system layout, has been adopted in the current prototype of the ATPC system. This solution is presented in Fig. 2.31, where a single device (item 1) is adopted, which is able to operate both as a compressor and as a vacuum pump, depending on which port is connected to the user and which one is connected to the atmosphere. For this purpose, the two 3/2 electro-valves indicated as items 7 and 8 in Fig. 2.31 are required. These valves normally connect the positive-pressure port of the machine to the system, and the other port of the same machine to the environment. In this way, the system is normally configured to execute an inflation actuation: when the control logic of the system determines that a tire needs to be inflated, it commands the actuation of the compressor, and commutes the vent valve (item 2) and the line valve (item 3) of the selected tire. On the other hand, when a deflation actuation is required, valves 7 and 8 are commuted in order to connect the vacuum port to the system and the other one to the environment. Again in this case, the vent valve and the line valve are commuted to allow communication between the central part of the system with the selected tire.

The vent valve maintains the central part of the system upstream of the wheel valve at atmospheric pressure, therefore reducing friction and wear on the rotating seals in the rotating junctions (items 6). Moreover, the vent valve that is open to the atmosphere ensures an outflow in the case the compressor is actuated accidentally, due to a malfunction of the system. Finally, a relief valve (item 5) limits the maximum pressure that can be reached in the tire during an inflation actuation, as well as the maximum pressure in the central part of the system in the case of a malfunction, e.g. if the line valve is not commuted during a commanded actuation.

Some of the CTISs on the market and in the technical literature allow the tires to be deflated directly through the on-wheel valve, in order to achieve fast tire deflation [207]. This solution is of special interest for those cases where the tire needs to adapt quickly to the kind of soil to allow adequate traction capability in critical situations, such as on military or emergency vehicles. In the studied application for passenger cars, tire deflation occurs via the central on-board unit, as it does in other known cases in the technical literature [192]: although this leads to longer actuation times, this solution is preferred to avoid the possible failure and clogging of a wheel-mounted deflation valve.

2.6.1 Experimental set-up to test the system components

A test bench has been built in compliance with ISO 6358 [273] and has been used to test one by one the system components, that is, both the commercial parts and the prototypes. The basic layout for testing pneumatic components in accordance to ISO 6358 is reported in Figure 2.32. It is basically composed by:

- a compressed air supply unit, including a filter (A);
- a pressure regulator with variable pressure setting (B);
- a shut-off valve (C),
- a flow rate measuring device (L or L');
- a temperature measuring pipe (D), where a temperature measuring device (E) is installed;
- an upstream pressure measuring pipe (F), where a pressure measuring device (I) is installed;
- the component under test (G);
- a downstream measuring pipe (H);
- a differential measurement device (J) installed in order to measure the differential pressure across the two pressure measuring pipes (in alternative, a pressure sensor can be installed on the second measuring pipe, and the differential pressure can be obtained as a difference between the two pressure measurements);
- a flow regulator (K).

According to ISO 6358, the choked flow conditions have to be verified in the component to be tested for higher pressure ratios than for the test bench components, and the measuring layout is therefore sized in order to avoid that the critical conditions may occur in the sections of the pipes and of the other components earlier than in the component to be tested. The temperature and pressure measuring pipes are meant to stabilize the flow. The pressure measuring pipes chosen for this application are of the G1/8 size (6mm diameter), i.e. is larger than the minimum geometric section of the component under test. The length of all the measuring pipes, as well as the diameter of the temperature measuring pipe, are sized accordingly.

The schematic of the test-bench layout built at the Politecnico di Torino for testing the components of the ATPC system is reported in Figure 2.33a. It is mainly

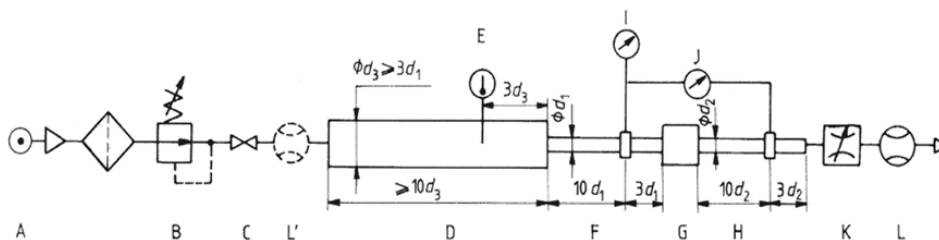


Figure 2.32: Test-bench layouts for testing pneumatic components according to ISO 6358 [273].

composed by an upstream measuring tube where pressure and temperature are measured, and a downstream measuring tube for the pressure, followed by a pressure regulator (VR) to vary the backpressure imposed to the component under test. It can be noted that two flow rate sensors (Q_1 and Q_2) have been used in order to obtain a characterization of the fluid losses, while the normative recommends the utilization of a single flowmeter under the hypothesis that no leakages occur. For this purpose, the testbed has been equipped with two high-accuracy Bronkhorst El-Flow thermal mass flow meters. Additionally, as the pressure upstream of the test component changes as a consequence of the regulation of the pressure downstream of the test component (through pressure regulator VR), a Bronkhorst El-Press electronic forward pressure controller has been used: the integrated electronics controls a proportional valve (PR) on the basis of the feed-back provided by a piezo-resistive pressure sensor (p_1). Another piezo-resistive pressure transducer (p_2) and a T-type thermocouple (TC) complete the installation.

This test bench has also been set up in a special configuration in order to test a toroidal pneumatic rotating joint under normal operating conditions. This component was specifically designed and prototyped, and considering that it represents one of the critical components of the system, the realization of a proper test campaign was considered of interest in order to analyze the pneumatic characteristics of this component under rotation at various speeds. For this purpose, the configuration shown in Figure 2.33b was set-up when required, considering the same general layout shown in Figure 2.33a. With reference also to Fig. 2.34, the component to be tested, i.e. the toroidal pneumatic rotating joint, is mounted on a shaft, that can rotate thanks to the coupling to an electric motor, whose speed can be regulated through an inverter. A Kistler 4520a torque-meter with a measuring range from 0 to 2 Nm and an accuracy within $\pm 0.5\%$ of the full-scale (i.e., ± 0.01 Nm) was also added in order to measure the resistive torque, which was expected to mainly be due to the bearing and the frictions on the rotating seals. The torque-meter is connected on one side to the electric motor and on the other side on the shaft, through bellows couplings with clamping hubs. The outer (statoric) part of the pneumatic rotating joint is constrained to the test-bench structure, while the inner (rotoric) part is installed on the rotating shaft through elastic rings able to transfer the torque. A flexible pipe, whose diameter is much larger than the minimum flow section of the component under test, connects the upstream flow measurement pipe of the ISO 6358 layout to the inner port of the rotating joint.

The toroidal pneumatic junction under test has an inner sealed channel, and an outlet port parallel to the rotation axis of the shaft, as it will be more deeply described in *Section 2.6.4*. In order to connect the outlet port of this pneumatic joint to the second measuring pipe, i.e. the one downstream the component to be tested according to the ISO 6358 layout, a second pneumatic junction is put in series to the component under test. This second joint is chosen among the commercially available rotating joints with a single inlet and single outlet port, with the two ports both located along the rotation axis. This component has negligible flow losses and friction torque with respect to the component under test, and therefore the effect of this component on the final results is minor. Therefore, the outlet port of the

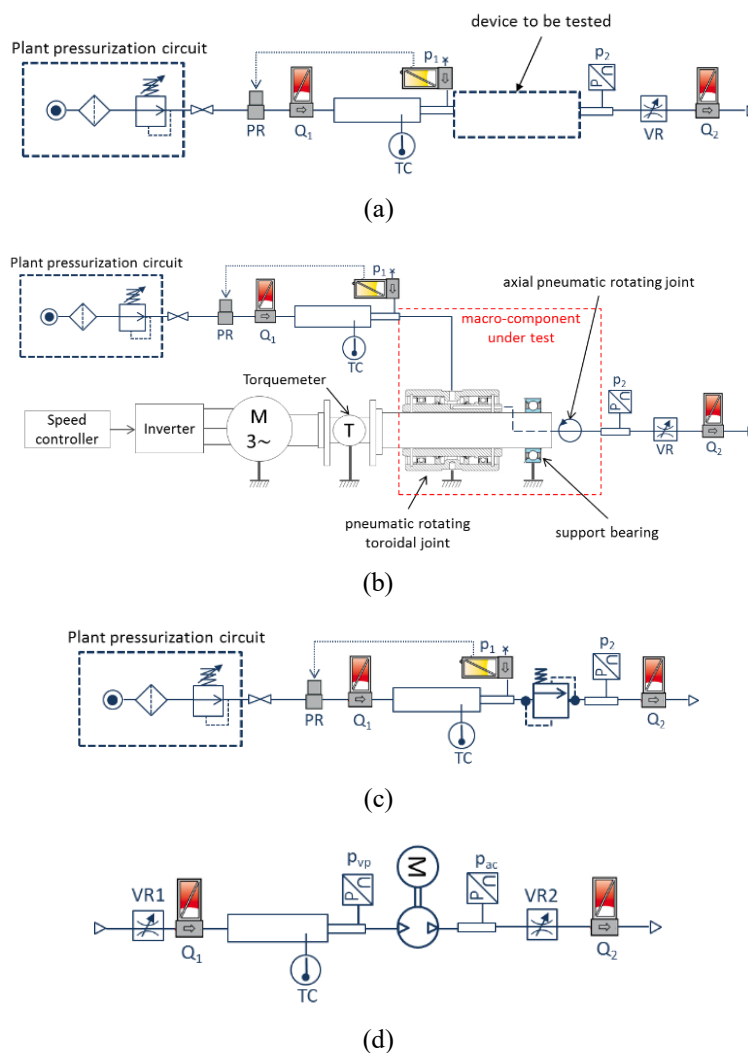


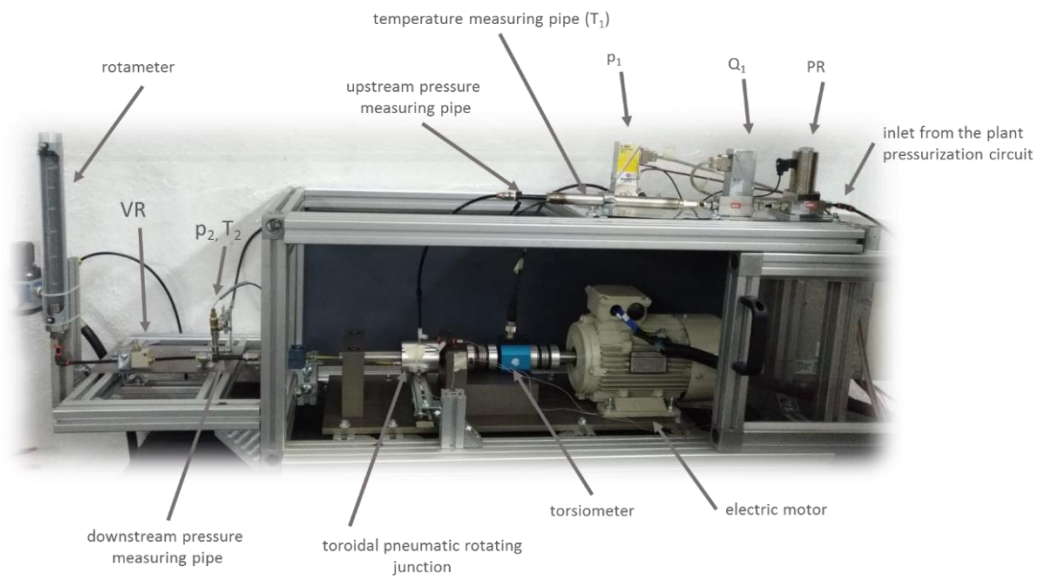
Figure 2.33: Test-bench layouts compliant with ISO 6358 [273] built to test several pneumatic components of the system (a), the toroidal pneumatic rotating joint under operating conditions (b), and additional layouts set-up to test an on-wheel deflation valve and a check valve (c) and the compressor/vacuum pump unit (d).

component under test is connected through a pipe to the inlet port of the rotoric part of the second axial pneumatic joint. Finally, the outlet of the second pneumatic joint is connected to the second measuring tube. All the components between the upstream measuring pipe and the downstream measuring pipe are considered as part of the component under test, as these parts are necessary in order to measure the characteristic of the component when it is rotating.

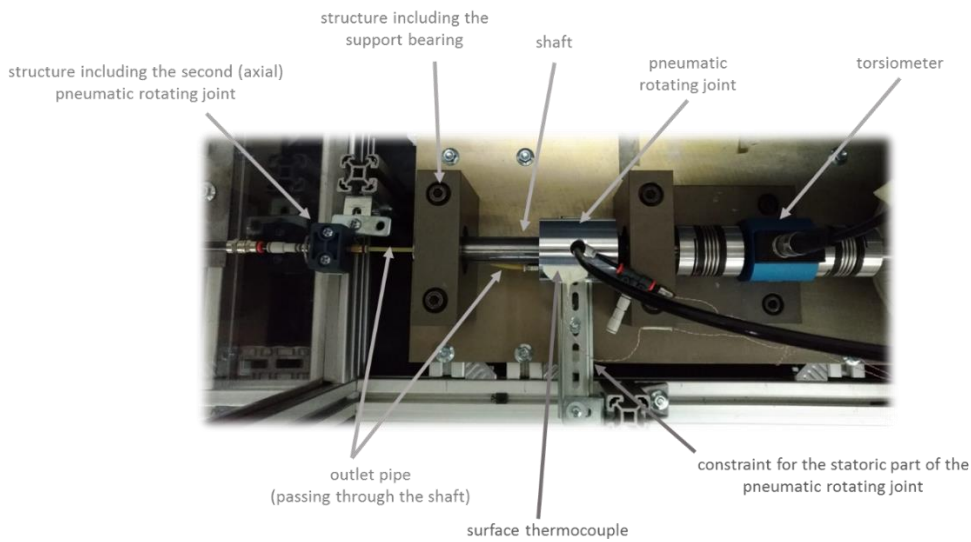
This layout allowed the characterization of the mechanical losses when the joint is rotating at different speed and with the inner seals pressurized at different pressure levels, as well as the pressure-flow characteristic to be obtained under rotating conditions. During these tests, additional thermocouples were added to measure the surface temperature of the statoric part, and the air temperature inside the sealed channel between the stator and the rotor and at the outlet of the second rotating joint. These additional measurements are used to monitor the working condition of the component. In particular, it was found out during preliminary tests that the component tends to reach a different thermal steady state condition for each pressure-flow-speed combination, and therefore the additional temperature measurements were useful to determine that the thermal transients were concluded before starting a measurement. Measurements are therefore performed at steady-state conditions. Additionally, monitoring the temperatures was used to check the health status of the inner parts, as a deterioration of the seals or of the bearing was expected to increase the temperatures of the component.

Using the same sensors as those used for the ISO 6358 configuration, different test layouts have been set-up in order to run also other specific tests. As an example, Fig. 2.33c shows the test-bench configuration used to test relief valves and similar components, while Fig. 2.33d shows the set-up used to carry out some characterizations of the compressor/vacuum pump unit. Concerning Figure 2.33c, the component to be tested is an in-line pressure regulating valve, which has been tested with the outlet port open to the atmosphere, i.e. with respect to the layout of Fig. 2.33a the final variable restrictor VR is removed from the test bench. Referring to Figure 2.33d, the layout was also adapted to test the characteristic of the compressor/vacuum pump machine used in the system layout described above: for this purpose the upstream measuring pipe is open to the atmosphere (and not fed with compressed air as in the other presented cases), and a variable restrictor (VR1) is added upstream the first measuring tube in order to simulate throttling at the compressor inlet. A second variable restrictor at the end of the second measuring pipe instead is used to simulate a pneumatic load on the compressor outlet, i.e. a backpressure.

Finally, starting from the layout of Fig. 2.31, measurements were performed to characterize the entire system under working conditions. These measurements were run by adding a number of piezo-resistive pressure sensors and thermocouples to the system, as well as the abovementioned flowmeters. This configuration and the corresponding results are described later on (*Section 2.6.6*).



(a)



(b)

Figure 2.34: Test-bench built to test several pneumatic components of the system. The pictures show the configuration setup to test the toroidal pneumatic rotating joint under operating conditions: (a) main view (b) top view.

All the signals provided by the sensors have been acquired through a test-bench acquisition device based on a National Instruments cRIO-9039, on which an analog input board and a thermocouple input board are fit. Additionally, an analogic output board installed on the same cRIO is used to remotely control the inverter that actuates the electric motor. All the required functionalities, i.e. remote control of actuators, live reading of the measurements, data logging, etc., have been implemented in an software developed in Labview environment within the research group that have been involved in the ATPC project. Later, in the most advanced phases of the project, the same test-bed software functionalities have been implemented through Veristand, in order to increase the flexibility in the usage of the software itself and to easily add new functionalities to the software.

2.6.2 Compressor/vacuum pump and valves

The compressor/vacuum pump machine chosen to set-up the layout of Fig. 2.31 is an oil less piston compressor with PTFE piston rings that is able to work to up to 8 bar and to generate a maximum vacuum of 93%, with respect to the local atmospheric condition. This machine allows a proper operating characteristic of the ATPC system to be obtained, and it has a weight of 2.3 kg and an absorbed electric power of 233W at 8 bar. However, it should be considered that the actual working characteristics of the compressor/vacuum pump depend on the circuit, and especially on the sections of valves 7 and 8 in Fig. 2.31. In fact, valve 8 determines a possible throttling of the compressor intake flow, which could cause a reduction in the compressor flow-rate characteristics. On the other hand, valve 7 generates an increase in the backpressure to the outlet flow generated by the vacuum pump, thereby reducing the outlet flow-rate during deflation operations. For this reason, and in order to choose the two 3/2 electro valves, the compressor has been tested in the Fig. 2.33d layout by varying the section of the passages upstream and downstream of the compressor through two variable restrictors, and the results are shown in Figure 2.35. It should be noted that all the pressures are indicated as gauge values.

With reference to Fig. 2.35a, the characteristic of the vacuum pump is reported under different working conditions. Each curve in Fig. 2.35a is obtained for a specific value of the effective section area (reported in the legend) of variable restrictor VR2 (cf. Fig. 2.33d) placed downstream of the compressor (at the flow outlet port). Each point on a curve is obtained from a steady-state test with a certain upstream pressure, where this pressure is adjusted through variable restrictor VR1, placed upstream of the compressor itself, i.e. at the flow inlet port. The graph shows only a slight dependence of the flow rate characteristics on the section diameter of

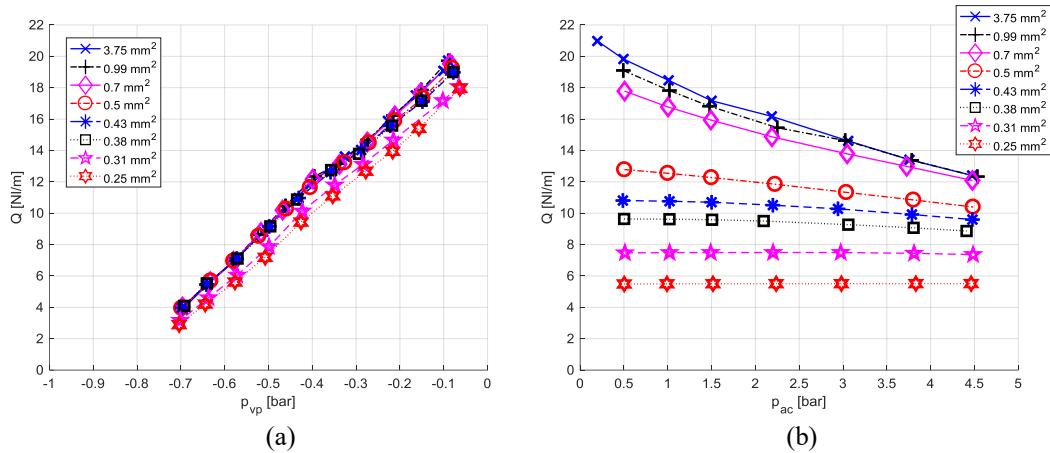


Figure 2.35: ATPC system: characteristics of the vacuum pump flow rate for several effective sections of the outlet port (a) and of the compressor for several sections of the intake port (b).

the downstream variable restrictor VR2, with negligible differences if the section is equal or larger than 0.38 mm².

Fig. 2.35b shows the flow-rate characteristics of the compressor obtained for different sections of variable restrictor VR1, placed upstream of the compressor itself. Each curve has been obtained by varying the pressure downstream of the compressor through variable restrictor VR2, placed at the flow outlet port. The flow has been stabilized for each combination of upstream section and downstream pressure, and the test has been recorded under steady-state conditions. The graph shows a significant influence of the obtained intake flow throttling at different sections. However, less difference can be noted among the curves if the effective flow section is larger than 0.7 mm².

Several commercially available electro-valves were tested on the ISO 6358 test-bench (cf. Fig 2.33a), including those with the smallest flow section and lightest weight, in order to individuate, for each of the ideal valves in Fig. 2.31, the lightest commercial valve with a suitable flow section. A solenoid valve was chosen for the item indicated as valve 7 in Fig. 2.31, which has an effective flow section of 0.57 mm² in choked flow conditions at an upstream pressure of 4 bar (gauge), and a geometric area of 1.77 mm². Similarly, for item 8 in Fig. 2.31, the selected solenoid valve has an effective flow section with an area of 3.8 mm² in choked flow conditions with an upstream pressure of 5 bar (gauge) and a geometric area of 7 mm².

All the other components along the line, and especially electro-valves 3, determine the pressure drop along the line. The larger this pressure drop is, the

higher the pressure at the compressor outlet and therefore the smaller the compressor flow rate. Choosing valves with a large section area has a negative effect, in terms of an increase in the system weight. Similarly, large diameters of all the passages and pipes decrease the distributed head losses, but increase the complexity of the integration of the system on-board. Therefore, an efficient system design has to take into account these aspects. The pressure drop along the line also affects the working conditions in deflation operations, since the higher the pressure drop is, the lower the vacuum level generated just upstream of the deflation valve (at the same vacuum level as the vacuum pump port) and therefore the lower the force acting to open the valve itself.

For this purpose, various commercial components have been tested in order to provide valuable data to choose the electro-valves and pipes. Similarly, tests were performed in order to characterize some preliminary designs for the on-purpose components, before validating the final design and setting up the prototype. When considering the whole line, from the compressor to a tire, the total pressure drop on the final prototype was quantified 1 bar as a maximum during normal inflation operations, where the maximum pressure drop was obtained for the lowest tire pressure. Considering that the range of pressure allowed in the tire is 1.8-3.2 bar, the maximum pressure downstream of the compressor ranges from between 2.8 bar and 3.8 bar in real working conditions. Therefore, the performance of the compressor was maintained in the high range for the flow rate, with a measured air flow rate, during inflation operations, of around 12.5-14 NL/min. This result is obtained with 0.85 mm diameter line control valves (item 3 in Fig. 2.31) of the effective section area.

2.6.3 On-wheel deflation valve

In order to make the system fail safe, the presence of a valve that is able to decouple the tire volume from the upstream environment is fundamental. This component is critical, due to its function, and it has to be placed in a protected position, but as close as possible to the on-rim connection port, in order to minimize the risk of failure downstream of the valve itself. It was decided to place the valve unit directly on the wheel, but this requires that it is opened only by means of pressure signals, in order to avoid the need for solenoids and electrical connections on the wheel. At the same time, in order to avoid an increase in the complexity of the design of the wheel-end components, a single duct is used to both provide the pressure signals that actuates the valves and to transport the incoming or outgoing flow rate from the tire. In the layout reported in Figure 2.31, two simple poppet-spring valves compose the on-wheel valve assembly (i.e., items 4.1 and 4.2). This design has resulted to be economic, robust, reliable and extremely simple.

The task of this valve unit is to ensure a disconnection of the tire volume from the upstream line when the system is not actuated, while allowing fluid connection when the system is actuated for inflation or deflation. The cracking pressure p_{def}^* of the deflation valve (item 4.2 in Fig. 2.31) is defined in order to determine the opening of the deflation valve only when a vacuum pressure (lower than atmospheric pressure, i.e. vacuum pressure is negative in Eqs. 2.39-2.43 as it is expressed in terms of gauge pressure) is realized upstream of the valve assembly 4 (cf. Figure 2.31). This ensures that the valve will remain closed if the central part of the system and the tire line are at atmospheric pressure or higher.

The p_{def}^* pressure setting of this valve determines the working range of the system. As p_{tire} is the pressure inside the tire and $p_{vacuum} = -0.8$ bar is the maximum vacuum under the actual working conditions (i.e., the minimum absolute pressure, which is reported as a negative value as it is expressed of in terms gauge pressure) upstream of valve group 4, the p_{def}^* pressure determines the minimum pressure at which it is possible to deflate the tire, that is:

$$p_{tire,def\ min} = p_{def}^* + p_{vacuum} \quad \text{Eq. 2.39}$$

As a consequence, the useful pressure range for the proper functioning of the system is:

$$p_{tire,def\ min} < p_{tire} < p_{def}^* \quad \text{Eq. 2.40}$$

In order to take advantage of the flexibility provided by the system, the working range of the system should be as close as possible to the tire working range between the minimum inflation pressure, $p_{tire,min}$, and the maximum inflation pressure, $p_{tire,max}$, as indicated by the tire manufacturer. The pressure setting of deflation valve 4.2 is therefore chosen in the interval

$$p_{tire,min} - p_{vacuum} < p_{def}^* < p_{tire,max} \quad \text{Eq. 2.41}$$

and depends on the level of vacuum that can be generated. In the specific case of the considered tire, the useful tire range, indicated by the tire manufacturer, is $1.8 \text{ bar} < p_{tire} < 3.2 \text{ bar}$, while the nominal inflation pressure, indicated by the vehicle manufacturer, is $p_{tire} = 2.2 \text{ bar}$. The cracking pressure of the deflation valve is chosen equal to 3 bar if the maximum vacuum is $p_{vacuum} = -0.8 \text{ bar}$, and the system can therefore be used in the $2.2 \text{ bar} < p_{tire} < 3 \text{ bar}$ range. It should be noted that this range is considered sufficient to obtain real advantages when using the system on the target application: in general, it is not advisable to work in the low-end of the tire working pressure range, while it would generally be necessary to increase the pressure to obtain fuel economy advantages. However, the cracking pressure setting may change depending on the real characteristics of the valve.

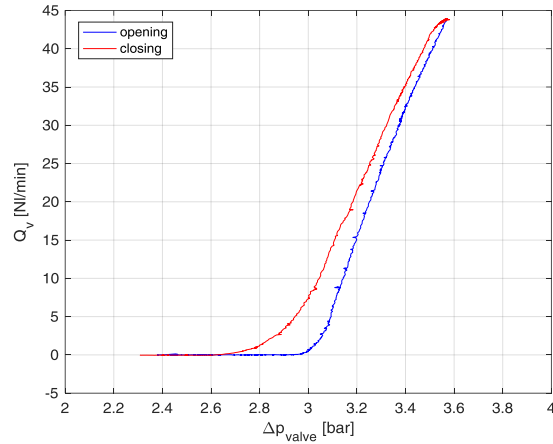


Figure 2.36: Characteristics of the designed on-wheel deflation valve.

Figure 2.36 shows the opening and closing characteristics of the on-wheel deflation valve designed at the Politecnico di Torino in order to realize the prototype of the ATPC system. The valve was designed as an in-line valve with a spherical poppet and a preloaded spring; it has a port diameter of 3 mm and a total inner length of the valve body of 12 mm. The spring pre-load is set to start the opening of the valve when the pressure prevailing on the sphere reaches $p_{def}^* = 3$ bar. A certain hysteresis can be noted when the valve is closing, which is typical of spring valves. It can be noted that the valve was designed to close during the returning stroke for a pressure of around 2.6 bar. This hysteresis actually extends the working range of the system: the minimum pressure that can be realized during a deflation operation is therefore:

$$p_{tire,def \min actual} = p_{def,closure}^* + p_{vacuum} \quad \text{Eq. 2.42}$$

where $p_{def,closure}^*$ is the pressure at which the valve closes in the real characteristic. As a consequence, $p_{tire,def \min actual} = 1.8$ bar in the studied case. Therefore, an accurate design of the valve spring allows the desired working range of the system to be obtained.

If $p_{tire} > p_{def}^*$, the valve is opened and the air pressurizes the line upstream of valve assembly 4. Although this situation increases friction and wear of the seals, as well as leakages, the system is still able to work properly and safely, since the line valve (item 3 in Figure 2.31) does not allow the tire volume to be connected to the central part of the system, unless an actuation is specifically commanded. This allows the maximum pressure at which the system can be operated to be increased, with a small increment in the friction on the pneumatic rotating joints (discussed

hereinafter). In the worst case, when the pipeline between line valve 3 and on-wheel assembly 4 is damaged, the pressure inside the tire would be limited to $p_{\text{tire}} = p_{\text{def}}^*$.

Finally, it should be considered that the valve closure at the end of an actuation is not always as gradual as in the complete characteristic shown in Fig. 2.36. In fact, when the vacuum source is switched off to stop deflation, the spring forces the valve to close almost instantaneously. A positive pressure can be provided to further force the closure of the valve.

2.6.4 Pneumatic rotating joints

In order to connect the stationary part of the system, i.e. the central group of electro-valves, to the wheel valve, pneumatic rotating junctions are needed. The kind and the shape of junction depends on the specific designed solution for the integration on-board. Two different kinds of rotating junctions have been considered for the ATPC system: for non-driving non-steering wheels, an as-small-as-possible rotating junction with axial intake and outlet ports in order to allow its integration within the wheel spindle; for driving wheels (steering or non-steering), a toroidal rotating joint to be installed on the traction half-shafts and with the outlet port parallel to the rotation axis. The designed solution avoids the need for drilled or hollow half-shafts, and this reduces the complexity of the design and of the installation. Both kinds of joints are required to have a single inlet and a single outlet, as each joint serves a single wheel.

Since the joints run with the wheels, they are expected to spin to up to 2000 rpm. Owing to the characteristics of the system, they need to work both at a high vacuum and with positive pressure, with a maximum pressure of around 4 bar so as to account for any tires that may work over a higher pressure working range. Finally, since the component will be located far from the brakes, no high thermal stress is expected, while the harshness of the installation environment, which can be subject to the presence of dust, mud, etc., should be considered. Low leakages and low resistant torques are additional requirements for a successful design.

For the axial rotating joint (non-driving non-steering wheels), an SMC commercial product has been applied to the prototype. Although it has not yet been certified for automotive applications, it has been found to satisfy the abovementioned requirements. It allows a flow of up to 136 Nl/min, and has a maximum allowed pressure of 10 bar and a maximum leakage of 1 l/min, spins up to 3000 rpm, with a negligible resistant torque, and it has an extremely compact design and a weight of only 25 g.

As far as the toroidal rotating joint is concerned, no commercial product was found on the market with a suitable performance to comply with the set requirements. As a consequence, a specific solution was designed and built as a prototype, as reported in Fig. 2.37. The component is basically made of an external statoric part (item 6 in Fig. 2.37) and an inner rotoric part (item 5 in Fig. 2.37), with bearings (1) and seals (2) to allow rotation and to transfer the air at the outlet port. An L-shaped duct connects the pressurized annular chamber to the outlet port of the joint, along a direction coaxial to the rotation axis. Special seals and lightweight materials allow correct operation to be obtained with rotating speeds of up to 3000 rpm and a maximum pressure of 10 bar. The double lip seals allow operation also under vacuum. The prototype has been tested under the test-bench configuration shown in Fig. 2.33b up to 1500 rpm and 4 bar upstream pressure, where the limits were chosen according to the expected limit conditions when the component is installed in the application for which it has been developed. It has to be underlined that in order to test this component, some additional pneumatic components are required, such as upstream and downstream flexible pipes to connect it to the measuring layout, as well a secondary pneumatic rotating joint between the outlet port of the component under test and the downstream pressure measuring pipe (c.f., *Section 2.6.1*). All these additional components cannot be avoided, and – as they are included between the upstream pressure measuring pipe and the downstream pressure measuring pipe – they have been considered as part of the component under test. Fig. 2.38 shows a comparison between the flow characteristics of the pneumatic rotating joint when it is measured in non-rotating conditions: Fig. 2.38a reports the characteristic measured in a layout where the additional components (upstream/downstream pipes, etc...) have been removed wherever it was possible, while Fig. 2.38b reports the characteristic measured when the component is installed in the layout of Fig. 2.33b and of Fig. 2.34. It can be observed that the choked flow rate with the maximum tested upstream pressure is about 84 l/min in Fig. 2.38a, while it is 56 l/min in Fig. 2.38b. Therefore, the effect introduced by the additional components added along the measuring layout is not negligible. Nevertheless, these additional components are unavoidable in order to install the device to be tested in the measuring layout. Additionally, it has to be mentioned that these additional components closely reproduce part of the upstream and downstream components that would be installed together with the pneumatic rotating joint for its implementation in the system layout.

For what concerns the tests performed when the component is under rotation, at first, it was observed that the component tends to reach a different steady-state temperature at different rotating speeds. Fig. 2.39a reports this behavior, where the temperatures reported in the graphs refer to the outer surface of the aluminum statoric part. This behavior can be explained considering that the higher is the speed, the higher are the friction between the seals and the inner surface of the aluminum rotoric part, and therefore the higher is the energy dissipated into heat. Nevertheless, with reference to Fig. 2.39b and 2.39c, the higher is the temperature of the joint, the

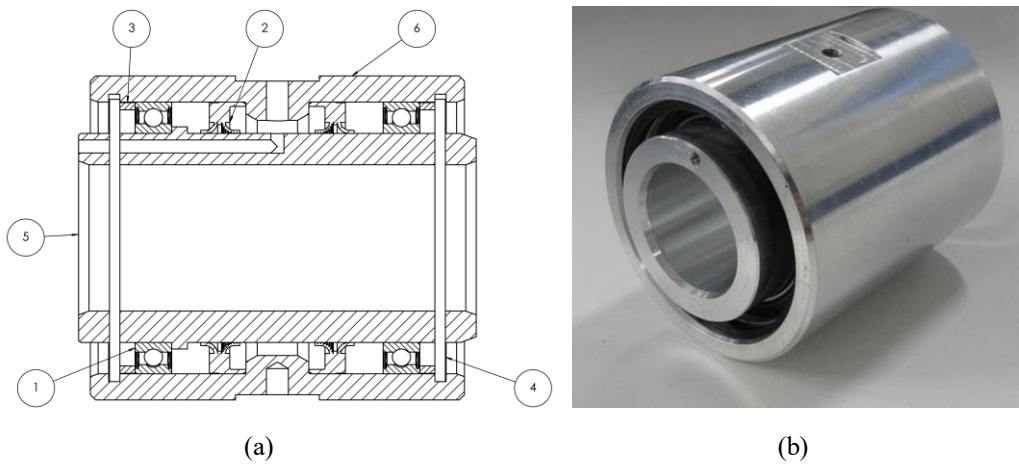


Figure 2.37: Toroidal pneumatic rotating joint of the ATPC system: (a) statoric part (6), rotoric part (5), bearings (1), seals (2), spacers (3) and seeger rings (4); (b) photograph of the prototype.

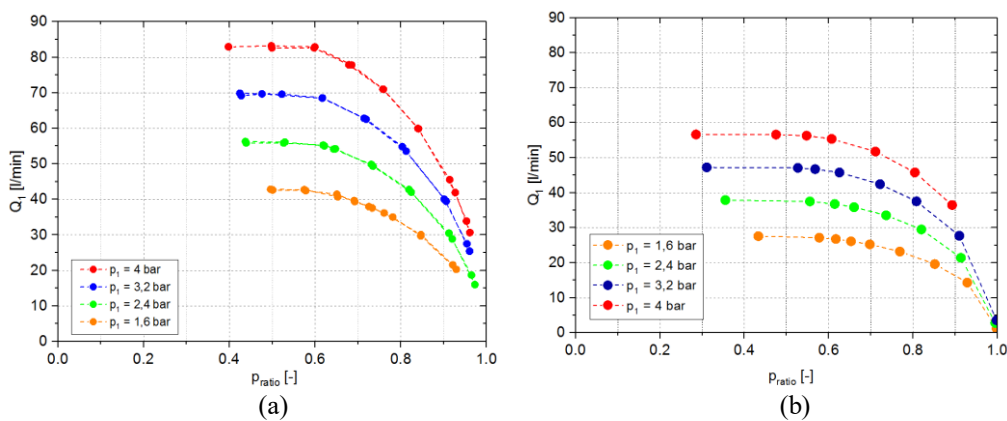


Figure 2.38: Volumetric flow rate characteristic of the pneumatic rotating joint of the ATPC system in non-rotating conditions: without any additional component upstream and downstream (a) and with the additional piping etc. that are needed to install it for measurements under rotating conditions (b).

lower is the mechanical resisting torque measured at the torsionmeter: this can be explained considering that the deformability of the seals increase as the temperature increases, and the resisting torque decreases as a consequence. In detail, Fig. 2.39b shows the torque measured at different speeds during the thermal transients reported in Fig. 2.39a, i.e. since the beginning of the test at ambient temperature till reaching the steady-state thermal condition. Moreover, Fig. 2.39c reports the average torque measured for each rotating speed after reaching the steady-state thermal behavior, as a function of the average steady-state temperature. The tests reported in Fig 2.39 refer to tests performed at zero-flow condition, and without pressurizing the inner chamber of the pneumatic rotating joint. The maximum steady-state resistant torque is 0.5 Nm, and it is measured at 500 rpm with an outer surface temperature of the joint of 55°C. The resistant torque as a function of temperature tends to decrease, and it is plausible that it would show an asymptotic value around 0.4 Nm for temperatures higher than 80 °C. Nevertheless, the measurement at 2000 rpm shows a behavior that is out of the expected trend, with the resistant torque increasing at higher temperature. This phenomenon was justified with a deterioration of the lubricant in the bearings of the pneumatic rotating joint due to temperatures that locally have overcome the applicability range for which the bearings are designed. This was also confirmed by dismounting the component and analyzing it after this phenomenon was highlighted. For the following tests, the component was reassembled with new bearings and seals in order to proceed with the testing activity, and the component was tested only up to 1500 rpm in order to avoid failures. Moreover, an updated version of the joint has been later designed, which involve different materials for improving heat dissipation and bearings that can work properly in a wider temperature range. The new component has not been tested yet.

The flow rate characteristic of the component was then tested under rotating conditions, at various speeds. Each measurement refers to the average steady state pressure and flow after the thermal transient. The results are reported in Fig. 2.40a-d in terms of mass flow rate as a function of the pressure ratio for various upstream pressure values. Finally, Fig. 2.40e reports the choked mass flow as a function of the rotating speed for various upstream pressure levels: it can be observed that the choked flow decreases when the component is rotating with respect to the values measured without putting the component under rotation. Nevertheless, spinning the joint between 500 and 1500 rpm the effect on the choked flow is only minor, with the flow slightly decreasing as the speed increases.

For the various rotating speeds and pressure conditions, also the steady state resistant torque was evaluated, and the results obtained at 500 rpm and 1500 rpm are reported in Fig. 2.41, for various upstream pressure levels and various values of

pressure ratios through the joint. The graphs show that the resisting torque does not vary significantly with the pressure ratio, while it tends to increase with the upstream pressure, due to the increase in the vertical force acting on the seals.

The highest measured resisting torque is about 1.4 Nm at 500 rpm and 4 bar upstream pressure.

Leakages were evaluated as the difference in the flow rate measured by the two flow sensors in Fig. 2.33b, and they were found to be within the measurement accuracy (± 2.4 NI/min maximum for the leakage flow, when the inlet flow rate is 100 NI/min). The weight of the entire assembled component is about 400 g. It is worth mentioning that the two rotating joints (the toroidal and the axial ones) in the test-bench configuration shown in Fig. 2.33b are in series, and the measured losses are therefore due to both junctions. However, the losses of the axial joints are known, as they are declared by the manufacturer, and are considered negligible

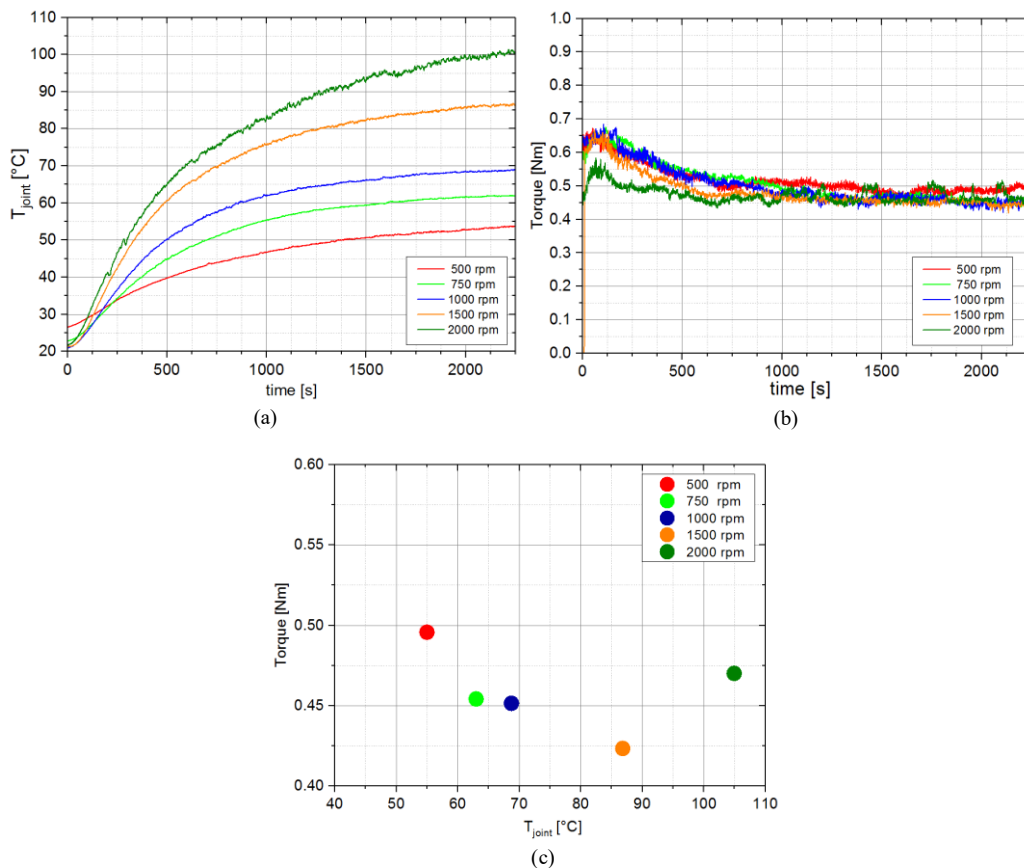


Figure 2.39: Time evolution of external surface temperature (a) and resistant torque (b) measured on the pneumatic rotating joint of the ATPC system, without putting the inner sealed chamber under pressure; steady state torque plotted as a function of the steady state temperature (c).

(both friction losses and flow leakages, since the flow leakages are declared as a maximum 0.1 Nl/min over the tested working range, i.e. up to 4 bar). Moreover, the measured resistant torque also includes the resistance of the rotating shaft support bearing.

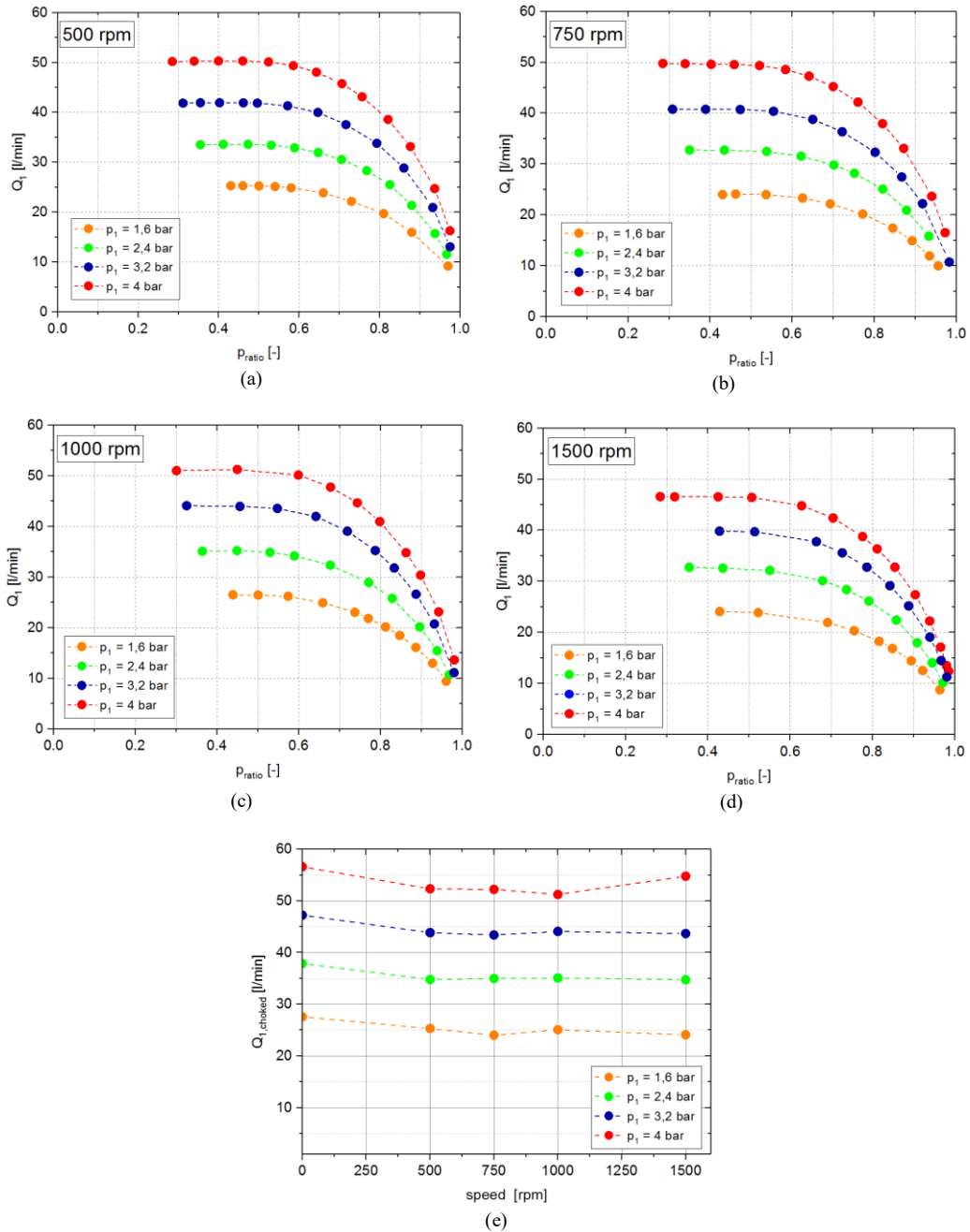


Figure 2.40: Pressure-flow characteristic of the pneumatic rotating joint of the ATPC system at various rotating speeds (a-d) and choked flow-rate as a function of rotating speed (e).

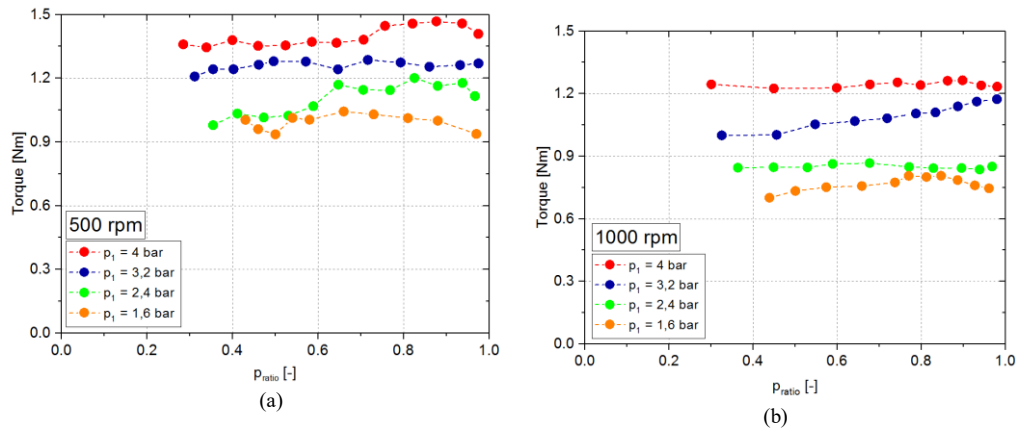


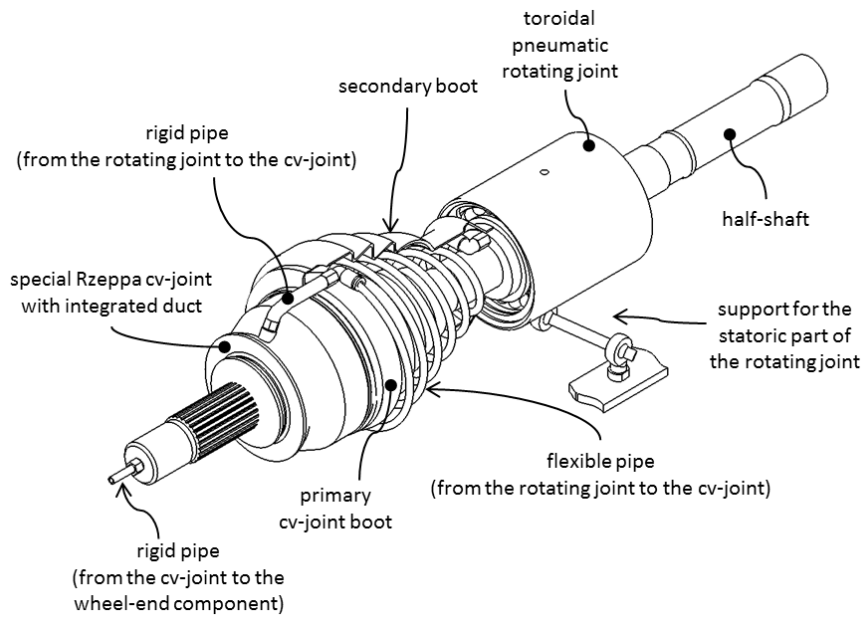
Figure 2.41: Resisting torque measured on the pneumatic rotating joint of the ATPC system as a function of the pressure ratio through the joint, for various inlet pressure levels, at 500 rpm (a) and 1000 rpm (b).

2.6.5 Integration of the system on-board

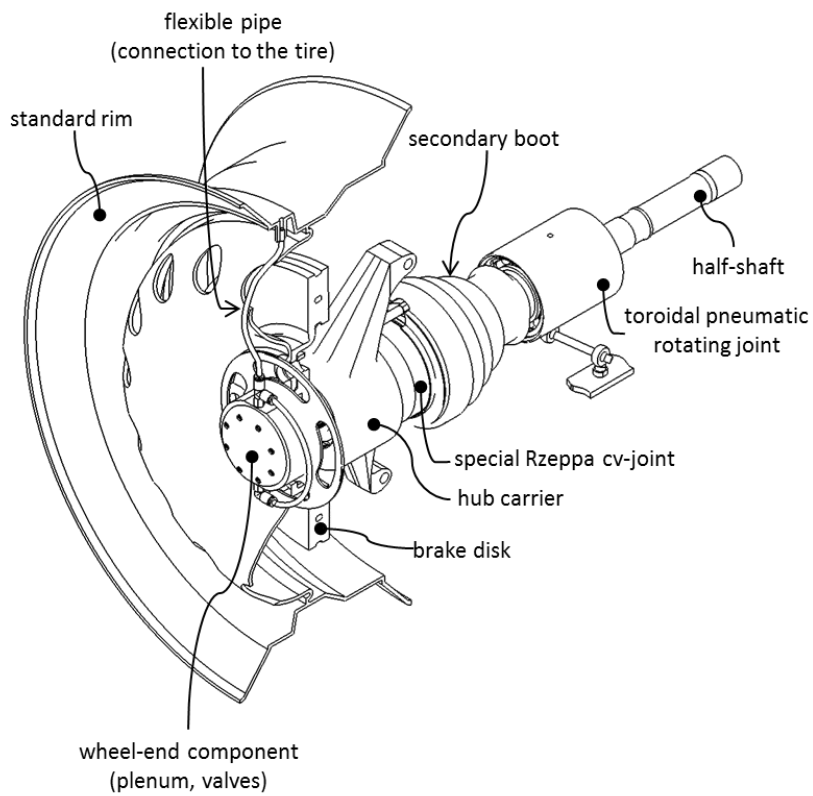
One of the aims of the study discussed in this *Section* is to achieve a design that could easily be integrated in standard wheel-end mechanical parts.

A standard driving wheel-end for a driving (and possibly steering) wheel for light-duty passenger applications usually includes: a Rzeppa constant velocity (cv) joint that transfers the torque from the half-shaft to the wheel-hub through a ribbed profile, where the hub is supported by a bearing or a bearing unit, whose external race is forced into a bore obtained within a hub carrier. The hub carrier also supports suspension components, as well as the braking cylinders-pad unit and the steering arm. The brake disc and the rim, on which a tubeless tire is installed, are fixed to the hub by means of screws.

The designed solution is presented in Fig. 2.42, where the figure does not represent the central part of the system: with reference to Figure 2.31, only the components downstream of electro-valves 3 are pictured in Fig. 2.42. The design involves the presence of a toroidal rotating pneumatic joint installed on the half-shaft, and of a special Rzeppa cv-joint, modified in order to host a through-conduit within the outer race and the output shaft. The connection between the pneumatic rotating joint and the conduit integral with the cv-joint is realized by means of a flexible pipe to ensure relative motion within the parts. The flexible pipe is helicoid-shaped, so that it can be wrapped around the cv-joint boot. This shape allows the



(a)



(b)

Figure 2.42: Integration of the ATPC system in the wheel-end of a driving wheel: assembly of the parts from the toroidal pneumatic joint to the cv-joint (a) and the wheel-end components (b).

required extendibility to be reached with a reduced radial displacement when the tube is subject to centrifugal forces due to rotation, therefore reducing the risk of damaging the tube itself. This pipe should be made of nylon, polyurethane or of any suitable plastic material that is able to provide the required mechanical properties (flexibility, superficial strength, etc...). Since the pipe should be placed close to the brakes and in a location that is usually exposed to environmental agents and dirt, the thermal properties and resistance to corrosion and chemical agents should also be considered when choosing the material of the pipe. The inlet port of the conduit integral with the cv-joint is connected to a rigid pipe, suitably shaped so that it can be adapted to the available space. A secondary boot is added as a cover for the pipe and the related connections, both as a protection device and to constrain the radial deformation of the pipe.

Two variations were designed for the wheel-end components and are described in more detail in [251, 274]: one is related to the installation of the system on a standard rim, while the other involves the realization of a special rim that directly integrates the wheel-end valves and the final ducts. Figure 2.42b reports the first of the two cases, where a special component, installed on the outer surface of the rim, integrates the on-wheel valve seats and an air chamber (plenum) and realizes the connection with the outlet port of the conduit integral with the cv-joint.

The outlet of the conduit within the cv-joint is connected to the air plenum through a rigid pipe. The wheel-end component hosts a dismountable insert and O-rings, which allow the pneumatic connection with the rigid pipe to be realized. In order to allow the wheel mounting and dismounting operations, and the assembly of the system itself, the wheel-end component has a dismountable cover. There is no relative motion between the rigid pipe integral with the cv-joint and the rim. The wheel-end component is connected to the port on the rim through a flexible hose, which can be connected to a special-purpose wheel valve that integrates this access, as well as to the usual port with a one-way valve to allow manual operations. The final pipe and the wheel-end component can be protected by means of a standard rim cover.

A non-driving wheel-end includes a stationary spindle, which is fixed to the suspension. A bearing is forced onto the spindle and supports the rotating wheel hub. The brake disk, or brake drum, and the rim are secured to the hub by means of screwed connections. The absence of a driving axle allows the adoption of the abovementioned axial pneumatic rotating joint, which has a cylindrical shape and can easily be integrated in the spindle. The solution is shown in Fig. 2.43. The outlet port of the rotoric part of the pneumatic joint is connected to a rigid pipe that rotates inside a through-hole drilled along the spindle axis and is supported by a small

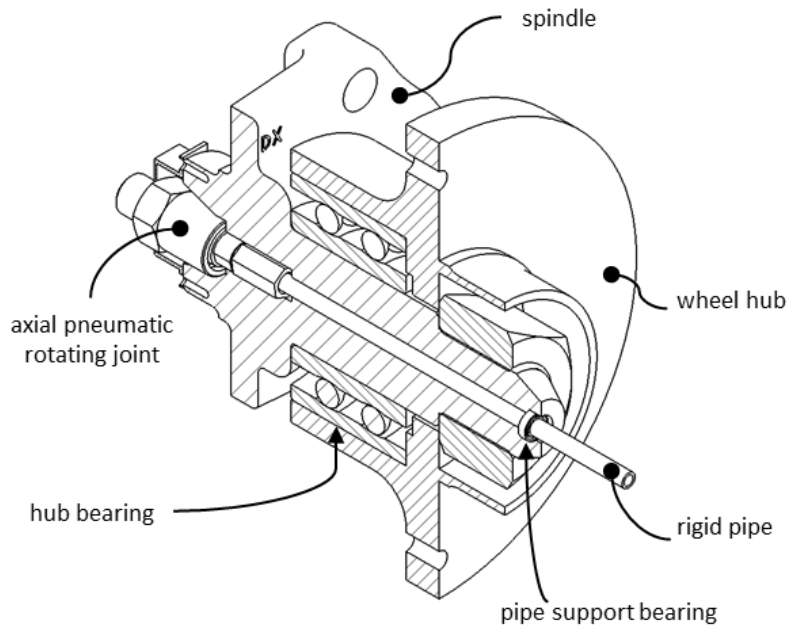


Figure 2.43: Integration of the ATPC system in the wheel-end components of a non-driving wheel.

bearing at the spindle extremity. The connection between this rigid hose and the wheel-end component is the same as that of a front driving wheel. As in the previous case, the wheel-end components integrate the valve seats to host the two wheel-end valves and the plenum, which is closed by a sealed cover.

Figs. 2.44-2.46 show some pictures of the prototype that has been set-up. In particular, Fig. 2.44 shows the solution for a front driving wheel with aluminum alloy rim, with evidence on the pneumatic toroidal rotating joint, on the wheel-end valve module integrated in the rim and on the outlet to the tire volume of the air duct integrated in the rim itself. Fig. 2.45 shows the solution for a rear non-driving wheel, with the axial rotating joint integrated within the spindle. Fig. 2.45 also refers to the installation of this solution on a standard steel rim, with the wheel-end valve module installed on the outer surface of the tire.

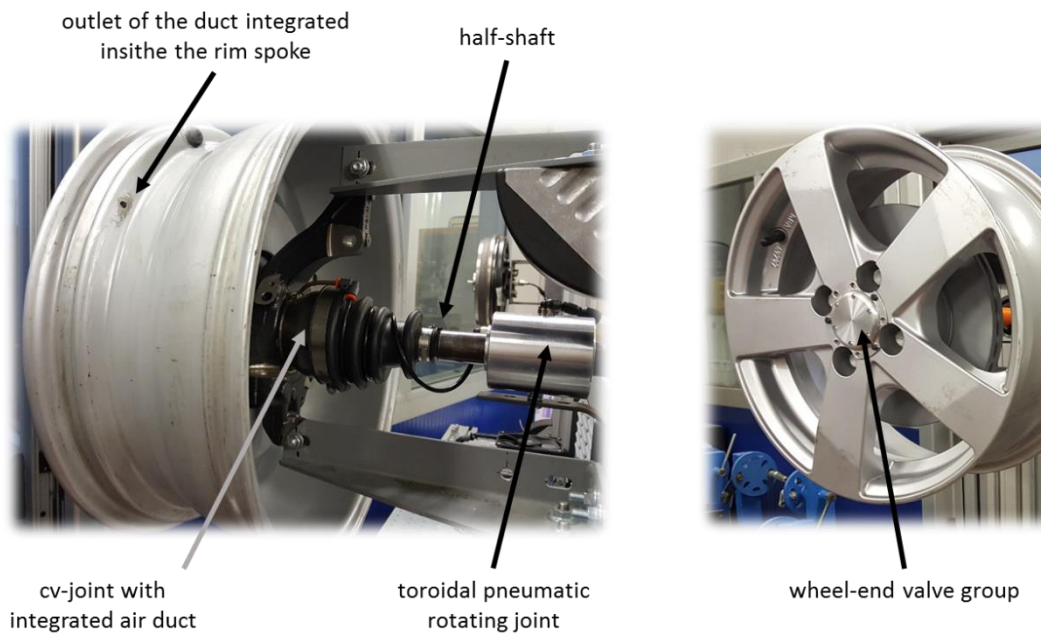


Figure 2.44: Integration of the ATPC system in the wheel-end components of a driving wheel: photo of the prototype showing the solution with wheel-end valves and the final duct integrated into an aluminum alloy wheel.

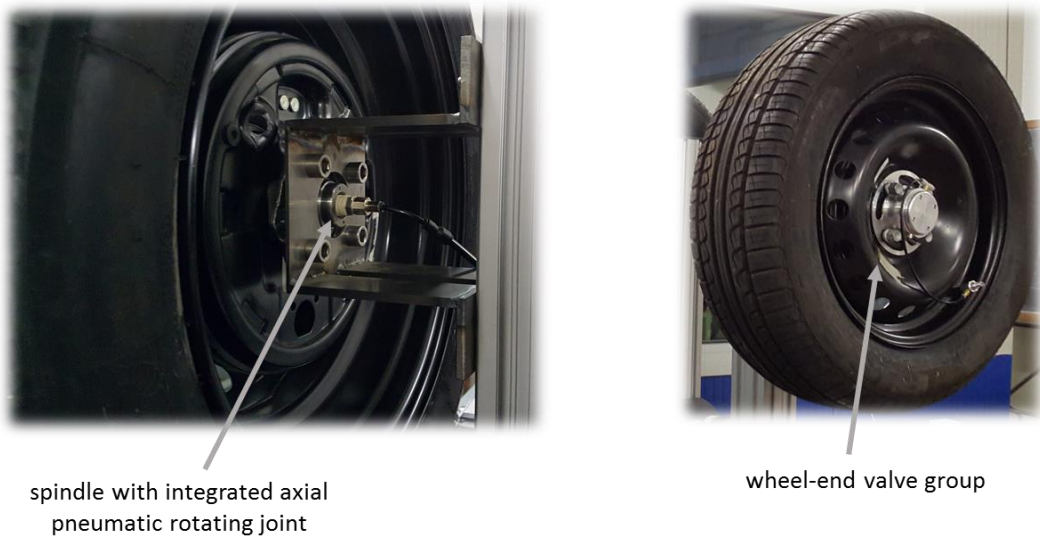


Figure 2.45: Integration of the ATPC system in the wheel-end components of a non-driving wheel: photo of the prototype showing the solution with wheel-end valves and the final duct fit on the external surface of a steel rim.

Fig. 2.46a shows the complete test-bench set-up for testing the system. A box has been built which integrates all the electronic hardware needed for the test bench, as well as the central actuators module of the ATPC system, i.e. the group including the compressor/vacuum pump, the central valves and the sensor(s). The electronic hardware is based on a National Instrument cRIO with input/output boards that manage analogic inputs and outputs, digital outputs and thermocouples inputs. The inputs and outputs channels are partially used internally in the box to receive data from the actuators unit and to command the compressors and the valves. The remaining channels are available on the front panel of the box, and can be used for additional sensors or actuators that can be needed during laboratory testing activities. The box can be powered alternatively at 230 V AC for usage in the laboratory, or at 12V DC for possible future on-board testing. Finally, some CAN input channels are also available for communication with on-board TPMS and for retrieving data from the main CAN network. More in detail, the inputs from the CAN network can be used for estimating the vehicle mass in the current running conditions, as well as load distribution among the wheels, and to calculate the optimal tire pressure on each axle according to logics oriented to fuel saving (as discussed in *Section 2.3*) and/or according to some algorithms meant to improve vehicle handling and stability. Specifically, an algorithm for real-time estimation of the vehicle loading condition and a second algorithm for setting tire pressure in order to improve vehicle handling have been also developed as a side-project, filed as patent applications [246, 275], implemented using the same electronic hardware here presented and tested in a Hardware-in-the-Loop environment with on-board data acquisitions. The development and testing of these algorithms is not discussed in this thesis work as they are outside of the scope of this dissertation, focused on the potential impact of some specific automotive technologies on energetics and environmental aspects.

Finally, Fig. 2.46b shows a CAD of the actuators block designed with a compact packaging for future application on-board.

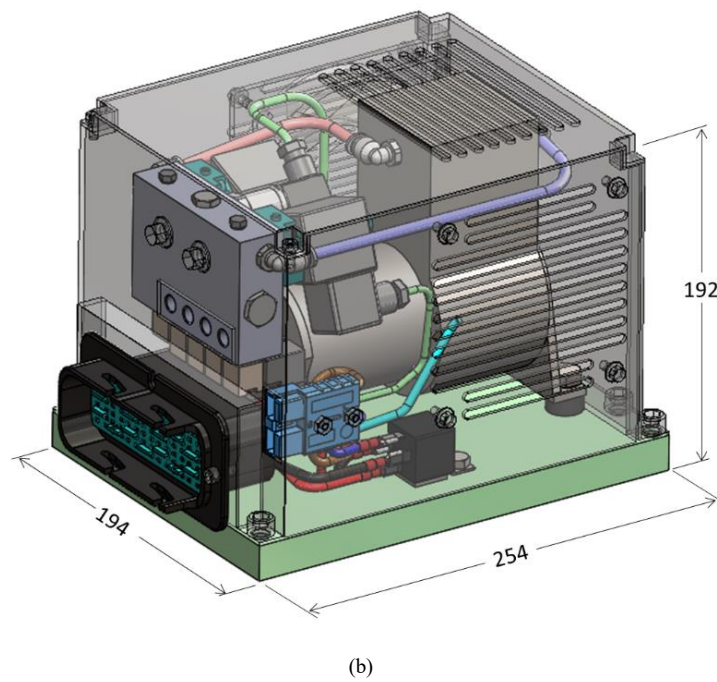
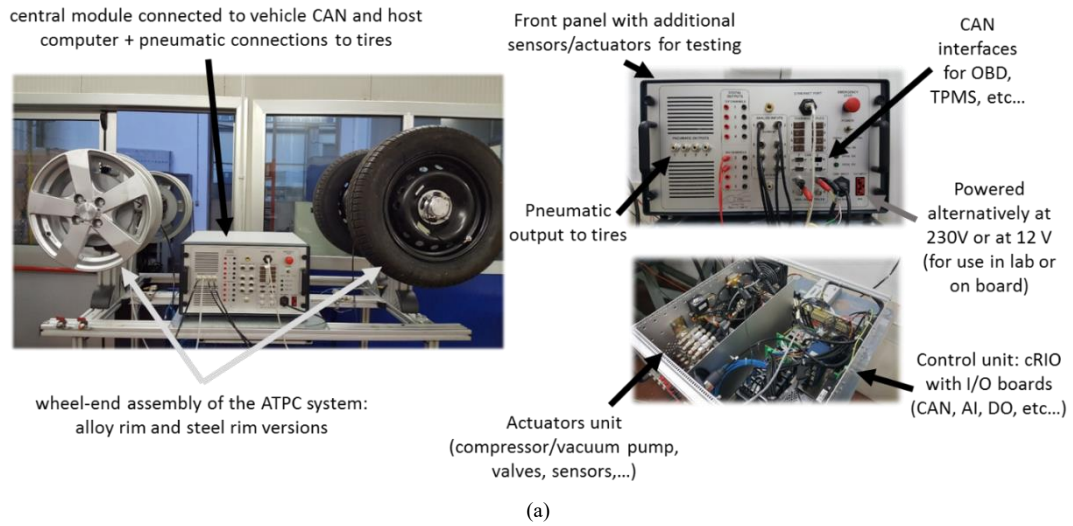


Figure 2.46: System prototype and test-bench used to test the performance of the complete ATPC system (a) and CAD of the final version of the system with the overall dimensions (b). Dimensions are reported in mm.

2.6.6 Performance of the ATPC system for passenger cars: characterization of the inflation and deflation times

The performance of the entire ATPC system prototype has been tested on a test bench, whose layout is represented in Figure 2.47. Pressure sensors were placed at the inlet and at the outlet of the compressor (p_{vp} and p_{ac} , respectively), upstream of the line valve (p_{blv}), upstream of the wheel valve (p_{bwv}), downstream of the wheel valve (p_{awv} , i.e. upstream of the tire inlet port) and inside the tire (p_{tire}). Temperature was also measured at the compressor outlet and inside the tire. Two Bronkhorst thermal mass flow meters were installed to measure the in-going flow to the tire during inflation operations (Q_{inf}) and outgoing from the tire during deflation operations (Q_{def}). The evolution of the tire pressure in time was measured during several actuations, and the actuation time needed to realize a desired pressure variation was evaluated.

Figure 2.48a shows the evolution of the tire pressure during the considered inflation tests. Several tests were repeated for different initial tire pressure levels within the working range of the system. Each test was performed by actuating the system till a higher pressure variation than 0.4 bar, with respect to the initial tire pressure, had been realized. Each test is reported as a blue solid curve in Fig. 2.48a. In the post-processing, each test was analyzed to calculate the actuation time needed to obtain smaller or equal pressure variations to the final one realized during the test. The pressure variation steps are indicated with red circles in Fig. 2.48a.

The results are shown in Fig. 2.48b as the actuation time needed to obtain a certain pressure variation; the pressure variation in time, with respect to the initial pressure, is reported and each curve refers to a different tire pressure at the beginning of the actuation (as reported in the legend). The system takes around 10 s to increase the tire pressure by 0.1 bar, and up to 43-48 s for a pressure variation of 0.4 bar. The graph shows a slight dependence of the actuation times on the initial tire pressure during inflation operations. This is because the compressor is working in a very narrow part of its characteristic. Fig. 2.48c shows the actual compressor working characteristic during the tested operating conditions; each set of points refers to a different test performed for a different initial tire pressure, and is represented with different shapes and colors (as reported in the legend). The highest actuation times are obtained for the highest initial tire pressure, since it corresponds to a higher compressor load for a given desired pressure variation. The results shown in Fig. 2.48 were obtained for the layout related to a non-steering and non-driving wheel, that is, when using the axial pneumatic rotating joint. Similar results were obtained for the layout of a driving steering wheel, but with slightly higher actuation times and a slightly greater dependence on the initial pressure, due to the

generally higher pressure drop along the complete line, as a result of the presence of the toroidal pneumatic rotating joint.

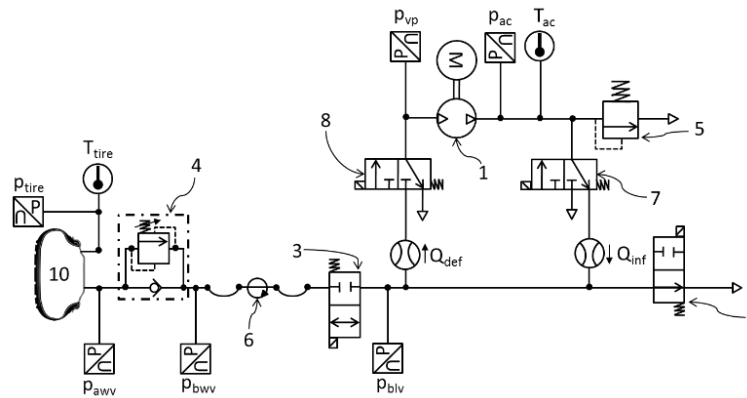


Figure 2.47: Test-bench configuration used to test the performance of the complete ATPC system.

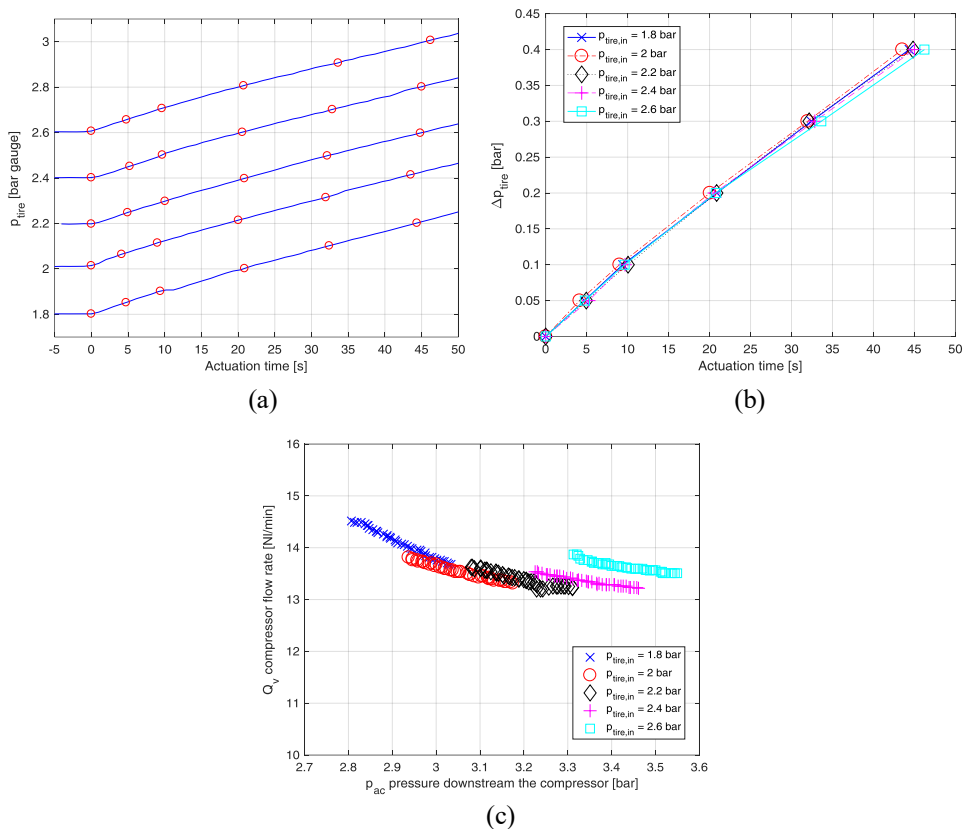


Figure 2.48: Inflation operations for the tested configuration of the ATPC system: tire pressure variation in time during the tested operations (a), tire pressure variations as a function of the actuation times (b) and actual compressor working characteristic in the considered operating conditions (c).

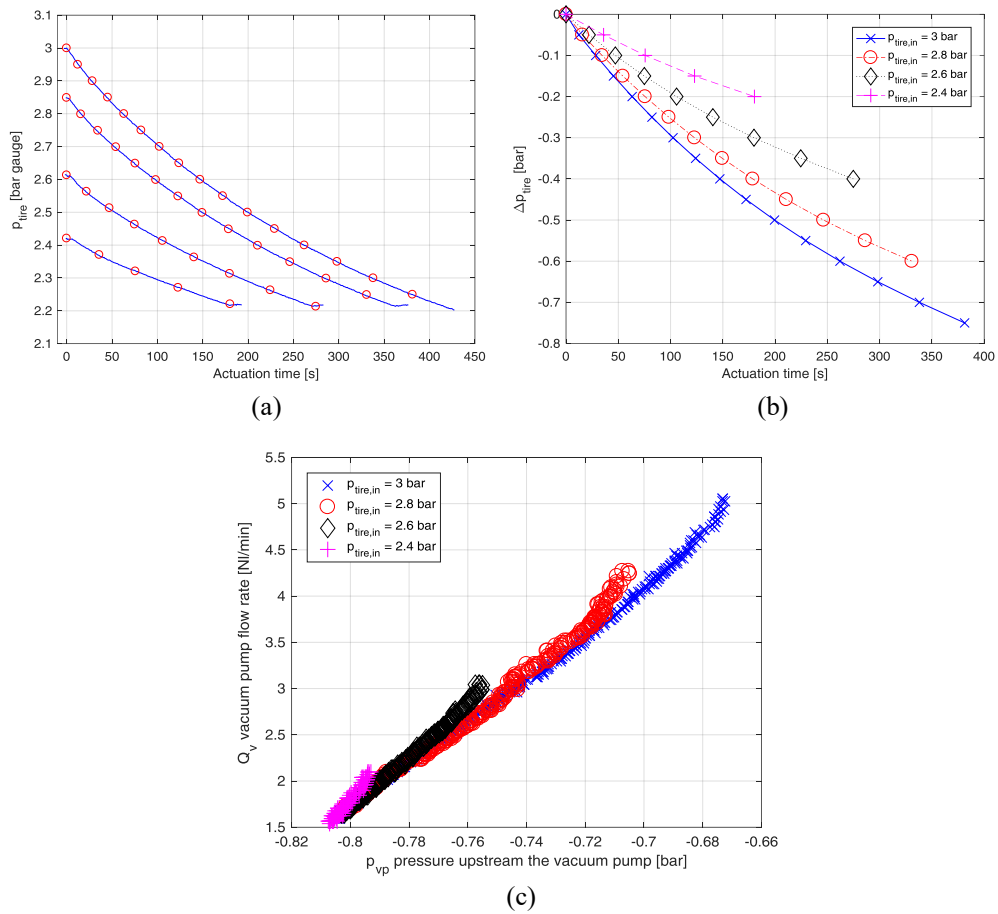


Figure 2.49: Deflation operations for the tested configuration of the ATPC system: tire pressure variation in time during the tested operations (a), tire pressure variations as a function of the actuation times (b) and actual vacuum pump working characterizing in the considered operating conditions (c).

Fig. 2.49 shows the results of similar tests performed to characterize the performance of the system during deflating operations. Fig. 2.49a reports the evolution in time of the tire pressure during a set of tests performed with different initial tire pressures, where each curve represents a different test and the red circles represent the pressure variation steps that were identified during the post-processing. Fig. 2.49b reports the pressure variation in time during an actuation, with respect to the in-tire pressure at the beginning of the actuation: each curve reports the results obtained for a test with a specific initial tire pressure (as reported in the legend). With reference to Fig. 2.49b, a high dependence of the actuation times on the initial tire pressure can be noted. In fact, the lower the tire pressure,

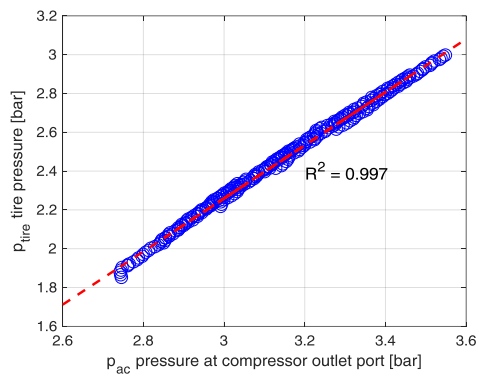
the higher the vacuum that is realized by the pump to maintain the force equilibrium necessary to keep the deflation valve open. According to the vacuum pump characteristics in Figure 2.35a, the higher the vacuum level (i.e., the lower the pressure at the vacuum port), the lower the vacuum pump flow rate. Achieving a pressure variation of 0.1 bar requires from 25 s, when the initial tire pressure is 3 bar, to 75 s, when the initial tire pressure is 2.4 bar. The actual vacuum pump characteristics in the tested working conditions for various tire pressures at the beginning of the actuation are depicted in Figure 2.49c. The results shown in Fig. 2.49 refer to the layout of a driving steering wheel, and similar results were obtained for a non-driving non-steering wheel.

2.6.7 Measuring tire pressure

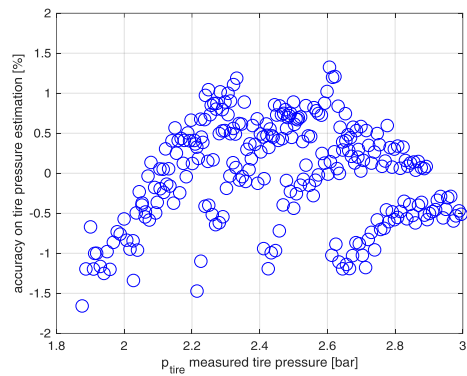
As previously discussed, if wired sensors are installed in the central part of the system, this solution requires an actuation when a measurement of the tire pressure is needed. This actuation allows the on-wheel valves to be opened, and therefore connects all the environments, from the compressor to the tire, in a continuous pneumatic line. Therefore, if the pressure drop along the line is known, the tire pressure can be estimated by measuring the pressure at a different point of the circuit.

This principle has been applied to the present system [251, 274]. For this purpose, the pressure drop along the line was characterized during the tests presented above. Figure 2.50a shows the result of this characterization: the tire pressure is plotted versus the pressure measured at the compressor outlet. This graph shows a very good linear correlation between the two quantities. The fitting coefficients of the linear interpolating function, reported with a dashed line in Fig. 2.50a, were calculated and applied to obtain an estimation of the tire pressure on the basis of the measured pressure at the compressor outlet. The estimated tire pressure is compared with the measured one in Fig. 2.50b and Fig. 2.50c: the estimation shows a root mean square error of 16 mbar when the measured pressure ranges between 1.8 and 3 bar, and the estimation accuracy ranges between -1.5% and 1.5%.

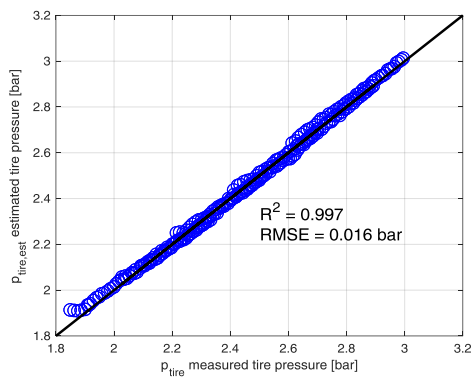
Similar results can also be obtained during deflation operations, if the tire pressure is correlated to the pressure measured upstream of the vacuum pump. This method can also be used to obtain feedback for a possible closed-loop actuation control of tire pressure.



(a)



(b)



(c)

Figure 2.50: Linear correlation between tire pressure and pressure measured at the compressor outlet port on the ATPC system (a), estimated and measured tire pressure (b) and accuracy of the tire pressure estimation (c).

2.7 Layout and on-board integration of the Advanced Central Tire Inflation System for commercial vehicles

Moving from the background developed on passenger cars, the layout of a system for autonomous management of tire pressure was also designed for commercial vehicles, as part of the project developed in collaboration with Iveco. The case studies of a light-duty commercial vehicle (LDV) and a heavy-duty commercial vehicle (HDV) were taken into account. This part of the study concerned the definition of the system layout and its integration on-board, while the detailed design and sizing of all the functional groups and sub-parts of the system has not been faced yet. Therefore, as this part of the project is still at a preliminary stage, the system or its components have not been prototyped nor tested yet, and also the design has to be considered as a preliminary one.

The layout of the system proposed for LDV and for the tractor of HDV is presented in Figure 2.51. The central part of the system, including the central manifold and the related valves (items 2, 3, 5, 7, 8, 9), as well as the compressor/vacuum pump (item 1) and the pneumatic rotating joints (item 6), is almost identical to the solution for passenger cars presented in *Section 2.6*. In the case presented in Figure 2.51a, as for the abovementioned case for passenger cars, the system is considered to be completely independent from other pneumatic systems that may be present on-board, therefore the system is represented with its own positive pressure source (item 1), which also serves as a vacuum pump. The electro-valves 7 and 8 connect the machine 1 to the central line, and allow to feed the central line with positive pressure for inflation operations, or to connect the same line to the vacuum source for deflation operations. Anyway, a pneumatic circuit is usually present on all HDVs, as well as on some LDVs: in this case an integration of the ACTIS (Advanced Central Tire Inflation System) with the existing circuits may be required, which can be obtained by eliminating from the layout of Figure 2.51a the item 1 and connecting the positive pressure intake port of the manifold to the main pneumatic line of the vehicle. In this latter case, a dedicated vacuum source is anyway likely to be needed for the ACTIS. This latter situation is depicted in Figure 2.51b: the 3/3 bistable electro-valve 17 is integrated in the manifold and connects the positive pressure source (from the main pneumatic circuit, through the dedicated 2/2 electro-valve 7') or the vacuum pump (item 1') to the central pressure line in the manifold. On both the positive pressure line and vacuum line two tanks are added (items 13 and 14) in order to maintain a minimum level of positive or negative pressure to properly feed the system whenever is required. Pressure in the two tanks is measured through dedicated pressure sensors (items 9' and 9'' in Fig. 2.51b). In both the cases, as for the system for passenger

cars, the pressure inside the tires is measured through a centralized sensor installed on the central manifold (item 9). In this design, a damping restrictor (item 15) is added in order to avoid pressure waves to be transmitted to the sensor.

For what concerns the valve groups in the terminal parts of the circuit, close to the tires, the solution designed for commercial vehicles differs significantly from the solution for passenger cars. The dedicated solution aims to solve two main issues that would arise if the design for passenger cars would be applied to commercial vehicles:

- in the design of Figure 2.31, the amplitude of the working pressure range (i.e., the difference between the maximum and the minimum pressure that can be operated by the system in normal working conditions) is limited by the maximum vacuum that can be generated, i.e. 1 bar maximum. It has been discussed in the previous sections as this solution is adequate for passenger cars. Anyway, the desired working pressure range for LDV is between 3.5 bar and 6 bar, while it is 4-10 bar for a HDV. Therefore the previous solution is not appropriate for these applications;
- in the solution for passenger cars, the deflation time is strongly limited by the equilibrium of the forces on the spool of valve 4.2, which changes as the pressure inside the tire decreases: given a certain vacuum level upstream of the valve, the flow area of the valve decreases as the pressure inside the tire decreases. If the deflation dynamics produced by that design is still adequate for the pressure variation dynamics in the case of passenger cars (c.f., *Section 2.8*), the same would not be satisfactory if applied to commercial vehicles.

Additionally, two different designs have been produced for single tires and for dual tires, considering that the traction wheels of trucks and of some commercial vans have dual tires (also named “twin tires”).

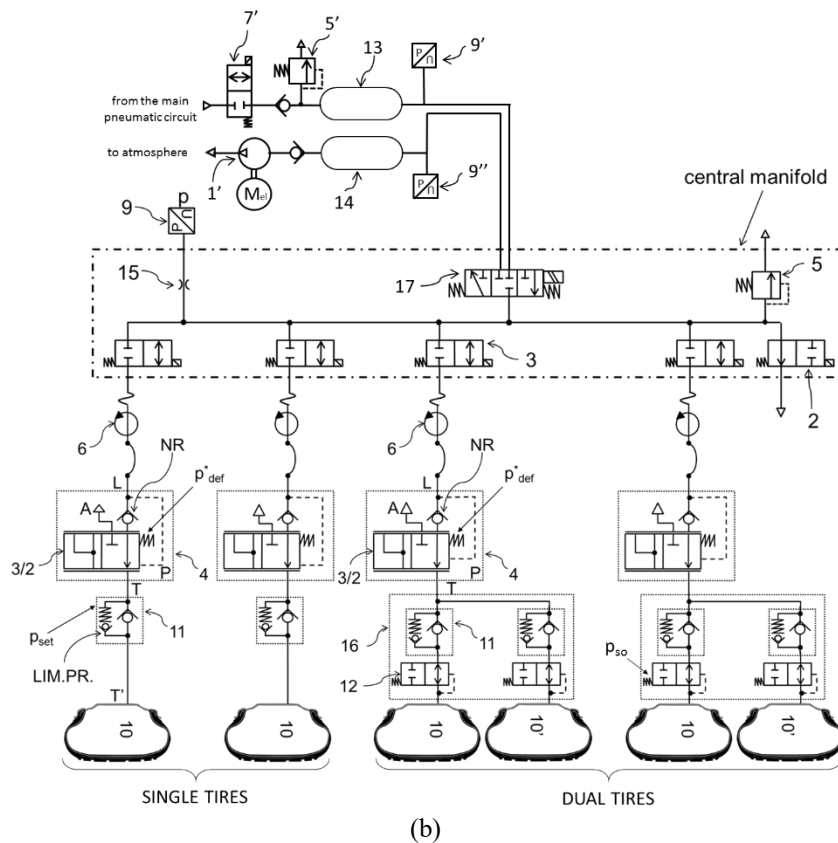
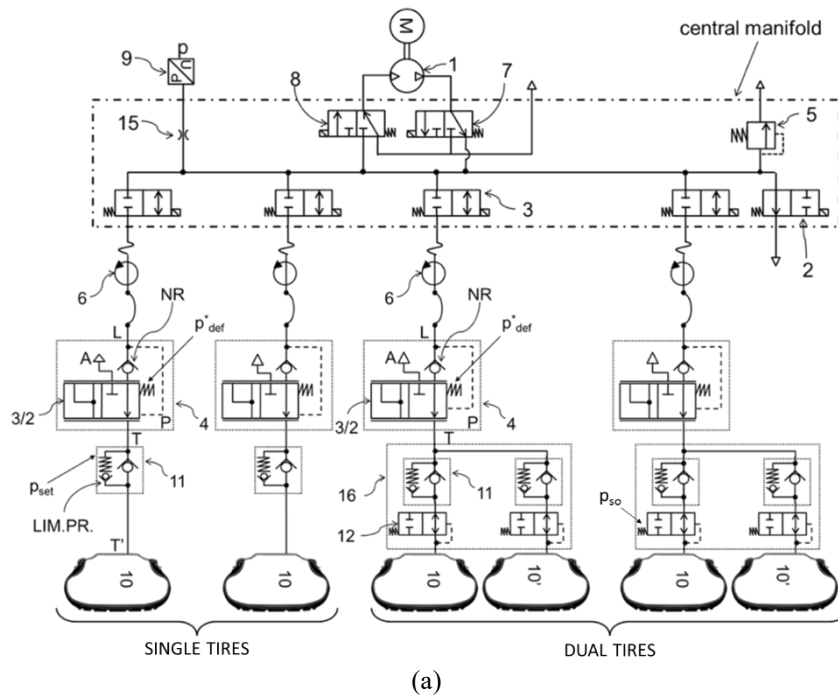


Figure 2.51: Schematic of the ACTIS system layout for the tractor of HDV and for LDV with rear dual tires: version with an independent source of compressed air source (a) and version integrated with the pre-existing on-board compressed air distribution line (b).

The wheel-end valve group is mainly composed by a 3/2 pneumatic valve (item 4) with vacuum piloting and a connection to the atmosphere, which serves as deflation valve, and a pressure limiter valve in parallel to a standard one-way valve (valve group 11). Valve 4 is a normally-open valve: the port L is normally connected to port T. At rest, the line upstream valve 4 is at ambient condition (due to the vent valve 2), and the preloaded spring (spring preload indicated in the figure as p_{def}^*) keeps the valve in the normally-open position, while the one way valve (NR) keeps the tire (port T) isolated from the line (port L). When the system is actuated for inflation, the valve keeps in the normal position so that the positive pressure flow from the main line can be fed to the tire. For deflation operations the vacuum pump is activated, therefore the pressure in the line upstream valve 4 (at port L) is $p_{\text{vacuum}} < p_{\text{amb}}$. This serves as piloting signal at port P, which opposes to the spring preload (p_{def}^*) and opens the 3/2 valve. The flow from the tire (T) to external environment (A) is allowed, while the flow to port L is blocked by the NR valve. The valve group 11 includes a standard one-way NR valve, and an in-line pressure limiter. The preload of the pressure limiter is set at the minimum allowed tire pressure (i.e. 4 bar on trucks, 3 bar on vans). During inflation, the flow from valve 4 (port T) to the tire (port T') is allowed in any case through the one-way valve. During deflation operation, the air flows from the tire (port T') to valve 4 (port T) through the pressure limiter, only if the pressure inside the tire (item 10) is higher than the pressure setting of the pressure limiter ($p_{\text{tire}} > p_{\text{set}}$). If tire pressure is lower than the pressure setting p_{set} , the tire cannot be further deflated by the system, while it can still be inflated.

Figure 2.52 shows a preliminary design of the valve group composed by valve 4 and the valve group 11. According to this design, valve 4 is a spool-spring proportional valve (item 4.1 in Figure 2.52): when the valve is piloted the spool is in an intermediate position between fully open and fully closed positions. The actual position of the spool is determined by the forces equilibrium on it, which depends on the valve geometry and on the pressures acting on it. The spool position will, in turn, determine the characteristic of the system during deflation operation. Also the other elements of the valve group have been designed in the form of poppet-spring valves, with the spring preloads calibrated according to the functional description above. Figure 2.52 shows how the functional schematic design was translated into a preliminary geometric model of the valve group. Such a geometric model has been further modified later on in order to allow the integration of the system with the wheel-end mechanics of the reference vehicles.

The geometry of valve 4, the forces equilibrium on it at various working conditions and the consequent characteristic during deflation have been deeply investigated through CFD simulations and the results have been used in order to

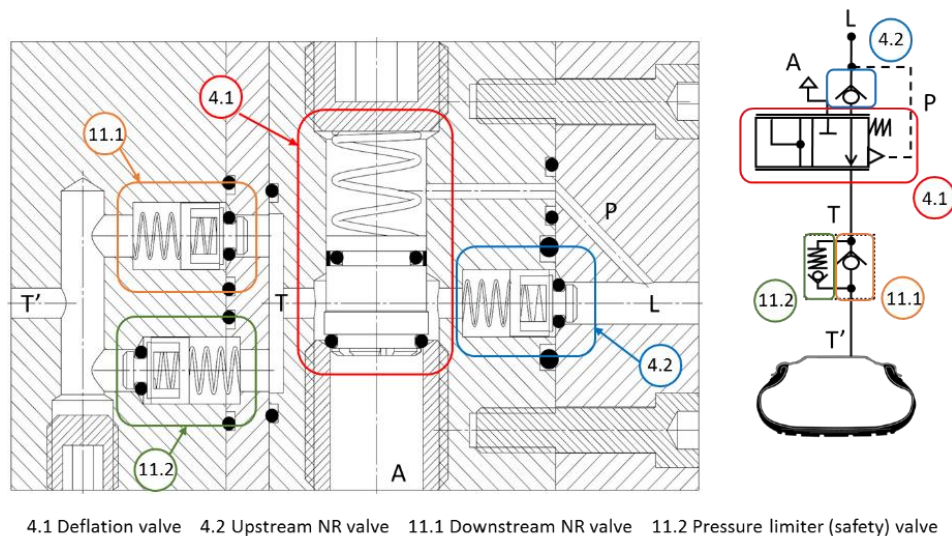


Figure 2.52: Preliminary design of the on-wheel valve group for single tires of LDV and HDV.

develop a 1D fluid-dynamic model of the valve group, to be integrated with the 1D model of the entire system. This part of the work has been developed by other members of the research group and therefore are not part of this dissertation. Nevertheless, some results of these simulations will be cited hereinafter where necessary for the sake of completeness.

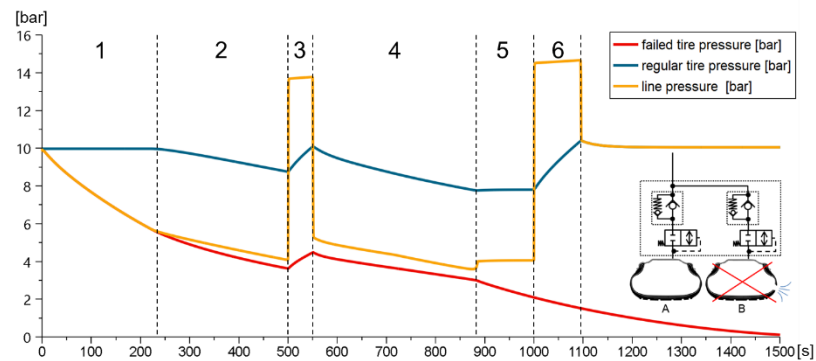
For dual tires, a single line provides air to both the tires. With reference to Fig. 2.51, the on-wheel valve group 16 allows to connect together the two tires, and includes some additional safety function to interrupt the communication between the tires if one of them suffers a failure (blowout, puncture, etc...). Valve 12 is a pneumatic shut-off valve piloted by the pressure in the tire. In normal operation, tire pressure is higher than the preload of the shut-off spring, p_{so} : the valve is kept normally-open. In this condition the twinned tires 10 and 10' are in communication between them and with the system: they can be inflated and deflated together, therefore the pressure in the two tires would be equalized. The pressure setting of the shut-off valve is lower than the one of the pressure limiter ($p_{so} < p_{set}$): in this way if tire pressure is lower than p_{set} but higher than p_{so} , the shut-off valve 12 is kept open and tires can still equalize their pressure as they can be inflated by the system. In case of a critical puncture or catastrophic failure of one of the two wheels, the pressure in the failed wheel would rapidly fall to low levels. As the pressure in the failed tire is lower than p_{so} , the shut-off valve closes and isolates the failed tire from the twinned tire. In this way, it is possible to keep the non-failed tire in a safe condition. It is also possible to maintain active the system functionalities on the non-failed tire, therefore it is possible to increase the pressure in it in order to partially compensate the failure. Figure 2.53 shows the working principle of the

valve group for dual tires in case of failure: the graph shows the evolution of the inflation pressure of a couple of twinned tires of an HDV in case one of the two tires is punctured, according to the results of 1D simulations performed in Amesim. Figure 2.53b shows the Amesim model that has been used to simulate the valve group [276]:

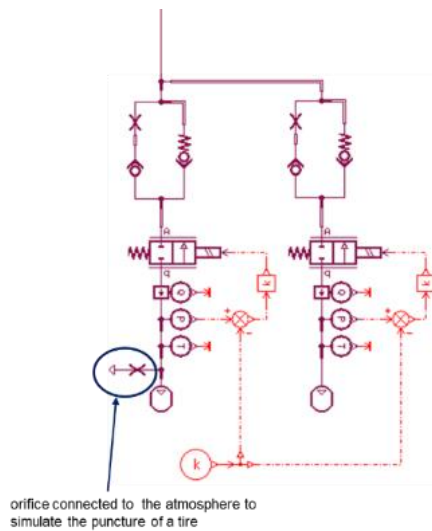
- the one-way valve (item 11.1 in Figure 2.52, as part of the valve group indicated as item 11 in Figure 2.51) has been modeled as an ideal one-way valve in series with a calibrated nozzle, and the flow area characteristic of the nozzle has been defined in order to match the flow characteristic of a commercial one-way valve, tested on the testbed described in *Section 2.6.1*;
- the pressure limiter valve (item 11.2 in Figure 2.52, as part of the valve group indicated as item 11 in Figure 2.51) has been modeled in order to match the opening-closing characteristic (including the hysteretic behavior) of a real in-line pressure limiter valve with nominal cracking pressure of 4 bar, where the characteristic of the real valve was obtained through tests on the abovementioned testbed;
- the shut-off valve has been modeled as a 2/2 logic valve, where the logic signal provided to the valve input is defined so that the valve switches to the closed position when the pressure inside the tire is equal or lower to 3 bar;
- tires are modeled as non-deformable pneumatic volumes;
- the puncture is simulated as an orifice open to the atmosphere.

The phases highlighted in the graph of Figure 2.53a depict the behavior of the system:

- phase 1: the pressure in the punctured tire (tire B, red line in Figure 2.53a) starts decreasing, with a rate of about 1bar/min. The common pipe that is connecting the two tires (upstream of valve groups 11) is initially at 10 bar, and its pressure instantaneously drops to compensate for the pressure in the punctured tire (c.f. “line pressure”, i.e. yellow line in Figure 2.53a). As a consequence, air would start moving from the non-punctured tire (tire A) to the common pipe, and from there to the punctured tire. Anyway, due to the preload on the pressure limiter valve on tire A, the pressure in the common pipe is initially not low enough to allow the opening of the pressure



(a)



(b)

Figure 2.53: Working principle of the wheel-end group for dual tires of LDV and HDV: example of the system response in case of a tire blowout (a) and Amesim model used to simulate it (b).

limiter valve of tire A. Therefore tire A keeps isolated and maintains its initial pressure.

- phase 2: the pressure in the punctured tire (and in the common pipe) becomes lower, so that the opening force on the pressure limiter of tire A (i.e., the pressure inside tire A) wins the closing resistance (the spring preload plus the pressure in the common pipe). Therefore, an air flow starts, which conducts air from tire A to tire B. This lasts until a certain threshold pressure is reached.

- phase 3: as the pressure is below a certain threshold, the system is actuated for inflation. At this stage, the central system has not recognized yet the presence of a puncture. The inflation actuation lasts for a certain period, during which the pressure inside the tires increases, but does not reach the target (i.e., 10 bar) due to the presence of the puncture. Notice that, in case of an open-loop control strategy the actuation time is computed from the actuation unit according to the expected pressure variation in time: after the actuation, the system checks again the pressure, and if this differs significantly from the expected one, the presence of a puncture is recognized. In case of a closed-loop control strategy (i.e., with continuous monitoring of tire pressure during the actuation), the system actuation continues until the target pressure is reached. Anyway, in order to limit the stress on the electrically-actuated system components, a maximum actuation time is possible: after this time has passed, the actuation is interrupted whichever is the pressure reached in the tires. In this latter case, the actuation unit still compares the expected pressure change that should be obtained during the completed actuation with the actual one: in case of a large mismatch between the two, again, the presence of a puncture is recognized.
- phase 4: the pressure inside both tires keeps decreasing, with the air flowing from tire A to tire B, until tire B reaches the pressure setting of the shut-off valve (i.e., 3 bar).
- phase 5: the shut-off valve of tire B switches to the closed position, so that the tire pressure in tire A is stabilized, while tire pressure from tire B keeps lowering till reaching the ambient pressure. If the shut-off valve would not be present, the air flow would continue from tire A to tire B and from there to atmosphere, until tire A would be at the pressure setting p_{set} of the pressure limiter.
- phase 6: the system checks the pressure again, and – as it is lower than the target – the system is actuated for inflation. If the shut off valve would not be present, the air provided from the compressor would be flowed to the atmosphere. As an alternative, as the system has recognized the presence of a puncture in phase 3, the system could isolate the tire group, thus avoiding to waste compressed air: in this way – in any case – the non-punctured tire would be kept at a critically low pressure. Thanks to the presence of the shut-off valve, instead, the system inflates the non-punctured tire back to the target pressure, while the punctured tire only is isolated.

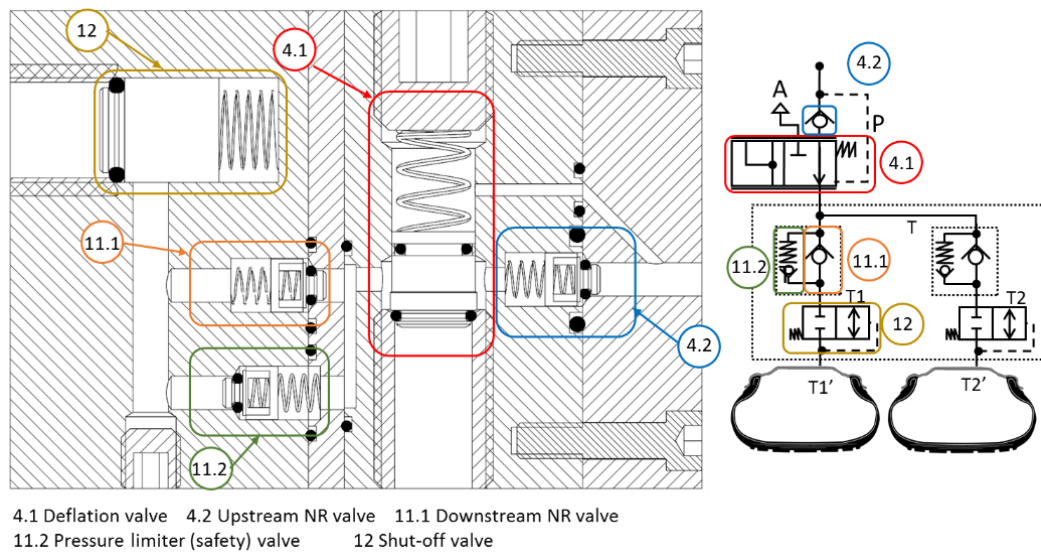


Figure 2.54: Preliminary design of the on-wheel valve group for dual tires of LDV and HDV.

Therefore, thanks to the proposed design, the system keeps its functionalities even in case of a punctured tire. In this case, although the puncture of one tire would reduce the load capacity of the axle, it would still be possible to drive it safely to destination, without the need to replace the punctured tire on the road. It is worth to remark that, according to the prescriptions of the tire manufacturers, the tires of commercial vehicles can be overloaded, provided that the maximum vehicle speed is limited accordingly: therefore, in the described case, the truck/van should reduce the driving speed to avoid excessive deformation of the overloaded tire.

Figure 2.54 shows the preliminary geometric definition of the functional group including valve 4 and valve group 16 (c.f. Figure 2.51).

2.7.1 Integration of the system on board: HDV

The integration of the system on board has also been studied, for both the HDV and for the LDV cases. As for the case of passenger cars, the design has been driven by the need to make the system integration feasible without major modifications on the standard mechanical components.

Figures 2.55-2.56 show the solution proposed for front steering (non-driving) wheels of an HDV [277]. With reference to Figure 2.55a, the standard wheel-end assembly on the front axle of the studied vehicle includes a spindle, which also serves as a steering knuckle (connected to the steering bracket, not shown in the

picture), on which is installed the wheel hub with its bearing. The wheel hub runs freely on the spindle and supports the wheel rim. The bearing unit is typically lubricated by oil: the oil-filled volume is limited by an oil seal on the spindle side (fitted on the hub extremity and with the sealing lip in contact with the spindle surface, seal not shown in the figures), and by a wheel cap on the rim side. The wheel cap also includes a screwed cap that can be removed to check the oil level and refill the volume when needed. In the proposed solution, the spindle has been modified in order to obtain a pass-through hole as a pneumatic connection, and a special wheel cap has been designed to replace the original one. With reference to Figure 2.56, the special wheel cap, which can be installed exactly as the standard one, includes the pneumatic rotating junction and all the valves included in the wheel-end valve block, i.e. valve 4 and valve group 11 with reference to Fig. 2.51.

The pneumatic rotating joint is of the axial type, as the one used for the rear wheels of the passenger car (c.f. *Section 2.6*). The pneumatic rotating joint is screwed in a dedicated seat on the special wheel cap, and the seat is sealed with a dedicated oil seal in order to avoid the contamination of compressed air with oil. The rotating joint is connected through a rigid pipe to a connector, which is then screwed in a special male fit-in connector with a spiral-like external shape. A female fit-in connector with a conjugated spiral-like profile is screwed in the spindle. The conjugated profiles of the parts of the connector allow to obtain a proper coupling of the two parts when the wheel cap is screwed on the hub. The sealing between the wheel cap and the conduit in the spindle is obtained through a radial o-ring fit on the male fit-in connector, which is compressed as the wheel cap is screwed on the

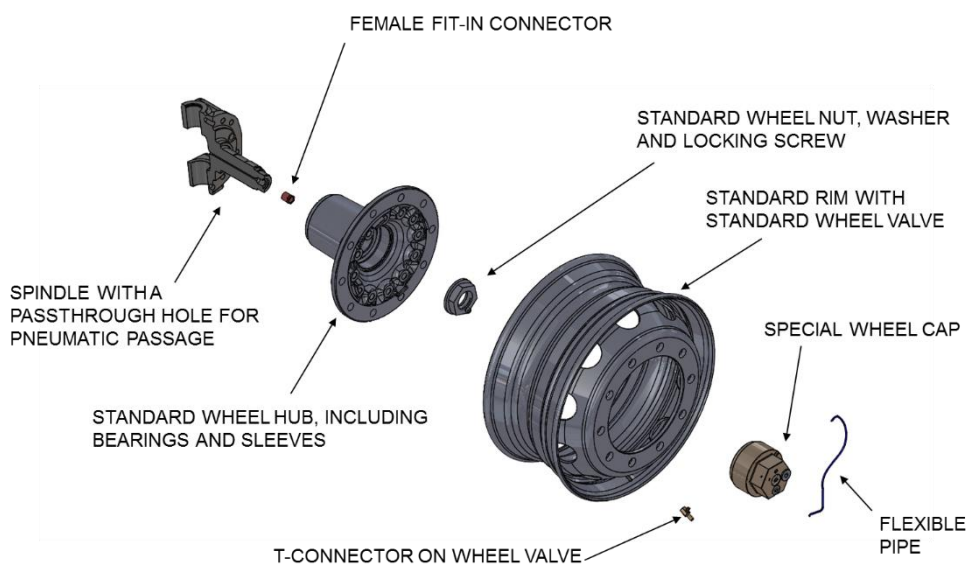
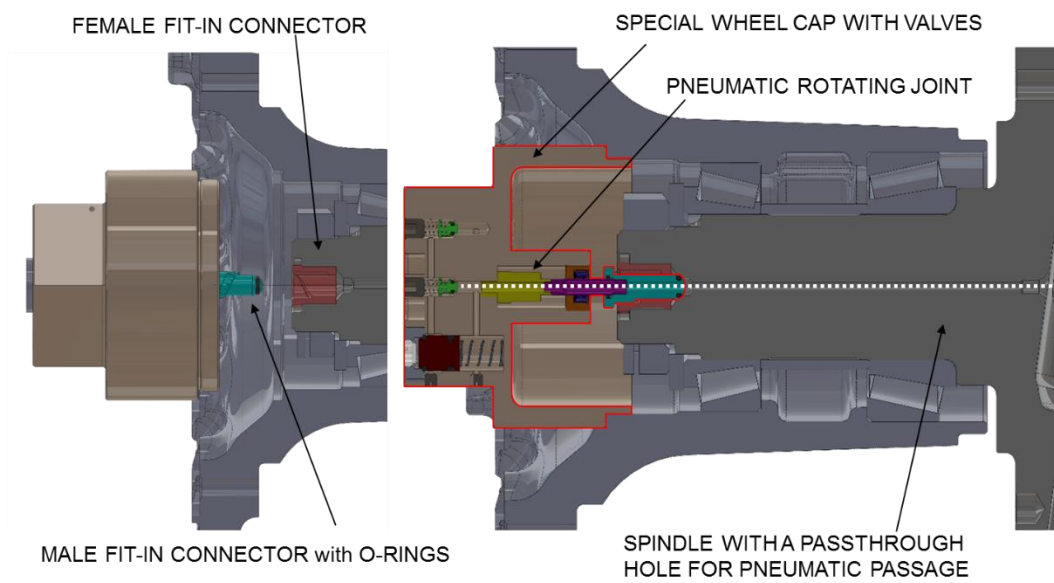
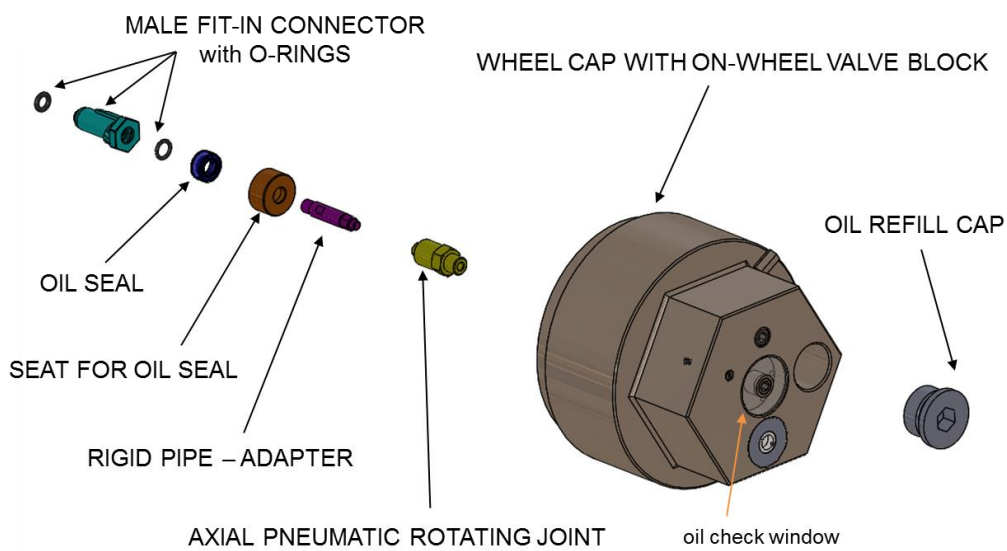


Figure 2.55: Integration of the ACTIS system on HDV: solution for front steering (non-driving) wheels: global view of the wheel-end assembly.



(a)

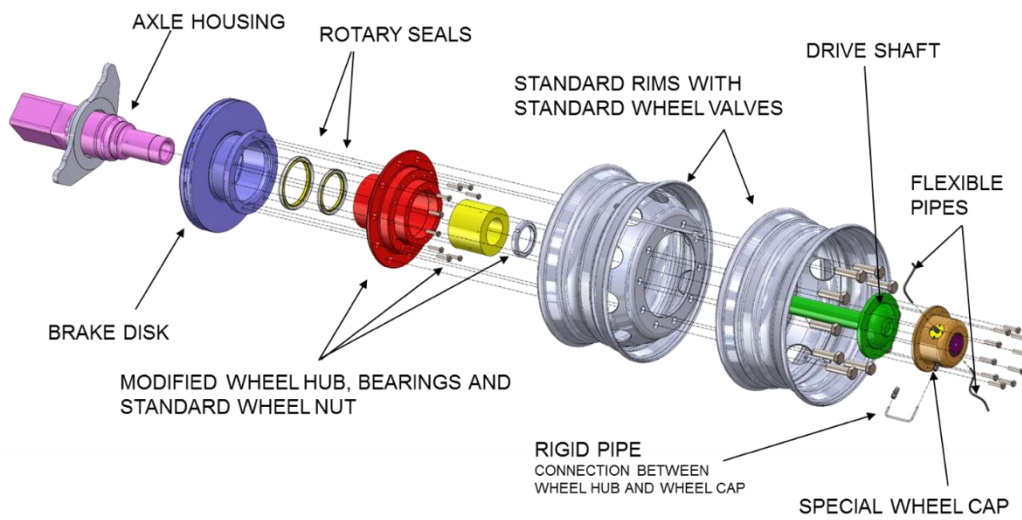


(b)

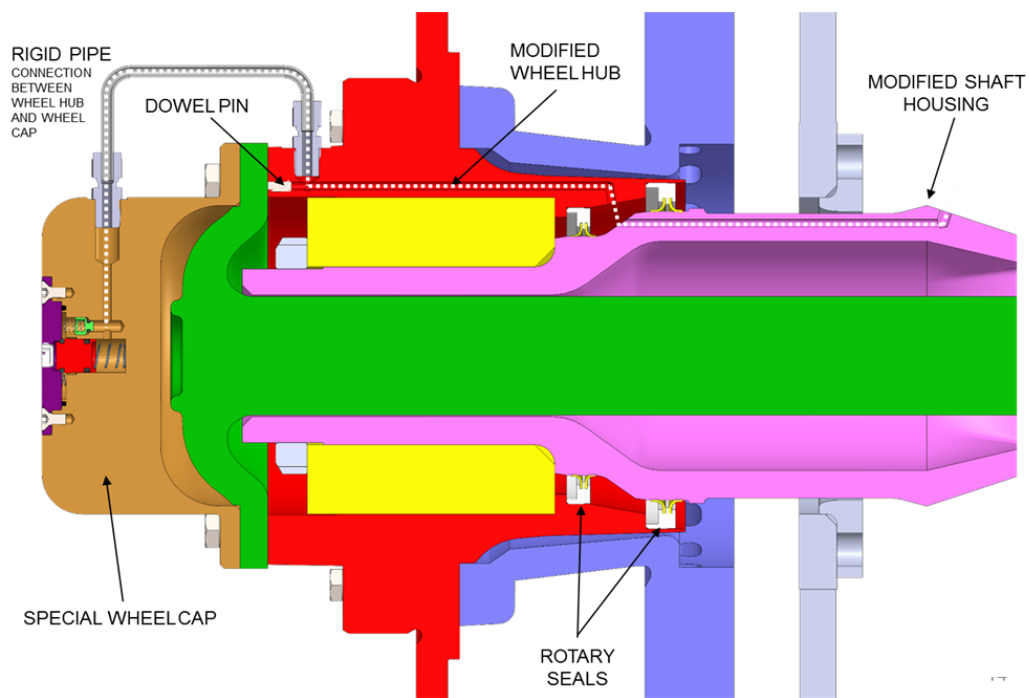
Figure 2.56: Integration of the ACTIS system on HDV: solution for front steering (non-driving) wheels: section (a) and exploded view (b) of the on-wheel valve block and its connection with the upstream parts of the circuit.

hub. In order to host the valves, the oil refill plug is moved from its original position (typically almost centered with respect to the wheel rotation axis): in order to keep the possibility to properly check the oil level, an oil check window in transparent plastic material is included in the front surface of the wheel cap. Some drilled holes in the cap, not visible in the pictures, put the oil check window in communication with the oil volume, without interfering with the pneumatic lines. A flexible pipe (Figure 2.55a) connects the outlet port of the wheel-end valve group to the tire through a T-connector. This latter is screwed on the standard wheel valve and includes the typical non-return valve in a dedicated port accessible for manual inflation operations.

Figure 2.57 shows the solution studied for the rear driving axle of an HDV. The axle has dual tires on each wheel. The drive shaft, that spins inside a shaft housing which contains lubricating oil, transfers the drive torque to the wheels through a wheel hub. The hub is supported by a bearing fit on the external surface of the axle housing. The brake disk and the rim are both connected to the wheel hub. In order to integrate the ACTIS, both the axle housing and the wheel hub have been modified in the proposed design: the first hosts a pass-through hole that allows the passage of air in the external shell of the housing (i.e., without interfering with the oil volume), while the latter integrates the seats to host two pneumatic rotating seals. The rotating seals are of the same type used for the toroidal rotating joint designed for passenger cars (c.f., *Section 2.6.4*), and present two lips in order to allow the seal to work both when positive and negative pressures are set in the sealed volume. The modified wheel hub also hosts a pass-through hole that connects the annular sealed chamber to a special wheel cap (not present in the standard design of the analyzed wheel-end assembly) through a rigid pipe. As for the previous case, the wheel cap integrates all the valves of the wheel-end valve group, i.e. valve 4 and valve group 16 in Figure 2.51. The wheel cap has two pneumatic outlet ports, one for each of the two twinned tires, which are connected to the tires volumes through flexible pipes and the abovementioned T-connectors.



(a)



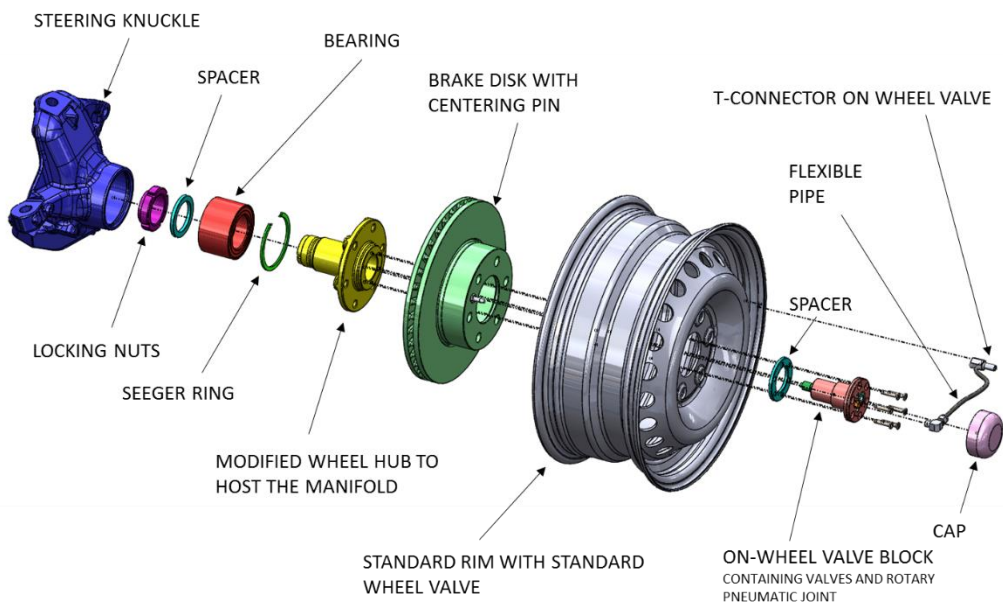
(b)

Figure 2.57: Integration of the ACTIS system on HDV: solution for rear driving wheels: global view of the wheel-end assembly (a) and section of the on-wheel valve block and its connection with the upstream parts of the circuit (b).

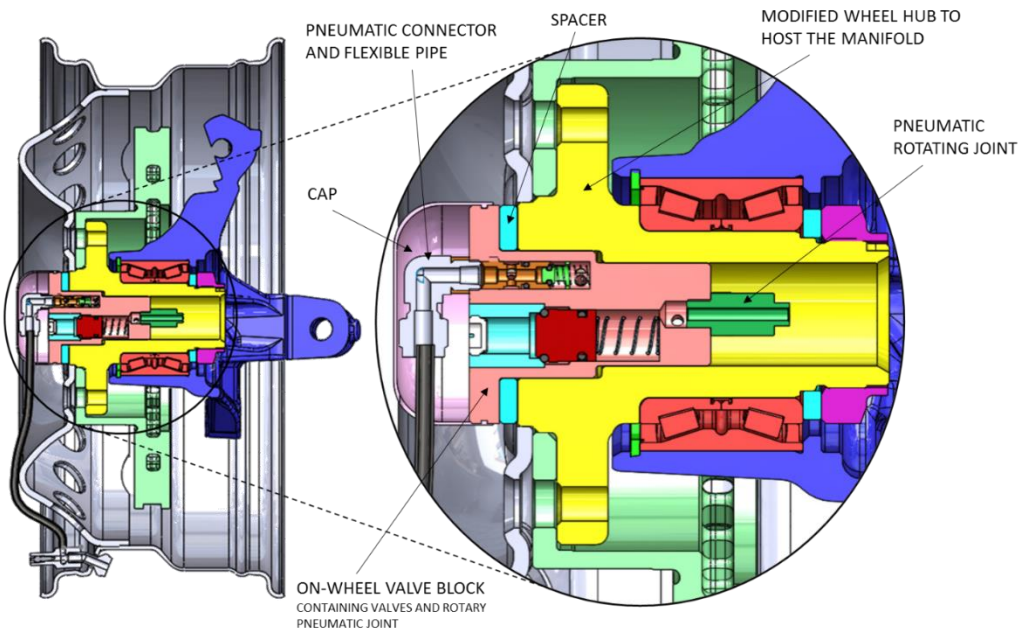
2.7.2 Integration of the system on board: LDV

Figure 2.58 shows the solution proposed for the steering non-driving wheels of a commercial van [278]. The wheel-end mechanics of a steering wheel for this kind of vehicle generally comprises a steering knuckle that hosts the statoric housing of a bearing. The bearing supports the wheel hub, on which the brake disk and the wheel rim are mounted. In the proposed solution, the wheel hub has been modified in order to host the on-wheel valve group. The on-wheel valve group hosts valve 4 and valve group 11, with reference to Figure 2.51, and it also integrates the axial rotating pneumatic joint. A flexible pipe connects the outlet port of the valve group to the T-connector on the standard wheel valve. A metallic cap completes the assembly and serves as a protection for the pneumatic connection on the outlet port of the on-wheel valve group.

Referring to Figure 2.59, the solution for the driving axle of a light commercial vehicle is reported with reference to a case where also driving wheels present single tires. The case of dual tires is also possible, and in this case the design of the on-wheel valve group would be retrieved from the HDV case. The driving axle of a commercial van typically comprises a flanged drive shaft that spins inside an axle housing supported by a bearing. The bearing is constrained through an housing cap, connected by means of screws to the axle housing. The brake disk and the rim are connected to the flanged extremity of the drive shaft. In order to allow the pneumatic communication from the stationary part of the system to the rotating one, a toroidal pneumatic joint is integrated between the housing cap and the flange on the driveshaft: the pneumatic rotating joint is made of two shells: a first shell is connected on the housing cap and integrates the pneumatic connector to communicate with the stationary part of the circuit, while the second shell supports the two double-lips seals and is integral to the flange on the drive shaft through screws. A hollow pin connects the outer shell of the pneumatic rotating junction to a connector placed on the external side of the wheels, which is also connected to the inlet port of the on-wheel valve block. As in other cases, the on-wheel valve block is a single component which integrates valves 4 and valve group 11 (c.f. Figure 2.51). The drive shaft is modified in order to host the on-wheel valve block.



(a)



(b)

Figure 2.58: Integration of the ACTIS system on LDV: solution for front steering non-driving wheels: global view of the wheel-end assembly (a) and section of the on-wheel valve block and its connection with the upstream parts of the circuit (b).

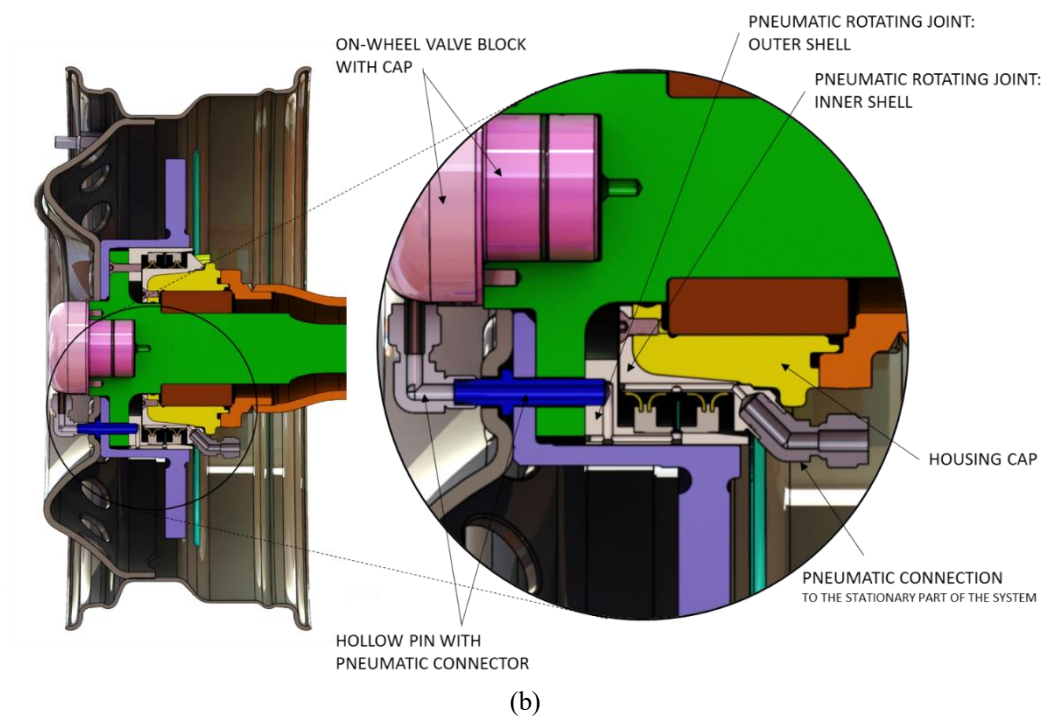
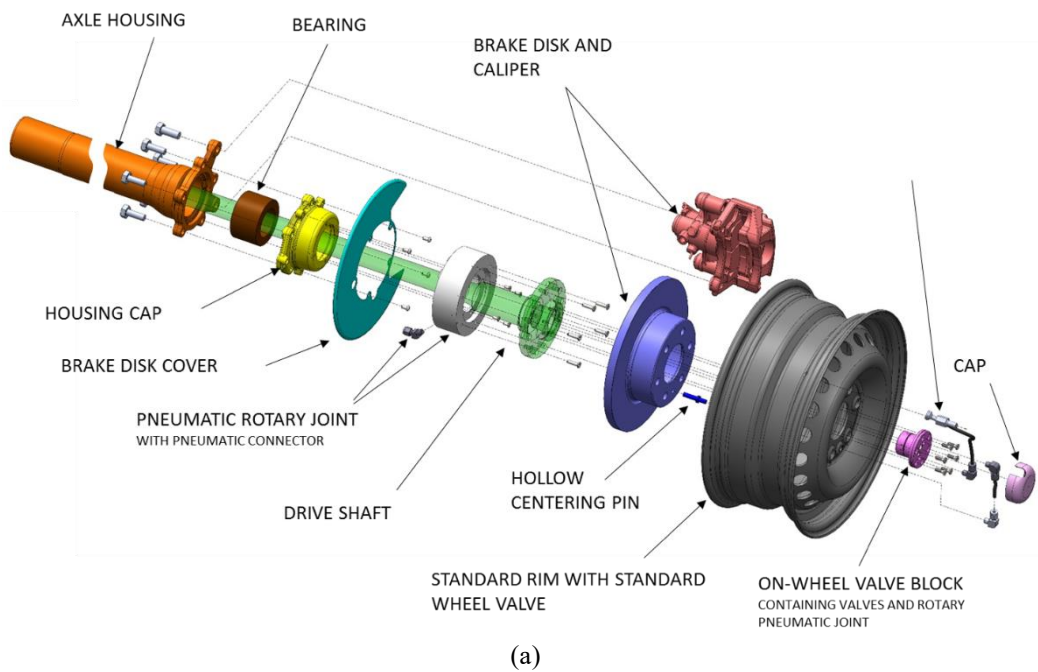


Figure 2.59: Integration of the ACTIS system on LDV: solution for rear driving wheels: global view of the wheel-end assembly (a) and section of the on-wheel valve block and its connection with the upstream parts of the circuit (b).

2.8 Effect of the dynamics of the actuation system on fuel consumption

In order to conclude the proposed analysis, an additional effect has to be considered in order to accurately assess the effects of an advanced CTIS on fuel economy and on the Total Cost of Ownership. This effect is related to the dynamics of the pneumatic actuation unit of the CTIS, i.e., on the time required for the system to vary the tire pressure from the present level to a target one. In fact, whenever the system dynamics is too slow, the fuel economy benefits could be reduced drastically. On the other hand, as the system dynamics depends to a great extent on the size of the system components, a system with fast dynamics would be extremely heavy, and the activation time would still be quite slow compared to the response dynamics of mechanical or electro-magnetic systems designed to adapt the vehicle behavior to high-frequency inputs. Therefore, system design choices may be critical from different points of view and should be the result of an accurate analysis to find the best compromise. For this reason, the TyPE software tool also allows the actual tire pressure to be simulated in each tire, to be calculated at each instant according to a set strategy and to be based on a map that provides the characterization of the system in terms of actuation time for various initial and final pressure levels.

All the simulations presented in *Sections 2.3-2.6* have been obtained by neglecting the effect related to the actuation dynamics. This was done in order to provide an extensive scenario of the potential benefits, regardless of the specific system design choices. Some additional simulations have also been conducted in a few specific cases in order to assess whether this effect is minor, or whether it may be critical for the validity of the abovementioned analysis.

It is worth underlining that the dynamic response of CTIS systems (and therefore also of the systems illustrated here) is inherently slow, so that the tire pressure could be only managed to adapt the vehicle behavior to a steady-state condition, e.g., passing from urban to highway driving, but it could not be used for fast transient operations, e.g., in a steering maneuver. The system dynamics is intimately related to the airflow rates in the system, and therefore to the size of the components, which is crucial in terms of the weight of the system and of the positioning of the on-board components: a fast-dynamic CTIS would result in a detrimental growth of the consumed energy, which would be much greater than the advantages obtained from pressure management, due to the huge increase in mass. As a reference, it should be considered that the mass of the ATPC system designed for passenger cars is about 4.4 kg and this allows an inflation actuation from 2.2 bar to 2.3 bar in about 10 s for each tire. The compressor currently used on the prototype built at the Politecnico di Torino has a nominal free flow of 35.4 l/min and weights 2.3 kg. In a first approximation, in order to reduce by 10 times the operating period for a reference actuation, the system would require a compressor with a flow rate 10 times bigger than the current one. Assuming that the current prototype has losses

that can be reduced in a future version, the target performance (actuation period 10 times lower than the current prototype) could be achieved with a compressor with a free flow of 280 l/min, whose weight is 25.4 kg. Additionally, with similar procedure, it can be estimated an increase of 8-9 kg on the central electro-valves module. Furthermore, other components of the system should be re-sized accordingly, which would determine a further increase of the system weight. Therefore, as a first-attempt, a system weight of at least 40-45 kg is estimated to reduce the actuation length by 10 times.

An increase of 40 kg in the mass of the reference passenger car would correspond to a 0.8-1% increase in fuel consumption in all the working conditions, while the system would only be able to improve fuel economy for certain specific situations. Furthermore, it should be taken into account that the increase in fuel consumption, due to the increase in curb mass, would affect the type-approval fuel economy, while the advantages that could be obtained from the system are mostly related to real-world driving. Finally, it should be underlined that a fast-dynamic response of the system would lead to advantages in vehicle handling behavior that are much smaller than those that can be obtained through other systems (e.g., active suspension systems).

Therefore, it is clear that proper sizing of the system components is critical to obtain the maximum advantage on fuel economy, which results from a trade-off between system dynamic performance and its weight on the intended system mission. Referring to “system mission” it is intended the expected utilization of the system during its application, which depends on the applied pressure management strategies, and on the typical mission of the target vehicle segment, including typical driving cycles/conditions (urban, extra-urban, highway, off-road,...) and loading conditions. The study proposed in this *Section* is therefore meant to be a validation *a posteriori* of the proposed designs and components sizing discussed in the previous *Sections*. The actuation dynamics for the current study is retrieved either from experimental data (for the system designed for passenger cars) or from 1D fluid-dynamic simulations (for the system designed for commercial vehicles). If accurate simulation models of the systems and of its sub-parts are available, it is then possible to easily test in simulation environment the effect on the actuation dynamics of different sizing choices for various components. The results obtained from the simulation model could then be used to evaluate in TyPE the effect of system sizing on the fuel consumption of the target vehicle on its typical mission profiles. This would allow an *a priori* evaluation of the best compromise in terms of actuation dynamics on fuel consumption. Direct co-simulation between TyPE and 1D fluid-dynamic simulation tools would, moreover, allow a true optimization of the size of various components of the system in order to obtain the minimization of fuel consumption on the intended system mission. Therefore, although only the *a posteriori* validation of the system design through fuel consumption estimations is discussed hereinafter, this can be intended as a first step towards the possible development of a dedicated tool for the *a priori* optimization of system design.

2.8.1 Passenger car

Although the previous simulations on the case-study related to passenger cars were performed using the FCA/Iveco software PerFECTS (c.f. *Section 2.3*), for this part of the study some additional fuel economy simulations of the passenger car were performed with the internal software tool TyPE (c.f. *Section 2.5*) in order to include the effect of the system dynamics. The results obtained from the characterization of the system in terms of actuation time as a function of the initial tire pressure and desired pressure variation as presented in *Section 2.6.6*, are provided in the form of a map to the simulation tool TyPE. Some real-world conditions were tested to simulate the effects of the system dynamics on a target actuation applied over a specific simulated driving cycle. The simulations were performed considering the reference vehicle and tires presented in Table 2.1.

Figs. 2.60a-b refer to the application of the abovementioned pressure management strategy during tire warm-up on an HWFET driving cycle. When the tire starts at ambient temperature, its rolling resistance is higher than the reference value, due to the low deformability of the rubber and the lower tire pressure with respect to a stabilized warm tire condition. In order to partially compensate for this effect, the considered pressure management strategy actuates an initial increase in the cold-tire pressure up to the pressure level that would be obtained at the end of the thermal transient. The pressure is then kept constant over time, and a certain amount of air mass is blown out to obtain an isobaric transformation as the temperature of the tire increases. Fig. 2.60a depicts this condition; the reported tire pressure is an equivalent tire pressure at an ambient temperature condition. Therefore, the isobaric transformation with a variable air mass as the temperature increases with the tire rolling time appears in this picture as a decreasing target pressure (at an ambient temperature) over time.

The graph in Figs. 2.60 shows the target pressure as a dashed line and the actual tire pressure in the four tires as solid lines. The system is actuated to inflate each tire individually, with a maximum pressure variation of 0.1 bar per tire in order to avoid excessive pressure imbalances between the tires on the same axle. Figs. 2.60a shows that the tire pressure reaches the target in about 120 s and then reproduces it within a tolerance band of ± 0.05 bar. Figs. 2.60b reports figures on the worsening of the fuel economy obtained in the case of a cold start with respect to the case of tire hot start. If no strategy is applied, the tire cold start increases fuel consumption by 1.78%. The application of the described warm-up strategy allows this worsening to be reduced to 1.06-1.10%. The case in which the real tire pressure evolution is considered shows a negligible worsening with respect to the case in which the ideal pressure variation that realizes the target pressure in Figs. 2.60a is considered.

Similarly, Figs. 2.60c-d refer to the adaptation of the tire pressure to the vertical load. Assuming a load variation by 10% with respect to the reference loading condition, the pressure is adapted to maintain the same vertical deflection of the tire

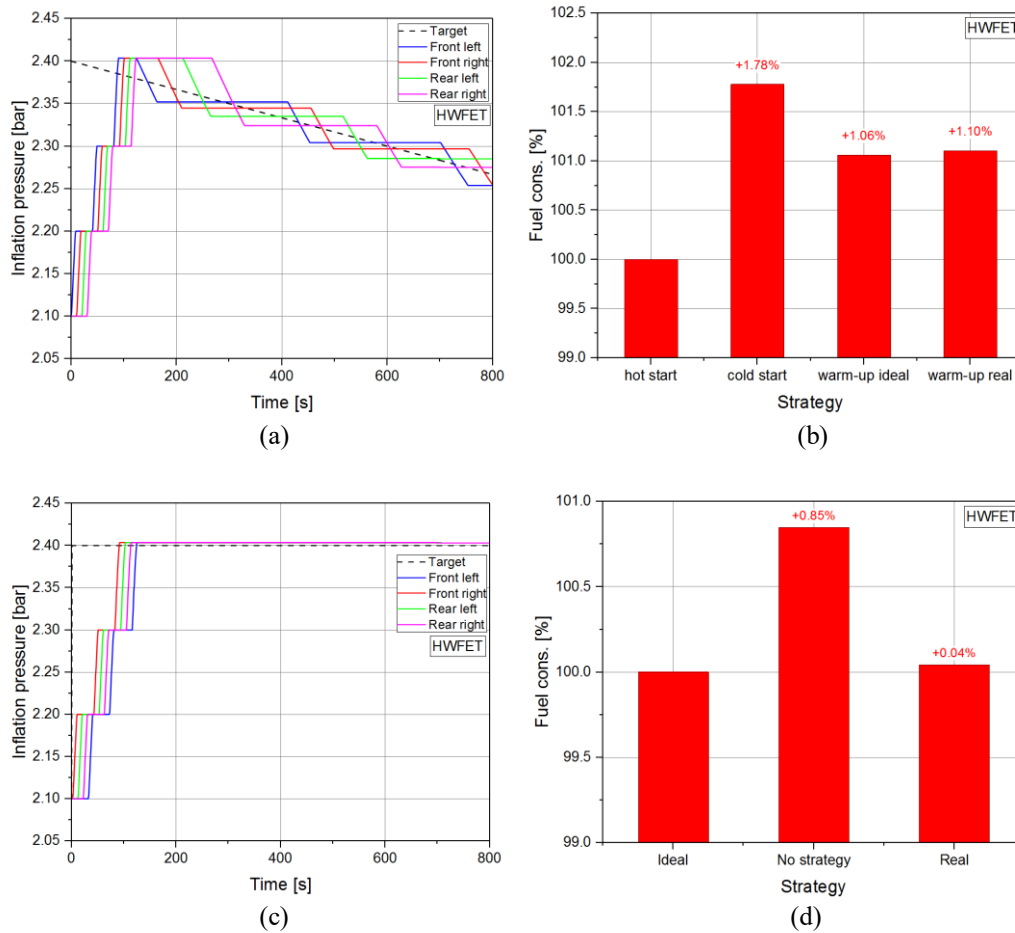


Figure 2.60: Effects of the ATPC system, accounting for the tested dynamics of the system, when tire pressure is adjusted during the tire warm-up period (a and b) and during a pressure adaption to a vertical load (c and d): tire pressure variation in time (a and c) and effect on fuel economy (b and d).

as in the reference tire pressure and vertical load case. The simulation was run with reference to an HWFET driving cycle. A mid-load condition was considered, evaluated as an average loading condition between the curb weight and the maximum possible load. The reference tire pressure is 2.1 bar at the curb weight condition. An increase to 2.4 bar was calculated to be suitable to the current load (c.f. Table 2.6). The real tire inflation pressure, according to the actuation dynamics of the system, reaches the target in about 120 s. Figs. 2.60d shows that taking into account the real system dynamics generates a very small variation (+0.04 %) in fuel economy, with respect to the ideal case. On the other hand, if the pressure were maintained at the reference level when the vertical load is increased and not adapted to the load variation, an increase in fuel economy of 0.85% would be obtained.

Therefore, as the simulations in which the real dynamics of the system (cf. previous paragraph) is implemented allow almost the same advantages to be obtained as the simulations in which an ideally instantaneous pressure variation is assumed, the pneumatic dynamics of the designed system results to be adequate for the dynamics of the target application.

2.8.2 Heavy-duty commercial vehicle

For this part of the study, the reference HDV was considered to be equipped with the designed ACTIS device, that has been described in *Section 2.7*. The system has been entirely modeled and simulated in a 1D flow simulation environment through Amesim [276]. As already mentioned, the modeling and simulation work will not be described here in detail, as it is not been developed by the author of this dissertation. Nevertheless, the results provided by the simulation models have been later implemented in this work in order to evaluate the effect of the actuation time of the designed system on the potential fuel economy advantage that the system itself could provide, as discussed in *Section 2.5*. Therefore, in the following, an overview of the system model is reported for the sake of completeness.

The solution that has been reported in the simulation model is the one that has been depicted in the schematic of Figure 2.51b: the system is considered to be equipped with its own main pneumatic circuit, and the ACTIS is considered as an added module on the existing pneumatic layout. For this purpose, the reference HDV has been assumed to be equipped with a mechanically-driven two-cylinders piston compressor with 628 cm³ total displacement and a maximum outlet pressure of 14 bar. The compressor has a maximum rotating speed of 3060 rpm and is driven mechanically by the internal combustion engine of the HDV, with a transmission ratio of 1.36. It has been simulated as an ideal fixed displacement machine with polytrophic compression and no mechanical losses. The compressor is operated in order to keep the downstream air tank (item 13 in Figure 2.51b) in the pressure range between 10.5 bar and 12.5 bar: when the pressure, measured by the pressure sensor (item 9' in Figure 2.51b) reaches the minimum value of 10.5 bar, a friction clutch is actuated to mechanically connect the compressor to the shaft of the engine. As the pressure inside the tank is restored to its maximum value (12.5 bar) the clutch is disengaged to limit the additional load on the engine. The tank has a volume of 60 liters and allows operation with a maximum pressure of 14 bar. A safety valve (item 5' in Figure 2.51b) opens at 13 bar to limit the maximum pressure that can be reached in the system. The maximum operating pressure of 12.5 bar with a maximum allowed pressure of 14 bar tolerated by the system components have been

set according to indications provided by Iveco as “best-practices” in use in the company. Also the compressor displacement and the transmission ratio of the engine-compressor coupling were provided by Iveco.

The vacuum source (item 1' in Fig 2.51b), required for operating the on-wheel valve (item 4 in Figure 2.51) for deflation operations, has been modeled as an ideal vacuum source able to provide continuously a 80% of vacuum grade (i.e., a relative pressure of -800 mbar). All the electrovalves of the system (items 2, 3 and 17 in Figure 2.51) have been chosen among those available on market with proper mechanical and flow characteristics to make them suitable for the application. The pressure flow characteristics, ISO 6358 compliant, of the chosen valves were available in the datasheets provided by the manufacturers, and were therefore implemented in the Amesim models of the valves. The pneumatic rotating joints were all modeled as pneumatic orifices whose characteristic was assumed equal to the ISO 6358 characteristic of the commercial axial pneumatic rotating joint mentioned in *Section 2.6*. Non-return valves (items 4.2 and 11.1 with reference to Figs. 2.52 and 2.54) have been modeled as ideal check valves in series to pneumatic orifices whose flow coefficient is given through a look-up table as a function of the pressure ratio: the characteristic of the orifice is reproduced from experimental tests performed on a commercial component, tested on the test-bench described in Figure 2.33c, while the ideal check valve is used to reproduce the functional behavior of the component. The pressure limiter valve (item 11.2 in Figs. 2.52 and 2.54) has been modeled as a pneumatic check valve with a cracking pressure of 3.95 bar and an opening-closing hysteresis of 0.2 bar, in order to obtain from the simulation model a flow-pressure characteristic as close as possible to that of a prototype valve realized at the Politecnico di Torino and tested on the test-bench described in Figure 2.33c.

Concerning the on-wheel deflation valve (item 4 in Figure 2.51), as mentioned in *Section 2.7*, a 3D model of the valve was set and CFD simulations were

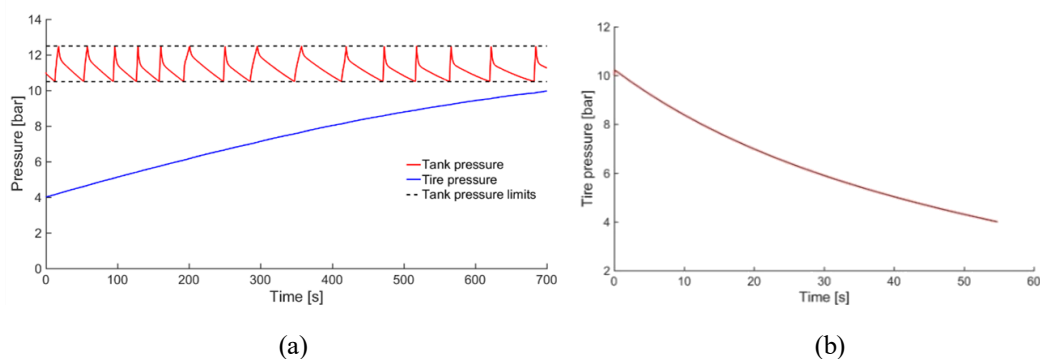


Figure 2.61: Inflation (a) and deflation (b) actuations as retrieved from Amesim 1D simulation model of the system for HDV.

performed in order to evaluate the forces equilibrium acting on the spool when the valve is operated for deflation in various working conditions (i.e. tire pressure varying from 4 bar to 10 bar with a pilot vacuum pressure of -800 mbar), and a flow-pressure characteristic of the valve was retrieved as a consequence from CFD simulations. This flow-pressure characteristic was implemented in Amesim as the characteristic of a pneumatic orifice in series with an ideal 2/2 valve: when the on wheel deflation valve is actuated for deflation, the ideal 2/2 valve opens the connection between the tire and the atmosphere, and air is forced to flow through the orifice that simulates the flow characteristic of the designed valve.

Finally, the shut-off valve for the on-wheel valve group for dual tires (item 12 in Figs. 2.51, 2.52, 2.54) was modeled as an ideal 2/2 pneumatic valve piloted through a logic signal depending on the pressure inside the tires, as already mentioned in *Section 2.7* with reference to Fig. 2.53.

The 1D model of the complete system has been then used to perform some simulations of inflation and deflation actuations. According to the results reported in Fig. 2.61, the system takes about 700 seconds to inflate an HDV tire of 165 liters from its minimum pressure of 4 bar to the maximum pressure of 10 bar, and it takes about 55 seconds to deflate the tire from its maximum pressure to the minimum one. The actuation times refer to the time needed to inflate or deflate a single tire.

Figure 2.62 shows the result obtained when applying the warm-up strategy on a *long-haul ACEA* mission, starting with cold tires (ambient temperature). The vehicle is considered to be empty, i.e. the simulation is run with a vehicle mass of 15 tons, and the initial cold tire pressures are set to 6 bar on the steer and drive axles, and to 4.5 bar on the trail axles, according to the isodeflection strategy. The warm-up strategy is applied which ideally requires an increase of tire pressure by 2 bar at the beginning of the cycle. The dashed lines in Figure 2.62a show the variation in time of the ideal tire pressure, set as a target by the simulated system control logic. It is worth pointing out that the tire pressure in Figure 2.62a is not the actual tire pressure at the actual temperature but an equivalent pressure under a cold tire condition. Each tire was not actuated for more than 0.5 bar at each step in order to avoid temporary pressure imbalances among the tires. Initially the system is actuated starting from the initial tire pressure in order to reach the desired target. The tire pressure reaches and overcomes the target pressure on all the axles after between 1300 s (on the steer axle) and 1800 s (on the trail axles) from the beginning of the cycle. After this initial transient, air is gradually blown out, and the actual pressure on all the tires keeps in a very narrow range around the target. Figure 2.62b shows the effect of this dynamics on fuel consumption. If the warm-up strategy was not applied, the effect in the simulated case would be an increase in fuel consumption of 1.56%, due to the tire cold start. The application of an ideal warm-

up strategy, with an instantaneous actuation at the beginning of the cycle, and a progressive variation of the tire pressure in all the tires, according to the target tire pressure in Figure 2.62a, would entirely compensate the negative effect of the tire cold start and would globally reduce fuel consumption by 0.06% with respect to the hot-start case. Owing to the dynamics of the real system shown in Figure 2.62a, the increase in fuel consumption, with respect to the hot-start case, is limited to 0.55%. Therefore, although the benefit provided by the actual strategy is reduced, with respect to the ideal one, it still allows a significant advantage to be obtained (about -1% on fuel consumption with respect to the case with tires cold start and no application of the warm-up strategy).

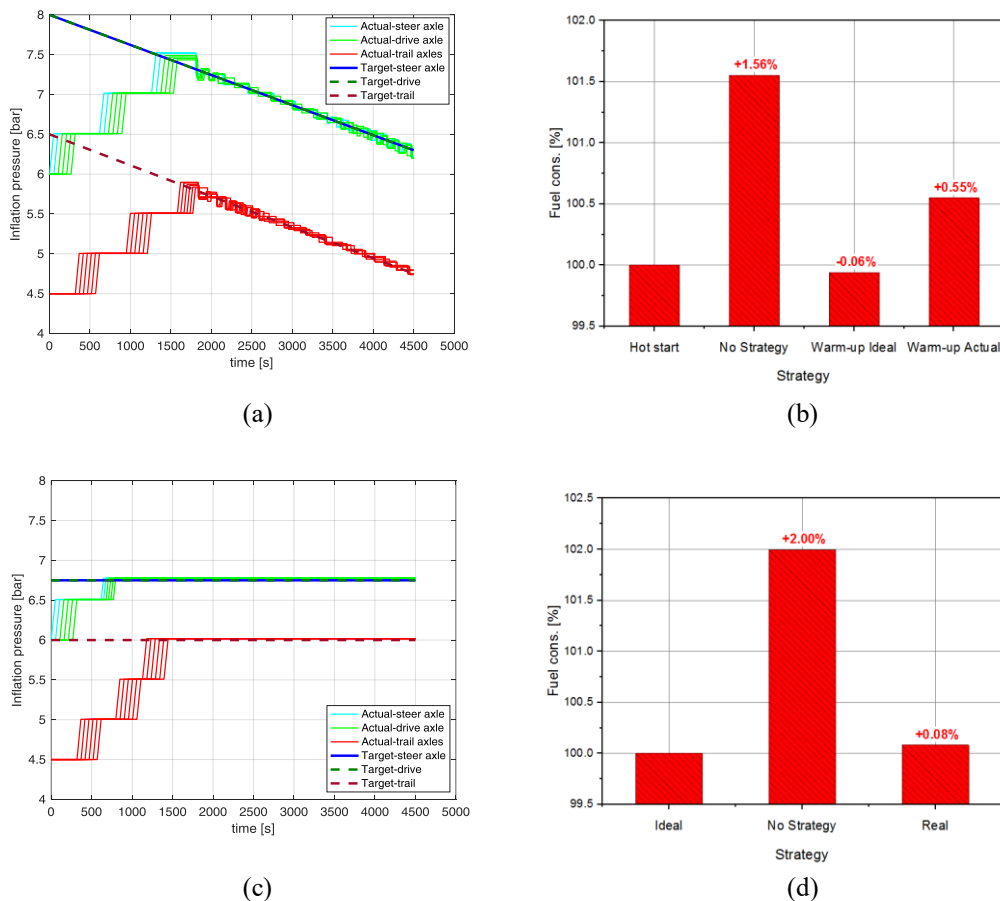


Figure 2.62: Effects of the ACTIS for HDV, accounting for the simulated dynamics of the system, when tire pressure is adjusted during the tire warm-up period (a and b) and during a pressure adaption to a vertical load (c and d) on a long-haul ACEA cycle: tire pressure variation in time (a and c) and effect on fuel economy (b and d).

Similarly, again taking the *long-haul ACEA* cycle as a reference, a load-adaptation according to the reference isodeflexion was simulated (cf. Figure 2.62c): the vehicle starts the trip with 6 bar on the steer and drive axles, and 4.5 bar on the trail axles, under the hypothesis that it was empty in the previous trip, and then increases the pressure to 6.75 bar on the steer and drive axles and to 6 bar on the trail axles in order to adapt to a new total load of 35 tons. With reference to Figure 2.62d, if the tire pressure was not adapted, the fuel penalty would be 2%, with respect to a case in which the correct pressure was set before starting the cycle. The automatic actuation of the system to compensate for the low pressure requires from 650 s to 1450 s to adapt the pressure to the desired level on all tires, which generates an increase in fuel consumption of only 0.08% with respect to the ideal case. In this case the difference with respect to an ideal instantaneous actuation is negligible, and significant fuel economy advantage can be obtained with the designed ACTIS system.

The ACTIS system performance estimated through simulation has been benchmarked against a commercially available CTIS previously tested internally by Iveco: this system showed a limited pressure working range (from 6 bar to 8.5 bar), with a total actuation time of 450s to increase the tire pressure from 4 to 8.5 bar, and being the inflation characteristic strongly non linear (i.e., actuation times increase substantially when moving towards the high-end of the working pressure range). The mentioned 450s inflation time was evaluated in the best case condition, with the lowest tested temperature at the compressor inlet, as the compressor performance was found to be strongly dependent on the inlet air temperature. The comparison between the designed ACTIS solution and the commercial CTIS is shown in Fig. 2.63. With respect to the mentioned commercial CTIS, the performance of the designed solution shows the following advantages:

- wider pressure working range (4-10 bar on the designed ACTIS, against 6-8.5bar of the commercial one) allows the maximum possible flexibility in the usage of the system. Especially, extending the higher limit of the working pressure range allows the effective implementation of fuel-saving strategies;
- the designed system shows an almost-linear inflation characteristic, with an average rate of 115s/bar, almost independent from the downstream pressure (i.e. the pressure in the tire). In the working range of the commercial CTIS (6-8.5 bar) the designed system shows a total actuation time of about 270s, whether the commercial one requires 450s;

- the commercial CTIS shows a shorter actuation time in the low pressure range between 6 and 7.5 bar, with about 52-57s required to increase the pressure from 6 bar to 7 bar, while the current ACTIS solution would require about 100s for the same pressure variation. Nevertheless, fuel-saving logics would move the interest more on the high-pressure range, where the designed system shows a better performance than the commercial one.

This benchmark comparison was not possible for deflation operations as the deflation times of the commercial CTIS were not evaluated during tests performed in Iveco. The system control logic was supposed to actuate one tire at a time.

This study has not been replicated also for the LDV as the Amesim model for the ACTIS designed for the LDV has not been set-up yet, therefore the simulations on the actuation times of the system are not available at the moment of writing.

Future studies on the topic will analyze the effect of system sizing on the fuel economy benefits achievable with an advanced CTIS in more detail. These data will then be exploited to design a CTIS devoted to maximizing the benefits, while limiting the system weight, as well as to designing efficient pressure management strategies.

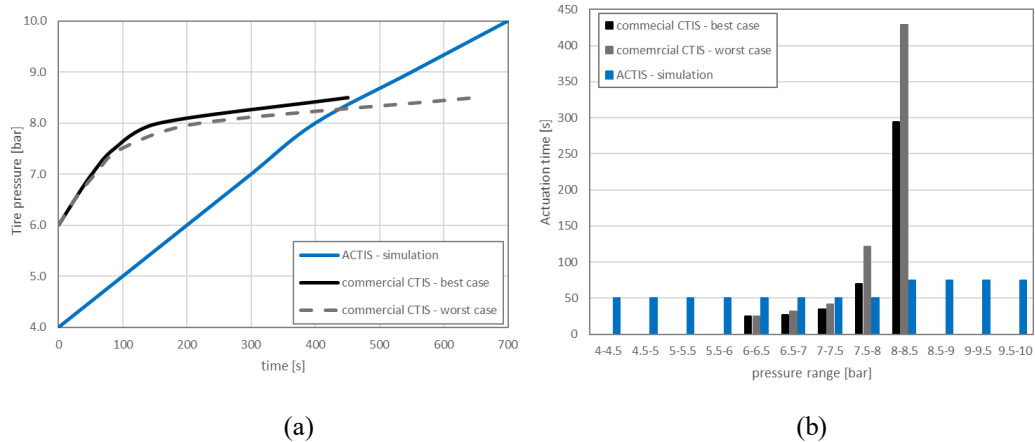


Figure 2.63: Benchmarking the designed ACTIS system for HDV against a commercial CTIS.

Chapter 3

Assessment of the potential combination of PCCI combustion and ACTIS technology on a light-duty commercial vehicle

Reducing the vehicle energy demand through a tire pressure management system can be effective in mitigating the fuel consumption increase of the PCCI combustion, while enabling its application to avoid the formation of NO_x and PM. The aim of the current *Chapter* is to analyze and present a case study related to the application on a reference vehicle of both the technologies presented in the previous *Chapters*. For this purpose, the case of a light-duty commercial vehicle is analyzed. The reference vehicle is the LDV taken as reference in *Chapter 2* and presented in Table 2.8. This vehicle, in its baseline configuration, is endowed with the diesel engine that has been object of the study discussed in *Chapter 1*, and whose main characteristic have been presented in Table 1.1. In its original configuration, the vehicle is endowed with the Euro VI version of the engine (i.e., the engine only works in conventional diesel combustion mode), and it is not endowed with any tire pressure management system. In the current *Chapter*, this baseline configuration will be compared with other possible configurations obtained by implementing the PCCI combustion mode and the abovementioned Advanced Central Tire Inflation System. Therefore, the following engine configurations have been considered:

- full conventional diesel combustion (CDC) engine: original calibration of the standard diesel engine tested on the whole engine map;
- PCCI/CDC “hybrid combustion mode” engine (also referred to as PCCI engine in the following): the standard CDC calibration is combined to the PCCI optimal calibration in the area where PCCI was calibrated on the upgraded engine (cf. *Chapter 1*)

each of which have been considered in two possible vehicle configurations:

- without the pressure management ACTIS system, i.e. in the baseline case with the reference pressure and in a typical misuse case;
- with the ACTIS system, i.e. applying the abovementioned strategies to adapt pressure to the payload and to adjust pressure during tire warm-up (cf. *Chapter 2*).

This comparison is based on computer simulations performed with the simulation tool TyPE (cf. *Section 2.5*), aiming at characterizing the behavior of the various vehicle-engine configurations on different driving missions/cycles in terms of fuel consumption, pollutant emissions, and urea consumption (as the baseline vehicle is endowed with SCR for the reduction of NO_x emissions).

For this purpose, the software tool TyPE has been adapted in order to provide results also in terms of emissions and urea consumption. According to what presented in *Section 2.5*, for each time instant of a driving cycle the software estimates the engine working point in terms of engine speed and load, and then interpolates a fuel consumption map in order to get an instantaneous fuel consumption. The fuel consumption map is obtained through a steady-state experimental test campaign. In order to develop a wider analysis on the potential effects of these technologies, the software was adapted in order to perform interpolations also on maps of specific gaseous emissions and urea consumption. All these maps have also been obtained from experimental steady-state tests. In general, it is well known that steady-state maps not always represent with a high accuracy the behavior of the engine when it works in transient conditions [279-281]. This approach can be improved by applying experimentally-derived correction coefficients that account for the emission discrepancies during engine speed and load transients [279] or by coefficients that account for the dynamic lag in exhaust temperature [280], or by using experimental engine performance maps built also as a function of the torque change rate [281]. Nevertheless, as no transient data were available for the PCCI engine, simple interpolation in steady-state engine maps as a function of engine speed and load was considered a valid estimation to perform a relative comparison among the different configurations, as for the analysis of *Chapter 2*. Future developments of the project might include the implementation of more sophisticated methodologies to improve the transient estimation of fuel consumption and exhaust emissions, while also explicitly taking into account the effect of tire pressure variations on road load.

With reference to the case of PCCI/CDC “hybrid combustion mode”, as a complete map is not available for the F1C PCCI engine (i.e., the PCCI engine was only calibrated in the area of interest for PCCI combustion, and a calibration of the engine in conventional diesel combustion was not preformed in the remaining areas

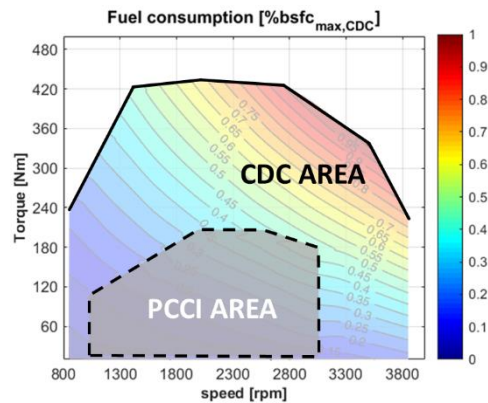


Figure 3.1: Combination of the CDC and PCCI engine performance maps for the simulations of the PCCI/CDC hybrid combustion mode.

of the engine map), the following assumptions were made to build the engine performance maps (fuel consumption, emissions and urea):

- the engine works in PCCI mode in the area calibrated on the PCCI engine;
- the engine works in conventional diesel combustion (CDC) outside the PCCI area, and the performance on the CDC area is the one measured on the standard engine with the reference Euro VI calibration;
- commutations between the two combustion modes are considered instantaneous;
- engine response during transients is simulated by interpolating maps obtained as combination of steady-state points, i.e. the effect of non-idealities during transients is neglected.

Therefore, the engine performance maps for the PCCI engine were obtained moving from the original maps of the CDC engine and replacing the areas where PCCI was calibrated on the upgraded engine with the performance measured on that engine (cf. Fig. 3.1). Nevertheless, the maps of the two combustion modes are obtained on two engines with different hardware specifications. The biggest difference among the two engine configurations is the compression ratio (CR). The effect on the full-load characteristic of low compression ratio engines designed for part-load operation in PCCI combustion modes is discussed in the technical literature [130, 131]. Lowering the compression ratio was found to not affect [131] or to have a minor effect [130] on the maximum engine bmep/torque, while engine exhaust temperatures are found to significantly increase with the reduction of CR

[130, 131]. The increase in exhaust temperature increased the work done by the exhaust gases on the turbine, which led to an increase in boost pressure and maximum bmep delivered by the engine in the low-end of the full-load characteristic [130]. This effect is only exploited at low speed [130], as at higher speed combustion phasing needs to be tuned in order to avoid exhaust temperature to overcome the turbine working limits. Moreover, the increase in exhaust temperature of the low CR PCCI engine in the CDC working area would be beneficial on the light-off of the DOC. The reduction on CR was also found to decrease CO emissions due to an improvement of air-fuel mixing, while fuel consumption was generally worsened in the low CR engines due to the need for advancing the injection event [130]. Nevertheless, in a low-compression ratio engine designed to run in PCCI in part-load and in CDC in the rest of the map, the CR should be chosen as a compromise between the various combustion modes. On the other hand, optimal CR in each combustion mode could be obtained by means of a variable compression ratio (VCR) system, such as one of those presented in the review paper by Asthana et al. [282]. The application of VCR systems to low-temperature combustion, and especially to HCCI, was already proposed in previous works as a way to obtain the HCCI combustion with various fuels compositions [283] or to adjust combustion phasing in a closed-loop control of HCCI combustion [284]. Other studies have shown the potentiality of variable valve timing (VVT) as a way to achieve low compression ratio for HCCI/PCCI operations through late intake valve closure without fuel penalties [285, 286]: in detail, as intake valve closure is retarded, the effective compression stroke of the engine is reduced (thus reducing the compression work done by the piston), while the effective expansion stroke is the geometrical one, therefore resulting in a substantial over-expansion at the end of the combustion cycle with respect to the in-cylinder pressure at the beginning of the compression [285]. Therefore, VVT is a suitable alternative to VCR systems, and it would allow to obtain a different effective compression ratio in different areas of the map. It is worth to underline that continuously adjustable VVT or VCR systems would allow a further degree of freedom in the optimization of both the PCCI and CDC combustion mode, which would potentially further improve the engine performance and extend the application area of PCCI, also allowing a gradual change from PCCI to CDC.

Apart from CR, other differences between the two hardware configurations of the engine are related to the different piston bowl geometry, lower injector static flow rate and smaller cone angle, and smaller turbocharger implemented on the PCCI engine (cf. Table 1.1). Narrowing the injector cone angle (without reducing the static flow rate) was found to be detrimental on the full-load characteristic (in CDC), possibly due to the interaction of the jet with the central dome in the piston bowl [130]. In the study case discussed in this dissertation the static flow rate of the

PCCI injector was reduced and the protrusion of the central dome of the piston bowl was largely reduced as well (cf. Fig. 1.2), in order to reduce the interaction of the jet from the narrow cone injector with the piston surface. Concerning the smaller turbo implemented on the PCCI engine, matched for part-load PCCI operation, its limitations in the high-load/high-speed region could be overcome by two-stage turbocharging, with a larger low-pressure turbo-group in series with the small high-pressure one, and with by-pass valves for the high-pressure stage (i.e., the so-called “regulated two-stage turbocharger” [287, 288]).

Therefore, considering the characteristics of the PCCI engine and the implementation of a two-stage turbo-group and of a VCR system, optimal calibration of the main combustion parameters (rail pressure, injector timing, boost pressure, EGR rate, etc...) in the CDC area could lead to a low interaction of the jet with the piston surface and proper fuel-air mixing, thus leading to a good performance of the PCCI engine also in the CDC area. Under the hypothesis that in the fully-upgraded PCCI engine it would be possible to obtain in the CDC area a calibration which allows performance similar to those of the CDC engine, differences between the two hardware configurations of the engine are considered virtually not affecting the CDC performance in the current analysis. Although this assumption, as well as considering instantaneous the transition from one compression ratio to another through a VCR or VVT system, are not rigorous as not validated yet by experimental evidence, they allowed to perform this study to provide a first feedback on the potentialities of a PCCI/CDC diesel engine, possibly applied in combination to the pressure management strategy, or to any other strategy/device to improve the on-board energy management.

It is worth recalling that the CDC engine tested at the Politecnico di Torino was not endowed with any after-treatment system, and therefore all the exhaust emissions are measured only as engine-out emissions, while the PCCI engine was endowed with a diesel oxidation catalyst, therefore the HC and CO emissions are evaluated both as engine-out emissions and at the tailpipe, i.e. upstream and downstream the DOC. NO_x and soot emissions are evaluated on the PCCI engine only as engine-out emissions, as no after-treatment system was installed for these emissions as the PCCI combustion mode is expected to produce ultra-low NO_x and PM emissions.

In order to allow a proper comparison on engine-out and tailpipe emissions, a further set of engine emission maps was also considered for the CDC EuroVI engine, that was obtained through steady state tests performed by FPT installing the complete ATS of the engine, including a DOC for HC and CO, an SCR for NO_x and a DPF for PM. Therefore, the engine performance maps for the PCCI engine are built as follows:

- fuel consumption map for the PCCI/CDC hybrid combustion mode engine is built combining the map of the CDC engine measured at the Politecnico di Torino with the partial map of the PCCI engine (also measured at the Politecnico di Torino). The fuel consumption of the CDC engine measured at the Politecnico di Torino is used as reference engine map for comparison;
- engine-out and tailpipe HC, CO and NO_x emissions, as well as urea consumption maps for the PCCI/CDC hybrid combustion mode engine, are built combining the maps of the CDC engine measured by FPT with the partial maps of the PCCI engine (measured at the Politecnico di Torino), where for the PCCI engine the engine-out NO_x emissions are equal to the tailpipe ones, and the urea consumption is considered null in the PCCI area. The HC, CO, NO_x and urea maps of the CDC engine measured by FPT are used as reference for the comparison;
- soot was only measured at the Politecnico di Torino, both during CDC and PCCI tests, and always without any DPF installed (i.e., only the engine-out soot emissions are available). Therefore, the engine-out soot map for the PCCI/CDC hybrid combustion mode engine is built combining the map of the CDC engine measured at the Politecnico di Torino with the partial map of the PCCI engine (also measured at the Politecnico di Torino).

As for the analysis of *Chapter 2*, the study is based on the simulation of three test cycles: a *Custom LDV highway* cycle, a *Custom LDV extra-urban* cycle and a *Custom LDV urban* cycle (cf. Table 2.10). The analysis is first performed considering each of these driving cycles in various vehicle loading conditions (from curb weight to the maximum payload), and then combining all the results in some reference annual missions considered as representative of the studied vehicle (as it was already presented for the ACTIS study in *Section 2.5*). In the following *Sections*, first the effect of introducing the PCCI/CDC hybrid combustion mode engine on driving cycle simulations will be discussed, and then the simulations that include the ACTIS system will be also analyzed. For the first comparison between PCCI and CDC all the simulations have been performed with the reference tire inflation pressure, i.e. with the nominal tire pressure of Table 2.8. For the following *Sections* including the effect of the ACTIS, the following cases are reported and discussed:

- a **baseline** case: the driving cycle is performed with the reference tire pressure, and the effect of tire cold start is included (i.e. the cycle is supposed to start when the tires are at ambient temperature and the increase

of the rolling resistance of cold tires is taken into account, according to what discussed in *Chapter 2*);

- a *misuse* case: the driving cycle is performed with tire pressure 25% lower than the reference one, and the effect of tire cold start is included;
- an *ACTIS* case: tire pressure is adapted to the vehicle load and is also varied during the tire warm-up period to mitigate the effect of tire cold starts, according to the cases discussed in *Chapter 2*.

3.1 Performance comparison between the PCCI engine and the standard diesel engine on single mission profiles

In this *Section* both the reference CDC Euro VI engine and the PCCI/CDC engine (that will be referred to as PCCI engine in the following, for simplicity) have been simulated on the reference driving cycles and their performance in terms of fuel consumption, pollutant emissions and urea consumption are compared. In this *Section*, all the simulations are performed with the reference tire pressure.

Fig. 3.2 shows this comparison on the *Custom LDV highway* cycle, and considering the reference mass of the vehicle (curb weight + driver). The graphs show the normalized cumulated fuel consumption and gaseous emissions, as well as urea consumption. With reference to Fig. 3.2a, fuel consumption is normalized with respect to the total fuel consumption of the CDC engine, and the graph shows that the implementation of the PCCI combustion mode in the PCCI area highlighted in Figure 3.1 would produce an increase by 1.7% on the cumulated fuel consumption. Figs. 3.2b and 3.2c report the engine-out and tailpipe emissions of CO and HC, normalized with respect to the Euro VI limits. It is worth to underline that the cycles considered for the current analysis are not valid for homologation purposes and are generally more severe than the reference cycle to which the Euro VI limits are referred. Therefore, the Euro VI limits are here used only as a reference for normalizations. In both cases, as discussed in *Chapter 1*, engine-out emissions increase significantly when PCCI is applied. Thanks to the presence of the DOC, most of the emissions of CO and HC can be treated effectively, and therefore both in the CDC and in the PCCI case tailpipe emissions are drastically lower with respect to the engine-out ones, and in both cases they are much lower than the Euro VI target. Nevertheless, in the CDC case the tailpipe emissions of CO and HC are

reduced almost to zero, while in the PCCI case there is still a non-negligible amount of these pollutants at the tailpipe.

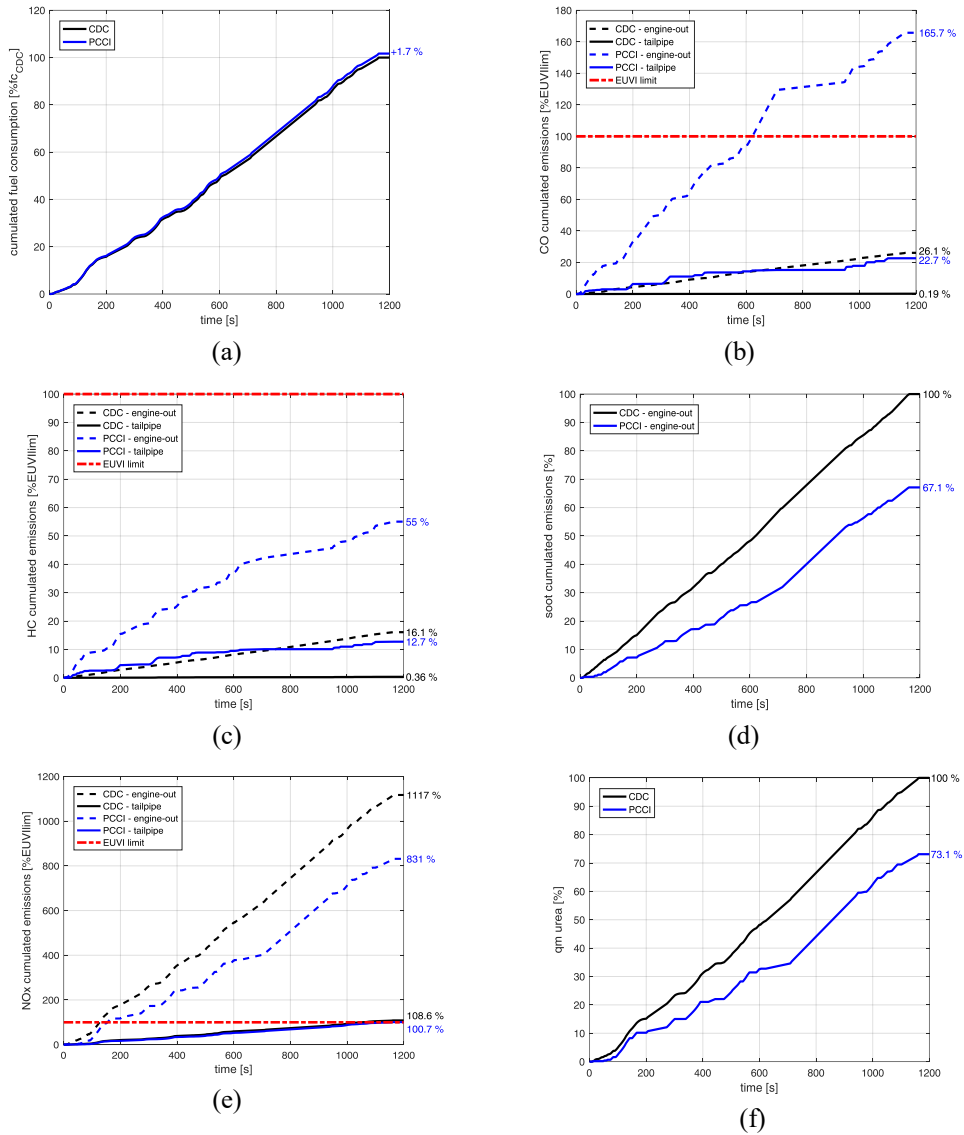


Figure 3.2: Engine cumulated fuel consumption, gaseous emissions and urea consumption on the LDV *highway* mission. Fuel consumption (a), soot engine-out emissions (d) and urea consumption (f) are reported in terms of percentage of the cumulated values at the end of the cycle with the reference CDC engine. CO (b), HC (c) and NO_x (e) emissions are reported as percentage of the Euro VI limits.

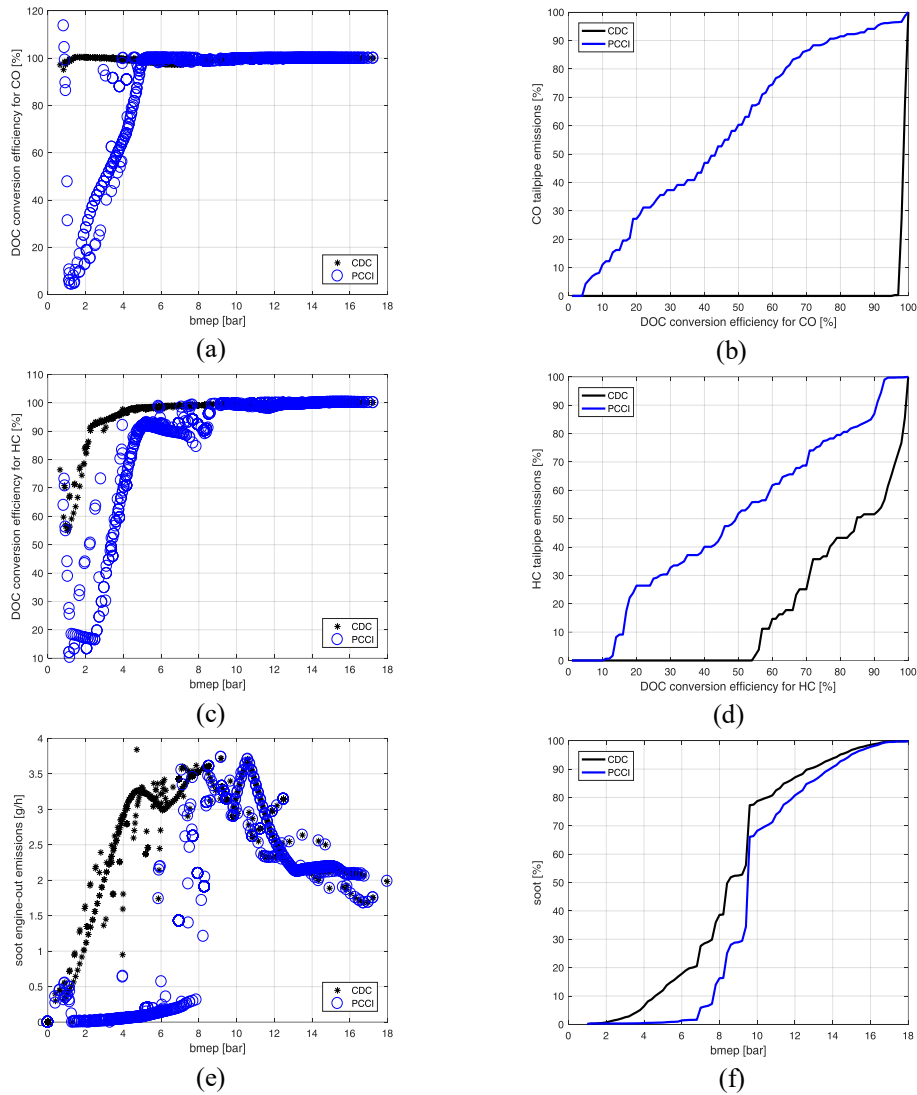


Figure 3.3: LDV *highway* cycle with the CDC and PCCI engines: DOC conversion efficiency for CO and HC emissions (a,c) and cumulated relative CO and HC tailpipe emissions (b,d) as a function of engine load; soot instantaneous (e) and cumulated relative emissions (f) as a function of engine load.

With reference to Figure 3.3, this is clearly due to the poor conversion efficiency of the DOC in the low-load area, when the low-temperature combustion is applied. Fig. 3.3a shows that for the CDC case the DOC conversion efficiency for CO is always higher than 95%, while in the PCCI case it is much lower up to 5 bar bmep, and increases almost linearly with the engine load in the low-load region, due to the increase in exhaust gas temperature. Fig. 3.3b shows that all the tailpipe emissions of CO in CDC case are produced with a very high DOC conversion efficiency, which allows to obtain the ultra-low tailpipe CO emissions of Figure 3.2b. Nevertheless, in the PCCI case, about 95% of the tailpipe CO emissions are

produced with a DOC conversion efficiency lower than 95%. Figs. 3.3c and 3.3d show the same analysis for HC emissions: in the CDC case the DOC conversion efficiency for HC is always higher than in the PCCI case in the low-load region, and up to around 8 bar bmep. While in the CDC case all the tailpipe HC emissions are produced with DOC conversion efficiency higher than 55%, in the PCCI case about 60% of the tailpipe HC emissions are produced with a DOC conversion efficiency lower than 55%.

Referring to Fig. 3.2d, engine-out soot emissions decrease by about 33% with the application of the PCCI combustion. This reduction was obtained by drastically reducing soot emissions below 8 bar bmep (cf. Fig. 3.3e and 3.3f): with CDC, about 37% of all the soot produced along the driving cycle are generated below 8 bar bmep, while with the PCCI engine this percentage is about 15%. As mentioned above, soot was only measured at the engine-out position, as no DPF was installed on both the CDC and on the PCCI versions of the engine. Moreover, as the soot only accounts for a fraction of the total PM emissions, the soot levels were not compared to the PM Euro VI limits. Concerning NO_x emissions (Fig. 3.2e), the application of the PCCI combustion mode allows to reduce both engine-out and tailpipe NO_x emissions. In particular, referring to the tailpipe NO_x emissions, in the *LDV highway* cycle the NO_x emissions overcame by 8.6% the Euro VI limit, while in the PCCI case they were almost at the limit. This corresponds to a reduction of tailpipe emissions by about 8.7% in the PCCI case with respect to the CDC case. This was again obtained through a reduction of NO_x emissions in the PCCI area to near-zero levels (Figs. 3.4a-b-c), and without injecting urea in the SCR when the engine is working in the PCCI combustion mode (Figs. 3.4d-e), which also produced an overall reduction of the urea consumption by 27% (Fig. 3.2f).

In addition to the previous figures, Fig. 3.5 and Fig. 3.6 show a comparison of the engine performance maps (bsfc, CO, HC, soot and NO_x emissions) in CDC (left column) and in the PCCI/CDC combustion modes (right column). CO and HC maps (Fig. 3.5c-d-e-f) refer to the tailpipe emissions, while soot and NO_x (Fig. 3.6) maps are relative to engine-out emissions. All the graphs are normalized on the maximum value reached considering both the combustion modes. Also the engine points relative to the specific cycle are reported on the map: it can be observed that in the *highway* cycle the engine is used mostly in the medium-high load region, with a large part of the cycle being out of the PCCI area.

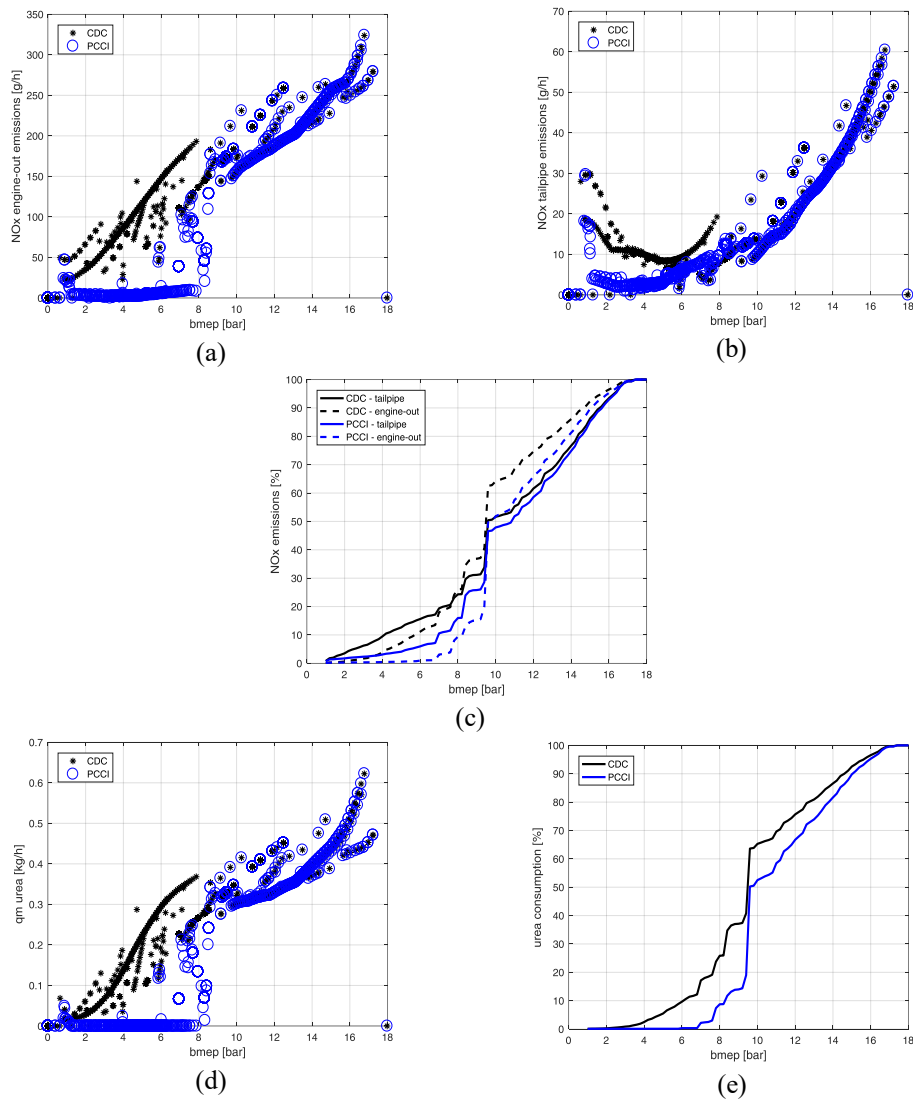


Figure 3.4: LDV *highway* cycle with the CDC and PCCI engines: NO_x instantaneous (a, b) and cumulated relative emissions (c) as a function of engine load; instantaneous and cumulated relative urea consumption as a function of engine load (d, e).

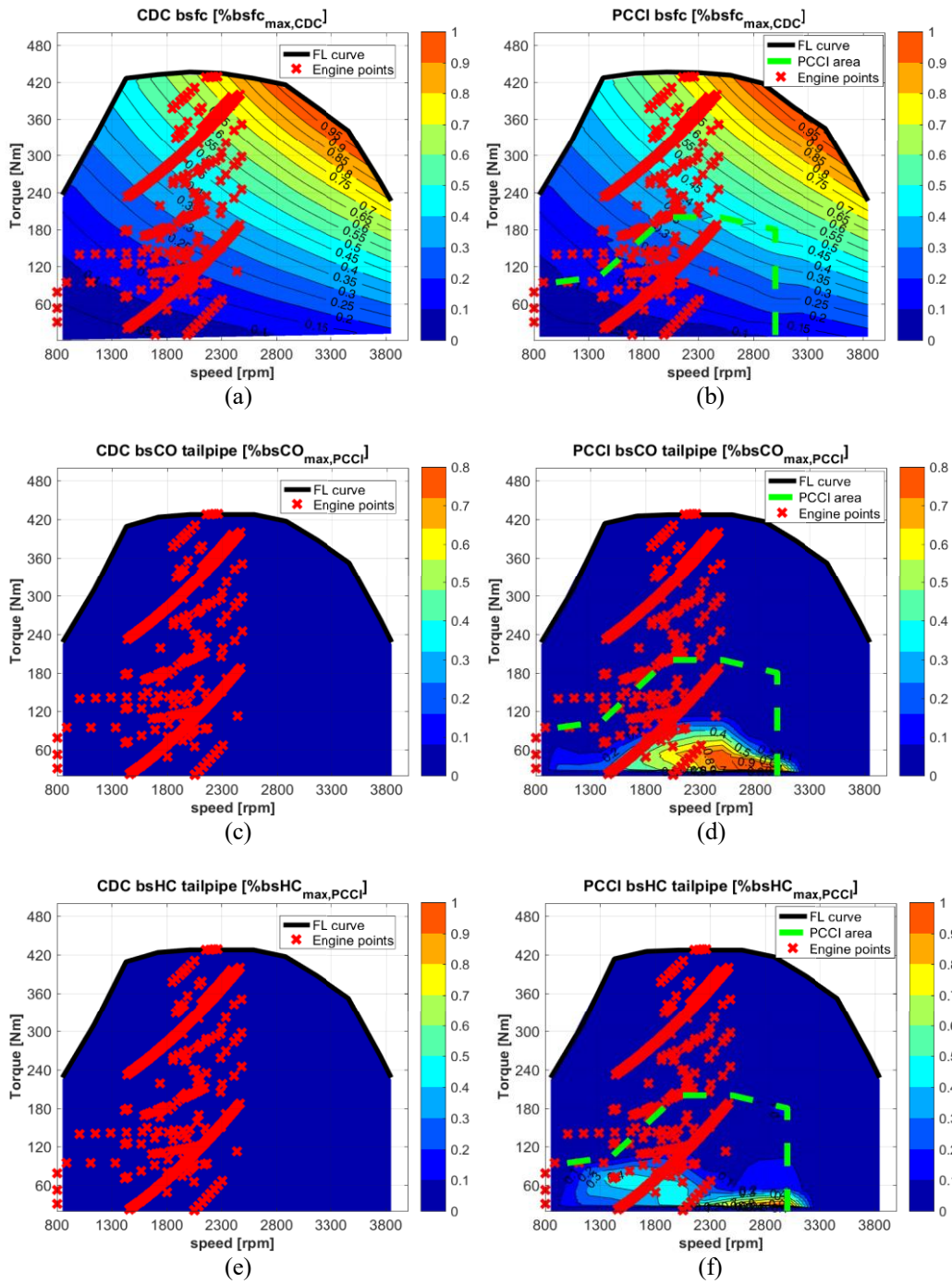


Figure 3.5: LDV *highway* cycle with the CDC and PCCI engines: normalized performance maps of bsfc and tailpipe CO/HC emissions.

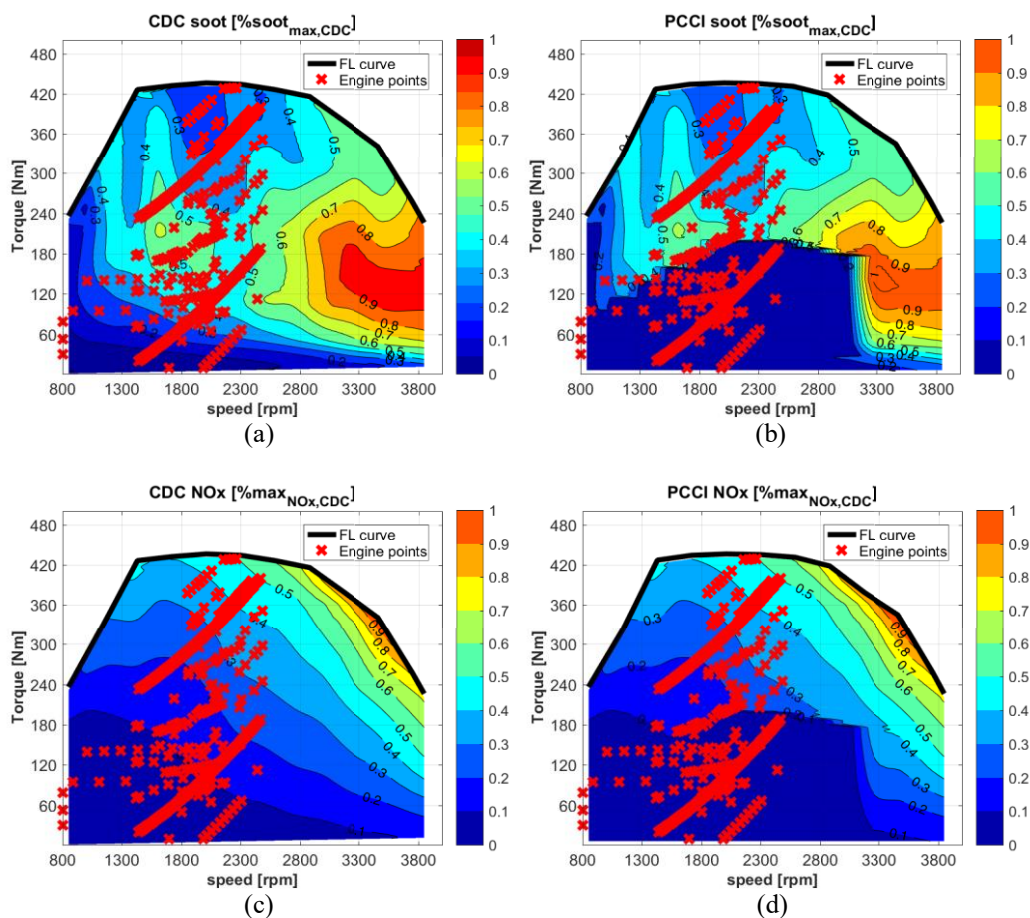


Figure 3.6: LDV *highway* cycle with the CDC and PCCI engines: normalized performance maps of engine-out soot and NO_x emissions.

As the vehicle payload increases, the engine working points move to higher loads, and therefore the engine works for a lower amount of time in the PCCI area. The comparison of the engine performance in CDC and PCCI cases as the vehicle mass increases is depicted in Figure 3.7, where all the data are reported in terms of relative variation with respect to the reference case with CDC engine and no payload. Where both engine-out and tailpipe emissions are reported, the figures are referred to the engine-out emissions of the CDC engine with no payload. Fig. 3.7a shows as the fuel consumption penalty of the PCCI case with respect to the CDC case (reported by the labels on the graph), tends to decrease as the vehicle mass increases. The same occurs in terms of CO and HC emissions: all the emissions in Figs. 3.7b-c have been normalized with respect to the emissions in CDC at the reference loading condition. It can be observed that HC engine-out emissions in CDC are almost constant with the increase of vehicle load, while the CO emissions

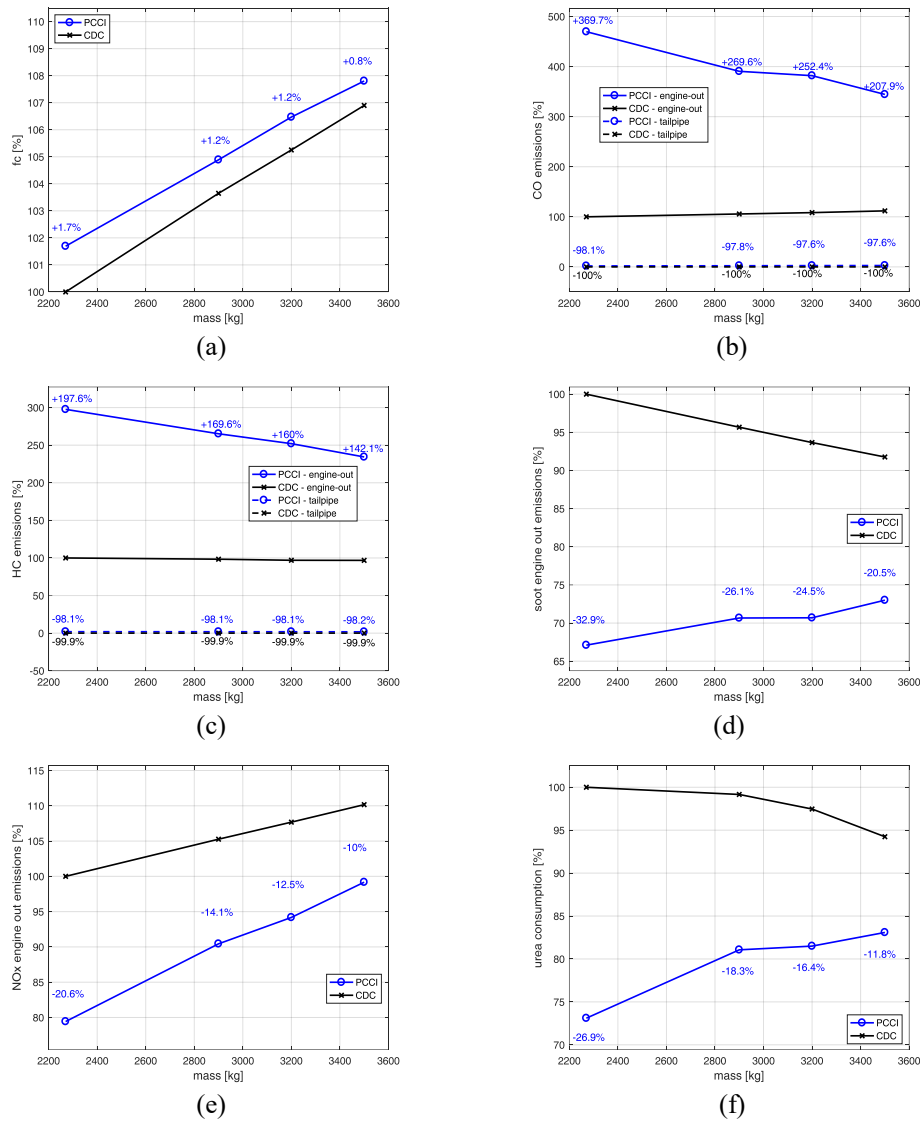


Figure 3.7: Engine cumulated fuel consumption, gaseous emissions and urea consumption on the LDV *highway* mission as a function of the vehicle mass.

tend to slightly increase. In both the cases, the penalty on engine-out HC and CO emissions on the PCCI engine tend to decrease as the vehicle mass increases. Figs. 3.7d-e show as in CDC the NO_x emissions tend to increase with the vehicle mass (as the engine load increases, and the combustion temperature increases as a consequence), while soot emissions decrease with the vehicle mass. Nevertheless, both the NO_x and soot emissions tend to increase with the vehicle mass as the engine works gradually less in PCCI combustion mode, thus reducing the benefit that can be obtained by the PCCI engine with respect to the CDC one. Also the benefit in terms of urea consumption reduces as a consequence (Fig. 3.7f).

A similar analysis has been also performed on the *LDV extra-urban* cycle and on the *LDV urban* cycle. Referring to the baseline loading condition, the fuel consumption penalty for the PCCI engine is 3.2% on the *Custom LDV extra-urban* cycle (Fig. 3.8a) and 4.9% on the *Custom LDV urban* cycle (Fig. 3.14a), being the latter a condition in which the engine mostly works at low loads, and therefore

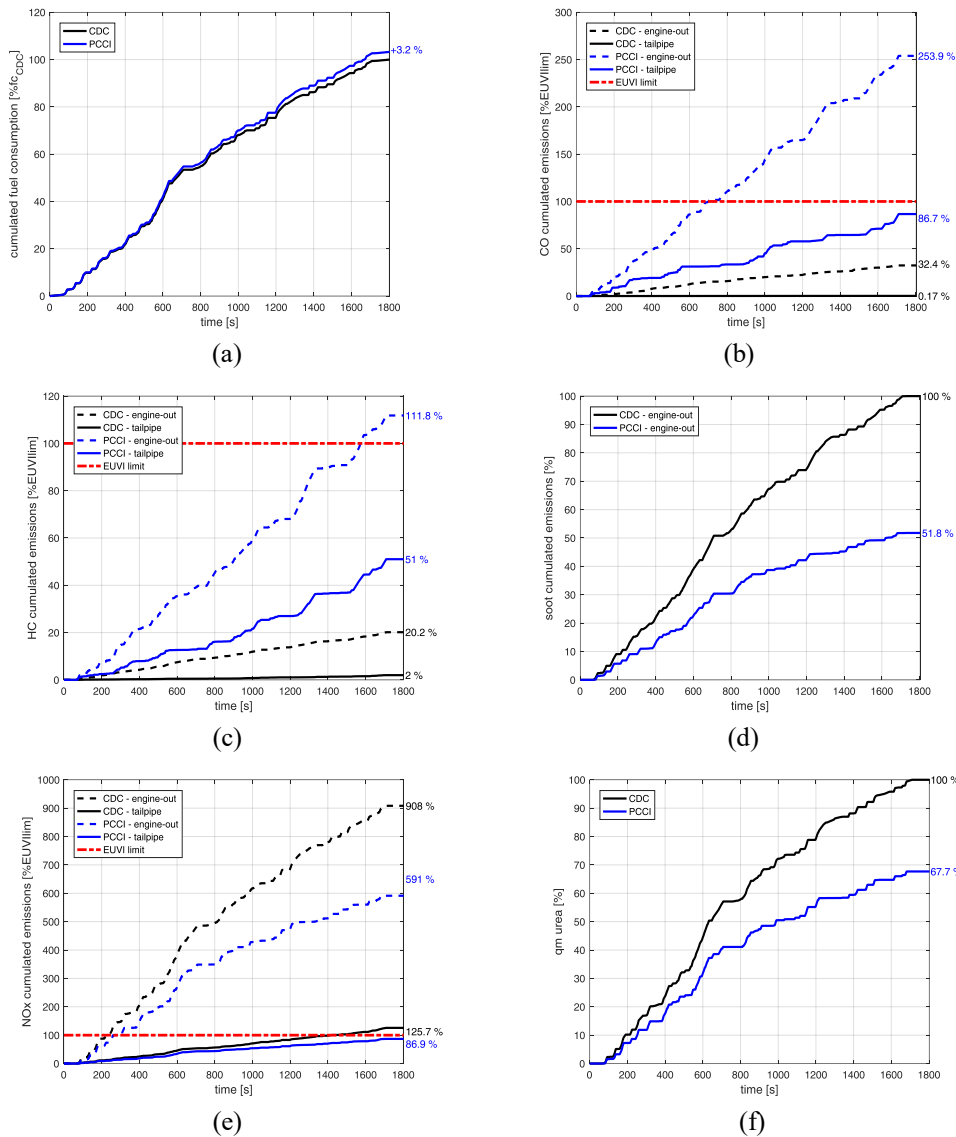


Figure 3.8: Engine cumulated fuel consumption, gaseous emissions and urea consumption on the *LDV extra-urban* mission. Fuel consumption (a), soot engine-out emissions (d) and urea consumption (f) are reported in terms of percentage of the cumulated values at the end of the cycle with the reference CDC engine. CO (b), HC (c) and NO_x (e) emissions are reported as percentage of the Euro VI limits.

spends most of the time in the PCCI area. Concerning CO and HC emissions, the graphs show a similar behavior as already discussed for the *LDV highway* cycle (Figs. 3.8b-c and 3.14b-c): in the *extra-urban* cycle, in PCCI mode 95% of the CO tailpipe emissions and 60% of the HC tailpipe emissions are produced with DOC conversion efficiencies lower than the minimum DOC conversion efficiencies obtained with the CDC engine (cf. Figs. 3.9a-b-c-d). Similarly, in the *urban* cycle, 95% of the CO tailpipe emissions and 75% of the HC tailpipe emissions are produced with DOC conversion efficiencies lower than 78% and 50%, respectively (cf. Figs. 3.15a-b-c-d). Soot engine-out emissions decrease by 48.2% on the *extra-urban* cycle and by 77.9% on the *urban* cycle (Figs. 3.8d and 3.14d, respectively) with the PCCI engine, while NO_x tailpipe emissions decrease by 38.8% on the *extra-urban* mission and by 86% on the *urban* one (Figs. 3.8e and 3.14e), with a reduction in urea consumption by 32.7% and 74.3% on the two missions (Figs. 3.8f and 3.14f). Figs. 3.9e, 3.10a-b-d, 3.15e and 3.16a-b-d show how soot production, NO_x emissions and urea consumption are distributed with respect to the engine load (bmep) in the PCCI and in the CDC cases for the *extra-urban* and *urban* cycles, respectively, and Figs. 3.9f, 3.10c-e, 3.15f and 3.16c-e show the same figure as percentage of the total emissions along the missions. Figures 3.11, 3.12 and 3.17, 3.18 show the engine working points for the simulated *extra-urban* and *urban* missions on the engine maps related to the CDC and to the PCCI engine.

Fig. 3.13 and Fig. 3.19 show the evolution of fuel consumption, emissions and urea consumption in the PCCI case and CDC case when the vehicle payload increases, with the same general trends already discussed for the *highway* cycle. On the *extra-urban* cycle, fuel consumption penalty due to PCCI consumption varies from 3.2% at the vehicle curb weight to 1.5% at the vehicle maximum load, the benefit on soot emissions and NO_x tailpipe emissions varies between 48% and 39% and from 31% to 18%, respectively, with the reduction of urea consumption being between 32% and 22% on the PCCI engine. In the *urban* mission, the fuel penalty ranges from 4.9% with no payload to 3.5% with the maximum payload, the reduction of soot emissions varies between 78% and 54% and for tailpipe NO_x emissions it ranges from 73% to 45%, with the reduction in urea consumption being between 74% and 42%.

It is worth to remark that the results here presented are based on custom driving cycles, and that none of these cycles are considered to be representative of an homologation procedure. Therefore, although in some of the graphs Euro VI limits were reported in order to provide a reference for the comparison, in none of the presented cases the emissions are compulsory required to comply with Euro VI limits. Additionally, it has to be considered that all the simulations here discussed are based on steady state tests performed on the hot engine, and therefore – as a

thermal model of the engine is not yet available for implementation in the software tool TyPE – engine cold starts are not taken into account.

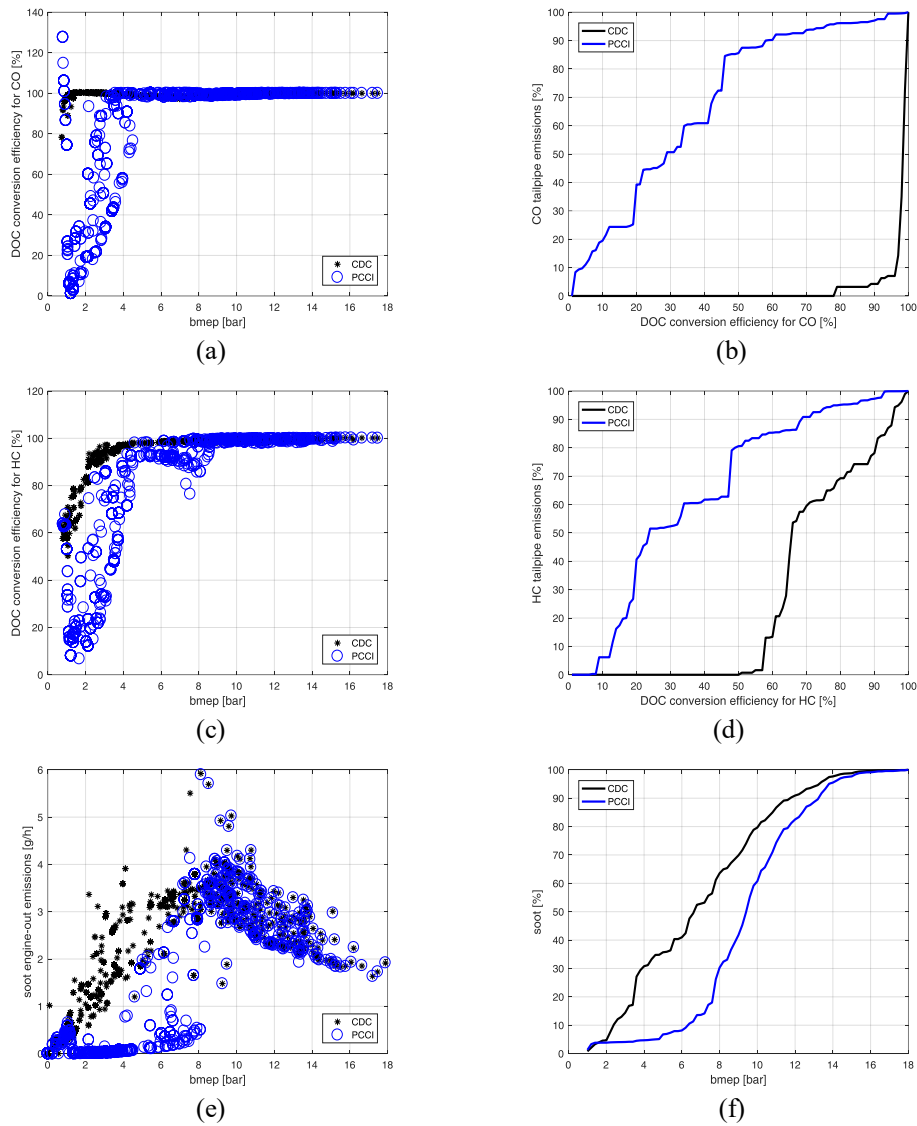


Figure 3.9: LDV *extra-urban* cycle with the CDC and PCCI engines: DOC conversion efficiency for CO and HC emissions (a,c) and cumulated relative CO and HC tailpipe emissions (b,d) as a function of engine load; soot instantaneous (e) and cumulated relative emissions (f) as a function of engine load.

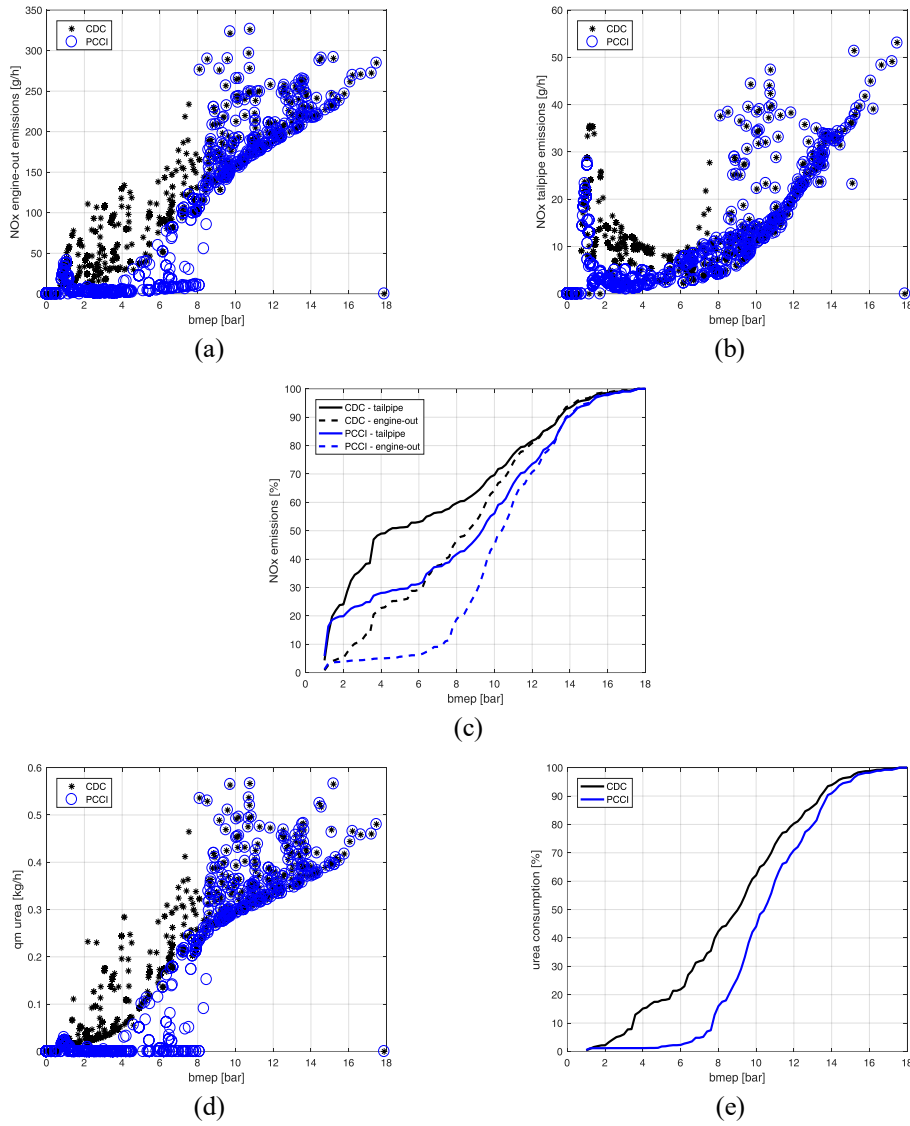


Figure 3.10: LDV *extra-urban* cycle with the CDC and PCCI engines: NO_x instantaneous (a, b) and cumulated relative emissions (c) as a function of engine load; instantaneous and cumulated relative urea consumption as a function of engine load (d, e)

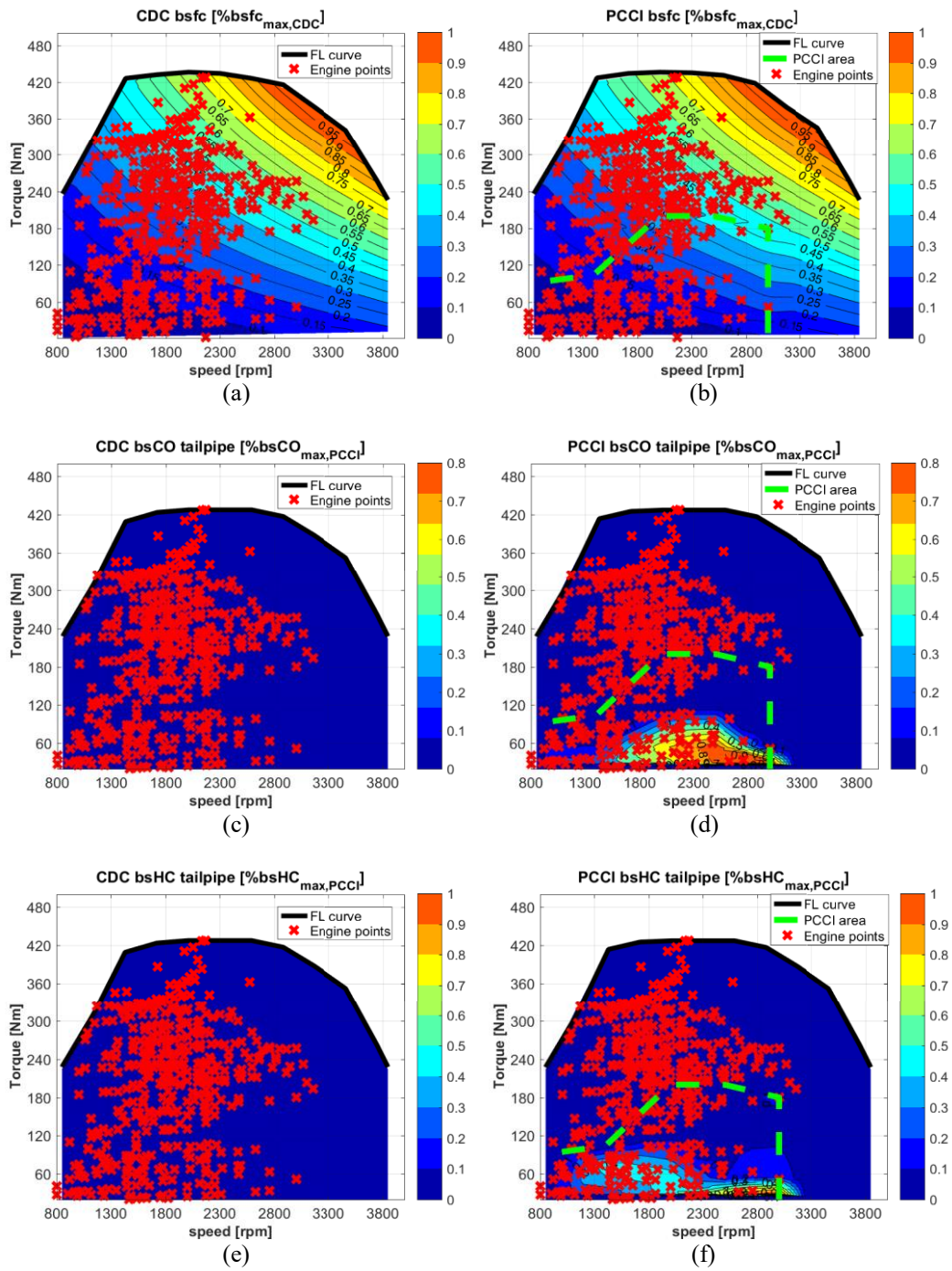


Figure 3.11: LDV *extra-urban* cycle with the CDC and PCCI engines: normalized performance maps of bsfc and tailpipe CO/HC emissions.

All the cases discussed in this *Section* have highlighted as the advantages in terms of NO_x and soot emissions due to PCCI combustion mode, discussed in *Chapter 1* on steady-state tests only, can be effectively exploited on real-world driving cycles. Nevertheless, the analysis has further highlighted the increase in fuel consumption due to the implementation of the PCCI combustion, which was in the range +0.5%-4.9% in the simulated cases. Next *Section* will be devoted mainly to analyze if this worsening effect on fuel consumption can be partially or fully mitigated by the introduction of a tire pressure management system.

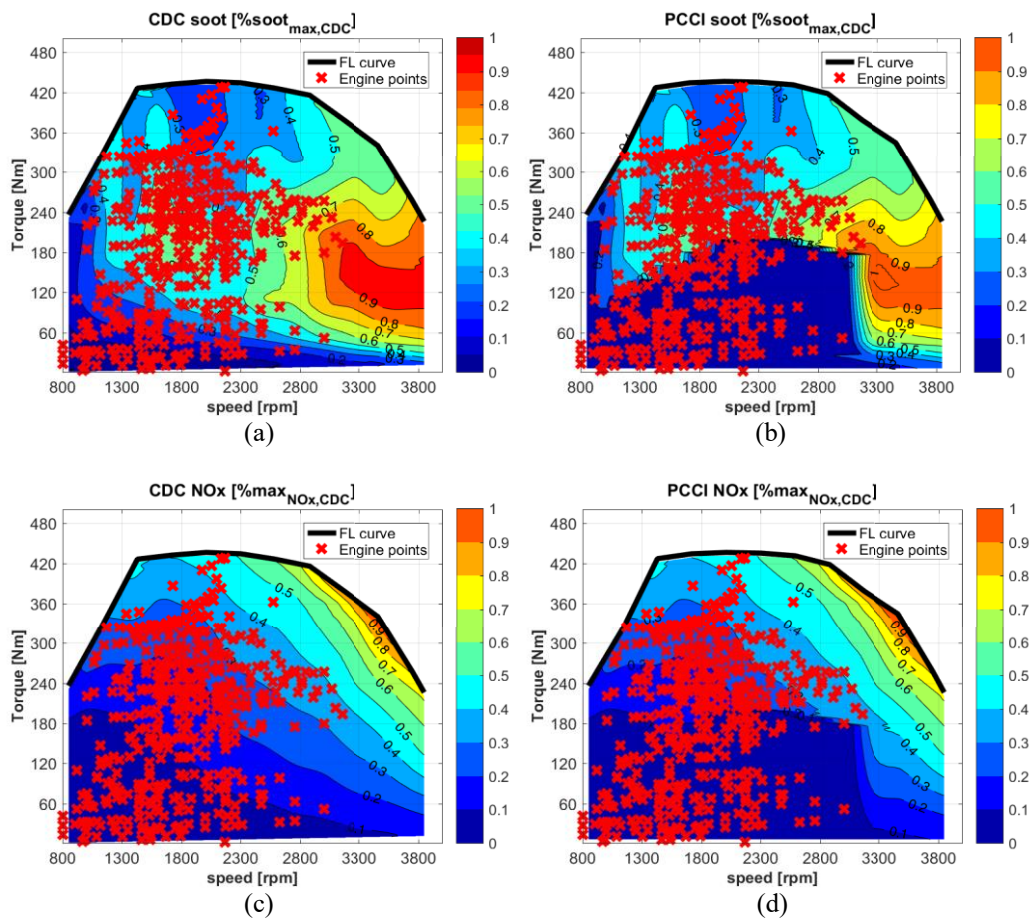
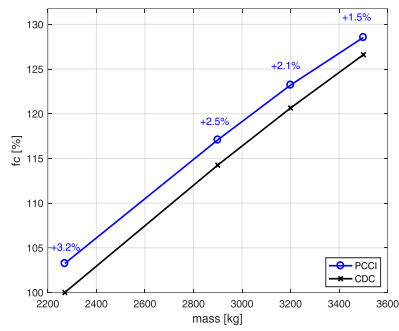
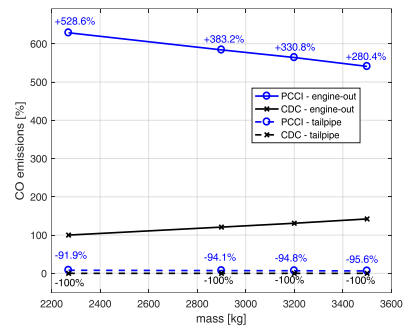


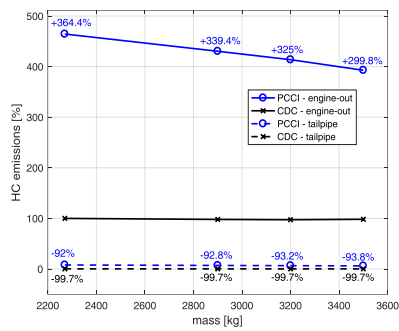
Figure 3.12: LDV *extra-urban* cycle with the CDC and PCCI engines: normalized performance maps of engine-out soot and NO_x emissions.



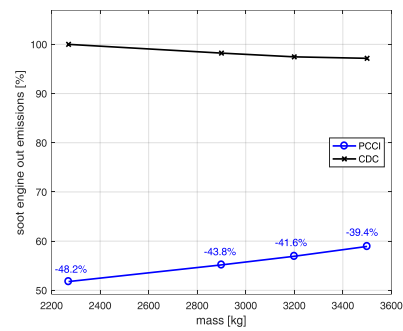
(a)



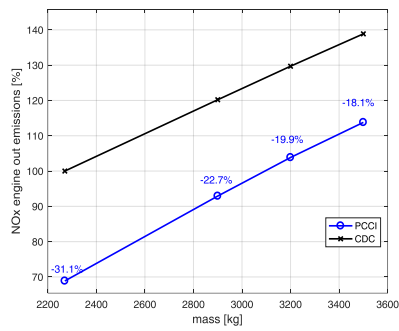
(b)



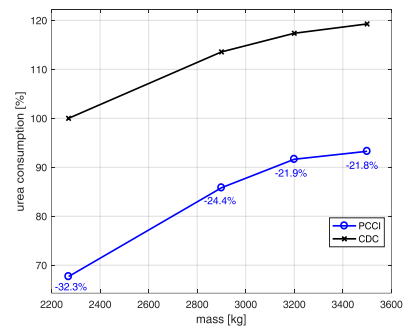
(c)



(d)



(e)



(f)

Figure 3.13: Engine cumulated fuel consumption, gaseous emissions and urea consumption on the LDV *extra-urban* mission as a function of the vehicle mass.

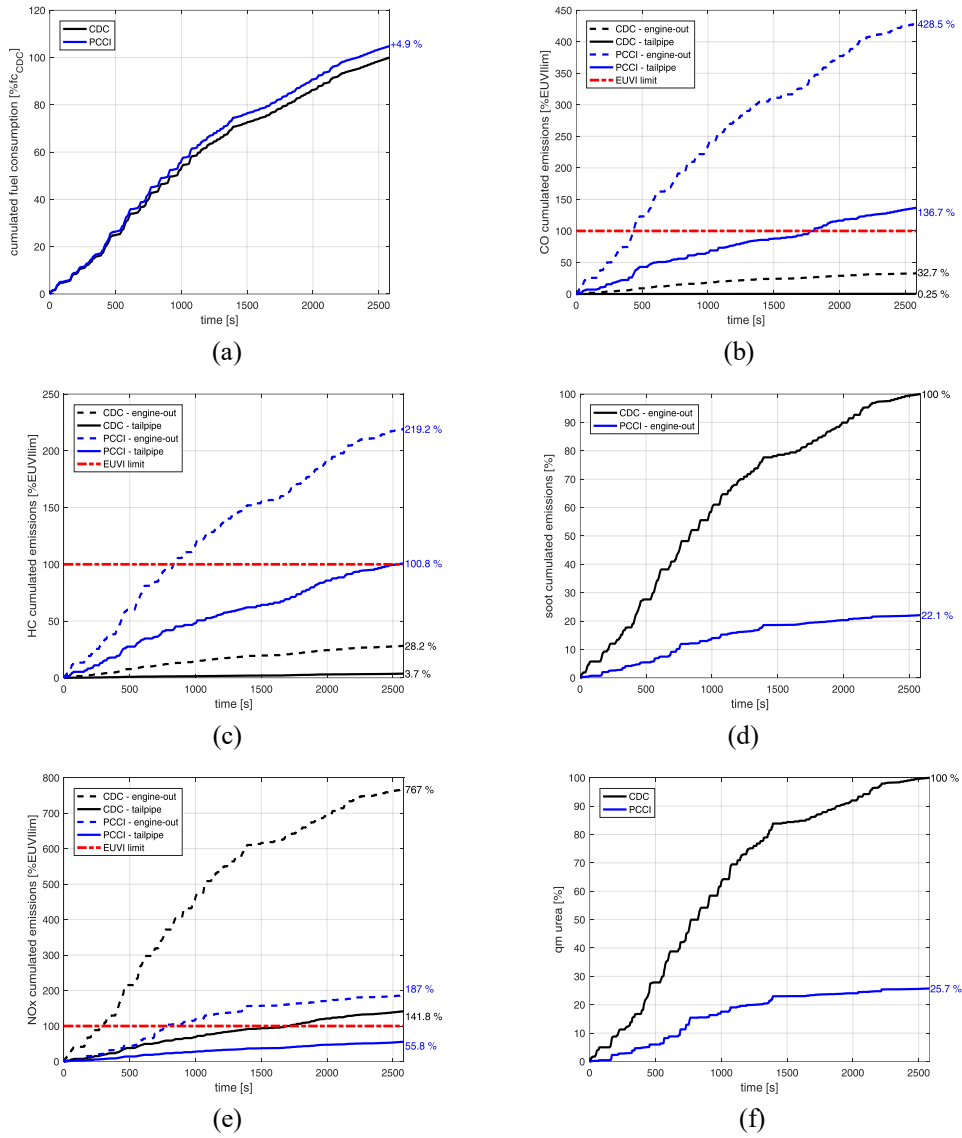


Figure 3.14: Engine cumulated fuel consumption, gaseous emissions and urea consumption on the LDV *urban* mission. Fuel consumption (a), soot engine-out emissions (d) and urea consumption (f) are reported in terms of percentage of the cumulated values at the end of the cycle with the reference CDC engine. CO (b), HC (c) and NO_x (e) emissions are reported as percentage of the Euro VI limits.

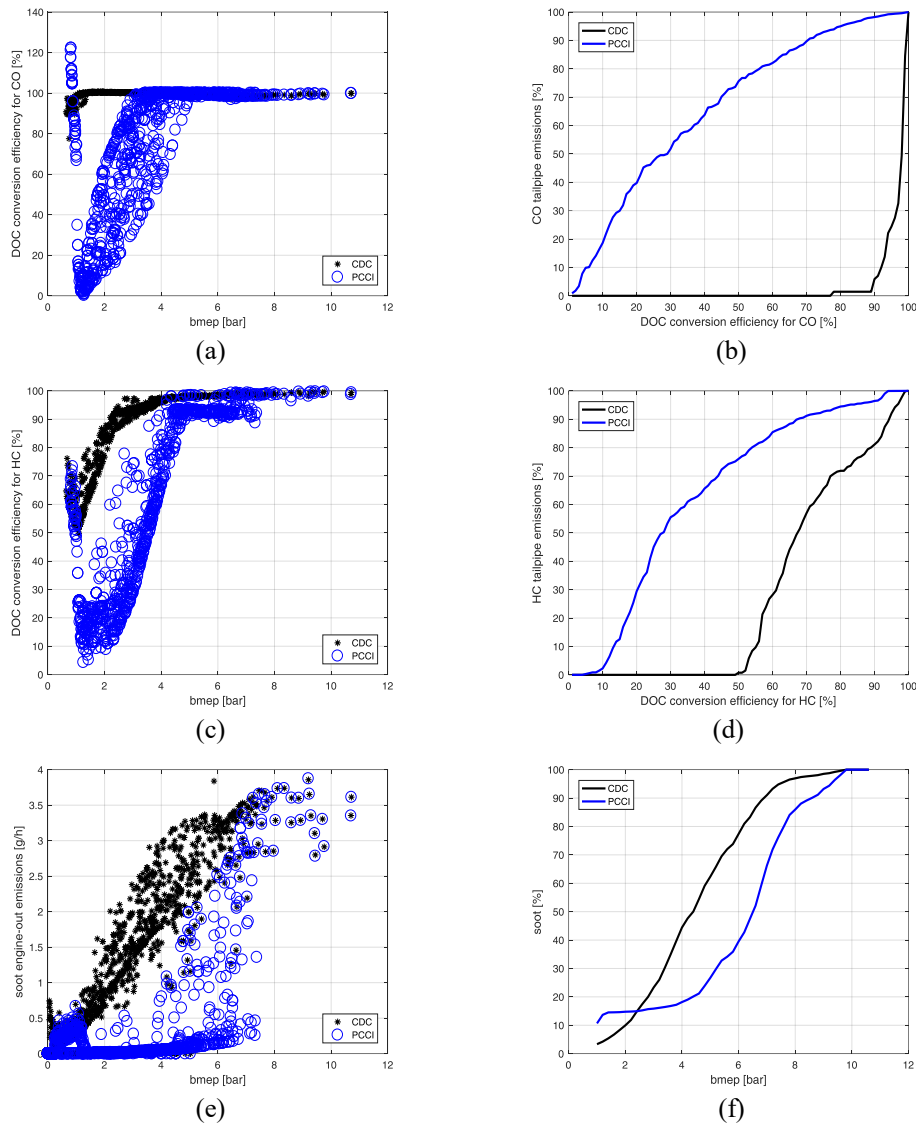


Figure 3.15. LDV *urban* cycle with the CDC and PCCI engines: DOC conversion efficiency for CO and HC emissions (a,c) and cumulated relative CO and HC tailpipe emissions (b,d) as a function of engine load; soot instantaneous (e) and cumulated relative emissions (f) as a function of engine load.

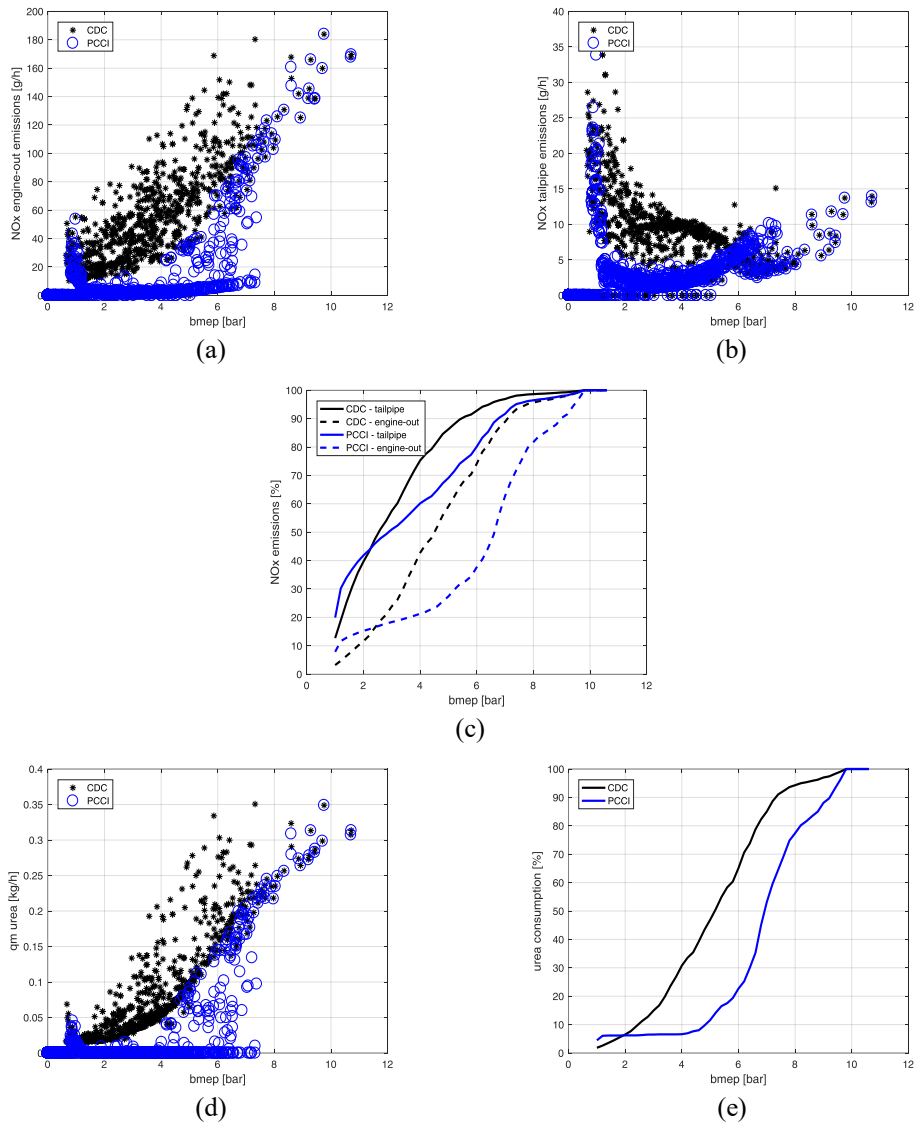


Figure 3.16: LDV *urban* cycle with the CDC and PCCI engines: NO_x instantaneous (a, b) and cumulated relative emissions (c) as a function of engine load; instantaneous and cumulated relative urea consumption as a function of engine load (d, e).

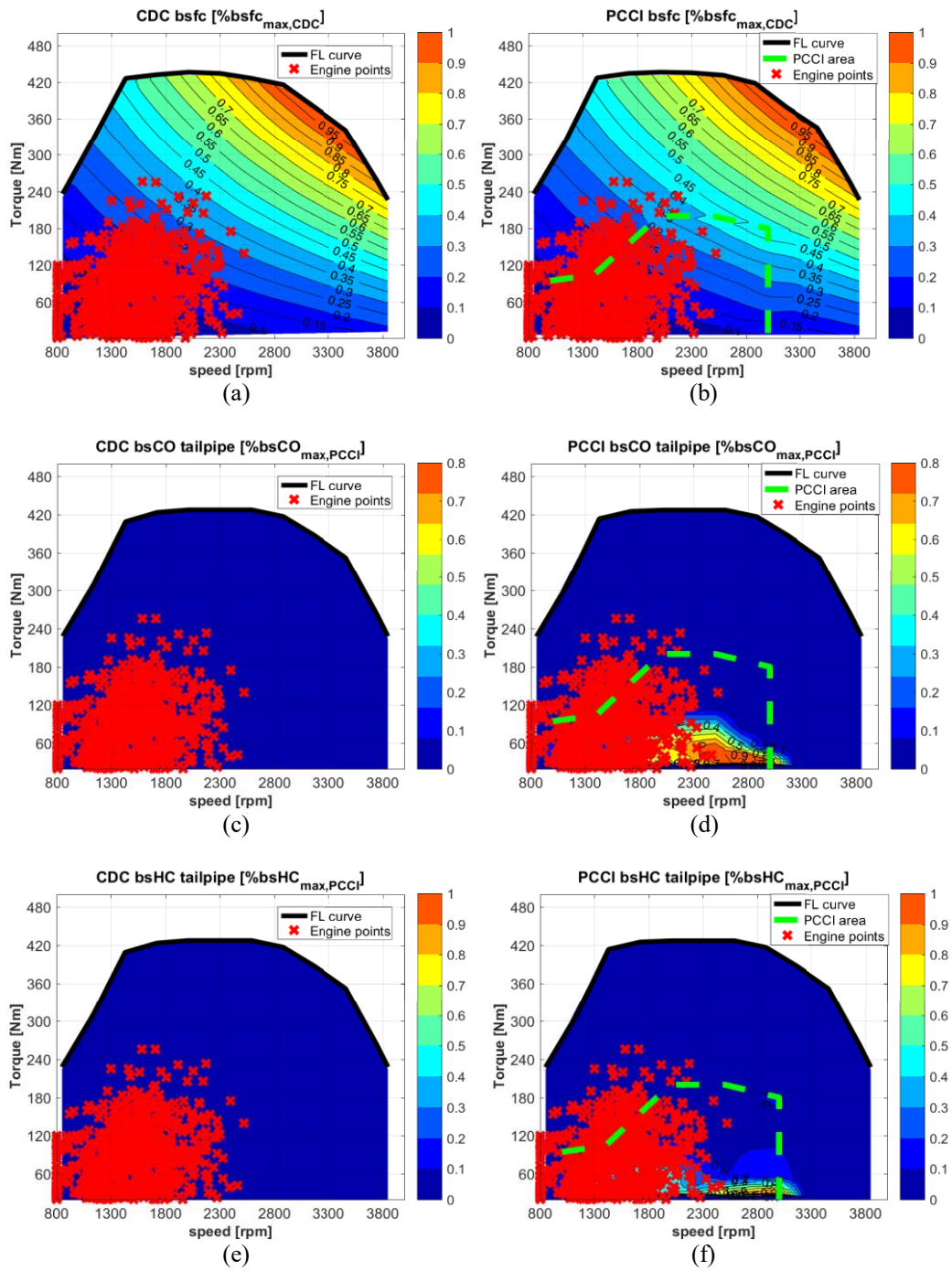


Figure 3.17: LDV *urban* cycle with the CDC and PCCI engines: normalized performance maps of bsfc and tailpipe CO/HC emissions.

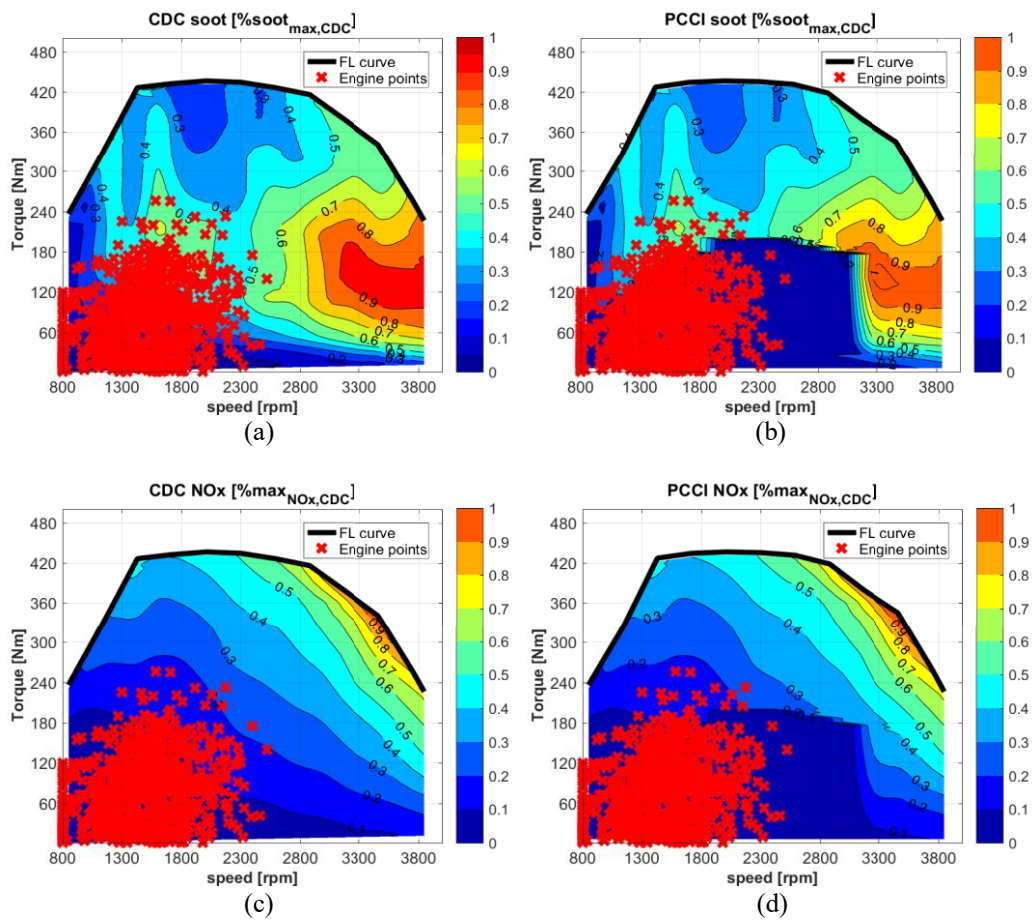
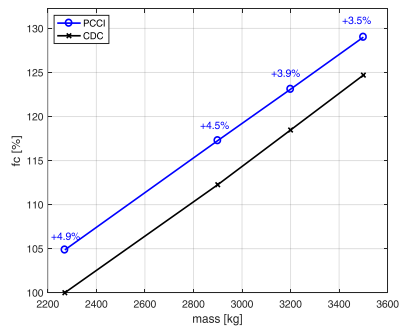
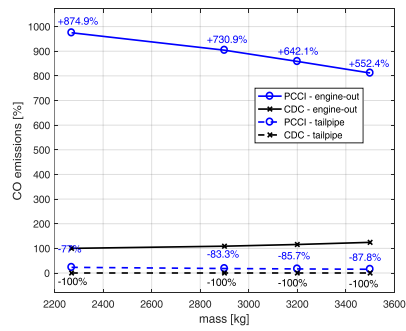


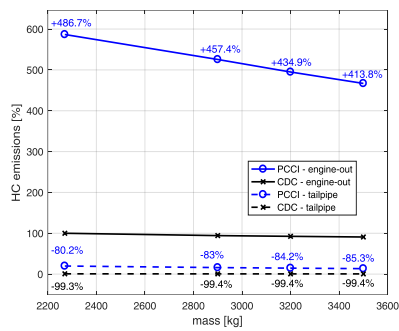
Figure 3.18: LDV *urban* cycle with the CDC and PCCI engines: normalized performance maps of engine-out soot and NO_x emissions.



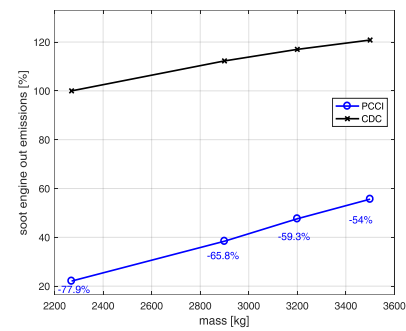
(a)



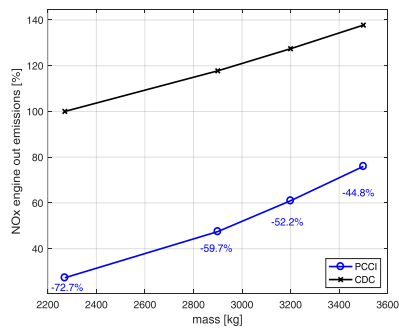
(b)



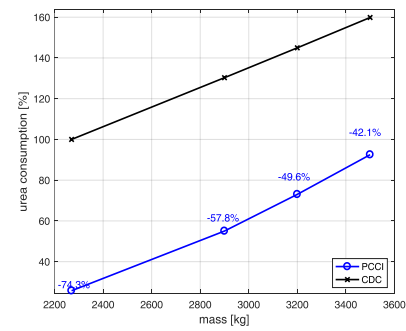
(c)



(d)



(e)



(f)

Figure 3.19: Engine cumulated fuel consumption, gaseous emissions and urea consumption on the LDV *urban* mission as a function of the vehicle mass.

Finally, this study has further remarked as the biggest limit for the implementation of PCCI combustion is the increase in HC and CO emissions. It is worth to underline that in all the simulated cases (including cases at various vehicle payloads, although not all these cases have been extensively reported graphically for the sake of brevity) tailpipe emissions of HC and CO were well below the Euro VI limits. Nevertheless, the increase of these gaseous emissions with respect to CDC case is remarkable, and could be even larger in case of cold starts. Therefore, the keypoint in the roadmap for the extensive introduction of this kind of combustion – or other low temperature combustion modes – on road engines is to find proper solutions for treating the HC/CO emissions with low temperature exhaust gases.

As an example of possible solutions to be implemented, in [289] the effect of hydrogen injection in the exhaust line was studied on a platinum and a platinum-palladium catalyst, showing generally a lower light-off temperature with the platinum one and using H₂ concentrations between 500 ppm and 2500 ppm. With the platinum catalyst the CO conversion efficiency reached 100% at about 100°C with 2500 ppm of H₂, lowering the light-off temperature by about 55°C with respect to the case where no H₂ was injected in the exhaust gases, while HC conversion efficiency of 90% was reached around 250°C with no hydrogen injection and around 185°C with 2500 ppm of H₂ [289]. The higher temperature required for proper oxidation of HC species with respect to CO is generally due to the high concentration of “medium-heavy” hydrocarbons (alkanes, alkenes, aromatics, etc.) [289]. Other possible solutions include the installation of a small pre-turbo DOC in addition to the main DOC, which was proven to be effective in reducing HC and CO emissions in a conventional diesel combustion engine [290], or electrically heated catalysts (EHC), which can increase the DOC temperature to about 180°C in 20s idling, where the DOC temperature without EHC would be 50°C [291]. Further improvements can be obtained through the implementation of dedicated post-injection strategies, since an optimization of the amount of fuel injected in the post-injection and the related timing have been demonstrated to increase the exhaust gas temperature [292, 293], although this also caused increase in fuel consumption in the cited studies. Also improving thermal insulation of the DOC could be considered as an additional solution to maintain the catalyst at proper working temperature, especially during transients from the CDC area to the PCCI one, i.e. when the exhaust gas temperature would decrease due to the variation of the engine operating conditions.

3.2 Combining the PCCI engine with ACTIS: simulations on single mission profiles

In this *Section*, the combined effect of PCCI combustion and tire pressure management is discussed. As mentioned above, the study has been performed by means of computer simulations using the engine performance maps of the CDC engine, and of the PCCI/CDC hybrid combustion mode case. For each of these two configurations, the vehicle has been simulated in all the pressure management conditions discussed in *Section 2.5*:

- a *reference* case with the nominal tire pressure and under the hypothesis of tires hot start;
- a *misuse* case, with tire pressure 25% lower than the reference case on all the tires;
- a case at reference tire pressure considering the effect of tire *cold-start*, i.e. applying to the tire rolling resistance at the reference tire pressure the percentage variation in time due to tire warm-up, according to the graph of Figure 2.20;
- a case of tires cold-start with the application of the *warm-up* strategy, where tire pressure is set to 1 bar above the reference tire pressure at the beginning of the test cycle, and air is then blown-out by means of the ACTIS as the tires warm-up, in order to reach the reference pressure at the end of the thermal transient. Fig. 3.20 shows the tire pressure adaptation during the tire warm-up with and without the warm-up tire pressure management strategy, in a case in which the vehicle is loaded at its reference loading condition, and with the pressure equalized on all the tires. Notice that Fig. 3.20 shows an instantaneous value of tire pressure normalized to ambient temperature, and therefore a decrease in the “cold” tire pressure consists actually in an isobaric air blow-out while tire inner temperature increases during the warm-up;
- a case of tire pressure adaptation to the vehicle loading condition (*iso-deflection* strategy), where tire pressure is adjusted linearly with the static load acting on each axle, from 3.5 bar for a load of 1135 kg per axle, to 5 bar when a load of 1750 kg per axle is applied. Tire pressure is kept constant along the cycle.

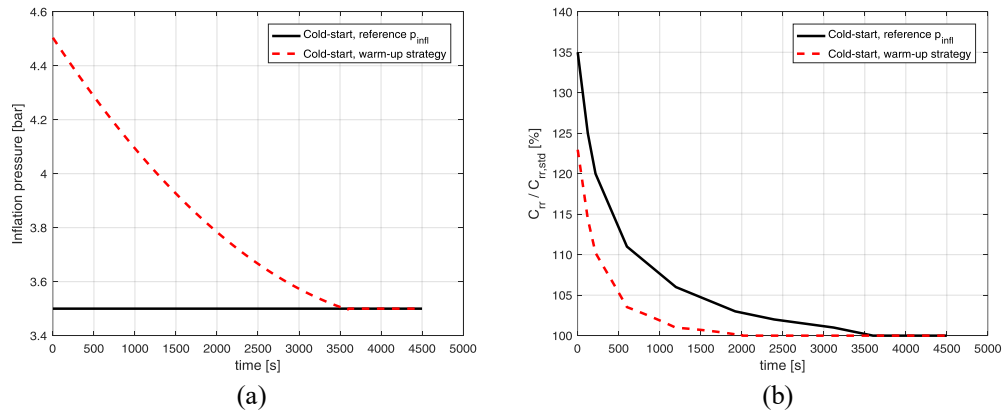


Figure 3.20: Tire inflation pressure (a) and the relative variation of tire rolling resistance (b) during a cold start, with (red dashed line) and without (black solid line) the warm-up tire pressure management strategy actuated through the ACTIS on the reference LDV.

Further details on the pressure management strategies were discussed in *Section 2.3.3* and *Section 2.5.2*. As mentioned above, the results have then been combined in three main cases for comparison: a *baseline* case (*reference* tire pressure with tire cold-start); a *misuse* case (25% lower tire pressure with tire cold start); an *ACTIS* case (*warm-up* and *iso-deflection* strategies). The results are reported in Figs. 3.21-3.26 for the *highway*, *extra-urban* and *urban* missions, respectively. It is worth to remark, as previously mentioned, that the engine is always simulated in warm conditions (i.e., after the warm-up transient), even when tires cold-start is taken into account. This is due to the fact that TyPE at the moment does not implement yet a thermal model to simulate engine warm-up.

Referring to the *highway* mission profile, with the CDC engine the fuel consumption in the *misuse* case worsens by 1.2-1.6% with respect to the baseline, while ACTIS allows a reduction by 1.2-3.1%, depending on the loading condition of the vehicle (Fig. 3.21a refers to the vehicle without payload, and Fig. 3.21b refers to the vehicle at its maximum payload). With the implementation of PCCI combustion, the relative worsening due to *misuse* (i.e., the delta between the PCCI engine in the *baseline* and *misuse* conditions) is aligned to the worsening due to *misuse* with the CDC engine (i.e., the abovementioned delta between the CDC engine in the *baseline* and *misuse* conditions). The combined implementation of PCCI and ACTIS allows to obtain fuel consumption slightly higher (+0.5% without payload) or lower (-2.2% with maximum payload) with respect to the baseline CDC case.

Soot engine-out emissions with the PCCI engine decrease by 26-33.4% without payload and by 15.3-21% with maximum payload, with respect to the baseline CDC case (Figs. 3.21c-d), being the soot reduction larger in the *ACTIS* case (where the

engine load is reduced) and smaller in the *misuse* case. Similarly, NO_x engine-out emissions (Figs. 3.21e-f) decrease by 13.9-22.1% with no payload and by 5.5-13.6% with maximum payload by means of the introduction of the PCCI combustion mode, being the highest reduction obtained when the ACTIS is also implemented. It is worth noting that, as also reported in literature [38, 267], engine-out NO_x emissions are also sensitive to pressure management in CDC: misuse increases NO_x emissions by 1.3-1.8%, while the implementation of advanced pressure management strategies reduce NO_x engine-out emissions by 1.4-3.5%. Due to the lower engine-out NO_x emissions with the PCCI case, and the reduction of engine-out NO_x emissions with the increase in the driveline efficiency, also urea consumption is reduced by 12-27.8% (Figs. 3.21g-h). Concerning engine-out CO and HC (Fig. 3.22a-b-c-d), in the CDC case they result to be slightly affected by tire pressure management with respect to the effect of the introduction of PCCI combustion. If the PCCI case is considered, it can be observed that the higher is the driveline efficiency (i.e., moving from the *misuse* case, to the *baseline* case, toward the *ACTIS* case) the higher are the HC and CO emissions: as the road load decreases, the engine load decreases as well. Moving the engine working points to lower bmep levels brings to a higher amount of time spent by the engine in the PCCI combustion area, with a subsequent increase in HC and CO emissions. Nevertheless, when tailpipe HC and CO emissions are considered and compared to the Euro VI limits (Figs. 3.22e-f-g-h), it can be observed that in any case the introduction of PCCI combustion worsens the tailpipe emissions, but the effect of tire pressure management is small.

With reference to Figs. 3.23-3.26, a similar behavior is also found on *extra-urban* and *urban* mission profiles, with the benefits and worsening effects of PCCI increasing as the engine spends more time in the PCCI area, i.e. moving from the *highway* to the *extra-urban* cycle, and from the *extra-urban* to the *urban* one. In terms of percentage variations on fuel consumption with respect to the CDC baseline case (Figs. 3.23a-b and 3.25a-b), the worsening effect of PCCI combustion combined to tire misuse is generally higher in lower loading conditions (i.e., with no payload) with respect to higher ones (i.e., with maximum payload), and higher moving from the *extra-urban* to the *urban* driving cycle. This is due to various effects: (1) increasing the vehicle mass, the negative effect on fuel consumption of PCCI combustion decreases as the engine load increases; (2) increasing the vehicle mass, the overall fuel consumption increases, and the relative worsening due to tire misuse applies therefore to a higher baseline fuel consumption; (3) moving from *extra-urban* to *urban* driving cycles worsens the overall fuel consumption of the PCCI engine. Reversely, the positive effect of ACTIS is higher when the vehicle mass increases, as the advantage due to iso-deflection strategy increases (c.f. Fig. 2.30) with the vehicle mass. Generally, the application of ACTIS allows to

compensate partially for the fuel penalty due to the PCCI combustion at low loading conditions, and totally or almost totally when the maximum payload is applied.

Engine-out soot emissions (Figs. 3.23c-d and 3.25c-d) are strongly reduced by the introduction of PCCI combustion, between 48.1% and 39.6% on the *extra-urban* mission (with no payload, and maximum payload, respectively) and between 77.3% and 53.4% on the *urban* mission, and the reduction of road load through ACTIS is generally beneficial on further reducing soot emissions with respect to the PCCI baseline and misuse cases. Also engine-out NO_x emissions (Figs. 3.23e-f and 3.25e-f) are strongly reduced by the introduction of PCCI, with a further positive effect due to ACTIS. Also in this case, it is remarkable the effect that tire pressure management has on engine-out NO_x emissions also in CDC, and especially in the case of maximum payload: in all the considered simulations, ACTIS reduced engine-out NO_x emissions by 1.2-1.4% with no payload and by 2.8-3.2% with the maximum payload, with respect to the baseline case. Urea consumption decreases by about 20% in the *extra-urban* mission with maximum payload up to more than 70% on the *urban* cycle with no payload (Figs. 3.23g-h and 3.25g-h).

In terms of engine-out CO (Figs. 3.24a-b and 3.26a-b) and HC (Figs. 3.24c-d and 3.26c-d) emissions, on *extra-urban* and *urban* driving cycles the trend looks generally opposite with respect to the *highway* case. While on the *highway* mission these emissions have generally shown the tendency to increase as the road load is decreased, on *extra-urban* and *urban* missions they generally tend to decrease with decreasing the road load, although these variations are considerably smaller than the effect of introducing the PCCI combustion. This is due to the fact that in the *highway* mission part of the engine working points that in the baseline case are in the low-emissions CDC area would move into the high-emissions PCCI area as the engine load decreases due to the reduction of road load. On the other hand, in *extra-urban* and *urban* missions a relatively high percentage of the engine working points during the cycle are already in the PCCI area in the baseline case, and therefore moving to lower loads has a secondary effect on HC and CO emissions. Tailpipe CO (Figs. 3.24e-f and 3.26e-f) and HC (Figs. 3.24g-h and 3.26g-h) emissions are always lower than the Euro VI limits, although much higher in the PCCI cases, with only a minor effect due to tire pressure management strategies. The most critical case is the *urban* cycle, especially for what concerns CO tailpipe emissions at low vehicle load (i.e., the condition in which the engine spends most of the time in PCCI mode, among those tested).

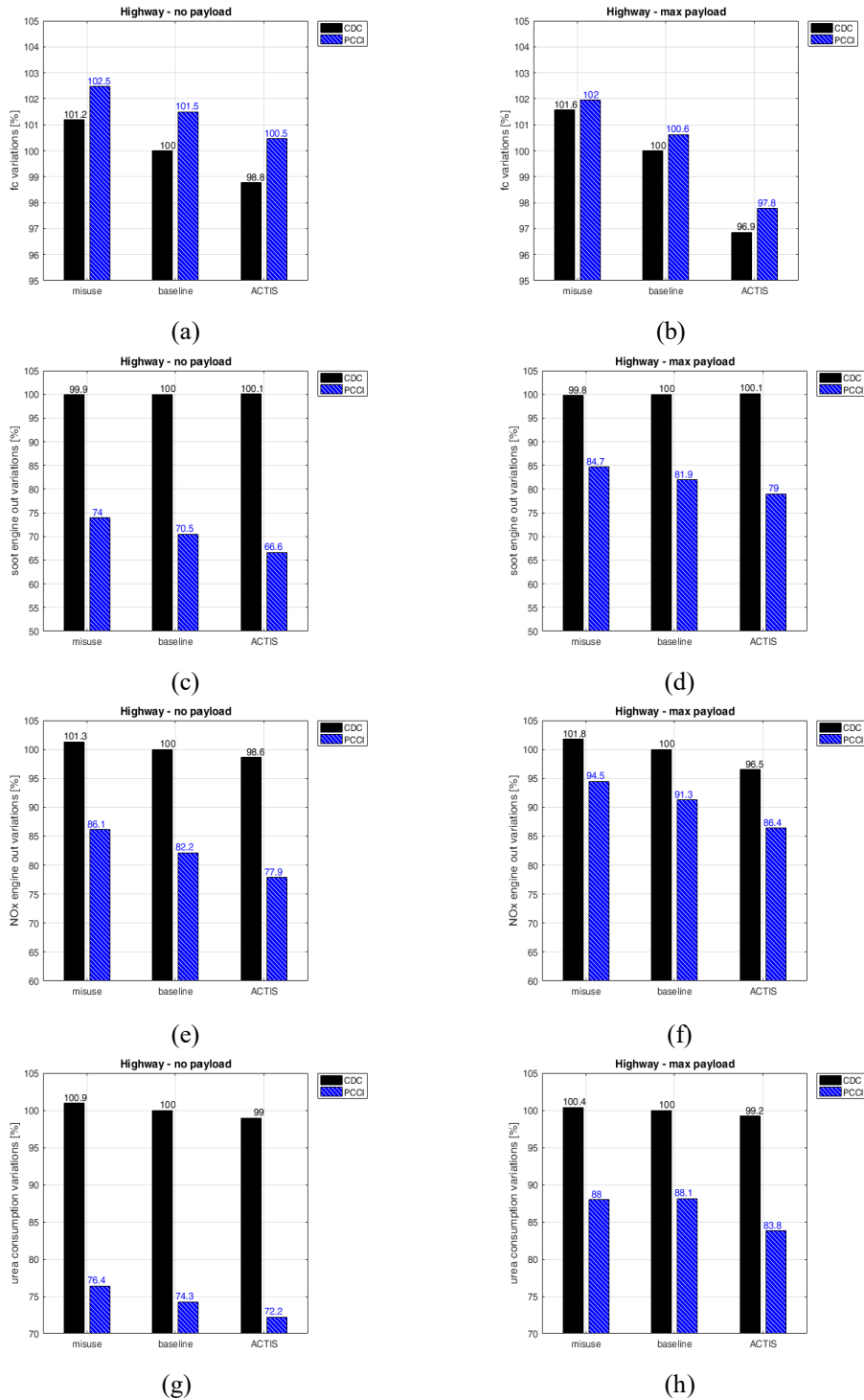


Figure 3.21: Results on LDV simulated on *highway* cycle. Fuel consumption, soot and NO_x engine-out emissions and urea consumption variations between the CDC and PCCI engines, with different tire pressure management situations: in a typical misuse case, when tires are always inflated at the nominal pressure (baseline) and in case of implementation of the ACTIS.

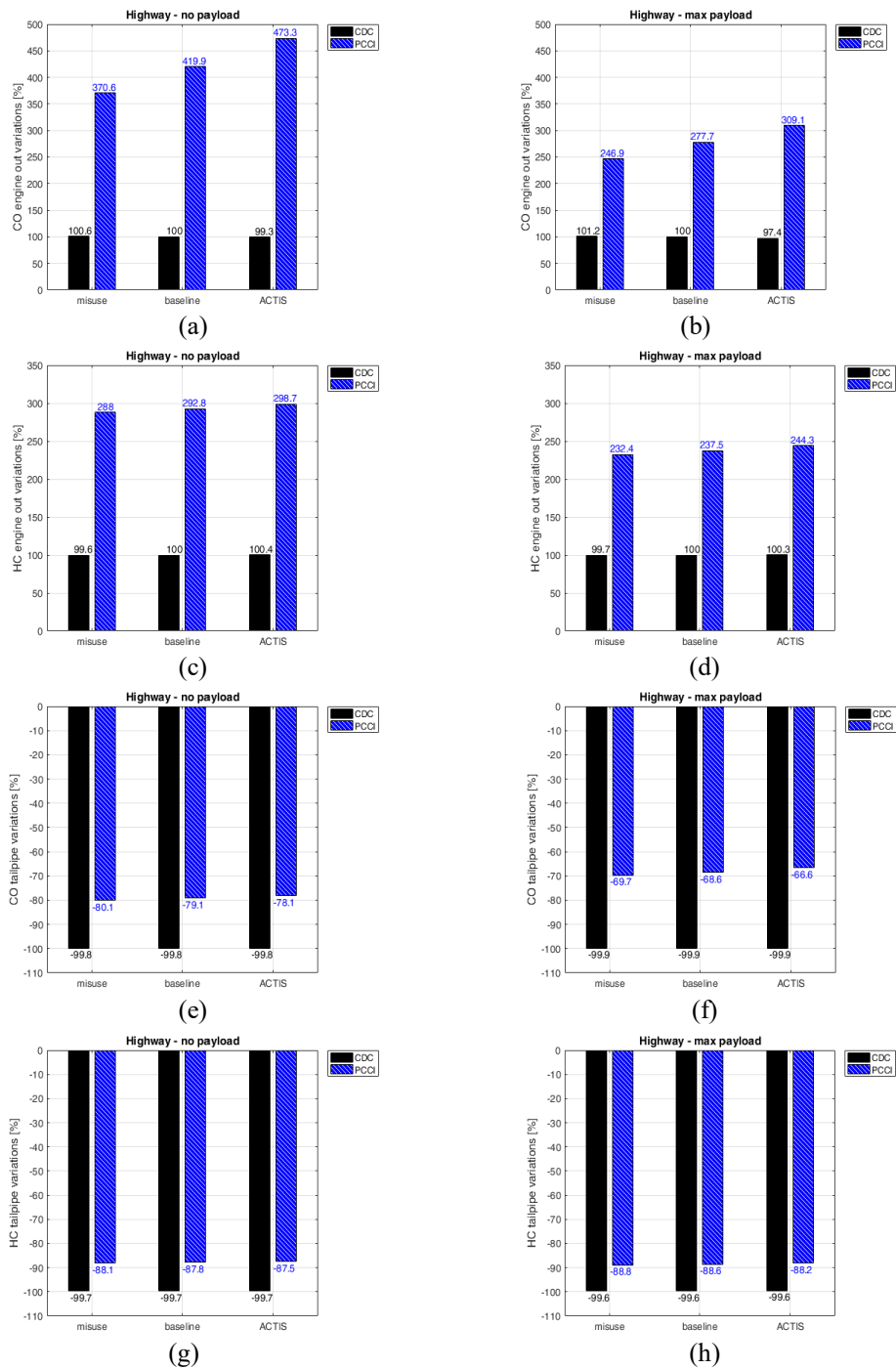


Figure 3.22: Results on LDV simulated on *highway* cycle. CO and HC engine-out and tailpipe emissions variations between the CDC and PCCI engines, with different tire pressure management situations: in a typical misuse case, when tires are always inflated at the nominal pressure (baseline) and in case of implementation of the ACTIS.

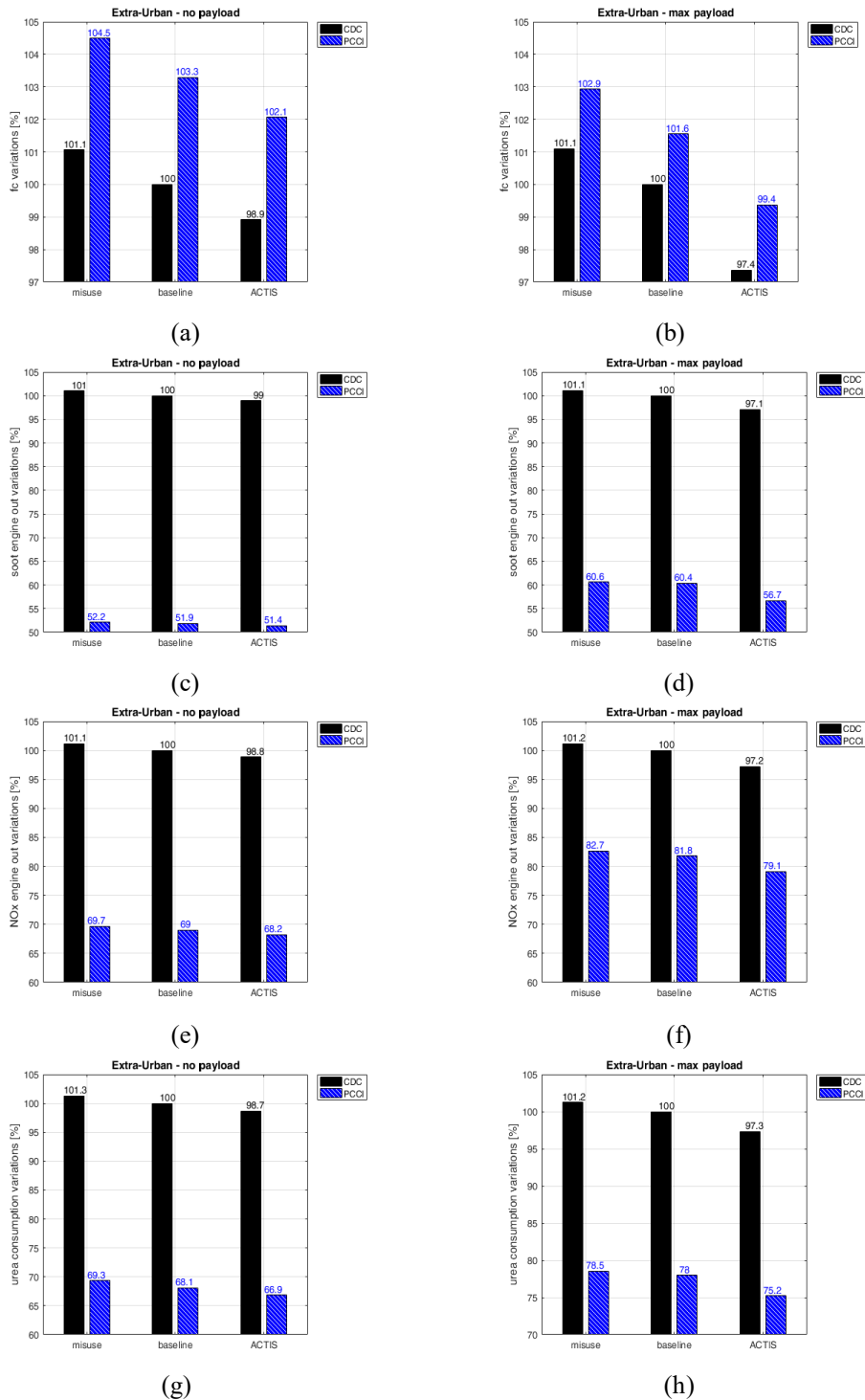


Figure 3.23: Results on LDV simulated on *extra-urban* cycle. Fuel consumption, soot and NO_x engine-out emissions and urea consumption variations between the CDC and PCCI engines, with different tire pressure management situations: in a typical misuse case, when tires are always inflated at the nominal pressure (baseline) and in case of implementation of the ACTIS.

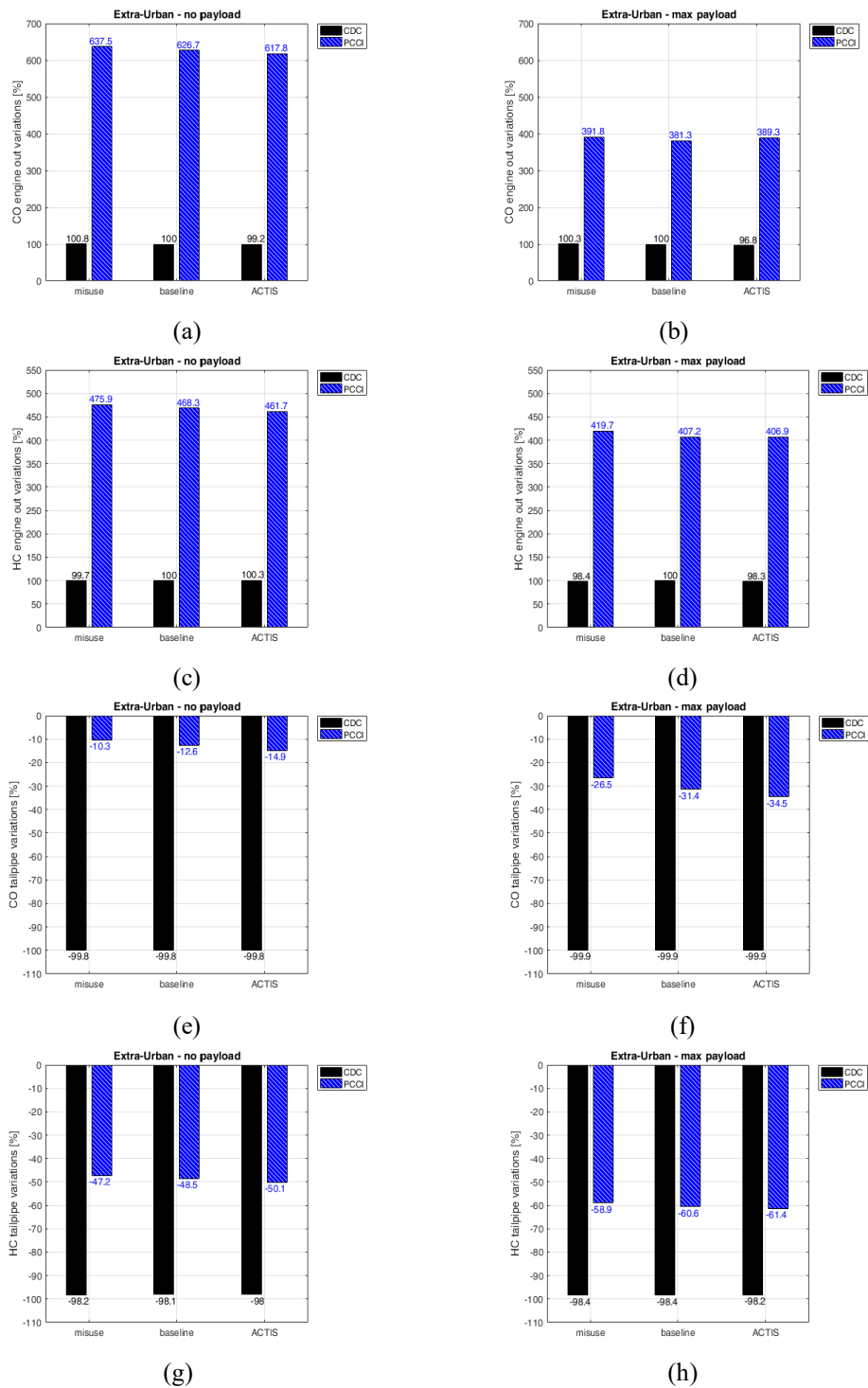


Figure 3.24: Results on LDV simulated on *extra-urban* cycle. CO and HC engine-out and tailpipe emissions variations between the CDC and PCCI engines, with different tire pressure management situations: in a typical misuse case, when tires are always inflated at the nominal pressure (baseline) and in case of implementation of the ACTIS.

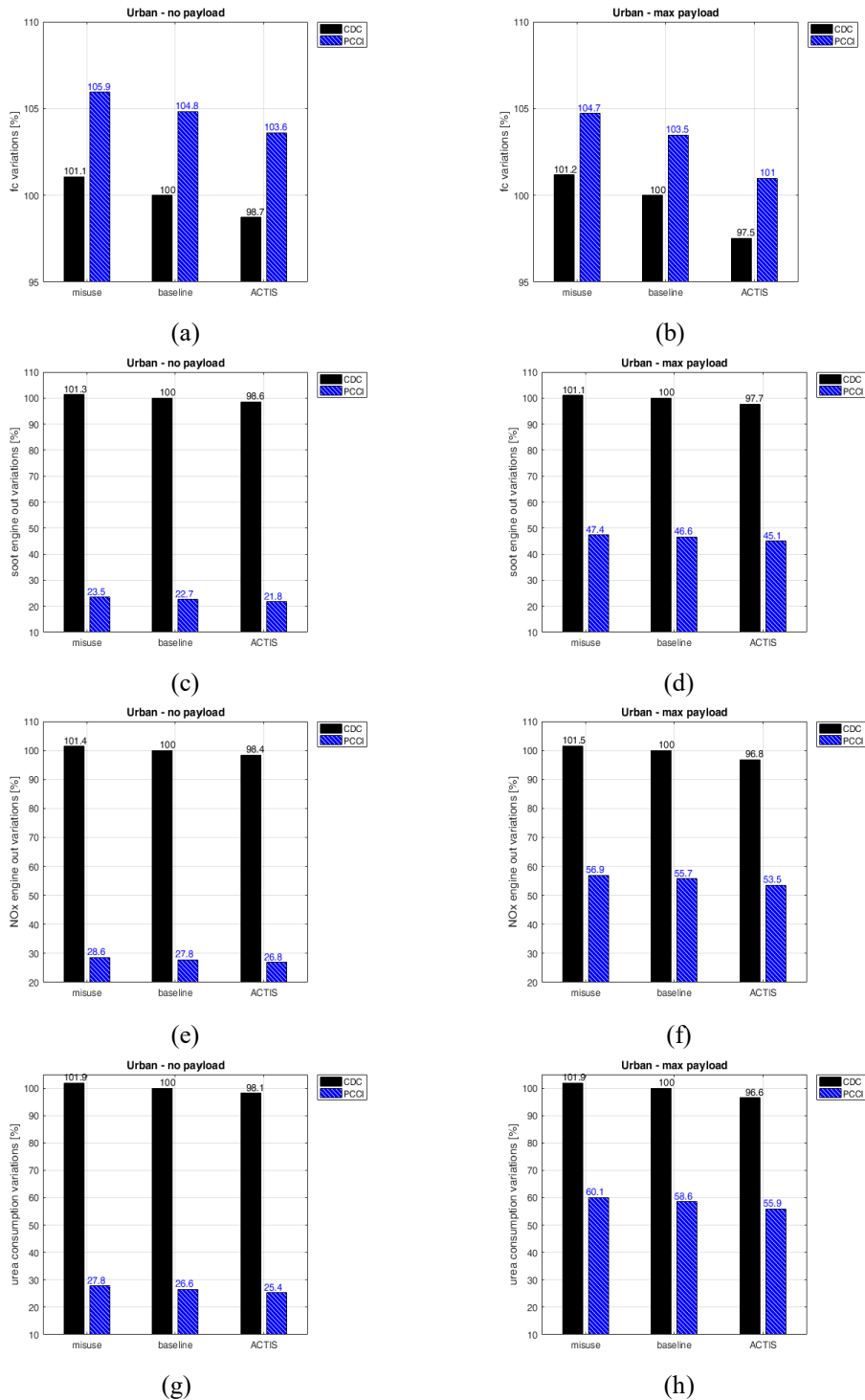


Figure 3.25: Results on LDV simulated on *urban* cycle. Fuel consumption, soot and NO_x engine-out emissions and urea consumption variations between the CDC and PCCI engines, with different tire pressure management situations: in a typical misuse case, when tires are always inflated at the nominal pressure (baseline) and in case of implementation of the ACTIS.

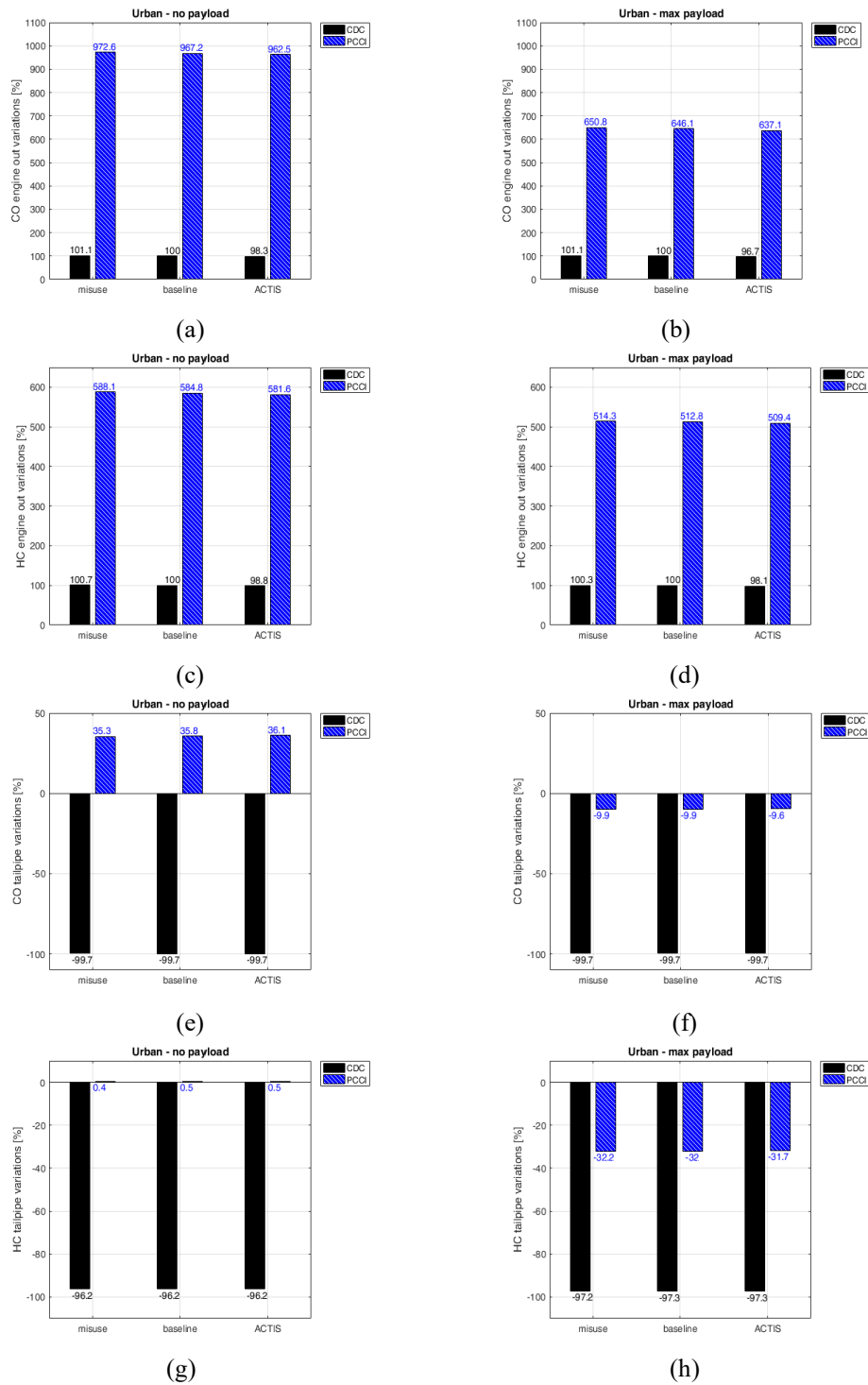


Figure 3.26: Results on LDV simulated on *urban* cycle. CO and HC engine-out and tailpipe emissions variations between the CDC and PCCI engines, with different tire pressure management situations: in a typical misuse case, when tires are always inflated at the nominal pressure (baseline) and in case of implementation of the ACTIS.

3.3 Combining the PCCI engine with ACTIS: effect on the total cost of ownership on annual missions

In order to conclude this analysis, the results of the previous simulations have been combined to evaluate three possible typical annual missions of light-duty commercial vehicles. The analysis is developed in analogy to what discussed in *Section 2.5.2*. This part of the analysis is mainly focused on evaluating the effect of these technologies on the in-use cost of the vehicle, i.e. on the Total Cost of Ownership (TCO). Other costs, such as purchase capital, maintenance cost and insurance are considered constant in all the cases, therefore, the results reported in Table 3.1 only refer to the effect of PCCI combustion and ACTIS on fuel consumption, tire wear and urea consumption. In the mentioned table, the results are reported both as relative variation and as absolute monetary variation with respect to the CDC baseline case, i.e. the case in which the standard engine with the conventional diesel combustion is applied and tire pressure is always maintained at its nominal level. For this analysis, the cost of fuel was considered as 1.4 €/l (cf. *Section 2.5*) and the cost of urea was taken as 1.49 €/l [294]. For tires, a cost of 160 €/tire was considered, with a total tire life of 50'000 km (cf. *Section 2.5*).

As already discussed in *Section 2.5.2*, tire misuse costs 35-56 €/year in terms of fuel consumption when CDC only is applied. Considering also the reduction of tire life and the increase in urea consumption due to the increase of engine loads, the total cost for tire misuse with the CDC engine is 52-84 €/year, depending on the type of mission that is considered. Still considering the vehicle endowed only with the CDC engine, the implementation of the ACTIS technology would allow a reduction in fuel consumption of 1.18-1.53% with respect to the CDC baseline case, which corresponds to an annual reduction by 85-123 €/year of the cost of fuel per vehicle. Moreover, ACTIS would allow to save from 26% to 32% of tire life, with a remarkable reduction of the cost of tires by 118-172 €/year. Including also a slight reduction of urea consumption due to the reduction of the engine load, the ACTIS technology applied to the vehicle endowed with the CDC case would allow to save 205-284 €/year with respect to the CDC baseline case. With respect to a common tire misuse case, the total economic benefit to the users by means of the ACTIS technology would range between 256 €/year and 367 €/year.

Considering the PCCI engine, if the baseline tire pressure condition is considered, the fuel consumption would be 1.6-2.4% higher than in the CDC baseline case, with an additional cost of fuel between 127-218 €/year. On the other hand, urea consumption would be reduced by 26-30%, with a reduction of the cost of urea by 36-55 €/year. Therefore the overall effect on the TCO of introducing PCCI combustion would be an increase ranging between 72 €/year and 162 €/year.

The application of the ACTIS technology allows to limit the worsening effect of PCCI on fuel consumption. Implementing both the PCCI engine and ACTIS, fuel consumption penalty with respect to the baseline CDC case is limited to maximum 1.2% (112 €/year) on the 70'000 km/year logistic mission, while in the 56'000 km delivery mission the fuel economy results only 0.13% worse than the CDC baseline case. If also the reduction of tire wear and urea consumption is considered, the ACTIS installed on the LDV endowed with the PCCI engine allows a reduction of TCO of between 103 €/year and 202 €/year with respect to the CDC baseline case, and of 155-280 €/year if compared to the CDC misuse case. Therefore, the implementation of PCCI combustion determines an increase in fuel consumption which can be partially or totally compensated by the introduction of the ACTIS technology. Moreover, from the TCO point of view, the additional cost of fuel is partially compensated by the reduction for the cost of urea used to reduce the NO_x in the SCR. Introducing also the ACTIS technology allows to further reduce the in-use vehicle costs, thus allowing a positive balance to be obtained on the TCO by the combination of the two technologies.

One additional aspect has not been considered in this analysis, which would reduce the difference on fuel consumption between the PCCI and CDC cases, and it is related to the regenerations of the DPF. As it is known, diesel particulate filters need to be periodically regenerated during operation, which is classically obtained through post-injections that allow to increase the temperature in the exhaust gases, therefore burning the PM accumulated in the filter. In the presented simulation, these periodical post injections have not been considered, therefore this is a worsening effect that would increase fuel consumption in the CDC case by 5.5-6%, if DPF regeneration occurs with soot loading around 6 g/l. Considering the ultra-low soot emissions of the PCCI combustion, that intervenes in the area of the engine map where typically soot/PM emissions are higher, it is then realistic to think that a CDC/PCCI hybrid combustion mode engine would be able to comply with the stringent Euro VI regulations without the usage of a DPF. Therefore in the PCCI engine fuel the post-injections for DPF regenerations could be avoided, thus improving the relative comparison between fuel economy of PCCI and CDC cases. Anyway, also the issues related to the activation of the DOC with low-temperature end-gases on the PCCI engine should be considered, and this would possibly be solved through the implementation of post-injection strategies to increase the temperature of exhaust gases when it is needed to reach the light-off temperature of the catalyst. The two effects would ideally compensate each other.

Furthermore, the absence of the DPF would reduce engine backpressure, therefore improving the pumping loop of the combustion cycle and thus improving fuel economy of the PCCI engine. This advantage anyway only would apply to the high-load areas of the engine map, where no EGR is recirculated: in lower load

areas, and especially in the PCCI area, the high request for EGR would require in any case a high engine backpressure, which is obtained in the PCCI engine through the operation of the engine backpressure flap (cf. Fig. 1.1).

It is worth to remark that only the in-use costs of the vehicle were considered. Purchasing cost was not taken into account, as the on-market cost of the proposed technology has not been estimated yet.

Table 3.1: Annual missions of the reference light-duty vehicle: effect of the combination of PCCI engine and ACTIS technology on the Total Cost of Ownership.

LDV parcel delivery mission - 40'000 km/year

		Urban	Extra-urban	Highway	% Load factor	Mission Load (kg)		
		35%	30%	35%	10%	2270		
		35%	30%	35%	35%	2900		
		35%	30%	35%	40%	3200		
		35%	30%	35%	15%	3500		
		Total fuel cons. (% ref.)	Delta cost of fuel (€/year)	Tire life variation (% ref.)	Delta cost of tire wear (€/year)	Urea consumption variation (% ref)	Delta cost of Urea (€/year)	Delta TCO (€/year)
CDC	Case #1 - baseline	0.00%	€ 0.00	0.00%	€ 0.00	0.00%	€ 0.00	€ 0.00
	Case #2 - misuse (underinflation)	0.63%	€ 35.50	-3.34%	€ 15.58	0.66%	€ 0.81	€ 51.89
	Case #3 - ACTIS	-1.51%	-€ 85.22	31.19%	-€ 118.09	-1.29%	-€ 1.60	-€ 204.91
PCCI	Case #1 - baseline	2.44%	€ 137.71	0.00%	€ 0.00	-29.65%	-€ 36.60	€ 101.12
	Case #2 - misuse (underinflation)	3.05%	€ 171.87	-3.34%	€ 15.58	-28.76%	-€ 35.49	€ 151.96
	Case #3 - ACTIS	0.97%	€ 54.69	31.19%	-€ 118.09	-31.97%	-€ 39.46	-€ 102.86

LDV logistic mission - 70'000 km/year

		Urban	Extra-urban	Highway	% Load factor	Mission Load (kg)		
		10%	80%	10%	15%	2270		
		10%	80%	10%	35%	2900		
		10%	80%	10%	35%	3200		
		10%	80%	10%	15%	3500		
		Total fuel cons. (% ref.)	Delta cost of fuel (€/year)	Tire life variation (% ref.)	Delta cost of tire wear (€/year)	Urea consumption variation (% ref)	Delta cost of Urea (€/year)	Delta TCO (€/year)
CDC	Case #1 - baseline	0.00%	€ 0.00	0.00%	€ 0.00	0.00%	€ 0.00	€ 0.00
	Case #2 - misuse (underinflation)	0.59%	€ 55.15	-3.34%	€ 27.01	0.72%	€ 1.54	€ 82.16
	Case #3 - ACTIS	-1.18%	-€ 110.04	26.21%	-€ 171.60	-0.96%	-€ 2.03	-€ 281.64
PCCI	Case #1 - baseline	2.34%	€ 217.72	0.00%	€ 0.00	-25.89%	-€ 54.89	€ 162.83
	Case #2 - misuse (underinflation)	2.92%	€ 271.72	-3.34%	€ 27.01	-25.09%	-€ 53.19	€ 245.54
	Case #3 - ACTIS	1.20%	€ 111.78	26.21%	-€ 171.60	-27.44%	-€ 58.18	-€ 118.00

LDV delivery mission - 56'000 km/year

		Urban	Extra-urban	Highway	% Load factor	Mission Load (kg)		
		10%	20%	70%	10%	2270		
		10%	20%	70%	35%	2900		
		10%	20%	70%	40%	3200		
		10%	20%	70%	15%	3500		
		Total fuel cons. (% ref.)	Delta cost of fuel (€/year)	Tire life variation (% ref.)	Delta cost of tire wear (€/year)	Urea consumption variation (% ref)	Delta cost of Urea (€/year)	Delta TCO (€/year)
CDC	Case #1 - baseline	0.00%	€ 0.00	0.00%	€ 0.00	0.0%	€ 0.00	€ 0.00
	Case #2 - misuse (underinflation)	0.69%	€ 55.88	-3.34%	€ 21.81	0.7%	€ 1.54	€ 77.69
	Case #3 - ACTIS	-1.53%	-€ 123.00	29.17%	-€ 154.16	-1.1%	-€ 2.29	-€ 277.16
PCCI	Case #1 - baseline	1.57%	€ 126.99	0.00%	€ 0.00	-25.8%	-€ 54.78	€ 72.21
	Case #2 - misuse (underinflation)	2.20%	€ 177.52	-3.34%	€ 21.81	-25.0%	-€ 53.08	€ 146.24
	Case #3 - ACTIS	0.13%	€ 10.24	29.17%	-€ 154.16	-27.5%	-€ 58.40	-€ 202.32

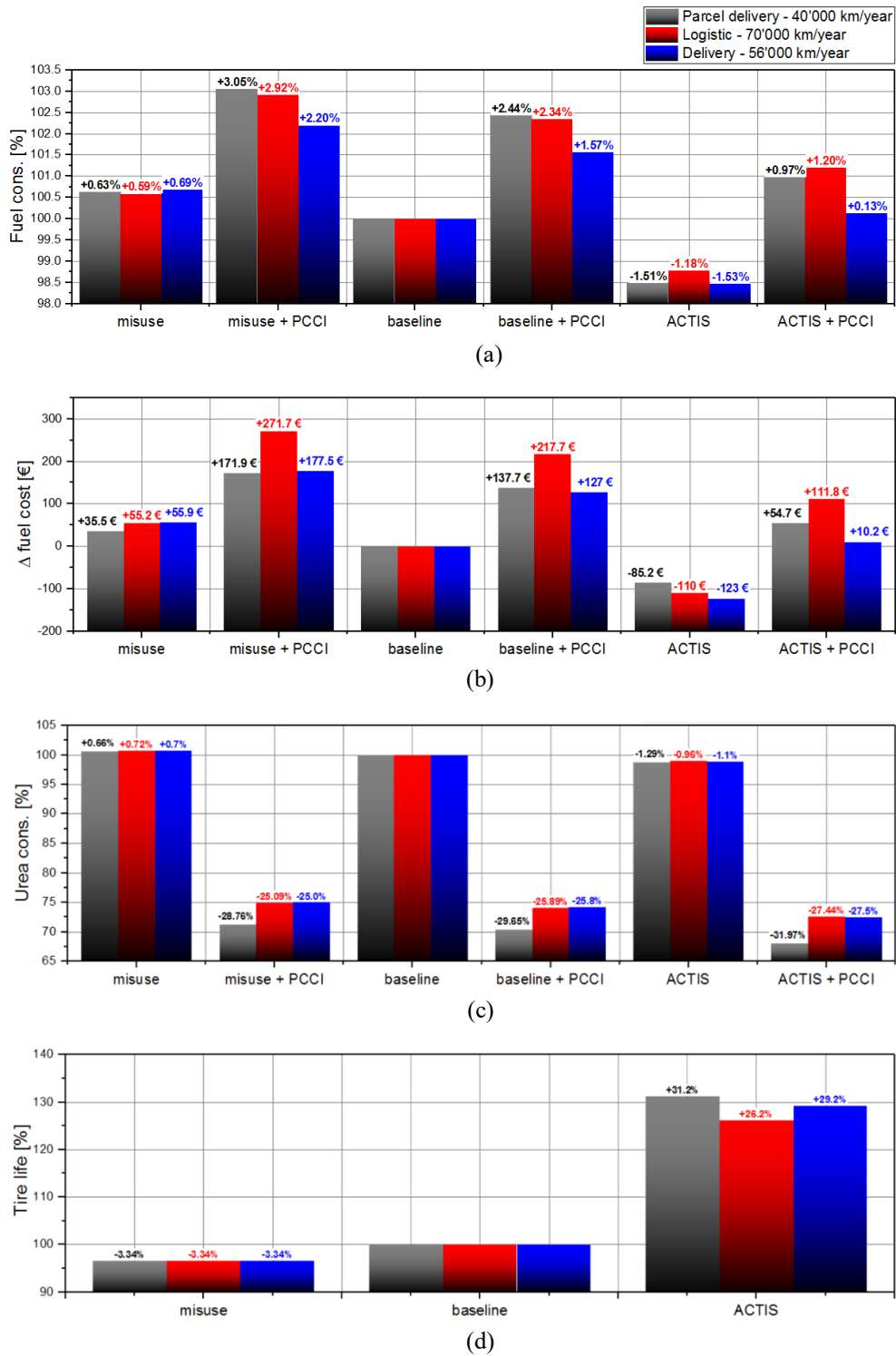


Figure 3.27: Annual missions of the reference light-duty vehicle: effect of the combination of PCCI engine and ACTIS technology on fuel consumption (a), cost of fuel (b), urea consumption (c) and tire life (d).

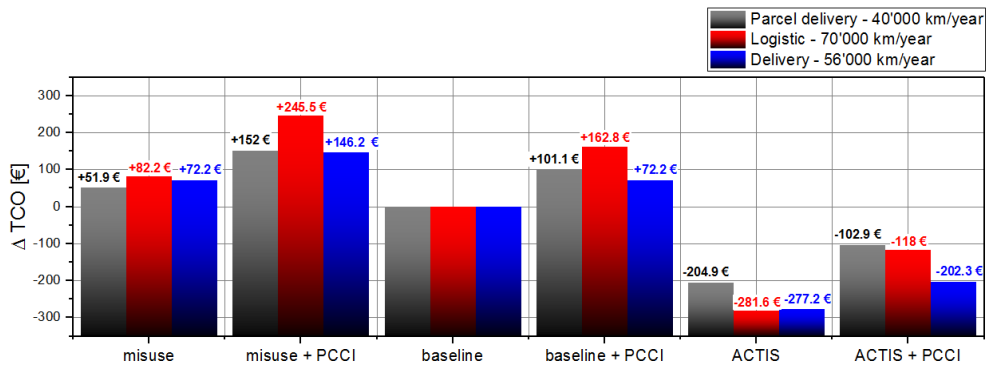


Figure 3.28: Annual missions of the reference light-duty vehicle: effect of the combination of PCCI engine and ACTIS technology on the Total Cost of Ownership.

Conclusions

The research work presented in this dissertation deals with the development of two different technologies, i.e. the implementation of PCCI diesel combustion for the reduction of in-cylinder formation of soot and NO_x , and the study of an automatic system for tire pressure management as a means for reducing the fuel consumption of a vehicle.

Concerning the assessment of the PCCI combustion, the project has been developed in collaboration with FPT Industrial on a 3.0 l diesel engine for commercial vehicles. In the first phase of the project, optimal calibration of PCCI combustion on a standard version of the engine allowed to reduce engine-out NO_x and soot by 90% and 99%, respectively, with reference to the original Euro VI calibration of the engine. This was obtained with an early injection strategy (SOI = 18°CA bTDC at 1800 rpm, 1 bar of bmep) and EGR rate higher than 66%. Nevertheless, it was possible to get the premixed combustion mode only up to medium speed (2000 rpm) and low load (bmep = 2 bar). In the tested engine points, a significant increase in fuel consumption and in HC and CO emissions was highlighted. As a further step of the project, a dedicated prototype version of the engine was set-up with reduced compression ratio, which allowed a reduction of engine-out soot of between 90% and 100% and a reduction of engine-out NO_x of between 85% and 97% in the engine working range up to 8.5 bar of bmep and up to 3000 rpm, with an increase in fuel consumption of between 3% and 11%, provided that the relative air-to-fuel stoichiometric ratio is maintained between 1.1 and 1.35. Due to the highly diluted charge and the early injection strategy, very high CO and HC emissions have been measured at the engine outlet: in most of the tested engine points these emissions were effectively oxidated by means of a DOC, but the DOC turned out to be ineffective on low load-low speed engine working points, where the light-off temperature of the catalyst was not reached due to the low temperature of the exhaust gases. Therefore, on one side the implementation of PCCI is demonstrated to be effective and feasible, provided that some further degrees of freedom in engine control is provided: this especially refers to the need for a PCCI/CDC “hybrid combustion mode” engine, which would require a variation of the effective compression ratio (through VCR or, possibly, VVT systems) moving from the PCCI to CDC areas of the map. On the other hand the main drawbacks of an engine of this type would be an increase in the fuel consumption, which should be addressed through other technologies for the reduction of the vehicle energy demand, and the critical reduction of the

temperature of the exhaust gases, which would require significant upgrades on the current after-treatment systems.

Due to the high variability of the PCCI combustion and of its stability to the boundary conditions, two further topics were investigated on the standard version of the tested engine, both in CDC and in PCCI: combustion phasing control, and accurate estimation of EGR rate. It was shown that a closed loop pressure-based control of MFB50 can significantly improve combustion stability, and extend the EGR tolerability of the engine. Open loop model-based combustion control, instead, does not produce significant improvements on the combustion stability, but has the potentiality to reduce calibration time, especially with reference to transient conditions which can potentially include switching from one combustion mode to another. Moreover, a semi-physical control-oriented model for the estimation of EGR mass flow rate, based on the nozzle flow equation and on the estimation of the exhaust temperature and pressure through statistical models, showed promising results when applied to a dataset significantly different from the original dataset of calibration, although a systematic error was highlighted. Statistical correlation of EGR rate to combustion phasing showed that in CDC the EGR has a significant effect only on the last phase of the combustion (i.e., the mixing-controlled phase), while in PCCI the major effect of EGR is in the first phases of the combustion process, as expected since the EGR is implemented in this case in order to increase the premixing time of the charge. The correlations between the EGR rate and combustion phasing were also proposed as a way to estimate the cylinder-to-cylinder EGR unbalance in those cases in which the cylinders are endowed with in-cylinder pressure sensors.

As the PCCI combustion shows an interesting potential in terms of the reduction of soot and NO_x with drawbacks in terms of fuel economy, a reduction of the vehicle energy demand is required to enhance the application of PCCI engines. As a possible countermeasure, Central Tire Inflation Systems were studied. The effect of tire pressure on fuel consumption was investigated, basing on computer simulations where the coast-down coefficients of the vehicle have been recalculated to account for tire pressure variations. The effect of tire pressure on the rolling resistance was calculated through a relation available in previous literature, and the validity of the proposed approach was verified by means of on-track coast-down tests performed at different tire pressures on a passenger car. Simulations have shown that typical misuse of tires on passenger cars increases fuel consumption up to 1% on urban and extra-urban driving, and up to 2% on highway driving. Applying a CTIS could allow to avoid this misuse, and further improve fuel economy by up to 1.6-2.4% by adapting tire pressure to the vehicle loading conditions, and by an additional 0.5% by adjusting tire pressure during tire warm-up period. Combining these results, it was estimated that fuel economy of a

passenger car would be improved by 1-1.4% on an annual basis with respect to a reference case where the nominal tire pressure is always maintained, and up to 2.8% with respect to a common misuse condition. This improvement in fuel economy means a reduction of the cost of the fuel for the drivers, but also a reduction of the carbon emissions and of the related social costs, which have also been quantified. Furthermore improving tire pressure management also means an improvement in road safety.

Moving from the experience on CTIS for passenger vehicles, the project was also extended to commercial vehicles, in a collaboration with Iveco. A dedicated software tool, which implements a simplified kinematic vehicle model for the estimation of engine working point moving from the vehicle speed profile, was developed in order to take into account explicitly of tire pressure on fuel economy simulations. It was found that typical misuse (i.e., tire pressure 25% lower than the reference) increases fuel consumption up to 1.5-3%, depending on the mission, on a HDV loaded at its maximum payload, and up to 1.8% on a fully loaded LDV (independently from the driving mission). Adapting tire pressure to the vehicle payload was estimated to reduce fuel consumption of an LDV up to 1.7% and to increase tire life by 23%, while it was practically not efficacious on HDV, where usually the reference pressure is set at the maximum payload and kept also at lower vehicle loads (which is detrimental on tire wear, but improves fuel economy). Additionally, adjusting tire pressure during tire warm-up was estimated to reduce fuel consumption by 1.4% on a fully loaded HDV and by 0.9% on a fully loaded LDV, when both are tested in a highway mission starting with cold tires. The reduction in fuel consumption that can be obtained on annual missions representative of the real-world usage of the target vehicles has been estimated in 1.7-1.9% on HDV and 1.7-2.1% on LDV, if the reference case for comparison is a common misuse condition. If the effect on tire mileage is also taken into account, the reduction in the Total Cost of Ownership estimated with an advanced CTIS is up to 920 €/year for an HDV and up to 350 €/year for an LDV.

A dedicated CTIS was first developed for passenger cars in order to overcome the limits that have constrained in the past the diffusion of this technology. An experimentally-driven design loop allowed to obtain the desired system performance in a lightweight solution. Also for the commercial vehicles dedicated system layouts have been proposed, together with a preliminary design of possible solutions for the integration of the system on-board. As the layout and sizing of a CTIS may be critical both from the perspective of the system weight as well as in terms of actuation time required to get a desired target pressure, the systems have been designed in order to be lightweight and to get acceptable performance for the intended system mission. In order to verify that the obtained performance was aligned to the requirements, some additional simulations were also performed on

the passenger car and on the HDV taking into account the measured (for passenger car) or estimated (for HDV, through 1D simulations) actuation times of the systems. It was found that, although the non-ideal actuation time leads to a reduction of the fuel economy benefit estimated in the case of ideal instantaneous actuations, the advantage that can be obtained is still significant and close to the expectations.

The combined effect of the two developed technologies (PCCI engine and CTIS) has also been assessed by means of simulations on an LDV on reference driving cycles. For this purpose, apart from the estimation of fuel consumption, also a first-attempt estimation of engine-out and tailpipe emissions was performed. Engine performance maps were built considering a PCCI/CDC “hybrid combustion mode” engine, which was obtained by ideally combining the PCCI optimal calibration of the prototype engine with the CDC calibration of the standard engine. The PCCI/CDC “hybrid combustion mode” engine, tested on single driving cycles, has the potentiality to reduce engine-out NO_x emissions by up to 20-73%, and soot by 33-78%, in highway and urban driving respectively. A significant increase in engine-out HC and CO emissions is remarked, although the tailpipe emissions with warm engine are estimated below Euro VI limits. Fuel consumption worsens by 1.6-2.4% on an annual basis due to PCCI combustion. If the PCCI engine is combined to the ACTIS technology, the worsening effect on fuel consumption is reduced to maximum 1.2% with respect to the baseline vehicle (with CDC only and reference tire pressure) on a 70'000 km/year logistic missions, while on a 56'000 km/year delivery mission the worsening in fuel economy is almost negligible (+0.13%). The implementation of PCCI combustion would also reduce the consumption of urea used for the reduction of NO_x in the SCR. This reduction has been quantified as 26-30% on an annual basis. Additionally, the usage of a smart CTIS would allow to increase tire life up to 26-31%.

Combining the previous effects (fuel consumption, urea consumption, tire mileage), the global effect of the two studied technologies results in a reduction of the TCO of the target LDV by 103-202 €/year with respect to a case where tire pressure is always maintained at the reference level, and up to 155-280 €/year with respect to a common tire misuse case.

This last analysis has highlighted as the combined effect of an engine technology and a vehicle technology allowed to get the target result in terms of the concurrent reduction of pollutant emissions and fuel consumption. Moreover, considering also some side effects of the considered technologies, an overall reduction of the TCO was highlighted, which makes the simulated LDV with PCCI engine and ACTIS technology also of interest from the market point of view, especially in case of a business application of the vehicle (as it is for the target commercial LDV).

Nevertheless, as mentioned in the previous *Chapters*, various aspects have not been considered in the current analysis, which may result in further benefits:

- reduction of engine backpressure (i.e., improvement in the pumping loop) as the DPF can be removed thanks to the soot-less PCCI combustion;
- reduction of fuel consumption thanks to the missing regenerations of the DPF;
- reduction of PM emissions related to tire wear thanks to the smart autonomous management of tire pressure;
- improvement of vehicle handling and road safety by avoiding tire misuse, and possibly thanks to the adaptation of tire pressure to the current vehicle conditions according to a multi-objective optimization that includes the effect of tire pressure on vehicle handling as well as on fuel consumption.

It is worth to remark that the current analysis has been developed starting from some simplifying hypothesis and practical simplifications that could be removed in future analysis to improve the results. For example, the approximations done in the kinematic vehicle model that was implemented in the simulation tool TyPE could be overcome by introducing the core module of TyPE (for the instantaneous evaluation of tire pressure effects on the coast-down coefficients) within fuel economy software tools more refined in terms of the description of the vehicle itself, i.e. implementing dynamic models of the vehicle and of the driver and warm-up models of the engine to simulate the effect of engine cold-starts. Similarly, the estimation of emissions on driving cycles was performed here by simply interpolating emission maps derived from steady-state tests, while some corrections could be implemented in future analysis to improve the estimations during transients. Additionally, future steps of the PCCI project could involve the implementation of the mentioned engine control functions on the PCCI prototype engine, the calibration of the CDC area on the PCCI engine (possibly implementing two-stage turbocharging and a VCR) and the analysis of some dedicated solutions to improve the performance of the DOC in low speed-low load engine points. For the ACTIS project, prototyping and testing the designed solutions for HDV/LDV would provide a further evaluation on the proposed design and its possible implementation on conventional vehicles.

References

1. Pasten, C., and Santamarina, J.C., “Energy and quality of life”, *Energy Policy* 49 (2012) 468-476, <https://doi.org/10.1016/j.enpol.2012.06.051>.
2. Lambert, J.G., Hall, C.A.S., Balogh, S., Gupta, A., and Arnold, M., “Energy, EROI and quality of life” *Energy Policy* 64 (2014) 153-167, <https://doi.org/10.1016/j.enpol.2013.07.001>.
3. Ecola, L., and Wachs, M., “Exploring the relationship between travel demand and economic growth”, Prepared for Federal Highway Administration, 2012.
4. U.S. Energy Information Administration, “EIA International Energy Outlook 2016”, May 2016.
5. Knutti, R., and Hegerl, G.C., “The Equilibrium sensitivity of the Earth’s temperature to radiation changes”, *Nature Geoscience* 1 (2008) 735-743, <https://doi.org/10.1038/ngeo337>.
6. Lelieveld, J., Evans, J.S., Fnais, M., Giannadaki, D., and Pozzer, A., “The contribution of outdoor air pollution sources to premature mortality on a global scale”, *Nature* 525 (2015) 367-371, <https://doi.org/10.1038/nature15371>.
7. U.S. Energy Information Administration, “Annual Energy Outlook 2014, with projections to 2040”, Washington, DC:Government Printing Office, 2014
8. Atabani, A.E., Badruddin, I.A., Mekhilef, S., et al., “A review on global fuel economy standards, labels and technologies in the transportation sector”, *Renewable and Sustainable Energy Reviews* 15 (2011) 4586-4610, <https://doi.org/10.1016/j.rser.2011.07.092>.
9. Glenn, H.T., “Automotive smog control manual”, 1968
10. Holmes, K., “A Century of Environmental Technologies for Light-Duty Vehicles”, *SAE Int. J. Engines* 10(2):160-172, 2017, <https://doi.org/10.4271/2017-01-0119>.
11. United States Environmental Protection Agency, “Timeline of Major Accomplishments in Transportation, Air Pollution, and Climate Change”, <https://www.epa.gov/transportation-air-pollution-and-climate-change/timeline-major-accomplishments-transportation-air>, accessed Oct. 2018.
12. Dieselnet, “Emission Standards – United States”, <https://www.dieselnet.com/standards/us>, accessed Oct. 2018.
13. Council of the European Communities, “Council Directive 70/220/CEE of 20 March 1970 on the approximation of the laws of the Member States relating to measures to be taken against air pollution by gases from positive-ignition engines of motor vehicles”, *Official Journal of the European Communities*, L76/1, 1970.
14. Pavlovic, J., Marotta, A., and Ciuffo, B., “CO₂ emissions and energy demands of vehicles tested under the NEDC and the new WLTP type approval test procedures”, *Applied Energy* 177 (2016) 661–670, <https://doi.org/10.1016/j.apenergy.2016.05.110>
15. Hooftman, N., Messagie, M., Van Mierlo, J., and Coosemans, T., “A review of the European passenger car regulations – Real driving emissions vs local air quality”, *Renewable and Sustainable Energy Reviews* 86 (2018) 1–21, <https://doi.org/10.1016/j.rser.2018.01.012>
16. Yang, L., Franco, V., Mock, P., Kolke, R., et al., “Experimental assessment of NO_x emissions from 73 Euro 6 diesel passenger cars”, *Environmental Science Technology* 49 (2015)14409–15, <https://pubs.acs.org/doi/10.1021/acs.est.5b04242>

17. Franco, V., Sánchez, F.P., German, J., and Mock, P., “Real-world exhaust emissions from modern diesel cars – a meta-analysis of PEMS emissions data from EU (Euro 6)”, white paper by International Council on Clean Transportation, 2014, available online: https://www.theicct.org/sites/default/files/publications/ICCT_PEMS-study_diesel-cars_20141010.pdf.
18. Kadijk, G., Van Mensch, P., and Spreen, J., “Detailed investigations and real-world emission performance of Euro 6 diesel passenger cars”, TNO report, 2015.
19. Johnson, T., "Vehicular Emissions in Review," SAE Int. J. Engines 9(2):1258-1275, 2016, <https://doi.org/10.4271/2016-01-0919>.
20. Dieselnets, “Emission Standards – EU: Cars and Light Trucks”, <https://www.dieselnets.com/standards/eu/ld.php>, accessed Oct. 2018.
21. LaStampa, “Il Parlamento europeo raddoppia i limiti delle emissioni per le auto”, <http://www.lastampa.it/2016/02/03/esteri/il-parlamento-europeo-raddoppia-i-limiti-delle-emissioni-per-le-auto-lbfHGbu3Khl6bVducWQcP/pagina.html>, accessed Oct. 2018.
22. The Guardian, “EU caves in to auto industry pressure for weak emissions limits”, <http://www.theguardian.com/environment/2015/oct/28/eu-emissions-limits-nox-car-manufacturers>, accessed Oct. 2018.
23. El Pais, “La UE duplica el límite de emisiones de los vehículos diésel en carretera”, https://elpais.com/economia/2016/02/03/actualidad/1454524292_307841.html, accessed Oct. 2018.
24. Epping, K., Aceves, S., Bechtold, R., and Dec, J., “The Potential of HCCI Combustion for High Efficiency and Low Emissions”, SAE Technical Paper 2002-01-1923, 2002, <https://doi.org/10.4271/2002-01-1923>.
25. Shuai, S., Ma, X., Li, Y., Qi, Y and Xu, H., “Recent progress in Automotive Gasoline Direct Injection Engine Technology”, Automotive Innovation 1 (2018) 95-113, <http://doi.org/10.1007/s42154-018-0020-1>
26. Mazda, “Skyactiv Technology”, <https://www.mazda.com/en/innovation/technology/skyactiv>, accessed Oct. 2018.
27. Hasegawa, R., and Yanagihara, H., “HCCI Combustion in DI Diesel Engine” SAE Technical Paper 2003-01-0745, <https://doi.org/10.4271/2003-01-0745>.
28. Parks, J.E. II, Prikhodko, V., Storey, J.M.E., Barone, T.L., et al., “Emissions from premixed charge compression ignition (PCCI) combustion and effect on emission control devices”, Catalysis Today 151 (2010) 278-284, <https://doi.org/10.1016/j.cattod.2010.02.053>.
29. Musculus, M.P.B., Miles, P.C., and Pickett, L.M., “Conceptual models for partially premixed low-temperature diesel combustion”, Progress in Energy and Combustion Science 39 (2013) 246-283, <https://doi.org/10.1016/j.pecs.2012.09.001>.
30. Iwabuchi, Y., Kawai, K., Shoji, T., and Takeda, Y., “Trial of New Concept Diesel Combustion System - Premixed Compression-Ignited Combustion”, SAE Technical Paper 1999-01-0185, 1999, <https://doi.org/10.4271/1999-01-0185>.
31. Splitter, D., Hanson, R., Kokjohn, S., and Reitz, R., “Reactivity Controlled Compression Ignition (RCCI) Heavy-Duty Engine Operation at Mid-and High-Loads with Conventional and Alternative Fuels”, SAE Technical Paper 2011-01-0363, 2011, <https://doi.org/10.4271/2011-01-0363>.
32. Glewen, W., Heuwetter, D., Foster, D., Andrie, M. et al., “Analysis of Deviations from Steady State Performance During Transient Operation of a Light Duty Diesel Engine”, SAE Int. J. Engines 5 (2012) 909-922 <https://doi.org/10.4271/2012-01-1067>.

33. Chung, J., Min, K., Oh, S. and Sunwoo, M., “In-Cylinder Pressure Based Real-Time Combustion Control for Reduction of Combustion Dispersions in Light-Duty Diesel Engines”, *Applied Thermal Engineering* 99 (2016) 1183-1189, <https://doi.org/10.1016/j.applthermaleng.2016.01.012>.
34. Carlucci, A.P., Laforgia, D., Motz, S., Saracino, R., et al., “Advanced Closed Loop Combustion Control of a LTC Diesel Engine Based on In-Cylinder Pressure Signals”, *Energy Conversion and Management* 77 (2014) 193-207, <https://doi.org/10.1016/j.enconman.2013.08.054>
35. Yang, F., Wang, J., Gao, G. and Ouyang, M., “In-Cycle Diesel Low Temperature Combustion Control Based on SOC Detection”, *Applied Energy* 136 (2014) 77-88, <https://doi.org/10.1016/j.apenergy.2014.09.014>
36. Hillion, M., Chauvin, J., Grondin, O., and Petit, N., “Active Combustion Control of Diesel HCCI Engine: Combustion Timing”, SAE Technical Paper 2008-01-0984, 2008, <https://doi.org/10.4271/2008-01-0984>.
37. Samuel, S., Morrey, D., Taylor, D., and Fowkes, M., “Parametric Study into the Effects of Factors Affecting Real-World Vehicle Exhaust Emission Levels”, SAE Technical Paper 2007-01-1084, 2007, <https://doi.org/10.4271/2007-01-1084>.
38. Barrand, J. and Bokar, J., “Reducing Tire Rolling Resistance to Save Fuel and Lower Emissions”, *SAE Int. J. Passeng. Cars - Mech. Syst.* 1 (2009) 9-17, <https://doi.org/10.4271/2008-01-0154>.
39. Bachman, L., Erb, A., and Bynum, C., “Effect of Single Wide Tires and Trailer Aerodynamics on Fuel Economy and NO_x Emissions of Class 8 Line-Haul Tractor-Trailers”, SAE Technical Paper 2005-01-3551, 2005, <https://doi.org/10.4271/2005-01-3551>.
40. Rexeis, M., Hausberger, S., “Trend of vehicle emission levels until 2020 – Prognosis based on current vehicle measurements and future emission legislation”, *Atmos Environ*, 43 (2009) 4689-4698, <https://doi.org/10.1016/j.atmosenv.2008.09.034>.
41. Combustion Diesel Particulate Filter (DPF) Testing system | Combustion <http://www.combustion.com/products/dpg>, accessed Oct. 2018.
42. Thorpe, A. and Harrison, R.M., “Sources and properties of non-exhaust particulate matter from road traffic: A review”, *Science of the total environment* 400 (2008) 270 – 282, <https://doi.org/10.1016/j.scitotenv.2008.06.007>.
43. Grigoratos, T. and Martini, G., “Non-exhaust traffic related emissions – Brake and tyre wear PM”, EUR - Scientific and Technical Research Reports, Publications Office of the European Union (2014), <https://doi.org/10.2790/21481>.
44. Chasapidis, L., Grigoratos, T., Zygogianni, A., Tsakis, A., et al., “Study of brake wear particle emissions of a minivan on a chassis dynamometer”, *Emiss. Control Sci. Technol.* 4 (2018) 271-278, <https://doi.org/10.1007/s40825-018-0105-7>.
45. Perricone, G., Matějka, V., Alemani, M., Valota, G., et al., “A concept for reducing PM10 emissions for car brakes by 50%”, *Wear* 396–397 (2018) 135–145, <http://dx.doi.org/10.1016/j.wear.2017.06.018>.
46. Timmers, V.R.J.H., and Achten, P.A.J., “Non-exhaust PM emissions from electric vehicles”, *Atmospheric Environment* 134 (2016) 10-17, <http://dx.doi.org/10.1016/j.atmosenv.2016.03.017>.
47. Mitchell, J.F.B., “The “greenhouse” effect and climate change”, *Reviews of Geophysics* 27 (1989) 115 -139, <https://doi.org/10.1029/RG027i001p00115>.
48. Houghton, J.T., Jenkins, G.J. and Ephraums, J.J. (eds), “Climate Change. The IPCC Scientific Assessment”, Cambridge Univ. Press, 1990.

49. Lashof, D.A. and Ahuja, D.R., “Relative contributions of greenhouse gas emissions to global warming”, *Nature* 344 (1990) 529–531, <https://doi.org/10.1038/344529a0>.
50. United Nations, “Kyoto Protocol to the United Nations Framework Convention on Climate Change”, 1998, available online: <https://unfccc.int/sites/default/files/kpeng.pdf>.
51. Dieselnets, “EU: Cars: Greenhouse Gas Emissions—ACEA Agreements”, https://www.dieselnets.com/standards/eu/ghg_acea.php, accessed Oct.2018.
52. European Parliament, “Regulation (EC) No 661/2009 of the European Parliament and of the Council of 13 July 2009 concerning type-approval requirements for the general safety of motor vehicles, their trailers and systems, components and separate technical units intended therefore”, *Official Journal of the European Union*, L200/1, 31 July 2009.
53. Dieselnets, “EU: Cars: Greenhouse Gas Emissions”, <https://www.dieselnets.com/standards/eu/ghg.php>, accessed Oct.2018.
54. European Parliament, “Regulation (EU) No 333/2014 of the European Parliament and of the Council of 11 March 2014 amending Regulation (EC) No 443/2009 to define the modalities for reaching the 2020 target to reduce CO2 emissions from new passenger cars”, *Official Journal of the European Union*, L103/15, 5 April 2014.
55. Statista, “Average annual OPEC crude oil price from 1960 to 2019 (in U.S. dollars per barrel)” <https://www.statista.com/statistics/262858/change-in-opec-crude-oil-prices-since-1960/>, accessed Oct.2018.
56. U.S. Department of Transportation, Bureau of Transportation Statistics, “National Transportation Statistics 2017”, 2017.
57. Dieselnets, “United States: Light-Duty Vehicles: GHG Emissions & Fuel Economy”, https://www.dieselnets.com/standards/us/fe_ghg.php, accessed Oct.2018.
58. Yang, Z., “Improving the conversions between the various passenger vehicle fuel economy/CO2 emission standards around the world”, International Council on Clean Transportation, available online: <http://www.theicct.org/blogs/staff/improving-conversions-between-passenger-vehicle-efficiency-standards>.
59. EU, “EU transport in figures – statistical Pocketbook 2014”, Luxembourg, 2014.
60. Ntziachristos, L., Mellios, G., Tsokolis, D., Keller, M., et al., “In-use vs. type-approval fuel consumption of current passenger cars in Europe”, *Energy Policy* 67 (2014) 403-411, <https://doi.org/10.1016/j.enpol.2013.12.013>.
61. Huo, H., Yao, Z., He, K., Yu, X., “Fuel consumption rates of passenger cars in China: Labels versus real-world”, *Energy Policy* 39 (2011) 7130-7135, <https://doi.org/10.1016/j.enpol.2011.08.031>.
62. Zhang, S., Wu, Y., Liu, H., Huang, R., et al. “Real-world fuel consumption and CO2 (carbon dioxide) emissions by driving conditions for light-duty passenger vehicles in China”, *Energy* 69 (2014) 247-257, <https://doi.org/10.1016/j.energy.2014.02.103>.
63. Tietge, U., Zacharof, N., Ligterink, N., Lambrecht, U., et al., “From Laboratory to Road: A 2015 Update of Official and “Real-World” Fuel Consumption and CO2 Values for Passenger Cars in Europe”, white paper by International Council on Clean Transportation, 2015, available online: https://www.theicct.org/sites/default/files/publications/ICCT_LaboratoryToRoad_2015_Report_English.pdf

64. Bielaczyc, P., Woodburn, J., and Szczotka, A., “A Comparison of Carbon Dioxide Exhaust Emissions and Fuel Consumption for Vehicles Tested over the NEDC, FTP-75 and WLTC Chassis Dynamometer Test Cycles”, SAE Technical Paper 2015-01-1065, 2015, <https://doi.org/10.4271/2015-01-1065>.
65. May, J., Bosteels, D., and Favre, C., “An Assessment of Emissions from Light-Duty Vehicles using PEMS and Chassis Dynamometer Testing”, SAE Int. J. Engines 7 (2014) 1326-1335, <https://doi.org/10.4271/2014-01-1581>.
66. Favre, C., Bosteels, D., and May, J., “Exhaust Emissions from European Market-Available Passenger Cars Evaluated on Various Drive Cycles”, SAE Technical Paper 2013-24-0154, 2013, <https://doi.org/10.4271/2013-24-0154>.
67. United Nations, “Paris Agreement”, 2015, available online: https://unfccc.int/sites/default/files/english_paris_agreement.pdf.
68. Reese, R. II, “Progress (and Challenges) along the Path to 2025”, presentation at the Engine Research Center 2015 Symposium, University of Wisconsin, Madison, June 2015
69. Conley, J. and Taylor, S., “Technological Evaluation of Fuel Efficiency Improvement Concepts to Meet Future Regulatory Requirements in the North American Market”, SAE Technical Paper 2002-01-2809, 2002, <https://doi.org/10.4271/2002-01-2809>.
70. Petitjean, D., Bernardini, L., Middlemass, C., and Shahed, S., “Advanced Gasoline Engine Turbocharging Technology for Fuel Economy Improvements”, SAE Technical Paper 2004-01-0988, 2004, <https://doi.org/10.4271/2004-01-0988>.
71. Schwaderlapp, M., Habermann, K., and Yapici, K., “Variable Compression Ratio - A Design Solution for Fuel Economy Concepts”, SAE Technical Paper 2002-01-1103, 2002, <https://doi.org/10.4271/2002-01-1103>.
72. Vaja, I., and Gambarotta, A., “Internal Combustion Engine (ICE) bottoming with Organic Rankine Cycles (ORCs)”, Energy 35 (2010) 1084-1093, <https://doi.org/10.1016/j.energy.2009.06.001>.
73. Yu, G., Shu, G., Tian, H., Wei, H., et al., “Simulation and thermodynamic analysis of a bottoming Organic Rankine Cycle (ORC) of diesel engine (DE)”, Energy 51 (2013) 281-290, <https://doi.org/10.1016/j.energy.2012.10.054>.
74. Shu, G., Zhao, M., Tian, H., Wei, H., et al., “Experimental investigation on thermal OS/ORC (Oil Storage/Organic Rankine Cycle) system for waste heat recovery from diesel engine”, Energy 107 (2016) 693-706, <https://doi.org/10.1016/j.energy.2016.04.062>.
75. Nakata, K., Nogawa, S., Takahashi, D., Yoshihara, Y. et al., “Engine Technologies for Achieving 45% Thermal Efficiency of S.I. Engine”, SAE Int. J. Engines 9 (2016) 179-192, <https://doi.org/10.4271/2015-01-1896>.
76. Ikeya, K., Takazawa, M., Yamada, T., Park, S. et al., “Thermal Efficiency Enhancement of a Gasoline Engine”, SAE Int. J. Engines 8 (2015) 1579-1586, <https://doi.org/10.4271/2015-01-1263>.
77. Holmberg, K., Andersson, P., Erdemir, A., “Global energy consumption due to friction in passenger cars”, Tribology International 47 (2012) 221–234, <https://doi.org/10.1016/j.triboint.2011.11.022>.
78. Oh, Y., Park, J., Lee, J., et al., “Modeling effects of vehicle specifications on fuel economy based on engine fuel consumption map and vehicle dynamics”, Transportation Research Part D 32 (2014) 287-302, <https://doi.org/10.1016/j.trd.2014.08.014>.

79. DeMarco, K., Stratton, J., Chinavare, K., and VanHouten, G., “The Effects of Mass and Wheel Aerodynamics on Vehicle Fuel Economy”, SAE Technical Paper 2017-01-1533, 2017, <https://doi.org/10.4271/2017-01-1533>.
80. Michelin, “The tyre. Grip.”, Ed. Société de Technologie Michelin, 2001.
81. LaClair, T.J., “Tire Rolling Resistance”, In: Walter, J. and Gent, A. (eds), “The Pneumatic Tire”, The National Highway Traffic Safety Administration, 2005.
82. Grosch, K.A., “Rubber Friction and Tire Traction”, In: Walter, J. and Gent, A. (eds), “The Pneumatic Tire”, The National Highway Traffic Safety Administration, 2005.
83. Michelin, “The tyre. Rolling Resistance and fuel savings”, Ed. Société de Technologie Michelin, 2002.
84. Clark, S.K., and Dodge, R.N., “A handbook for the rolling resistance of pneumatic tires”, Industrial Development Division, Institute of Science and Technology, The University of Michigan, 1979.
85. Le Gal, A., Guy, L., Orange, G., et al. “Modelling of sliding friction for carbon black and silica filled elastomers on road tracks”, *Wear* 264 (2008) 606-615, <https://doi.org/10.1016/j.wear.2007.05.002>.
86. Pearce, J.M. and Hanlon, J.T., “Energy conservation from systematic tire pressure regulation”, *Energy Policy* 35 (2007) 2673-2677, <https://doi.org/10.1016/j.enpol.2006.07.006>.
87. Bridgestone, “European drivers increasingly negligent about the maintenance of their tyres”, www.bridgestone.eu/corporate/press-releases/2013/04/european-drivers-increasingly-negligent-about-the-maintenance-of-their-tyres/, 2013, accessed 15 May 2017.
88. U.S. Department of Transportation, National Highway Traffic Safety Administration, “Tire Pressure Monitoring Systems, Control and Displays”, RIN 2127-AI33 Federal Motor Vehicle Safety Standards, 49 CFR Part 571 (Docket No. NHTSA 2000-8572), 2001.
89. European Parliament, “Regulation (EC) No 1222/2009 of the European Parliament and of the Council of 25 November 2009 on the labelling of tyres with respect to fuel efficiency and other essential parameters”, *Official Journal of the European Union*, L342/46, 22 Dec. 2009.
90. European Parliament, “Regulation (EC) No 443/2009 of the European Parliament and of the Council of 23 April 2009 setting emission performance standards for new passenger cars as part of the Community's integrated approach to reduce CO₂ emissions from light-duty vehicles” *Official Journal of the European Union*, L140/1, 5 June 2009.
91. U.S. 106th Congress, “Transportation Recall Enhancement, Accountability and Documentation (TREAD) Act”, Public Law 106-414, Nov. 1 2000.
92. Morgadinho, L., Oliveira, C. and Martinho, A., “A qualitative study about perceptions of European automotive sector’s contribution to lower greenhouse gas emissions”, *Journal of Cleaner Production* 106 (2015) 644-654, <https://doi.org/10.1016/j.jclepro.2015.01.096>.
93. Turrentine, T.S., and Kurani, K.S., “Car buyers and fuel economy?”, *Energy Policy* 35 (2007) 1213–1223, <https://doi.org/10.1016/j.enpol.2006.03.005>.
94. Simmons, R.A., Shaver, G.M., Tyner, W.E. and Garimella, S.V., “A benefit-cost assessment of new vehicle technologies and fuel economy in the U.S. market”, *Applied Energy* 157 (2015) 940-953, <https://doi.org/10.1016/j.apenergy.2015.01.068>.

95. Singh, N., Rutland, C., Foster, D., Narayanaswamy, K. et al., "Investigation into Different DPF Regeneration Strategies Based on Fuel Economy Using Integrated System Simulation", SAE Technical Paper 2009-01-1275, 2009, <https://doi.org/10.4271/2009-01-1275>.
96. Organisation Internationale des Constructeurs d'Automobiles (OICA), "World Vehicles in use – Commercial Vehicles", <http://www.oica.net/category/vehicles-in-use/>, accessed Oct. 2017.
97. European Automobile Manufacturers Association (ACEA), "Trucks fact sheet", http://www.acea.be/uploads/publications/factsheet_trucks.pdf, accessed Oct. 2017.
98. European Automobile Manufacturers Association (ACEA), "Vans fact sheet", http://www.acea.be/uploads/publications/factsheet_vans.pdf, accessed Oct. 2017.
99. European Automobile Manufacturers Association (ACEA), "Trucks, Vans and Buses", <http://www.acea.be/automobile-industry/trucks-vans-buses>, accessed Oct. 2017.
100. Zhu, H., Bohac, S.V., Nakashima, K., et al., "Effect of fuel oxygen on the trade-offs between soot, NO_x and combustion efficiency in premixed low-temperature diesel engine combustion", Fuel 112 (2013) 459-465. <https://doi.org/10.1016/j.fuel.2013.05.023>.
101. Kawanami, M., Horiuchi, M., Leyrer, J., Lox, E. et al., "Advanced Catalyst Studies of Diesel NO_x Reduction for On-Highway Trucks", SAE Technical Paper 950154, 1995, <https://doi.org/10.4271/950154>.
102. Hirata, K., Masaki, N., Ueno, H., and Akagawa, H., "Development of Urea-SCR System for Heavy-Duty Commercial Vehicles", SAE Technical Paper 2005-01-1860, 2005, <https://doi.org/10.4271/2005-01-1860>.
103. Jiao, Y., "Euro VI HDD Engine Technology Overview", Ricardo presentation, May, 2015.
104. Laguitton, O., Crua, C., Cowell, T., Heikal, M.R., et al., "The effect of compression ratio on exhaust emissions from a PCCI diesel engine", Energy Conversion and Management 48 (2007) 2918-2924, <https://doi.org/10.1016/j.enconman.2007.07.016>.
105. Agarwal, A.K., Singh, A.P., and Maurya, R.K., "Evolution, challenges and path forward for low temperature combustion engines", Progress in Energy and Combustion Science 61 (2017) 1-56, <https://doi.org/10.1016/j.pecs.2017.02.001>.
106. Akihama, K., Takatori, Y., Inagaki, K., Sasaki, S. et al., "Mechanism of the Smokeless Rich Diesel Combustion by Reducing Temperature", SAE Technical Paper 2001-01-0655, 2001, <https://doi.org/10.4271/2001-01-0655>.
107. Zhao, H., Ladommatos, N., Abdelhalim, S.M., and Hu, Z., "The effects of carbon dioxide in exhaust gas recirculation on diesel engine emissions", Proceedings of the Institution of Mechanical Engineers, Part D: Journal of Automobile Engineering 212 (1998) 25-42, <https://doi.org/10.1243/0954407981525777>.
108. Hashizume, T., Miyamoto, T., Hisashi, A., and Tsujimura, K., "Combustion and Emission Characteristics of Multiple Stage Diesel Combustion", SAE Technical Paper 980505, 1998, <https://doi.org/10.4271/980505>.

109. Reveille, B., Kleemann, A., Knop, V., and Habchi, C., "Potential of Narrow Angle Direct Injection Diesel Engines for Clean Combustion: 3D CFD Analysis", SAE Technical Paper 2006-01-1365, 2006, <https://doi.org/10.4271/2006-01-1365>.
110. Kimura, S., Aoki, O., Ogawa, H., Muranaka, S., et al., "New Combustion Concept for Ultra-Clean and High-Efficiency Small DI Diesel Engines", SAE Technical Paper 1999-01-3681, 1999, <https://doi.org/10.4271/1999-01-3681>.
111. d'Ambrosio, S., and Ferrari, A., "Effect of exhaust gas recirculation in diesel engines featuring late PCCI type combustion strategies," *Energy Conversion and Management* 105 (2015) 1269-1280, <http://dx.doi.org/10.1016/j.enconman.2015.08.001>.
112. Kamimoto, T., and Bae, M., "High Combustion Temperature for the Reduction of Particulate in Diesel Engines", SAE Technical Paper 880423, <https://doi.org/10.4271/880423>.
113. Carlucci, A.P., Ficarella, A., and Laforgia, D., "Control of the combustion behaviour in a diesel engine using early injection and gas addition", *Applied Thermal Engineering* 26 (2006) 2279-2286, <https://doi.org/10.1016/j.applthermaleng.2006.03.016>.
114. Zhao, Y., Wang, Y., Li, D., Lei, X., et al., "Combustion and emission characteristics of a DME (dimethyl ether)-diesel dual fuel premixed charge compression ignition engine with EGR (exhaust gas recirculation)", *Energy* 72 (2014) 608-617, <https://doi.org/10.1016/j.energy.2014.05.086>.
115. Ying, W., Li, H., Longbao, Z., and Wei, L., "Effects of DME pilot quantity on the performance of a DME PCCI-DI engine", *Energy Conversion and Management* 51 (2010) 648-654, <https://doi.org/10.1016/j.enconman.2009.10.023>
116. Torregrosa, A.J., Broatch, A., Novella, R., and Mónico, L.F., "Suitability analysis of advanced diesel combustion concepts for emissions and noise control", *Energy* 36 (2011) 825-838, <https://doi.org/10.1016/j.energy.2010.12.032>.
117. Torregrosa, A.J., Broatch, A., García, A., and Mónico, L.F., "Sensitivity of combustion noise and NO_x and soot emissions to pilot injection in PCCI Diesel engines", *Applied Energy* 104 (2013) 149-157, <https://doi.org/10.1016/j.apenergy.2012.11.040>.
118. Han, D., Ickes, A.M., Bohac, S.V., Huang, Z., et al., "HC and CO emissions of premixed low-temperature combustion fueled by blends of diesel and gasoline", *Fuel* 99 (2012) 13-19, <https://doi.org/10.1016/j.fuel.2012.04.010>.
119. Cheng, X.B., Hu, Y.Y., Yan, F.Q., Chen, L., et al., "Investigation of the combustion and emission characteristics of partially premixed compression ignition in a heavy-duty diesel engine", *Proceedings of the Institution of Mechanical Engineers, Part D: Journal of Automotive Engineering* 228 (2014) 784-798, <https://doi.org/10.1177/0954407013513012>.
120. Abd-Alla, G.H., "Using exhaust gas recirculation in internal combustion engines: a review", *Energy Conversion and Management* 43 (2002) 1027-1042, [https://doi.org/10.1016/S0196-8904\(01\)00091-7](https://doi.org/10.1016/S0196-8904(01)00091-7).
121. Hong, K.S., Lee, K.S., Song, S., Chun, K.M., et al., "Parametric study on particle size and SOF effects on EGR cooler fouling", *Atmospheric Environment* 45 (2011) 5677-5683, <https://doi.org/10.1016/j.atmosenv.2011.07.036>.

122. Abarham, M., Zamankhan, P., Hoard, J.W., Styles, D., et al., "CFD analysis of particle transport in axi-symmetric tube flows under the influence of thermophoretic force", *International Journal of Heat and Mass Transfer* 61 (2013) 94-105, <https://doi.org/10.1016/j.ijheatmasstransfer.2013.01.071>.
123. Abd-Elhady, M.S., Malayeri, M.R., "Asymptotic characteristics of particulate deposit formation in exhaust gas recirculation (EGR) coolers," In *Applied Thermal Engineering*, Volume 60, Issues 1–2: 96-104, 2013, <https://doi.org/10.1016/j.applthermaleng.2013.06.038>.
124. Kim, H.M., Park, S.K., Choi, K.S. et al., "Investigation on the flow and heat transfer characteristic of diesel engine EGR cooler", *Int.J Automot. Technol* 9 (2008) 149–153, <https://doi.org/10.1007/s12239-008-0019-4>.
125. Hikosaka, N., "A View of the Future of Automotive Diesel Engines", SAE Technical Paper 972682, 1997, <https://doi.org/10.4271/972682>.
126. Yanagihara, H., "Compression-ignition type engine", U.S. Patent 6,182,632, February 6, 2001.
127. Coma, G., Gastaldi, P., Hardy, J. P., and Maroteaux, D., "HCCI combustion: dream or reality?," *Proceedings of the 13th Aachen Colloquium on Vehicle and engine technology*, 513–524, 2004.
128. Ishii, H., Koike, N., Suzuki, H., and Odaka, M., "Exhaust Purification of Diesel Engines by Homogeneous Charge with Compression Ignition Part 2: Analysis of Combustion Phenomena and NO_x Formation by Numerical Simulation with Experiment", SAE Technical Paper 970315, 1997, <https://doi.org/10.4271/970315>.
129. Pinchon, P., Walter, B., Réveill  , B., Miche, M., "New concepts for diesel combustion", *Proceedings of the Conference on thermo and fluid dynamic processes in diesel engines*, 395–414, September 9-12, 2004.
130. Catania, A., d'Ambrosio, S., Finesso, R., Spessa, E. et al., "Combustion System Optimization of a Low Compression-Ratio PCCI Diesel Engine for Light-Duty Application", *SAE Int. J. Engines* 2 (2009) 1314-1326, <https://doi.org/10.4271/2009-01-1464>.
131. Beatrice, C., Giacomo, N., and Guido, C., "Benefits and Drawbacks of Compression Ratio Reduction in PCCI Combustion Application in an Advanced LD Diesel Engine", *SAE Int. J. Engines* 2 (2009) 1290-1303, <https://doi.org/10.4271/2009-01-1447>.
132. Murata, Y., Kusaka, J., Daisho, Y., Kawano, D. et al., "Miller-PCCI Combustion in an HSDI Diesel Engine with VVT", *SAE Int. J. Engines* 1 (2009) 444-456, <https://doi.org/10.4271/2008-01-0644>.
133. Jain, A., Singh, A.P., and Agarwal, A.K., "Effect of split fuel injection and EGR on NO_x and PM emission reduction in a low temperature combustion (LTC) mode diesel engine", *Energy* 122 (2017) 249-264, <https://doi.org/10.1016/j.energy.2017.01.050>.
134. Lee, J., Chu, S., Cha, J., Choi, H., et al., "Effect of the diesel injection strategy on the combustion and emissions of propane/diesel dual fuel premixed charge compression ignition engines", *Energy* 93 (2015) 1041-1052, <https://doi.org/10.1016/j.energy.2015.09.032>.
135. Torregrosa, A.J., Broatch, A., Novella, R., Gomez-Soriano, J., et al., "Impact of gasoline and Diesel blends on combustion noise and pollutant emissions in Premixed Charge Compression Ignition engines", *Energy* 137 (2017) 58-68, <https://doi.org/10.1016/j.energy.2017.07.010>.

136. Srihari, S., Thirumalini, A., and Prashanth, K., “An experimental study on the performance and emission characteristics of PCCI-DI engine fuelled with diethyl ether-biodiesel-diesel blends”, *Renewable Energy* 107 (2017) 440-447, <https://doi.org/10.1016/j.renene.2017.01.015>.
137. Srihari, S., Thirumalini, S., “Investigation on reduction of emission in PCCI-DI engine with biofuel blends”, *Renewable Energy* 114 (2017) 1232-1237, <https://doi.org/10.1016/j.renene.2017.08.008>.
138. Mei, D., Yue, S., Zhao, X., Hielscher, K., et al., “Effects of center of heat release on combustion and emissions in a PCCI diesel engine fuelled by DMC-diesel blend”, *Applied Thermal Engineering* 114 (2017) 969-976, <https://doi.org/10.1016/j.applthermaleng.2016.12.064>.
139. Godiño, J.A.V., Aguilar, F.J.J-E., and García, M.T., “Simulation of HCCI combustion in air-cooled off-road engines fuelled with diesel and biodiesel”, *Journal of the Energy Institute* 91 (2018) 549-562, <https://doi.org/10.1016/j.joei.2017.04.002>.
140. Natarajan, S., Abhinav Shankar, S., and Meenakshi Sundareswaran, A.U., “Early Injected PCCI Engine Fuelled with Bio Ethanol and Diesel Blends – An Experimental Investigation”, *Energy Procedia* 105 (2017) 358-366, <https://doi.org/10.1016/j.egypro.2017.03.326>.
141. Singh, A.P., Jain, A., and Agarwal, A.K., “Fuel-Injection Strategy for PCCI Engine Fueled by Mineral Diesel and Biodiesel Blends”, *Energy Fuels* 31(2017) 8594-8607, <https://doi.org/10.1021/acs.energyfuels.6b03393>.
142. Lucchini, T., D’Errico, G., Onorati, A., Frassoldati, A. et al., “Modeling Non-Premixed Combustion Using Tabulated Kinetics and Different Flame Structure Assumptions”, *SAE Int. J. Engines* 10 (2017) 593-607, <https://doi.org/10.4271/2017-01-0556>.
143. Lucchini, T., D’Errico, G., Cerri, T., Onorati, A. et al., “Experimental Validation of Combustion Models for Diesel Engines Based on Tabulated Kinetics in a Wide Range of Operating Conditions”, *SAE Technical Paper* 2017-24-0029, 2017, <https://doi.org/10.4271/2017-24-0029>.
144. Lucchini, T., Della Torre, A., D’Errico, G., Onorati, A., “Modeling advanced combustion modes in compression ignition engines with tabulated kinetics”, *Applied Energy* 247 (2019) 537-548, <https://doi.org/10.1016/j.apenergy.2019.04.062>.
145. Brooks, T., Lumsden, G., and Blaxill, H., “Improving Base Engine Calibrations for Diesel Vehicles Through the Use of DoE and Optimization Techniques”, *SAE Technical Paper* 2005-01-3833, 2005, <https://doi.org/10.4271/2005-01-3833>.
146. Simpson, T.W., Poplinski, J.D., Koch, P.N., and Allen, J.K. “Metamodels for computer-based engineering design: survey and recommendations”, *Engineering with Computers* 17 (2001) 129–150, <https://doi.org/10.1007/PL00007198>.
147. Montgomery, D.C., “Design and Analysis of Experiments”, 5th Edition, Wiley, 2000.
148. Benajes, J., Novella, R., Pastor, J.M., Hernández-López, A., et al., “Optimization of the combustion system of a medium duty direct injection diesel engine by combining CFD modeling with experimental validation”, *Energy Conversion and Management* 110 (2016) 212-229, <https://doi.org/10.1016/j.enconman.2015.12.010>.
149. Dec, J.E., “A conceptual model of DI diesel combustion based on laser-sheet imaging”, *SAE Technical Paper* 970873, 1997, <https://doi.org/10.4271/970873>.

150. Kiplimo, R., Tomita, E., Kawahara, N., and Yokobe, S., "Effects of spray impingement, injection parameters, and EGR on the combustion and emission characteristics of a PCCI diesel engine", *Applied Thermal Engineering* 37 (2012) 165-175, <https://doi.org/10.1016/j.applthermaleng.2011.11.011>.
151. Hardy, W.L., and Reltz, R.D., "A study of the effects of high EGR, high equivalence ratio and mixing time on emissions levels in a heavy-duty diesel engine for PCCI combustion", SAE Technical Paper 2006-01-0026, 2006, <https://doi.org/10.4271/2006-01-0026>.
152. Ryan, T.W., Callahan, T.J., "Homogeneous Charge Compression Ignition of Diesel Fuel", SAE Technical Paper 961160, 1996, <https://doi.org/10.4271/961160>.
153. Imarisio, R., Peters, B., Rossi Sebastiano, G.M., Pinson, J., et al., "Diesel Strategies Towards Fuel Neutral European Emission Standards", International Symposium Diesel Engine: The NO_x & PM Emissions Challenge, ATA paper no.04A5010, 2004.
154. Asad, U., and Zheng, M., "Efficacy of EGR and boost in single-injection enabled low temperature combustion", *SAE Int. J. Engines* 2 (2009) 1085-1097, <https://doi.org/10.4271/2009-01-1126>.
155. Northrop, W., Bohac, S., Chin, J., and Assanis D., "Comparison of filter smoke number and elemental carbon mass from partially premixed low temperature combustion in a direct-injection diesel engine", *J. Eng. Gas Turbines Power* 133 (2011) 102804, <https://doi.org/10.1115/1.4002918>.
156. Box, G.E.P., and Cox, D.R., "An analysis of transformations", *Journal of the Royal Statistical Society. Series B (Methodological)* 26 (1964) 211–252.
157. European Commission, "Commission Regulation (EU) No 582/2011 of 25 May 2011 implementing and amending Regulation (EC) No 595/2009 of the European Parliament and of the Council with respect to emissions from heavy duty vehicles (Euro VI) and amending Annexes I and III to Directive 2007/46/EC of the European Parliament and of the Council Text with EEA relevance", *Official Journal of the European Union*, L 167/1, 25 June 2011,
158. Zheng, M., Reader, G. T, and Hawley, J. C., "Diesel engine exhaust gas recirculation - a review on advanced and novel concepts", *Energy Conversion and Management* 45 (2004) 883-900, [https://doi.org/10.1016/S0196-8904\(03\)00194-8](https://doi.org/10.1016/S0196-8904(03)00194-8).
159. Liu, B., Cheng, X., Liu, J., Pu, H. et al., "Combustion and Particulate Matter Emission Characteristics for Diesel Engine Run by Partially-Premixed Low-Temperature Combustion Mode", SAE Technical Paper 2017-01-2398, 2017, <https://doi.org/10.4271/2017-01-2398>.
160. Katare, S. and Laing, P., "Hydrogen in Diesel Exhaust: Effect on Diesel Oxidation Catalyst Flow Reactor Experiments and Model Predictions", *SAE Int. J. Fuels Lubr.* 2 (2009) 605-611, <https://doi.org/10.4271/2009-01-1268>.
161. Kuzuyama, H., Machida, M., Kawae, T., Tanaka, T. et al., "High Efficiency and Clean Diesel Combustion Concept using Double Premixed Combustion: D-SPIA", SAE Technical Paper 2012-01-0906, 2012, <https://doi.org/10.4271/2012-01-0906>.
162. Fuyuto, T., Taki, M., Ueda, R., Hattori, Y. et al., "Noise and Emissions Reduction by Second Injection in Diesel PCCI Combustion with Split Injection", *SAE Int. J. Engines* 7 (2014) 1900-1910, <https://doi.org/10.4271/2014-01-2676>.

163. Nishi, M., Ikeda, H., Iida, N., Kuzuyama, H. et al., "Numerical Assessment of Controlling the Interval between Two Heat-Release Peaks for Noise Reduction in Split-injection PCCI Combustion", SAE Technical Paper 2015-01-1851, 2015, <https://doi.org/10.4271/2015-01-1851>.
164. Willems, F., Doosje, E., Engels, F., and Seykens, X., "Cylinder Pressure-Based Control in Heavy-Duty EGR Diesel Engines Using a Virtual Heat Release and Emission Sensor", SAE Technical Paper 2010-01-0564, 2010, <https://doi.org/10.4271/2010-01-0564>.
165. Yu, S., Choi, H., Cho, S. et al., "Development of Engine Control Using the In-Cylinder Pressure Signal in a High Speed Direct Injection Diesel Engine", *Int.J. Automot. Technol.* 14 (2013) 175-182, <https://doi.org/10.1007/s12239-013-0019-x>.
166. Catania, A.E., Finesso, R., Spessa, E., "Predictive Zero-Dimensional Combustion Model for DI Diesel Engine Feed-Forward Control", *Energy Conversion and Management* 52 (2011) 3159-3175, <https://doi.org/10.1016/j.enconman.2011.05.003>.
167. Finesso, R., Spessa, E., Yang, Y., Alfieri, V. et al., "HRR and MFB50 Estimation in a Euro 6 Diesel Engine by Means of Control-Oriented Predictive Models", *SAE Int. J. Engines* 8 (2015) 1055-1068, <https://doi.org/10.4271/2015-01-0879>.
168. Baratta, M., Finesso, R., Misul, D., and Spessa, E., "Comparison between Internal and External EGR Performance on a Heavy Duty Diesel Engine by Means of a Refined 1D Fluid-Dynamic Engine Model", *SAE Int. J. Engines* 8 (2015) 1977-1992, <https://doi.org/10.4271/2015-24-2389>.
169. Dong, T., Liu, B., Zhang, F., Wang, Y., et al., "Control Oriented Modeling and Analysis of Gas Exchange and Combustion Processes for LTC Diesel Engine", *Applied Thermal Engineering* 110 (2017) 1305-1314, <https://doi.org/10.1016/j.applthermaleng.2016.09.001>.
170. Heywood, J.B., "Internal Combustion Engine Fundamentals", McGraw-Hill Education, 2018, ISBN: 12-601-1610-7.
171. Finesso, R., Marello, O., Misul, D., Spessa, E., et al., "Development and Assessment of Pressure-Based and Model-Based Techniques for the MFB50 Control in a Euro VI 3.0L HD Diesel Engine", SAE Technical Paper 2017-01-0794, 2017, <https://doi.org/10.4271/2017-01-0794>.
172. d'Ambrosio, S., Finesso, R. and Spessa, E., "Calculation Of Mass Emissions, Oxygen Mass Fraction And Thermal Capacity Of The Inducted Charge In SI And Diesel Engines From Exhaust And Intake Gas Analysis", *Fuel* 90 (2011) 152-166, <https://doi.org/10.1016/j.fuel.2010.08.025>.
173. Ladommatos N., Abdelhalim S., Zhao H., and Hu. Z., "Effects of EGR on Heat Release in Diesel Combustion", SAE Technical Paper 980184, 1998, <https://doi.org/10.4271/980184>.
174. Maiboom, A., Tauzia, X., Hétet, J.F., "Experimental study of various effects of exhaust gas recirculation (EGR) on combustion and emissions of an automotive direct injection diesel engine", *Energy* 33 (2008) 22-34, <https://doi.org/10.1016/j.energy.2007.08.010>.
175. Agarwal, D., Singh, S.K., and Agarwal, A.K., "Effect of Exhaust Gas Recirculation (EGR) on performance, emissions, deposits and durability of a constant speed compression ignition engine", *Applied Energy* 88 (2011) 2900-2907, <https://doi.org/10.1016/j.apenergy.2011.01.066>.

176. Maiboom, A., Tauzia, X., Hétet, J.F., “Influence of EGR unequal distribution from cylinder to cylinder on NO_x-PM trade-off of a HSDI automotive Diesel engine”, *Applied Thermal Engineering* 29 (2009) 2043-2050, <https://doi.org/10.1016/j.applthermaleng.2008.10.017>.
177. Sakowitz, A., Reifarth, S., Mihaescu, M., and Fuchs, L., “Modeling of EGR Mixing in an Engine Intake Manifold using LES”, *Oil & gas science and technology* 69 (2014) 167-176, <https://doi.org/10.2516/ogst/2013118>.
178. Griffin, J., Ganseman, C., Baerts, C., Burkholder, N. et al., “Cooled EGR Rate Measurement with a Thermal Anemometer for EPA02 Heavy Duty Diesel Engine Emission Control”, SAE Technical Paper 2003-01-0263, 2003, <https://doi.org/10.4271/2003-01-0263>.
179. Wahlström J., and Eriksson L., “Modelling diesel engines with a variable geometry turbocharger and exhaust gas recirculation by optimization of model parameters for capturing non-linear system dynamics”, *Proceedings of the Institution of Mechanical Engineers Part D Journal of Automobile Engineering* 255 (2011) 960-986, <https://doi.org/10.1177/0954407011398177>.
180. Castillo, F., Witrant, E., Talon, V., and Dugard, L., “Simultaneous Air Fraction and Low-Pressure EGR Mass Flow Rate Estimation for Diesel Engines”, *IFAC Proceedings Volumes, Volume 46, Issue 2, 2013, Pages 731-736*, <https://doi.org/10.3182/20130204-3-FR-2033.00070>.
181. Diop, S., Moraal, P.E., Kolmanovsky, I.V., and Van Nieuwstadt M., “Intake oxygen concentration estimation for DI diesel engines”, *Proceedings of the 1999 IEEE International Conference on Control Applications* 1 (1999) 852-857, <https://doi.org/10.1109/CCA.1999.807777>.
182. Guardiola, C., Gil, A., Pla, B., and Piqueras, P., “Representation limits of mean value engine models”, *Lecture notes in control and information sciences* 418 (2012) 185–206, 2012, https://doi.org/10.1007/978-1-4471-2221-0_11.
183. Yang, Z., Winward, E., O'Brien, G., Stobart, R. et al., “Modelling the Exhaust Gas Recirculation Mass Flow Rate in modern Diesel Engines”, SAE Technical Paper 2016-01-0550, 2016, <https://doi.org/10.4271/2016-01-0550>.
184. d’Ambrosio, S., Ferrari, A., and Spessa, E., “Analysis of the Exhaust Gas Recirculation System Performance in Modern Diesel Engines”, *J. Eng. Gas Turbines Power* 135 (2013) 081601, <https://doi.org/10.1115/1.4024089>.
185. Goodman, A.W. and Goodman, G., “Generalizations of the Theorems of Pappus”, *The American Mathematical Monthly* 76 (1969) 355-366, <https://doi.org/10.2307/2316426>.
186. Nakayama, S., Fukuma, T., Matsunaga, A., Miyake, T. et al., “A New Dynamic Combustion Control Method Based on Charge Oxygen Concentration for Diesel Engines,” SAE Technical Paper 2003-01-3181, 2003, <https://doi.org/10.4271/2003-01-3181>.
187. Vassallo, A., “Experimental EGR rate and unbalance evaluation”, GM internal report, 2010.
188. European Automobile Manufacturers Association (ACEA), “ACEA Position Paper: Reducing CO₂ Emissions from Heavy-Duty Vehicles”, January 2016.
189. Delgado, O., and Muncrief, R., “New Study on Technology Potential for EU TractorTrailers”, Presentation at Road to Efficiency Workshop, Brussels, June 2016.

190. SAE Truck And Bus Tire Pressure Management Systems Committee, "Tire Pressure Systems – Management (CTIS) Type for Medium and Heavy Duty Highway Vehicles", SAE Standard J2848/3, 13 Feb. 2012.
191. Turek, T.J., "Tire inflation control system.", U.S. Patent No. 2,634,783. 14 Apr. 1953.
192. Schultz, G. R., "Wheel end valve for central tire inflation system", U.S. Patent No. 4,678,017. 7 Jul. 1987.
193. Braun, E.R., and Schultz, G.R., "Tire valve assembly for central tire inflation system", U.S. Patent No. 4,754,792. 5 Jul. 1988.
194. Medley, M.A. and Miler, D.P., "Central Tire Inflation Wheel Assembly and Valve". U.S. Patent No 2013/0276902 A1. 24 Oct., 2013
195. Schultz, G.R., and Ruzicka, L. M., "Adaptive inflation control for vehicle central tire inflation system", U.S. No. 5,180,456. 19 Jan. 1993.
196. Scholer, R.A., "Tire inflation system", U.S. Patent No. 4,763,709. 16 Aug. 1988.
197. Goodell, F.L., "Automatic control for central tire inflation system", U.S. Patent No. 5,327,346. 5 Jul. 1994.
198. Meydiou, M., and Battochio, C., "Inflation circuit, in particular for a tire mounted on a wheel, and corresponding wheel", U.S. Patent No. 7,367,371 B2. 6 May 2008.
199. Braun, E.R., and Schultz, G.R., "Central tire inflation system", U.S. Patent No. 4,640,331. 3 Feb. 1987.
200. Hurrell, G.L.II, "Vehicle tire pressure management system with easily removed wheel and tire", U.S. Patent No. 5,221,381. 22 Jun. 1993.
201. Genna, R.A., "Automatic tire pressure control system for a vehicle", U.S. Patent No. 5,587,698. 24 Dec. 1996.
202. Stech, C.G., "Axle to axle sealed airway for an onboard automatic tire inflation system", U.S. Patent No. 8,869,850 B2. Oct. 2014.
203. Colby, J., "Revolutionary Developments in Wheeled Military Vehicles", SAE Technical Paper 490193, 1949, <https://doi.org/10.4271/490193>.
204. Keller, R., "Operational Testing of Central Tire Inflation Systems Proves the Benefits of Low Tire Pressure in Logging Operations", SAE Technical Paper 933056, 1993, <https://doi.org/10.4271/933056>.
205. Mahoney, J., Sweet, B., Copstead, R., and Keller, R., "The Potential Use of Central Tire Inflation During Highway Load Restriction Periods", SAE Technical Paper 942245, 1994, <https://doi.org/10.4271/942245>.
206. Verhoff, D. and Mittal, C., "Central Tire Inflation Systems: The Basics of How the Systems Function and Installation/Operational Issues", SAE Technical Paper 942252, 1994, <https://doi.org/10.4271/942252>.
207. Freigang, A., "Application of the Eaton® Tire Pressure Control System to the Commercial Truck", SAE Technical Paper 942248, 1994, <https://doi.org/10.4271/942248>.
208. Besselink, I.J.M., Schmeitz, A.J.C. and Pacejka, H.B., "An improved Magic Formula/Swift tire model that can handle inflation pressure changes", Vehicle System Dynamics 48 (2010) 337-352, <https://doi.org/10.1080/00423111003748088>.

209. Collier, B. and Warchol, J., “The Effect of Inflation Pressure on Bias, Bias-Belted and Radial Tire Performance”, SAE Technical Paper 800087, 1980, <https://doi.org/10.4271/800087>.
210. Millar, P., Woodward, D., Friel, S. and Woodside, A., “An investigation of the variation of contact area with inflation pressure”, 5th International Conference Bituminous Mixtures and Pavements, 2011.
211. Australian Government, Department of Resources, Energy and Tourism, “Fuel for thought. Identifying potential energy savings in the Australian road and rail sector”, February 2012.
212. U.S. Department of Transportation – Federal Motor Carrier Safety Administration, “Advanced Sensors and Applications: Commercial Motor Vehicle Tire Pressure Monitoring and Maintenance”, February 2014.
213. Ogunwemino A.A., “Economic Analysis of Continuous Monitoring of Commercial Truck Tire Pressure Using Tire Pressure Monitoring Systems (TPMS) and RFID Technologies”, University of Nebraska – Lincoln, Dec. 2011.
214. Augsburg, K., Ivanov, V.; Kruchkova, K., Höpping, K. et al., “Project Adtyre: towards dynamic tyre inflation control”, Proceedings of the FISITA 2012 World Automotive Congress. Lecture notes in Electrical Engineering 198 (2013) 185-198, https://doi.org/10.1007/978-3-642-33795-6_16.
215. Höpping, K. and Augsburg, K., “Dynamic tire pressure control system - analysis of the effect to longitudinal vehicle dynamics and fuel consumption”, Shaping the future by engineering: 58th IWK, Ilmenau Scientific Colloquium, Ilmenau, Germany, September 8-12, 2014.
216. Seymour, S., and Pivonka, D., “Active Tire Controller Device”, U.S. Patent No. 2012/0221196 A1. 30 Aug. 2012.
217. U.S. Department of Transportation – Federal Motor Carrier Safety Administration, “Fleet Study of Brake Performance and Tire Pressure Sensors”, July 2009.
218. Technavio Research, “Global Automotive Automatic Tire Inflation System Market - Drivers and Forecast 2017-2021”, 2017.
219. Taghavifar, H., and Mardani, A., “Investigating the effect of velocity, inflation pressure, and vertical load on rolling resistance of a radial ply tire”, Journal of Terramechanics 50 (2013) 99-106, <https://doi.org/10.1016/j.tterra.2013.01.005>.
220. Genta, G., and Morello, L., “The Automotive Chassis. Volume 1: Components Design”, Springer, 2009.
221. Hoever, C., and Kropp, W., “A model for investigating the influence of road surface texture and tyre tread pattern on rolling resistance”, Journal of Sound and Vibration 351 (2015) 161-176, <https://doi.org/10.1016/j.jsv.2015.04.009>.
222. Grappe, F., Candau, R., Barbier, B., et al., “Influence of tyre pressure and vertical load on coefficient of rolling resistance and simulated cycling performance”, Ergonomics 10 (1999) 1361-1371, <https://doi.org/10.1080/001401399185009>.
223. Calwell, C., Ton, M., Gordon, D., et al., “California state fuel-efficient tire report: Volume II”, California Energy Commission, January 2003.
224. Pneumatici sotto controllo, “Resistenza al rotolamento”, www.pneumaticisottocontrollo.it/resistenzaRotolamento.html 2012, accessed December 2014.
225. Thomson, R. W., “Improvement in Carriage-Wheels”, U.S. Patent No. 5,104. 8 May 1847.
226. Wolff, F. O., “Pressure Indicator for Pneumatic Tires”, U.S. Patent No. 905,778. 1 Dec. 1908.

227. ISO 18164:2005, "Passenger car, truck, bus and motorcycle tyres - Methods of measuring rolling resistance".
228. Paroue, L., "Pressure-Indicating Device", U.S. Patent No. 1,183,486. 16 May 1916.
229. Dare, S.G., "Tire Deflating Indicator", U.S. Patent No. 1,208,508. 12 Dec. 1916.
230. Vignotto, A., Savarese, C., Le Reun, P., and Nicastri, F., "Hub-bearing assembly allowing pressurized air to be supplied to the tire of a motor vehicle wheel", U.S. Patent No. 7,488,046 B2. 10 Feb. 2009.
231. Krisher, J. A., "Tire inflation system for live spindle wheel end", U.S. Patent No. 6,283,186 B1. 4 Sep. 2001.
232. Wang, J., Marsaly, O. and Rogers, L., "Vehicle wheel assembly with a hollow stud and internal passageways connected to a CTIS", U.S. Patent No. 7,168,468 B2. 30 Jan, 2007.
233. Tarasinski, N., Sobotzik, J., Kneer, B. and Glaser, F., "Tyre pressure regulating system", U.S. Patent No. 2007/0144171. 28 Jun, 2007.
234. SAE Recommended Practice, "Road Load Measurement Using Onboard Anemometry and Coastdown Techniques", SAE Standard J2263, Rev. Dec. 2008.
235. US Environmental Protection Agency, "Data on Cars used for Testing Fuel Economy. 2017 Test Car List Data", <https://www.epa.gov/compliance-and-fuel-economy-data/data-cars-used-testing-fuel-economy>, accessed Oct. 2017.
236. Borgarello, L., Galliera, E., Avanzo, A., and Fagianò, A., "Roller bench urban cycles identification for light commercial vehicles fuel consumption", Italian Journal of Applied Statistics 22 (2010) 353-362.
237. Piu, A., Galliera, E., Petrolo, D., Pettiti, M., et al., "Fiat Group methods for fuel consumption: SW PerFECTS", 11th Stuttgart International Symposium on Automotive and Engine Technology, Stuttgart, Germany, February 22-23, 2011.
238. Ricci, C., Storer, D., Berzi, L., "ASTERICS - 314157 D1.1 – Definition of State of the Art and possible update by the new methods development", Report of the European project ASTERICS, 2013, http://www.asterics-project.eu/userdata/file/Public%20deliverables/ASTERICS-D1.1-Definition-of-State-of-the-Art_UNIFI_M10_FINAL.pdf, accessed July 2019.
239. Sina, N., Nasiri, S. and Karkhaneh, V., "Effects of resistive loads and tire inflation pressure on tire power losses and CO₂ emissions in real-world conditions", Applied Energy 157 (2015) 974-983, <https://doi.org/10.1016/j.apenergy.2015.04.010>.
240. Brusarosco, M., Mancosu, F., Arosio, D., "Method and system for determining a tyre load during the running of a motor vehicle", U.S. Patent No. US 8,874,386 B2. 28 Oct. 2014.
241. Chaklader, A.C.D., "Vehicle weight and cargo load determination using tire pressure", U.S. Patent No. US 6,449,582 B1, 10 Sept. 2002.
242. Keller, L., Griesser, M., Köbe, A., Säger, P., "Method for determining the load exerted on a vehicle tire", U.S. Patent No. US 7,013,721 B2. 21 Mar. 2006.
243. Elliott, J.A., Fulmer, B.T., "Method for determining axle load of a moving vehicle", U.S. Patent No. US 6,688,168 B1. 10 Feb. 2004.
244. Katou, M., "Vehicle load weight detecting apparatus", U.S. Patent No. US 8,096,174 B2. 17 Jan. 2012.

245. Singh, K.B., Fenkanyn, J.M., Patel, A., et. al., “Vehicle tire load estimation”, European Patent EP 2,722,202 A1. 23 Apr. 2014.
246. Vitolo, R., d'Ambrosio, S., Vigna, L.F., et al., “Apparatus and method for estimating loading conditions of tires”, Italian Patent application 102018000005764, May 28th, 2018.
247. Mallet, E., “Tire contribution to CO₂ emissions”, 1st SAE Torino Conference on CO₂ Reduction for Transportation Systems, 2016.
248. De Gennaro, M., Paffumi, E., Martini, G., and Scholz, H., “A pilot study to address the travel behaviour and the usability of electric vehicles in two Italian provinces”, Case Studies on Transport Policy 2 (2014) 116-141, <https://doi.org/10.1016/j.cstp.2014.07.008>.
249. JRC – Joint Research Center, 2015, “Individual mobility: From conventional to electric cars”, 2015.
250. European Automobile Manufacturers Association (ACEA), “Fact sheet: Cars”, <http://www.acea.be/publications/article/fact-sheet-cars>, accessed August 2017.
251. Vitolo, R., d'Ambrosio, S., Salamone, N., et al., “On-board centralized system for regulating the pressure of tyres of a motor vehicle”, Patent Application WO 2017/089915 A1. 24 Nov. 2015.
252. EPA - United States Environmental Protection Agency, “Social Cost of Carbon. EPA Fact Sheet”, https://www.epa.gov/sites/production/files/2016-12/documents/social_cost_of_carbon_fact_sheet.pdf, accessed Oct 2016.
253. IPCC, “Summary for Policymakers. In: Climate Change 2014: Mitigation of Climate Change. Contribution of Working Group III to the Fifth Assessment Report of the Intergovernmental Panel on Climate Change”, 2014.
254. European Environment Agency, “Transport fuel prices and taxes”, <https://www.eea.europa.eu/data-and-maps/indicators/fuel-prices-and-taxes/assessment-6>, accessed September 2017.
255. TUV, “Final Report. Survey on motor vehicle tyres & related aspects (ENTR/02/045), Commissioned by The European Commission Enterprise Directorate General. 2003.
256. Michelin, “Limited mileage warranties”, http://www.michelinman.com/content/dam/master/Michelin/pdf/limited_mileage_warranties.pdf, 2013, accessed August 2017.
257. European Commission Directorate General Energy and Transport, “Framework Contract TREN/A1/56-2004, Lot 2: Economic assistance activities, Final Report. Cost-benefit assessment and prioritization of vehicle safety technologies (ref. TREN-ECON2-002)”, 2006.
258. European Automobile Manufacturers Association (ACEA), “Commercial Vehicles and CO₂”, http://www.acea.be/uploads/publications/20101013_Commercial_Vehicles_CO2.pdf, accessed Oct. 2017.
259. IPCC, “Climate Change 2014: Synthesis Report. Contribution of Working Groups I, II and III to the Fifth Assessment Report of the Intergovernmental Panel on Climate Change”, 2015, ISBN 978-92-9169-143-2.
260. DieselNet, “Engine Exhaust Back Pressure”, https://www.dieselnet.com/tech/diesel_exh_pres.php#emi, accessed Oct. 2017.
261. DieselNet, “Emission Standards; United States; Heavy-Duty Vehicles: GHG Emissions & Fuel Economy”, https://www.dieselnet.com/standards/us/fe_hd.php, accessed Oct. 2017.
262. European Commission, “European Commission; Climate Action; EU Action; Reducing emissions from transport; Road transport: Reducing CO₂ emissions from vehicles; Reducing CO₂ emissions

- from Heavy-Duty Vehicles”, https://ec.europa.eu/clima/policies/transport/vehicles/heavy_en, accessed Oct. 2017.
263. CONVENIENT, “Complete Vehicle ENergy-saving Technologies”, <http://www.convenient-project.eu>, accessed Oct. 2017.
 264. DieselNet, “Emission Standards; United States; Cars: GHG Emissions & Fuel Economy”, https://www.dieselnets.com/standards/us/fe_ghg.php, accessed Oct. 2017.
 265. Goodyear, “Radial Truck Tire And Retread Service Manual”, 2002.
 266. Michelin, “Technical Information. Michelin: Truck and Bus Tyres”, Edition 24.
 267. Guillou, M., and Bradley, C., “Fuel Consumption Testing to Verify the Effect of Tire Rolling Resistance on Fuel Economy”, SAE Technical Paper 2010-01-0763, 2010, <https://doi.org/10.4271/2010-01-0763>.
 268. Janssen, M., and Hall, G., “Effect of Ambient Temperature on Radial Tire Rolling Resistance”, SAE Technical Paper 800090, 1980, <https://doi.org/10.4271/800090>.
 269. Franco V., Delgado O., and Muncrief R., “Heavy-duty vehicle fuel-efficiency simulation: A comparison of US and EU tools”, The International Council on Clean Transportation, 2015, http://www.theicct.org/sites/default/files/publications/ICCT_GEM-VECTO-comparison_20150511.pdf, accessed Oct. 2017.
 270. ETRTO Standards Manual, 2008.
 271. Michelin, “Truck Tire Operator’s Manual and Limited Warranty”, https://www.michelintruck.com/assets/pdf/MLN_Truck_Tire_Warranty.pdf, 2011, accessed Oct. 2017.
 272. Ministero delle infrastrutture e dei trasporti, “Autotrasporto merci conto di terzi, valori indicativi di riferimento dei costi di esercizio dell’impresa”, <http://www.mit.gov.it/documentazione/autotrasporto-merci-conto-di-terzi-valori-indicativi-di-riferimento-dei-costi-di>, accessed Oct. 2017.
 273. ISO 6358-1:2013(E), “Pneumatic fluid power – Determination of flow-rate characteristics of components using compressible fluids – Part 1: General rules and test methods for steady-state flow”.
 274. Vitolo, R., d’Ambrosio, S., Salamone, N., et al., “On-board centralized system for regulating the pressure of tyres of a motor vehicle”, Patent application WO2017/089916 A1. 24 Nov. 2015.
 275. Vitolo, R., d’Ambrosio, S., De Mattei, E., “Apparatus and method for computing tire pressures”, Italian Patent application 102017000128722. November 10th, 2017.
 276. Salamone N., “PoliTO – Iveco Contract: ACTIS performance on HDV and LDV. Study of the system layout: simulation of the performance on proposed configurations for HCV”, internal report, November 6th, 2018
 277. Salamone N., Vitolo R., “PoliTO – Iveco Contract: ACTIS performance on HDV and LDV. Integration of the system on board: Description of the proposed solution for the steering axle of a HCV”, internal report, September 28th, 2018.
 278. Salamone N., “PoliTO – Iveco Contract: ACTIS performance on HDV and LDV. Integration of the system on board: Description of the proposed solution for a LCV: wheel assembly”, internal report, January 7th, 2019.

279. Giakoumis, E.G., and Alafouzos, A.I., “Study of diesel engine performance and emissions during a Transient Cycle applying an engine mapping-based methodology”, *Applied Energy* 87 (2010) 1358–1365, <https://doi.org/10.1016/j.apenergy.2009.09.003>.
280. Pelkmans, L., Debal, P., Hood, T., Hauser, G. et al., “Development of a Simulation Tool to Calculate Fuel Consumption and Emissions of Vehicles Operating in Dynamic Conditions”, SAE Technical Paper 2004-01-1873, 2004, <https://doi.org/10.4271/2004-01-1873>.
281. Gao, Z., Conklin, J.C., Daw, C.S. and Chakravarthy, V.K., “A proposed methodology for estimating transient engine-out temperature and emissions from steadystate maps”, *International Journal of Engine Research* 11 (2010) 137-151, <https://doi.org/10.1243/14680874JER05609>.
282. Asthana, S., Bansal, S., Jaggi, S., and Kumar, N., “A Comparative Study of Recent Advancements in the Field of Variable Compression Ratio Engine Technology”, SAE Technical Paper 2016-01-0669, 2016, <https://doi.org/10.4271/2016-01-0669>.
283. Christensen, M., Hultqvist, A., and Johansson, B., “Demonstrating the Multi Fuel Capability of a Homogeneous Charge Compression Ignition Engine with Variable Compression Ratio”, SAE Technical Paper 1999-01-3679, 1999, <https://doi.org/10.4271/1999-01-3679>.
284. Haraldsson, G., Tunestål, P., Johansson, B., and Hyvönen, J., “HCCI Combustion Phasing with Closed-Loop Combustion Control Using Variable Compression Ratio in a Multi Cylinder Engine”, SAE Technical Paper 2003-01-1830, 2003, <https://doi.org/10.4271/2003-01-1830>.
285. Helmantel, A., Gustavsson, J., and Denbratt, I., “Operation of a DI Diesel Engine With Variable Effective Compression Ratio in HCCI and Conventional Diesel Mode”, SAE Technical Paper 2005-01-0177, 2005, <https://doi.org/10.4271/2005-01-0177>.
286. Nevin, R., Sun, Y., Gonzalez D., M., and Reitz, R., “PCCI Investigation Using Variable Intake Valve Closing in a Heavy Duty Diesel Engine”, SAE Technical Paper 2007-01-0903, 2007, <https://doi.org/10.4271/2007-01-0903>.
287. Christmann, R., Schmalzl, HP., Schmitt, F. et al., “Regulated 2-stage turbocharging for passenger car and commercial vehicle engines”, *MTZ Worldw* 66 (2005) 6-9, <https://doi.org/10.1007/BF03227726>
288. Buchwald, R., Lautrich, G., Maiwald, O., and Sommer, A., “Boost and EGR System for the Highly Premixed Diesel Combustion”, SAE Technical Paper 2006-01-0204, 2006, <https://doi.org/10.4271/2006-01-0204>.
289. Herreros, J.M., Gill, S.S., Lefort, I., Tsolakis, A. et al., “Enhancing the low temperature oxidation performance over a Pt and a Pt–Pd diesel oxidation catalyst”, *Applied Catalysis B: Environmental* 147 (2014) 835– 841, <https://doi.org/10.1016/j.apcatb.2013.10.013>.
290. Maunula, T., Suopanki, A., Torkkell, K., and Härkönen, M., “The Optimization of Light-duty Diesel Oxidation Catalysts for Preturbo, Closed-coupled and Underfloor Positions”, SAE Technical Paper 2004-01-3021, 2004, <https://doi.org/10.4271/2004-01-3021>.
291. Kim, C., Paratore, M., Gonze, E., Solbrig, C. et al., “Electrically Heated Catalysts for Cold-Start Emissions in Diesel Aftertreatment”, SAE Technical Paper 2012-01-1092, 2012, <https://doi.org/10.4271/2012-01-1092>.
292. Stadlbauer, S., Waschl, H., Schilling, A., and del Re, L., “DOC Temperature Control for Low Temperature Operating Ranges with Post and Main Injection Actuation”, SAE Technical Paper 2013-01-1580, 2013, <https://doi.org/10.4271/2013-01-1580>.

293. Neely, G., Sarlashkar, J., and Mehta, D., “Diesel Cold-Start Emission Control Research for 2015-2025 LEV III Emissions”, SAE Int. J. Engines 6 (2013) 1009-1020, <https://doi.org/10.4271/2013-01-1301>.
294. Automobile.it, “Scopri cos’è e a cosa serve AdBlue, il nuovo additivo per i diesel”, <https://www.automobile.it/magazine/come-funziona/adblue-5348>, accessed March 2018.

Abbreviations and Acronyms

ABS	Antilock Braking System
ACEA	Association des Constructeurs Européens d'Automobiles (European Automobile Manufacturers' Association)
ACTIS	Advanced Central Tire Inflation System
AFM	Accumulated Fuel Mass
ATPC	Active Tire Pressure Control
ATS	After Treatment System
bmep	brake mean effective pressure
bsfc	brake specific fuel consumption
CA	Crank Angle
CAD	Computer Aided Design
CAFE	Corporate Average Fuel Economy
CARB	California Air Resources Board
CDC	Conventional Diesel Combustion
CFD	Computational Fluid Dynamics
CLD	Chemiluminescence Detector
CN	Combustion Noise
CoV	Coefficient of Variation
CR	Compression Ratio
CTIS	Central Tire Inflation System
DI	Direct Injection
DOC	Diesel Oxidation Catalyst
DoE	Design of Experiments
DPF	Diesel Particulate Filter
ECU	Electronic Control Unit
EGR	Exhaust Gas Recirculation
EHC	Electrically Heated Catalyst
EMEA	Europe, Middle East, and Africa
EPA	Environmental Protection Agency
EU	European Union
FCA	Fiat Chrysler Automobiles
FPT	Fiat Powertrain Technologies

FSN	Filter Smoke Number
FTP	Federal Test Procedure
GDI	Gasoline Direct Injection
GDP	Gross Domestic Product
GHG	Green-House Gases
HCCI	Homogeneous Charge Compression Ignition
HDV	Heavy-Duty (commercial) Vehicle
HWFET	Highway Fuel Economy Test
ICCT	International Council on Clean Transportation
ICE	Internal Combustion Engine
ID	Ignition Delay
IFP	Institut Français Du Pétrole
imep	indicated mean effective pressure
JRC	Joint Research Center
LDV	Light-Duty (commercial) Vehicle
LNT	Lean-NO _x Trap
LTC	Low Temperature Combustion
MFB	Mass Fraction Burned
NDIR	Non Dispersive Infra-Red
NEDC	New European Driving Cycle
NHTSA	National Highway Traffic and Security Agency
NSC	NO _x Storage Catalyst
OEM	Original Equipment Manufacturer
OFAT	One-Factor-at-A-Time
PAH	Polycyclic Aromatic Hydrocarbons
PCCI	Premixed Charge Compression Ignition
PEMS	Portable Emission Measurement Systems
PerFECTS	Performance and Fuel Economy for Cars and Trucks Simulation
PFP	Peak Firing Pressure
PM	Particle Matter
PN	Particle Number
RCCI	Rate-Controlled Compression Ignition
RDE	Real Driving Emissions
RMSE	Root Mean Square Error
RP	Rapid Prototyping

RSM	Response Surface Metodology
SCC	Social Cost of Carbon
SCR	Selective Catalytic Reduction
SOC	Start of Combustion
SOF	Solubile Organic Fraction
SOI	Start of Injection
TCO	Total Cost of Ownership
TDC	Top Dead Center
TPMS	Tire Pressure Monitoring System
TyPE	Tyre Pressure Effect
UNFCCC	United Nations Framework Convention on Climate Change
VCR	Variable Compression Ratio
VGT	Variable Geometry Turbocharger
VVT	Variable Valve Timing
WHSC	Worldwide Harmonized Stationary Cycle
WHTC	Worldwide Harmonized Transient Cycle
WLTC	Worldwide Light-Duty Test Cycle
WLTP	Worldwide Light-Duty Test Procedure